1000 times closer to a continuous atom laser

Steady-state strontium with unity phase-space density

Bennetts, S.P.

1000 times closer to a continuous atom laser:

Steady-state strontium with unity phase-space density

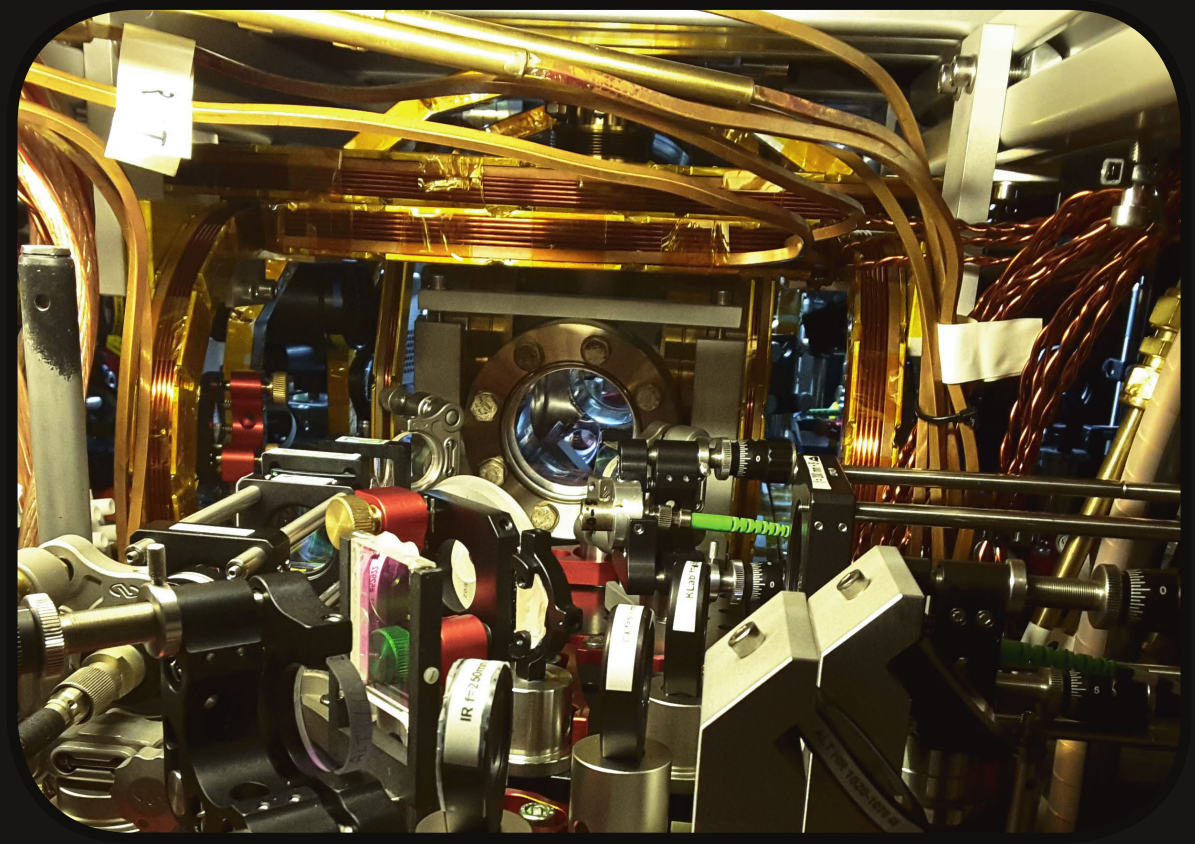

Shayne Bennetts

1000 times closer to a continuous atom laser:

Steady-state strontium with unity phase-space density

ACADEMISCH PROEFSCHRIFT

ter verkrijging van de graad van doctor
aan de Universiteit van Amsterdam
op gezag van de Rector Magnificus
prof. dr. ir. K. I. J. Maex
ten overstaan van een door het College voor Promoties ingestelde
commissie, in het openbaar te verdedigen in de Agnietenkapel
op vrijdag 25 oktober 2019, te 14:00 uur

door

Shayne Peter Bennetts

geboren te Darwin

Promotiecommissie

Promotor	prof. dr.	F. E. Schreck	Universiteit van Amsterdam
Co-promotor	dr.	B. B. Pasquiou	Universiteit van Amsterdam
Overige leden	dr.	S. Blatt	Ludwig-Maximilians-Universität
	prof. dr.	D. Guéry-Odelin	Université Paul Sabatier
	prof. dr.	F. Koenderink	Universiteit van Amsterdam
	prof. dr.	H. B. van Linden van den Heuvell	Universiteit van Amsterdam
	dr.	R. J. C. Spreeuw	Universiteit van Amsterdam

Faculteit der Natuurwetenschappen, Wiskunde en Informatica (FNWI)

The research reported in this thesis was primarily funded by the NWO through Vici grant No. 680-47-619 and mostly carried out at the Van der Waals-Zeeman Institute, Institute of Physics, University of Amsterdam.

Significant additional support was obtained through the European Quantum Technologies Flagship iqClock project (www.iqclock.eu) funded by the European Union's Horizon 2020 research and innovation programme under grant agreement No 820404, the European Research Council (ERC) under Project No. 615117 QuantStro, the NWO through Veni grant No. 680-47-438, the Australian Government through an Australian Postgraduate Award and the Ministry of Education of the Republic of China (Taiwan) through an MOE Technologies Incubation Scholarship. Early parts of this work was carried out at the Department of Quantum Science, Research School of Physical Sciences and Engineering at the Australian National University.

Summary

Since antiquity, humanity has strived for ever greater control of the world around us. In 1960 we first demonstrated ultimate control over light in the form of the first laser and a year later a steady-state laser made this control eternal. It took another 35 years to extend this to matter. With the first achievement of a pure Bose-Einstein Condensate (BEC) in 1995 we realised for the first time a pure quantum mechanical state of matter and shortly after, a matter-wave laser. This new ability to control matter sparked the revolution in ultracold physics that we see today with applications ranging from time standards to quantum simulation to quantum information and sensing. But 25 years on, these states remain fleeting. They survive at most a few minutes before they dissipate and are lost from our world. Yet the physics says there should be a way to provide stimulated gain, to replenish losses, to make these states eternal. The goal of our research is to try to realise this, to make a steady-state BEC, and with it, a steady-state matter-wave laser.

To make a BEC you first need to laser cool a sample of atoms as cold as possible, then you turn off all resonant light and finally you evaporatively cool them to reach degeneracy. The incorporation of these two incompatible steps, laser cooling and evaporation, is what made BEC possible in a practical sense, but it also made it very hard to make a steady-state system. In 2012 our group demonstrated a "cloak of invisibility" for a BEC. Using Stark shifts, a BEC was made transparent, showing it is possible for a BEC to coexist and form in the presence of small intensities of resonant cooling light. With this in hand we set about trying to make the first steady-state BEC.

The measure of how close you are to forming a BEC is the phase-space density (PSD). This describes how cold and dense your sample is. For values above 2.6 a BEC can form. When we started, the highest steady-state phase-space density demonstrated was a sample of one hundred thousand chromium atoms with a PSD of 0.0004. We now have a PSD around 1, just a heartbeat away from the critical value of 2.6. But this thesis is about much more than just one number.

This thesis will describe, the Strontium Continuous Atom Laser (SrCAL) machine that we built and the many lessons we learned. The path to a steady-state BEC is uncharted. To navigate us there we designed and built a unique and flexible strontium quantum gas machine, a machine designed from the beginning to be a steady-state device. Few non-alkali

quantum gas machines have ever been built and only a handful of them are for strontium, so making a new quantum gas machine is always a challenge. Learning how to build such a machine is not something you will learn in class, or from the literature. The best resources we have are the theses of those who came before us so an important part of this thesis is to document some of that hard won knowledge, to aid future builders in the construction of both pulsed and steady-state degenerate gas machines. I also describe the technical detail needed for future users of SrCAL to wield this tool with mastery.

The result was a unique ability to make steady-state ultracold gases. Using a steady-state magneto-optical trap (MOT) on the narrow 7.4 kHz red transition we achieved a phase space density of 1×10^{-3}. This improved the state of the art phase-space density for steady-state MOTs by more than two orders of magnitude, an unusual event given that MOTs have now been around for more than 30 years.

New ways to protect a BEC from resonant light were developed and demonstrated. This allowed BECs to survive for the first time even within MOT beams with lifetimes of around 1 s. The ability to protect a BEC from the strong blue transition of strontium was also demonstrated for the first time, validating our baffled twin chamber design. We produced a BEC surrounded by a reservoir of thermal atoms designed to replenish it. We were able to hold and protect this BEC within 2 mm of a steady-state red MOT and in full view of the MOT light, but we were not able to couple fresh atoms from our MOT to the reservoir without melting the BEC. For this reason we developed a second approach towards steady-state BEC.

A new architecture was developed and demonstrated for constructing guided atomic beams. It produced the highest phase-space density ever achieved in a continuous ultracold beam experiment, improving the state of the art by around three orders of magnitude. Our steady-state guided atomic beam of ^{88}Sr attained a peak PSD of $1.5(4) \times 10^{-4}$, a flux of $3.3(3) \times 10^{7}\,\mathrm{s}^{-1}$ and radial temperatures as low as $0.89(8)\,\mu\mathrm{K}$. Furthermore, by demonstrating on the order of 30% conversion efficiency from the flux captured by the MOT into a high PSD beam, we showed the practicality of our approach for future steady-state beam sources. This could have important implications for ultracold beam generation in applications from ion beams, to sympathetic cooling, to atom lasers. It could also be the ideal source for an active optical clock based on a steady-state superradiant laser.

We used this beam to continuously transport atoms from a steady-state red MOT to a protected dark trap accumulating and cooling them there. Here, in a protected dipole trap we produced a steady-state sample with a PSD approaching degeneracy, 1.7 ± 1.1. This result is another three orders of magnitude beyond the already record phase-space density produced by our red MOT. In fact, from this steady-state sample a BEC can form within 250 ms simply by turning off the slower laser beam that loads new atoms into the protected

trap. We believe this tantalizingly close result was limited primarily by the lifetime of atoms in the this trap.

Finally, we developed and demonstrated a new Sisyphus type slowing and cooling technique. The Sisyphus Optical Lattice Decelerator (SOLD) uses Sisyphus cooling within an excited state lattice to slow and cool atoms without using radiation pressure. This approach can be more photon efficient than radiation pressure based techniques and it eliminates the need for counter-propagating resonant beams. It has other applications from molecule cooling to slowing and trapping anti-hydrogen.

Our system is now being upgraded to use a SOLD decelerator to slow and cool atoms from our atomic beam. It is hoped that this will extend the lifetime of atoms in our reservoir trap. Together with a new dark-state free transparency transition at 487 nm, we are hoping to tip our system into steady-state quantum degeneracy.

Five years ago the highest steady-state phase-space densities were on the order of 4×10^{-4}. We are now at 1, just a heartbeat away from the critical value of 2.6 needed to make a steady-state BEC. Along the way, new records were demonstrated for steady-state MOTs and ultracold beams. We developed new ways to slow, to cool and to protect atoms from resonant light and we now stand at the dawn of a new era in which eternally existing states of pure matter become reality.

Samenvatting

Sinds de oudheid streeft de mensheid naar een steeds grotere controle over de wereld om ons heen. In 1960 demonstreerden we de ultieme controle over licht in de vorm van de eerste laser en een jaar later maakten we met een laser in stabiele toestand deze controle eeuwig. Het duurde nog eens 35 jaar om dit tot materie uit te breiden. Met de eerste realisatie van een puur Bose-Einstein-condensaat (BEC) in 1995 realiseerden we voor het eerst een pure kwantummechanische toestand van materie en kort daarna een laser van golfende materie. Deze nieuwe mogelijkheid om materie te beheersen leidde tot de revolutie in ultrakoude fysica die we vandaag zien met toepassingen variërend van tijdstandaarden tot kwantumsimulatie tot kwantuminformatie en nieuwe detectie technologie. Maar 25 jaar later blijven deze toestanden vluchtig. Ze overleven hoogstens een paar minuten voordat ze verdwijnen. Toch zegt de natuurkunde dat er een manier moet zijn om dit verval tegen te gaan. Constante input moet verliezen kunnen tegengaan en de condensaat aanvullen, om deze toestand eeuwig te maken. Het doel van ons onderzoek is om dit te proberen te realiseren, een stabiel BEC te maken, en daarmee een continue laser van atomen.

Om een BEC te maken, moet je eerst een monster van atomen zo koud mogelijk afkoelen, dan schakel je al het resonante licht uit en koel je verder af door middel van afdampen om condensatie te bereiken. De integratie van deze twee incompatibele stappen, laserkoeling en verdamping, heeft BEC's mogelijk gemaakt, maar het heeft het ook heel moeilijk gemaakt om een stabiel systeem te creëren. In 2012 demonstreerde onze groep een "onzichtbaarheidsmantel" voor een BEC. Met behulp van Stark-verschuivingen werd een BEC transparant gemaakt, wat aantoont dat het mogelijk is om een BEC te vormen in aanwezigheid van een kleine hoeveelheid resonant koellicht. Met dit in de hand probeerden we de eerste stabiele BEC te maken.

De maat voor hoe dicht je bij het vormen van een BEC bent, is de fase-ruimtedichtheid (PSD). Dit beschrijft hoe koud en dichtheid de wolk is. Voor waarden boven 2,6 kan een BEC worden gevormd. Toen we begonnen, was de hoogste stabiele fase-dichtheid die werd aangetoond een gas van honderdduizend chroomium atomen met een PSD van 0,0004. We hebben nu een PSD van ongeveer 1, slechts een fractie verwijderd van de kritische waarde van 2,6. Maar dit proefschrift gaat over veel meer dan slechts één cijfer.

Dit proefschrift beschrijft de Strontium Continuous Atom Laser (SrCAL) -machine die

we hebben gebouwd en de vele lessen die we daarbij hebben geleerd. Het pad naar een stabiel BEC is onbekend. Om ons daarheen te navigeren, ontwierpen en bouwden we een unieke en flexibele strontium-kwantumgasmachine, een machine die vanaf het begin werd ontworpen om een stabiele toestant te creëren. Er zijn maar enkele niet-alkalische kwantumgasmachines gebouwd en slechts een handvol daarvan is voor strontium, dus het maken van een nieuwe quantumgasmachine is altijd een uitdaging. Leren hoe je zo'n machine moet bouwen, zul je niet in college of uit de literatuur leren. De beste middelen die we hebben zijn de proefschiften van degenen die voor ons zijn gekomen, dus een belangrijk onderdeel van dit proefschrift is om een deel van die hard verworven kennis te documenteren, om toekomstige bouwers te helpen bij de bouw van zowel gepulseerde als stabiele gecondenseerde gasmachines. Ik beschrijf ook de technische details die nodig zijn voor toekomstige gebruikers van SrCAL om deze machine volledig te beheersen.

Het resultaat van dit werk is de een uniek vermogen om stabiele ultrakoude gassen te maken. Met behulp van een steady-state magneto-optische val (MOT) op de smalle 7.4 kHz rode overgang bereikten we een faseruimte-dichtheid van 1×10^{-3}. Dit verbeterde de ultramoderne fase-ruimtedichtheid voor stabiele MOT's met meer dan twee ordes van grootte, een bijzonder resultaat gezien het feit dat MOT's nu al meer dan 30 jaar bestaan.

Er zijn nieuwe manieren ontwikkeld om een BEC tegen resonant licht te beschermen. Hierdoor konden BEC's voor het eerst overleven, zelfs binnen MOT-stralen met een levensduur van ongeveer 1 s. Het vermogen om een BEC te beschermen tegen de sterke blauwe overgang van strontium werd ook voor het eerst aangetoond. Dit bevestigde het vernuft in ons bijzondere ontwerp met twee kamers boven elkaar. We produceerden een BEC omringd door een reservoir van thermische atomen ontworpen om het condensaat aan te vullen. We waren in staat om deze BEC vast te houden en te beschermen binnen 2 mm van een stabiele rode MOT en in het volle zicht van het MOT-licht, maar we konden geen nieuwe atomen van onze MOT koppelen aan het reservoir zonder het BEC te smelten. Om deze reden hebben we een tweede benadering voor stabiele BEC's ontwikkeld.

Een nieuwe architectuur werd ontwikkeld en gedemonstreerd voor het construeren van geleide atoomstralen. Dit produceerde de hoogste fase-ruimtedichtheid ooit bereikt in een continu ultrakoud atoombundel experiment, het verbeterde deze techniek met ongeveer drie orden van grootte. Onze stabiele geleide atoomstraal van ^{88}Sr bereikte een piek PSD van $1.5(4) \times 10^{-4}$, een flux van $3.3(3) \times 10^{7}\,\mathrm{s}^{-1}$ en radiale temperaturen zo laag als $0.89(8)\,\mu\mathrm{K}$. Bovendien toonden we door het demonstreren van 30% conversie-efficiëntie van de flux die door de MOT wordt opgevangen maar de hoge PSD-bundel, de bruikbaarheid van onze aanpak voor toekomstige bundel experiementen. Dit kan belangrijke implicaties hebben voor het genereren van ultrakoude bundels in toepassingen van ionenstralen en het sympathische koelen tot atoomlasers. Het zou ook de ideale bron kunnen zijn voor

een actieve contuinue superluminisente lasende optische klok met toepassingen voor tijdstandaarden en detectie technologieën.

We gebruikten deze bundel om atomen continu te transporteren van een rode MOT in een stabiele toestand naar een beschermde donkere val alwaar de atomen zich verzamelden en afkoelde. Hier produceerden we in een beschermde dipoolval een stabiele wolk met een PSD die condensatie naderde, 1.7 ± 1.1. Dit resultaat is nog eens drie orden van grootte voorbij de reeds record fase-ruimtedichtheid geproduceerd door onze rode MOT. Uit dit stabiele monster kan in feite een BEC worden gevormd binnen 250 ms door eenvoudig de afremmende laserstraal uit te schakelen die nieuwe atomen in de beschermde val laadt. Wij geloven dat dit nagenoeg ultieme resultaat vooral werd beperkt door de levensduur van atomen in deze val.

Ten slotte hebben we een nieuwe Sisyphus-type vertraagings- en koeltechniek ontwikkeld en gedemonstreerd. De Sisyphus Optical Lattice Decelerator (SOLD) maakt gebruik van Sisyphus-koeling in een rooster voor de aangeslagen toestand van de atomen waarin deze vertragen en afkoelen zonder stralingsdruk te gebruiken. Deze benadering kan meer foton-efficiënt zijn dan op stralingsdruk gebaseerde technieken en elimineert de noodzaak voor een paar van twee tegengestelde laserbundels. Het heeft andere toepassingen, van het koelen van moleculen tot het vertragen en vangen van anti-waterstof.

Ons systeem wordt nu geüpgraded om een SOLD decelerator te gebruiken om atomen van onze atoomstraal te vertragen en af te koelen. Het is te hopen dat dit de levensduur van atomen in onze reservoirval zal verlengen. Samen met een nieuwe transparante transitie op 487 nm welke geen donkere grondtoestanden bevat hopen we in ons experiment in stabiele condensaat te creëren.

Vijf jaar geleden waren de hoogste fase-dichtheden in stationaire toestand in de orde van 4×10^{-4}. We staan nu op 1, slechts een fractie verwijderd van de kritische waarde van 2,6 die nodig is om een continue BEC te maken. Onderweg werden nieuwe records gedemonstreerd voor stabiele MOT's en ultrakoude bundels. We hebben nieuwe manieren ontwikkeld om atomen te vertragen, te koelen en te beschermen tegen resonant licht en we staan nu aan het begin van een nieuw tijdperk waarin eeuwig bestaande staten van pure kwuantum materie werkelijkheid worden.

Contents

Chapter 1

Introduction

Since antiquity humanity has strived for ever greater control of the world around us. For millennia, control was always one of degree, we aimed to control the macroscopic behaviour while accepting we could do little at the microscopic level. An understanding of the quantum mechanical nature of light and matter has, over the past century, led us to the realisation that perfection and state purity even within macroscopic systems is now within our grasp.

One of the most important first realisations of this was the maser. It combined two concepts. Firstly, the quantum mechanical concept of stimulated emission in which a photon can be effectively cloned [1, 2]. Secondly, a feedback mechanism in the form of a resonant cavity. Together you have a system which will drive towards a single, pure, macroscopically occupied, quantum mechanical state. The first machine to demonstrate "microwave amplification by stimulated emission of radiation" was an ammonia maser built by Charles Townes, James Gordon and Herbert Zeiger in 1953 [3]. More than fifty years later hydrogen masers at 1.4 GHz continue to provide continuous wave radiation with state of the art purity and short term temporal stability. This remains a key part of today's clock and time keeping technology.

For all its successes, it was not the maser but the laser which has permeated our everyday lives. Taking the same ideas of stimulated emission and feedback and applying them at optical instead of microwave frequencies, one can create a pure state of optical rather than microwave radiation. The first demonstration was a flash lamp pumped ruby laser made by Theodore Maiman in 1960 [4]. This pulsed laser was a highly multimode device so it wasn't pure, but it did demonstrate light with unrivalled spatial and temporal purity. The following year the first continuous laser, a helium-neon laser was demonstrated by Ali Javan, William Bennett and Donald Herriott [5]. The helium-neon laser demonstrated a linewidth as low as 10 kHz on a transition of 474 THz and thus took another big leap towards the ideal of a macroscopic pure state of light. Today, no-one would question the importance of the laser both from an applied point of view and from a fundamental

perspective. The single mode laser is at the heart of the quantum revolution taking place in quantum sensing and quantum information as it provides a pure clean state with which to interact and manipulate objects at the quantum level.

Our ability to produce macroscopically occupied pure states of matter and manipulate them is taking a little longer to develop but, like the laser before it, the principle relies on stimulated scattering and feedback. If a gas of bosons is cooled to very low temperatures at high densities, Bose enhanced scattering (analogous to stimulated emission) can scatter atoms into a single macroscopically occupied ground state. This phenomenon known as Bose-Einstein Condensation (BEC) was first predicted for light by Bose [6] and extended to matter by Einstein in 1924 [7]. While this concept was used in 1938 to explain superfluidity observed in helium, it took 70 years to develop the tools and ideas needed to create a pure BEC.

In 1995, the groups of Eric Cornell and Carl Wieman at JILA [8] and Wolfgang Ketterle from MIT [9] succeeded in creating the first pure BECs in rubidium and sodium respectively. This was the first creation of a macroscopic pure state of matter and was thus a major step for humanity's ability to control matter. Although their creation mechanisms were inherently pulsed, these macroscopically occupied states survived for tens of seconds allowing a broad range of experiments to be conducted. Over the past 25 years the field of ultra-cold atoms has blossomed and revelled with these new tools and capabilities [10–14].

In 1997 Ketterle's group showed [15] that by out-coupling a small proportion of a BEC from its trap, pulses of coherent matter-wave can be created. This was coined the first 'pulsed atom laser'. This output had the potential to provide macroscopic numbers of atoms on demand with ultimate control of their state, motion and position. Over the following years numerous improvements were demonstrated [16] including a continuous out-coupling mechanism [17] and the replacement of a depleted condensate with a fresh (but incoherent) batch of condensate [18, 19].

For more than 50 years the laser has provided users with pure, coherent states of light on demand for as long as you want. In atomic physics despite numerous attempts we have not yet had our 'continuous matter-wave laser' or 'steady-state BEC' moments. The goal of this thesis work was to try to make that moment happen.

1.1 Why make a steady-state BEC and atom laser?

Nearly 20 years ago Wolfgang Ketterle described what he thought might be the potential uses of a newly demonstrated atom laser [20]. Surprisingly little has changed in the intervening time:

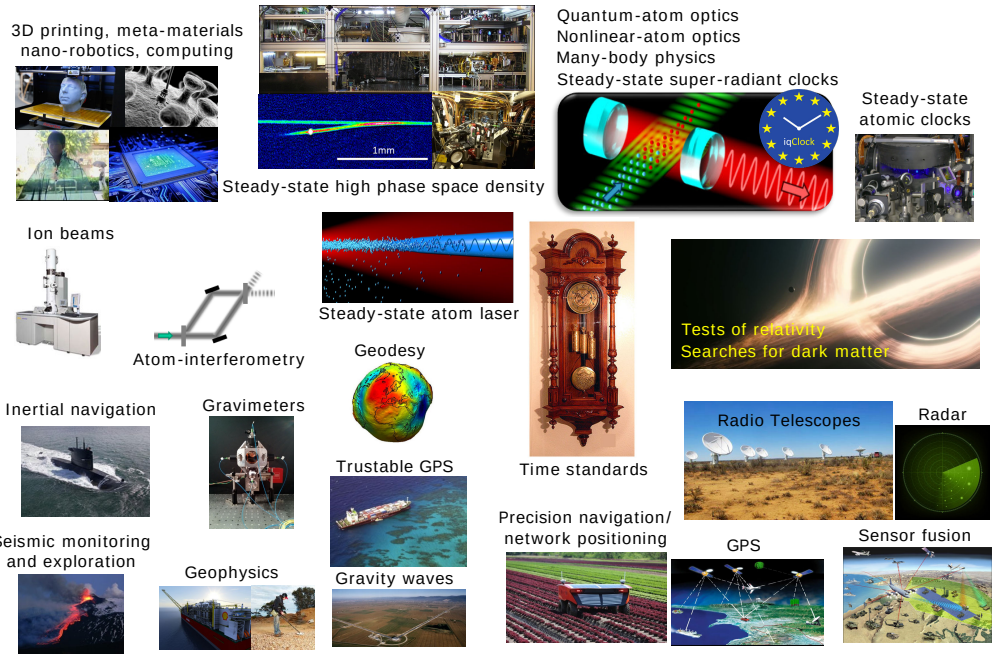

FIGURE 1.1: **Potential applications.** A few of the possible applications to which a steady-state BEC or a steady-state atom laser might be able to contribute.

Although a basic atom laser has now been demonstrated, major improvements are necessary before it can be used for applications, especially in terms of increased output "power" and reduced overall complexity. The atom laser provides ultimate control over the position and motion of atoms at the quantum level, and might find use where such precise control is necessary, e.g. for precision measurements of fundamental constants, tests of fundamental symmetries, atom optics (in particular atom interferometry and atom holography) and precise deposition of atoms. Since the matter-wavelength of atoms can be extremely short (it decreases inversely proportional to the atomic velocity), the ultimate limit to the spatial resolution is not the matter-wavelength, but the size of the atom.

It was this final application of "precise deposition" or 3D printing that originally drew me to the challenge of trying to make a steady-state atom laser. As the spatial resolution of lithographic systems approaches the size of an atom the inevitable demise of Moore's law draws close. Without the ability to reduce feature size in a layer, any growth in computational capacity must be accompanied by growth in the number of chip layers or chip area and thus a linear increase in the number of manufacturing processes and cost.

Yet there is a potential solution, we only use two of the three available dimensions. But semiconductors are just the tip of the iceberg. Right now we are witnessing a revolution in the way we think about materials.

Meta-materials formed by structuring and mixing traditional materials are attracting phenomenal interest with potential applications ranging from energy harvesting to stealth. Yet this is all conducted by structuring and mixing classical materials. Quantum meta-materials and devices have the potential for dramatically broader possibilities as observed by phenomena like high temperature superconductivity. The problem is, how do you efficiently print devices structured on an atomic or near atomic scale (without a crazy good crystal grower)?

Another key area was highlighted by the 2016 Nobel prize in chemistry for the development of molecular machines. The painstaking effort needed to produce even a few devices cries out for radical new ideas and new solutions.

But today, there are no clear solutions for solving this problem. Maybe atom lasers could help? As Wolfgang Ketterle pointed out above, resolution is at least in principle no problem. Fluxes from atom lasers of 1×10^6 atoms/s are reasonable and 2D MOTs already deliver cold beams of 1×10^{11} atoms/s with plenty of scope to scale. But materials are a challenge as the materials you might want to print with are not alkali metals but more likely semiconductors or organics or noble metals for which there are few laser cooled species. Maybe with sympathetic cooling and maybe with the entrainment of materials in an atom laser beam the refrigeration power of laser cooling might be brought to bare on a broad array of other species. Perhaps one day this work might contribute to opening these doors and making these dreams reality.

There are of course other nearer term applications for atom lasers, and in particular a steady-state atom laser.

1.1.1 Time standards: Superradiant clocks

The precision obtained from optical atomic clocks [21–25] has doubled almost every year for nearly thirty years, an exponential growth rate that looks extraordinary even when compared to the famous "Moore's law". Recent strontium optical lattice clock work from the group of Ye has now reached precisions of 5×10^{-19} with an hour of averaging [26, 27]. In fact the precision of optical clocks now exceeds that of the caesium time standard by more than two orders of magnitude[1]. Yet, the question always remains, "What needs to be improved to get that next order of precision?".

[1] The NIST CsF2 clock reportedly reaches to a fractional uncertainty in the low 1×10^{-16}.

An optical lattice clock [28] is a passive device. You build a laser, lock that to the narrowest linewidth optical reference cavity you can make [29, 30], then you periodically measure the difference between your laser and the frequency of an atomic transition and feedback to your laser. Longer interrogation times and better precision can be obtained by trapping your sample in a magic wavelength lattice [31, 32]. It is possible to find very narrow optical transitions (eg bosonic ^{88}Sr $^1S_0$-$^3P_0$ [33, 34]), but it is getting very hard to build a better reference cavity with which to stabilize your laser [35–37]. A question naturally arises: is it possible to use the output from a very narrow transition directly as a clock output and entirely bypass the reference cavity limitation? Let us assume that we can cool and trap 1×10^7 atoms emitting on a 1 mHz transition. Assuming we can capture the output from 10% of the solid angle, then we might expect to be able to collect an output on the order of 0.1 fW. This is sadly not even close to being enough to lock a laser, even with a very narrow locking bandwidth. Of course we would want to rapidly head towards even narrower linewidths, so even a marginal solution wouldn't be particularly exciting.

In 2005 [38] and 2009 [39] two papers proposed building an optical maser using superradiance in the "bad cavity" regime as a solution. Superradiance is a collective effect in which identical atoms can effectively phase lock and produce an enhanced emission rate [40]. In fact, the emission into a mode can grow as the square of the number of emitters (N^2) instead of in proportion to the number of emitters (N). It is important that the cavity be in the "bad cavity" regime, where the linewidth of the gain medium is narrower than the linewidth of the cavity, otherwise the cavity will frequency pull the laser output frequency. With 1×10^7 superradiant atoms in a cavity it now becomes in principle possible to emit an output on the order of 10 nW, a power 4 orders greater than what might be required for a locking system. Of course at these levels other limitations would come into play, like the need to repump or replenish atoms at a rate of at least 1×10^{11} s^{-1} but we can at least see there is a possible solution.

In 2012 Thompson's group demonstrated a pulsed superradiant laser with repumping on the rubidium 6 MHz line [41]. Four years later they extended this to strontium, firstly on the kHz line [42] and then on the ^{87}Sr mHz line [43]. Now, they are proceeding to try to produce a steady-state superradiant laser in strontium. It is here that our work can possibly help. This thesis will describe the production of sources which might be suitable for providing the gain medium for just such a superradiant laser. This is what I am now building for the iqClock project (section 8.3).

In addition to the superradiant clock, a steady-state source of near degenerate atoms may also be able to improve conventional optical lattice clocks. This is because lattice clocks rely on comparing their laser to an atomic sample which needs to be constantly refreshed. During the production of a new sample there will be a gap where there is no

atomic reference to compare the laser with. Thus, we end up with a periodic sampling of a continuous quantity.

This is in fact a pervasive problem often referred to as the Dick effect [44]. If a continuous signal is periodically sampled, noise at higher frequencies can be effectively mixed down to the baseband where it affects the long term signal. Ideally the solution is to continuously sample the quantity you wish to measure or failing that, at least make the sampling gaps very short. To get around the intermittent signal/sample problem, clock groups have built multiple clocks and multiplexed them [45] to remove measurement dead time, but having a steady-state sample like the ones developed in this thesis could provide an alternate if not simpler route.

1.1.2 Quantum sensors using clocks

So far, no other quantity has been measured as precisely as time and frequency. For this reason, there is much sense to be found in measuring physical quantities in terms of a frequency which can be compared with a reference clock.

With fractional uncertainties of better than 1×10^{-18} optical clocks are now entering the territory where they are able to sense both general and special relativistic effects to extraordinary precision. Clocks see tidal forces, they see gravitational red shifts and they see time dilation at walking speed. The list of radical potential applications for clocks is growing every year with proposals including:

- Tests of general relativity [25].
- Gravitational wave detection [46].
- Searches for variations of fundamental constants [47].
- New gravitational couplings [48].
- Searches for dark matter [49–52].
- Gravitational potential sensing for geodesy [25].
- Quantum many-body physics [53, 54].

But applications for clocks didn't begin only once they reached such extraordinary precisions. With a more compact and robust superradiant clock we can equally imagine continued improvements in less exotic applications such as GPS, GPS reliability (with a good clock you can see when someone is hijacking your GPS signal - or your predator drone [55]) network positioning and synchronization (keeping 5G basestations and other assets synchronized), phased array radars for astronomy [56] or military [57] and geolocation by sensor fusion.

1.1.3 Quantum sensors using atom interferometry

Atom interferometers [58] are continuing to grow in importance across a broad range of sensor domains. While atom interferometers tend to have a poor bandwidth compared to some traditional sensor technologies (such as MEMS devices) they offer much better absolute accuracy. For this reason cold atom interferometers are finding an important place in inertial navigation units and gravimeters. For physicists however, the most exciting application area at the moment is probably the potential for a cold atom interferometer based gravitational wave detector. A space based cold atom gravity wave detector could offer lower frequency sensitivity bands complementary to planned optical sensors. Even more importantly for this work, proposals for such a device call for strontium cold atom sources [59] and because of the targeted extremely low frequency bands, a steady-state degenerate device might be particularly appropriate for this application.

A selection of references is provided on some of the work done on applications of cold atom interferometers:

- Complete inertial navigation measurement units [60–63].[2]
- Gyroscopes [64–67].
- Gravimeters (and accelerometers) [60, 68–75] and gradiometers [74, 76] for geodesy, anomaly detection [77] such as mapping underground structures
- Magnetic sensors [76]
- Searches for dark matter [51].
- Gravity wave detectors [59, 68, 78, 79].

One issue for all these sensor applications is that current atom interferometers are pulsed devices. In the same way the Dick effect [44] impacts the performance of clocks it also impacts the performance of atom interferometers. This might be particularly important for the gravitational wave proposals, where the interest in atom interferometers is precisely for their ability to detect low frequency signals. There are important research lines pushing towards both continuous systems [66, 80] and quantum degenerate systems [81–84]. A steady-state degenerate source of atoms might be able to contribute significantly in both directions.

[2] Many inertial sensor technologies like the MEMS devices you might find in your phone are cheap to fabricate and often have excellent frequency bandwidths compared with atom interferometers but they suffer from poor offsets. When these signals are integrated over long times for example for maritime applications the result can be highly inadequate. Precision inertial measurement units are increasingly relying on atom interferometers for absolute accuracy and zeroing higher bandwidth technologies which is critical for precision applications. [62]

1.1.4 Fundamental questions

Whether you can call applications with no clear application an application is debatable. But nevertheless, much interesting science comes from pushing the boundaries of what is possible and from studying things that don't make sense. This is often without regard to the importance or even existence of some immediate application. Quantum atom optics remains a relatively young field. While it may not be the 1990s and 2000s where everything was new, I still firmly believe there is still much territory which remains to be explored and it helps to think about where the interesting gaps might be and which of those gaps our work might help with.

Quantum atom optics If a quantum noise limited atom laser can be constructed there are a great many analogies which could be explored measuring everything from the noise figure of a matter-wave amplifier [85], to a squeezed matter-wave [86], to entanglement or the teleportation of matter. Unlike quantum optics, the book of quantum atom optics has barely been started beyond a few proposals.

Nonlinear atom optics Nonlinear atom optics is another big field in optics but an area which has barely been started in atom optics despite the incredible nonlinearities available. Directions range from squeezing to self modulation to bistability [87]. In optics an important theme is harnessing nonlinear systems to perform computation and complex control tasks like all optical packet switching. The potential for applications is boundless.

Many-body physics, cavity-atom optics, superradiance and synchronization Many-body physics, interactions and synchronization of matter-waves is an area very closely linked to superradiance. This is part of what we hope to explore with the steady-state superradiant iqClock machine. Recent work includes studying phase synchronization inside a superradiant laser [88], synchronization across ensembles [89] and coherent single atom superradiance [90] as well as many body physics effects in a superradiant laser [91].

They said we couldn't For me, a good reason to try to do something is because people said it couldn't be done. A steady-state atom laser fits that description, literally.

1.1.5 Other applications

Atomtronics Without gain, optics and electronics would be pretty boring. In developing a steady-state atom laser we will also develop a steady-state gain medium which might make a significant impact for the field of atomtronics [92–94].

Cold chemistry and sympathetic cooling Cold chemistry [95, 96] is one of the most exciting areas of AMO physics today. Cold molecules is both experimentally and theoretically rich and challenging. It also has applications like the search for an electron dipole moment (EDM) and quantum simulation and computation which could have far reaching impacts for physics and beyond, but cooling a sample of molecules is extremely challenging. Setting aside molecule specific approaches, the best way to cool a material without closed (or even known) laser cooling transitions is to sympathetically cool it [97]. Sympathetic cooling [98] means immersing the material of interest in a dense (high collision rate) bath of something you can cool and which will not react with the substance you want to cool. Ideally you would use helium because you can cool helium to a few K before it condenses and because it is inert. Unfortunately it is difficult to cool helium gas much below 1 K, so reaching ultracold temperatures requires creative efforts. One approach is finding something you can laser cool to further cool your (already cold) sample, or finding something you can laser cool to to cool your helium to further cool your sample. An atom laser could be thought of as a never ending coolant supply for exotic species. Strontium is less reactive than the alkalis and is energetically stable for interactions with some interesting dipole molecules like SrF. For strontium, the sympathetic cooling of SrF looks like a promising place to start, as it has laser cooling transitions and has been well studied by the DeMille group [99–101]. SrF has many interesting applications like EDM [102, 103], dipolar physics [104] and quantum simulation [105].

Ion beams The atomic beam we produce in section 6.1 has state-of the art phase-space density and could be ionised to make a record ion beam brightness. Ion beam brightness is important for both ion beam microscopy and milling applications. A steady-state atom laser would improve the state of the art by many orders on top of what we will demonstrate here.

1.2 Making Bose Einstein condensates

At low temperatures it is useful to think of particles as quantum-mechanical wavepackets with an extent on the order of their thermal de Broglie wavelength λ_{dB} rather than as 'billiard balls' [10].

$$\lambda_{dB} = \sqrt{\frac{2\pi\hbar^2}{mk_BT}} \tag{1.1}$$

where:

m = mass of the particle
k_B = Boltzmann's constant
T = the temperature of the gas

The phase-space density provides a measure of how far away a system is from having the particle wavefunctions overlap and interfere.

$$PSD = n\lambda_{dB}^3 = n\left(\frac{2\pi\hbar^2}{mk_BT}\right)^{3/2} \tag{1.2}$$

where:

PSD = phase-space density
n = particle density

When particles are sufficiently cold and dense their deBroglie wavelengths begin to overlap and their behaviour becomes strongly dependent on the quantum mechanical properties of the particles. At high phase-space density, scattering will be affected by the wavefunctions of the surrounding particles. Bosons will be stimulated to scatter into the same state and a macroscopically occupied state can form, a BEC. It can be shown that this phase change occurs for phase-space densities greater than 2.612 [10]. The phase-space density also provides a measure of the number of particles in the ground state [10].

Another way of describing this phase change condition is in terms of a critical temperature, an experimental parameter which we can measure in order to see how close we are to the BEC phase change threshold.

$$T_c = 0.5273\frac{2\pi\hbar^2}{mk_B}n^{2/3} \tag{1.3}$$

There are several signatures we often use experimentally to search for the existence of a condensate. These are shown in figure 1.2. The usual signature of the phase transition is the bimodal distribution observable just below the critical temperature. In most circumstances this is used as the proof of a BEC. Secondary signatures can be an inversion in the aspect ratio of the cloud during a time of flight and a variation in the aspect ratio in dependence of the trapping powers and frequencies.

In principle a sufficiently low temperature and sufficiently high density of identical bosons is sufficient to give a phase change. In practice it is also necessary to have some scattering to thermalize the sample and provide gain to the ground state, otherwise the formation time scales will be excessive. This is particularly noteworthy for strontium where atoms of the most abundant isotope, ^{88}Sr are essentially non-interacting having a scattering length of around -1a_0.

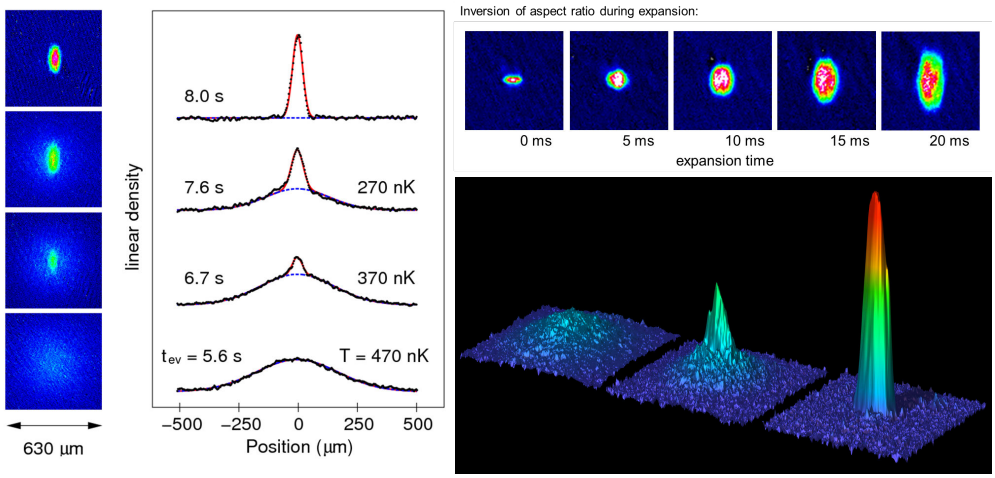

FIGURE 1.2: **The signatures of BEC.** As a cloud is cooled past its critical temperature a condensate will grow out from the thermal cloud. As the condensate becomes ever more pure the thermal cloud will fade to nothing. The bimodal distribution is the primary (and often only) signature used to verify the existence of a BEC. Other signatures can include a change in the aspect ratio in dependence of the trapping frequencies and an inversion in the aspect ratio during expansion. Data is reproduced from [106, 107].

There were several concerted efforts to try to make the first BEC.

Evaporative cooling was developed as a method to cool spin polarized hydrogen by the groups of Jook Walraven and Isaac Silvera in Amsterdam [108–110] and by Daniel Kleppner and Thomas Greytak's groups at MIT [111, 112]. With heroic effort hydrogen was finally condensed in 1998 [112] with an enormous condensate size of 1×10^9 atoms, although it is unlikely that there remains a working hydrogen condensate machine today.

Alkali atoms possess extremely closed laser cooling transitions at accessible wavelengths which are ideal for laser cooling. This was the basis of a separate set of efforts to laser cool dilute vapours of alkali gases to degeneracy. While numerous tricks like the dark SPOT MOT [113] were developed to boost phase-space densities it was the combination of laser cooling with a final evaporative cooling step (using ideas developed from the hydrogen efforts) which provided the necessary leap needed to reach degeneracy. Figure 1.3 shows just how dramatic this leap was with an improvement in phase-space density of 12 orders of magnitude in just two years.

Surprisingly little has changed over the past 25 years. A BEC is still made by:

1. A large sample of atoms is captured using a magneto-optical trap (MOT). This MOT can be loaded from a background vapour [113–115] or using a directed beam from

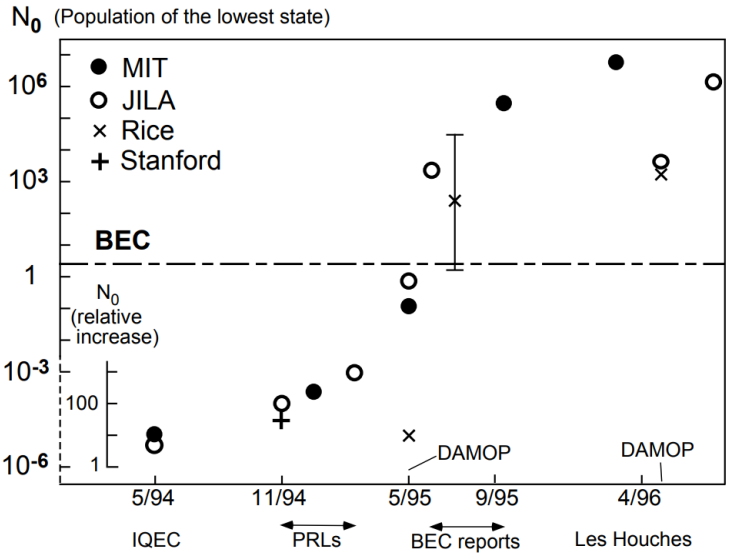

FIGURE 1.3: **Evolution of phase-space density during the race for a BEC.** Once an evaporation step was combined with laser cooling the phase-space density was improved by 12 orders of magnitude within 2 years (Plot taken from [10]).

a 2D MOT [116], a Low Velocity Intense Source (LVIS) [117] or an oven/Zeeman slower [118] combination.

2. By varying the laser intensities and frequencies this gas sample can be cooled to reach the laser cooling limits.
3. The sample must next be loaded into a conservative trap, either magnetic or optical.
4. Resonant light must be removed to prevent it from heating the sample.
5. A loss channel is introduced to create a controlled evaporation sequence.

This sequence has a number of steps which are mutually incompatible and thus must be performed in a time sequential manner. Particularly notable is the removal of all laser cooling light before beginning evaporation.

It is the incompatibility of laser cooling and evaporation which I would contend has prevented the development of a steady-state system able to produce BEC. Evaporation has always been needed to go beyond the limits that can be reached with steady-state laser operation.

A number of atoms have now been laser cooled and many of them have been condensed. Some have proven easy to generate large condensates owing to their favourable scattering properties and optical transition properties, while others required heroic efforts to produce tiny, unstable condensates. For our work it is useful to start with those species which have produced particularly favourable outcomes.

Species	Condensed flux (atoms/s)	Condensed number and cycle time
H	$3.3\text{x}10^6$	$\sim 1\text{x}10^9$ @ $\sim$5min [112, 119]
^{23}Na	$2\text{x}10^6$	$1.2\text{x}10^8$ @ 60s [120]
	$3.3\text{x}10^5$	$2\text{x}10^7$ @ 60s [121]
	$1.7\text{x}10^5$	$5\text{x}10^6$ @ 30s [15]
^{87}Rb	$1.07\text{x}10^6$	$2.3\text{x}10^6$ @ 2.14s [122]
	$3.8\text{x}10^5$	$3.8\text{x}10^6$ @ 10s [122]
	$3.3\text{x}10^5$	$2\text{x}10^7$ @ 60s [121]
	$2.7\text{x}10^5$	$4\text{x}10^4$ @ 1.5s [75]
	$1.3\text{x}10^5$	$2\text{x}10^6$ @ 15s [123]
	$1\text{x}10^5$	$1\text{x}10^4$ @ 1s [75]
	$3.4\text{x}10^4$	$3.4\text{x}10^4$ @ 0.953s [124]
^{4}He*	$1\text{x}10^6$	$1.5\text{x}10^7$ @ 15s [125]
	$3.3\text{x}10^4$	$5\text{x}10^5$ @ 15s [126]
	$6.7\text{x}10^2$	$4\text{x}10^4$ @ 60s [127]
^{84}Sr	$2.2\text{x}10^5$	$1.1\text{x}10^7$ @ 50s [128]
	$5\text{x}10^4$	$1\text{x}10^5$ @ 2s [128]
	$4.9\text{x}10^4$	$2.3\text{x}10^5$ @ 4.7s [129]
	$1.9\text{x}10^4$	$1.5\text{x}10^5$ @ 8s [106]
^{39}K	$3.6\text{x}10^4$	$4\text{x}10^5$ @ $\sim$11s [130]
	$1.2\text{x}10^3$	$3\text{x}10^4$ @ 25s [131]
^{86}Sr	$1.2\text{x}10^4$	$2.5\text{x}10^4$ @ 2.1s[128]
	$1.1\text{x}10^3$	$5\text{x}10^3$ @ 4.7s [132]
^{40}Ca	$6.7\text{x}10^3$	$2\text{x}10^4$ @ 3s [133]
^{174}Yb	$6.7\text{x}10^3$	$1\text{x}10^5$ @ 15s [134]
	$2.3\text{x}10^2$	$5\text{x}10^3$ @ 22s [135]
^{168}Er	$3.4\text{x}10^3$	$7\text{x}10^4$ @ 20.5s [136]
	$1.5\text{x}10^3$	$3\text{x}10^4$ @ 20s [137]
^{88}Sr	$3.3\text{x}10^3$	$3\text{x}10^4$ @ 9s [138]
^{52}Cr	$3.1\text{x}10^3$	$5\text{x}10^4$ @ 16s [139]
^{85}Rb	$2.7\text{x}10^3$	$4\text{x}10^4$ @ 30s [123]
	$1.8\text{x}10^3$	$8\text{x}10^4$ @ 44s [140]
^{133}Cs	$2\text{x}10^3$	$6.5\text{x}10^4$ @ 32s [141]
^{170}Yb	$5.8\text{x}10^2$	$7\text{x}10^3$ @ 12s [142]
^{164}Dy	$3.3\text{x}10^2$	$1.5\text{x}10^4$ @ 45s [143]
^{41}K	83	10^4 @ 120s [144]
^{7}Li	73	$1.4\text{x}10^3$ @ 200s [145]
		$1\text{x}10^3$ @ 5min [146]

TABLE 1.1: **Demonstrated condensate production rates for various species.** Listed is an (incomplete) list of the rates of condensate production for various species. This should be regarded as merely indicative of the relative ease of condensate production for different species. Flux can usually be increased by an order of magnitude or more by turning up your oven temperature or with a more concerted effort to improve sources and lasers. It is also possible to consider the production of condensates in parallel, for example [147] evaporated an array of four condensates in parallel.

Table 1.1 provides an overview of the rates at which various species have been condensed. Both the cycle time and the overall production rates are relevant, as a short cycle time could be considered as being closer to a steady-state system owing to a higher starting phase-space density. There are several good species with production rates over 1×10^5 per second but one species in particular becomes very common.

^{87}Rb is the most common alkali used for BEC production, in fact 50% of BEC machines use this species[3]. It is easy and inexpensive to make the lasers, the 780 nm cooling transition is next to the 785 nm lasers developed for CD Burners. The laser cooling is powerful and needs only one easy repump detuned by just 6.8 GHz from the cooling transition. Polarization gradient cooling in MOTs delivers typical MOT temperatures of just a few tens of µK, well below the Doppler cooling limit of 140 µK. It has outstanding scattering properties and the designs for 2D-MOTs in particular are very well developed, with typical compact sources delivering fluxes well over 1×10^{10} atoms/s. In short, BEC with ^{87}Rb is now very easy. Steady-state BEC with ^{87}Rb is on the other hand very hard and has been tried by numerous groups. The steady-state phase-space densities from rubidium MOTs are typically on the order of 1×10^{-6} or below, with pulsed systems able to reach 10^{-3}-10^{-5}. This leaves the need for a lot of evaporation and deep tight traps to evaporate efficiently from such low starting points. Given the incompatibility of evaporation and laser cooling, reaching steady-state is hard.

^{84}Sr is mostly interesting because it is an alkali earth metal rather than an alkali so it has two electrons in the outer shell instead of one and it thus possesses a much richer level and transition structure. It has an accessible transition at 689 nm, with a 7.4 kHz linewidth which allows laser cooling to hundreds of nK even without sub-Doppler cooling processes. ^{88}Sr can be pulsed laser cooled to phase-space densities of 0.1 when loaded in a dipole trap, leaving a much lower hurdle for evaporation. A problem for strontium is that only ^{84}Sr has suitable scattering properties for thermalization, and ^{84}Sr is rare with a natural abundance of just 0.56%. Despite these challenges this is the species we will pursue in this work, using approaches made possible by the richness of strontium's electronic structure.

1.3 Pulsed atom lasers

The first atom laser was demonstrated in 1997 by Ketterle's group [15]. It used an RF output coupler to change the state of atoms in a magnetically trapped BEC from a trapped to an untrapped state, resulting in a pulse of atoms forming a coherent burst of matter-wave with a defined phase relative to the source BEC: an atom laser. The first atom laser results are shown in figure 1.4 (B). A review of atom lasers and their production can be found in [16].

[3] A further 25% of machines use the other alkalis, https://www.uibk.ac.at/exphys/ultracold/atomtraps.html

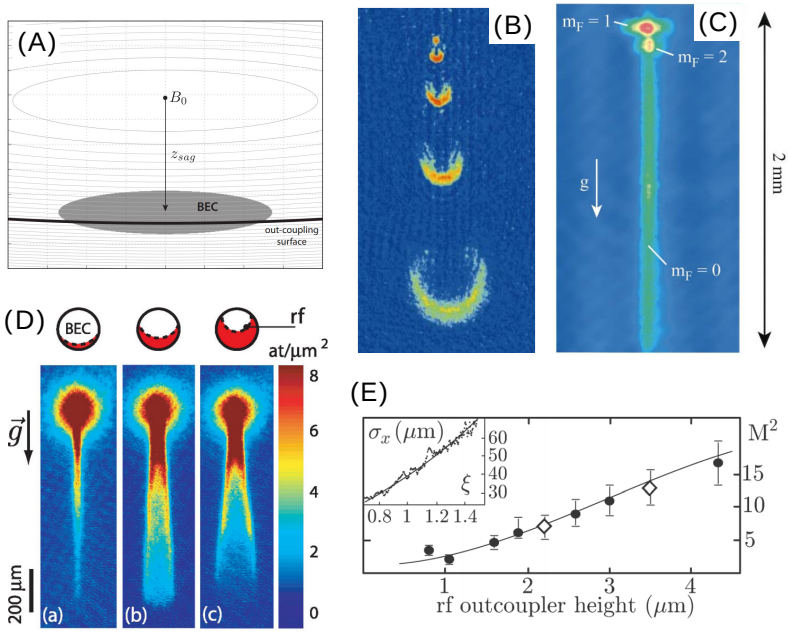

FIGURE 1.4: **RF Outcoupling.** (A) An RF outcoupler works by producing spin flips on a spherical surface from trapped to untrapped states, after which the atoms will fall under gravity from [16]. (B) The first atom laser from [11, 15]. (C) The first continuous outcoupler producing a quasi-CW atom laser from [17]. (D) The beam quality from an atom laser produced by RF outcoupling depends critically on the distance between the RF out-coupling surface and the bottom of the BEC. Shown are atom laser beams produced at heights of (a) 0.37 μm, (b) 2.22 μm and (c) 3.55 μm respectively from [148]. (E) The variation in the M^2 of the atom laser with out-coupling height from [148].

The concept of an atom laser is simple and the analogies with optical lasers are rich, but all atom lasers so far have had to operate within the confines of a finite size source of atoms which can not be coherently renewed. Thus, all atom lasers are either pulsed, operate quasi-continuously or would have an output phase that changes randomly across renewal events. Even within these limitations there has still been a wealth of work done demonstrating better output couplers from condensates, beams with better spatial mode quality (spatial coherence) and continuous output couplers. I will now briefly step through some of the most interesting and important developments from the past two decades.

Pulsed RF outcoupler The first demonstration of an atom laser [15] used a pulsed RF source to periodically transfer atoms in a ^{23}Na BEC from a trapped to untrapped magnetic sublevels of the ground state (see figure 1.4 (B)). Untrapped atoms then

accelerated away under gravity. Three variations on this approach were explored. Firstly an RF frequency was chosen resonant with the magnetic splitting between the m_F=-1 and m_F=1 states and the RF pulse length set at 5 cycles (6.6 µs). By varying the RF pulse amplitude the proportion coupled could be varied in accord with the Rabi frequency. A second method swept the RF frequency for 1 ms and varied the RF amplitude. This resulted in better output amplitude control as the spatial variation in the magnetic bias field was rendered mute. Finally the bias field of the magnetic trap could be set to zero in the trap centre leading to outcoupling via spin flips although the amplitude was essentially uncontrolled.

Continuous RF outcoupler The first demonstration of a continuous output coupler [17] again used RF coupling between trapped and untrapped magnetic sublevels, see figure 1.4 (C)). By making the bias field of their magnetic trap extremely stable they were able to tune the location of their outcoupling within the condensate by tuning the RF frequency, improving the effective linewidth and transverse beam quality, but spatially there is always a broad annulus across the condensate outcoupled limiting the beam quality. Additionally, there is significant interaction of the beam with the condensate while leaving the condensate, further distorting the beam. The beam quality of continuous RF outcouplers was studied by the group of Aspect [148, 149] and some of the key results are included in figure 1.4 (D-E).

Raman outcoupler A Raman outcoupler can provide a solution to the interaction and beam quality problems found with RF outcouplers. The advantages of Raman are firstly that optical beams can be focussed tightly into a condensate or even form a dipole waveguide to guide the outcoupled beam and secondly, counter-propagating Raman beams impart a $2\hbar k$ momentum kick to the outcoupled beam so they quickly exit the condensate avoiding interactions. Raman outcoupling was demonstrated in [150] and [151]. In [150] a time orbiting potential trap was used forcing the use of a syncronized pulsed Raman outcoupling leading to a 20 kHz maximum operating frequency rather than a true continuous output as in [151]. A detailed comparison was made in [152] between RF and Raman outcouplers. Results of atom lasers produced using Raman outcoupling are shown in figure 1.5.

Bragg outcoupler Until now atom lasers have been made by changing the state of atoms in a BEC from a trapped to an untrapped state. Alkalis like rubidium have both fine and hyperfine splitting of their ground states so there is an abundant choice of stable states which can be used. Strontium has no such splitting of the ground state. For strontium it might be possible to excite condensed atoms to the metastable $^3P_0$ or $^3P_2$ states but inelastic collision losses for these states is concerning, particularly at high densities.

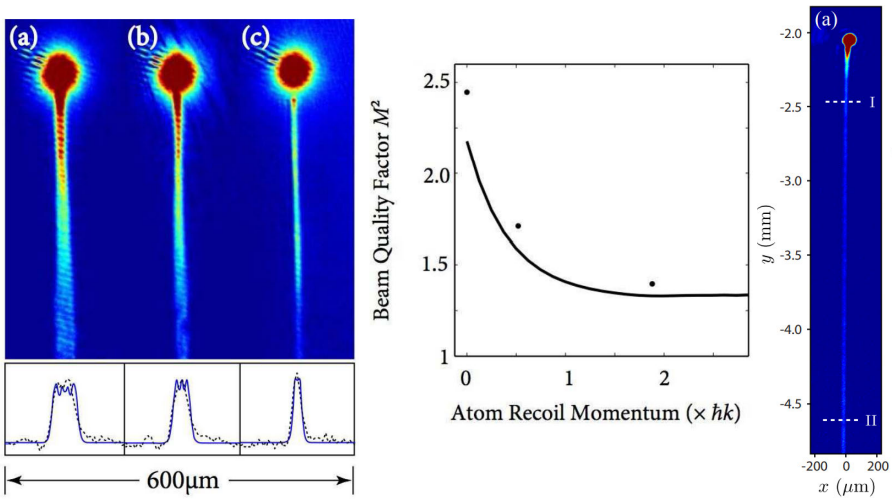

FIGURE 1.5: **Raman outcouplers.** Raman transitions can be used instead of RF transitions to coherently change the state of atoms in a BEC from a trapped to an untrapped state. (left) Atom lasers produced from a ^{87}Rb BEC using (a) RF outcoupling, compared with (b,c) Raman transitions with the two Raman beams at 30° and 140° respectively from [153]. (center) A comparison of the M^2 of the resulting atom laser in dependence of the recoil momentum imparted by the Raman beams from [153]. (right) Raman outcoupled atom laser from [16].

Another approach if the trap is very weak would be to try Bragg outcoupling. A Bragg transition looks much the same as a Raman transition except that we change only the momentum state, we do not change the atom's internal state. Bragg uses two beams; an atom absorbs a photon from one beam and emits into the second beam so there is no spontaneous event which would destroy coherence. Since the state is unchanged, enough momentum must be imparted from the photon recoils to push the atoms out of the trap. Large Momentum Transfer (LMT) multi-photon Bragg beamsplitters is an important line of research for the atom interferometry community. Bragg transfers of 10-20 $\hbar k$ are relatively easy [154, 155] with momentum transfers of $100\hbar k$ having been demonstrated [156].

Modelocking — tunnelling through a lattice A different approach was demonstrated by the Kasevich group [157]. If a BEC is placed on a thick blue detuned light sheet the tunnelling rate and flux will be exponentially dependent upon the barrier height and thus unstable. If you use a lattice instead of a sheet this sensitivity is largely removed and atoms will tunnel through the barrier under force of gravity. But rather than getting a continuous output you get a pulsed output. Effectively each lattice site acts

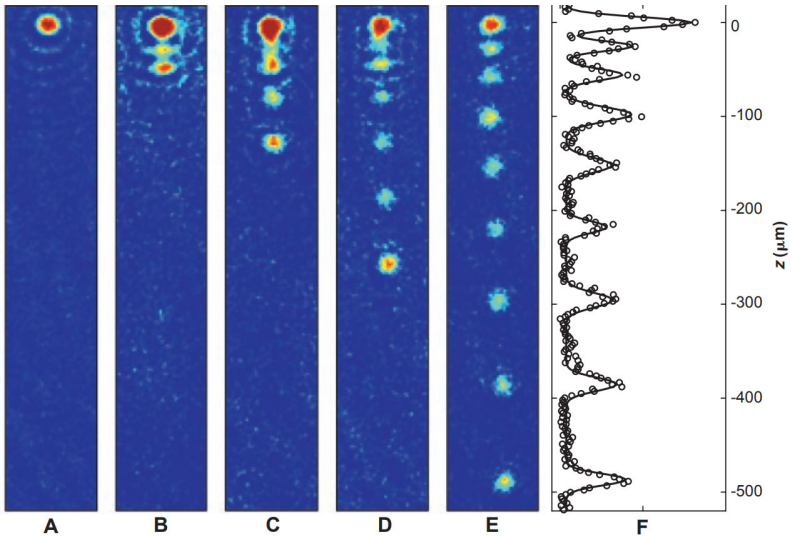

FIGURE 1.6: **Modelocked atom lasers.** A modelocked atom laser can be produced from atoms tunneling through a lattice barrier [157]. (A) Absorption image of a Bose-Einstein condensate in a TOP trap. (B-E) Absorption images after fixed holding times in the optical lattice showing the time development of the pulse train; 3 ms (B), 5 ms (C), 7 ms (D), and 10 ms (E). (F) The integrated absorption profile for (E), obtained by summing over the horizontal cross-sections with a fit to a series of gaussian pulses. Figure reproduced from [157].

as a coherent emitter of matter-waves which interfere in the same way as the many frequencies of a modelocked laser interfere to create a pulsed output.

This effect can also be considered atoms escaping while they are non-adiabatically undergoing Bloch oscillations, or, in the case of just two wells, the AC Josephson effect. The modulation frequency f_{mod} of the pulsed output will be proportional to the potential difference between adjacent lattice sites $f_{mod} = mg\Lambda_{Lat}$ where m is the atomic mass, g is acceleration due to gravity and Λ_{Lat} is the lattice period. This gives 2.2 kHz $\cdot$ μm^{-1} in lattice spacing for ^{84}Sr under bare gravity. The flux will be dependent upon the lattice depth, condensate population and the cross sectional area. It is of course possible to increase the frequency by increasing the lattice gradient, for example with a dipole gradient and one can imagine generating complex waveforms by painting the lattice with a complex potential landscape.

Quantized couplers An idea related to the modelocked output coupler is making a deep 2D lattice and rotating it by 90° so that gravity will pull atoms through a sieve of 1D tubes. This is something I wanted to try. The conductance through a deep 1D

tube is quantized and thus you can define and control the flux precisely. You can also imagine painting a potential on a 2D array of tubes to make a phased array atom laser or to block specific tubes to paint a picture. Needless to say I believe there could be a lot of interesting things you might do with such an architecture if you had the source to feed it. The idea of the quantized conductance through a 1D waveguide has now been demonstrated by Esslinger's group [158] but I would like to think that it is just the tip of the iceberg.

Beyond the simple architecture of a BEC with an output coupler, there is of course a plentiful array of atom laser and amplifier architectures which might be harnessed to various ends. On top of the atom optics approaches already considered, the world of optics has furnished us with more than 50 years of creative designs from which to draw inspiration.

Matter-wave amplification An alternate approach to outcoupling atoms from a condensate into an atom laser beam is to use a condensate as a source for a matter-wave seed. There are two configurations which have been demonstrated, superradiant Rayleigh scattering [159–163] and superradiant Raman scattering [159, 164, 165].

Parametric amplification It is also possible to use four wave mixing of matter-waves to produce matter-wave amplification analogous to an optical parametric amplifier (OPA) or an optical parametric oscillator (OPO).

Ring vs trap Atom lasers produced so far have been based on outcoupling atoms from a trapped BEC using a coherent process such as Raman output coupling [166]. In these systems the 'resonator' has zero length, it is the BEC itself. An alternative architecture is the cavity in which a travelling wave of atoms is resonated in a ring in the same way as an optical laser [167]. A phase contrast imaging video playing BEC pong might also be pretty cool.

Bragg grating A "laser like" approach to creating an output coupler is to use a lattice as a distributed Bragg reflector for a cavity. We may tailor the spectral and reflectance properties of a grating as desired using many of the same techniques used for fibre Bragg grating design and manufacture [168]. This was demonstrated by the group of Guéry-Odelin [169].

1.4 Paths towards steady-state BEC and atom lasers

If we can make a steady-state BEC then we can outcouple a steady-state atom laser using the methods described in section 1.3. Thus, we shall focus on the challenges of making a steady-state BEC.

There have been several demonstrations in which a trap was periodically refilled with new condensates. This was first demonstrated by loading batches [18] and later by loading adiabatically [19]. Importantly, in both cases there was no phase relationship between the trapped condensate before and after each refilling event. While there was a continuously available reservoir of condensed atoms these were not steady-state systems nor did they preserve the coherence of the condensate. For us, we will distinguish a steady-state BEC as being one in which the phase remains coherent and predictable as one would require for steady-state atom interferometry[4].

There are two approaches by which we can increase the phase-space density (or brightness) of a system without destroying coherence. These approaches are in no way unique to BEC or matter-waves, they are also the ways in which we make brighter optical lasers:

Incoherent pumping We can create a population inversion providing gain through stimulated scattering. This can be combined with feedback in the form of a trap or resonator or the system can be seeded by a macroscopically occupied state in the form of an amplifier. In all these systems the stimulated process of scattering a new atom into the ground state condensate *must* be accompanied by the scattering of a thermal atom or photon which can carry away the entropy.

Coherent pumping We can also combine beams by constructively interfering them. If we measure the phase difference between two condensates or matter-waves and then provide feedback they can be constructively interfered on some form of beam splitter forming a brighter coherent source. In this case, the entropy is removed by the feedback process.

I will now describe some of the approaches taken and milestones achieved in the quest for a steady-state BEC over the past 20 years.

[4] *Predictable* is a provocative claim. There must of course be some degree of phase diffusion coming from the varying chemical potential as atoms enter and leave the BEC mode randomly. This is analogous to the phase diffusion we see in an optical laser which gives rise to the Schawlow-Townes linewidth. Yet we can in most respects consider the phase of a laser to be predictable within the linewidth limits describing the oscillator. The same should be true of a matter-wave oscillator. Studying how this linewidth varies with the amplitude of the oscillator/BEC, with the gain in the system, the pumping rates, inversion or with the strength of the coupling to the thermal and vacuum baths (scattering length) are just a few of the many unexplored areas which motivate this pursuit.

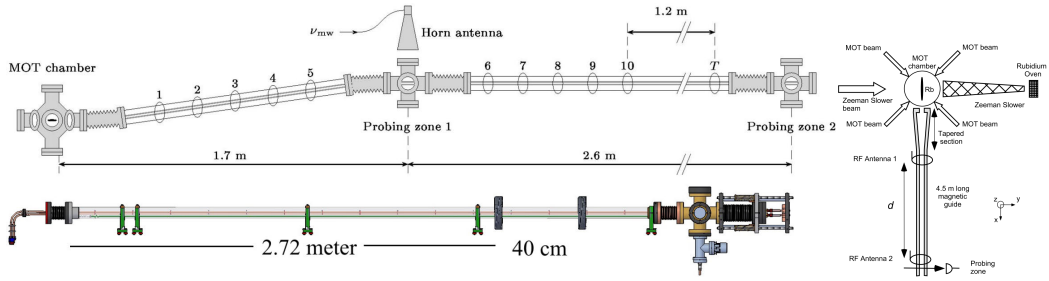

FIGURE 1.7: **Waveguide evaporation.** Perhaps the first concerted effort to produce a steady-state atom laser and one of the most spectacular was carried out by the group of David Guéry-Odelin from 1999 until 2008 (with some ongoing modelling work). (top, right) This work was based on evaporatively cooling a magnetically guided rubidium beam along a 4.3 m path. (bottom) One of the postdocs, Johnny Vogels, who worked on the Guéry-Odelin beam line went on to build a very similar device and pursued this from 2004 until some time around 2011 [184]. Figures reproduced from [170, 172] and [184].

1.4.1 Evaporation and cooling

Evaporation Some of the most spectacular efforts to make a steady-state atom laser have been those using evaporation to cool a beam of atoms propagating along a waveguide. Much of the pioneering work in this area was carried out by the group of David Guéry-Odelin from 1999 until 2008 [170–183] with some ongoing numerical and other related work since then. This work was based on evaporatively cooling a magnetically guided steady-state ^{87}Rb beam. The experiment began [172] with a flux of 7×10^9 atoms per second at 550 µK with a phase-space density of 2×10^{-8}. The initial velocity was $0.9\,\mathrm{m \cdot s^{-1}}$ which was slowed to $0.6\,\mathrm{m \cdot s^{-1}}$ by gravity in combination with a tilt in the guide. Over the 4.3 m path a series of 10 RF antennas were used to evaporatively cool the beam which was magnetically guided by 4 water cooled cubes generating gradients of $800\,\mathrm{G \cdot cm^{-1}}$. One of the particular challenges with magnetic waveguides is the 'wash-boarding' effects you can get from nonuniformities in the guide. The experiment reached a steady-state phase-space density of 2×10^{-7}. One of the postdocs from this experiment, Johnny Vogels, went on to build a copy of it and pursued this line from 2004 until some time around 2011 [184]. Some diagrams showing these machines are included in figure 1.7. This group also demonstrated ideas which were later used in other efforts such as the idea of removing hot atoms from a magnetically guided beam by absorbing the beam edges on a material surface [179].

The group of Georg Raithel also pursued evaporation of ^{87}Rb from magnetic waveguides from around 2000 until some time around 2012 [185–188]. In their final work

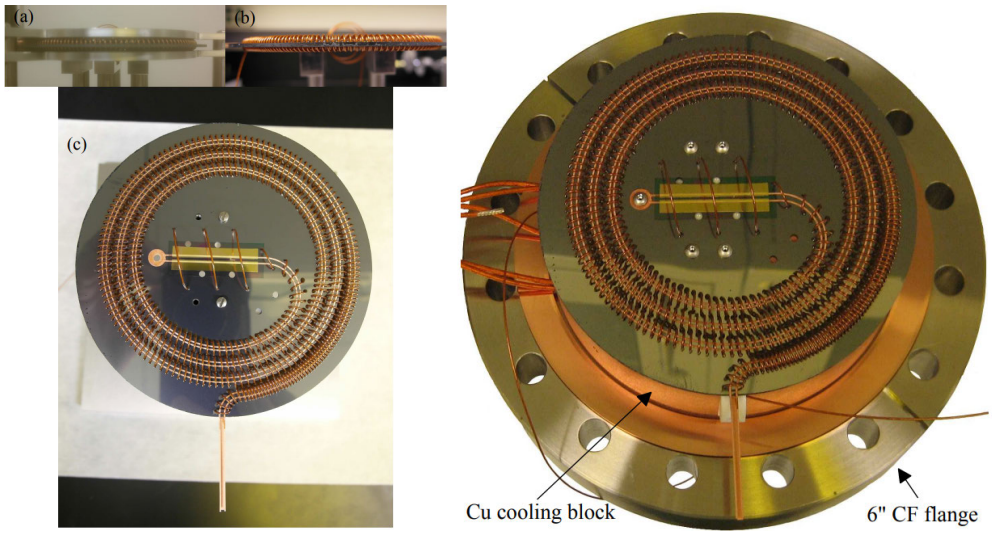

FIGURE 1.8: **Waveguide evaporation on a chip.** The group of Georg Raithel also pursued evaporation of rubidium from magnetic waveguides from around 2000 until some time around 2012. Perhaps the most spectacular effort was the 0.7 m waveguide built on a silicon wafer shown above. Figures reproduced from [185].

(that I could find) they produced [185] a beautiful magnetic waveguide 0.7 m long coiled on a silicon wafer as shown in figure 1.8. I never found results from this work but the engineering which went into it is gorgeous.

One of the objectives of our work here was to try evaporation from an optical guide along the same lines as this previous work. Strontium provides us with much higher starting phase-space densities than rubidium which should make our task easier. The machine we built was designed to have a 0.05-0.1 m Bessel beam optical dipole trap acting as a guide for evaporation. We have not yet had the time to try this approach but we have produced some guided strontium beams (section 6.1) which could be considered precursor steps. It remains something we are looking at.

Direct cooling with a dimple trap If a dimple is placed within a reservoir it is possible to locally increase the density without affecting the temperature. This will push the local critical temperature above the reservoir temperature and a BEC can form in the dimple. With a sufficiently deep dimple the density increase can be large enough to push the critical temperature above what can be achieved using only laser cooling. As long as the dimple is dark enough it is possible to generate BEC in this way using only laser cooling. This approach was described in a variety of theoretical proposals [173, 189–191] and it is the basis of the laser cooling to degeneracy paper

from our group [192]. To make this scheme steady-state, you need to make the dimple extremely dark, the laser cooling very weak and find a way to refill the reservoir without heating it. This approach is the basis of the work described in this thesis and will be described in more detail in section 1.5.

Direct cooling in a lattice There was heroic effort (and progress) in the quest to reach phase-space densities high enough for degeneracy by direct laser cooling. These began with efforts like the dark spot MOT [113], Raman cooling [193, 194] and velocity selective coherent population trapping [195] and in the end focussed on using such techniques on atoms trapped within deep lattices. Vladan Vuletic [196] and Andrew Kerman [197] in Chu's group, and Han and others from David Weiss's group [198, 199] as well as others [200] made great progress in the late 90s. The ultimate result during this first series of attempts was produced by Han [198] in 2000 where a pulsed 3D Raman sideband cooling sequence in a deep lattice reached a phase-space density of 0.03 in caesium. A few months later Katori's group [201] pulsed laser cooled ^{88}Sr loaded in a dipole trap to a phase-space density exceeding 0.1 using just simple Doppler cooling on the 7.4 kHz line. These records stood for well over a decade until finally, in 2017 the group of Vuletic [202] revisited this area using ^{87}Rb. They demonstrated that Raman sideband cooling in a lattice interlaced with phases of thermalization can reach quantum degeneracy.

Other direct cooling A creative steady-state magnetic loading and Sisyphus cooling scheme was developed by the group of Axel Griesmaier and Tilman Pfau. This approach [203–206] is described in figure 1.9. Griesmaier *et al.* [205] demonstrated a steady-state phase-space density of 4×10^{-4} for chromium loaded in a dipole trap. This work held the record for the highest steady-state phase-space density until the work described in this thesis.

A feedback mechanism is an essential part of any atom laser the same way it is for an optical laser. Without feedback there is no linewidth narrowing and there will be a short coherence length. In optics a laser without feedback is an amplified spontaneous emission (ASE) source. If a beam of atoms were to evaporatively cool past the transition temperature, without a seeding matter-wave source a condensate would grow from vacuum fluctuations and would be in effect a matter-wave ASE source. The same is true of all the unseeded matter-wave amplifiers we will discuss. There might be many interesting theoretical and experimental questions to be asked about how the coherence of such a beam might behave: Would the coherence propagation depend on the speed of the beam? Would it break up into coherent domains? These are questions which could be explored with the machine we have built.

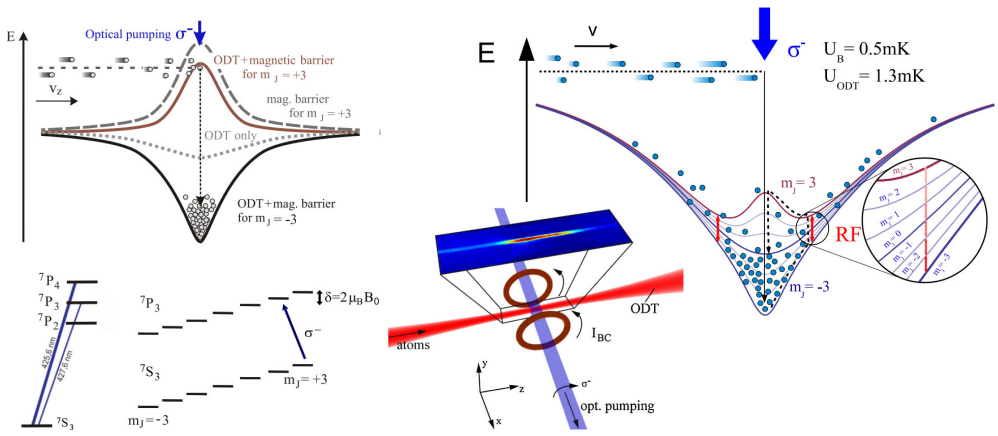

FIGURE 1.9: **Steady-state chromium with PSD=4×10^{-4}.** The chromium work lead by Axel Griesmaier and Tilman Pfau used a novel magnetic deceleration and loading scheme followed by a Sisyphus cooling scheme to demonstrate a steady-state phase-space density of 4×10^{-4} [205]. Until our work [207] this was the highest demonstrated steady-state phase-space density. Figures reproduced from [203, 205]

1.4.2 Scattering

All the previous approaches were based on the idea of "cooling to degeneracy". The next set of approaches instead begin with condensates or material with a high phase-space density produced by normal means offline perhaps in parallel or in a separate chamber. These pump condensates can be carried using a dipole trap or a lattice and then used to provide gain to a seed condensate or matter-wave you wish to coherently refill or amplify. The key is to preserve the coherence, which means there must be a mechanism for removing the entropy between the pump and the seed condensates.

Most of these approaches are based on some sort of 4-wave mixing or scattering process which can be stimulated by the presence of a strong matter-wave. If you wish to perform matter-wave amplification at least one of the input beams in a 4-wave mixing process (optical beam 1, optical beam 2, matter-wave before interaction, matter-wave state after interaction) must be seeded from vacuum fluctuations in order to remove the entropy. Table 1.2 summarizes the nomenclature used for the different types of scattering as this can be confusing.

Pumping using resonant light If you create two mode-matched condensates in different electronic states it is possible to pump or stimulate one condensate to scatter into the other and thus provide gain. This conceptually elegant approach was described

TABLE 1.2: **Scattering types.** Nomenclature used for the different types of scattering.

Scattering Type	Optical Pump 1	Optical Pump 2	Change of internal state?	Suitable for matter-wave amplification?
Resonant	Resonant	None	Yes	Yes [208]
Rayleigh	Off-resonant	None	No	Yes[d]
Superradiant Rayleigh	Off-resonant	None[a]	No	Yes [159–163]
Bragg	Off-resonant	Off-resonant	No	No[b] [163]
Raman	Off-resonant	Off-resonant	Yes[c]	No[b]
Superradiant Raman	Off-resonant	None[a]	Yes[c]	Yes[159, 164, 165]

[a] Although there is no second optical pump beam an output matter-wave is seeded from vacuum fluctuations and previous interactions. This seeded matter-wave output is phase matched and further stimulates and enhances the scattering process. This is the 'superradiant' aspect.

[b] Bragg and Raman scattering have fully defined output matter-wave phases so there is no way to remove the entropy needed to automatically ensure phase matching. But using feedback it is possible to coherently combine condensates and thus provide gain or amplification [163].

[c] Although no resonant light is present the difference between the two optical frequencies matches the difference between two internal states so an internal state is changed via a "virtual" state.

[d] Insufficient gain?

by [209, 210] and demonstrated by Robins *et al.* [208] in 2008. They showed condensate gain and output of an atom laser. Their scheme used ^{87}Rb and is described in figure 1.10. This system achieved pump to seed transfer efficiencies of 35% with 7×10^5 atoms in the pump condensates. Pumping depleted the pump condensate over a period of 0.2 s thus demonstrating a peak transfer rate of 1×10^6 atoms/s. After depletion, new condensates need to be manufactured and loaded, a process taking on the order of 30 s but nevertheless this demonstrated conceptually the feasibility of such an approach.

Superradiant lasers An approach studied by Helmut Ritsch [211] has proposed that a thermal beam used to pump a steady-state supperradiant laser might emerge as a steady-state atom laser provided it enters the system cold and dense enough. This is an approach I hope to explore as part of the iqClock project.

Superradiant Rayleigh Scattering Superradiant Rayleigh scattering and matter-wave amplification has been demonstrated by several groups in [159–162] generally in the form of amplified spontaneous emission source. In Rayleigh scattering an incident off resonant photon is scattered without changing an atom's internal state. In the presence of a strong matter (or optical) wave the scattering process can be stimulated. When scattering atoms from a condensate this process can be further enhanced by the initial correlations in the atoms. On average the recoiling atoms move the same

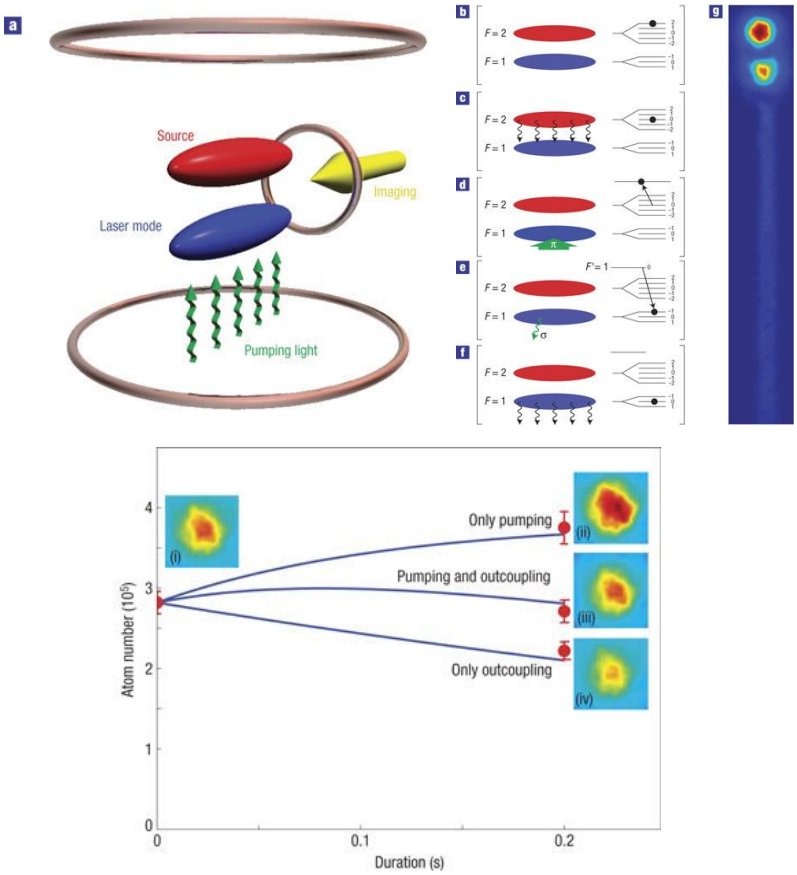

FIGURE 1.10: **A pumped atom laser.** The steps for creating a pumped atom laser using ^{87}Rb: (a) Begin with two trapped condensates, one condensate in F=1, m_F=-1 (blue) and a second in F=2, m_F=2 (red). These condensates will be spatially offset due to their different magnetic states. (b) A radio-frequency field spin-flips the red condensate from m_F=2 to the magnetically untrapped m_F=0 state. (c) The untrapped atoms fall under gravity. (d) When the falling atoms overlap with the blue condensate a π pulse is used to optically excite the falling atoms to the F'=1 excited state. (e) These excited atoms are stimulated to emit a photon and scatter into the same mode as the blue condensate, providing gain to the blue condensate. The atomic momentum of the falling atoms is cancelled by the absorption and emission of the photons (d,e). (f) Optionally a second radio-frequency field can be used to out-couple the atoms from the F=1, m_F=-1 to the untrapped m_F=0, thus forming an atom laser. (g) Absorption image of the experimental system, showing source, laser mode and output beam. (bottom) The evolution of the atom number in dependence of pumping and atom laser out-coupling. Figure reproduced from [208]

way so a recoiling matter-wave can build up from vacuum fluctuations. This output matter-wave is phase matched further enhancing the scattering process providing the superradiant aspect. If the condensate is elongated (cigar shaped) photons scattered down the length of the condensate have a much greater chance of stimulating scattering than photons scattered in other directions. Thus, there is gain for these optical modes and the corresponding matter-wave modes. Note that scattering down the length of such a condensate will be strongly suppressed if the pump polarization is parallel to the long axis of the condensate. Similarly, a scattered matter-wave will interfere with the original condensate forming a grating which stimulates scattering of incident photons into the corresponding optical mode resulting in gain for the optical mode and the original matter-wave mode. Since the speed of the matter-wave is slow compared to light, the scattered matter-wave remains long after the scattered light has left the condensate and can stimulate coherent scattering across multiple independent pump light pulses. In the same way, we may begin with a seed matter-wave rather than noise thus demonstrating a matter-wave amplifier. A problem with superradiant Rayleigh amplifiers is that since there is no change of state between the original pump BEC and the amplified matter-wave, there is nothing to prevent this process from cascading [159] to produce gain for an array of matter-wave momentum states. An example of superradiant matter-wave amplification is reproduced from [159] in figure 1.11.

Superradiant Raman scattering When superradiant Rayleigh scattering is suppressed by using a pump polarization parallel to the orientation of the condensate and when there is a particular state strongly favoured by a Raman transition it is instead possible to scatter atoms using a Raman transition. The threshold pump intensity is significantly higher than for Rayleigh scattering. The processes for stimulated and superradiant Raman scattering are very similar to those of Rayleigh scattering except that the transfer is unidirectional and can't be cascaded since atoms in the output matter-wave do not see the Raman pump pulse as the detuning is so much larger. This results in a much cleaner transfer from the pump condensate to the resulting output matter-wave. Like Rayleigh, this process may act as a coherent amplifier for a matter-wave. Superradiant Raman scattering and amplification has been demonstrated in [159, 164, 165].

1.4.3 Coherent combination

Finally, we can use coherent combination to produce constructive interference for a chosen matter-wave. In these systems *all* the input waves are defined, there are no vacuum inputs

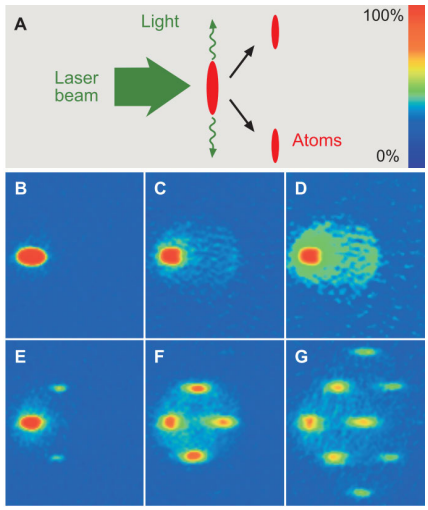

FIGURE 1.11: **Superradiant Rayleigh scattering.** An example of superradiant Rayleigh scattering (figure reproduced from [159]). (A) An elongated condensate is illuminated with a single off-resonant laser beam. Collective scattering leads to photons scattered predominantly along the axial direction and atoms at 45°. (B to G) Absorption images show the atomic momentum distribution after their exposure to a laser pulse of variable duration. When the polarization was parallel to the long axis, superradiance was suppressed, and normal Rayleigh scattering was observed (B to D). For perpendicular polarization, directional superradiant scattering of atoms was observed (E to G) and evolved to repeated scattering for longer laser pulses (F and G). The pulse durations were 25 (B), 100 (C and D), 35 (E), 75 (F), and 100 (G) ms. The field of view of each image is 2.8 mm by 3.3 mm. The scattering angle appears larger than 45° because of the angle of observation. All images use the same color scale except for (D), which enhances the small signal of Rayleigh scattered atoms in (C). Figure reproduced from [159].

so it is critical to phase match the input matter-wave to produce a constructive rather than destructive (or random) feedback.

Parametric amplification BEC constitutes a highly nonlinear medium. Using three wave or four wave mixing between condensates with different momenta you can generate gain. Phillips, Deng, Hagley and others [212] showed that it is possible to transfer atoms from a pump to a seed condensate in a four-wave mixing process and thus produce matter-wave amplification. This is analogous to an optical parametric amplifier or an optical parametric oscillator.

Coherent combination Mixing of matter-waves does not have to be via nonlinear interactions. We can also make a Bragg or Raman beam splitter, for example with a $\pi/2$ pulse to mix two momentum or electronic states. If the phase of the input matter-waves is

chosen correctly and maintained via a feedback mechanism you can constructively interfere the input matter-waves and thus produce gain for a chosen mode. This is easier said than done because the phase of a matter-wave can only be defined in a relative sense. We always need to interfere a matter-wave with some other matter-wave local oscillator to measure a phase. On the positive side matter-waves move slowly so compared with optics it could be much easier to implement fast feedback loops to maintain locks. There has been much work discussing measurement and feedback schemes [213, 214].

1.5 Steady-state BEC - Why here, why now?

In 2013 our group published the first BEC using only laser cooling to remove entropy [192]. This was achieved by placing a dimple in a reservoir of laser cooled atoms. The dimple raised the local density sufficiently that the critical temperature in the dimple exceeded the temperature of the laser cooled reservoir. The key new idea was the realization that with such a narrow 7.4 kHz cooling transition in strontium, it is feasible to locally Stark shift the resonance of the cooling transition by tens or even hundreds of linewidths. In this way a dark spot was produced which was much darker than any previous dark spot, enough to even protect a BEC under resonant light. Thus, this long proposed route to BEC [173, 189–191] finally became reality.

This achievement made the related goal of a steady-state BEC and a steady-state atom laser finally seem within reach. No longer was it necessary to turn off the light on the laser cooling transition and no longer was an evaporative cooling sequence necessary. From a laser cooled cloud loaded in a reservoir dipole trap all the way to BEC, there was no need to change the dipole trap powers and no need to change the laser intensities or frequencies. A steady-state system appeared on the verge.

There were apparently two problems left to solve to make a steady-state BEC:

1. We needed to build a new machine in which the BEC location is completely protected from the 30.5 MHz linewidth blue cooling light. There is no way we can protect a BEC from blue light by Stark shifting, the shifts required are just too big. Therefore, protection would need to come from a multichamber design with in-vacuum baffles to protect against scattered blue light.
2. A steady-state machine would need to be able to produce a steady-state red MOT cold enough to couple to and replenish the atoms in the reservoir. This MOT would need to capture and load atoms sent from a second chamber using only the weak 7.4 kHz 689 nm transition.

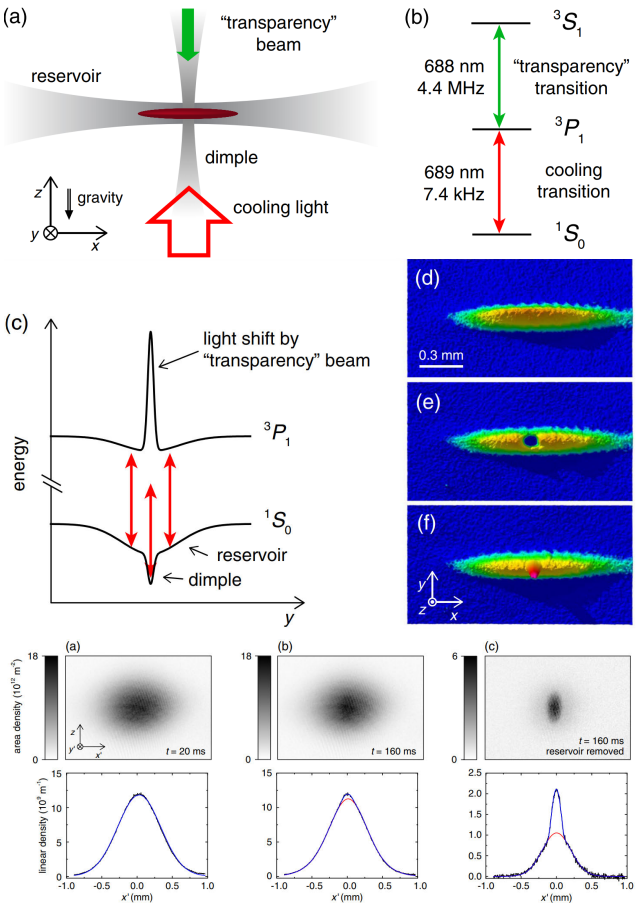

FIGURE 1.12: **Laser cooling to degeneracy.** (a) The laser and dipole trap configuration (b) The cooling transitions and the transparency transition used to Stark shift the $^3P_1$ state. (c) Resulting potential energy landscape for the $^1S_0$ ground and $^3P_1$ excited states. (d) Absorption image on the $^1S_0$-$^3P_1$ transition of atoms loaded into the reservoir trap. (e) Absorption image on the $^1S_0$-$^3P_1$ transition of atoms loaded into the reservoir trap with the transparency beam applied which shifts a patch out of resonance imaging light. (f) Absorption image on the $^1S_0$-$^3P_1$ transition of atoms loaded into the reservoir trap with the dimple (but not transparency) beam applied. (bottom-a,b) Formation of a BEC in 160 ms. (bottom-c) Improved visibility by 'blowing away' the reservoir. Figures reproduced from [192].

In December of 2013 I moved from working on rubidium with Nick Robins at the Australian National University to join Florian's group and begin designing a new strontium machine to meet these goals. We started with no funding hoping to borrow a bit of money from the RbSr/SrMic grant and Florian's start up grant. In 2014 Benjamin received a Veni grant and the following year Florian received a Vici grant which together with the scholarships Chun-Chia and I brought with us (from Australia and Taiwan) made building this new machine possible. This thesis is the story of the following five years and our strontium continuous/perpetual atom laser (SrCAL/SrPAL) machine.

1.6 Thesis Outline

This thesis will describe our work which aimed to build the first steady-state source of BEC and a steady-state atom laser.

It will not be a succinct account of our design, results and conclusions, the way I would write a paper. Instead it will describe failures and mistakes as much as it will describe successes. Most of all it will describe lessons we learned the hard way, things I wish I had known before we started, the things you will never learn from reading papers. This thesis is written in the hope that these words might spare future machine builders some of our trials and it is written as a manual for future users of our machine.

In the following chapter (chapter 2) I will describe the properties of strontium, our species of choice. The aim is to introduce strontium to the reader as well as provide a reference containing the data, properties, equations and tools that we use in the lab every day. This way, during the next US government shutdown we can still find our repump transitions even though the NIST atomic spectra database [215] might be offline.

Chapter 3 describes the detailed design and construction of our strontium continuous atom laser (SrCAL) machine. This should be read in conjunction with Chun-Chia's thesis [216] which describes particularly the laser systems in greater detail. While I have tried to provide a lot of pictures which show detail far beyond the text, in the end the CAD designs should also be considered important if not essential supplementary material.

Our first attempt to make a steady-state BEC is described in chapter 4. Our concept was to take the architecture demonstrated by the laser cooling to degeneracy work [192] and couple it with a steady-state MOT on the 7.4 kHz transition. This was the initial architecture we had in mind when we were designing the machine. In this work we achieved the highest ever steady-state phase-space density in an ultracold atomic system. We developed protection schemes that could protect a BEC even under intense resonant red light with lifetimes of 1 s and we showed that we could protect a BEC from scattered resonant blue light.

Chapter 5 reproduces our paper published in PRL [207]. It describes our steady-state red MOT which achieved a phase-space density of $(1.2 \pm 0.2) \times 10^{-3}$. Today this remains the highest ever steady-state phase-space density published. The phase-space density exceeded that of all previous steady-state MOTs by more than two orders of magnitude.

Chapter 6 will describe our second attempt at making a steady-state BEC. Here we created a dipole trap guided atomic beam with a peak phase-space density of $(1.4 \pm 0.6) \times 10^{-4}$. This beam, co-aligned with a dark cylinder, transported atoms away from our steady-state red MOT to a darker region. The atoms were then slowed and loaded into a second dipole trap with a protected dimple where we attempted to condense them. By moving our atoms to a cold dark place and minimizing the light we applied we managed to reach a steady-state phase-space density of 1.7 ± 1.1. This result is a further three orders of magnitude better than the current published state of the art steady-state phase-space density. Perhaps mistakenly we haven't published this result, because it lies so close to our goal of degeneracy, a much bigger and higher impact result. I will end this chapter with a description of the improvements we have now made or are making to try to push this phase-space density over the limit and finally reach degeneracy.

Chapter 7 reproduces a preprint [217] we wrote on a new deceleration technique we demonstrated, the Sisyphus optical lattice decelerator. This techniques uses a lattice on only the excited state to slow atoms instead of using radiation pressure. The advantages of this approach are that we achieve a colder sample, we reduce the required light intensities and we don't need to use a counter-propagating resonant beam to slow our beam of atoms. The technique we experimentally demonstrated can in principle be used to slow a broad range of species. Similar techniques have been proposed to slow anti-hydrogen [218]. This is one of the ways we are trying to improve the performance of our system in order to reach degeneracy.

I will end with a few brief remarks on the paths to steady-state BEC that we did not take and which I hope might still be taken with the SrCAL machine or its successor.

Chapter 2

Strontium: The tool box

Atoms are our tools and by knowing them we can manipulate and bend them to our will. This chapter will describe and discuss the key properties of strontium used throughout this work.

2.1 Physical properties

Property	Value
Molar Mass	$87.62\,\mathrm{g}\cdot\mathrm{mol}^{-1}$
Density (room temperature)	$2.64\,\mathrm{g}\cdot\mathrm{cm}^{-3}$
Melting Point	$777\,^{\circ}\mathrm{C}$
Boiling Point	$1377\,^{\circ}\mathrm{C}$
Thermal Conduction	$35.4\,\mathrm{W}\cdot\mathrm{m}^{-1}\cdot\mathrm{K}^{-1}$
Thermal Expansion	$2.25\times10^{-6}\,\mathrm{K}^{-1}$
Resistivity	$1.32\times10^{-7}\,\Omega\cdot\mathrm{m}$
Heat of Fusion	$84.8\,\mathrm{J}\cdot\mathrm{kg}^{-1}$
Heat of Vaporization	$1610\,\mathrm{J}\cdot\mathrm{kg}^{-1}$
Specific Heat Capacity	$301\,\mathrm{J}\cdot\mathrm{kg}^{-1}\cdot\mathrm{K}^{-1}$

TABLE 2.1: Physical properties of strontium.

Strontium is a light weight alkaline-earth metal. Its key physical properties are summarized in table 2.1. The partial vapour pressure for Sr [219, 220], P (Pa) is given as a function of temperature T (in K) by equation 2.1 and plotted in figure 2.1.

$$\log_{10}[P] = 14.232 - \frac{8572}{T} - 1.1926\log_{10}(T) \tag{2.1}$$

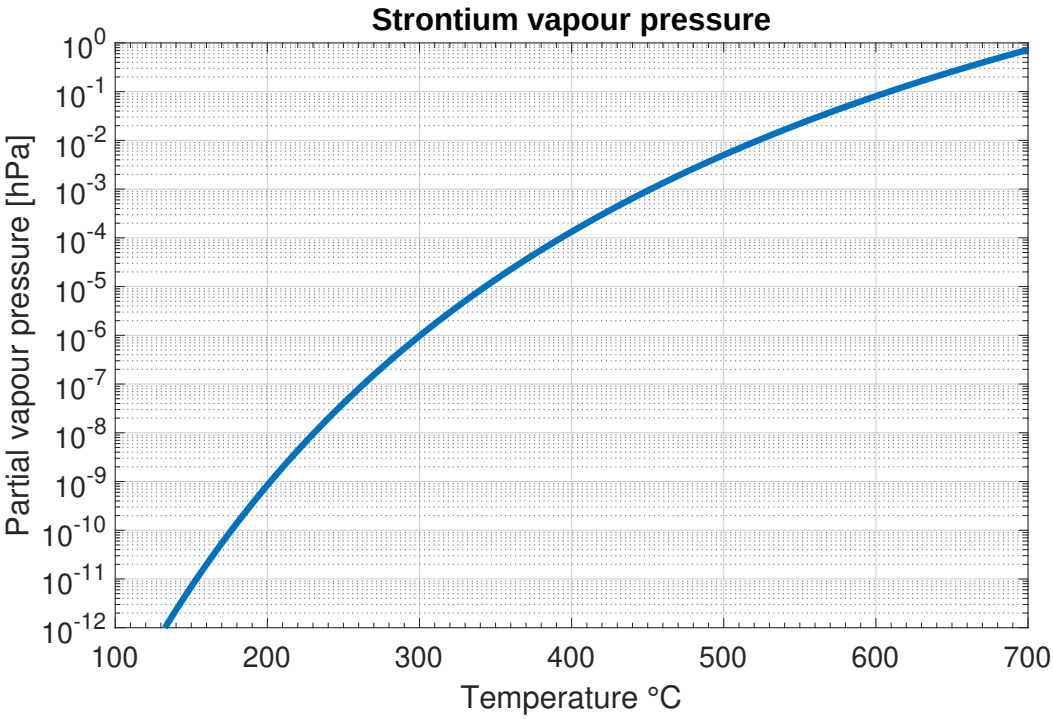

FIGURE 2.1: Partial vapour pressure curve for strontium.

2.2 Isotopes

There are four natural isotopes of strontium, three bosons and a fermion. Table 2.2 summarizes their properties.

Perhaps surprisingly in popular culture strontium is known as a radioactive "bogeyman" attributed to the creation of mutants such as *Strontium Dogs* [221]. These refer to ^{90}Sr, a man made isotope with a radioactive half life of 28.8 years. This isotope decays by beta radiation and because it can chemically displace calcium it is easily absorbed and retained within biological systems, making it dangerous. Its half life makes ^{90}Sr ideal for radioisotope

isotope	mass [amu]	natural abundance	statistics	nuclear spin
^{84}Sr	83.913425(3)	0.56%	bosonic	0
^{86}Sr	85.9092607309(91)	9.86%	bosonic	0
^{87}Sr	86.9088774970(91)	7.00%	fermionic	9/2
^{88}Sr	87.9056122571(97)	82.58%	bosonic	0

TABLE 2.2: Naturally occurring isotopes of strontium, data taken from [215].

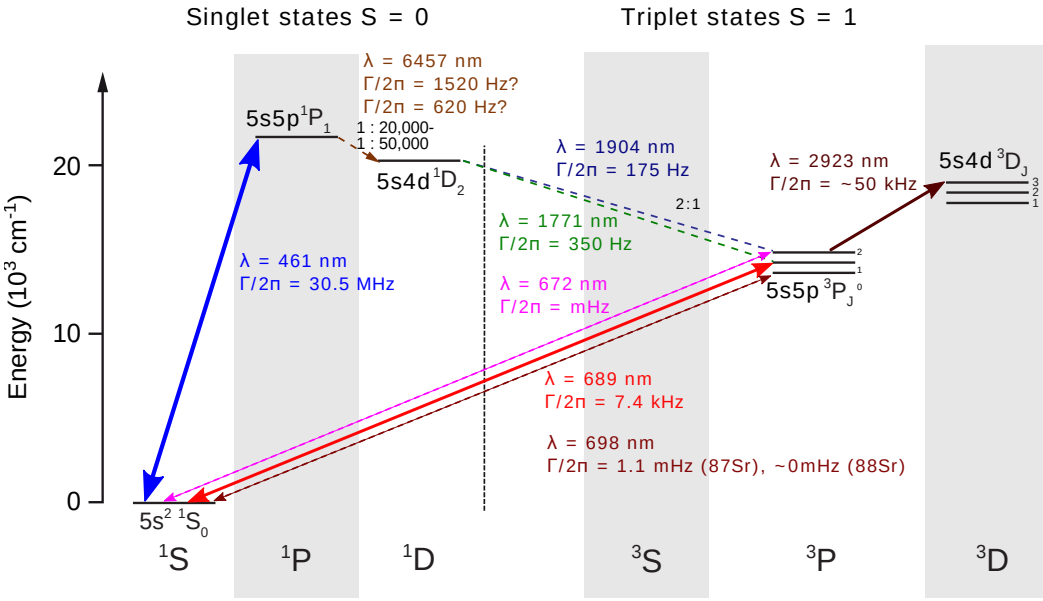

FIGURE 2.2: **Strontium laser cooling transitions.** Level diagram for strontium showing the broad 461nm and narrow 689nm cooling transitions as well as the $^1S_0$-$^3P_2$ and clock ($^1S_0$-$^3P_0$) transitions. The ionization threshold is at 45 932.09 cm^{-1} (5.69485 eV). The position of the levels is taken from [215].

thermoelectric generators (RTGs) (think of *The Martian* [222]) to provide long term power for remote devices. ^{90}Sr RTGs are said to have been deployed widely in Russian lighthouses but because it is a beta decay it needs heavy shielding so less ideal for space applications. It was also deployed widely across Europe from Chernobyl in the mid 80s as well as globally by bomb testing. We do not use ^{90}Sr.

As we shall discuss later the scattering properties are such that we need to use ^{84}Sr for processes requiring thermalization or evaporative cooling but this isotope has a very low natural abundance. For this reason I got a quote for 9g of 82% enriched ^{84}Sr from Oak Ridge produced using a calutron. This was sold by the milligram, which was quoted at 1.53M€. In our work we use natural strontium.

2.3 Laser cooling transitions

Strontium is graced with both broad and narrow laser cooling transitions. These transitions are illustrated in figure 2.2 and their properties are summarized is table 2.3.

To capture and rapidly laser cool large fluxes of atoms efficiently we require a broad laser cooling transition. The 30 MHz 461 nm transition fits this requirement almost perfectly. The

	Unit	Application		
		Broad cooling transition	Narrow cooling transition (intercombination line)	IR cooling transition
Wavelength (vacuum) λ	nm	460.862	689.4490985	2923.36
Lower State		$5s^2\ ^1S_0$	$5s^2\ ^1S_0$	$5s5p\ ^3P_2$
Upper State		$5s5p\ ^1P_1$	$5s5p\ ^3P_1$	$5s4d\ ^3D_3$
Frequency (^{88}Sr)	THz	650.503226	434.8289942	102.550486
Γ	2π MHz	30.5	7.4×10^{-3}	$\approx 50 \times 10^{-3}$
Lifetime τ[a]	ns	5.2	21.5×10^{3}	$\approx 3 \times 10^{3}$
I_{sat}[b]	$mW \cdot cm^{-2}$	40.76	2.95×10^{-3}	0.26×10^{-3}
a_{max}[c]	$m \cdot s^{-2}$	9.44×10^{5}	153	255
$T_{Doppler}$[d]	µK	732	0.178	1.2
$v_{Doppler}$[e]	$mm \cdot s^{-1}$	144	0.035	0.238
$v_{capture}$[f]	$m \cdot s^{-1}$	14	0.005	0.146
T_{Recoil}[g]	µK	1.07	0.480	0.0267
v_{Recoil}[h]	$mm \cdot s^{-1}$	10.3	6.9	1.62

TABLE 2.3: **Strontium cooling transition properties.** Key transitions for strontium, and some resulting properties. Properties are evaluated for ^{84}Sr. [215].

[a] $\tau = \Gamma^{-1}$ [223]
[b] $I_{sat} = (\pi/3) \cdot (hc/(\lambda^3\tau))$ [223]
[c] $a_{max} = h/(\lambda m) \cdot (\Gamma/2)$ [223]
[d] $T_{Doppler} = \hbar\Gamma/(2k_B)$ [223]
[e] $v_{Doppler} = \sqrt{\hbar\Gamma/m}$ [223]
[f] $v_{capture} = \Gamma\lambda/(2\pi)$ [223]
[g] $T_{Recoil} = h^2/(k_B\lambda^2 m)$ [223]
[h] $v_{Recoil} = h/(\lambda m)$ [223]

only wrinkle is that this transition is not completely closed. There is a weak 620-1520 Hz transition to the $^1D_2$ state. Because of the 5.2 ns lifetime of the $^1P_1$ state the chance of decaying to $^1D_2$ is very small, somewhere in the range of 1:20,000 [224] and 1:50,000 [225], but this is significant. The $^1D_2$ state has a lifetime of around 350 µs from which it can decay to either the $^3P_1$ or $^3P_2$ states with a ratio of 2:1 respectively [226]. An atom in the $^3P_1$ state eventually drops back to the ground state and is returned to the system but the $^3P_2$ state is metastable with a 500 s lifetime [227] effectively removing these atoms from the cycling transition. This can be an asset or a liability. The $^3P_2$ state is magnetically trappable and thus it can be used as a dark state to collect and store laser cooled atoms. This is used on both the RbSr and the SrMic machines as the loading mechanism. Alternatively, it can be a loss as it is for the atom laser machine. We discuss this in more detail in the section on

Path	Wavelength (vacuum) [nm]	Frequency [THz]	Lower State	Upper State	Ref
Red	322.2585322	930.2855567	5s5p $^3P_1$	5s20s $^3S_1$	[215, 230, 231]
	318.1889236	942.1838277	5s5p $^3P_1$	Sr II Limit	[215]
Blue	418.6599924	716.0762038	5s5p $^1P_1$	5s20d $^1D_2$	[215, 232]
	412.6476232	726.5095959	5s5p $^1P_1$	Sr II Limit	[215]

TABLE 2.4: **Additional wavelengths which can be used to access Rydberg transitions.** Laser wavelengths required to access Rydberg states or for ionization of strontium via the blue or red paths.

repumping transitions (Section 2.5).

The 461 nm transition can not cool atoms below 1 mK. Fortunately a second transition at 689 nm, the intercombination line is able to address this. With a linewidth of just 7.4 kHz this transition is able to directly Doppler cool into the nanokelvin range while still being strong enough to provide sufficient radiation pressure to support atoms against gravity in a MOT. This sweet linewidth gives strontium a special place among the alkaline-earths, able to get colder than ytterbium (556 nm, 183 kHz) but not so weak as calcium (657 nm, 414 Hz/ 8.6 $m \cdot s^{-2}$).

A little discussed and thus far untested potential cooling transition for the $^3P_2$ state lies at 2923 nm. $^3P_2$ is magnetically trappable as well as completely dark and protected from the first stage 461 nm cooling light. In a conventional pulsed machine it is easy to turn off your blue light when you want to use red to get colder. But, for a steady-state machine, being unable to protect against the blue light and being unable to turn it off is a major challenge. In the work we present in this thesis this challenge is addressed by moving the atoms a long way and around a corner so there is no line of sight with the harmful blue light, allowing you to cool with the gentle red transition. This is an awkward, brutish solution to the problem which results in a large machine and heavy losses. An elegant solution is perhaps to use the 2923 nm transition towards $^3D_3$ which has a larger but still narrow ($\approx$50 kHz) [228, 229] linewidth to cool and directly load atoms from a blue MOT into a waveguide for transport to a dark protected place, where they can be returned to the ground state and used or condensed. We will discuss this more later (Section 6.1).

Although we barely touch upon it in this work Rydberg atoms remain highly topical so we will briefly mention them. Accessing Rydberg states can be achieved by many paths. One commonly used route is to use the $^3P_1$ or $^1P_1$ states as an intermediary. The red path where an atom is first raised to the $^3P_1$ state using 689 nm is a little more challenging as it requires 320 nm UV lasers (albeit of very low power). The other option, the blue path first excites to $^1P_1$ using 461 nm and requires only an easily constructed 415 nm laser. These are

summarized in table 2.4. Constructing the laser is of course only part of the problem, the other issue is the need to stabilize the laser to a reference cavity.

2.4 Metastable states and the clock transition

The ^{3}P states in strontium are metastable in that they can not in principle decay to $^1S_0$ by a single photon. In practice they can decay through higher order processes but they have long lifetimes. The $^3P_1$ lifetime is quite modest at 21 µs as spin-orbit interaction mixes some $^1P_1$ state contribution into $^3P_1$ [34, 107]. As a result, this state is not typically referred to as metastable. The $^3P_2$ state has a calculated lifetime of 1000 s [34, 233] reduced in practice to around 500 s by thermal radiation exciting the ^{3}D states which can decay to the ground state via $^3P_1$ [107, 227]. The $^3P_0$ state is the clock state. For $^3P_0$ spin-orbit interactions are absent and with bosons $I = 0$ so there is also no hyperfine coupling. In this case the dominant decay path will be a two-photon decay with a lifetime calculated to be thousands of years [234]. However, in the presence of thermal blackbody radiation excitation to the $^3D_1$ on the 3 µm transition, opens a decay channel via $^3P_1$ in much the same way as for $^3P_2$. For the fermionic ^{87}Sr, the nuclear magnetic dipole moment couples $^3P_0$ to other states of the same parity such as $^1P_1$ and $^3P_1$ resulting in a lifetime of the order of 100 s [34, 107, 234, 235]. In addition, transitions from the metastable ^3P states to higher singlet states can be used to quench the lifetime of these metastable states [133, 236].

Transitions to the metastable states are shown on figure 2.2. For fermionic ^{87}Sr the 698 nm $^1S_0$-$^3P_0$ strontium clock transition at 429.228 004 229 873 65(37) THz [22, 237] (429.228 066 418 008 3(19) THz [238] in ^{88}Sr) is currently used in today's most precise clocks [26, 28]. In addition to metrology the exquisite precision of this transition offers the potential for studying physics on very small energy scales and thus forms the basis of many proposals across quantum computation, simulation and sensing [25, 46–54, 239]. Atom interferometry on this transition has been proposed for a new generation of space-based gravitational wavesensors [46, 59]. One down side is the problematic 3 µm transition out to $^3D_1$ which is Stark shifted by thermal blackbody radiation. This is intensively studied for clock applications [240, 241].

Most clocks use ^{87}Sr rather than ^{88}Sr for its comparatively broad mHz level transition and its fermionic suppression of the interaction shift. For ^{88}Sr the transition strength can be tuned using an external magnetic field to induce a coupling to other states of the same parity, the same way the internal magnetic field does in ^{87}Sr. Another approach is to introduce a weak Raman coupling [242] although this has the difficulty that it is hard to control the resulting Stark shifts. In the outlook (section 8.3) we will briefly describe our work towards building a steady-state superradiant clock using this transition.

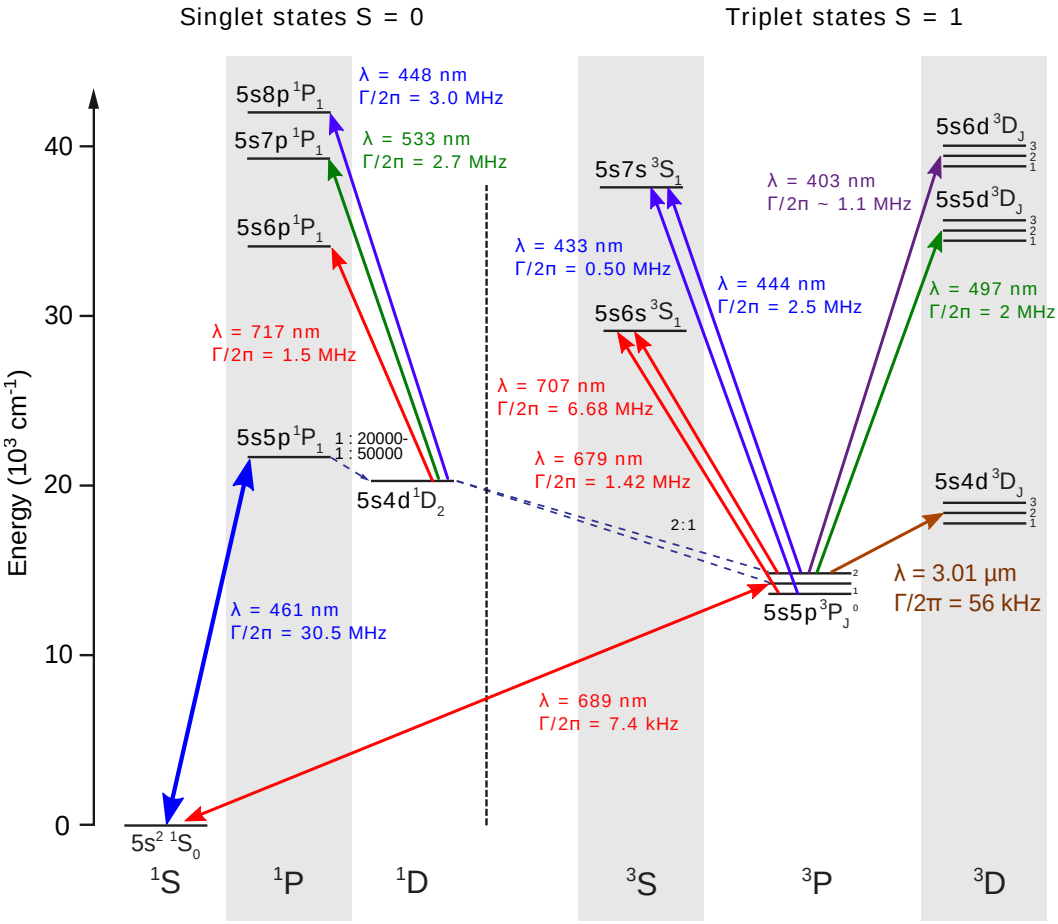

FIGURE 2.3: **Strontium repump transitions.** Level diagram for strontium showing actual and potential transitions suitable for repumping $^3P_0$ and $^3P_2$. Our machine presently uses the 679 nm, 707 nm transitions while other machines in our group use the 497 nm transition. We are currently also characterizing the 448 nm repump option [244].

The 671 nm $^1S_0$-$^3P_2$ fermionic transition is magnetically sensitive so it is not used as a clock. It may however be useful for magnetic sensing and in quantum simulation experiments where you wish to use or measure the magnetic properties or need to access additional magnetic sublevels. The location of this transition was recently probed by the SrMic team [243].

Wavelength (vacuum) [nm]	Frequency [THz]	$\Gamma\,[(2\cdot\pi)^{-1}$, MHz]	Lower State	Upper State
3011.831	99.53826	0.056	$5s5p\ ^3P_2$	$5s4d\ ^3D_2$
496.9328	603.2857	2.04	$5s5p\ ^3P_2$	$5s5d\ ^3D_2$
403.3517	743.2532	1.1	$5s5p\ ^3P_2$	$5s6d\ ^3D_2$
707.2022	423.9134	6.70	$5s5p\ ^3P_2$	$5s6s\ ^3S_1$
679.2894	441.3325	1.42	$5s5p\ ^3P_0$	$5s6s\ ^3S_1$
443.9289	675.3164	2.47	$5s5p\ ^3P_2$	$5s7s\ ^3S_1$
432.7661	692.7355	0.493	$5s5p\ ^3P_0$	$5s7s\ ^3S_1$
716.9117	418.1721	1.50	$5s4d\ ^1D_2$	$5s6p\ ^1P_1$
533.1294	562.3259	2.70	$5s4d\ ^1D_2$	$5s7p\ ^1P_1$
448.1803	668.9105	3.02	$5s4d\ ^1D_2$	$5s8p\ ^1P_1$

TABLE 2.5: **Strontium repump transitions.** Repump transitions for strontium [215]. The linewidth for the 403 nm transition is from [245, 246].

2.5 Repump transitions

In our atom laser work the presence of the metastable states results in loss. For this reason we must repump atoms that fall into $^3P_0$ and $^3P_2$ back to the ground state via some intermediate state. There are many possible paths and for the most part it is a question of finding the simplest laser to make. Figure 2.3 shows a range of repump transitions which have been used or considered for repumping.

There are three basic repumping approaches.

Repump via $^3D_2$ After pumping from $^3P_2$ to the $^3D_2$ states an atom must either decay to the ground state via $^3P_1$ or return to $^3P_2$ with a ratio of approximately 3:1 respectively [245]. Importantly to first order ($\approx 1\%$ [245]) there is no path to the metastable $^3P_0$ state so a single laser is sufficient to eventually send the entire $^3P_2$ population to the ground state. There are several wavelength choices. The 497 nm 5d $^3D_2$ is commonly used and is used in both the RbSr and SrMic machines. [107]. There was not sufficient power available to also use the existing laser for the SrCAL machine. At the time of construction single mode diode lasers at 497 nm were not available so a very expensive frequency doubled system would have been required. Recent work [247] indicates that this wavelength is now available, so this looks much more attractive for future work. The availability of blue ray diodes makes the 403 nm 6d $^3D_2$ transition attractive. This was explored by Simon Stellmer [245] but the high lying energy level suffers from a higher branching ratio to the ground state [245]. A third 3 µm 4d $^3D_2$ option is made difficult by the cost of lasers in the mid-IR, the difficulty of working in the mid IR due to the incompatibility of cameras, powermeters, IR

cards, optics and the need for specialized vacuum chamber windows such as ZnSe or CaF_2. These difficulties effectively rule out the 4d $^3D_2$.

Repump via $^3S_1$ The $^3S_1$ decays to $^3P_{0,1,2}$ in the ratio 1:3:5 so unlike $^3D_2$ it can decay to both the $^3P_0$ and $^3P_2$ metastable states. For this reason repumping using these levels always requires two lasers, one from $^3P_0$ and one from $^3P_2$. Within the ladder of $^3S_1$ states the 6s $^3S_1$ and 7s $^3S_1$ have relatively accessible wavelengths but in practice it is the 6s $^3S_1$ requiring 679 nm and 707 nm which clearly stands out due to the ease of laser construction. This is the repump scheme used in SrCAL as well as numerous machines within other groups [225].

Fast repump from $^1D_2$ A new approach we (our master student Jens Samland) are currently trying is intercepting decaying atoms and repumping directly from the $^1D_2$ state before they decay to $^3P_2$. This is not a general repumping scheme as it will not affect atoms that have already decayed to $^3P_2$. Thus it is useless in schemes where $^3P_2$ is used as a reservoir to collect and store atoms such as the pulsed loading schemes of typical strontium BEC machines [106]. However, unlike all the other repumping schemes this approach can be fast as it doesn't pass through the long lived $^1D_2$ state with its ≈350 µs decay time. This is important if we want to repump atoms within a Zeeman slower where a repump time ≪100 µs is necessary to avoid drifting out of resonance. The 717 nm and 448 nm options via the 6p $^1P_1$ and 8p $^1P_1$ are easily accessible in terms of laser diode technology. The 717 nm option was explored previously [248–250] but [250] found that unfavourable branching ratios to the ^3P states limited effectiveness as a repump. Preliminary results using 448 nm have shown it to be very effective as a repump but there are several problems with trying to employ this to repump a Zeeman slower [244][1].

2.5.1 How closed is $^1S_0$-$^1P_1$?

There is a divergence of opinion on how closed the $^1S_0$-$^1P_1$ cycling transition is. Essentially, the value of Γ for the $^1P_1$-$^1D_2$ has been measured or calculated with two inconsistent sets of results. [225, 251] measure a loss rate to $^1D_2$ of 1:50,000 while [224, 246, 252] suggest a value of 1:20,000. The results are summarized in table 2.6. Our Zeeman slower optimizations

[1] A wrinkle in this cunning plan is that the σ^+ Zeeman slower pumps the atom to the $^1P_1$ m_J=+1 state which decays to the $^1D_2$ m_J=(0,+1,+2) states. To repump all magnetic sublevels we need a σ^- transition, the opposite of the Zeeman slower polarization so the Zeeman shift will anti-compensate the Doppler shift throughout the slower. As a result, a GHz broad comb of lines with ≈10 MHz spacing would be needed to repump atoms along the entire slower. Sadly this greatly increases the technical difficulty of this approach. A second problem is that atoms which decay from $^1P_1$ to $^1D_2$ are exceptional. In order for an atom to decay by this channel it must have spent an improbably long time in the $^1P_1$ during which it will have travelled a significant distance down the slower, maybe enough to already break the slower trajectory, something no repump can fix.

Type	Year	$\langle {}^1D_2 \| D \| {}^1P_1 \rangle$	Γ [2π Hz]	Loss rate	Reference
Expt.	1986		$(3.85 \pm 1.47) \times 10^3$	$1{:}(4.95 \pm 1.91) \times 10^4$	[251]
Theory	1992		1.7×10^4	$1{:}1.1 \times 10^4$	[246]
Theory	2001	1.9 a.u.	9.06×10^3	$1{:}2.1 \times 10^4$	[252]
Expt.	2003		$(3.85 \pm 0.12) \times 10^3$	$1{:}(4.95 \pm 0.16) \times 10^4$	[225]
Theory	2018	1.956 a.u.	9.6×10^3	$1{:}1.99 \times 10^4$	[224]
Expt.			$(9.3 \pm 1.9) \times 10^3$	$1{:}(2.05 \pm 0.35) \times 10^4$	

TABLE 2.6: **How closed is $^1S_0$-$^1P_1$?** There are two bodies of opinion on how closed the $^1S_0$-$^1P_1$ transition is. One says the loss rate is 1:20,000 the other says 1:50,000.

suggests that 1:20,000 might be an underestimate[2] but we have not made a careful study yet.

2.6 AC Stark shifts

Light that is intense but far detuned from any resonances will interact with an atom, shifting the energy levels and creating conservative forces without scattering light or changing an atom's electronic state. These AC Stark shifts, also known as light shifts, are the basis of optical dipole traps which we use extensively. The potential and scattering rate for a two-level system in a field far detuned from a resonance ($\Gamma_{sc} \ll \Gamma$) are given by [253] and summarized in box 2.6.1.

For the most part, these are the equations that we use for modelling dipole traps. We usually just sum terms for the blue 461 nm and red 689 nm transitions to get the potential of the $^1S_0$ ground state.

The Stark shift not only affects the potential of the $^1S_0$ ground state but also the excited states. Since the transitions originating from these states are different, an induced light shift will generally be different for different states. As a result, transition frequencies will vary as an atom moves within a light field of varying intensity. This can be a major problem for efficiently cooling on a narrow line transition where this AC Stark shift can be very large compared with the linewidth. Equations and transition data for calculating the Stark shifts can be found in numerous papers and theses but mostly it is focussed on the $^3P_0$ clock state. Significant uncertainty remains in what is known about many of the transition rates for weaker transitions, particularly the weak transitions to excited states. Therefore

[2] We do find that the current on our first Zeeman slower coil matters yet all atoms decelerated by this coil require more than 20,000 photons to stop. However, this could be due to the large proportion of the population that requires more than 20,000 photons, ie most might not make it but there are a lot of them so it still affects the flux noticeably.

Box 2.6.1: Potentials and scattering rates in dipole traps (2 level system).

$$U_{\mathrm{dip}}(\boldsymbol{r}) = -\frac{3\pi c^2}{2\omega_0^3}\left(\frac{\Gamma}{(\omega_0-\omega)}+\frac{\Gamma}{(\omega_0+\omega)}\right) I(\boldsymbol{r}) \tag{2.2}$$

$$\Gamma_{\mathrm{sc}}(\boldsymbol{r}) = \frac{3\pi c^2}{2\hbar\omega_0^3}\left(\frac{\omega}{\omega_0}\right)^3\left(\frac{\Gamma}{(\omega_0-\omega)}+\frac{\Gamma}{(\omega_0+\omega)}\right)^2 I(\boldsymbol{r}) \tag{2.3}$$

where:

$I(\boldsymbol{r})$ = Intensity as a function of position $\boldsymbol{r}$ [$\mathrm{W}\cdot\mathrm{m}^{-2}$],
ω = Light frequency [$\mathrm{rad}\cdot\mathrm{s}^{-1}$],
ω_0 = Transition frequency [$\mathrm{rad}\cdot\mathrm{s}^{-1}$],
Γ = Transition linewidth [$\mathrm{rad}\cdot\mathrm{s}^{-1}$],
Δ = Detuning $(\omega-\omega_0)$ [$\mathrm{rad}\cdot\mathrm{s}^{-1}$],
Γ_{sc} = Scattering rate [$\mathrm{rad}\cdot\mathrm{s}^{-1}$],
U_{dip} = Dipole trap potential energy [J].

Within the rotating wave approximation ($\Delta \ll \omega_0$) they can be simplified to:

$$U_{\mathrm{dip}}(\boldsymbol{r}) = \frac{3\pi c^2}{2\omega_0^3}\frac{\Gamma}{\Delta} I(\boldsymbol{r}) \tag{2.4}$$

$$\Gamma_{\mathrm{sc}}(\boldsymbol{r}) = \frac{3\pi c^2}{2\hbar\omega_0^3}\left(\frac{\Gamma}{\Delta}\right)^2 I(\boldsymbol{r}) \tag{2.5}$$

Box 2.6.2: Stark shifts in multi level atoms.

$$U_{\mathrm{i}} = -\frac{\alpha_i I}{2\epsilon_0 c}$$

$$\alpha_i = 6\pi c^3 \epsilon_0 \sum_{k,m_k} \frac{A_{Jki}(2J_k+1)}{\omega_{Jki}^2(\omega_{Jki}^2-\omega^2)} \begin{pmatrix} J_i & 1 & J_k \\ m_i & p & -m_k \end{pmatrix}^2 \tag{2.6}$$

where:

ω	= Light frequency [rad·s^{-1}]
ω_{Jki}	= Transition Frequency between states k and i (i the state whose Stark shift is being evaluated) [rad·s^{-1}]
α_i	= Polarizability of state i
I	= Intensity [W · m^{-2}]
A_{Jki}	= Einstein A_J coefficient for a transition between fine structure states k and i [rad·s^{-1}]
m_i	= Spin projection of state i
j_i	= j value of state i
p	= polarization of the light (-1=σ^-, 0=π, 1=σ^+)
$\begin{pmatrix} J_i & 1 & J_k \\ m_i & p & -m_k \end{pmatrix}$	= Wigner 3-j symbol [255]

results obtained should be treated as a guide rather than quantitatively precise. We use the transition data from [254] which is used with equation 2.6 in box 2.6.2.

We observe differential Stark shifts between the ^{1}S$_0$ and ^{3}P$_1$ $m_J = 0$ state when we cool atoms loaded into our 1.07 µm wavelength dipole trap on the non-magnetic 689 nm line. Experimentally this is around 50 kHz when using a linearly ($\sigma^+ + \sigma^-$) polarized dipole trap with power 1.6 W focussed to a $1/e^2$ waist of 15 µm×350 µm. This corresponds to a peak power of 19 kW · cm^{-2} for which the calculated peak differential shift is tabulated at 46 kHz in table 2.7. The calculated and experimentally observed shifts are in good agreement giving some confidence in these models. Improved or augmented data sets might be found in the work of references [224, 234, 241, 256, 257] and others. Significant efforts are ongoing to better understand and model these shifts as blackbody radiation in the vicinity of the 2.6 µm ^{3}P$_0$ - ^{3}D$_1$ transition can cause large shifts on the scale of clock precisions [240].

Upper State	Dipole Trap Polarization	Calculated Shift kHz
$^3P_1\ m_J = 0$	π	122
$^3P_1\ m_J = 0$	σ	46
$^3P_1\ m_J = 1$	σ^-	11
$^3P_1\ m_J = 1$	π	46
$^3P_1\ m_J = 1$	σ^+	156

TABLE 2.7: **The importance of dipole trap polarization.** Calculated differential Stark shifts for a dipole trap using 19 kW · cm^{-2} of linearly polarized light at 1.07 µm.

2.6.1 Trapping frequencies in Gaussian beams

An atom trapped in a dipole trap will oscillate. For small oscillations the trap can be approximated as harmonic and we have simple expressions for the trapping frequencies in standard geometries [253]. Key properties of Gaussian beams are summarized in box 2.6.3.

For a focussed beam with a trap depth U (given by equation 2.2) and for an atom of mass m, we have the following trapping frequencies in the radial ω_r and axial ω_z directions.

$$\omega_r = \sqrt{\frac{4U}{mW_0^2}} \tag{2.10}$$

$$\omega_z = \sqrt{\frac{2U}{mz_R^2}} \tag{2.11}$$

A second common geometry is a standing wave or lattice. In this case we have a rather large axial trapping frequency due to the high field gradients. Note that U still refers to the maximum lattice depth which takes account of power in both forward and counter-propagating beams.

$$\omega_z = k\sqrt{\frac{2U}{m}} \tag{2.12}$$

2.6.2 Transparency lasers

One of the key tools we use in this work is the ability to locally AC Stark shift the $^3P_1$ level out of resonance with the 689 nm red MOT cooling light. This key idea was proposed and demonstrated in "laser cooling to degeneracy" [192] as a means of protecting a BEC from scattering in the presence of red cooling light. A list of suitable transitions is summarized in table 2.8 and shown in figure 2.4. While Stark shifting in the MHz range is feasible for

Box 2.6.3: Gaussian beams.

We will recall that a Gaussian beam has the following properties [253]:

$$I(r,z) = \frac{2P}{\pi W_0^2} \exp\left(-2\frac{r^2}{W^2(z)}\right) \tag{2.7}$$

$$W(z) = W_0\sqrt{1+\left(\frac{z}{z_R}\right)^2} \tag{2.8}$$

$$z_R = \pi W_0^2/\lambda \tag{2.9}$$

where:

W_0 = The $1/e^2$ radius waist
P = The power
r = The radial coordinate
z = The axial coordinate
I = The intensity
z_R = The Rayleigh range
λ = The wavelength
k = $2\pi/\lambda$

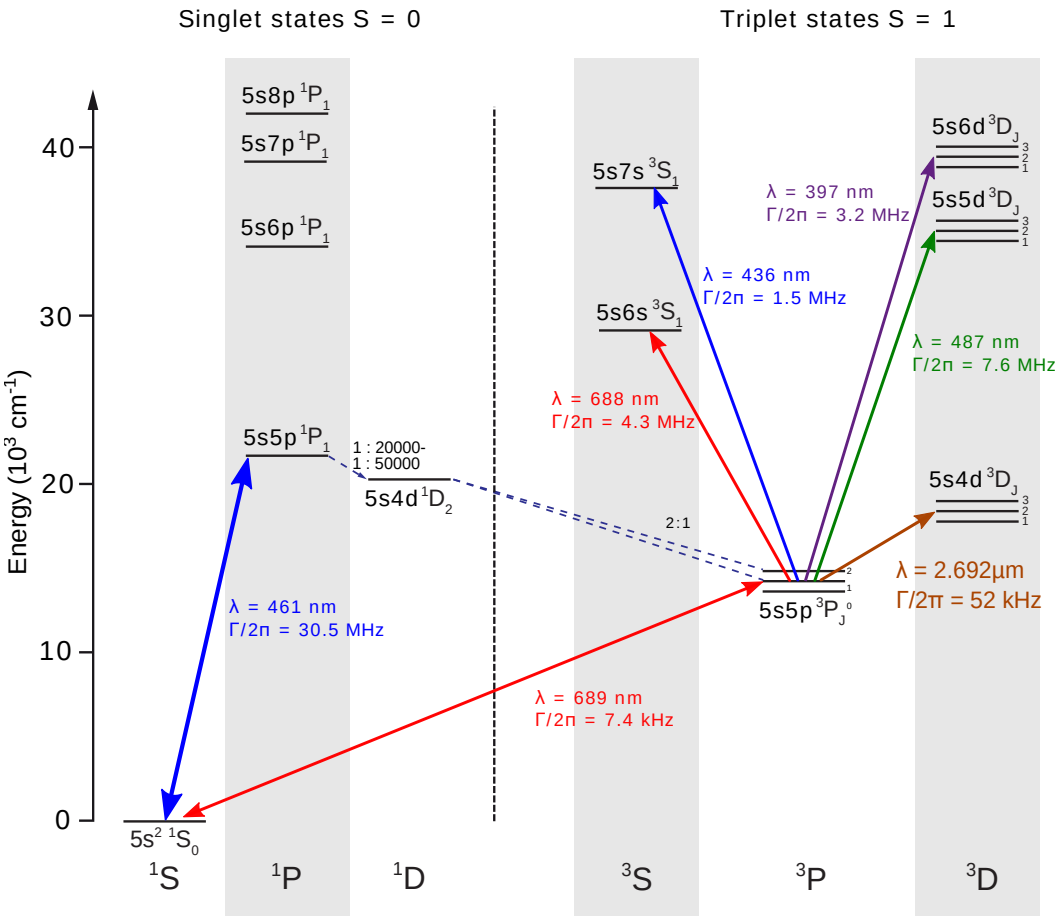

FIGURE 2.4: **Strontium transparency transitions.** Level diagram for strontium showing the actual and potential transitions for Stark shifting the $^3P_1$ transition in order to make it "transparent" and protected from 689 nm cooling light. In the work described here we use the 688 nm transition although we are presently developing the 487 nm transition as a dark state free alternative.

protecting against photons on the 7.4 kHz transition, shifting the GHz necessary to protect against photons on the 30.5 MHz transition is not.

Stark shifting using the $^3P_1$-$^3S_1$ transition In this work and in the original laser cooling to degeneracy work [192] the 688 nm $^3P_1$-$^3S_1$ transition was used. This laser wavelength is easily accessible although being so close to the 689 nm laser cooling transition means that amplified spontaneous emissions (ASE) must be filtered out to avoid excess heating. In hindsight this was possibly not the easiest solution. The problem is that if you use a single light shifting beam there is always a dark state in a J=1 to J=1

Wavelength (vacuum) [nm]	Frequency [THz]	$\Gamma/(2\pi)$ [MHz]	Lower State	Upper State
688.0211	435.7315	4.30	5s5p $^3P_1$	5s6s $^3S_1$
436.2937	687.1345	1.54	5s5p $^3P_1$	5s7s $^3S_1$
2692.189	111.3564	0.052	5s5p $^3P_1$	5s4d $^3D_2$
487.3851	615.1038	7.64	5s5p $^3P_1$	5s5d $^3D_2$
397.0386	755.0713	3.19	5s5p $^3P_1$	5s6d $^3D_2$

TABLE 2.8: **Strontium transparency transitions.** "Transparency" transitions for strontium used to locally Stark shift the $^3P_1$ state [215]. The linewidth for the 397 nm transition is from [234]. The linewidth for the 2.7 µm transition is from [229].

transition meaning at least one m_J magnetic sublevel will not be Stark shifted resulting in incomplete protection. This problem will be addressed in detail in section 4.3.

Stark shifting using the $^3P_1$-$^3D_2$ transition Another approach is to use a J=1 to J=2 transition eliminating the problem of dark states and allowing all magnetic sublevels to be shifted. The $^3D_2$ levels offer suitable options at 487 nm and 397 nm (the mid-IR 2692 nm transition is difficult in both a practical and laser sense and it is not considered further). To Stark shift a transition, high intensities are needed with a large detuning to avoid scattering. One issue with the 487 nm and to a lesser degree the 397 nm transition is that they are both close to the broad 461 nm resonance compared with 688 nm. This limits lifetimes at high intensities. Although 397 nm has a greater detuning from 461 nm compared with 487 nm it is expensive to buy and has limited power output, which combine to make the 397 nm option less attractive compared with 487 nm. We are currently developing a 487 nm laser for the transparency application.

2.6.3 Magic wavelengths

We described how different states may experience different Stark shifts in a dipole trap leading to spatially varying transition frequencies. For an optical lattice clock where atoms must be trapped in a dipole trap lattice for long interrogation times this would be a disaster. As we have already seen differential Stark shift on the order of 100kHz are typical, which would be catastrophic for a clock on a mHz transition. Fortunately there is a solution. A *magic* wavelength Stark shifts two states by the same amount, allowing the ground state potential to form a trap without affecting the level spacing and thus the transition. An *anti-magic* wavelength Stark shifts two states by the same amount in opposite directions. For example we plot the $^1S_0$ and $^3P_0$ polarizabilities in the presence of a π polarized dipole beam in figure 2.5, clearly showing the intersections corresponding to magic wavelengths.

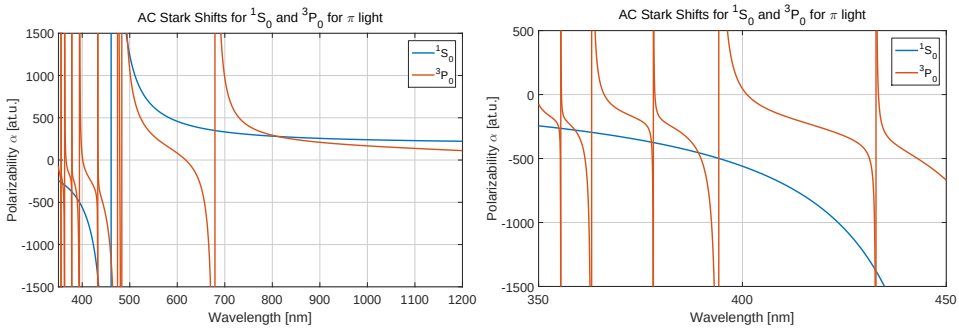

FIGURE 2.5: **Strontium $^1S_0$ and $^3P_0$ polarizabilities.** Polarizabilities of the $^1S_0$ and $^3P_0$ states in the presence of a π polarized dipole beam in atomic units $(4\pi\epsilon_0 a_0^3)$ where a_0 is the Bohr radius.

In figure 2.6 we plot the difference in the polarizabilities for each of the ^3P states which look rather like spaghetti plots. Alongside we plot the locations of the magic wavelengths for each of the states and for each dipole trap polarization, along with the slope of the polarizability with respect to wavelength. It is this last property, the slope (along with losses, whether it is trapping or anti-trapping and the availability of laser technology) which largely determines the relative usefulness of these potential magic wavelengths. Having a very gentle slope provides some tolerance for the dipole or lattice laser wavelength.

In table 2.9 we list a selection of the most suitable magic wavelengths along with their slopes based on the model. Some experimental wavelengths are also listed. Using a magic dipole trap for the potential landscape in the final cooling stages in the atom laser was not implemented in the work described here due to the lack of a suitable laser. However, it remains high on our "wish list" for its potential to cool colder and better. For the superradiant optical clock work we are now embarking on, operation at magic wavelengths is critical. Likewise, for cooling in an optical tweezers setup.

2.7 Isotope shifts

All the isotopes of strontium are readily accessible by using a couple of AOMs to compensate for the isotope shifts before generating the various cooling beams. These shifts are listed in table 2.10. The fermionic isotope ^{87}Sr is a little more complicated due to its hyperfine structure. In practice typically two frequencies are required in a $^1S_0$-$^3P_1$ MOT running on ^{87}Sr, one tuned to the F=11/2 state and another mixing or stirring frequency on the 9/2 state [266]. Making the SrCAL machine run on ^{87}Sr was a passion of Chun-Chia's, which turned out to be quite difficult. We did however get this working. This is also a very

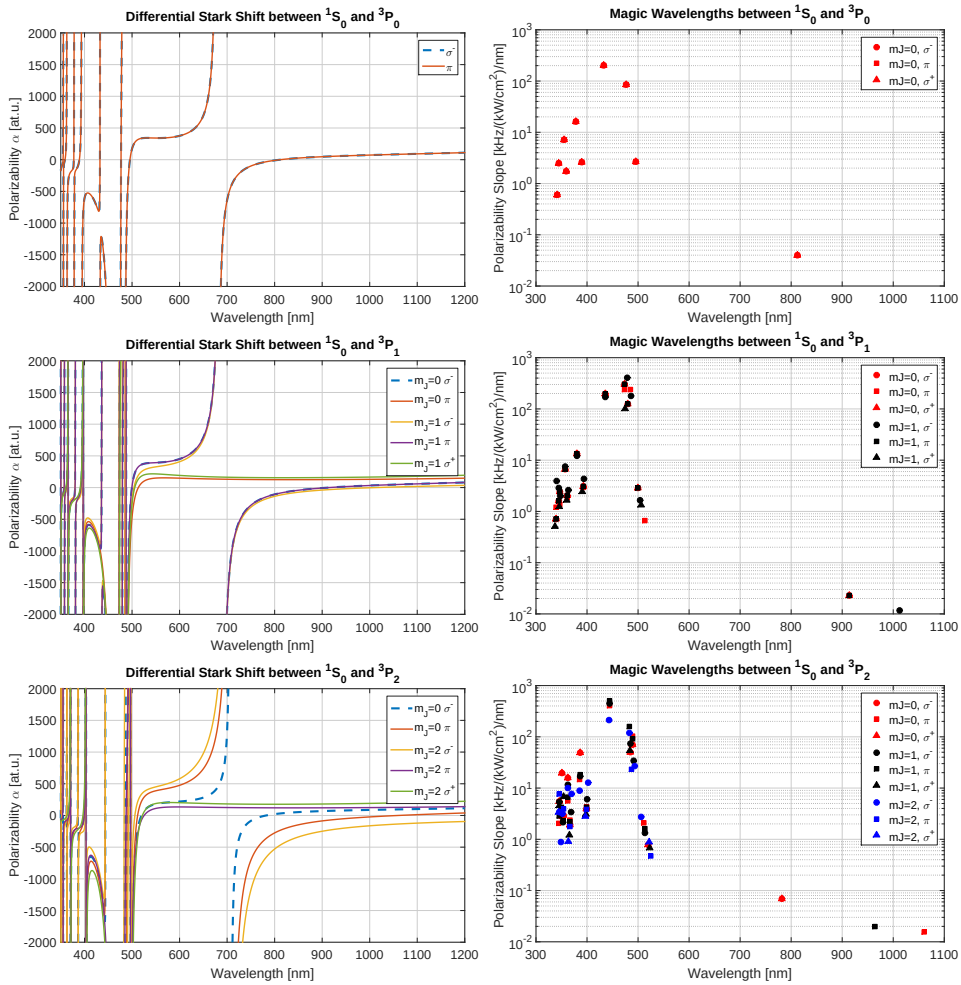

FIGURE 2.6: **Strontium $^1S_0$-^3P_J magic wavelengths.** (left) Plots of the difference in the polarizability (in atomic units $(4\pi\epsilon_0 a_0^3)$ where a_0 is the Bohr radius) between the $^1S_0$ and various ^3P states. (right) Magic wavelengths and the slopes of the differential polarizabilities extracted from the plots on the left. The smaller the slope the easier a magic wavelength is to use.

Upper State	Light Polarization	Wavelength (vacuum) [nm]	Light shift slope [kHz/(kW · cm^{-2}/nm)]	^{1}S$_0$ Polarizability [a.u.]
^{3}P$_0$	π	358.9[a]	1.75	-277.98
^{3}P$_0$	π	389.2[b]	2.60	-454.40
^{3}P$_0$	π	495.6[c]	2.68	1379.01
^{3}P$_0$	π	811.7[d]	0.040	278.82
^{3}P$_1$ $m_J = \pm1$	$\sigma\pm$	391.06	2.44	-470.36
^{3}P$_1$ $m_J = 0$	σ	392.33	3.09	-481.65
^{3}P$_1$ $m_J = \pm1$	π	392.33	3.09	-481.65
^{3}P$_1$ $m_J = 0$	π	392.57	2.93	-483.87
^{3}P$_1$ $m_J = 0$	σ	499.67[e]	2.87	1249.51
^{3}P$_1$ $m_J = \pm1$	π	499.67[e]	2.87	1249.51
^{3}P$_1$ $m_J = \pm1$	$\sigma\mp$	503.9	1.67	1140.92
^{3}P$_1$ $m_J = \pm1$	$\sigma\pm$	505.7	1.32	1101.71
^{3}P$_1$ $m_J = 0$	π	513.2[f]	0.67	964.32
^{3}P$_1$ $m_J = 0$	σ	913.9[g]	0.023	253.71
^{3}P$_1$ $m_J = \pm1$	π	913.9[g]	0.023	253.71
^{3}P$_1$ $m_J = \pm1$	$\sigma\mp$	1012	0.012	1101.71
^{3}P$_2$ $m_J = \pm2$	$\sigma\pm$	396.7	2.83	-524.28
^{3}P$_2$ $m_J = \pm1$	$\sigma\pm$	397.8	3.10	-536.03
^{3}P$_2$ $m_J = 0$	π	399.0	4.29	-548.71
^{3}P$_2$ $m_J = \pm1$	π	399.1	4.18	-549.33
^{3}P$_2$ $m_J = 0$	σ	399.2	3.94	-550.77
^{3}P$_2$ $m_J = \pm2$	π	399.3	3.82	-551.60
^{3}P$_2$ $m_J = \pm2$	$\sigma\mp$	506.0	2.73	1095.74
^{3}P$_2$ $m_J = 0$	π	511.7	2.11	988.53
^{3}P$_2$ $m_J = \pm1$	$\sigma\mp$	513.1	1.32	966.80
^{3}P$_2$ $m_J = \pm1$	π	513.6	1.60	958.35
^{3}P$_2$ $m_J = 0$	π	519.8	0.79	873.63
^{3}P$_2$ $m_J = \pm2$	$\sigma\pm$	521.7	0.89	850.90
^{3}P$_2$ $m_J = \pm1$	$\sigma\pm$	523.1	0.67	834.86
^{3}P$_2$ $m_J = \pm2$	π	525.4	0.48	811.15
^{3}P$_2$ $m_J = 0$	σ	782.2	0.070	289.25
^{3}P$_2$ $m_J = \pm1$	π	963.8	0.020	245.40
^{3}P$_2$ $m_J = 0$	π	1060.4	0.016	233.54
^{3}P$_2$ $m_J = \pm1$	$\sigma\mp$	1076.3	0.0010	231.98
^{3}P$_2$ $m_J = \pm2$	$\sigma\mp$	1908.5	0.0068	201.62

TABLE 2.9: **Selected ^{1}S$_0$-^{3}P$_J$ magic wavelengths.** Selected calculated "magic" wavelengths, the local slope of the polarizability for the ^{1}S$_0$ - ^{3}P states and the value of the polarizability of the ^{1}S$_0$ state in atomic units ($4\pi\epsilon_0 a_0^3$) where a_0 is the Bohr radius.

[a] Too UV for typical laser technology.
[b] Experimentally used at 389.889(9) nm [258].
[c] Close to 461 nm
[d] Experimentally used at 813.428(1) nm [28, 259–261], 813.427 37(20) nm [262].
[e] Calculated by [224] at 500.65(50) nm.
[f] Calculated by [224] at 520(2) nm using new data from Safronova [241, 256]. Possibly used by [224] at 515.2 nm although they state they need to tune their polarization to achieve magic operation, presumably they purchased their 515 nm laser based on earlier calculations and the uncertainty in the location of this magic wavelength is larger than the laser tuning.
[g] Experimentally used at 914(1) nm [263].

	^{84}Sr	^{86}Sr	^{87}Sr F_{upper}	^{87}Sr	^{88}Sr
$^1S_0$ - $^1P_1$	−270.8	−124.8	7/2 9/2 11/2	−9.7 −68.9 −51.6	0
$^1S_0$ - $^3P_1$	−351.49	−163.81	7/2 9/2 11/2	1352.0 221.7 −1241.4	0
$^3P_0$ - $^3S_1$ [264]					0
$^3P_1$ - $^3S_1$	≈ 200	≈ 100	9/2	≈ 54	0
$^3P_2$ - $^3S_1$					0
$^3P_2$ - 5s5d $^3D_2$	−91.8	−47.5			0
$^3P_2$ - 5s5d $^3D_3$	−91.6	−46.6			0

TABLE 2.10: **Strontium isotope shifts.** Isotope shifts of the Sr isotopes, in MHz relative to ^{88}Sr. Most data is taken from [107] which in turn is largely derived from [234, 265] with the exception of the repump lines ($^3P_0$ - $^3S_1$ and $^3P_2$ - $^3S_1$) where this data was measured experimentally using a *High Finesse WSU-30* wavemeter which has a nominal accuracy of 30 MHz.

	^{84}Sr	^{86}Sr	^{87}Sr	^{88}Sr
^{84}Sr	124	32	−56	1800
^{86}Sr	32	830	164	98
^{87}Sr	−56	164	97	55
^{88}Sr	1800	98	55	−1

TABLE 2.11: **Strontium scattering lengths.** Scattering lengths between the strontium isotopes, given in units of a_0 taken from [107]. The values are averages of the values given in [267] and [268], and the uncertainty is a few a_0 except for the two very large values, where the uncertainty is larger.

important isotope for the superradiant optical clock project but having motivated this I, like Chun-Chia, will leave you in suspense waiting for Rodrigo's thesis in a few years time.

2.8 Scattering properties

Identification of the excellent scattering properties of ^{84}Sr (despite its exceptionally low abundance) was the key step towards making Bose-Einstein condensates of strontium [106]. The scattering length between the various strontium isotopes in their ground states is listed in table 2.11.

Scattering between atoms in the metastable states was also explored as a potential way of thermalizing ^{88}Sr and thus making BECs but the inelastic scattering rates were found to be far too high to be useful [269]. The inelastic scattering rates are listed in table 2.12.

States	Inelastic scattering loss rate β_{in} $[\mathrm{cm}^3 \cdot \mathrm{s}^{-1}]$
^{84}Sr $^1S_0$ - $^1S_0$	very small
^{87}Sr $^1S_0$ - $^1S_0$	very small
^{87}Sr $^1S_0$ - $^3P_0$	small [270]
^{87}Sr $^3P_0$ - $^3P_0$	1×10^{-11} [270]
^{88}Sr $^1S_0$ - $^1S_0$	very small
^{88}Sr $^1S_0$ - $^3P_0$	2×10^{-12} [271]
^{88}Sr $^3P_0$ - $^3P_0$	2×10^{-11} [269]
^{88}Sr $^3P_2$ - $^3P_2$	1×10^{-10} [269]

TABLE 2.12: **Strontium inelastic scattering rates.** Inelastic scattering loss rate coefficients for strontium. The elastic to inelastic scattering rates were approximately the same for ^{88}Sr $^3P_0$-$^3P_0$ scattering [271]. This data is very limited and there is definitely a need to go and measure some more of these properties.

2.9 Optical Feshbach resonances

Bosonic strontium with its non-magnetic ground state doesn't have magnetic Feshbach resonances, but it does have optical Feshbach resonances (OFRs). These photoassociation (PA) resonances are hard to miss when you have a dense sample as they can be observed just a few hundred kHz red detuned from the 689 nm cooling transition. In principle these can allow the continuous tuning of the scattering length but they are accompanied by strong Sr_2 molecule formation. These have been studied in some depth [277, 278] but with typical sample lifetimes of around 1 ms, there is little hope of tuning the scattering properties to thermalize a sample for evaporative cooling. There have also been some efforts to optimize this molecule production process [276, 279] but for us this was a loss which plagued us. The locations of molecular bound states in the potentials corresponding to $^1S_0$+$^3P_1$ at long inter-particle distances are included in table 2.13. These can induce optical Feshbach resonances and losses around the 689 nm cooling transition.

2.10 Zeeman shifts

The Zeeman shift for small magnetic fields can be calculated from equation 2.14 as shown in box 2.10.1. In the case of bosons there is no nuclear angular momentum so $I = 0$ while for ^{87}Sr $I = 9/2$. The resulting Zeeman shifts are tabulated for the lower levels of strontium in table 2.14. For the molecular bound states in the $^1S_0$+$^3P_1$ potentials the Zeeman shifts are given in table 2.13.

	J	Symmetry	v	Binding Energy E/h [MHz]	Linear Zeeman Shift g	$\lvert m' \rvert$	Quadratic Zeeman coefficient $-\bar{q}$	Ref
^{88}Sr	1	0_u^+	1	$-0.435(37)$	0.666(14)	0	0.325(34)	[272, 273]
						1	0.546(44)	
			2	$-23.932(33)$	0.232(2)	0	0.0181(6)	
						1	0.0444(13)	
			3	$-222.161(35)$	0.161(2)	0	0.0023(6)	
						1	0.0066(4)	
			4	$-1084.093(33)$	0.142(2)	0	0.0019(7)	
						1	0.0041(3)	
			5	$-3463.280(33)$	0.193(3)	0	0.0016(8)	
						1	0.0029(5)	
			6	$-8429.650(42)$	0.931(13)	0	0.0008(6)	
						1	0.0060(13)	
		1_u	1	$-353.236(35)$	0.625(9)	0	0.0126(26)	
						1	0.0077(10)	
			2	$-2683.722(32)$	0.584(8)	0	0.0080(18)	
						1	0.0034(11)	
			3	$-8200.163(39)$	$-0.149(2)$	0	0.0112(12)	
						1	0.0040(4)	
	3	0_u^+	1	-0.63	0.270(2)	0	0.130(5)	[273]
						1	0.102(5)	
						2	0.095(6)	
						3	0.090(4)	
			1	-132	0.173(2)	0	0.0041(15)	
						1	0.0043(5)	
						2	0.0061(9)	
						3	0.0060(14)	
^{86}Sr	1	0_u^+	1	$-1.633(10)$	0.490			[274, 275]
			2	$-44.246(10)$	0.214			
			3	$-348.742(10)$	0.206			
^{84}Sr	1	0_u^+	1	$-0.338(10)$/ $-0.320(10)$	0.736	0		[275, 276]
						1		
			2	$-23.010(10)$	0.242			
			3	$-228.380(10)$	0.116			

TABLE 2.13: **Strontium low lying molecular bound states.** Locations of the low lying molecular bound states supported by the potentials corresponding to $^1S_0+^3P_1$ at long inter-particle distances, as well as what is currently known about their Zeeman shift coefficients. The Zeeman shift of a line is given by $\Delta\nu = g\mu_B m'B + \bar{q}\mu_B B^2$ where $\mu_B = e\hbar/(2m_e)$ is the Bohr magneton [273].

Box 2.10.1: Zeeman Splitting.

$$\Delta_{\text{Zeeman}} = \vec{\mu} \cdot \vec{B} \tag{2.13}$$

$$= m_F g_F \mu_B B \tag{2.14}$$

$$g_F = g_J \frac{F(F+1) - I(I+1) + J(J+1)}{2F(F+1)} + g_I \frac{F(F+1) + I(I+1) - J(J+1)}{2F(F+1)}$$

$$g_J = g_L \frac{J(J+1) - S(S+1) + L(L+1)}{2J(J+1)} + g_S \frac{J(J+1) + S(S+1) - L(L+1)}{2J(J+1)} \tag{2.15}$$

where:

B = Magnetic field strength,
μ_B = Bohr magneton $e\hbar/(2m_e)$ =1.400 MHz/G,
μ_N = Nuclear magneton is $e\hbar/(2m_p)$ =762.3 Hz/G,
F = The total angular momentum $J + I$,
J = The total electronic angular momentum $L + S$,
L = The electronic orbital angular momentum,
S = The electronic spin angular momentum,
I = The nuclear angular momentum,
g_L = The electron orbital Landé g-Factor $g_L = 1 - m_e/m_{\text{nucleus}} \approx 1$,
g_S = The electron spin Landé g-Factor $g_S = 2.0023193043737(80) \approx 2$,
g_I = The nuclear Landé g-Factor $g_I = -0.1422\mu_N/\mu_B$. Boyd [234] measures a Zeeman shift of Δ =−108.4(4) Hz/G. in ^{87}Sr. We equate using $\Delta = g_I \mu_N$.
m_F = The projection of the angular momentum onto the B field (-F:1:F).

Isotope	State	Quantum Numbers I	L	S	J	F	g_F	$(\Delta_{\text{Zeeman}}\,[\text{kHz}])/m_F B$
Bosonic	$^1S_0$	0	0	0	0	0	0	0
	$^1P_1$	0	1	0	1	1	1	1399.5
	$^3P_0$	0	1	1	0	0	0	0
	$^3P_1$	0	1	1	1	1	3/2	2099
	$^3P_2$	0	1	1	2	2	3/2	2099
	$^3S_1$	0	0	1	1	1	2	2799.1
	$^3D_2$	0	2	1	2	2	7/6	1632.8
Fermionic	$^1S_0$	9/2	0	0	0	9/2	≈ 0	-0.108
	$^1P_1$	9/2	1	0	1	7/2	$-2/9$	-311.1
						9/2	4/99	56.4
						11/2	2/11	254.5
	$^3P_0$	9/2	1	1	0	9/2	≈ 0	-0.108
	$^3P_1$	9/2	1	1	1	7/2	$-1/3$	-466.7
						9/2	2/33	84.7
						11/2	3/11	381.6
	$^3P_2$	9/2	1	1	2	5/2	$-6/7$	-1199.8
						7/2	$-1/7$	-200.1
						9/2	2/11	254.4
						11/2	51/143	499.1
						13/2	6/13	645.9

TABLE 2.14: **Zeeman splitting for small fields.** The Zeeman-splittings for small fields for the lower states of strontium. Not all figures are significant.

Chapter 3

The Strontium Continuous Atom Laser (SrCAL) Machine

The fundamental concept behind the continuous atom laser machine is to try to demonstrate cooling atoms to degeneracy in space rather than in time. This involves flowing atoms through a series of spatially separated and isolated cooling stations. The initial concept design for the machine and the final CAD drawing of the vacuum system are shown in Figure 3.1. This chapter will describe this machine and how it was constructed. We shall do this by following the path of the atoms on their journey from a block of strontium metal at 800 K to their arrival a second later in a cloud at 1 µK with unity phase-space density.

3.1 Oven

At room temperature the vapour pressure for strontium is negligible (see figure 2.1) so we begin our journey in an oven. The design of the oven is shown in figure 3.2. It consists of a nipple filled with strontium pieces and externally heated to generate a vapour pressure. This vapour is ejected into the machine through a microtube array which acts as a collimating nozzle to dramatically improve the on-axis brightness. In this section we shall describe the key elements of the oven and its construction.

Reservoir The reservoir consists of a 128 mm long DN35 nipple in 316L stainless steel from Vacom. It was loaded with seven 5 g ampoules of natural strontium metal pieces (99.95% from Alfa Aesar). As strontium oxidises rapidly in air the loading process was carried out in a makeshift glove box set up around the oven with disposable plastic drop sheets (normally for painting) that was overpressured and flushed with nitrogen. The objective was to open the ampoules, load the strontium into the reservoir, close the reservoir flange and pump the machine down to vacuum within 15 minutes. It turned out that the glass ampoules were much harder to break than anticipated so

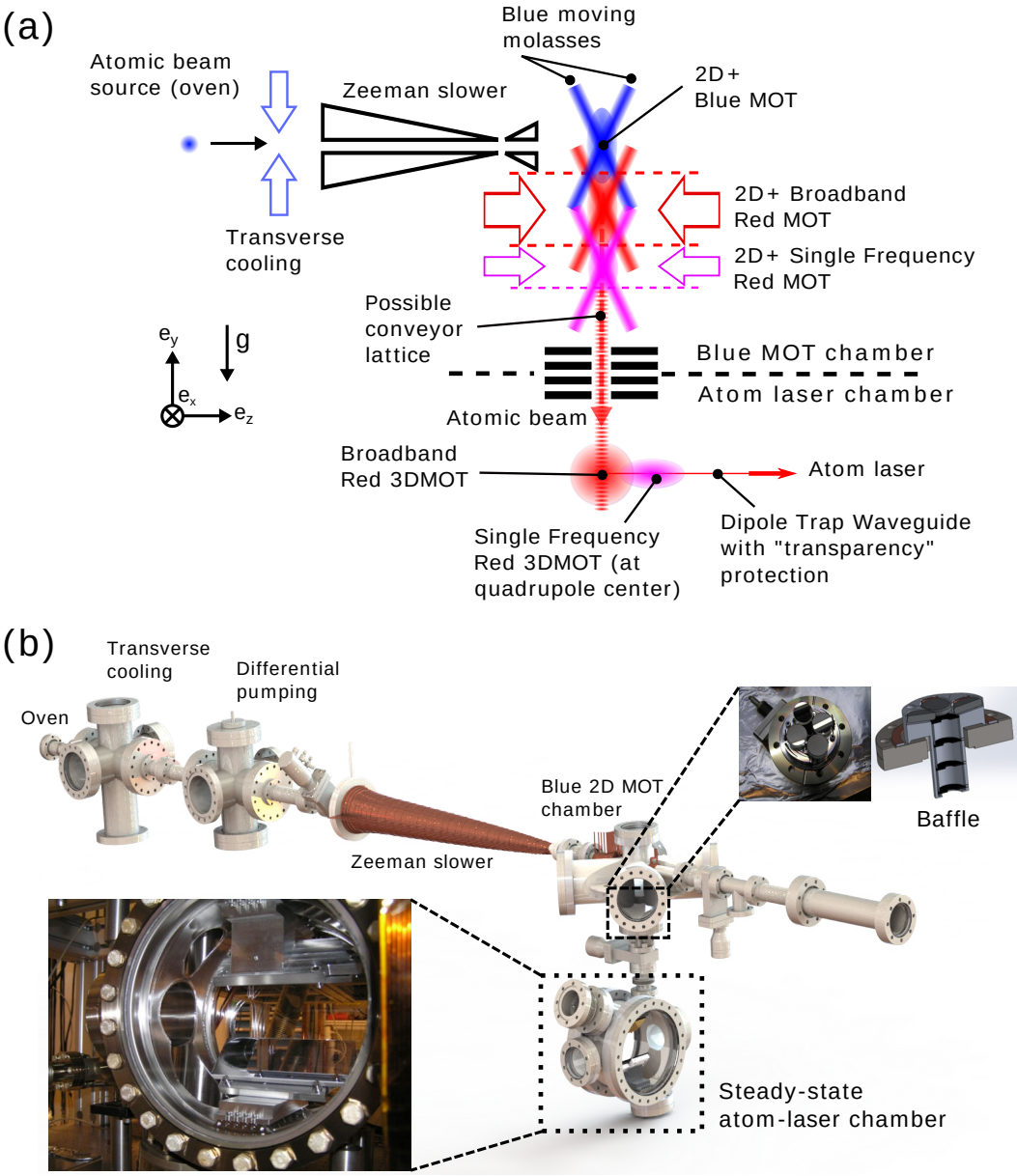

FIGURE 3.1: **Strontium Continuous Atom Laser machine.** (a) Initial concept design for the continuous atom laser experiment. Different laser cooling steps are implemented sequentially in space. (b) The final CAD configuration with insets of key components. A number of the features of the initial concept design were not implemented on the final machine such as the conveyor, while other aspects were significantly altered such as the $2D^+$ Red MOT modified to a 2D molasses.

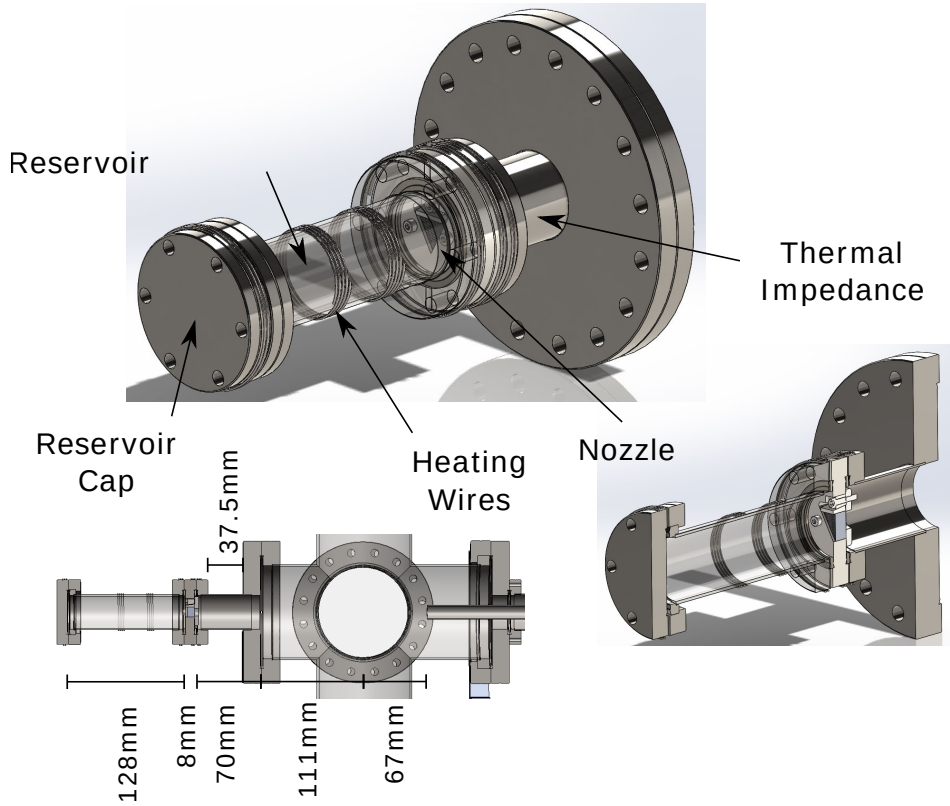

FIGURE 3.2: **Oven design.** Design of the oven subsystem. Inset at the bottom shows a cross section indicating distances.

many well laid plans had to be set aside in favour of a big hammer. This in turn created havoc by adding the need to pick through the shattered glass to extract and place by tweezers as much strontium as possible into the reservoir. It is estimated that around 30 g of the original 35 g made it into the reservoir. The process ended up taking about 20 minutes. This process was improved in the SrMic experiment by using a single 25 g ampoule, by scoring the ampoule at the glass workshop so that it was easy to open, by building a better glove box using perspex sheeting which provided much better visibility and by accepting that 15 minutes is still a long time so for difficult processes like opening the ampoule it is OK to do this in air and only then place it in the glove box to load the reservoir.

Heating The oven is heated by eight Thermocoax ZEZI 10/50-50-50/2xCM 10/KZ 0510/500mm heating elements. These cables have a 50 cm long hot zone with 25 cm long cold zones

TABLE 3.1: Properties and operating parameters for the SrCAL oven heating elements.

Name	Length [cm]	Resistance [Ω]	Standby current [A] (23/08/2017)	PSD1 current [A] (25/01/2018)
Oven 1	50.0	7.02	1.15	1.27
Oven 2	48.7	6.58	1.15	1.32
Oven 3	48.0	6.65	1.15	1.27
Oven 4	47.8	6.55	1.15	1.32
Oven 5	50.0	7.04	0.47	0.80
Oven 6	50.5	6.99	0.47	0.80
Oven 7	50.5	7.13	0.62	0.90
Oven 8	48.0	6.42	0.62	0.90

on each side ceramically insulated with an inconel 600 alloy sheath. The outer diameter is 1 mm. The heater array consumes approximately 60 W at high flux output. The location of the heating elements is shown in figure 3.3. They are secured under stainless steel hose clamps with a protective layer of stainless steel shim ≈0.2 mm thick placed between the heating element and the hose clamp. This acted as both a heat and mechanical shield. The operating currents and the electrical properties of each heater are listed in table 3.1. The heated zone extends significantly beyond the location of the nozzle in the transverse cooling direction. This is to try to reduce radiative heat losses from the nozzle. Conduction from the flange to the center of the nozzle is actually quite small because the microtubes forming the nozzle only contact at points along their sizes and there are many layers of tubes between the conductively heated flange and the nozzle center. This increases the importance of heating the surrounding area to reduce radiation losses and minimize the chance of clogging the nozzle center.

Temperature sensing The temperatures in the oven were monitored by K type thermocouples placed as shown in figure 3.3. Since they were much thinner than the 1 mm diameter heating elements they easily slid between the heating spirals under the shim between the hose clamps and the heaters. These sensors are not robustly secured and if they are pulled it is possible to pull the thermocouple completely out of the oven box so care is needed when working near the thermocouples. The way the wiring is secured and terminated is also shown in figure 3.3. The temperatures measured for each of the sensors at standby and high flux operating points is listed in table 3.2. For low temperature sensing (<300 °C) thermocouples were made by spot welding thermocouple wire (Omega Part: GG-KI-24-300M) and insulating the wire with Kapton tape as shown in figure 3.3 (top, left). For higher temperatures we purchased ready made thermocouples from Omega, part TJ2-CAXL-IM15U-600(?).

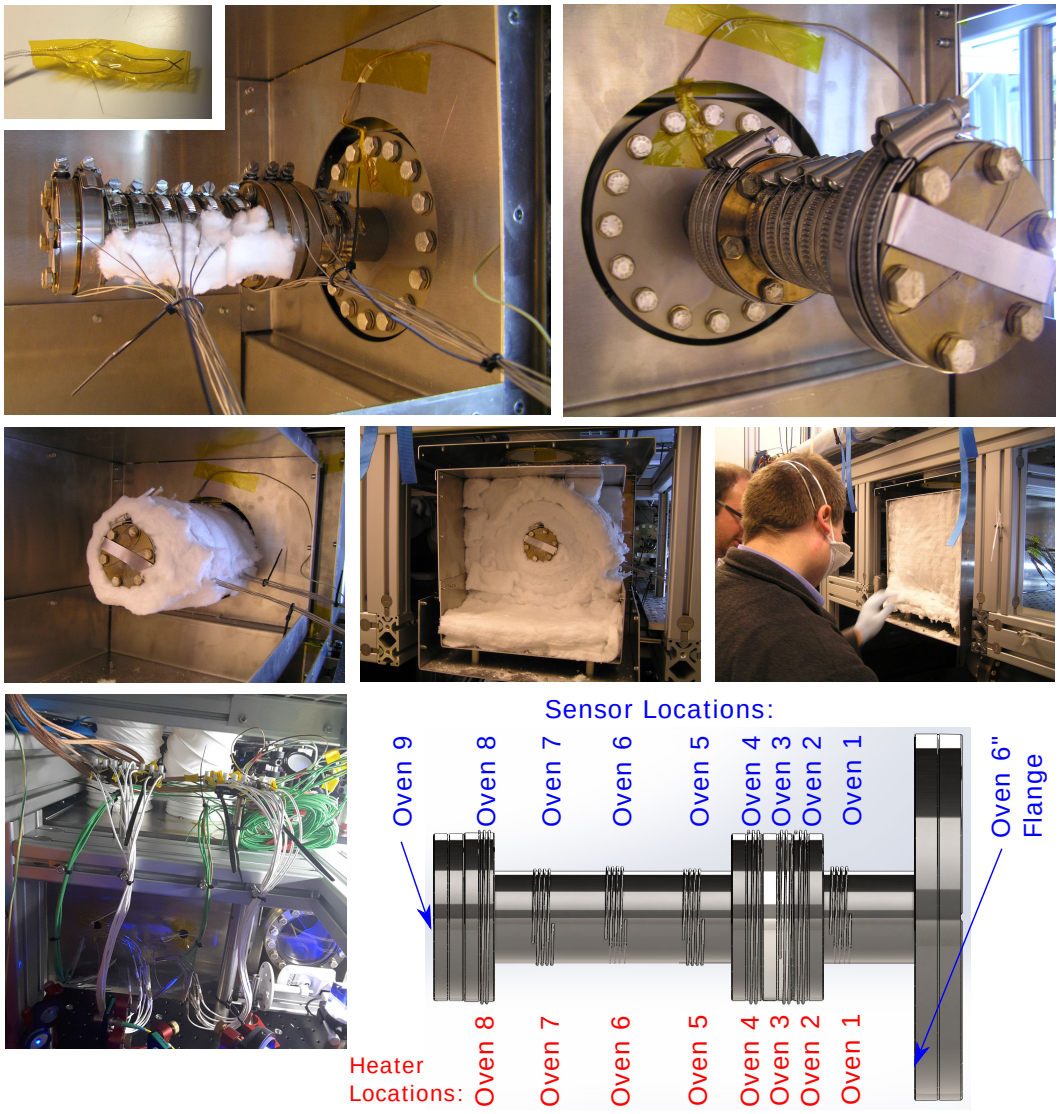

FIGURE 3.3: **Oven construction.** Construction of the oven and the configuration of the oven heating elements and thermocouples.

TABLE 3.2: **Oven temperatures.** Temperature sensor values for the SrCAL oven for standby and maximum (so far) operation.

Name	Standby temperature [°C] (23/08/2017)	PSD1 temperature [°C] (25/01/2018)
Oven outer box	31	35
Oven 6" flange	70	94
Oven 1	286	362
Oven 2	414	528
Oven 3	412	528
Oven 4	414	530
Oven 5	394	525
Oven 6	376	520
Oven 7	366	513
Oven 8	340	480
Oven 9	340	479

Temperature profile A temperature gradient between the nozzle and the back of the reservoir must be maintained to prevent strontium depositing in and blocking the nozzle. For this reason we maintain a difference of around 50 K between the nozzle peak temperature and the lowest temperature at the back of the reservoir. The poor conduction between the nozzle flange where temperatures are measured and the center of the microtube nozzle combined with radiation losses must be considered when deciding what temperature gradient is appropriate. The real gradient to the nozzle center will be significantly smaller than the apparent measured gradient. It would be valuable to do some modelling of this to better understand these limits. During the first 6 to 12 months of operation it was noted that the flux captured by our MOT gradually declined, particularly while operating at high temperatures[1]. Initially the fear was that this could be due to the gradual blocking of the nozzle microtubes. Searches were made of the fluorescence profile at the transverse cooling section to try to detect a lower than expected signal in the beam center but nothing was clear. We also tried lowering the temperature at the back of the reservoir and increasing the nozzle temperature in a bid to evaporate away any strontium which might block the nozzle but no improvement was noted. While nothing is for certain I attribute the flux evolution to the migration of strontium from the hot zone near the nozzle to the back of the reservoir, a process which now appears to have essentially stopped. Compared to when we initially started operation we now require temperatures approximately 40 K-50 K hotter for a similar fluorescence level which would be consistent with such

[1] A similar observation was made by Simon on the RbSr machine [107] in which he suspected this was related to an increase in the atomic beam divergence from the nozzle. In the case of the RbSr oven this was due to the migration of the strontium from inside the oven to the other side of the microtubes due to operation at very high temperatures. Migration to outside our oven is certainly not an issue in our case.

a theory. The fluorescence levels for the 2D blue MOT are periodically recorded for known camera settings to keep track of long term performance drifts.

Insulation I always held a great fear of leaks developing in the CF seals due to rapid or differential heating or cooling. Such a leak within the oven reservoir might not be immediately apparent while it oxidised our strontium. If it occurred on the UHV side of the nozzle it might ruin the vacuum requiring a time consuming rebuild of the oven. This fear was in no small part derived from the leaks observed to develop at flanges during the low speed ramps baking the machine which were fixable by tightening up the gaskets. To minimize the potential for developing such leaks the oven was strongly insulated to immediately guard against power failure and power increases and decreases were carried out in small steps (25 mA steps for heaters 1-4 and 50 mA steps for heaters 5-8). A UPS, monitoring, email and phone alarm system was developed to call for help if any problems were detected (this will be described in section 3.7.4). The oven was insulated by a 150-200 mm thick layer of Superwool 607 (RS Components 840-5529) essentially eliminating thermal loss through the sides. The remaining thermal losses are mainly from conduction along the DN100 to DN35 reducing nipple and radiation in the direction of the transverse cooling. To try to reduce heat conduction and allow the oven nozzle to be safely placed as close as possible to the transverse cooling (to maximize the solid angle) we tried to minimize the wall thickness of the DN100 to DN35 reducing nipple. A 70 mm long 0.25 mm wall thickness 316Ti tubulation was purchased from Novotek through Demaco, the thinnest wall the supplier was willing to offer. Once installed the weld to the DN100 flange was found to leak. An alternate part was sourced from Vacom who were only willing to supply down to a wall thickness of 1 mm. This is the tubulation installed. While there were never any major incidents on the SrCAL oven to test these protection measures the monitoring system and then the UPS both failed on the similarly designed SrMic oven resulting in an uncontrolled fall to room temperature. When the problem was discovered the power supplies were turned back on resulting in a very rapid rise back to 550 °C. This all occurred without any monitoring but no problems were detected resulting from this harsh treatment so it might be that this system is over engineered.

Cooling Figure 3.3 shows the double layer sheet metal box used to house the oven. The inner box filled with mineral wool insulation is surrounded by a second box with two 125 mm diameter air inlets at the top. One inlet rises about 1 m to the table roof and is fitted with a fan designed to blow cool room air through the box. The second pipe rises only about 10 cm to the electronics area which has a negative pressure

FIGURE 3.4: **The "bird cages".** Jan Kalwij from the workshop bending the "bird cages". The inner and outer boxes used to insulate the oven and the heated Zeeman slower window assemblies.

maintained by the building air exhaust. Baffles within the double layer box guide the air flow to try to get a broadly even cooling over the entire inner box. In fact, the fan proved unnecessary as the outer box temperature never exceeds 35 °C even with the fan off so this is how it is operated (one less fan which can fail and trigger temperature alarms). The sheet metal boxes were water cut from 2 mm aluminium and then bent in an impressive feat of workmanship by Jan Kalwij from the workshop (Figure 3.4). They were assembled using insertnuts. In hindsight these were over engineered except for one key point, it should have been split into two separate pieces allowing the box to be assembled around the wiring rather than requiring the wires to be threaded through holes. One should be very mindful of this if you ever need to disassemble the oven enclosure.

Gaskets Nickel gaskets are used on the DN35 connections to allow high temperature operation while the DN100 connection is cold enough to allow the use of a standard silver plated copper gaskets.

Power supplies Initially, linear power supplies (Digimess HY3003, Farnell 4283211) were used to drive the oven heating coils. These supplies proved to be notoriously unreliable and most eventually completely failed. The low efficiency also resulted in a short UPS lifetime of only ≈10 minutes. They were therefore replaced as they failed with precision switched mode power supplies (B& K Precision BK1666, Farnell 2321448) which increased UPS lifetime to around an hour.

3.1.1 Oven nozzle design

The choice of microtube dimensions and choosing the number of microtubes for an oven nozzle can best be addressed through flow calculations.

TABLE 3.3: Knudsen Flow regimes.

Molecular Flow	$10 < K_n$
Transition Flow	$0.1 < K_n < 10$
Slip Flow	$0.001 < K_n < 0.1$
Continuum/Viscous Flow	$K_n < 0.001$

The flow through a tube may be characterized according to the Knudsen number[2], K_n,

$$K_n = \frac{\lambda}{2R} = \frac{p*}{p_s} = \frac{k_B T_s}{\sqrt{2}\pi(2a_s)^2(2R)p_s}, \tag{3.1}$$

where:

λ = mean free path,
$p*$ = pressure at which the mean free path equals the channel diameter,
k_B = Boltzmann constant,
T_s = source temperature,
a_s = scattering length/radius,
p_s = pressure of the source,
R = radius of the tube.

It is convenient to classify flow into a number of regimes [280] listed in table 3.3. From a purely utilitarian perspective the key difference between these regimes is that in the molecular flow regime the flux varies with pipe radius as R^3 while in the viscous regime it varies as R^4. A second key change is that the angular divergence of a beam emerging from a pipe changes from an essentially collimated beam determined by tube geometry in the case of molecular flow to one varying as $\cos(\theta)$ in the viscous flow regime irrespective of the tube geometry. Thus, even though increasing pressure will increase the flux it is possible that the peak brightness of a beam will decrease. Unfortunately, the reality of oven design is that we tend to operate in the crossover from molecular to transitional flow which somewhat complicates the analysis. Appendix A describes the equations, assumptions and approximations used for estimating the flow through the oven nozzles and for estimating the angular distribution of the resulting atomic beam. Here we shall focus on two particular geometries, one used in the atom laser (and microscope) oven and a second corresponding to the oven designed by Erik Wille [281] and also used in the original strontium BEC/RbSr machine [107]. The geometries and summary results are listed in table 3.4.

[2]Note that this equation uses the tube diameter as the characteristic length in defining the Knudsen number. It is also possible to use the tube length, a trap for mixing and matching theory from sources using different conventions.

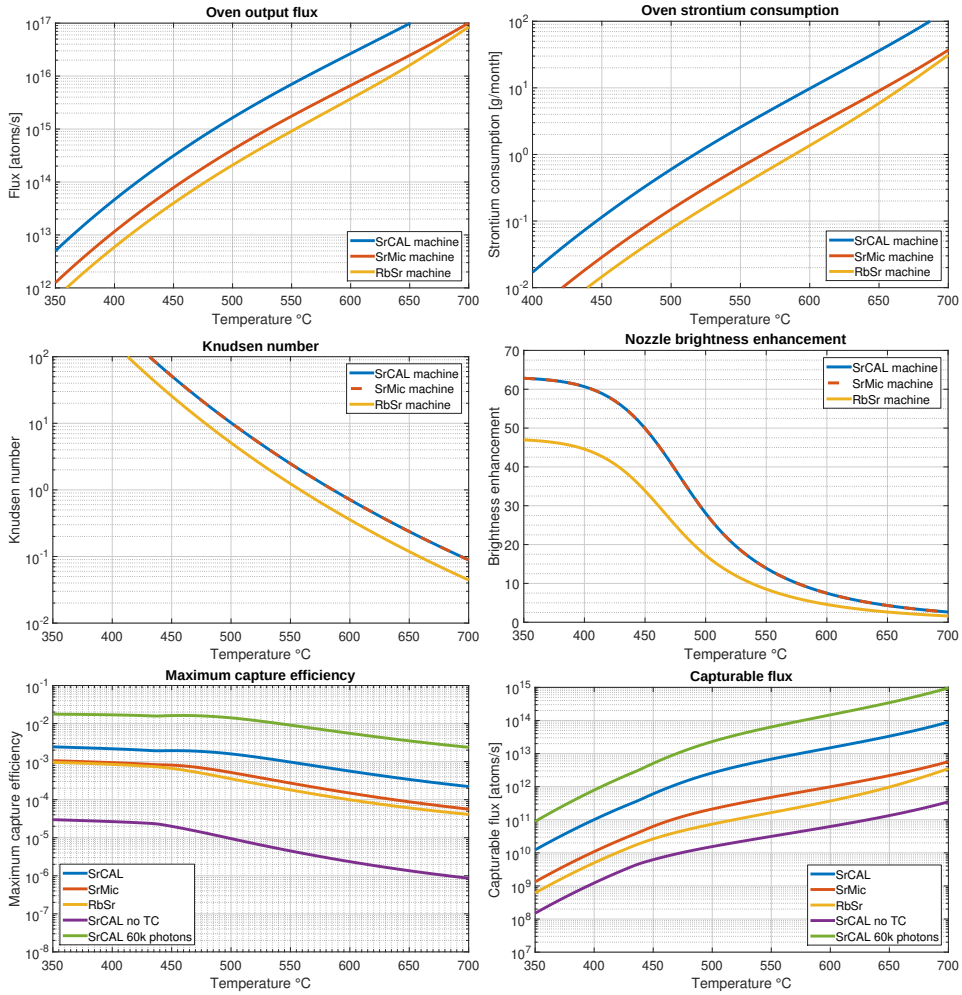

FIGURE 3.5: **Oven performance plots.** The nozzle parameters for the SrCAL, SrMic and RbSr configurations. The velocity capture range assumes scattering 20,000 Zeeman slower photons. Also plotted are calculated curves for a reduced angular capture range on the SrCAL machine (SrCAL no transverse cooling - TC) where the angular capture range of 0.12° is an estimate without transverse cooling and a curve assuming the ability to scatter 60,000 Zeeman slower photons (which is what was thought possible at the time of design).

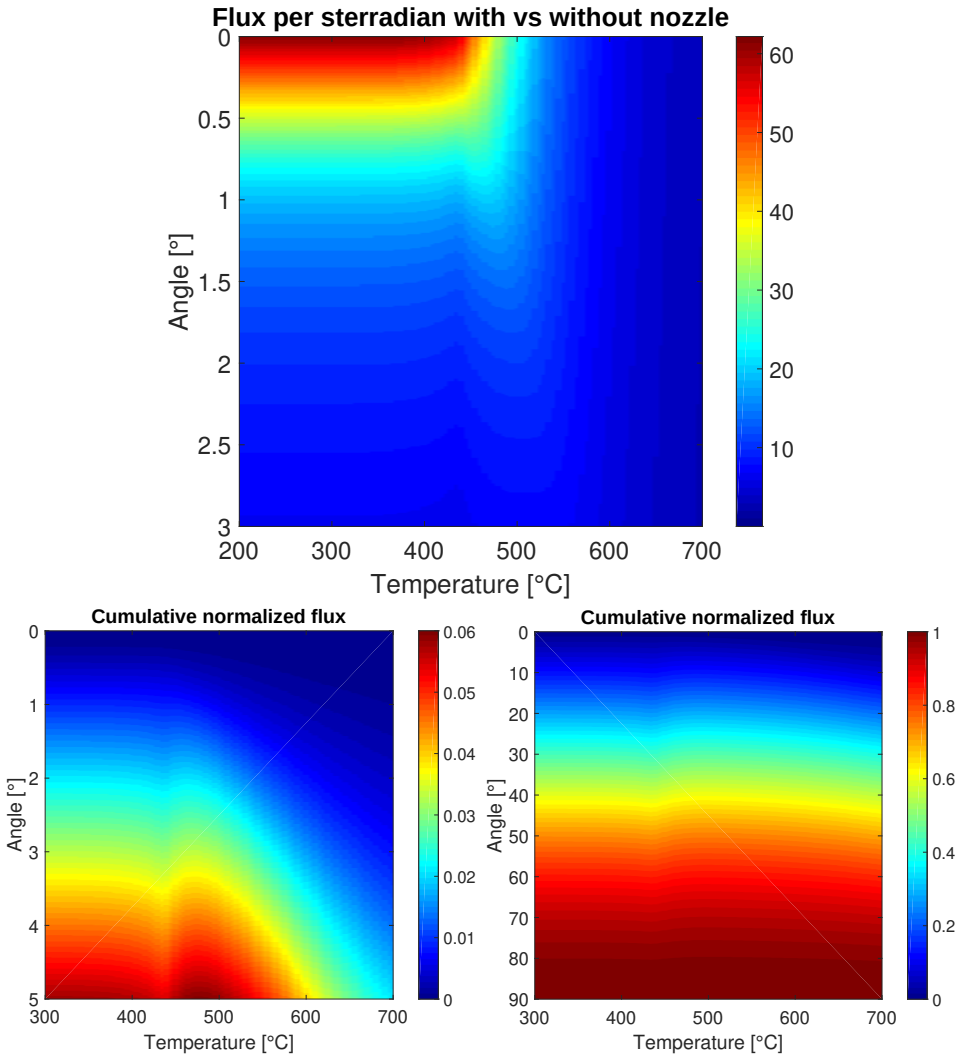

FIGURE 3.6: **Oven flux angular distributions.** Angular flux distributions for the SrCAL machine as a function of temperature. Top: the normalized flux per steradian as a function of angle. The bright axial collimated beam is deceptive in that despite the impressive enhancement the relevant solid angle is small. This means that the overall flux contained within this bright feature is small. (bottom) The cumulative flux contained within a given angle around the axis. This shows the tiny proportion of total flux which is contained within the collimated axial beam. Note that the distortion at around 440 °C corresponds to the border between molecular and transitional flow regimes where the equations are dubious.

TABLE 3.4: **Calculated performances from the oven.** Nozzle configuration and calculated performance parameters for the RbSr machine [107], the Continuous Atom Laser (SrCAL) machine at both 500 °C and 550 °C and the strontium microscope (SrMic) machine (which used a scaled down version of the SrCAL oven). In these plots it is assumed that the capture velocity is limited to the momentum of scattering 20,000 461 nm photons in a Zeeman slower.

Parameter	RbSr	SrCAL 500 °C	SrCAL 550 °C	SrMic
Tube inner diameter [µm]	200	110		110
Tube outer diameter [µm]	300	190		190
Tube length [mm]	12	8		8
Exit aperture diameter [mm]	1	10		5
Number of tubes	60	2510		630
Reservoir Sr mass [g]	25	30		25
Operating temperature [°C]	550	500	550	550
Knudsen number	1.2	10	2.5	2.5
Flux [at/s]	9.1×10^{14}	1.6×10^{15}	7.0×10^{15}	1.7×10^{15}
Flux [g/month]	0.33	0.60	2.56	0.64
Lifetime [years,months]	6y3m	4y2m	1y	3y3m
Nozzle brightness enhancement	8.5	28	14	14
Assumed capture angle [°]	1	2	2	1
Capture efficiency	1.8×10^{-4}	1.6×10^{-3}	9.7×10^{-4}	2.7×10^{-4}
Capturable flux [atoms/s]	1.6×10^{11}	2.6×10^{12}	6.8×10^{12}	4.8×10^{11}

To offer some insight into the nozzle properties we plot curves for the flux and the angular distributions from the nozzles in figure 3.5 and figure 3.6. There are a few important realizations which come from looking at these graphs. Firstly ovens are impressively wasteful in their use of strontium, we capture and use around 0.1% of the atoms emitted. The second realization is that beyond about 500 °C the oven moves well into the transitional flow regime where the effectiveness of the nozzle is heavily compromised. It would be ideal to measure the angular distributions and fluxes from the built oven to cross check the theory and close the design loop. To this end an ECDL was built at 461 nm but the laser was repurposed as a replacement master laser before measurements were able to be made.

The clearest way to improve the performance would be to avoid entering the transitional flow regime. This could be achieved without sacrificing flux by increasing the number of tubes (which becomes impractical) or by using shorter or wider tubes to reduce the aspect ratio (at a cost of reduced peaking factor at lower temperatures).

3.1.2 Oven nozzle construction

Constructing the oven nozzle was a long and painstaking process. The design and images of the completed oven nozzle are shown in figure E.1. The design draws from the old oven developed by Erik Wille and Florian Schreck [281] as well as more recent work from the Weld group [282]. The design consists of a double faced DN35 SS316L flange into which a

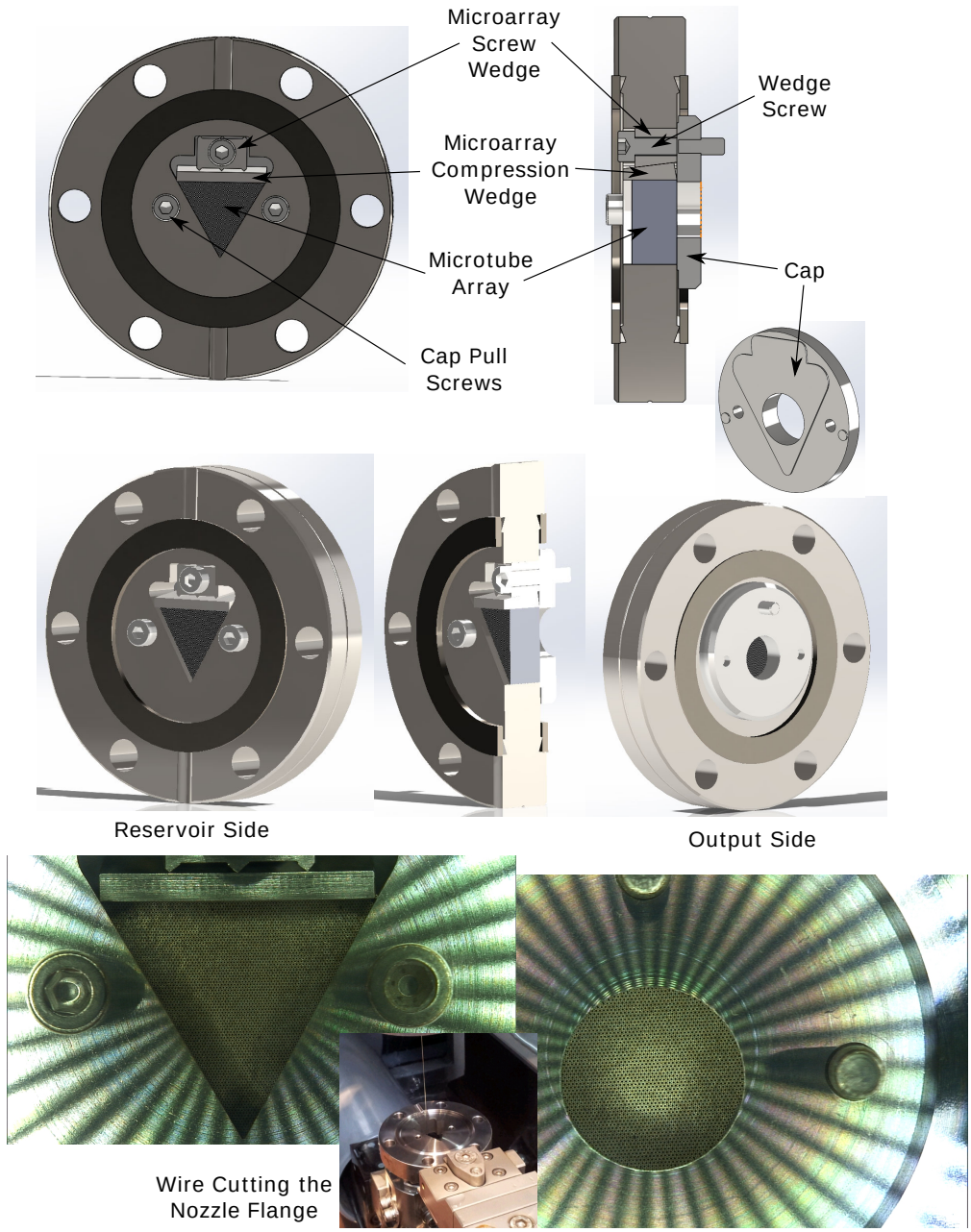

FIGURE 3.7: **Oven nozzle.** (Top) Design of the oven nozzle. (Bottom) microscope images taken of the finished loaded oven nozzle.

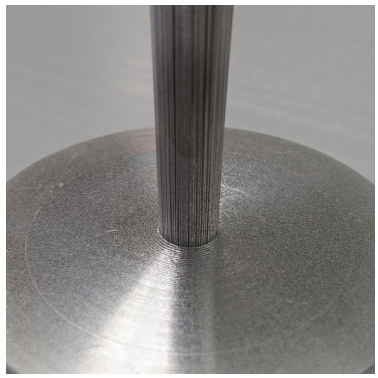

FIGURE 3.8: **Brazing an oven nozzle.** The first 10 mm diameter oven test nozzle loaded with microtubes before brazing.

60° triangle was wire cut allowing close stacking of a triangular array of microtubes. To secure the tubes a microarray compression wedge was placed on top of the array and a counter wedge of opposite angle, the microarray screw wedge on top of that. By using a screw to pull the screw wedge towards the cap a pressure is generated pushing the microtube array down and securing it. The screw wedge is designed with a series of knives machined into the top and bottom surfaces to apply pressure while avoiding virtual leaks. To seal the open areas of the nozzle and restrict the output to those microtubes in the centre of the flange (aligned with the differential pumping tubes) the cap had a 10 mm diameter output aperture and was attached so as to seal the output side of the nozzle. A protrusion on the underside of the cap 1 mm larger than the cutout of the flange ensures sealing while restricting the sealing surface to an annulus 1 mm across. This was done to try to avoid virtual leaks. The cap was held to the flange by several cap pull screws. This was the final but not the first design tried.

We also tried to vacuum braze to both mechanically secure the microtube array and to fill the gaps between the tubes for improved thermal conduction. An additional advantage of this approach is that the oven is much simpler to make and much more compact. A picture of the tube array before brazing is shown in figure 3.8. We tried a nickel based filler material and the brazing supplier recommended a braze temperature of 1020-1040 °C. They also expressed concerns that there might be grain growth through the tube walls roughening the inner surface and therefore recommended staying as low as possible in temperature if the smoothness of the tubes is important (which it is!). The results were disappointing. The filler material only ended up filling the gaps in the outer layers of the array, it did not penetrate through to the center of the array. It was also very uneven longitudinally. The inner tubes were not mechanically secure and the conduction to the

centre was little improved. At the time we did not have a wire cutter here at UvA[3] so it was not worth paying for the resulting array to be cut clean so I don't have pictures after brazing. If we used a lower temperature filler material to get better flow (without risking roughening the tube surface) and with much more testing and optimization it is easy to imagine brazing being the right choice for making oven nozzles. The brazing supplier (www.bodycote.com) also recommended nickel plating the tubes and holder to get better and lower temperature wetting and adhesion. A better array loading procedure like the triangular holder used in the final design could also give an array with far fewer defects which would have helped. However, without the equipment to do any of this in house it cost us 450€ per trial and we had neither the time nor the money to perfect this process.

A different approach that was also considered was using glass microstructure arrays. Photonic crystal fibres in fused silica are often made by taking thousands of glass tubes and drawing them into a rod usually while pressurizing the holes to prevent surface tension from closing them. Canes of millimetre diameter are typically an intermediate stage of fiber production and a piece of a cane might make an ideal nozzle. Usually these processes are suited to delivering metres of material rather than the few millimetres needed for an oven and as a result they are probably cost prohibitive unless you can get offcuts from a manufacturer. Other microtube array applications include filtration plates and image intensifiers for night vision equipment. The arrays for night vision equipment look particularly promising but they tend to be a sensitive technology, so the lack of an easy supply for these components stopped us from trying this approach, but maybe there are new suppliers now. Another obvious question is whether strontium will react with or clogg a fused silica microtube array based nozzle. Fear of reaction and strontium sticking is the reason we use sapphire rather than fused silica for our Zeeman slower windows but it would appear from the AO Sense website that they may be using glass microtube nozzles which maybe answers this question. We have also heard there are problems with clogging in 3D printed titanium nozzles used for strontium which may be related to the difficultly of achieving a smooth tube surface.

The nozzles we used were built with blood, sweat and many tears from T-33RW stainless 304 tubes supplied by Cadence Inc. We also priced tubes from other suppliers but they were cost prohibitive for the tens of thousands of tubes we needed[4] (each nozzle requires 5,000 tubes and we built several over the development process). The tubing we used came as a bundle of five foot lengths and was measured to have an inner diameter of 110 µm

[3] Technically we did but it was an oil immersion machine and there was no way we were putting microtubes in an oil bath!

[4] Discussions with Markus Debatin from Freiburg at DPG in 2018 suggested that there might be a supplier in Switzerland able to provide ready cut tubes at an affordable price so we will look into this again for the iqClock ovens.

FIGURE 3.9: **Strontium Continuous Atom Laser machine.** Jig used to hold the microtubes in the wire cutting machine in order to cut the microtubes to length. Approximately 10-20% of the tubes slid out of the holder during the cutting process in the wire cutting machine. This significantly complicated the loading process as the bad tubes needed to be removed from the array by tweezers, a particularly labour intensive process.

and an outer diameter of 190 µm. Cutting the tubing with pliers closed the tube ends and a Dremel made a mess of the ends so we needed to wire cut the tubes to size. Ron Manuputy came up with a process for turning this bundle of tubing into a clean cut array of 8 mm long tubes. The steps are outlined in figure 3.9. First the bundle was tight wrapped in paper and Dremel cut to 30 mm long. A brass holder with a glass window clamped ≈10 mm in front was placed on an angle and gradually loaded with tubes tamping the array down regularly to ensure as regular a packing as possible. Once full, the array was pressed down and kept under tension by an array of spring washers. Additional clamps were placed around the tubes on each side to secure the ends. This was then wire cut. The wire cutter ran slowly often stopping with errors as individual tubes bounced around giving an unreliable and constantly changing electrical connection. Although the array appeared very secure, on a micro scale a significant proportion of the tubes were in fact not clamped and moved under the applied forces. Microscope images of the wire cut faces of the outer (showing some closed ends) and inner cut faces demonstrate the irregularity of the array and the numerous gaps which caused problems. A second monolithic version of the holder was prepared for the final tube preparation in hope of generating 3 useful blocks of cut tubes, the lack of securely held tubes again caused problems for the wire cutter and a side view shows a large number of tubes which slid out of the holders during cutting. The end block was used as the initial supply of tubes as this was the least affected by sliding microtubes however at least 10% of the tubes were defective. The wire cutter left the tubes in a filthy state (we did use a deionized water cutter not an oil immersion one!). To clean them, they were ultrasonically bathed in ethanol and acetone constantly changing the solvent once filthy for many hours until at last the solvent remained visibly unpolluted, and finishing with an acetone bath. They were then dried in an oven at 80 °C for a few hours .

The process of loading the microtubes in the nozzle was carried out under a microscope. The oven cap (Figure E.1) was replaced by a (clean!) disk of perspex allowing observation of the full triangular array of microtubes while at the same time providing a hard flat reference surface backed by gravity to locate the microtubes. The tubes were then gradually loaded into the triangular cut out using a pair of tweezers to achieve a defect free filling. The biggest problem was the large number of defective microtubes resulting from the tubes sliding around while on the wire cutter. Some were too short, some too long, some were nicked in one place and cut elsewhere while still more had non flat end faces. The defective items had to be grabbed from among the mass of loaded tubes with tweezers and every time the array needed to be resettled and the next defective item located. With around 5000 tubes needing loading and a 10-20% defect rate, this was tedious. The final row needed an exact number of tubes to complete the row defect free and get a secure robust array. In the final array at least 4 defective tubes can still be observed and the final tube in the final row

got jammed by the wedge but the array otherwise came out well. The plastic cap was then replaced by the stainless 316 cap with an aperture and pressure was applied to the array with the screw wedge to lock everything into position.

Overall the ovens were successful and I would not hesitate to use the design again.

3.2 Transverse cooling

After the oven, the first stage of the atoms' journey is a transverse cooling section. Here the beam from the oven is cooled by a 4-pass optical molasses on the 461 nm transition in both transverse axes. Since atoms are generally travelling at speeds of hundreds of meters per second we have only a few hundred microseconds to cool them. The maximum transverse velocities we are interested in can be estimated from the 15 mm diameter of the differential pumping tubes and the distance of 180 mm from the oven nozzle to the center of the transverse cooling giving an acceptance angle up to 4.8°. The requirements for the transverse cooling intensities are listed in table 3.5 for speeds corresponding to the scattering of both 2×10^4 and 5×10^4 photons in the Zeeman slower (see section 2.5.1 for a discussion on which would be the appropriate maximum number to assume scattered). We set a target intensity of $I_{sat}/4$.

TABLE 3.5: **Transverse cooling requirements.**

Parameter	Unit	Case 1	Case 2
Photons scattered in Zeeman slower		2×10^4	5×10^4
Axial speed	$m \cdot s^{-1}$	206	516
Transverse speed[a]	$m \cdot s^{-1}$	17	43
Photons needed for transverse cooling		1.67×10^3	4.17×10^3
Required scattering rate	MHz	4.3	26.9
Required Intensity	I_{sat}	0.047	0.39

[a]The maximum transverse velocities we are interested in can be estimated from the 15 mm diameter of the differential pumping tubes and the distance of 180 mm from the oven nozzle to the center of the transverse cooling giving an acceptance angle up to 4.8°.

For an 80×20 mm beam obtaining a power of $I_{sat}/4$ requires 160 mW which is not realistic from a blue slave laser. By multipassing the beam we can recycle the power and reduce this power requirement. A 4-pass geometry can reduce this to 40 mW which is very reasonable from a slave laser. Initially large mirrors were tried with a diagonal multipass geometry but this didn't work well. Later Chun-Chia replaced it with a configuration using

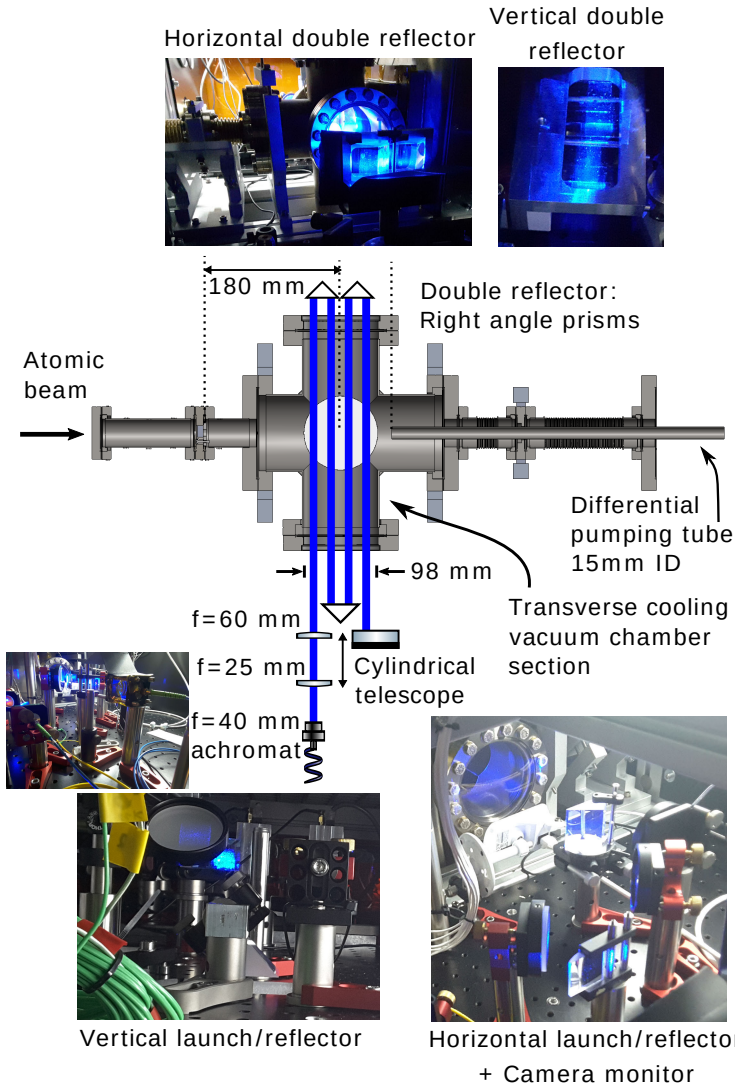

FIGURE 3.10: **Transverse cooling.** Here we show the transverse cooling section and the geometry of the optics. A camera is used to monitor the transverse cooling fluorescence which is used to injection lock the slave lasers.

a series of offset corner cubes[5] as shown in figure 3.10. Although power is important, a highly balanced and uniform beam profile is much more important, otherwise the atomic beam will likely finish with a nonzero final mean deflection or more likely, a deflection varying with position. This is also known as a non-collimated atomic beam. With early implementations we found our transverse cooling to reduce flux rather than increase it due to nonuniformities so one is advised wherever possible to first get a MOT running before adding the transverse cooling so that you have a signal to optimize. For this reason we also spatially filter our slave laser output with a single mode polarization maintaining fiber (Thorlabs P3-405BPM-FC-1) and align the transverse cooling beam based on the MOT atom numbers. We also found that diffraction rings and beam imperfections from our collimating optics can be responsible for major losses. Details like the collimation, lens type and lens size are unexpectedly important and we tried and tested a number of collimating lenses including singlets and achromats. The collimation is done using a free space collimator on a cage mount. This section is wrapped in tape to greatly reduce the incidence of dust damage to the fiber tip which periodically occurs and often requires repolishing the fiber tip. A 2.4× telescope is used to increase the beam size in the horizontal axis to give 9.6 mm×23 mm $1/e^2$ diameter. The use of singlet lenses in the horizontal telescope gives a non gaussian shaped beam in this axis as can be observed in some of the images in figure 3.10. The power of the beams was typically 30 mW per axis giving an average intensity of $I = I_{sat}/3$. The detuning was typically 18 MHz red detuned. The viewports used for the transverse cooling are fused silica with a 461 nm AR V-coating (Demaco A0650-5-AR461).

3.3 Vacuum system

Next the atoms encounter a series of differential pumping stages included to try to improve the vacuum quality, and a mechanical shutter to block the atomic beam. At this point we will actually deviate from our atom journey for a short while to describe the entire vacuum system in coarse detail. We will also describe the supporting structure, the construction processes and the bake. The layout of the vacuum system is shown in figure 3.11 along with the framework used to support the structure.

[5] A word of caution, although the corner cube configuration is a great way to retro-reflect a beam or to tile linearly polarized beams for a molasses it is not a good choice for generating MOT beams. The total internal reflections cause a polarization dependent phase shift by the same principle you use to make a Fresnel rhomb. This means the reflection of a circularly polarized beam will not be circular. We have seen time and again people try to use corner cubes in their 2D MOTs only to waste lots of time then take them apart and replace them with 2 metal coated mirrors. You can use metal (typically silver) mirrors which do not exhibit a phase shift (but they will flip the handedness of a circularly polarized beam on each reflection). If you use a dielectric or totally internally reflected mirror you may assume nothing about the reflected polarization from a circular input.

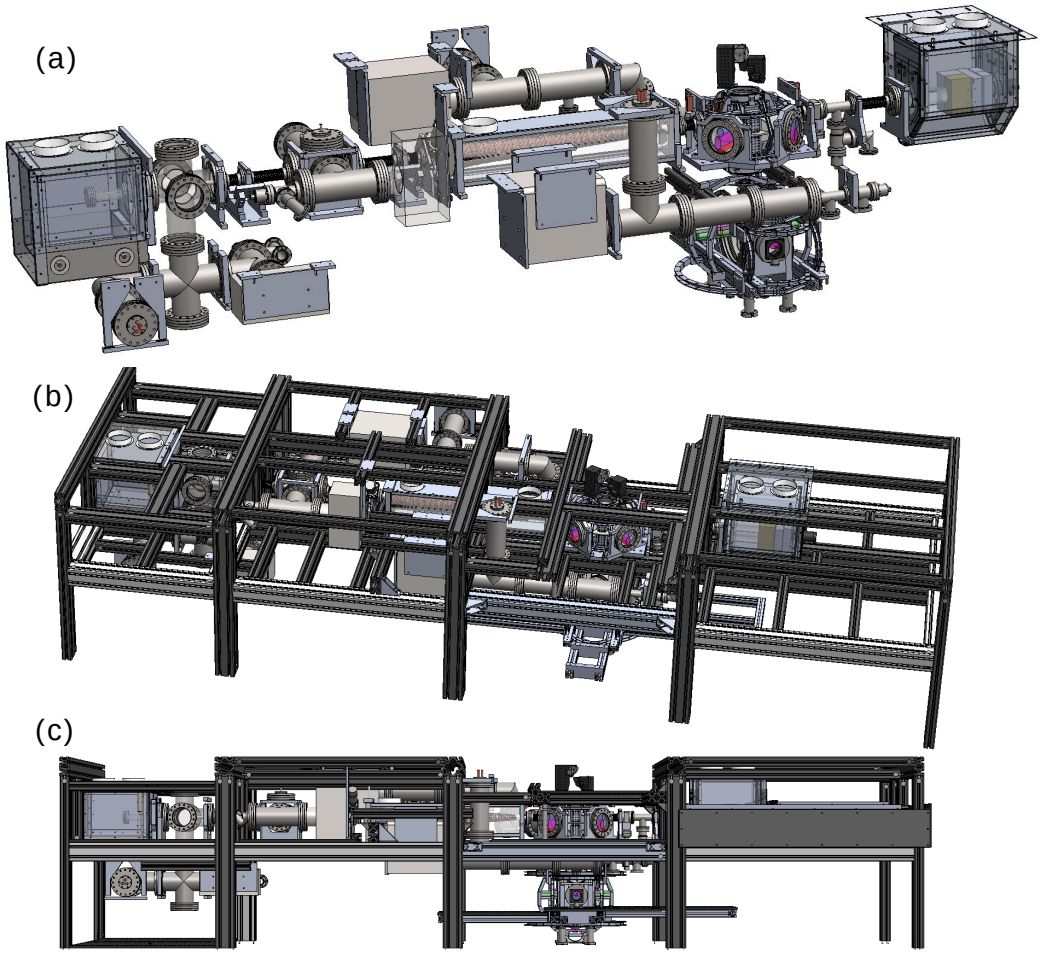

FIGURE 3.11: **The SrCAL vacuum system.** (a) The vacuum system with some of the clamping structures. (b) The vacuum system along with the framework which supports the structure. (c) Side view (in perspective view) showing the large open space around the main lower chamber.

The concept of the machine design was that the top half of the machine should act as "infrastructure" delivering a continuous, intense, cold, slow beam of atoms for use in the lower, atom laser chamber. The design was limited by the existing (newly built at the time) roof electronics support structure which restricted us to a 1 m machine height. As a result the space available in the lower half is marginal. We did reconfigure the roofing structure a little adding numerous access panels to allow aligning the optics while sitting in the roof space (which we often did) and we moved the HEPA filter to another part of the machine. The new designs for the iqClock machines will hopefully replace the entire upper storey with something the size of a old fashioned CRT monitor, which will hopefully make this original concept of cold atoms on tap more practical.

3.3.1 Support structures and framework

Clamping Building a 4 m long UHV vacuum system by bolting together lots of small pieces is asking for trouble as every weld and every gasket is an opportunity for a leak. Worse still, the weight and vacuum forces over long lever arms and distances, the temperature differentials and differential expansion coefficients during a 350 °C bake make this even trickier. Yet the ability to buy most pieces inexpensively, off the shelf and have them all welded by experts gives a reliability which outweighs these disadvantages. To work with lots of joints, we need stress relief in the form of bellows throughout the machine breaking it into manageable pieces. Where possible the structure is supported by multiple clamps at opposite ends of the same piece to avoid stressing the joints. The positioning of most clamps is adjustable to match the machine and where ever possible form a "3 point mount" to avoid over-constraining the system. In one place, on the 4 arms of the 2D MOT upper chamber I initially had clamps for all 4 arms which generated excessive stress so one of the clamps had to be removed. Throughout the machine a 3 mm stainless steel shim is typically used between the clamp and flange to reduce thermal conduction from the chamber during baking and to offer greater flexibility in fine tuning clamp positions by adjusting the shim thickness. Most clamps support the sides of flanges allowing the system to in principle slide along the clamp to reduce thermal expansion or vacuum contraction stress. Over the following years I have seen others weld mounting points to the sides of their chambers and tubes, a concept I have grown quite fond of. Tubes are able to flex a little with stress whereas a flange with a gasket does not need much stress to start to leak. Monolithic chambers like the ones from Kimball Physics on the other hand are massive and thus much more resistant to any stress induced warping than flanges, making them also an excellent mounting point choice. The huge DN200

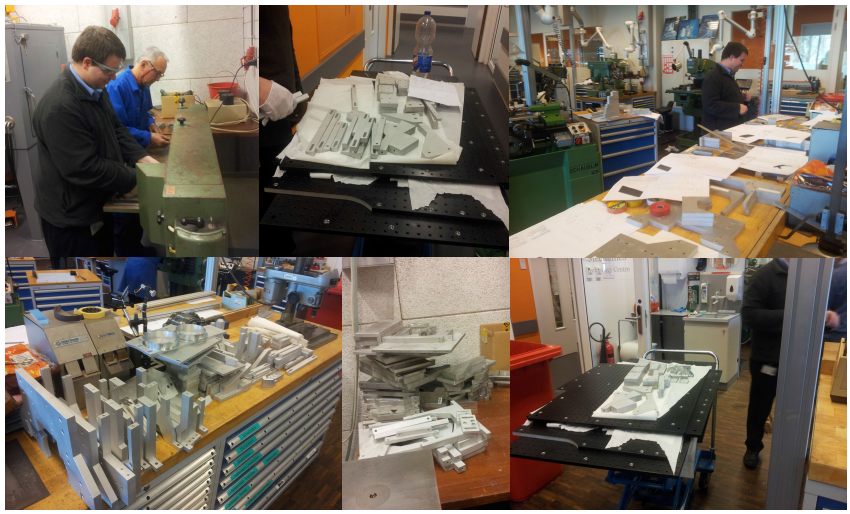

FIGURE 3.12: **Clamps.** Construction of the clamps to support the SrCAL machine.

window flanges on the bottom chamber developed numerous small stress related leaks during the first two bakes (but not the final bake) which had to be resealed by tightening up the sealing bolts afterwards.

Framework All the supports in the SrCAL machine rigidly fix the chamber to the supporting structure so it is very important that the support doesn't flex significantly as it is loaded, especially as the optics and support structures are added after the final bake as this could introduce leaks. In fact we also used the support structure to mount breadboards containing the laser and distribution systems. There are even places where beams are coupled to optical fibers on neighbouring breadboards which have been stable for months in the absence of temperature fluctuations so the structure was very rigid. But a rigid structure provides no relief for thermal stresses from temperature changes. The support structure is aluminium while the chamber and optical table are stainless steel which caused me much anxiety over the years. Most parts of a vacuum chamber can move a little without causing problems for a machine so if I were to do it again I would try to include more soft clamping. Options include viton spacers which can work to around 230 °C, compressed thin walled stainless tubing, flexures and springs (which Georgios successfully tried for supporting his SrMic chamber during his bake).

The aluminium profile framework for the machine was purchased cut to size and with all the required holes from Item. The reason I used Item profiles was that the strength and rigidity of their 50 mm and 100 mm profiles (parts 0.0.624.56, 0.0.624.60,

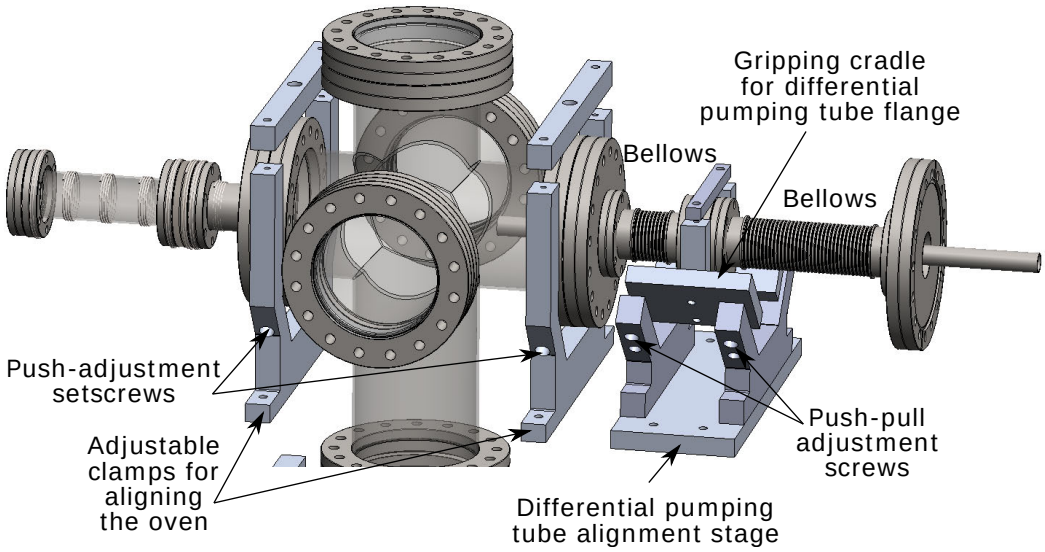

FIGURE 3.13: **Alignment clamps.** The clamping structures used to align the differential pumping tubes and the oven with the Zeeman slower tube.

0.0.624.52) is unparalleled and they are compatible with the 25 mm hole spacing of the optical table. This way the entire structure can simply be bolted to the optical table using some slightly shortened universal fasteners (part 0.0.632.07) without the need for disruptive angle brackets. It would be easy to turn the manufacture of all the clamp structures into a complex and expensive manufacturing project. We used a local waterjet cutting shop to cut all the clamps complete with most of their holes directly from plate aluminium for not much more than the material cost. To make it prettier I sand blasted the parts to clean them up. They needed deburring and, where appropriate, threading and a few extra holes but the clamps project went very quickly and easily, and I would strongly recommend this approach again. A picture of the completed clamps is shown in figure 3.12.

Alignment There are three places where the vacuum chamber itself needs to be aligned. The oven and the two differential pumping tubes needed both angle and position adjustment to align them to the Zeeman slower tube. The alignment structures were based on sitting the vacuum system on long set screws in a 3 point configuration in two places which gives four degrees of freedom, position and tilt. The structures are shown in figure 3.13. Hydrolic bellows (Lesker MHT-CF-C03) allow independent movement of the different sections. Alignment of these sections was performed after the high temperature bake while in the process of adding the Zeeman slower

gate valve and before loading the strontium into the oven. A DN35 viewport was mounted in place of the oven nozzle and a HeNe laser was installed and aligned to fill the Zeeman slower tube without clipping from misalignment with the sides. Irises were installed to mark this location which remain in the machine today. Next, each differential pumping tube could be positioned and tilted to avoid clipping the transmitted HeNe beam. The entire transverse cooling structure needed to be moved and tilted to align the oven. The nozzle was installed and its position was adjusted looking for beam clipping while a triangular diffraction pattern from the microtube array was the target for adjusting the oven tilt. It was envisaged that these alignments would be adjusted to optimize the flux from the system but this was before feeling the strength of the forces the vacuum system was able to exert on these structures. After pumping down for the first time before the high temperature bake I played a little with these alignment structures. A slight release of the screws clamping the differential pumping tube flange and the vacuum forces will take control and yank the tubes back to their equilibrium position. In doing do they will remove any alignment you might have made. For this reason I would rely on our original pre-bake alignment rather than trying to adjust or optimize them. A better solution here might have been to weld or thread some mounting points to the differential pumping tube flanges rather than relying on simply gripping the flange edge with a clamp.

3.3.2 Assembly processes

Assembly Wherever possible the system is assembled with silver plated screws using plate nuts and silver coated gaskets. Exceptions include windows where annealed gaskets are used and the oven where high temperature nickel gaskets are used. The silver screw plating allows high temperature operation without the threads seizing and without needing to use copper oxide paste (Messy! Yuk!). A trick I saw used on Rene Gerritsma's ion trap machine was to use threaded rod for at least some of the screws around the viewports. This gives an easy mounting point to attach a (light weight) optical system, something which might have been really useful and something which now features extensively in the iqClock designs. Our assembly process began by inspecting the knife edges of a part and then wherever possible ultrasonically bathing (small parts) first in acetone (99% VWR 20063.365) and then in ethanol (99.9% ACS grade, Brunschwig Chemie ET00162500) typically for 10 minutes or until clean. Kimwipes (Thorlabs KW32) with ethanol were then used to clean the ends of a part taking particular note around the knife edge. The process was repeated until no dirt was visible on the kimwipe after cleaning. This process took

place on the HEPA filtered optical table wearing power free nitrile gloves on a bench lined with oil free 38 µm thick aluminium foil (Part Al-Fl-24-0015 from Demaco) for cleanliness and some limited knife edge protection. Gloves were changed regularly but we didn't go to the lengths of bunny suits or dedicated tool sets as a bake should take care of any small residual contaminants. Unfortunately the lab was a mess when we were putting the SrCAL machine together so a lot of particles can still be seen on the inner surfaces of chamber windows which is a source of shame. Later all the electronics work and cardboard boxes full of parts for the SrCAL and SrMic machines were moved to a dedicated store room and we claimed additional space for doing electronics. This improved the lab dramatically before the SrMic machine was built. We didn't have a torque wrench when we assembled the chambers and judged by eye the even compression of the gasket. Later we realised a feeler gauge was the ideal tool for getting an even assembly and we started compressing our gaskets to a flange spacing of ≈250 µm. We did not tighten our gaskets metal to metal for fear that in event of a leak there would be no way to further compress the gasket to fix it. Some of the connections leaked a little mostly around the viewports when we first leak checked the system. This was easily corrected by tightening the bolts a little and reducing the flange to flange separation to ≈150 µm. In discussions with other groups we found that a target flange spacing of 100 µm-150 µm is more typical.

Leak checking To leak check the system we used an SRS RGA100 with an electron multiplier[6] which we hooked up the pump station near the turbo pump. We applied helium moving the jet over all flange joints and all welds on the machine. We found there was always a small delayed (typically 30 s) leakage through all our fused silica windows. This surprised us a little. The delay was a clear signature quite different from the leaks we saw through welds and gaskets. This signal decreased as you moved the helium gas jet away from the window and onto the gaskets of the viewports, so we assumed it was intrinsic to the viewport itself. Our viewports were specified to leak rates better than $1 \times 10^{-10}\,\mathrm{bar \cdot cm^3 \cdot s^{-1}}$ and $2 \times 10^{-10}\,\mathrm{bar \cdot cm^3 \cdot s^{-1}}$ depending on manufacturer. It turned out that fused silica has a particularly high helium diffusion rate [283, 284]. An equation for the diffusion is given by

$$\frac{dQ}{dt} = \frac{KA\Delta p}{d}, \tag{3.2}$$

where

[6] The electron multiplier was only used at pressures below 1×10^{-8} mbar and only ever operated for a few hours when a measurement needed to be made to preserve the lifetime.

dQ/dt = Mass flow in $\mathrm{cm}^3 \cdot \mathrm{bar} \cdot \mathrm{s}^{-1}$,
A = Window surface area [cm^2],
Δp = Differential helium pressure across the window,
d = Window thickness [mm], and
K = Permeation rate [$7.6 \times 10^{-9}\,\mathrm{cm}^3 \cdot \mathrm{bar} \cdot \mathrm{mm} \cdot \mathrm{s}^{-1} \cdot \mathrm{cm}^{-2} \cdot \mathrm{bar}^{-1}$] [283].

For our DN200 windows the calculated diffusion rate for a full atmosphere of helium across the entire window is $2.4 \times 10^{-7}\,\mathrm{bar} \cdot \mathrm{cm}^3 \cdot \mathrm{s}^{-1}$. It is easy to understand how we can detect this diffusion with our RGA. Fortunately helium is rare in the atmosphere (5×10^{-6}) so its diffusion is tolerable and the diffusion for other gases is tiny [283]. Kodial (7056) glasses have diffusion more than an order of magnitude smaller [283], while aluminosilicate glasses can have diffusion rates nearly five orders of magnitude smaller [284]. This will be important for future applications like sealed vacuum systems [284]. In hindsight we probably could or should have used Kodial glass viewports for their better temperature range as well as other properties like cost and helium diffusion rates. We never needed the transmission range of fused silica.

3.3.3 Transverse cooling and differential pumping section

Next I will step through the machine and describe the design of the individual sections. We begin with the oven, transverse cooling and differential pumping section shown in figure 3.14. This section has two pumping chambers, the first includes the oven and windows for transverse cooling and the second has a mechanical shutter to block the atomic beam in order to protect the back window and the gate valve. The shutter is less important in the SrCAL machine than in the RbSr and SrMic machines where it is helpful to stop fast atoms which would otherwise bombard the MOTs and BECs[7]. In our case the sensitive parts are in a whole other chamber. Differential pumping tubes with a 15 mm inner diameter connect the different pumping chambers and both sections. Both chambers include a rebuilt Varian $75\,\mathrm{l} \cdot \mathrm{s}^{-1}$ starcell ion pump from Duniway and a titanium sublimation pump (TSP) (300 mm long VG Scienta part ZST22-300). A compilation of the pumping rates is listed in table 3.6[8]. Both ion pumps are driven by the same ion pump controller, a Terranova 751A[9] from Duniway with two output connectors. Since the ion pumps draw tiny currents at the

[7] Although BEC can also be made and used with the shutter open in these machines. Florian's opinion is that the shutter is mainly useful for keeping the strontium off the back window.

[8] I think a small word is in order discussing vacuum pumps. A number of people have said over the years "Why would you use those big old fashioned ion pumps when you can get a little red one from SAES with 25 times the pumping speed?" I am a fan of the SAES pump technology bringing a clean powerful pump to a compact package. This is great for small machines and compact demonstrators but it is an expensive pump and I am not convinced it is able to compete with the raw pumping power of traditional approaches as described in table 3.6.

[9] These pump controllers were by and large trouble free except that twice the fuse (and the plastic IEC power connector in which the fuse was held) exploded. This little 3am bang tripped the circuit breakers and all our

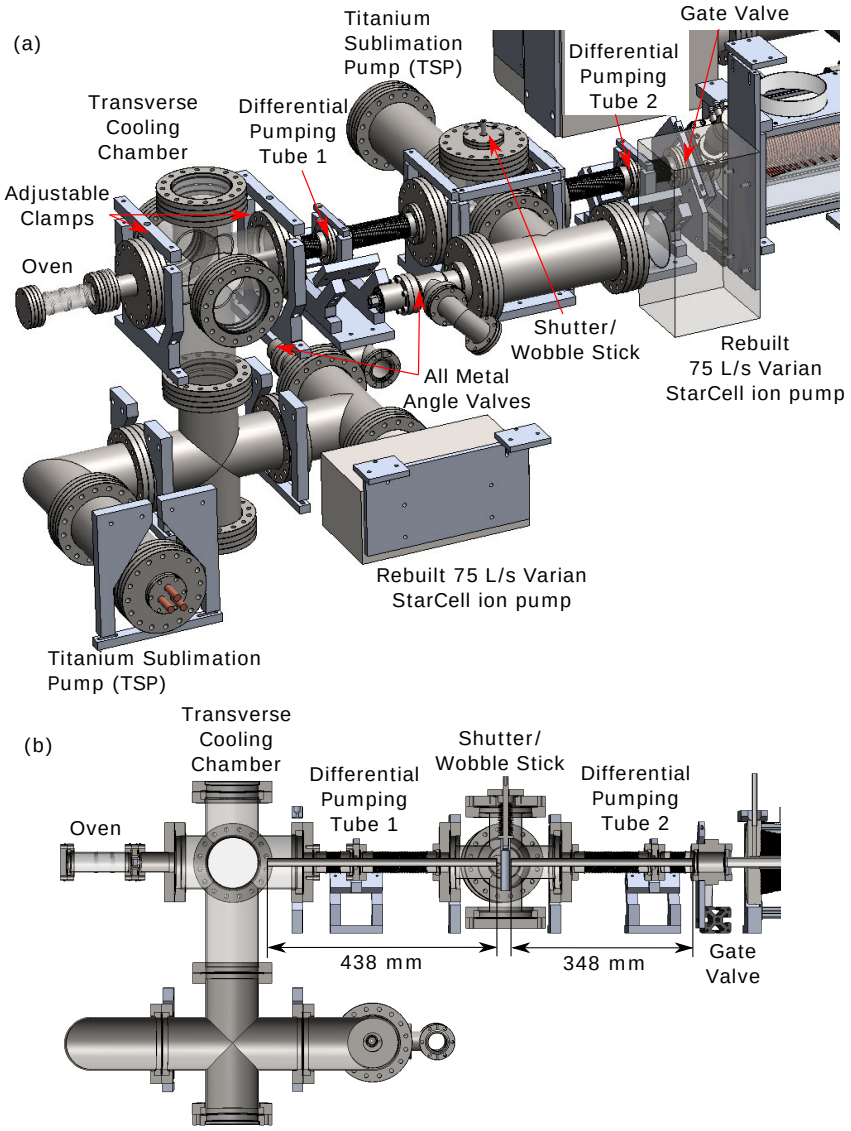

FIGURE 3.14: **Transverse cooling and differential pumping.** The transverse cooling and differential pumping section of the vacuum chamber.

10 µA level there is no load issue from driving multiple pumps from the same controller. The only down side is that we don't have records of the individual pump currents. There is no line of sight between the TSPs and the ion pumps. This was deliberate to try to avoid creating titanium deposits or flakes which might bridge the ion pump causing a leakage current. Details of some of these components will now be described.

TABLE 3.6: **Pumping speeds.** A summary of the pumping speeds for a titanium sublimation pump on a DN100 300 mm long nipple, a (rebuilt) Vacion 75 $l \cdot s^{-1}$ ion pump and a SAES NXT D-2000 pump. Pump rates for some gases are not specified by the manuals and these are listed as '-'.

Gas	TSP with 1000 cm^2 area [$L \cdot s^{-1}$]	Rebuilt 75 Lps Starcell pump	NEXTorr D 2000-10
H_2	3000	-	2000
H_2O	3000	-	-
CO	9000	-	1100
N_2	4000	25	640
O_2	2000	-	1700
CO_2	8000	-	-
CH_4	0	-	32
Argon	0	20	10
Helium	0	-	-
Cost	≈1 k€	≈2 k€	≈12 k€

Mechanical shutter The mechanical atomic beam block (shutter) is located between the two differential pumping tubes as shown in figure 3.14. It is essentially a wobble stick (Part WBL-275 from Demaco) able to move in an out the atomic beam. The diameter of the stick is however too small to block the beam so we clamped a 20 mm diameter aluminium (6061- as we know this aluminium is regularly used for UHV) pipe to the bottom. On the RbSr machine the wobble stick was squished in a press to make it bigger but in our case we needed much too large a size ratio increase. Since installation I have had nightmares about the pipe falling off the wobble stick. This could have been avoided by notching the wobble stick so that the clamping screw could clamp reliably even in the presence of large temperature cycling (like our bakes) or by using gravity to our advantage instead of disadvantage and turning the system upside down (which was later done on the SrMic machine). Another little point of note is that the air pressure pushes the wobble stick into the chamber with quite some

alarms making for a little excitement. After the second event pieces of the power connector and the fuse were found throughout the lab.

force. Normally a plastic ball handle (unsuitable for baking) is fitted to the end of the stick providing a limiting stop[10].

Gate valve At the end of the second differential pumping tube a pneumatic DN35 gate valve allows the separation of the oven section of the machine from the Zeeman slower and subsequent sections. This allows the oven to be repressurized and the reservoir reloaded with strontium while maintaining UHV in the rest of the machine[11]. Part of the reason for the mechanical beam block was to protect the gate valve from being coated with strontium for fear this coating might flake or oxidize, ruining the seal. We wanted to use all metal gate valves from VAT so that we could bake the whole system to 350 °C and since these valves had been used in earlier machines like RbSr. However, they were too expensive so we purchased valves with Kalrez seals (better temperature range than Viton) and copper bonnets. We were very worried about using elastomer o-rings in the machine. We heard that on the helium machine at VU they get a pressure burst to 1×10^{-8} mbar every time they open their valve[12]. First we purchased valves from MDC but that didn't go well[13]. We then purchased replacement valves with a special cleaning procedure from Demaco (part GVMP-1502-CF-S32). I'm not sure that the special cleaning added anything but cost but I wouldn't hesitate to use these valves or similar valves again before a Zeeman slower. We also observe the pressure burst every time we open the valve but being on the other size of the Zeeman slower it didn't seem to affect the 2D MOT chamber.

Differential pumping Differential pumping tubes were included to reduce the flow of background gas from the oven to the 2D MOT and atom laser chambers where we want good vacuum quality. The size of the differential pumping tubes was chosen as 15 mm inner diameter, more or less the same as the Zeeman slower tube diameter (16 mm). This caused essentially no apperturing to the atomic beam from the 10 mm diameter oven. We made the tubes as long as possible without extending the overall vacuum chamber length. We can examine their performance using molecular flow

[10] Beware - without the handle attached there is a risk of air pressure pushing the wobble stick all the way into the chamber and breaking the bellows

[11] Reloading the oven reservoir with strontium is something I had hoped to avoid. In principle if it can be done quickly without oxidizing the strontium in the machine and with minimal water contamination it might be a painless procedure - but things rarely work out that way. When the RbSr oven was changed over to introduce rubidium to a purely strontium machine, the strontium in the machine oxidized covering the transverse cooling windows in a white power which had to be scraped off. Any long process will also introduce water vapour to the machine which will need to be baked out. Normally this wouldn't be a big problem but for us the laser systems had to be build around the vacuum system due to space constraints so any bake is likely to be a long disruptive process.

[12] We recently discovered the same is true from a similar valve on the strontium clock at Torun in Poland.

[13] We have not purchased any products from MDC since this experience.

TABLE 3.7: **Differential pumping tubes.** Here we list the geometry and conductances of the differential pumping tubes and the series of four baffles between the upper and lower chambers which is described in section 3.3.4. We also estimate the gas load reduction between sections assuming the main load is from the oven and neglecting the pump capacity from the TSPs as a rough guide to the effectiveness of the differential pumping. We can add the conductance of a series of tubes as $1/C = 1/C_1 + 1/C_2 + ...$ The "effective load reduction" is the ratio of the gas load which will impinge on the subsequent system, the lower the better.

Tube	Diameter [cm]	Length [cm]	Conductance [$l \cdot s^{-1}$]	Pump [$l \cdot s^{-1}$]	Effective load reduction
Differential pump 1	1.5	43.8	0.93	75	0.012
Differential pump 2	1.5	34.8	1.17	75	0.005
Zeeman slower	1.6	92.0	0.54		
Baffles	0.8	4×	1.46	150	0.01

equation 3.3 to describe the flow through a tube [285, 286]. The conductances of the three tubes in the system are shown in table 3.7.

The conductance through a pipe is given by

$$\begin{aligned} C_{\text{tube}} &= \frac{1}{6}\sqrt{\frac{2\pi k_B T}{m}}\frac{d^3}{L} \\ &= 12.1\frac{d^3}{L} \end{aligned} \tag{3.3}$$

where

C = Conductance [$l \cdot s^{-1}$],
d = pipe inner diameter [cm],
L = pipe length [cm],
T = Temperature, 300 K, and
m = Molecular mass $\approx 1 \times 10^{-25}$ kg for air.

With hindsight, the TSPs in the transverse cooling and differential pumping sections are completely redundant and should not have been included. The pressures in the oven section are sufficiently high that the TSP saturates within days at most (if not hours). Furthermore the differential pumping tubes and Zeeman slower provide an enormous isolation so that the pressure at the 2D MOT chamber is essentially unaffected by the oven. It might be that the ion pump in the second differential pumping chamber and the second differential pumping tube are also redundant but that would be a bigger call. The effective isolation with two pumping stages is the multiplication of the two effective load reductions from

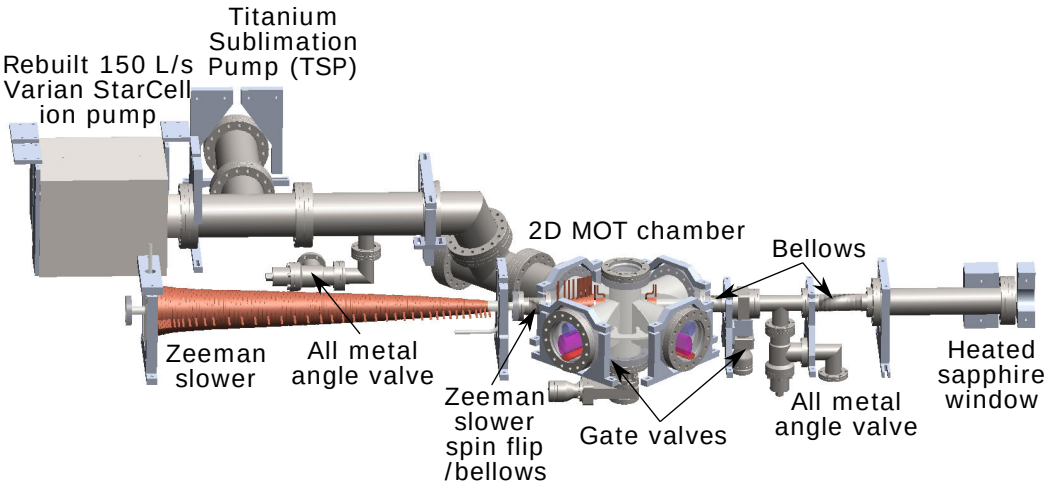

FIGURE 3.15: **2D MOT Chamber vacuum system.** The vacuum system for the 2D MOT chamber including the heated Zeeman slower window.

table 3.7 giving 6×10^{-5}. If we were to drop the second differential pumping tube and the second pump we have an effective load reduction of 4.6×10^{-3}. For the SrCAL machine we have additional isolation through the baffles between the 2D MOT and atom laser chambers and we don't do quantum gases in the upper chamber, just MOTs so for the SrCAL it is probably safe to say the second differential pump tube and ion pump are redundant. At design time the need for the second pump and differential pumping tube was discussed but we took a conservative approach.

3.3.4 2D MOT chamber section

After the transverse cooling and differential pumping come the Zeeman slower and then the 2D MOT section also known as the blue chamber or upper chamber. I won't say much about the Zeeman slower here as the vacuum system is essentially just a pipe. The 2D MOT chamber is shown and described in figure 3.15. Within this chamber there is a wire cut mirror holder as well as mirrors and neutral density filters which will be described in the section on the 2D MOT (section 3.5.2). Section 3.5.2 will also describe the rather unusual shape of the chamber and how that came to be. Here we will only discuss the differential pumping properties of this series of baffles.

Pumping This chamber is pumped by a rebuilt $150\,\mathrm{L \cdot s^{-1}}$ Varian Starcell ion pump from Duniway and a titanium sublimation pump (TSP) (300 mm long VG Scienta part ZST22-300) (see also table 3.6). The ion pump is located around 1 m from the chamber to reduce the effects of the ion pump magnetic field but more importantly to free the

space around the chamber for coils, magnets and optics. A DN100 pipe connects to the vacuum chamber providing high conductance.

Zeeman slower heated window section The pumps of the 2D MOT chamber also pump the heated Zeeman slower back window. This will be discussed in more detail in section 3.4.4 but in brief we need to heat the back window to 180 °C and make it from Sapphire so that strontium doesn't stick and coat it, which would make it reflect the Zeeman slower light. In case something bad happens to this window we include a gate valve (part GVM-1502-CF-M) and an all metal angle valve (VAT 54132-GE02) so that the section can be sealed off and independently pumped and baked without breaking vacuum in the main chambers. The gate valve has only been closed a couple of times but it's presence does not seem to adversely affect the vacuum quality which can be achieved in the 2D MOT chamber.

Baffles A series of four orifices baffle the lower chamber from scattered blue light and also form a differential pumping section between the top and bottom chambers. We can calculate the conductance through this baffle in the molecular flow regime from [285, 286] using equation 3.4 with the results included in table 3.7 along with the results for the other differential pumping tubes. The impact of the baffle is to essentially provide a 20dB isolation between the pressures of the upper and lower chambers.

$$\begin{aligned} C_{\text{tube}} &= \sqrt{\frac{k_B T}{2\pi m}} \cdot A, \\ &= 11.6A \end{aligned} \tag{3.4}$$

where

C = Conductance [$\text{l} \cdot \text{s}^{-1}$],
A = orifice area [cm^2],
T = Temperature, 300 K, and
m = Molecular mass $\approx 1 \times 10^{-25}$ kg for air.

3.3.5 Atom laser chamber section

The final vacuum section is the atom laser chamber[14]. This is detailed in figure 3.16. We begin immediately below the baffles between the upper and lower chambers. Here there is

[14]The atom laser chamber is also known as the red MOT chamber or the lower chamber.

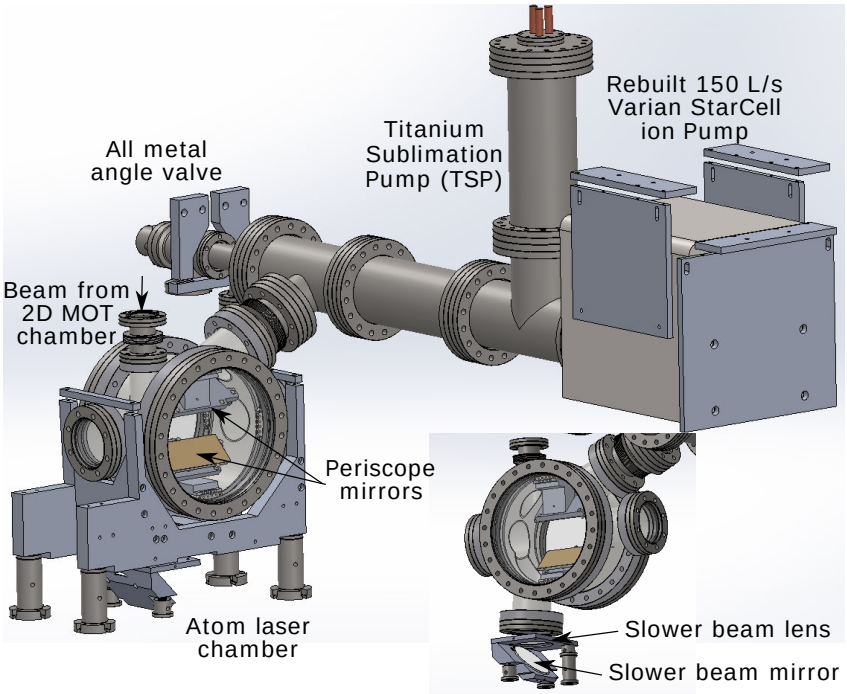

FIGURE 3.16: **Atom laser chamber.** The final vacuum section is the atom laser chamber and its pumping system.

a gate valve (part GVM-1502-CF from Demaco with a kalrez seal[15]). The purpose of this gate valve was so that the bottom chamber could be replaced or modified once we had a steady-state BEC and atom laser. This would allow the inclusion of a cavity for a steady-state superradiant laser or optimization towards a continuous atom interferometer. We had great misgivings about using these elastomer sealed valves in the UHV final chamber and as we will discuss in the next section these remain unresolved. Like the 2D MOT chamber, the atom laser chamber is pumped by a rebuilt $150\,\mathrm{L}\cdot\mathrm{s}^{-1}$ Varian Starcell ion pump from Duniway and a titanium sublimation pump (TSP) (300 mm long VG Scienta part ZST22-300) (see also table 3.6). Again the ion pump is located around 1 m from the chamber in part to reduce the effects of the ion pump magnetic field but more importantly to free the space around the chamber for coils and optics. In chamber mirrors are mounted on flexure mounts using the same techniques as in the top chamber. This along with the chamber design will be described in detail in section 3.6. Welded bellows were included between the chamber and the gate valve and between the chamber and the pumping section with the idea that this might be needed for a future interferometer where we might want to vibrationally isolate the chamber (at least to first order).

3.3.6 Baking

We conducted two bakes of the machine. The first was a high temperature hydrogen bake targeting 300-350 °C designed to remove as much hydrogen from the steel as possible. This first bake was conducted without any of the lower temperature rated components like windows, in chamber optics, their aluminium holders and gate valves. The second low temperature bake targeted around 200 °C and aimed to remove water and any residual volatile materials from the machine.

The high temperature bake should be as hot as possible without damaging anything and it should last as long as your patience. Hydrogen is usually the main gas load in a steel chamber as it diffuses out of the walls. By increasing the temperature the diffusion rate can be increased allowing the hydrogen to escape the steel and be pumped out reducing the future gas load from the chamber. This is particularly effective for thin steel like tubes where you can deplete the entire material thickness of hydrogen. There is a second related technique which can be used to reduce the hydrogen load from a chamber, the air bake. If you heat steel to a few hundred °C it will oxidise and change colour. This oxide layer can act as a barrier to hydrogen encasing it within the steel. The air bake is a quick process while the vacuum bake can take months but in principle the vacuum bake can reduce a hydrogen gas load further. The RbSr machine, like the machines before it had a long

[15]This valve has imperial threads instead of metric to allow the use of the kimball physics close couplers to keep the distances compact.

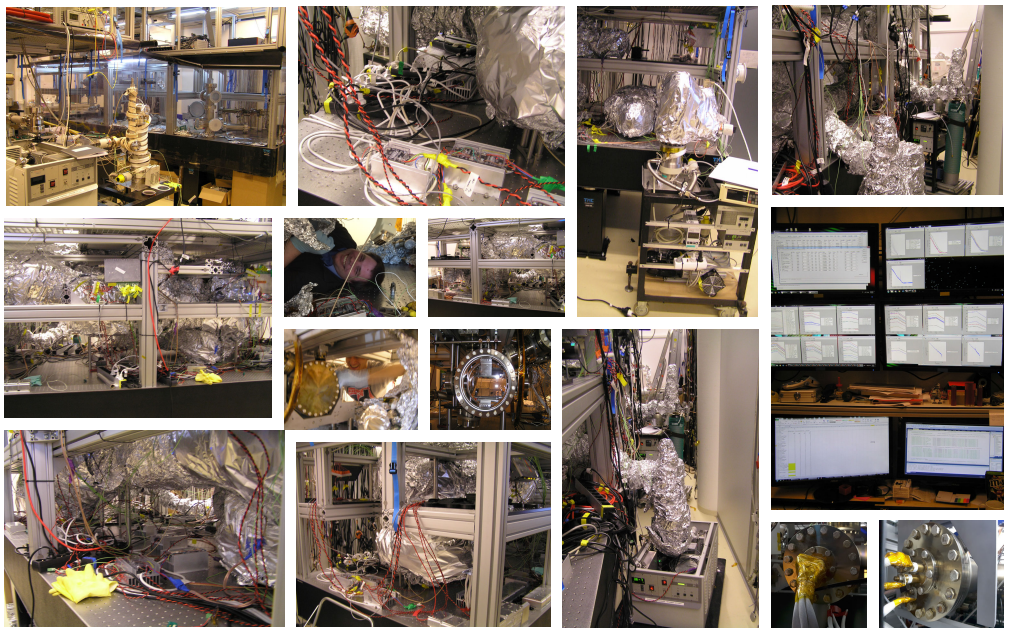

FIGURE 3.17: **Baking setup.** The machine during the bakeouts.

vacuum bake so that is what we did. A different approach is to entirely avoid using materials loaded with hydrogen. Options include titanium (which is expensive to buy and very expensive to machine), aluminium[16] and glass. Another option is to heat treat your steel chamber, essentially a hydrogen bake on speed. This should be incorporated into the manufacturing process as steel knife edges are not rated for operation above 450 °C and at high temperature they dull so some post processing will likely be required. The SrMic chamber was accidentally made out of a magnetic steel by the manufacturer and they offered a heat treatment process as a remedy for this. A bonus of this heat treatment process was that the chamber also had a very low hydrogen load[17]. This heat treatment will also harden the steel making it more brittle as well as non-magnetic and hydrogen degassed.

To heat our chamber we wrapped it in heating tapes (Omega parts STH102-060, STH102-080 STH052-100) and flange heating bands (Omega part MBH00236, MBH00274 and MBH00336). These heating elements were driven at 230 V AC by a solid state relay, Omega part SSR330DC25 with groups of two relays mounted on an Omega FHS-7 heatsink for cooling (with additional holes tapped for dual relay mounting). Due to the limited number of relays typically one or two heating elements of the same type and in close proximity

[16] Aluminium is soft and requires an explosive bonding technique to clad the flanges with a layer of steel in which knife edges can be machined. Five years ago this was a speciality product but now it is increasingly widely available so aluminium chambers are looking increasingly exciting.

[17] I believe that CERN also heat their steel tube sections to 800 °C to degas them.

were grouped in parallel electrically. No more than 3 kW was placed on any 3.6 kW mains circuit, and 12 circuits were used for the bake with 4 additional spare circuits left available for debugging and to handle failures. Temperatures were monitored using thermocouple wires (omega part GG-KI-24-300M) which we spot welded and insulated with Kapton tape as shown in figure 3.3 (far top left). Typically we tried to place several thermocouples for each heating element. We aimed for monitoring places of average temperature as well as hot and cold extremes to keep an eye on the variation of the baking within the machine. The machine was wrapped in many layers of thin 16 µm household aluminium foil to insulate the chamber and thus reduce the temperature variations (not to mention the heat load on the room). We tried to use large sheet wrapping with the aim of minimizing convection around the chamber to keep the heat in. During the first bake we also tried to recycle some of the 38 µm thick aluminium "UHV" foil left over from the vacuum assembly. We found it conducted much more and provided a comparatively poor insulation so we stopped the bake and removed this thick foil replacing it with standard cheap household foil which worked much better[18]. In all cases the temperature sensors and heating bands were secured to the chamber with kapton tape and, where necessary, fibreglass ribbons. This tape performs well at temperatures below 250 °C but our high temperature bakes, went higher. Where possible we tried to put the sensors under the fibre glass heating bands and used excessive amounts of tape to try to compensate for the expected tape failures. Most of our sensors remained in place even during the high temperature bake. The monitoring and alarm system was originally developed for the bakes and remains in use monitoring the machine today. It is discussed in section 3.7.4.

We used three turbo pump stations to maintain vacuum but shortly after we had pumped down for the window bake one of our primary membrane pumps failed [19]. We also had several heating bands short during the high temperature bake. This was a wicked problem because it would knock out several other heaters on the same mains circuit and it took several occurrences to identify which heating band was defective. The rapid temperature fluctuations were also a problem which could have caused failure had it occurred around viewports or feedthroughs. Fortunately all the problematic heating bands were identified before the final window bake but the TSP on the atom laser chamber section experienced some rather nasty thermal shocks. Other causes for excitement included the partial melting of the polyethylene roofing material (which by design softens at around

[18] A word of caution. We had several instances of heating bands shorting with the foil or the chamber. Although the table is grounded a set of thick rubber gloves and much caution is recommended when handling the aluminium foil with live heating bands.

[19] This tested our alarm system as I had already left and had to race back to find our turbo grinding under the load trying to maintain vacuum and hitting temperatures of 65 °C. The turbo survived, the vacuum was maintained and we repaired the primary so all worked to plan.

80 °C[20]) and the complete failure of the room air conditioning system which caused us to rapidly shut down the high temperature bake for fear of melting or damaging things and restart it again after the air conditioning had been fixed. See figure 3.19 for the logs.

Our chamber is supported by aluminium clamps and intertwined with an aluminium framework. One problem is that aluminium softens above 200 °C and loses most of it strength by 350 °C. For this reason, all the main support beams (which consisted of hollow aluminium profiles) were forced air cooled during the bakes. Additional steel posts (mostly Thorlabs 0.5″ and 1″ optical posts with setscrews on top for fine length adjustment) were introduced to support the chamber from below as an insurance against aluminium clamps softening and many of the aluminium clamps were removed to reduce heat conduction and avoid cold spots[21]. To get a more uniform bake, the temperature profile was fine tuned spatially by adding or subtracting aluminium foil insulation.

To protect the window surfaces we folded protection covers from 2 mm thick aluminium plate which slipped over all the window flanges. These also provided a thermally conductive surface in order to produce a uniform thermal environment around the window and thus minimize thermal gradients across the window.

Window bakes are risky as a loss of power can lead to a rapid temperature drop and thermal gradients which can crack or implode windows. To reduce this risk a large amount of thermal mass was added around the windows for the window bake (see figure 3.18). The hope was that in the event of power failure this would give our windows at least a sporting chance of survival. For the iqClock project the machines we are designing are quite small, small enough to insert in a well insulated and high thermal mass oven. The hope is that we will have an entire oven which is window safe and immune to power failure. A picture of the oven we made and are currently testing is in figure 3.18.

The records of the temperatures and vacuum pressures for the bakes are included in figures 3.19, 3.20 and 3.21.

[20] This is required by fire safety regulations so that in the event of a fire there are no obstructions to the fire sprinklers.

[21] This was the cause of a small disaster which cost us a month. At the end of the window bake after a 24 hour day babysitting the final temperature ramp the aluminium foil was removed, the aluminium clamps were reattached and these additional steel support posts were removed. This had been almost completed and we were preparing for celebratory drinks at the bar. I removed the final steel support post from under the atom laser chamber pump section without first checking the aluminium clamps had been secured. This pump section moved around 1 mm flexing two of the joints and introducing a large leak which sent our ion pump current spiralling. Applying acetone quickly showed two problem joints (next to the ion pump). They were resealed by tightening the bolts and compressing the joints metal to metal. A leak check found no leak but the pressure was significantly affected and the chamber probably had acetone from the leak check. After a couple of days going through the 7 stages of grief with a strong focus on denial the decision was made to repeat the window bake on the 2D MOT and atom laser chambers. The second window bake was done with much slower ramps and we didn't get the leaks which formed around some of the window gaskets in the first window bake so maybe there was some good that came from this. There was also a little learning lesson in this - don't do vacuum when you are exhausted!

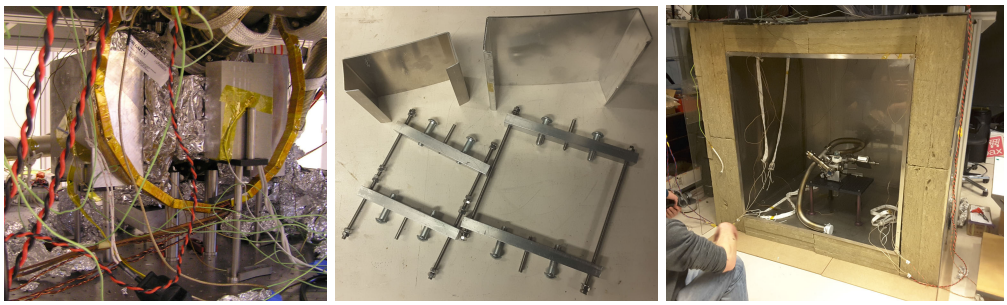

FIGURE 3.18: **Window protection.** (left) For the SrCAL bakes we added thermal mass around the windows to try to reduce thermal gradients in the event of a power failure. (middle top) Folded aluminium covers were placed over all the windows to create a more uniform thermal environment and protect the window surfaces. (middle bottom) Tools for separating uncooperative flanges. (right) The new oven we made for the iqClock bakes has internal dimensions of 1.2 m high, 1 m wide and 1.4 m long. It is made from thick mineral wool insulation with an internal steel box. The hope is that with a reasonable thermal mass this oven will be intrinsically safe for windows against power failures. Initial tests have shown a $1/e$ time constant of around 10 hours.

3.3.7 Vacuum quality

We do not have any pressure gauges in the machine so we rely on the atoms and on the currents through the ion pumps to indicate the vacuum quality. A history of our machine's operating temperatures and ion pump currents since we first started the oven is plotted in figure 3.22. During the weeks after the final window bake our ion pump currents remained at the limits of the display on our controller and we were very happy. But then ion pump currents started to rise.

Depression was starting to set in as the combined currents from our two $150\,\mathrm{L}\cdot\mathrm{s}^{-1}$ ion pumps nudged 6 µA. Our operating voltage was 7 kV giving a corresponding pressure of [287] 1×10^{-9} mbar. Strangely, flashing the TSP didn't make any difference so things were a little fishy. After 6 months of this we decided to try something radical and 'hi-pot' the ion pumps [287]. We borrowed a 12.5 kV, 1 mA power supply and to our glee we managed to make lots of sparks burning off the whiskers and reducing the ion pump currents all the way back to the values we had when we started. Thus it was concluded that our pressures were actually good and the ion pump currents were just part of some wicked sense of humour on the part of our experiment. To our dismay just a few weeks later the current spiked up again and seemed to acquire a bipolar personality, happy one day sad the next but this gave us no real cause to doubt the vacuum quality. On one of the sad days with a high controller current the fuse on the controller exploded and it did it again a few weeks later (figure 3.22). After this we hi-potted the pumps again and reduced the voltage on the pumps to 5 kV. With the lower voltage the pumping rate also decreased. We started finding

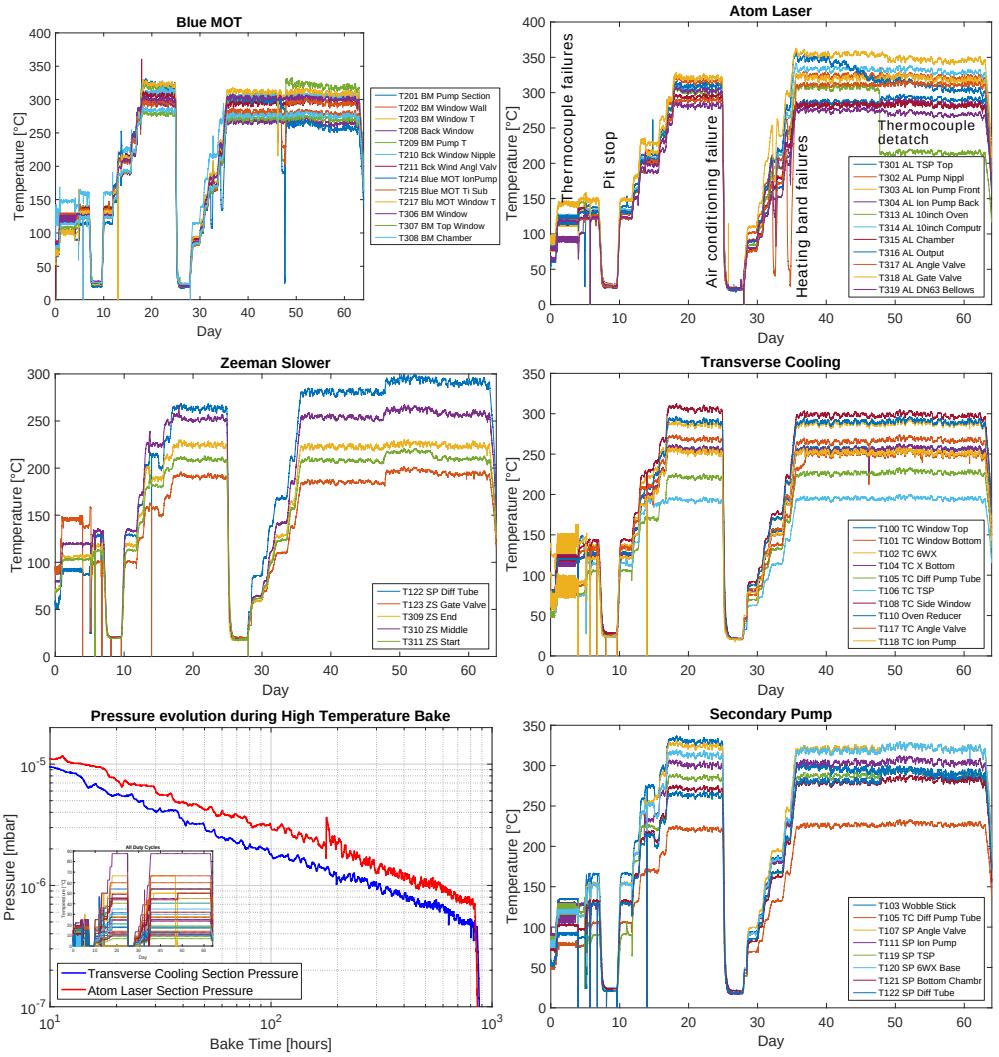

FIGURE 3.19: **Hydrogen bake records.** The logs of the temperatures and pressures during the hydrogen bake. There were several heating band and thermocouple failures during this bake but the most notable event was the failure of the room air conditioning system. To avoid the risk of anything melting or burning we immediately lowered the temperature as fast as we dared and restarted the bake after the air conditioning was repaired.

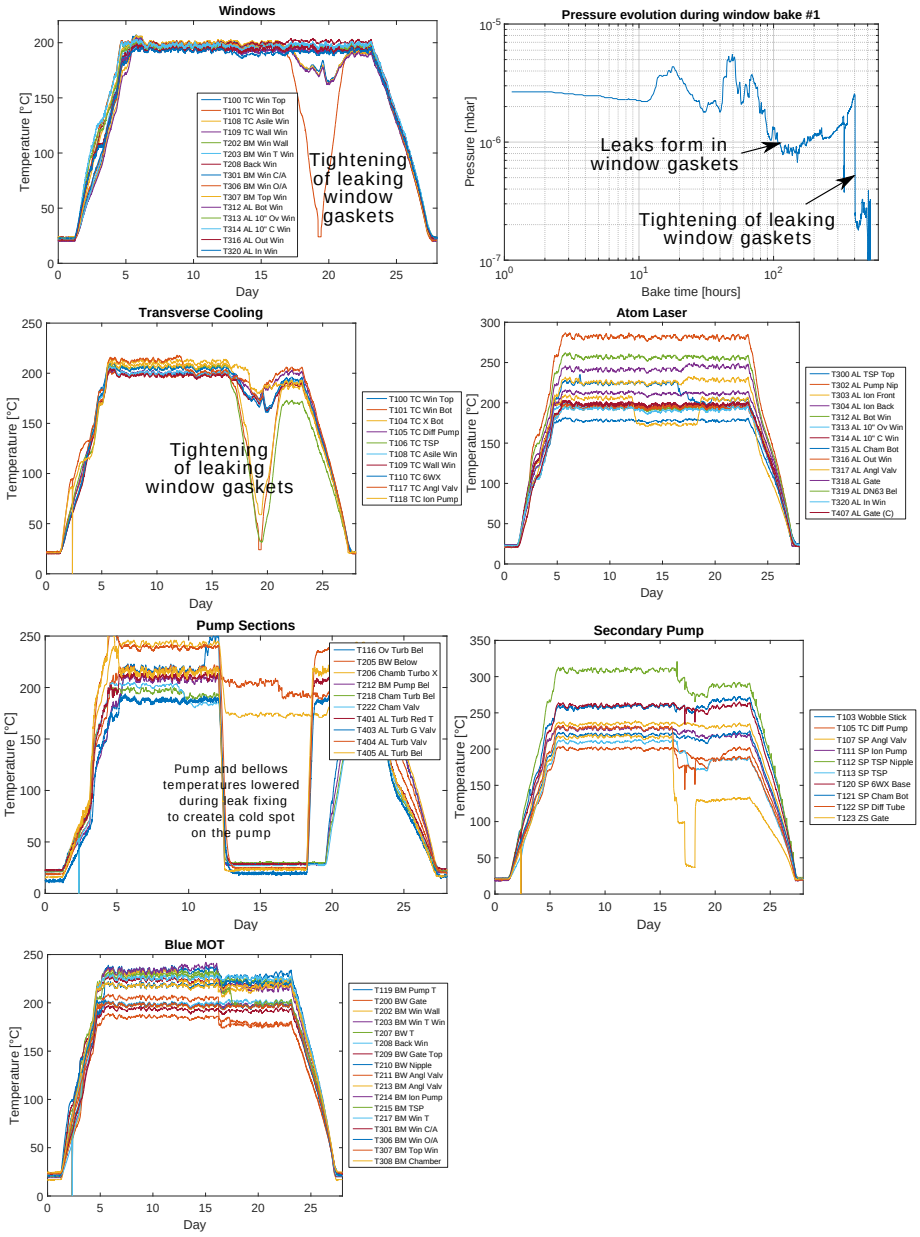

FIGURE 3.20: **Window bake records.** The logs of the temperatures and pressures during the first window bake. During this bake a number of window gaskets began leaking. As the leaks grew we became more and more worried and eventually decided to try to repair them. Helium checking identified the likely culprits and the temperatures around these windows was dropped to room temperature. To prevent these windows forming a machine cold spot and condensing all the rubbish from the bake we also dropped the pumps and the bellows to room temperature in a bid to condense rubbish on these instead. Tightening the bolt dramatically reduced the pressure and the bake continued.

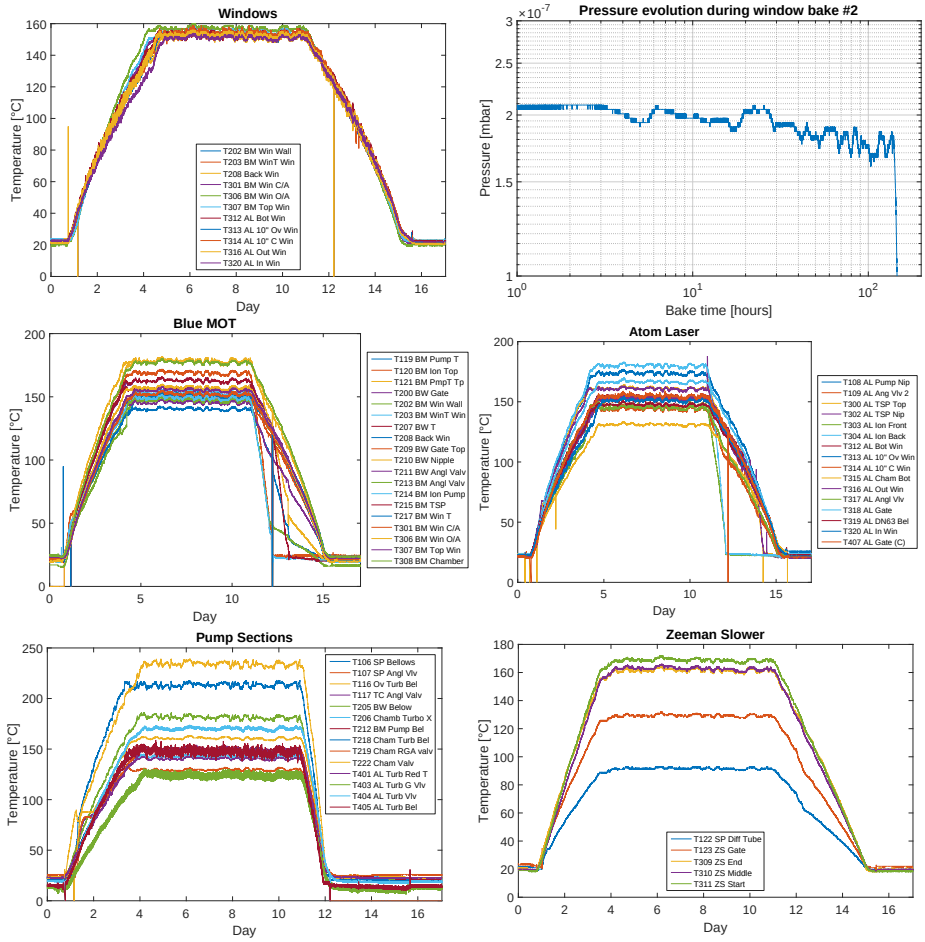

FIGURE 3.21: **Second window bake records.** The logs of the temperatures and pressures during the second window bake. Only the atom laser and 2D MOT sections were rebaked, the Zeeman slower gate valve was sealed.

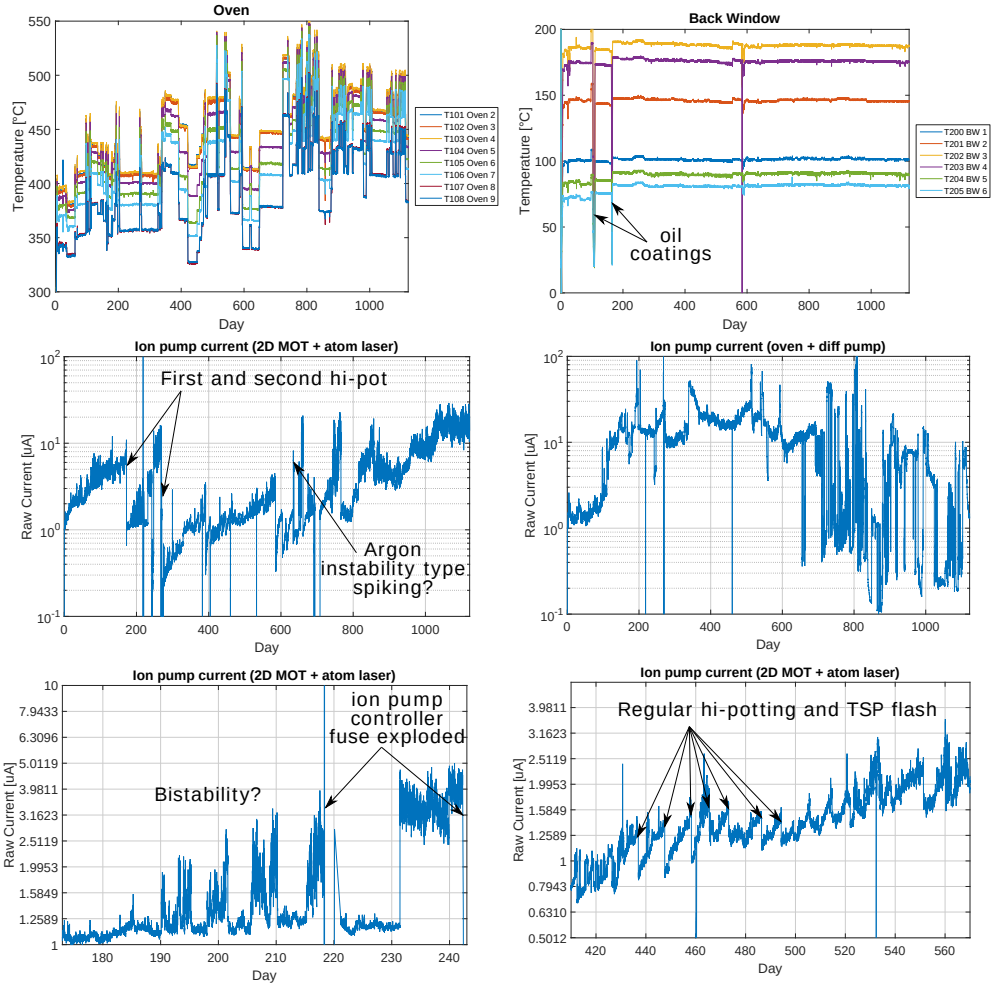

FIGURE 3.22: **Temperature and pressure logs.** The logs of the temperatures and ion pump currents for the machine. Oil coating were events where the back Zeeman slower window became covered in oil (see section 3.4.4).

the TSP in the atom laser chamber would start to saturate and flashing it would make an improvement to the ion pump currents after as little as a week. For a year I would flash the atom laser section TSP and hi-pot the atom laser section ion pump every week or few. The ion pump for the 2D MOT section also had a large leakage current but flashing its TSP didn't make any impact. It was concluded that the pressures in the 2D MOT section were still OK and we tried to ignore the leakage current. When the atom laser ion pump was not hi-potted for a few weeks we started to notice a behaviour where the pump current would increase exponentially over a few weeks and spike before dropping down to a low value again. Initially we thought it might be arcing and burning off whiskers but such a pathology is also similar to what was described as Argon instability in [287]. We went back to using 7 kV to reduce the need for TSP flashing and after the second attempt at making a steady-state BEC 6.2 I stopped attending to the system and let it evolve naturally. The leakage current eventually stabilized at around 20 µA. By hi-potting at day ≈1200 (shortly after the end of the graphs plotted in figure 3.22) it was clear that most of the current was leakage current which again reduced to the <1 µA with a hi-pot and a TSP flash.

While the vacuum quality is much better than the ion pump currents would indicate there remains an impact from flashing the TSP in the lower atom laser section. Thus, there is an unanticipated gas load on the system. We wondered if a joint had opened up in the machine since the end of the bake so after almost two years we hooked up a turbo pump with an RGA and baked the pump station out. Once again the leak checking found no hint of a problem indicating some residual volatile component or more likely a virtual leak. To be sure, we tried heating the bottom chamber section again. We couldn't easily heat the chamber itself because of all the surrounding optics so instead we created a cold spot next to the turbo pump by peltier cooling a nipple to −26 °C and gently heated what we could to around 80 °C. Nothing changed. Maybe we have a dreaded virtual leak in a weld or maybe it is just leakage through the gate valve which I regret placing in the UHV. The short answer is we do not know where this gas load comes from.

I have also asked myself many times why the leakage currents are so bad on our ion pumps. The best answer I have is that our old second hand ion pumps are not of the same quality as new ones[22]. While these leakages probably make little difference for the pumping performance they do mask our ability to debug and monitor our vacuum quality. For this reason in the future I would prefer to use new ion pumps and include a gauge so there is at least the option for getting a better handle on the real vacuum level.

In the end it is the lifetime of the atoms in our system which matters. The $1/e$ lifetime of a ^{84}Sr MOT in the atom laser chamber is around 12 s while the BEC lifetime in a dipole trap

[22] There is another potential cause I have wondered about. In the atom laser chamber the TSP is above its ion pump (but not within line of sight). This might increase the chances of titanium particles or flakes being deposited in the ion pump which might lead to increased leakage currents.

tends to be 2.5-3.5 s[23] I think it is safe to assume that our BEC lifetime is not vacuum limited. In fact, for trying to make a steady-state BEC, it is heating from resonant light which is the overwhelming limitation leading to lifetimes on the order of 1 s. While the vacuum may not practically limit us, it is not the >1 min MOT lifetimes I had hoped for and expected.

3.4 Zeeman slower

The objective of the Zeeman slower design was to obtain the absolute maximum possible flux with little regard to size, weight or power requirements.

3.4.1 Zeeman slower design

We shall now step through the various design choices that went into making our slower. For the impatient, the key decisions are summarized in table 3.8. It would be very nice to know if the number of blue photons that can be scattered before an atom falls into the $^1D_2$ state is closer to 2×10^4 or 5×10^4 (see section 2.5.1). This makes a big difference to what would be considered a suitable Zeeman slower length choice. At the time of design it was though that the number of photons which could be scattered was 5×10^4 and that this value was precisely known [225].

Choosing η and ϵ A major design decision for a Zeeman slower is its η or ϵ value. The magnetic field of a slower is designed so that an atom is assumed to be able to follow a trajectory with a constant deceleration of ηa_{max}, where a_{max} is the maximum deceleration possible given a fully saturated resonant transition. In atoms like strontium which have high saturation intensities, a related parameter ϵ is often used, where the ratio is quoted in terms of the maximum acceleration achievable given the assumed laser intensity available. This is summarized in equation 3.5.

$$\begin{aligned} a &= \eta a_{max} \\ &= \eta \frac{h}{\lambda m}\frac{\Gamma}{2} \\ &= \epsilon \frac{h}{\lambda m}\frac{\Gamma}{2}\frac{I}{I_{sat}} \Big/ \left(1 + \frac{I}{I_{sat}}\right) \\ \eta &= \epsilon \frac{I}{I_{sat}} \Big/ \left(1 + \frac{I}{I_{sat}}\right) \end{aligned} \tag{3.5}$$

[23] If you measure it by other methods you can fit lifetimes of 9 s but I don't believe these numbers and we will discuss this further in section 4.3.2.

where

h = Plank's constant,
λ = wavelength (461 nm),
Γ = scattering rate (2π 30.5 MHz),
I = laser intensity,
m = mass of ^{84}Sr (1.25×10^{-25} kg), and
I_{sat} = saturation intensity (40.7 mW $\cdot$ cm^{-2}).

If $\epsilon = 1$ the slower is very lossy as it assumes there are no defects such as spatial variations in the beam intensity or imperfections in the magnetic field that would result in atoms unable to follow the required deceleration curve. On the other hand an $\epsilon = 0.1$ will result in a slower 10 times longer which eventually becomes impractical to make and will also suffer some inefficiencies from divergence of the atomic beam. What is considered an appropriate value for ϵ varies within the literature. Erik Wille suggested $1/3 < \eta < 2/3$ [281]. Most strontium references tend to use $\epsilon = 0.75$ as this in principle gives the strongest restoring force against defects towards the target trajectory [288, 289]. Others allow for more loss so that they are more tolerant to lower laser powers, and have designed for $\epsilon = 0.6$ [290]. In the literature this typically leads to an ($0.35 < \eta < 0.6$), which in turn corresponds to an assumed intensity of $1.5I_{sat} < I < 4I_{sat}$. In our case we have a large beam and we were concerned about absorption from our high flux reducing the effective intensity. We also worried about our available Zeeman slower power since we were using injection locked diode lasers giving ≈ 90 mW, whereas others often used doubled tapered amplifiers or TiSaphs). Thus we chose a conservative value $\epsilon = 0.75$, $I = 0.5I_{sat}$ ($\eta = 0.25$) as the target for our design.

Detuning At the end of the Zeeman slower atoms must travel a short distance to a MOT where they can be trapped and cooled. It is therefore critical that they rapidly cease interacting with the Zeeman slower, which requires that they quickly detune from resonance. In practice this is achieved by offsetting the slower laser frequency by many linewidths from resonance and ending the slower with a compensating B field. This is the spin flip Zeeman slower design. We designed for a slower offset frequency of 432 MHz, the same as was used in the RbSr machine. This detuning is large enough to allow a MOT to sit in middle of the Zeeman slower beam with minimal impact. It is also possible to reduce this detuning (and the corresponding magnetic field) at the cost of coupling the alignment of the Zeeman slower and the MOT used to capture the atoms, but we saw no reason to deviate from a working design choice.

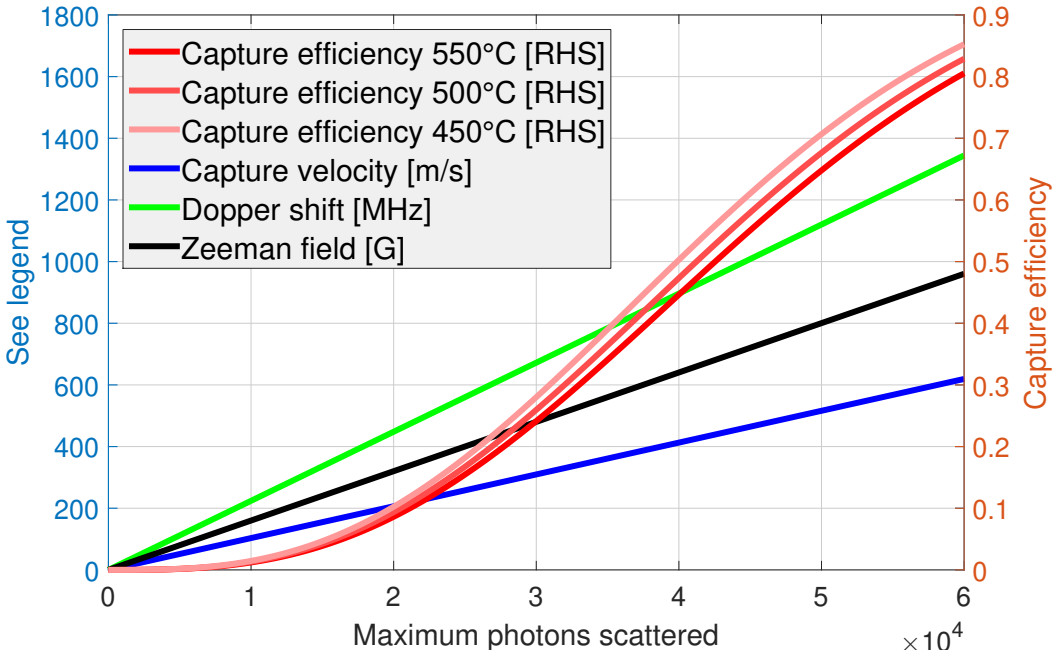

FIGURE 3.23: **Impact of Zeeman slower length.** Here we plot the theoretical capture efficiency for 450 °C, 500 °C and 550 °C thermal sources as a function of the number of slowing photons scattered. Also plotted are the corresponding capture velocities, frequency detuning and the required magnetic field variation.

Length Aside from practical challenges there is little down side to making a longer Zeeman slower. The relative change in path length is small and atoms travel at high speed through the extra tube until they reach their resonance condition. In principle, additional length should simply increase the atom number which can be captured albeit with diminishing returns. Figure 3.23 plots the proportion of atoms which can be captured from a 550 °C thermal beam of ^{84}Sr and the corresponding velocities, Doppler shifts and Zeeman slower fields required. It is clear that efficiently capturing flux requires scattering on the order of 3×10^4 photons but that little is to be gained beyond around 6×10^4 photons. In strontium, the 461 nm cooling cycle is not completely closed. At the time of design it was thought that we could typically cycle up to 5×10^4 photons before decay to the $^1D_2$ state so there is little point to designing a slower for atoms travelling so fast that they need to cycle a lot more than 5×10^4 photons to stop. Our slower was designed with a length long enough and a field strong enough to scatter at most 6×10^4 photons.

New results [224] have suggested that the 461 nm cooling cycle is not as closed as we thought and the number of photons that can be scattered may be as low as 2×10^4. This is discussed in section 2.5.1. If we check figure 3.23 we can see that the Doppler shift corresponding to scattering 2×10^4 photons happens to be around 450 MHz which almost exactly corresponds to only the spin flip section of our slower. If the 2×10^4 number is correct it would turn out that our beautiful big coil offers only a modest improvement for the machine flux. More than that, the big coils on all three machines, RbSr, SrCAL and SrMic would seem to be largely redundant for strontium (although still needed for the rubidium in RbSr). Experimentally we do find the big coils improve flux so before ditching the big coil for new designs this should be further investigated.

The potential losses through $^1D_2$ also led to some thinking about how we might be able to repump atoms quickly directly from the $^1D_2$ to put them back on the Zeeman slower path before they are lost. Our work on the the 448 nm repump mentioned in section 2.5 and described in Jens' master's thesis [244] focused on this. Although 448 nm appears to work well as a repump there appear to be some problems with applying it to a Zeeman slower. The Zeeman slower polarization acts on largely unpopulated magnetic sublevels instead of the populated ones so it isn't efficient and using the opposite polarization means both the Zeeman shift and the Doppler shifts need to be covered by a high power multi gigahertz wide comb of repump lines which is not easy to make. Other wrinkles are also discussed in Jens' thesis [244].

Laser power The more atoms you try to slow the more light will be absorbed and scattered.

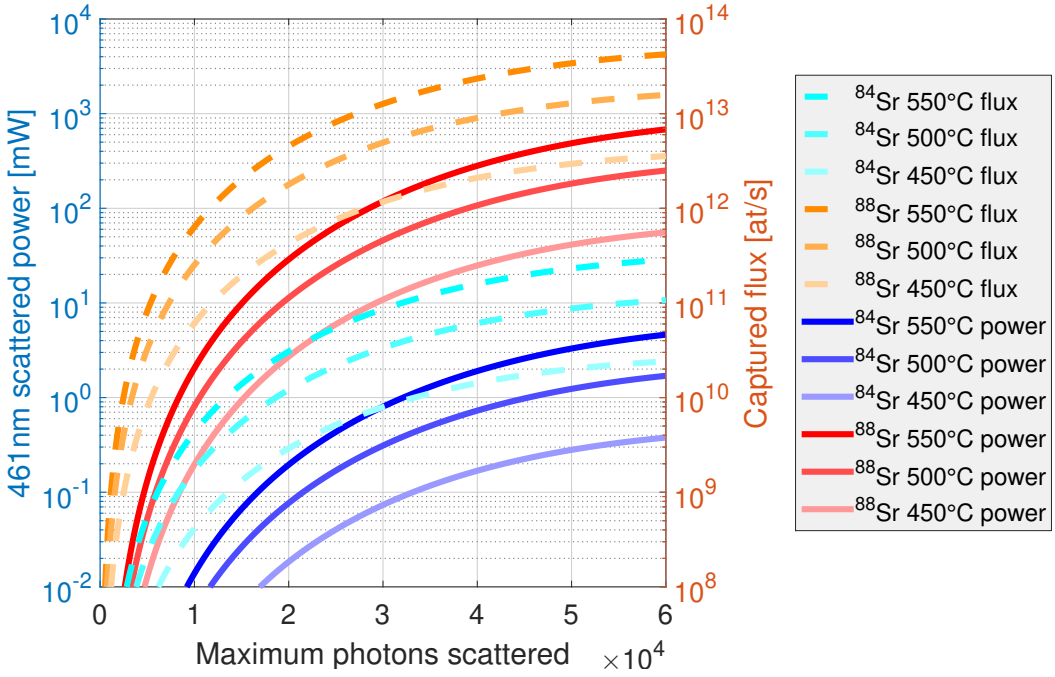

FIGURE 3.24: **Impact of Zeeman slower length on scattered Zeeman slower laser power.** Here we plot the theoretical flux which can be captured as a function of the maximum number of slowing photons which can be scattered per atom. The amount of Zeeman slower light which would be scattered to capture that flux for various isotopes and oven temperatures is also plotted.

If the amount of light scattered reduces the Zeeman slower beam intensity such that atoms are no longer able to follow the slower deceleration curve then the number of atoms which can be caught will saturate. The power scattered as a function of oven temperature, number of photons scattered and isotope is plotted in figure 3.24. Our machine is designed to run on ^{84}Sr where scattering is a few mW at most but since the ^{88}Sr isotope shift is only 278 MHz and the Zeeman slower can span 1.3 GHz[24], scattering on ^{88}Sr remains a concern. If we can scatter at most 2×10^4 photons due to the decay to $^1D_2$ it would mean that at most our system will scatter a few 10 mW even on ^{88}Sr at the highest oven temperatures. Our current Zeeman slower laser power is around 60-75 mW (after several uncoated surfaces) depending on which diode current we injection lock at so this would be fine. On the other hand, if we can scatter up to 5×10^4 photons then we would need a slower laser of several watts to efficiently capture ^{88}Sr. During design we imagined injection locking 1 W 461 nm multimode diodes for use on the Zeeman slower, so even at 5×10^4 photons the scattering seems acceptable for the fluxes our oven can reach. In 2015 Chun-Chia injection locked these diodes but found the power obtained did not justify the additional complexity and stability problems introduced by their multimode nature. About 6 months later, another group published similar work [291] so it was never formally documented. MSquared lasers also offer 461 nm doubled TiSa sources with 1.5 W so in principle absorption at very high fluxes can always be solved with more laser power (and more money).

Laser beam size We want to have enough intensity on the atoms at all points in the atomic beam and at all points along the Zeeman slower. Figure 3.25 shows the geometry of the Zeeman slower beam in the machine. At the entrance to the Zeeman slower, the beam size is approximately square and around 20 mm×20 mm. The design intensity is $0.5I_{sat}$ implying a requirement for at least 80 mW beam power which is ≈ 90 mW, including uncoated window losses. The available power is currently around 75 mW. Figure 3.25 also shows that there is significant structure in the beam so we would probably like to have I_{sat}. For these reasons it would probably have been better to focus the slower beam to around 12 mm×12 mm at the oven[25].

A summary of the design decisions is included in table 3.8.

[24] Fortunately ^{88}Sr lies to the blue of ^{84}Sr so the final section of the slower will be free from this effect.

[25] We recently tried refocussing the slower beam and the flux improved by 11× with an optimal beam size of 11 mm×11 mm measured 0.8 m past the oven location. This means that all the work described in this thesis could have been performed with a significantly lower oven temperature but it doesn't change conclusions as we did push the flux to saturation when trying to make steady-state BEC.

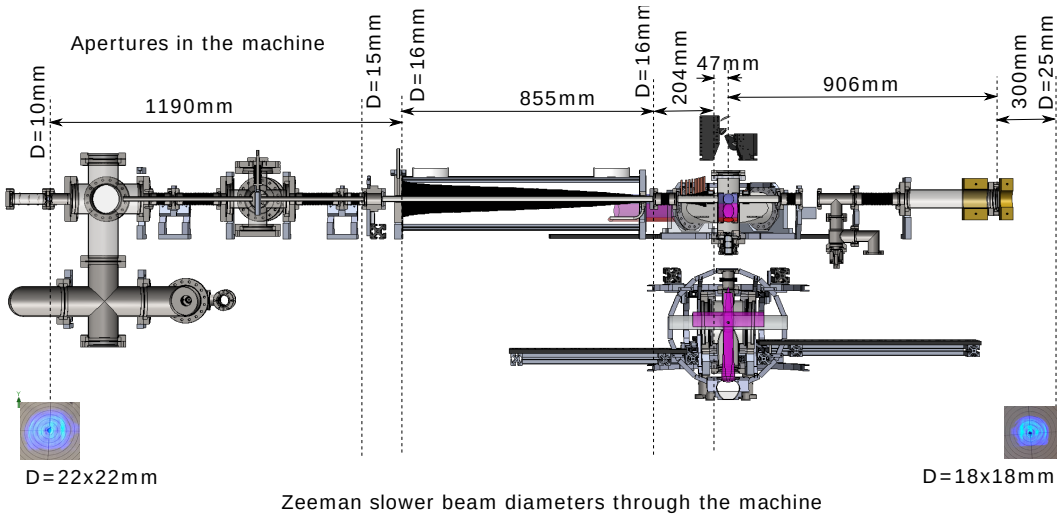

FIGURE 3.25: **Zeeman slower beam geometry.** Here we show the beam shape of the Zeeman slower beam and the apertures in the machine through which the beam propagates. To increase available power the Zeeman slower beam from the slave is not mode filtered by a fibre explaining the structured rectangular shape.

TABLE 3.8: **Zeeman slower design decisions.**

Parameter	Value
Intensity	0.5 I_{sat}
ϵ parameter	0.75
η parameter	0.25
Beam size at the oven	12×12 mm
Beam size at launch	18×18 mm
Required power[a]	52 mW
Endpoint detuning	432 MHz
Maximum capture	6×10^4 photons
Maximum capture velocity	$600\,\mathrm{m \cdot s^{-1}}$
Magnetic field variation	950G
Maximum Doppler shift	1350 MHz

[a]This assumes a uniform illumination. Real beams will require higher power levels to account for losses and non-uniformities in the illumination.

3.4.2 Coil configuration

Three separate coils were used to generate the field giving some ability to optimize the actual field on the experiment. Two sections (ZS1 and ZS2) were constructed from flat copper enamelled wire (Part CS4175: 4.57 mm×1.01 mm (4.401 mm^2) copper, Magnetemp

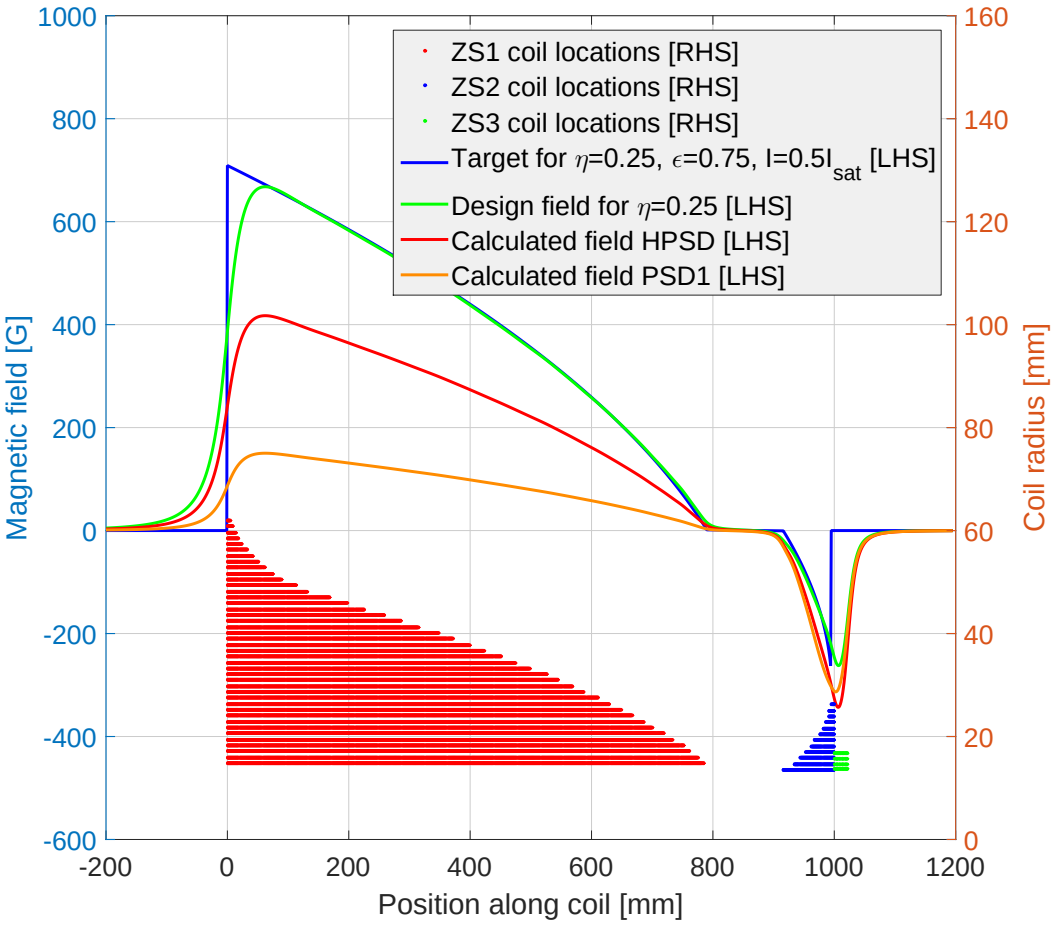

FIGURE 3.26: **Zeeman slower design.** Here we plot the locations of all the coils along the Zeeman slower (RHS=right hand side axis) and the fields generated using both the design currents and the actual currents the experiment optimized to (LHS=left hand side axis). The current and field on the first (large) coil optimized to very different values at different times over the years and only ever seemed to make a marginal effect. Plotted are the fields corresponding to the optimal currents during the steady-state MOT work labelled "HPSD" (Section 5) and during the unity phase-space density work 18 months later labelled "PSD1" (section 6.2). One possible explanation for the insensitivity of the first coil is that we might only be able to scatter 2×10^4 blue photons before decay to $^1D_2$. This would take place entirely within the post spin flip region in which case the main coil would bring only a marginal benefit (for a discussion see section 2.5.1). A second explanation is that we need more Zeeman slower laser power and that absorption is reducing the effectiveness of the first coil. This second explanation would be consistent with an optimization that depends on the oven temperature.

TABLE 3.9: **Zeeman slower coil currents.** Design and optimized operating currents for the Zeeman slower coils during the steady-state red MOT II work labelled "HPSD" (Section 5) and during the unity phase-space density work 18 months later labelled "PSD1" (section 6.2).

Coil name	ZS1	ZS2	ZS3
Design current	8 A	−9 A	−125 A
Current during SSMOT	5 A	−12.5 A	−160 A
Current during HPSD	1.8 A	−14.5 A	−128 A

CA200 grade 2 wire from Hi Wire Ltd (spsx.com)). The final coil nearest the MOT (ZS3) consisted of 4×4 mm square annealed EN12441 copper tubing with a 1 mm wall thickness (from www.coleandswallow.com), which was insulated with kapton tape and water cooled. The field for the designed current and the calculated field using the currents optimized using the machine are plotted in figure 3.26. The design and actual currents are listed for each coil in table 3.9 and the number of turns in each layer is listed in table C.5. A second mirror coil, the "compensation coil" was placed on the opposite side of the 2D MOT roughly symmetrically about the 2D MOT. This coil also used 4×4 mm square copper tubing so that it could run large currents. The purpose of this coil was to cancel the field from the slower coils at the MOT location. It was found that it was not needed, in part due to the mu-metal shielding used, and for now the power supply has been repurposed. More details on the coil properties can be found in appendix C.

It is important to reduce the magnetic field as rapidly as possible at the end of the slower to quickly take the slower laser out of resonance with the atoms. A second important reason is that the atoms at the end of the slower travel slowly and are transversally hot, so the atomic beam diverges rapidly. The closer the capture MOT can be to the end of the Zeeman slower the more efficient the capture is. To try to increase the magnetic field gradient a 2 mm thick mu-metal shield made by magneticshield.co.uk was placed between the final slower coil and the MOT. The effect of this shield was modelled using Maxwell (Ansys) using the properties of mu-metal from magneticshield.co.uk. In hindsight soft iron would probably also have done a good job as was used for example in [288]. Plots of the axial B field gradient and the modelled geometry are shown in figure 3.27 both with and without the shield. Including the shield reduced the peak field in the slower by around 10% from 222G down to 200G but it reduced the residual field at the location of the 2D MOT by 6× from 3G to 0.57G.

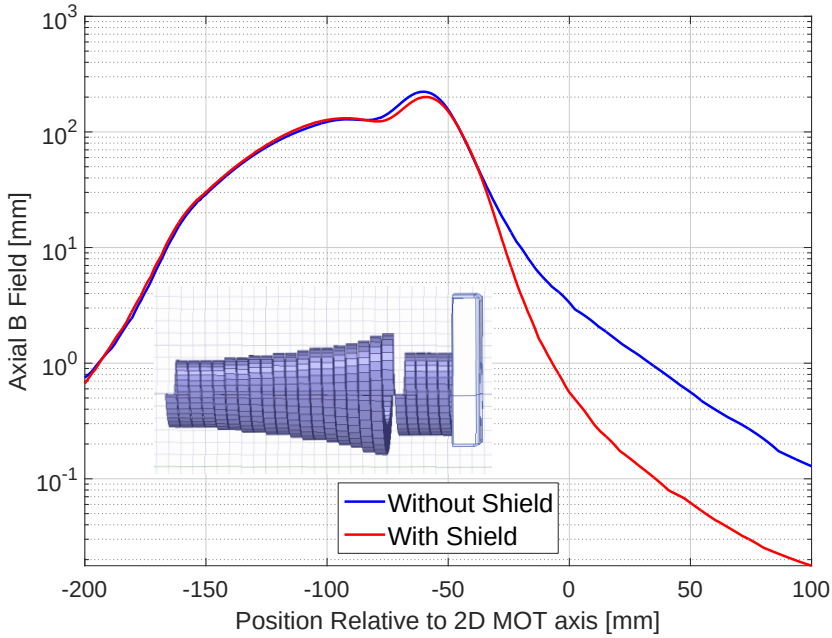

FIGURE 3.27: **Mu-metal shielding.** The axial B field with and without mu-metal shielding. (Overlay) The coil and shield geometry used in the model. The scale and position of the shield and coils correspond to the horizontal axis.

3.4.3 Zeeman slower construction

Our main Zeeman slower coil is wrapped on a 16 mm inner diameter (1.5 mm wall) stainless steel 316 pipe within a 25.4 mm outer diameter (1.65 mm wall) pipe forming a cavity for water cooling. The design is shown in figure 3.28. The construction techniques are shown in figure 3.29. One detail not obvious from the pictures is that bending the rectangular copper tubing of ZS3 and the compensation coil requires first annealing the copper tubing to make it soft. This was done by heating it red hot with an oxy-acetylene torch and then quenching it in a pipe full of water. After one or two bends the tube will again harden so it must be handled with care. The ZS1 coil is contained within an air cooled box as the outer surface can exceed 45 °C at the 8 A design current. This can create air currents which disturb optical beam paths and also disturb the temperature stability of the machine. Technical details of the power supplies and other relevant data can be found in appendix C.

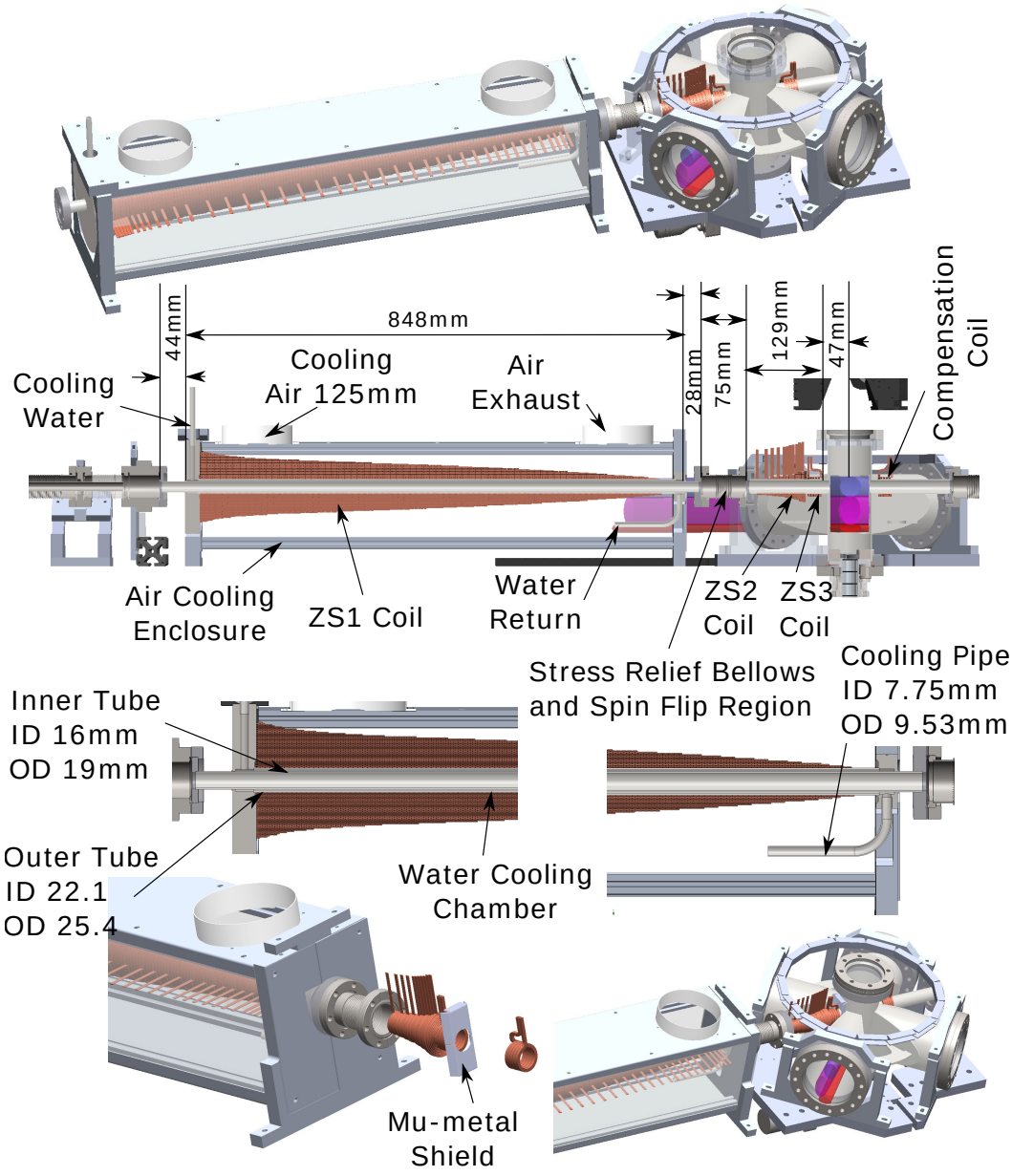

FIGURE 3.28: **Zeeman slower mechanical design.**

FIGURE 3.29: **Making the Zeeman slower.**

3.4.4 Zeeman slower back window

We can see from figure 3.23 that if we can scatter at most 2×10^4 blue photons (see section 2.5.1) then we can slow at most 10% of the atoms. Furthermore, if we operate on ^{84}Sr with 0.56% abundance this proportion is reduced to 5.6×10^{-4}. The vast majority of the strontium atoms as well as all the molecules and other contaminants from the oven fly straight through the slower and slam into the back window through which the Zeeman slower beam must shine. If you operate at high flux for a significant period of time this back window will become coated in strontium metal and your Zeeman slower will cease to work. There are at least three solutions to this problem. You can use a sapphire back window and heat it to around 200 °C, which prevents strontium atoms from sticking to the window (used by the RbSr machine [107] and the AO Sense source among others). You can use an in vacuum reflective mirror (typically polished stainless steel) instead of a window accepting that there will be some reduction in reflectivity as the surface becomes coated in strontium. We have heard of this option being used and it was studied in [292]. A third direction is using a transverse cooling section to first bend slow atoms of the desired isotope away from the main beam after which they can be slowed and captured with high efficiency. This also avoids having hot atoms flying through your MOT as well as depletion of your Zeeman slower beam power by atoms of the wrong isotope. Many others just operate at low flux with intense slower beams and ignore the problem entirely.

During design we strongly considered the option of using a transverse cooling section to preselect slow atoms of the desired isotope but eventually went with the option we knew from the RbSr machine, a heated sapphire window. We know from experience with our transverse cooling section that it is easy for small misalignments to significantly reduce rather than increase flux so it was assumed that relying on deflecting the desired atoms out of the beam could be prone to misalignment problems. One of the big problems with having a heated window on your machine is that vacuum windows break when rapidly thermally cycled. The windows we use are rated for no more than 2-3°C $\cdot$ min^{-1} which is easily exceeded in the event of a power failure and a rapid cooling, unless there is sufficient insulation and heat capacity in the system. I also considered and developed designs for placing a heated sapphire plate within the vacuum system in the middle of a nipple. This would eliminate the need to heat a flanged window (or even a flange) and thus it would eliminate the risks of leaks or catastrophic failure in the event of power failure. Again we ended up deciding to stick to the technology we knew rather than risk the unexpected. If I built another machine I would again strongly consider all the options mentioned as the heated viewport approach is a big, ugly, brutish approach which carries a risk for catastrophic failure in the event of a power outage.

With hindsight I would say that my concerns about rapid thermal cycling creating leaks in the oven may have been exaggerated but in the case of the heated viewport I remain as paranoid now as the day we designed. To mitigate the risks a number of steps are taken:

- The viewport is uncoated sapphire to avoid sticking (Torr Scientific part VPZ64S-LN-200[26]).
- A DN63 viewport is used instead of DN35 and a bellows is incorporated so that, if one part of the viewport becomes coated with strontium, the window can be shifted so that the beam travels through another part of the viewport.
- A typically 10 cm thick insulating layer of Superwool 607 (RS Components 840-5529) is used to surround the heated viewport and thermal mass.
- Two layers of AR coated BK7 windows (Thorlabs WG12012-A) act as a transparent heat shield for the viewport. The inner window was later removed as will be discussed.
- Approximately 4.9 kg of aluminium blocks were wrapped around the viewport acting as a thermal inertia.
- A UPS (AEG Protect C.1000 from Conrad) drives the heating element (a DN63 flange heater from Omega, part MBH00236) giving approximately 50 min of backup power and an alarm system monitors the system (see section 3.7.4).
- Heating and cooling was performed by adjusting the power supply voltages in small steps at typically no more than $0.5\,^{\circ}\mathrm{C}\cdot\mathrm{min}^{-1}$.
- A gate valve sealing the back window from the machine and an angle valve for attaching a turbo pump are included allowing the back window to be replaced in event of strontium coating or in case a leak develops without rebaking the whole machine.
- A double layer sheet metal box houses the thermal insulation and forms an air cooling outer box. Forced air cooling is provided but proved unnecessary. This outer box prevents air currents and thermal load which would reduce the machine stability.

The design and construction details are shown in figure 3.30 and are closely related to the oven system (see section 3.1). The heating element was initially powered by a Digimess PM6003 (Farnell 1664826) 60 V 3 A but was later replaced by an Aim-TTi PL601 (Farnell 1510523) after *all* the Digimess power supplies driving the oven failed one by one. The operation was at 55.51 V, 608 mA. Temperature is monitored using home made thermocouples and our homemade temperature monitor boards in the same way as for the oven (see section 3.1). The temperature profile through the system is shown in figure 3.30.

[26] We had hoped to buy the 450 °C version rather than the 200 °C version but that was withdrawn from sale at the time due to technical problems.

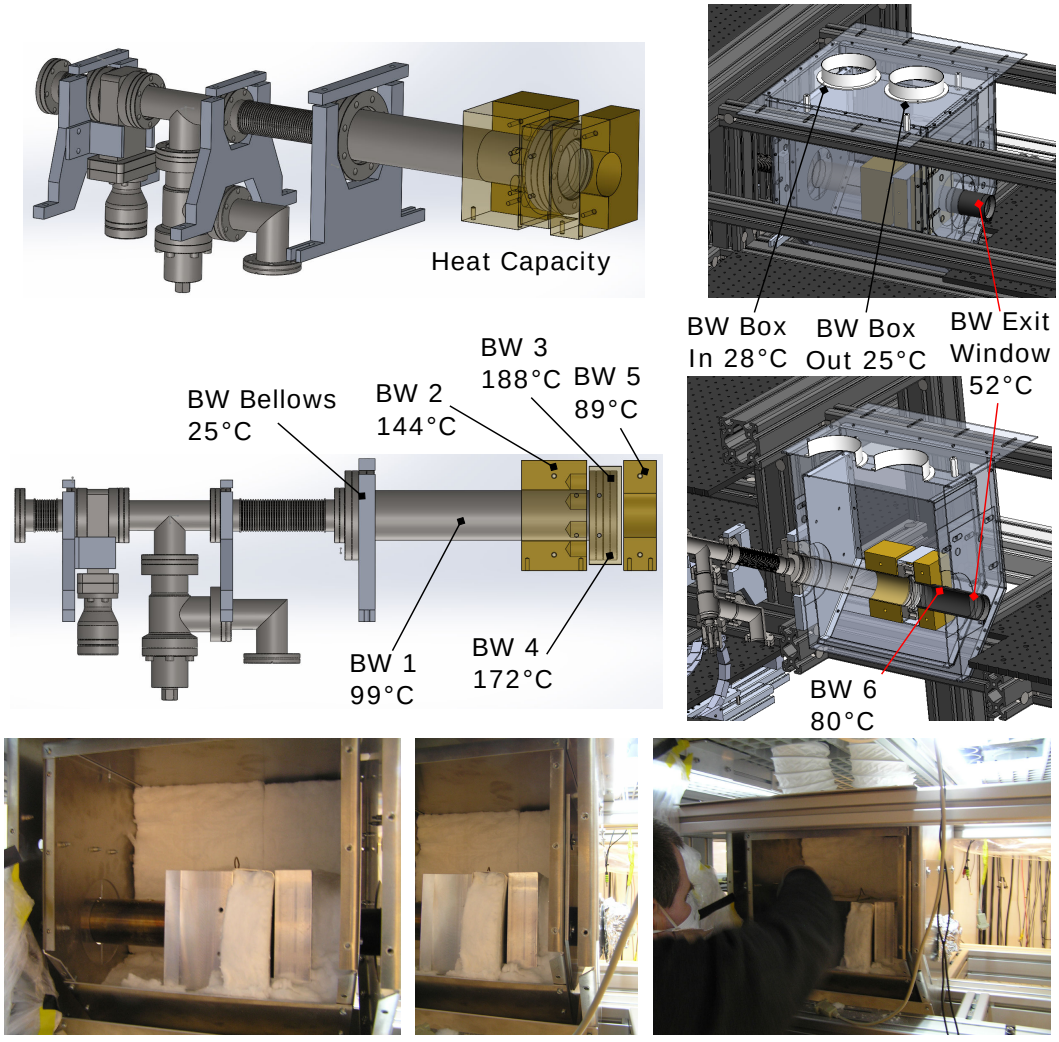

FIGURE 3.30: **Heated Zeeman slower window.** Shown is the design of the heated back window section as well as details of its construction. The rear sapphire window is heated to around 180 °C to prevent strontium not stopped from the Zeeman slower from sticking to it.

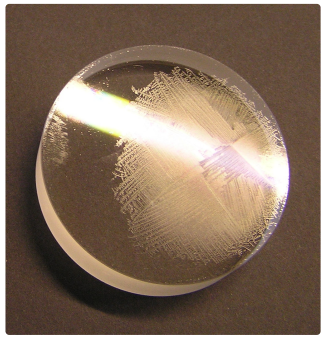

FIGURE 3.31: **Oil coated Zeeman slower back window.** This picture shows the inner surface of the inner heat shield window which was found to be coated with oil presumed to have been evaporated from the heat capacity blocks.

We were fortunate enough not to have any long power outages so we never tested whether our protection measures were sufficient.

After four months of operation it was noted that the system performance appeared to have significantly declined and to our horror we discovered the back window appeared to more or less completely scatter the Zeeman slower beam. Fearing that we had painted the window with strontium or worse the heat shield windows were removed to get a better look. We found the inner heat shield window to be covered in oil (as shown in figure 3.31). It is assumed that this oil came from inadequate cleaning of the aluminium heat capacity blocks which were machined and added as a last minute design change. The window being the coldest part of the system acted as a cold finger and collected oil vapour. The windows were cleaned and replaced. Things ran well for a few weeks and then one April night it happened again. The cause of this second event was traced to the back window temperature being accidentally raised instead of the oven temperature the previous night. The higher temperature appeared to have vapourized a new higher temperature oil fraction. This time the inner heat shield window was not replaced in the hope that any future oil might condense on the lens tube before making it to the window. No further oil coating events were noted over the following 3 years but the potential remains if the back window temperature is raised too high.

3.5 Capturing and transferring atoms

Having slowed them with a Zeeman slower, atoms must next be captured, cooled and transferred to a place free from blue photons. At their final destination they can only be stopped and held using red MOT light and dipole traps. Since red MOT light is very weak

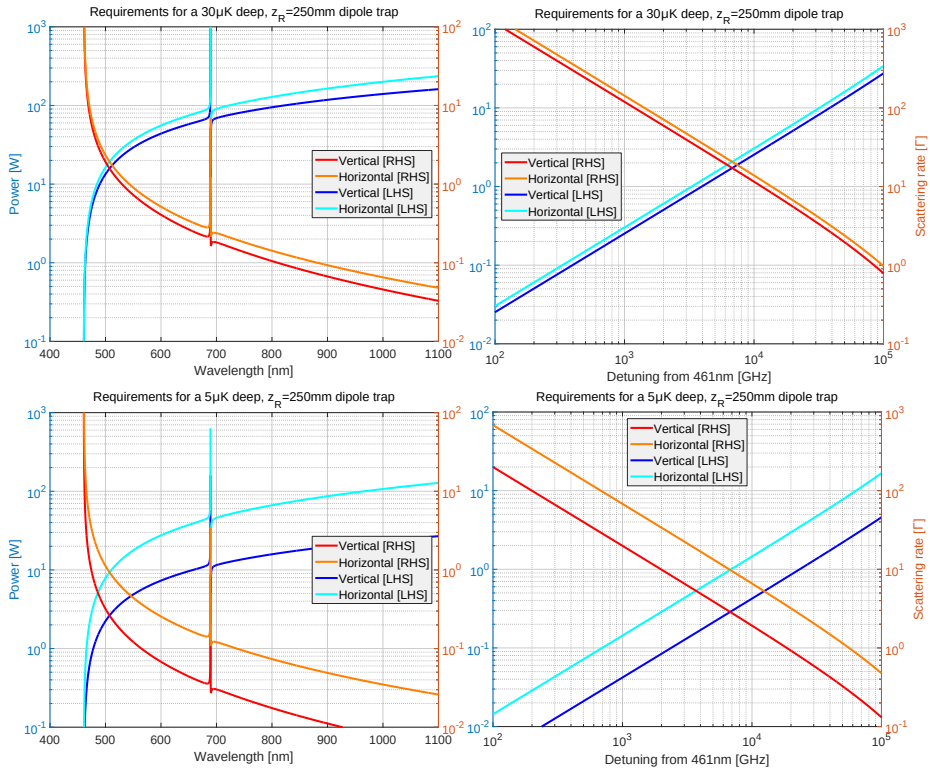

FIGURE 3.32: **Dipole waveguide power requirements.** (top) Here we plot the power requirements and the resulting scattering for dipole traps 30 μK deep (at the Rayleigh range) for beams with a Rayleigh range of 250 mm. Both vertical (along the axis of gravity) and horizontal waveguide orientations are plotted showing the impact of gravitational sag. The plots on the right show a close up around the 461 nm resonance. (bottom) The same set of plots for a 5 μK deep (at the Rayleigh range) dipole trap showing the much greater relative impact of gravitational sag.

and may only support accelerations of less than 15g, any transfer must minimally rely on radiation pressure deceleration. Two basic approaches can be imagined; transferring atoms while trapped in a dipole trap or lattice, or creating an intense, cold, slow atomic beam which can be recaptured at the destination[27]. Both approaches were considered and the SrCAL machine was designed so that both approaches could be implemented without changing the vacuum system should the first choice fail.

Lattice transfer By loading atoms into a deep red detuned lattice, they can be trapped and no longer accelerated by gravity. This keeps energies low and minimizes the need for dissipation at the destination. A Bloch acceleration and deceleration [293, 294] can be used to transfer atoms rapidly over large distances but this is intrinsically a time

[27] One could also use a magnetic guide for atoms in $^3P_2$ but this likely to be lossy.

sequential rather than a steady-state process, making it philosophically undesirable for our steady-state machine. Of course, with several transfer channels and a large reservoir at the destination this pump noise could in principle be made small. Alternatively, one can use a simple conveyor lattice but there is a trade off between transfer time and speed, and there are additional challenges in unloading (for example using an angled blue detuned dipole trap "wall" to gradually nudge atoms out of their lattice wells) and dissipating the momentum of the atoms at their destination. The biggest problem with lattice schemes is that they require a high power coherent laser in order to create a guide big enough to propagate the long distances needed without significantly diverging, yet deep and detuned enough to hold relatively hot atoms without excessive scattering. Figure 3.32 plots out the power requirements for making 500 mm long dipole traps of 30 µK and 5 µK depth as a function of wavelength and orientation. At 464 nm, two 250 mW lasers would be sufficient for a vertically propagating 30 µK lattice. This is borderline feasible even without the complexity of a frequency doubled system. In conclusion, lattices remain interesting[28] but the lasers are a challenge unless we relax the target specification in terms of propagation distance or depth. We shall therefore focus our attention on the second approach, the atomic beam.

Beam A cold, slow, beam can be created in many ways but the usual suspects are the LVIS (low velocity intense source) [117] and the 2D MOT [116] and its variants. These architectures can also be combined with additional molasses cooling or a dipole guide to better confine the atomic beam and improve the capture efficiency at the destination. An LVIS where the output forms due to a dark spot in a MOT is not a great choice in our case because the MOT beams follow the direction of atomic beam propagation. This would mean shining a blue beam directly into our protected chamber, not a great plan. Thus, we focus on the 2D MOT approach. An important design choice is whether to transfer up, down or across relative to gravity. Transferring across without a guide will result in a loss of atomic beam intensity as different velocity classes follow different trajectories, so we immediately eliminate this option. Transferring up usually requires that the atoms travel within the MOT beam and that the MOT beams pass through the protection baffles which might be challenging. Loss of slow atoms due to gravity might also be a concern. We did not long consider an upward propagation as this would also mean placing the oven/slower vacuum system along the optical table where we had hoped to place our laser systems. Furthermore, we would then need to place our dipole traps and atom laser work high above the optical

[28] Particularly for the iqClock kHz superradiant laser.

table where stability and laser safety is more challenging. We chose a downwards propagating atomic beam.

A blue 2D MOT has a capture velocity of several tens of $m \cdot s^{-1}$ but will only reach temperatures in the mK range while a broadband red MOT has a capture range on the order of $1\,m \cdot s^{-1}$, corresponding to 10 mK, and can in principle cool to 0.35 µK. Neither MOT can both capture atoms from a Zeeman slower and make them µK cold. Thus, a series of cooling stages is required to first capture the hot, fast, Zeeman slower output and then to cool it to a cold and dense enough beam to propagate efficiently to the next chamber. The resulting transfer system is a series of 2D MOTs feeding one another (blue, broadband red[29], single frequency red) mimicking the cooling stages of time sequential machines. The objective was for an atomic beam as small as possible to efficiently transfer through a small (8 mm diameter) aperture in baffles used to shield the second chamber from blue light. It needs to be slow and cold so that it can be efficiently recaptured using only the red transition at the destination. Table 3.10 summarizes "back of the envelope" parameters for such as system. One problem immediately sticks out from these estimations. The time for a red MOT to compress is long, approaching 100 ms. This in turn requires axial speeds on the order of $0.1\,m \cdot s^{-1}$ for realistic beam sizes. Unfortunately the axial temperature from a 2D blue MOT is of the order of several meters per second. Therefore a moving molasses would also be required along the axial direction to cool the atoms and keep them in the 2D red MOT long enough to sufficiently cool and compress. The significance of this recompression time should not be underestimated. For short time scales a MOT acts like a lens for atoms, increasing the transverse velocity spread as it pushes atoms as hard as possible towards the axis. A prematurely ended MOT will have a very large divergence and an appalling transfer efficiency. Our system was also designed to be able to add a vertical dipole trap to help guide the beam to the second chamber (Figure 3.32) but laser availability was a problem so this was never implemented.

A second major technical challenge arises in such an architecture. The typical magnetic field gradient used for a MOT on the blue transition is $40\,G \cdot cm^{-1}$ while a MOT on the red transition typically uses $\approx 1\,G \cdot cm^{-1}$[107]. Temporally this is trivially solved by varying the MOT coil current, but we aim for a series of MOTs in space where there is a rapid handover from the blue to red MOT beams, so as to avoid a large atomic beam spread at the exit from the blue MOT. One critical point is that the field gradient can never become negative within the MOTs for risk of having regions of "anti-MOT" which explode the atomic beam. A second critical point is that the quadrupole centers through all the MOTs must remain lined

[29] The linewidth of the red cooling transition is only 7.4 kHz which corresponds to a Doppler velocity range of only $\pm 5\,mm \cdot s^{-1}$. For a red MOT to be able to robustly capture the 10 mK, $1\,m \cdot s^{-1}$ output of a blue MOT it is necessary to frequency broaden (modulate) the red light by several MHz. This artificially broadened MOT can capture a much larger range of velocity classes (1 MHz=$0.689\,m \cdot s^{-1}$).

TABLE 3.10: **Parameters for 2D MOTs.** "Back of the envelope" estimates for the characteristic parameters of MOTs on the different cooling transitions. This informed the design choices made.

Parameter	Unit	Blue MOT	Broadband red MOT	Single frequency red MOT
Assumed input speed v	$\mathrm{m \cdot s^{-1}}$	30	0.99	0.044
Settling time τ_p[a]	ms	0.015	3.10	0.14
Settling beam size d[b]	mm	0.46	3.09	0.0062
Estimated final temperature T_f[c]	µK	1×10^4	20	1
Estimated final velocity v_f[d]	$\mathrm{m \cdot s^{-1}}$	0.99	0.044	0.01
Compression time τ_x[e]	ms	0.46	69	0.62
Axial MOT beam size B	mm	30	50	10
Maximum axial velocity[f]	$\mathrm{m \cdot s^{-1}}$	65	0.72	16

[a] $\tau_p = mv/(\hbar k/\Gamma)$, Γ is the transition linewidth, m is the mass.
[b] $d = \tau_s d$.
[c] Estimates based on observed data from our machines.
[d] $v_f = \sqrt{k_b T_f / m}$.
[e] $\tau_x = d/v_f$. This rough estimation is determined by our assumed input speeds. Monte Carlo simulations also indicated times of the order of 100 ms for the red MOTs.
[f] B/τ_x

up otherwise atoms will be accelerated to try to chase this moving minimum, again leading to high atomic beam divergences.

In summary, our design requires:

- A blue $2D^+$ MOT to efficiently capture the output from the Zeeman slower. To axially cool the resulting beam and direct the output downwards, a power imbalanced blue molasses was envisaged on axis in the central region of the blue MOT. This could eject a beam downwards which is capturable by the following broadband red MOT.
- A broadband red 2D MOT with a moving molasses on axis to produce a beam with mm size and ≈10 µK temperatures. The axial moving molasses needs to be slow enough to hold the atoms in the MOT long enough to avoid any potential for a prematurely ended MOT yet fast enough to avoid losses.
- An optional single frequency red MOT to reduce the axial temperature to the ≈1 µK range. An axial moving molasses could optionally cool the atoms into a faster moving frame to reduce the transfer time and thus the beam spread at the next stage. Ideally this would target a velocity less than that which will inevitably be gained from the gravitation acceleration during the transfer.
- A magnetic field configuration which provides a gradient on the order of $40\,\mathrm{G \cdot cm^{-1}}$ in the blue region and $1\,\mathrm{G \cdot cm^{-1}}$ in the red region, which never goes negative and which has a linear, well aligned quadrupole center.

The architecture described should in principle be able to produce a very small, (≈1 mm)

diameter cold (≈1 μK) beam ideal for transfer but there is a simpler configuration which can produce an equally cold (but larger) beam. The red MOT stages can be replaced by red molasses. The removal of the spatial compression means that the beam size will always be limited by the expansion from the hot blue MOT to something on the order of 5 mm-10 mm diameter but it has numerous important advantages:

- It eliminates the need for complex moving molasses beams along the axial direction of the red MOTs.
- It eliminates the risk of prematurely ending the MOT before the atom positions have reached their equilibrium. The velocity dampening time in a molasses is much shorter than the position dampening time in a MOT as described in table 3.10[30].
- Unlike a MOT, a molasses gives a monotonically improving temperature.
- It eliminates the risk of negative magnetic field gradients exploding your MOT.
- It eliminates the requirement to align all the quadrupole centres along the axis.

In order to convert our MOT to molasses in the red region we merely need to reorient the magnetic field so as to allow a significant nonmagnetic π component and to spectrally separate the π from the σ transitions[31]. This can be done by applying a bias field in the vertical axis (the axis of the 2D quadrupole magnetic field) of comparable strength to the fields in the red MOT region, but small compared with fields in the blue MOT region which will retain their quadrupole character[32]. The blue MOT will not work well on axis as it will contain significant amounts of incorrect σ polarization while the red molasses will perform badly far from axis as there will be minimal π component but hopefully there can be a reasonable compromise.

We built the configuration assuming we would use MOTs not molasses (although we never built the single frequency red MOT lasers and optics). In fact it wasn't until we got up to trying to align the quadrupole centres that we really saw the technical difficulty of this approach. It was at that time the molasses option was recognised and tested. It turned out that the efficiency of the molasses configuration in transferring atoms to the lower chamber was fine (≈25%) so the headache of aligning the axial moving molasses beams and the quadrupole centres was abandoned and we moved on to the next problem. It is an open question as to how well (better?) the MOT approach might work but the molasses performed fine and was much easier, so this is what I would implement on a

[30] Position compression is then entirely taken care of by the blue MOT, which is fast.

[31] A molasses works only on non-magnetic transitions or, as used in alkalis, a magnetic transition in zero B-field.

[32] We use our vertically oriented Helmholtz coil set to generate a 1.46G bias field in the upwards direction to turn our red MOTs into red molasses. This bias field tilts the field orientation, giving a strong non-magnetic π transition near the axis. Furthermore it creates an offset field everywhere in space. Along the axis of the 2D quadrupole field (created by the permanent magnets), this bias allows the separation of the magnetic $^1S_0$-$^3P_1$ m_J=±1 transitions from the non-magnetic $^1S_0$-$^3P_1$ m_J=0 transition allowing us to spectrally discriminate against MOT like transitions which have a slow time scale to reach equilibrium.

new machine. There has long been a discussion on whether the need for rapidly varying MOT gradients could also have been avoided by designing for the molasses configuration from the beginning. I would contend that the spatially varying field gradient remains an essential part of the molasses architecture otherwise you will either disrupt the Blue MOT by introducing some of the wrong σ light near the axis or you will disrupt the molasses by eliminating the π component. Having a spatially varying field gradient largely eliminates this trade off.

For now we will describe the machine we built with all the detail required for the MOT architecture. For a new molasses machine much of the additional moving molasses optics could be discarded but I would recommend keeping the magnetic configuration in a similar form.

3.5.1 2D MOT magnetics

There are several ways to make a spatially varying MOT gradient. You could use high current wires in the usual race track configuration but with a spatially varying separation from the axis but it is uncertain if a ratio of $10\times$ in field gradients is practical[33]. A second option is to use an array of permanent magnets with varying polarity, position and strength to tailor the desired field profile. It would be best to place the magnets as close as possible to the axis as this will determine the spatial resolution with which the field gradient can be varied. A way in which permanent magnets can be used to create a 2D quadrupole field is illustrated in figure 3.33 for both two and four magnet configurations. With four magnets you get stronger and more uniform fields but it requires free space for magnet arrays on all four sides of a MOT. For us this is impossible due to the presence of a Zeeman slower, so we use the two magnet geometry. The lasers should propagate along the diagonals.

An equation for the magnetic field from a rectangular permanent magnet in an aligned rectangular coordinate system is shown in equation 3.6 adapted from [295, 296]. Properties needed for the calculations can be found in box 3.5.1.

A numerical optimization routine was developed to adjust the position, number, type and direction of an array of magnets in order to try to best match a target field gradient profile. This optimization routine could select from a library of commercially available magnets. The target chosen was a magnetic field gradient of $2\,\mathrm{G}\cdot\mathrm{cm}^{-1}$ in the red MOT regions and $20\,\mathrm{G}\cdot\mathrm{cm}^{-1}$ in the blue MOT region. Severe penalties were imposed should the gradient fall below $1\,\mathrm{G}\cdot\mathrm{cm}^{-1}$ while relatively minor guidance was provided towards $20\,\mathrm{G}\cdot\mathrm{cm}^{-1}$ in the blue MOT region. The resulting optimized configuration of permanent

[33] A typical blue MOT on the RbSr machine uses a $40\,\mathrm{G}\cdot\mathrm{cm}^{-1}$ field gradient and below $10\,\mathrm{G}\cdot\mathrm{cm}^{-1}$ few atoms are captured. This may be related to the use of a magnetic trap to collect the $^3\mathrm{P}_2$ atoms. On RbSr, bosonic red MOTs operate at $1\,\mathrm{G}\cdot\mathrm{cm}^{-1}$ while for ^{87}Sr gradients tend to be around $3\,\mathrm{G}\cdot\mathrm{cm}^{-1}$.

Box 3.5.1: Magnetic field from a permanent magnet.

$$
\begin{aligned}
B_x(x,y,z) = &+\frac{\mu_0 m_x}{4\pi}\sum_{i,j,k=0}^{1}(-1)^{i+j+k}\,\mathrm{atan}\left(\frac{(y-y_j)(z-z_k)}{(x-x_i)\sqrt{(x-x_i)^2+(y-y_j)^2+(z-z_k)^2}}\right)\\
&-\frac{\mu_0 m_y}{4\pi}(-1)^{i+j+k}\,\mathrm{asinh}\left(\frac{z-z_k}{\sqrt{(x-x_i)^2+(y-y_j)^2}}\right)\\
&-\frac{\mu_0 m_z}{4\pi}\sum_{i,j,k=0}^{1}(-1)^{i+j+k}\,\mathrm{asinh}\left(\frac{y-y_j}{\sqrt{(x-x_i)^2+(z-z_k)^2}}\right)\\
B_y(x,y,z) = &\frac{\mu_0 m_y}{4\pi}\sum_{i,j,k=0}^{1}(-1)^{i+j+k}\,\mathrm{atan}\left(\frac{(x-x_i)(z-z_k)}{(y-y_j)\sqrt{(x-x_i)^2+(y-y_j)^2+(z-z_k)^2}}\right)\\
&-\frac{\mu_0 m_z}{4\pi}\sum_{i,j,k=0}^{1}(-1)^{i+j+k}\,\mathrm{asinh}\left(\frac{x-x_i}{\sqrt{(y-y_j)^2+(z-z_k)^2}}\right)\\
&-\frac{\mu_0 m_x}{4\pi}\sum_{i,j,k=0}^{1}(-1)^{i+j+k}\,\mathrm{asinh}\left(\frac{z-z_k}{\sqrt{(x-x_i)^2+(y-y_j)^2}}\right)\\
B_z(x,y,z) = &\frac{\mu_0 m_z}{4\pi}\sum_{i,j,k=0}^{1}(-1)^{i+j+k}\,\mathrm{atan}\left(\frac{(x-x_i)(y-y_j)}{(z-z_k)\sqrt{(x-x_i)^2+(y-y_j)^2+(z-z_k)^2}}\right)\\
&-\frac{\mu_0 m_x}{4\pi}\sum_{i,j,k=0}^{1}(-1)^{i+j+k}\,\mathrm{asinh}\left(\frac{x-x_i}{\sqrt{(x-x_i)^2+(y-y_j)^2}}\right)\\
&-\frac{\mu_0 m_y}{4\pi}\sum_{i,j,k=0}^{1}(-1)^{i+j+k}\,\mathrm{asinh}\left(\frac{x-x_i}{\sqrt{(y-y_j)^2+(z-z_k)^2}}\right)
\end{aligned}
\tag{3.6}
$$

where:

(x_0, y_0, z_0) = Coordinates of a corner of the rectangular magnet (magnet axes must be aligned with the coordinate system)

(x_1, y_1, z_1) = Coordinates of the opposite corner of the rectangular magnet

(m_x, m_y, m_z) = Magnetism vector $M = B_R/\mu_0$ in the direction of the internal magnetic field

B_R = Residual Magnetism, a property of the magnet grade

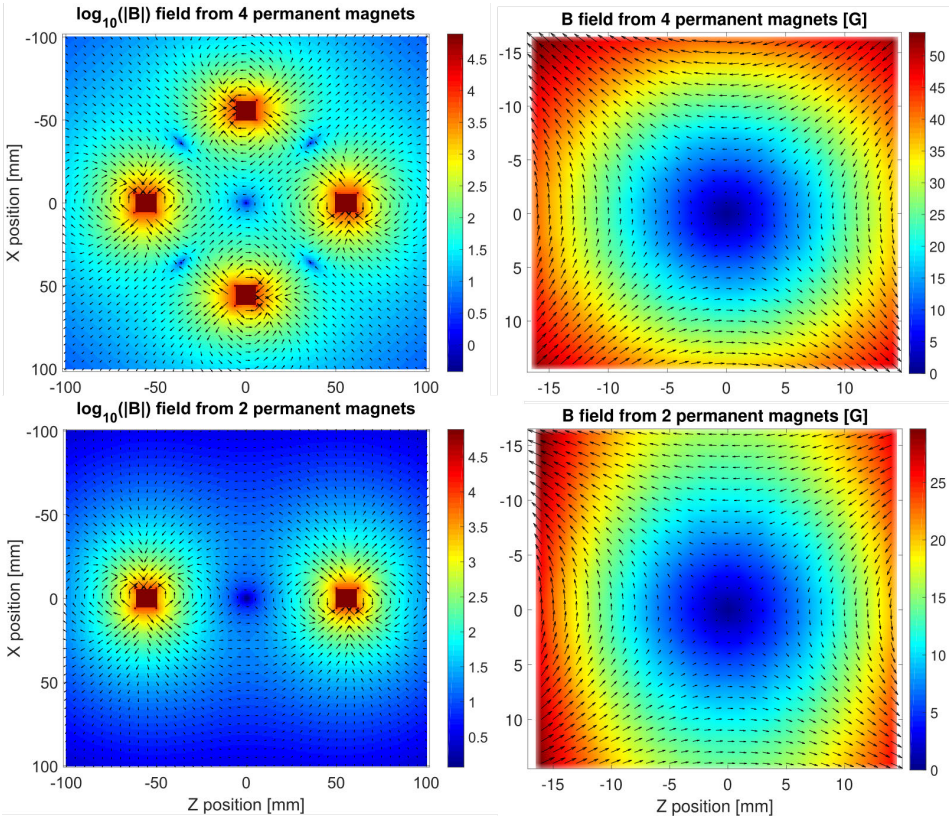

FIGURE 3.33: **Concept for creating a 2D quadrupole field with permanent magnets.** (top left) Here we plot the four permanent magnet configuration for constructing a 2D quadrupole field. On a large scale it may not be apparent but if we zoom in (top right) we can see the central region forms a quadrupole field. The lasers for the MOT should propagate along the diagonals. (bottom) A close approximation to the four magnet geometry can be made using just two magnets, at least in the central region. This version is less uniform and has half the strength but it frees two sides for the placement of other structures like a Zeeman slower and its beam.

magnets is listed in table 3.12. The array described is assumed to be symmetric and duplicated about the axis so only two identical arrays need to be fabricated. A summary of the fields achieved using the permanent magnet array design is plotted in figure 3.34.

The design of the array was developed in isolation from other system components such as the fields from coils and the mu-metal shield (see figure 3.27). The coils just linearly add field offsets but the mu-metal is highly nonlinear and difficult to calculate. Furthermore there is typically significant variation in the strengths of magnets so the design was treated as a guide. To turn this guide into capability the magnet locations need to be able to be fine tuned and the field produced needs to be verified and mapped experimentally.

TABLE 3.11: **Properties of permanent magnets.** Properties of selected magnet grades used in our calculations. We mostly use low temperature neodymium magnets N35 - N52. For the iqClock project, where we are considering in chamber magnets which would need baking we are also looking at Y35 ferrite magnets and high temperature 42SH neodymium magnets. Data is taken from https://www.supermagnete.nl/eng/data_table.php

Grade	Residual Magnetism B_R [G]	Coercive field strength bHc [kOe]	Coercive field strength iHc [kOe]	Energy product [MGOe]	Maximum Temperature [°C]
N30	10800-11200	9.8-10.5	$\geq$12	28-30	$\leq$80
N33	11400-11700	10.3-11	$\geq$12	31-33	$\leq$80
N35	11700-12100	10.8-11.5	$\geq$12	33-35	$\leq$80
N38	12200-12600	10.8-11.5	$\geq$12	36-38	$\leq$80
N40	12600-12900	10.5-12.0	$\geq$12	38-40	$\leq$80
N42	12900-13200	10.8-12.0	$\geq$12	40-42	$\leq$80
N45	13200-13700	10.8-12.5	$\geq$12	43-45	$\leq$80
N48	13700-14200	10.8-12.5	$\geq$12	45-48	$\leq$80
N50	14000-14600	10.8-12.5	$\geq$12	47-51	$\leq$80
N52	14200-14700	10.8-12.5	$\geq$12	48-53	$\leq$65
42SH	12900-13200	10.8-12	$\geq$20	40-42	$\leq$150
Y35	4000-4100	2.20-2.45	2.26-2.51	3.8-4.0	$\leq$250

The concept for the magnet array mount was a holder with many carriages into which various magnets can be swapped with their individual positions fine adjustable using screws. The first designs for a brass and aluminium structure were rather complex and the feedback from workshop on their manufacturability was...shall we say "clear and robust". I then set about designing new versions which could be printed on our Dimension Elite 3D printer from ABS plastic. 3D printing is a wonderful new technology but the strength and resolution of parts produced is in no way comparable to what you can do with a good operator using aluminium. When designing for a 3D printer one must take into account the granularity of the printing process. The printer works with a 3D translation stage and a printing head which extrudes a continuous bead of plastic on the work pieces as it moves around. A second support material can be used to fill voids allowing more complex parts and straight walls. This support material is later dissolved in a bath of hot sodium hydroxide. The dimensions of the bead and the recommended minimum wall thickness (two beads side by side) is summarized for our printer in table 3.13.

How do you make precision adjustment using such low resolution tools? One way is to post process, drill and tap threads in the plastic pieces. This is a lot of work and the threads

TABLE 3.12: **Permanent magnet array configuration.** Permanent magnets and their locations relative to the center of the blue 2D MOT. These magnets arrays are located either side of the 2D MOT (symmetric about the Z=0 mm plane) on the machine. The supplier SM refers to supermagnete.nl and the supplier K&J refers to K&J Magnetics (www.kjmagnetics.com).

Magnet	Block	Direction (along Z)	Center Position Y [mm]	Center Position X [mm]	Center Position Z [mm]	Width X [mm]	Width Y [mm]	Width Z [mm]	Part	Grade	Supplier
1	1	-1	-100.81	57	0	10	10	10	W-10-N	N42	SM
2	1	1	-100.88	68.5	0	12	12	12	W-12-N	N48	SM
3	2	1	-89.78	69	0	10	10	10	W-10-N	N42	SM
4	4	-1	-67.30	54.5	0	7	7	7	W-07-N	N42	SM
5	5	1	-58.80	75	0	10	10	10	W-10-N	N42	SM
6	9	1	-22.17	43.76	3.175	3.175	3.175	3.175	B222G-N52	N52	K&J
7	9	1	-22.17	43.76	0	3.175	3.175	9.525	B222G-N52	N52	K&J
8	9	1	-22.17	43.76	-3.175	3.175	3.175	3.175	B222G-N52	N52	K&J
9	9	1	-24.14	49.35	3.175	6.35	6.35	6.35	B444-N52	N52	K&J
10	9	1	-24.14	49.35	-3.175	6.35	6.35	6.35	B444-N52	N52	K&J
11	9	-1	-24.17	53.5	0	7	7	7	W-07-N	N42	SM
12	10	-1	-8.55	48	6	12	24	12	W-12-N	N48	SM
13	10	-1	-8.55	48	-6	12	24	12	W-12-N	N48	SM
14	11	1	7.04	49	6	12	24	12	W-12-N	N48	SM
15	11	1	7.04	49	-6	12	24	12	W-12-N	N48	SM
16	11	1	0.94	76	0	12	12	12	W-12-N	N48	SM
17	15	1	38.14	56	0	12	12	12	W-12-N	N48	SM
18	15	1	38.35	68	0	10	10	10	W-10-N	N42	SM

TABLE 3.13: **3D printer resolution.** Resolutions for the ABS plastic Dimension Elite 3D printer.

	Unit	Low resolution	High resolution
Layer thickness	mm	0.254	0.178
Bead width	mm	0.457	0.318
Minimum wall thickness	mm	0.915	0.635

are not strong (neodymium magnets are stronger:-). I also looked at making groove and bump arrays so you could release a magnet carriage and push it to the next groove and re-secure it, but again, once you release a piece to move it, the neodymium magnets have a way of taking control of the situation. The way we came up with was to print holders for pieces of threaded rod. This way a low resolution structure could be printed with the

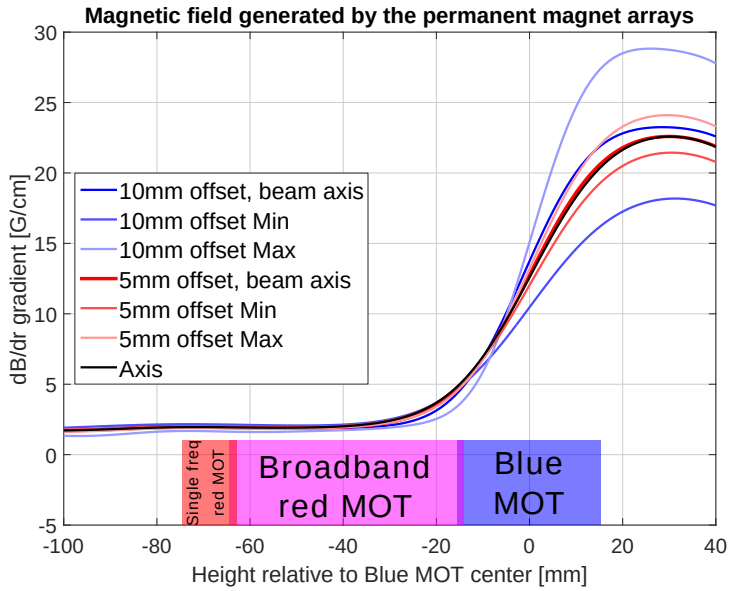

FIGURE 3.34: **Magnetic field gradients achieved using the permanent magnet array design.** Here we plot the magnetic field gradient variation with height showing the variation achieved between the blue MOT and red MOT regions.

properties, strength and precision of a stainless steel thread. This was the principle behind the magnet carriage design and their adjustment. A second problem is how to insert and remove the magnet arrays. This wasn't a problem until Vacom decided they needed to weld stainless steel plate wedges between the arms on the vacuum chamber. I convinced them to put a big hole allowing the magnet array to exist but sliding the array in from any direction was not possible. Thus this precision magnet array had to be able to be disassembled into small pieces and reconstructed on site with high precision. For this I printed tongue and groove structures to dowel the pieces together. Threaded rods down the sides secured the structure and the tolerances were such that by applying pressure with a locking nut it was no longer possible to slide the magnet carriages and the structure become essentially monolithic and quite stable. Figure 3.35 show the design and construction of the magnet arrays.

To measure the actual magnetic fields produced by the magnet arrays another system was developed. We were fortunate to be able to borrow an old Leapfrog Creatr 3D printer platform from Rudolf Sprik which had been stripped of its printing head. This gave us a huge computer controlled 3D translation stage upon which a 3D printed holder with three Texas Instruments DRV5053RAQLPG hall effect probes (Farnell 2455499) was mounted to simultaneously measure the magnetic field in all three axes. Each sensor had a nominal

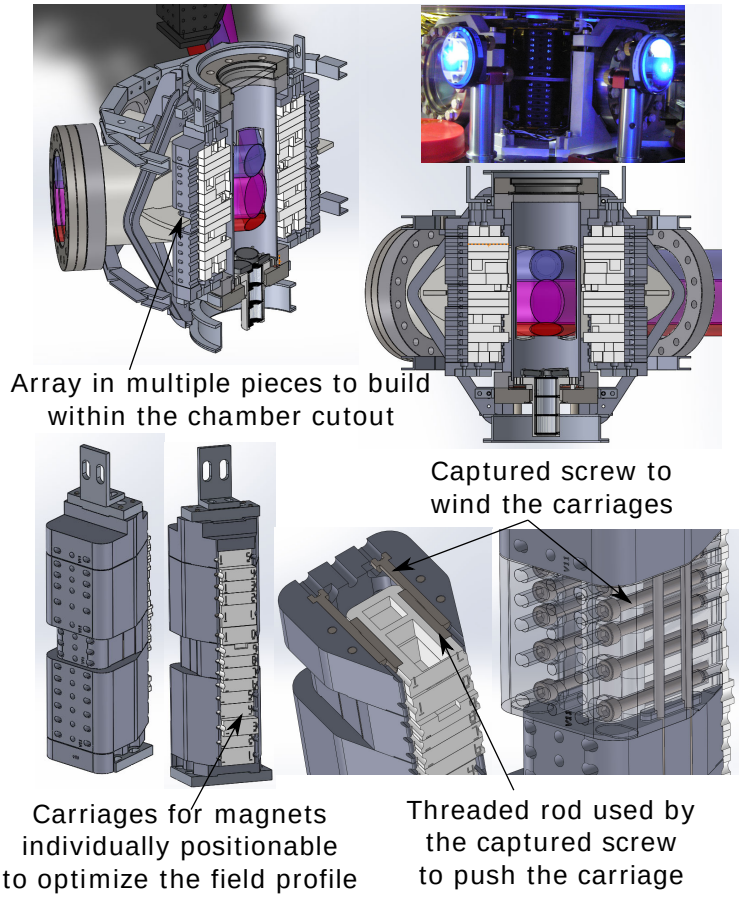

FIGURE 3.35: **Magnet array design and construction.** Here we show the design of the 3D printed holders for the magnet arrays including the precision screw adjustment provided by inserting pieces of threaded rod within the structure. The array also had to be disassembled and reassembled on site to accommodate the vacuum chamber support wedges.

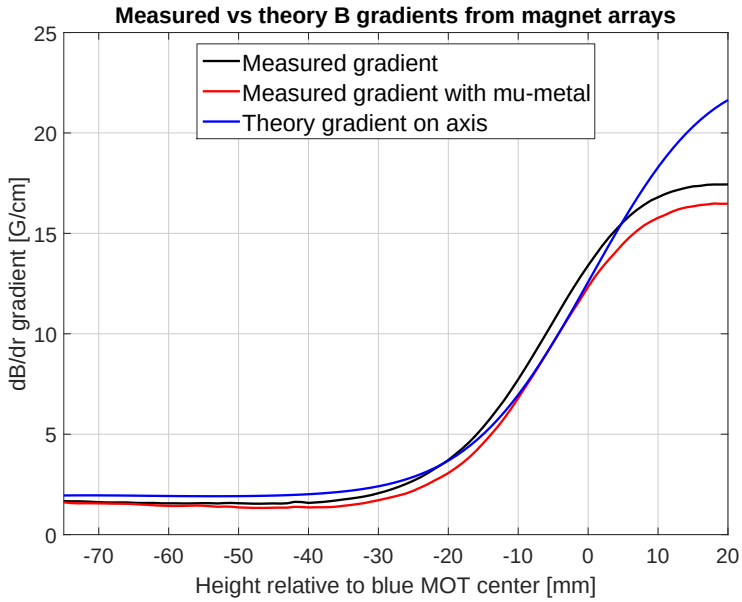

FIGURE 3.36: **Designed and measured field gradients for the permanent magnet arrays.** The design field gradients are the on axis fields while the measured gradient are averaged over a 25 mm square roughly centred on the quadrupole center.

sensitivity of $4.5\,\mathrm{mV}\cdot\mathrm{G}^{-1}$, saturated at 180G and had a nominal noise level of $22mV_{pp}$ which corresponds to $\pm$2.5G. A fact that went unnoticed at the time of the characterization is that the specification actually only specifies that the sensitivity is within the range from $2.0\,\mathrm{mV}\cdot\mathrm{G}^{-1}$ to $7.0\,\mathrm{mV}\cdot\mathrm{G}^{-1}$ which is a rather wide margin compared to the nominal value. The sensor locations for the three axes were as close as possible but they still had several mm separations which was accounted for by postprocessing the results. Data was logged using Matlab with a National Instruments PCI6259 data card. To reduce noise, measurements were only recorded while the printer was stationary and averaged over a period of 1 s at 1 kHz for five separate passes. Matlab was used to control the printer using a serial over USB interface to send G-code commands to the printer. Fields were measured for the magnet array, the background and the magnet array with the mu-metal shielding pieces (before mounting it in the machine). The results are summarized in figure 3.36. Examples of the details are plotted in figures B.1, B.2 and B.3 of appendix B for the center locations of the blue, broadband red and single frequency red MOTs respectively.

The match between the predicted and measured field gradient shapes was excellent but at high fields the measured magnitudes varied by 25% from theory. The results were good enough to move on so no further investigation of this deviation was conducted. Although it wasn't realised at the time, this deviation was almost certainly due to variation

in probe sensitivity from the assumed nominal value for the part. A calibration was never performed and the original probe appears to have been cleaned away at some point over the intervening years. While the gradients were good, the alignment of the quadrupole centres was not, especially with the inclusion of the MuMetal shielding. Adjustment was included in the arrays to be able to trim the field strength to avoid fields approaching zero and causing an exploding MOT. This was envisaged by varying the axis-magnet spacing but there was no way to translate individual magnets in the X direction parrallel to the Zeeman slower. It is likely this quadrupole shift could be corrected to first order using the Zeeman slower and compensation coils but this is a global shift. A smaller variation in the location of the quadrupole zero can also be seen in scans without MuMetal but these shifts were mostly in the Z axis where adjustment existed to fine tune the magnet locations and trim the field strengths and zero locations. Before embarking on a long and arduous process of trimming the magnet locations we tested replacing the red MOTs with red molasses and were pleasantly surprised by the performance so no further adjustment was made of the magnet arrays[34].

Three sets of magnetic field bias coils are provided to adjust the location of the quadrupole center essentially at the exit of the blue MOT in order to align the atomic beam with the aperture to the lower chamber. These coils also provide the option of increasing the gradients should the field from the magnet arrays approach zero or a negative value. Each coil set includes three circuits which can be used to provide both Helmholtz and anti-Helmholtz configurations, as well as adjust the available strength of the Helmholtz and anti-Helmholtz coil sets.

Since we use a molasses configuration we are not sensitive to field gradients becoming zero or negative so we do not use the anti-helmholtz coil pairs. The horizontal Helmholtz coil pairs are used to optimize the beam transfer through to the lower chamber. The vertically oriented Helmholtz coil set provides a 1.46G bias field in the upwards direction to turn our red MOTs into red molasses (by tilting the field orientation, giving a strong non-magnetic π transition). The technical details of these coils including their orientations can be found in appendix C.

Finding a way to squeeze these coils around the chamber was very challenging and we resorted to custom made coil holders for the horizontal axes and pre-winding these coils around the chamber before the high temperature vacuum bake. Additional constraints included requiring being able to install the magnet arrays and windows after the bakes and the rather difficult set of wedges added by Vacom to the chamber design. The result was a little crazy and the name stuck so these coils are named the short and tall “crazy coils”.

[34] With a touch of sadness given the level of obsession which had been devoted to developing 3D printed magnet mounts with this fine adjustment:-(

The high temperature bake did some bad things to the enamel insulation on these coils. Significant variations in the coil resistances were measured between before and after the bake (see table C.5). Extreme care should be used when physically interacting with these coils. The vertical coils are known as the blue MOT vertical coils and although one coil experienced the high temperature bake, it was not nearly as hot so its enamel remains in good shape. Each coil includes a single turn of 4 mm×4 mm square copper tubing which is used to flow water and cool the coil. The square tubing ends were filed round and silver soldered into 8 mm brass pipes which were swagelocked to 8mm annealed soft copper tubing. The copper then descended to below the optical table where it was swagelocked to plastic tubing for vibrational isolation and strain relief before connecting to the water manifolds and their flow adjustment valves. Other details can be found in appendix C. Figure 3.37 shows the design and construction of these coils.

3.5.2 2D MOT optical and vacuum system

The optical configuration generating the beams for the 2D MOT chamber as well as the imaging systems used is included in figure 3.38. The design consists of a series of three 2D MOTs stacked one below the other beginning with a 2D blue MOT, followed by a 2D broadband red MOT and finishing with a (never implemented) 2D single frequency red MOT. In addition to the 2D MOT beams, the design also called for a series of molasses beams in the vertical direction to control the speed with which atoms move through these MOTs. This is necessary to give the atoms long enough in the MOT for them to coalesce near the axis. The vertical molasses beams consist of independent counter-propagating beams allowing a moving molasses (for the red) and a power imbalanced molasses (for the blue) to be implemented. These are each implemented as two crossed beams to maintain symmetry while avoiding sending light into the lower chamber. At the bottom of the 2D MOT chamber a baffle is needed to minimize the transfer of blue light to the next chamber. Another design consideration is keeping the magnet arrays as close as practical to the MOT axis to rapidly vary the field gradient between the blue and red MOT regions which means keeping the chamber diameter as small as possible. The design we came up with relies on mounting four mirrors in the chamber as shown in figure 3.39. Also shown is the optical layout used to generate these vertical beams.

In chamber mirror holder Designing mounts for holding optics in UHV was new to me. The basic design principles for avoiding virtual leaks and poor vacuum are that surfaces should not touch, gaps should be as large as possible, materials should be selected for vacuum compatibility and everything must be thoroughly cleaned. The design is shown in figure 3.40. It was developed in partnership with Ron Manuputy

FIGURE 3.37: **Design and construction of the bias coils.** Here we show the design and construction of the bias coils around the 2D MOT chamber.

from the workshop and made by Jan Kalwij. We wire cut a flexure into an aluminium holder and press fitted hourglass shaped stainless steel pins with square shaped bottoms into round holes in the flexure to grab mirrors. We chose standard 1″ silver mirrors[35] to avoid the polarization problems you get with dielectric mirrors. To allow a more symmetric molasses we provided two mirrors symmetric about the axis. We could not easily separate the addressing of the blue, broadband red and single

[35]This was maybe not the best choice as the mirrors in the atom laser chamber grew a thick (hundreds per cm^2) layer of fur during the bake.

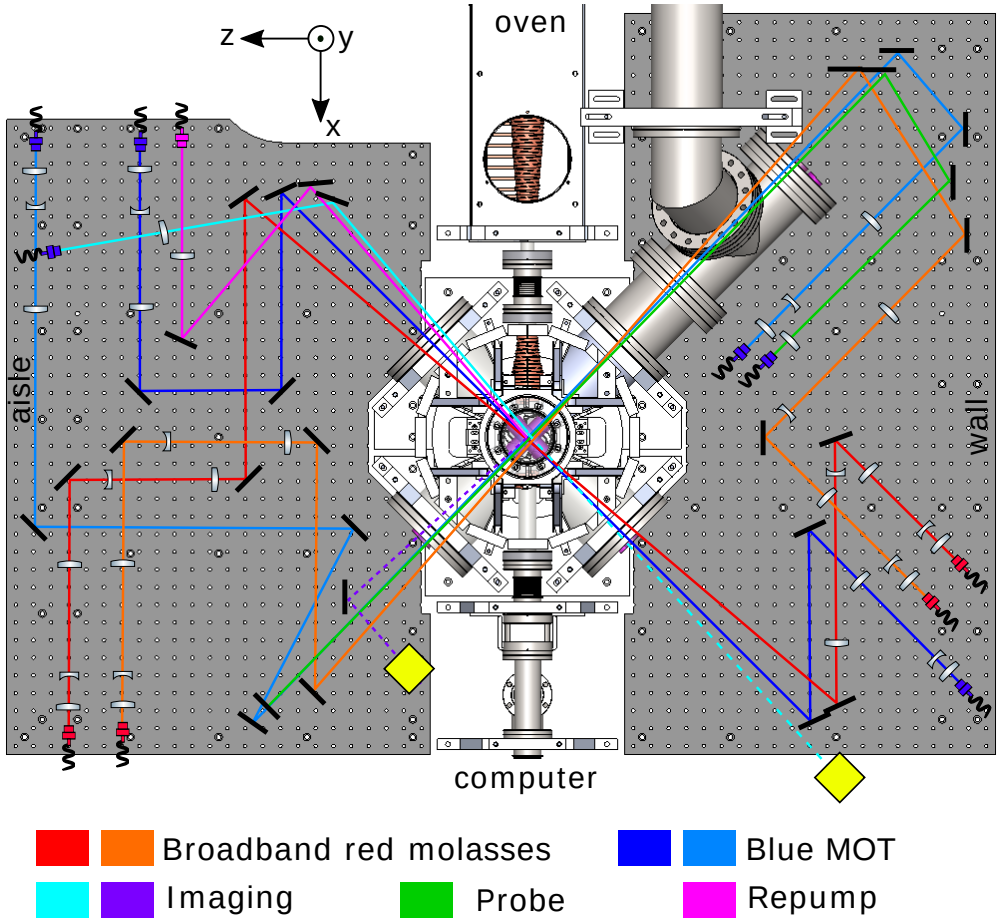

FIGURE 3.38: **2D MOT optical configuration.** Here we show the optical layout for the horizontal beams in the 2D MOT chamber.

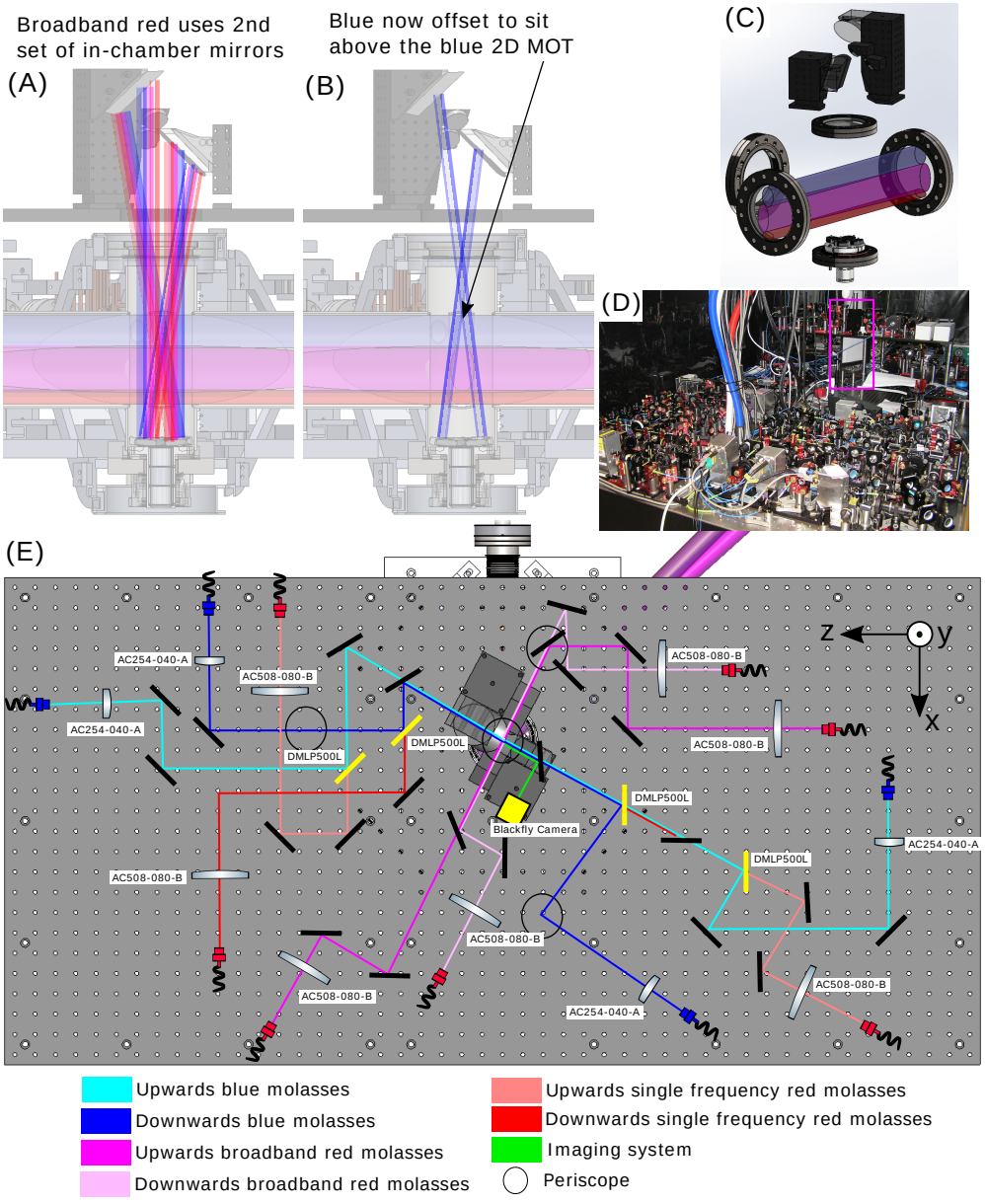

FIGURE 3.39: **2D MOT vertical optical configuration.** (A) Here we show the initial optical layout for the vertical beams for the 2D MOT chamber. (B) The current downward blue push beams used in the machine to plug the top of the 2D blue MOT. (C) The mirror arrays used to direct the vertical beams into the chamber and the in chamber mirrors. (D) The mock up of the in chamber mirrors built to align the vertical beams is outlined in the pink box. (E) Optical layout of the optics generating the vertical beams for the 2D MOT chamber.

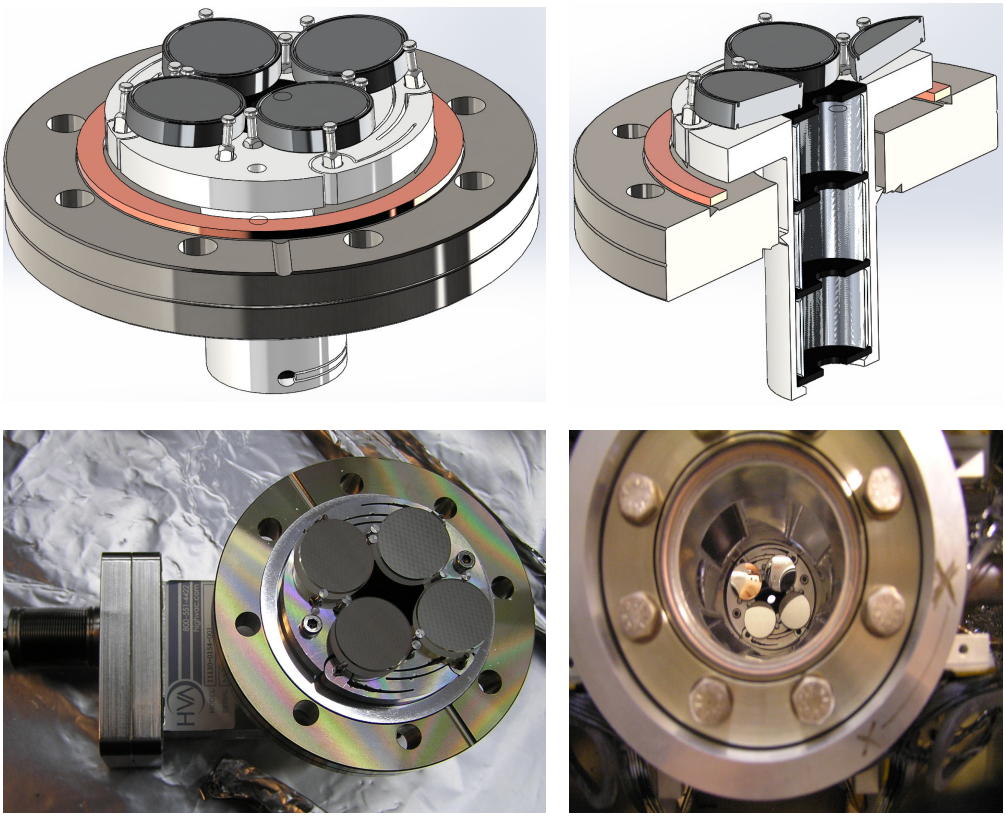

FIGURE 3.40: **2D MOT in vacuum optics.** Here we show the design and construction of the in-vacuum mirrors and the baffle within the UHV 2D MOT section.

frequency red MOT regions using a single mirror to reflect the counterpropagating beams. Therefore a separate mirror set was used for the broadband red MOT vertical moving molasses beams.

Baffle We examined a variety of options for baffling the lower chamber from the blue light in the 2D MOT chamber. The main problem with transfer tubes is that grazing incidence light will always be transmitted to some degree so we converged on using a series of orifices. There are not many options for UHV rated black materials. Anodised surfaces are absolutely not UHV compatible. We considered the copper oxide techniques used by the DeMille group [100] but we settled on using AR coated neutral density filters (Thorlabs NE60B-A) with an 8 mm hole drilled in the center for the atomic beam to pass[36]. The baffle also provides differential pumping isolating the vacuum between the two chambers by 20dB, as was discussed in section 3.3.4.

[36]Today we would also look at the coatings from Acktar.com.

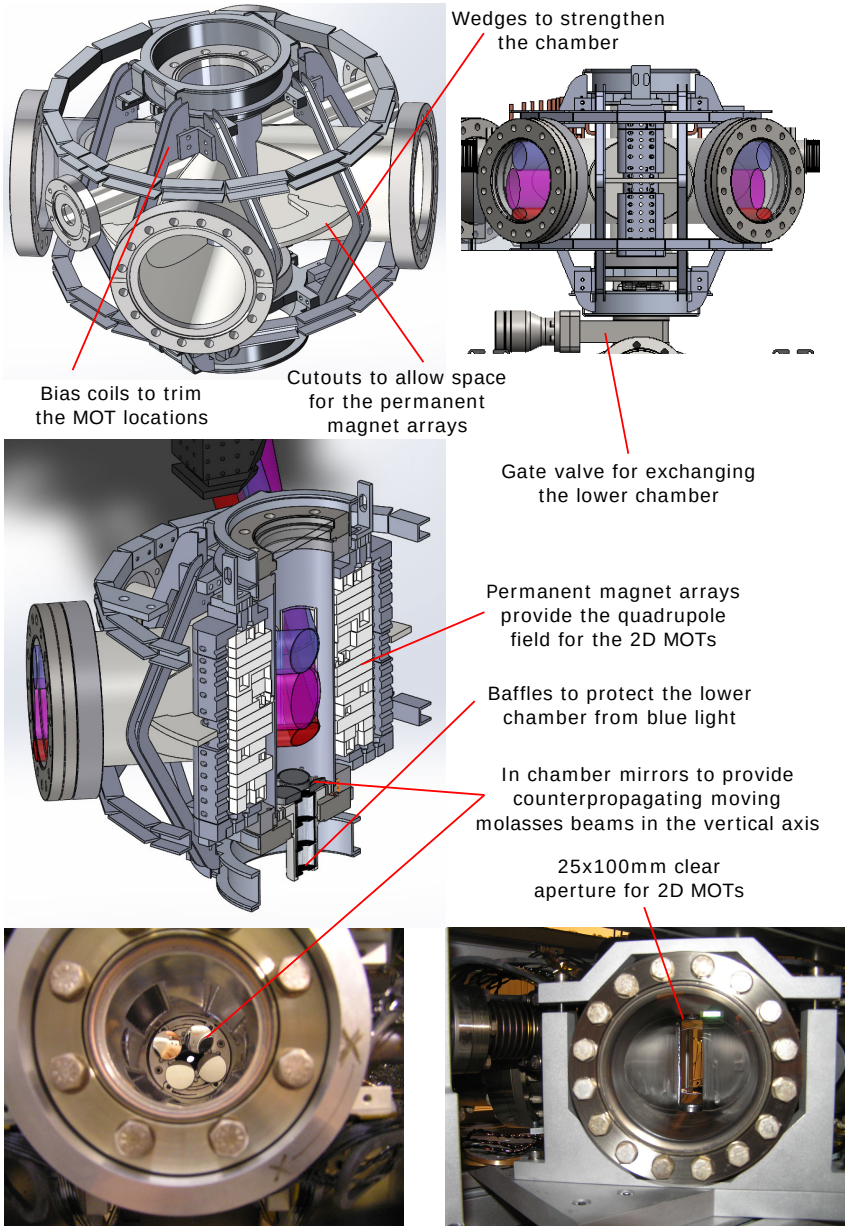

FIGURE 3.41: **2D MOT chamber.** Here we show the design and features of the 2D MOT chamber.

The baffle filters are held within the same mount as the in-chamber mirrors. Flexures secure the disks transversally while axially they are spaced at 20.5 mm centres by a series of 19 mm long rings. More detail can be seen in figure 3.40.

Vacuum chamber The objectives of the vacuum chamber design were to keep the Zeeman slower-MOT separation as small as possible, allow a 25 mm diameter Zeeman slower beam, allow the permanent magnets to be as close to the axis as possible, provide optical axes for a 25 mm×100 mm long MOT region, provide space for the in-chamber optics and vertical access for a conveyor and do this using commercially available viewports. The design is shown in figure 3.41. The chamber was made by Vacom.

Pre-alignment To make it easier to rough align, a mock up of the in chamber optics was made (figure 3.39). Being able to inspect the beam without a vacuum chamber in the way was particularly valuable for getting the positioning of the vertical molasses beams right. This was done by Chun-Chia while we were baking the machine and the final optics breadboards slid into the machine for fine adjustment. The beams, their geometries and powers are listed in table 5.2, table 5.3, table 5.4 and table 5.5.

Alignment The alignment of the 2D MOT section optics, particularly the blue MOT beams, is quite sensitive. Initially we align this system by power and mode matching the beams and adjusting the polarizations so that it has the correct circular polarization as judged by a S&K polarimeter. We then geometrically align the beams. We have cameras (Point Grey Blackfly BFLY-PGE-23S6M-C) which we use to monitor the 2D blue MOT fluorescence in real time[37]. By looking at the blue MOT fluorescence from two orthogonal sides and sometimes the vertical axis, we then try to make an intense linear blue MOT. The fluorescence from the red molasses is not visible but we found this is also alignment insensitive. As long as the beams are power balanced and the polarizations are vertical, little effort is needed for the red molasses. Initially to get the red frequency, modulation and power correct, we placed a back reflected probe beam using the blue transition (of the correct linear polarization) into first the bottom of the 2D MOT chamber and later the atom laser chamber. Looking at the probe fluorescence (figure 4.2) is how the red molasses and blue MOT were first optimized. Now that we have a working red MOT in the lower chamber, we always fine adjust the blue MOT alignment and the Zeeman slower alignment to maximize the fluorescence from the red MOT in the lower chamber. We never saw much improvement from the red vertical molasses beams on the bosonic isotopes. These may yet prove useful for polarizing the fermions. The same is true for the counterpropagating blue vertical molasses beam, but we do use the forward propagating vertical blue beams essentially for plugging the top of the 2D blue MOT.

The generation of the beams will not be discussed here. Information can be found in Chun-Chia's thesis [216].

[37] Using a C++/Matlab program I wrote

Here we tried to describe the machine as it was designed and first built. Of course the main change in the upper chamber from the present system is the use of a 2D red molasses instead of a 2D red MOT. The power and AOMs for the vertical red molasses beams were repurposed for use in the lower chamber early on, although the molasses beam optics remain in place. We also find that the extent of the broadband red molasses beams is excessive and the beam height could be apertured by at least a factor of two with no performance impact. The power on the 2D blue MOT beams is less than ideal, as we continue to improve fluxes with more power. That said, we still get a flux of 30% with blue MOT powers of 3 mW per beam instead of 10 mW per beam, so the power is not critical.

Another obvious question is "why don't you retro-reflect the MOT/molasses beams and thus double your power?". We did look into this but found the system less stable and less reliable. In fact we rebuilt the MOT optics for the lower chamber to remove the retro reflections to make the system more stable. We tried a polymer waveplate (ITOS WP140HE) for the blue which can give a low cost alternative for big waveplates. Chun-Chia found these used and discussed in Bjorn Kock's thesis from Birmingham [297]. We also tried a telescope to be able to use our 0.5" waveplates with our big 30 mm diameter beams. We have recently discovered a lower cost supplier of waveplates in China (crylight.com). The quality from them has been good and they offer 30 mm waveplates as standard products.

Although the broadband AR coatings on the 2D MOT chamber DN100 windows (Demaco part A0650-5-BBAR425-760) performed fine in the red they scattered strongly at 461 nm (10% loss per pass). We did not test them before building them into the vacuum system, which was a mistake[38].

3.6 The atom laser chamber

The atom laser chamber is the heart of the SrCAL machine. It was envisaged to be a flexible workspace in which to use the cold atomic beam delivered from above. It was also imagined that this chamber might be replaced once we figured out how to make a steady-state atom laser. We imagined a future chamber incorporating a cavity for trying a steady-state superradiant clock or perhaps something dedicated towards a steady-state atom interferometer or sensor.

At the time of design we knew we wanted to be able to try two basic approaches in this chamber for making a continuous atom laser. The first was making a steady-state BEC using the Innsbruck architecture [192] and then outcoupling a continuous atom laser. The second direction was evaporation in a waveguide in the style of David Guéry-Odelin [170,

[38] We recently read a horror story from JILA (Appendix A of [27]) about some of their broadband coatings on fused silica viewports which also scattered about 10% at 461 nm.

172] and Georg Raithel [185, 187, 298, 299]. Another direction for creating a steady-state atom laser is using cavity cooling on a beam similar to the superradiant laser architecture. This approach was studied by Helmut Ritsch [211] and might mix nicely with the iqClock superradiant clock project.

3.6.1 Design and construction

The design objectives for the lower chamber were:

- A long horizontal space of around 10 cm where an optical waveguide can be placed for waveguide evaporation and with optical access to allow both top and horizontal imaging of the evolution and hopefully condensation within the waveguide.
- The ability to place MOT or molasses beams anywhere along this waveguide for loading, cooling or to create a MOT.
- The ability to place a vertical conveyor lattice to feed atoms from the top chamber.
- A gate valve to the top chamber to allow changing the chamber design without rebaking the top chamber.

The chamber design along with many of its features is shown in figure 3.42. Like the upper chamber it was made by Vacom from stainless steel 304.

Periscope mirrors A key feature is the long in-chamber periscope which gives access to the vertical axis. This is formed by a pair of custom, protected, silver coated mirrors from Altechna. I was once asked why we didn't extend these mirrors all the way across on the bottom. There are two answers to this. Firstly, we use metal (silver) coated mirrors to avoid tampering with the polarizations of the reflected beams but silver coated mirrors have a low damage threshold. This would limit the intensity of any conveyor or lattice beam we might want to use to assist in the transfer of atoms from the upper chamber. The second reason is that the vertical slower beam is by far the highest power and the most frequency broadened red laser. By having the insertion viewport for this beam out of sight from the atom laser or BEC location we can avoid some of the heating from scattered light from this beam. Another fun fact we discovered about protected silver coated mirrors in vacuum is that they grow fur when you bake them (see figure 3.43). At the end of the window bake where we heated the in chamber mirrors to somewhere in the 150 °C-200 °C range for a few weeks we unwrapped our chamber and were surprised to find the mirrors when viewed from the side had a forest of multi-mm long whiskers growing from the mirror surface (hundreds per cm^2). We don't believe this ever really caused us problems but it would be worth reconsidering the use of silver mirrors for in chamber optics which need baking. The

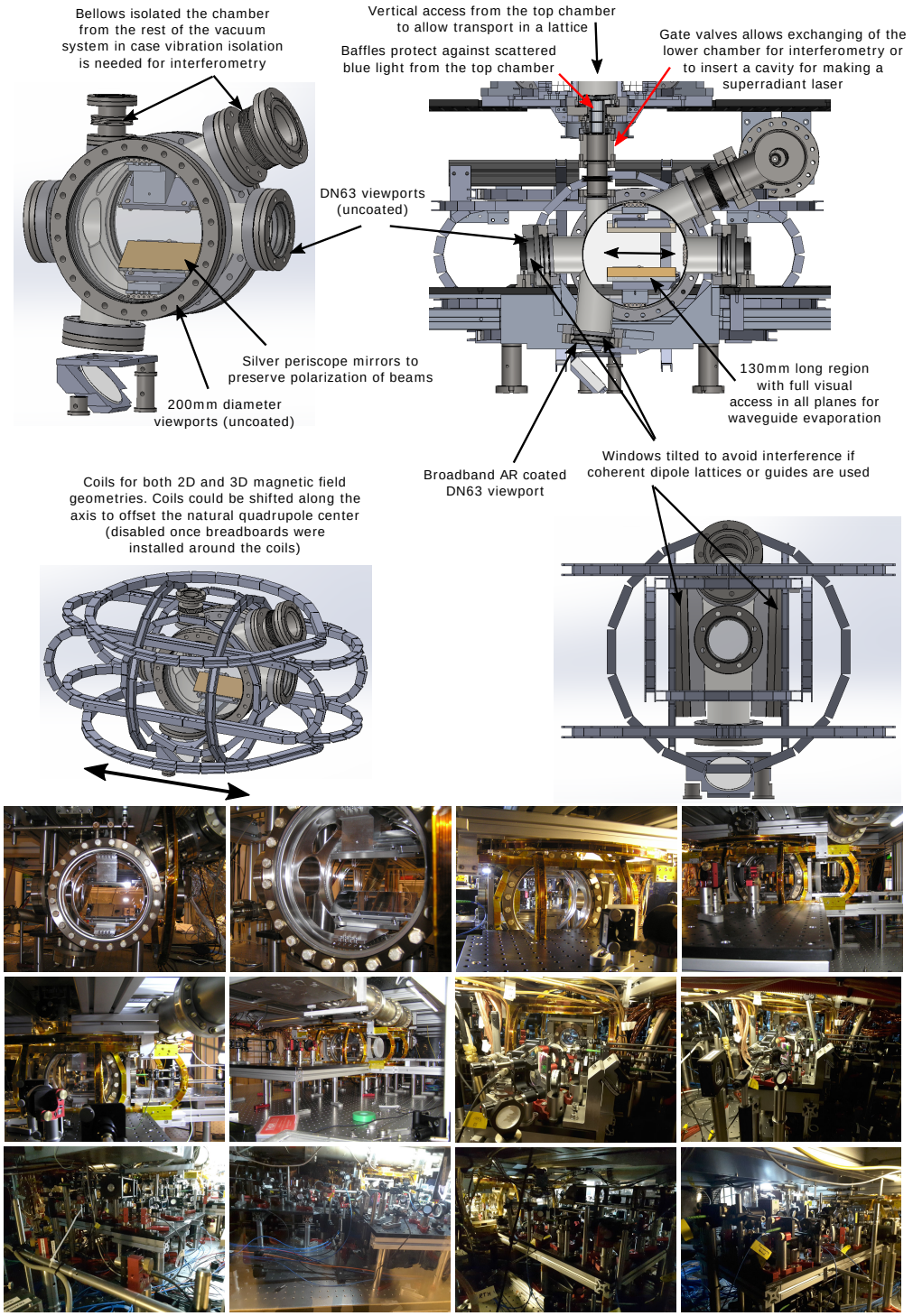

FIGURE 3.42: **Atom laser chamber design and features.** .

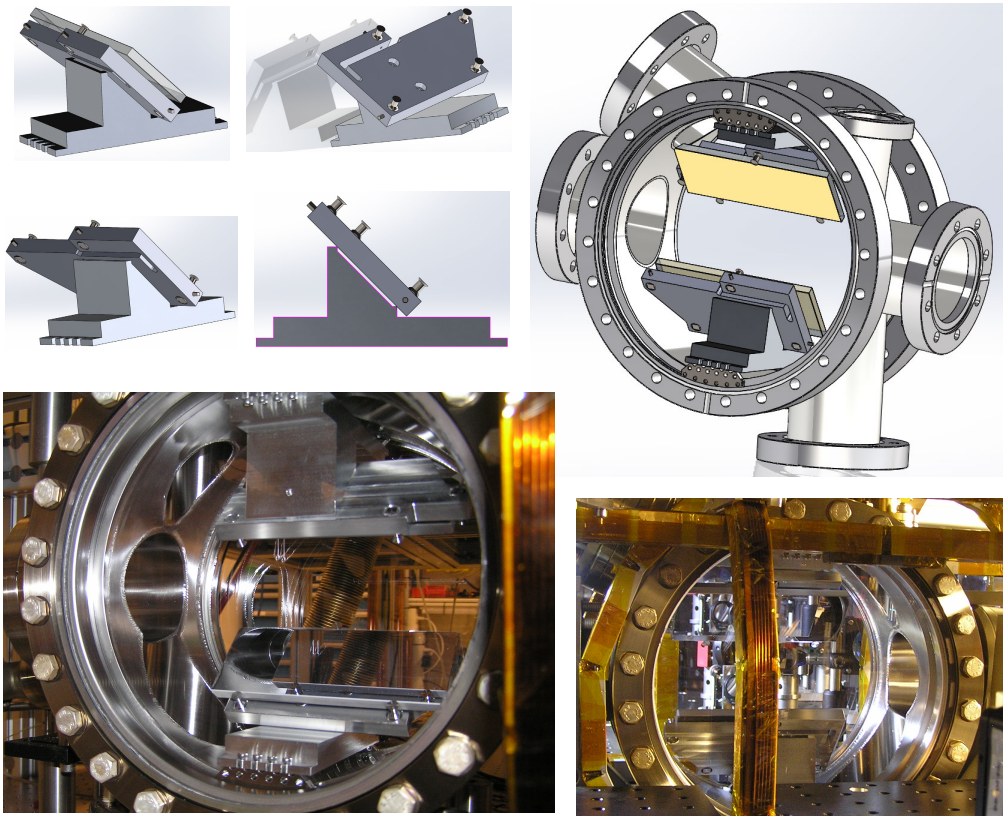

FIGURE 3.43: **Atom laser chamber mirrors.** Here we show the design and construction of the in-vacuum mirrors for the atom-laser chamber.

damage threshold of the silver coated mirrors must be carefully considered when choosing the dimple dipole trap intensities, otherwise you will be sad.

The mirrors were held in the chamber by a customized holder we made from aluminium 6061. It was attached to the chamber using groove grabbers (Kimball Physics) which were fixed to grooves machined into the DN200 window flanges with the same dimensions as found on the Kimball Physics chambers. The holder detail is shown in figure 3.43 and has many similarities to the mirror mount made for the top chamber. Like in the top chamber a flexure structure was wire cut into the aluminium and the mirrors themselves sit on stainless steel pins with square bases press fitted into round holes. Vented screws from Vacom were used. Ideally screws should be avoided entirely for UHV but I reasoned that since there were already screws in the groove grabbers a few more would not matter. As discussed earlier, the vacuum in this chamber is not what we had hoped for so careful attention should be paid to the

design of these mirror holders to check if they were not the cause of the mysterious virtual leak.

Gate valve At the bottom of the baffle from the upper chamber we have a manual gate valve (Demaco GVM-1502-CF). We were very worried about using these elastomer sealed valves in the UHV section as they are only rated for pressures down to 1×10^{-10} mbar (they specify a helium leak rate of $\leq 2 \times 10^{-9}$ mbarL/ sec. We were however short on cash at the time and the all-metal valves were much more expensive as well as having a much larger form factor. We do see a pressure burst when the valve is opened typically on the order of 1×10^{-8} mbar but it dissipates in a matter of minutes. A similar valve is used in the top chamber without any noticeable vacuum issues, which makes us think that in principle these valves can be OK even in UHV. That said, I think this is a likely source of our virtual leak and I would be very reluctant to use one in a UHV chamber again (at least put it the other side of the baffle so there is some differential pumping!). The VAT 481 series valves specify leakage rates more than an order of magnitude smaller.

Bellows Between the gate valve and the chamber, and between the chamber and the pumping section we included welded bellows[39]. These allowed isolating the chamber from the rest of the machine and securely bolting it to the optical table. This reduces the potential for stress and differential movements which may play a role when we are bouncing very small and very alignment sensitive beams like the transparency or dimple dipole trap beams off the in chamber mirrors. It also was imagined as a way to isolate the main chamber from vibration which might be important in an interferometry application.

Windows The bottom chamber is centred around two uncoated DN200 fused silica windows from Lesker (part 450027). These windows are each tilted away from vertical at 1.5° so there is a 3° mutual angle to try to avoid the potential for interference effects from the uncoated surfaces. Scatter off these windows is a major consideration when placing cameras to look at fluorescence from very dim red MOTs. The two DN63 horizontal chamber end windows are also uncoated (Demaco A0650-3-CF). The window on the source side is tilted in the vertical to point down at 3° in order to avoid interferences while the second window on the far side of the chamber is square.

[39] Vacuum chambers can fly. To reduce heat loss and get a more even temperature, before the window bake we removed the aluminium support structure and left the lower chamber sitting on a cradle we made for it. When we first pumped the system down to our surprise the lower chamber lifted itself off the support cradle and compressed and slightly twisted the bellows trying to minimize their lengths. We then had to improvise collars around the bellows to keep them happily stretched and not twisted before we baked. After the bake the chamber was once again reattached to the table and this surprise lies waiting to strike again.

The final fused silica DN63 window allows the red slower beam to pass from below. It has a broadband AR coating (Demaco A8003-1-CF) primarily to try to minimize the rescatter of any blue light from the top chamber. There is some dust, particularly fiber glass from the heating bands in the bottom chamber on the inner surfaces of the windows. This is a little embarrassing. The cleanliness of the room, particularly the area around the atom laser chamber when we installed the windows was poor. One theory is that our virtual leak is outgassing from this dust, but I doubt that one.

Magnetics Two sets of coils were built for the atom laser chamber, a set of racetrack coils provides a 2D geometry with the axis along the z direction while a second set of round coils provides a 3D geometry roughly centred on the atom laser chamber. The coils are shown and described in appendix C and in particular, figure C.1. There was some uncertainty over where on the z axis the best place would be for the 3D quadrupole center. For this reason the Z coils were made to be able to be moved along rails in the Z direction. We soon realised that we needed to place optics as close to the chamber as possible so we built optical breads with cutouts for the coils effectively fixing the coils at their initial location and removing this adjustment. Since we now use a MOT centred directly below the apertures to the 2D MOT chamber it would have been better to slide the coils 4-5 cm towards the wall. This would have reduced the field distortion the atoms experience after they pass through the baffles which affects the slower performance a little. This distortion which is observable in simulations comes from one of the Z coils which runs close to the path of the atoms. We never really used the round coils for the X axis as this is also served by the horizontal racktrack coils so these coils were mostly used for implementing a feedforward correction to compensate noise from the other machines in the X axis. The vertical axis similarly has some redundancy.

Images showing the coil construction are included in figure 3.37. These coils were constructed using formers made from lengths of aluminium U profile. The profile sides were segmented every ≈2 cm allowing them to be bent around laser cut wooden formers. The ends were then joined with a plastic plate to avoid eddy currents. Before winding the formers were wrapped with kapton tape insulating them. To wind the coils a foot-pedal operated welding turntable was used to spin the coil holder and the wire reel was mounted on a rod and tensioned by hand. Typically three separate circuits were wrapped on each former. Cooling was achieved by wrapping a 4×4 mm copper tube with a 2 mm inner diameter within the former and running water through it. The pressure from from 2 m pipe is no problem but it is important to expand the diameter back up in the piping to and from. During coil wrapping bulldog clips were

used to hold the system together until it could be secured with cable ties and then kapton tape. 45 °C thermal switches were used to monitor the temperature of the coils but they would probably survive a coiling failure without any issues given the low currents we typically operate with.

The details of how the red MOT and subsequent systems were made to work will be left for chapter 4.

3.7 Other aspects

Here we will briefly step through some of the details on supporting infrastructure for the machine.

3.7.1 Lasers and optics

A lot of optics and lasers were developed for the SrCAL machine. Much more information on the laser systems can be found in Chun-Chia's thesis [216], which should be considered companion reading to this document. With the exception of the 1 µm wavelength dipole trap laser, we designed all our lasers. The parts were manufactured by our workshop and they were made to work mostly by Chun-Chia (with some cursing)[40]. This section will briefly summarize some of the systems developed.

Slave lasers The slave lasers were the first lasers we made and were very simple, basically a copper block with a diode collimator (Thorlabs LT230P-B) which was peltier cooled on a base with provisions for a cylindrical telescope. In principle they can be operated below dew point as there is a nitrogen purge port. The final version is shown in figure 3.44. I have seen others make a press fit hole for the laser diodes in a similar copper block to improve centring and I periodically wonder about moving the cooling to the side to remove the potential for movement across the peltier but these lasers have not given cause to change anything. Another change over the years is in how adventurous we have been willing to be with our diode laser suppliers. Initially we used to stick to Nichia, Roithner and Eagleyard (Toptica) while now we source many of our lasers from eBay, Amazon, Aliexpress and CNI laser with a little less

[40] We learned a lot. At this point I think we have a library of electronics and laser designs which give reasonable performances (we are still missing a good PID). Occasionally we still get comments like "it is silly to make your own lasers and electronics when you can just buy these from Toptica". We applaud this sentiment but we need a little help with the implementation. We accept bank transfers, paypal and cash. For the SrCAL machine a number somewhere in the mid six figures would be a good start but a number in the low seven figures would probably be a safer bet. We appreciate your support.

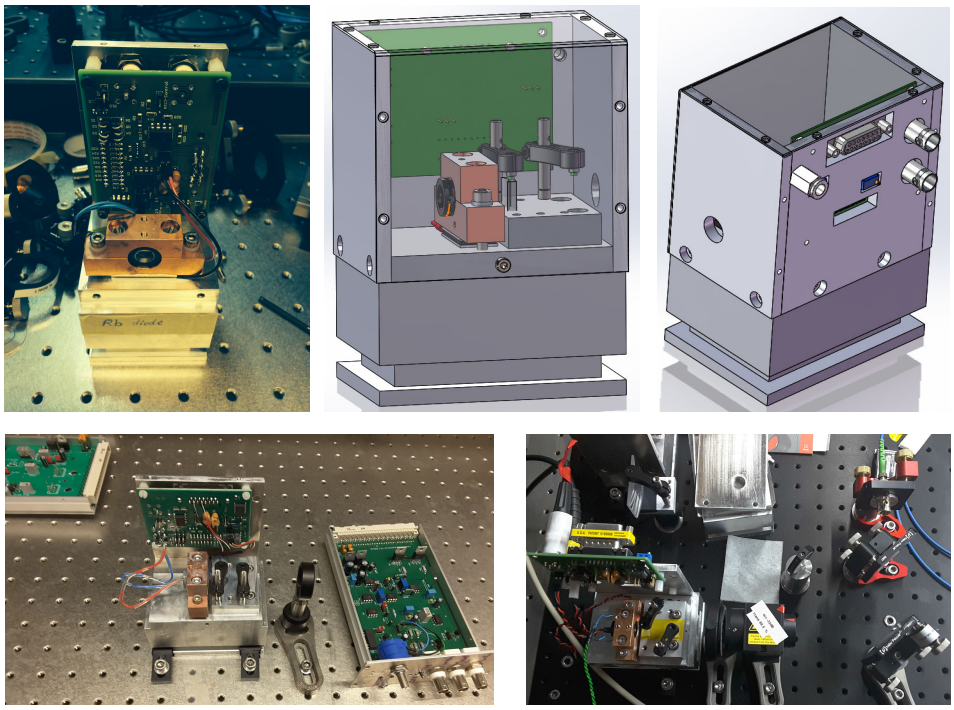

FIGURE 3.44: **Slave lasers.** (top left) The first edition of our slave laser module. Usually a 15×15 mm peltier is used rather than the 15×30 mm unit in the picture. (top right) The third edition of the slave laser is our current standard. (bottom) Examples of assembled (but not injected) slave lasers.

wavelength reliability but at a dramatically lower cost. Some of the standard diodes and lenses we use are listed in table 3.14.

Littrow external cavity diode lasers Our Littrow ECDL laser designs grew from some lasers I put together back at ANU [300]. The objective there was to make a cavity which was very stable against vibrations and thus with a very low linewidth but with little regard for the tuning range. Tim van Leent [301], our first SrCAL master student took a variation on these designs and came up with a variety of flexure based grating mount designs. He put together 461 nm and 689 nm ECDLs. Before he had tested them we needed to make ECDLs for the 688 nm transparency laser and the 679 nm and 707 nm repump lasers so we simply copied these first designs. A collection of images showing the evolution of our ECDL design is shown in figure 3.45. The repump lasers were put together by our second master student Zhoumuyan Geng [302] with help from Chun-Chia. All these lasers suffered from a rather small mode hop free tuning range which made them hard to lock and the massive bulk which was intended to keep the laser thermally stable made them hard to temperature tune. Eventually I

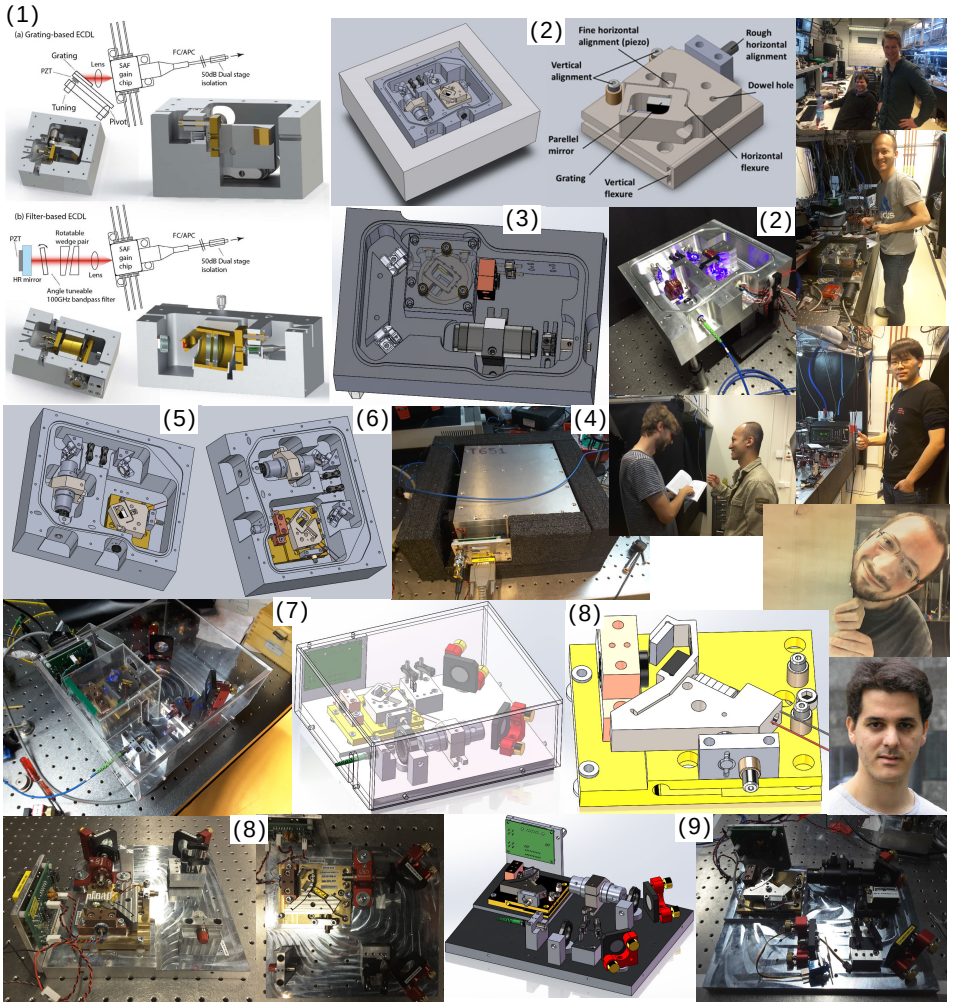

FIGURE 3.45: **Evolution of the external cavity diode lasers (ECDLs) produced to run the SrCAL machine.** (1) First designs - filter and Littrow ECDL designs from [300]. (2) First edition 461 nm master laser. (3) An alternate flexure design we considered as a first laser but never built. Before the first edition had been tested, we needed to make ECDLs for transparency and repump lasers so the first edition was just duplicated. For this reason the initial design lingered longer than it should have. (4) 688 nm transparency. (5) 707 nm with improved tuning adjustment. (6) 679 nm repump with diode separated from the housing and housing sealed to get below dew point. (7) 461 nm upgraded master without the large housing, on a simple baseplate improving accessibility and manufacturability (8) 448 nm repump with shorter cavity length and ideal pivot point. (9) 487 nm transparency with longer isolator and including an onboard AOM.

TABLE 3.14: **Slave laser optics.** Laser diodes and lenses used for slave lasers. Parts are supplied by Thorlabs unless otherwise specified. The telescope is used to expand the beam in the horizontal axis in order to symmetrize it.

Parameter	Blue	Red	High Power Red
Wavelength	461 nm	689 nm	689 nm
Diode supplier	Nichia	Thorlabs	Thorlabs
Part number	NDB4216	HL6738MG	HL6750MG
Rated power	100 mW	30 mW	50 mW
Collimator focal length	3.1 mm	3.1 mm	3.1 mm
Collimator part	C330TMD-A	C330TMD-B	C330TMD-B
1st telescope lens focal length	−15 mm	−25 mm	−15 mm
1st telescope lens part	LK1753L1-A	LK1426L1-B	LK1753L1-B
2nd telescope lens focal length	40 mm	40 mm	40 mm
2nd telescope lens part	LJ1402L1-A	LJ1402L1-B	LJ1402L1-B
Fiber collimator focal length	11 mm	7.5 mm	7.5 mm
Fiber collimator part	S&K 60FC-4-A11-01	S&K 60FC-4-A7.5-02	S&K 60FC-4-A7.5-02
Fiber part	P3-405BPM-FC-5	P3-630PM-FC-5	P3-630PM-FC-5

designed a new ECDL with the pivot in the ideal location [303, 304], a short cavity to reduce the susceptibility for running multimode and a small thermal mass so it is easy to tune. This design was used on the 448 nm repump laser and is partially used on the latest 461 nm master. The mode hop free tuning range is at least several GHz even without any feedforward, it is easy to lock to cavities and it will stay locked to a 461 nm spectroscopy cell for days at a time. We are now producing additional ECDLs with this design at 461 nm, 487 nm, 688 nm, 679 nm and 707 nm for the SrCAL and iqClock machines.

Littrow ECDLs are great for systems that need large tuning ranges but they will never have the robustness of cat-eye or filter based designs [305–309]. We have heard many reports of the cat eye designs being used successfully in other labs and I am keen to put one together. The problem I always had was finding a suitable source for the in cavity filters. The filters used in [300] were custom made and exorbitantly expensive. More recently we have seen inexpensive filters from Laser Components and Andover suggested as potential options. I used to look for extremely sharp narrow filters but these filters tended to be lossy or not so narrow and difficult to find. There is however a body of work from Rob Scholten's lab [309] where instead of looking for narrow filters they looked for broad filters with a sharp edge, an approach which has been highly successful (`http://www.moglabs.com/cateye-diode-laser.html`). Thus, I am looking forward to trying a laser or two with a cat-eye design to see how the

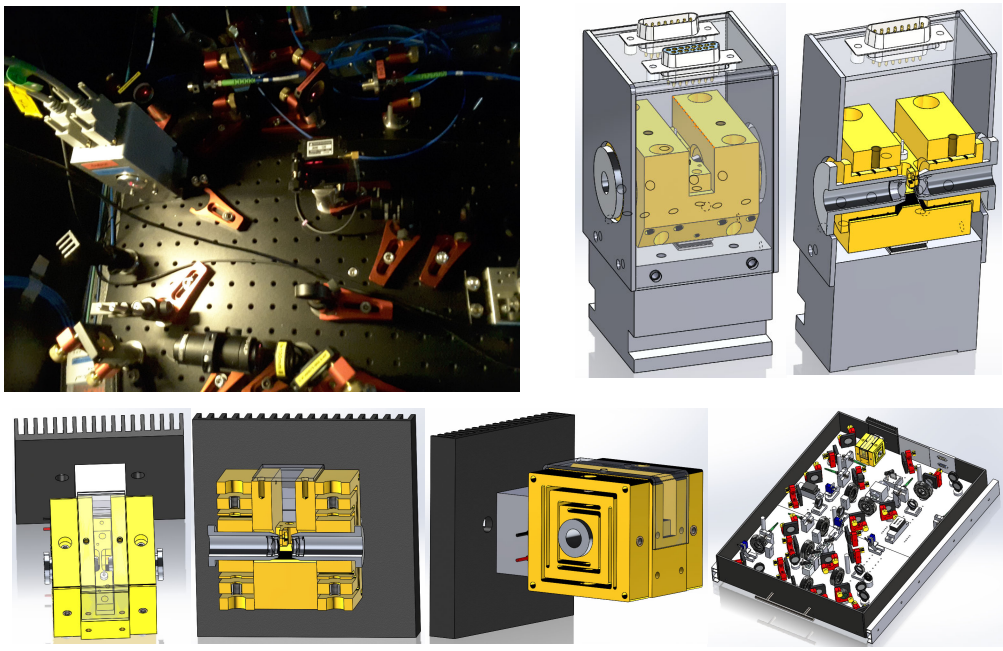

FIGURE 3.46: **Tapered Amplifiers.** (top) Our first edition of the tapered amplifier design. This unit is still in use amplifying the transparency beam. The optical adjustment consists of SM05 thread to adjust the focus of the aspheric lenses and a three point set screw to translate the lenses. At my request Jan from workshop made the threads a very close match and the first time I assembled it without grease the thread seized - embarrassing. Always use apiezon L or similar grease on these high tolerance threads. The two parts that the threads are made in are brass and aluminium to try to reduce the potential for the threads seizing. Another problem we had was that the setscrews for lens translation dug into the brass distorting it when tightened. Again this caused seizing. (bottom) The second edition was designed and manufactured using flexures instead of setscrews for lens translation. This version has not been tested yet as we made do with the working system.

performance compares.

Tapered amplifiers For rubidium, the tapered amplifier (TA) at 780 nm is the obvious way to generate hundreds of milliwatts of power for applications like 2D MOTs. The quality of TA chips for strontium is far less exciting. At 689 nm the power is limited to 500 mW and the chips can be unreliable in our experience. We heard they were also withdrawn from sale by Toptica for a time due to the reliability problems. In the blue at 461 nm TA chips don't even exist. Nevertheless, 500 mW is much more than the 50 mW diode lasers deliver even conceding the poor mode quality expected from TAs.

We made a TA using a EYP-TPA-0690-00500-2003-CMT02-0000 chip from Eagleyard (Toptica) to get more power for the 688 nm transparency beams. Initially we had

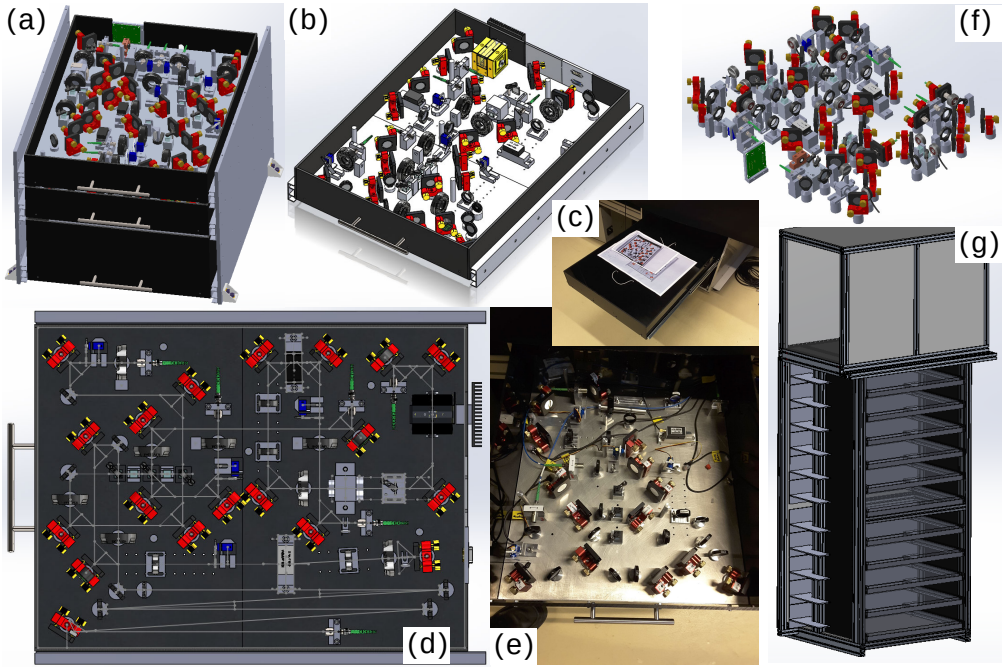

FIGURE 3.47: **Drawer breadboards.** (a-e) Our first edition optical drawers. To create more space we started placing optics in drawers. As long as the optics board is not rigidly coupled to the drawer this proved very stable (we mount on 0.5" cubes of sorbathane). The base plates here are 25 mm thick aluminium. We did not mill the surface flat, just drilled holes for mounting optics. One issue with the first version is that the fibres trailed out the back so they can be broken if care is not taken. The drawer rails also did not roll smoothly which was annoying. (f-g) The iqClock design can stack 11 breadboards worth of optics. An early design example is included from the iqClock laser systems. If the design is correct it is very easy but if there is a design mistake it is a nightmare to drill or tap new holes in the board accurately and without removing all the optics.

around 200 mW at 800 mA drive after our isolator using a 15 mW seed (which is not really enough). This was in broad agreement with the specification curve accounting for isolator losses and the less than ideal seed power. We were able to fiber couple 120 mW after an AOM for 800 mA, but we never really pushed the power for fear of degrading the TA chip and didn't spend much time to optimize the system. We always turned the current from 800 mA to 250 mA when not operating the machine to extend the lifetime but the TA was always left on because we found it needed regular realignment if it was turned fully off and on. We recently upgraded the seed to 30 mW and with that we now match the manufacturer's performance curves (even after 3 years of operation). This indicates that reliability, at least if you operate them very gently is not a problem. Images and details of the system can be found in figure 3.46.

Drawer laser breadboards Long ago we ran out of laser breadboard space on the SrCAL machine. We have commandeered a third of a neighbouring table and we are still short. To house the transparency laser filtering and distribution breadboard we tried something different and made the breadboard into a drawer and stuck it under the optical table (actually we made three drawers of optics). The designs and built breadboards are shown in figure 3.47. Initial results were disastrous, every time you opened or closed the drawer the fibres misaligned. This was due to stress on the breadboard plate which formed the drawer base. Instead we tried sitting the breadboard plate on four 0.5" cubes of sorbathane (Thorlabs SB12B) rubber. The breadboard was then found to be extremely stable even under large temperature fluctuations (the space under the optical tables is not temperature stabilized). In fact we found the 2 m long path length ASE filter, which on the main optical table was quite unstable, became stable. There was however one major design problem with this first drawer breadboard. The number of degrees of freedom provided was the theoretical minimum so there was an order in which the beams had to be aligned which made it difficult to tweak up and maintain. There should have been enough adjustment provided that every beam could be individually aligned. The entire iqClock laser system (figure 3.47), which is now under construction is based on racks each with 11, 581×690 mm breadboards (the biggest plates we can process on our CNC mill in a single pass[41].). The outputs are all fibre coupled for transfer to the iqClock machines. Each breadboard sits within a drawer frame on a 0.5" cube of sorbathane and the optics screw into pre-designed hole positions. One of the keys to making this work is having a somewhat predictable beam propagation to ensure waists are of the correct size and located in the centres of their respective AOMs within a reasonable tolerance. We have found that practically speaking slaves have astigmatic beams which complicates their propagation. Over long distances and through many elements the beams become impossible to predict so we first mode-clean our outputs with short PM fibres giving us a nice symmetric and predictable round beam. Another option may be to replace the cylindrical telescope in the slaves with an anamorphic prism pair so that poor focussing is eliminated but the initial waist sizes will never be perfectly matched.

Cavities and spectroscopy cells Our repump lasers are PDH locked to high (≈ 5000) finesse Fabry Pérot cavities using Zerodur spacers in vacuum. On the other hand, our 461 nm master laser is locked to a saturated absorption feature on a high temperature spectroscopy cell. Details of the construction and locking of these cells and cavities

[41] The maximum usable area is 500×600 mm.

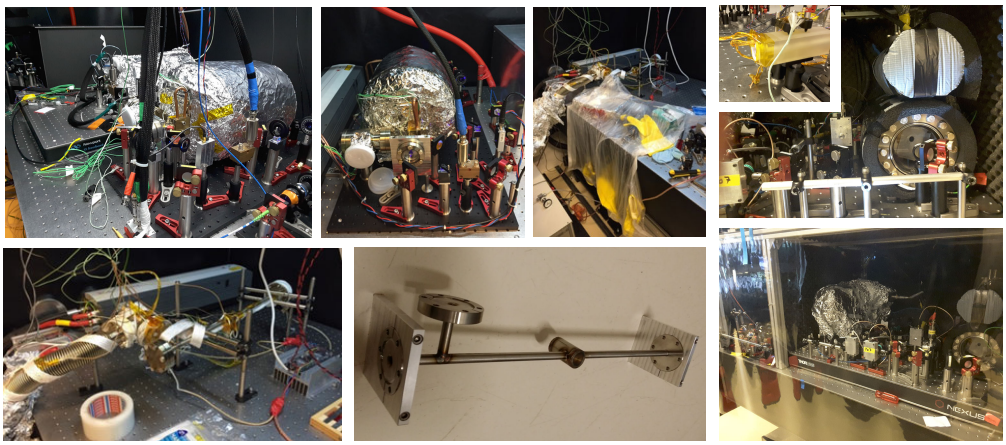

FIGURE 3.48: **Cavities and Cells.** (left) 400 °C strontium vapour cell with water cooled ends constructed to lock the blue maser laser. The design for the cell for the red laser is similar but operates at 600 °C for higher vapour pressure. Note the copper cooling pipe used to keep the ends cool, and the makeshift glove box used to load the strontium. For more details see Tim's thesis [301]. (right) In vacuum high (5000) finesse Fabry Pérot cavities used to lock the repump lasers. The top picture shows the zerodur spacer with the Torr seal glued mirrors and piezo and kapton insulated wires. See Jens' thesis for more details [244].

can be found in the theses from our master students. Tim van Leent talks about the construction and locking of a spectroscopy cell [301] while Jens Samland [244] will describe putting a cavity together and PDH locking his 448 nm master to it. A few photos are in figure 3.48. We still would like to put together a locking cell for the repump lasers based on a hollow cathode lamp [310] or a home made cell with an electronic discharge similar to the work in Kai Bongs' group [297].

Fabry Pérots and other items A lot of other optics mounts and devices were made over the years, ranging from electro optic modulators to Fabry Pérot cavities to general mounts for polarizing cubes and optical fiber collimators. I have pasted together a collection of examples in figure 3.49.

3.7.2 Electronics and control

Most of the electronics for the machine was built by Chun-Chia and I, based on designs developed at the University of Austin Texas and later refined at Innsbruck. In some cases we started from populated boards and in other cases it was from bare PCBs, and on a couple of occasions it began in Altium. A few pictures from the construction are in figure 3.50. I will not describe most of the details here but simply pass through a few of the design choices which are not already covered elsewhere. There is in fact a wealth of information contained

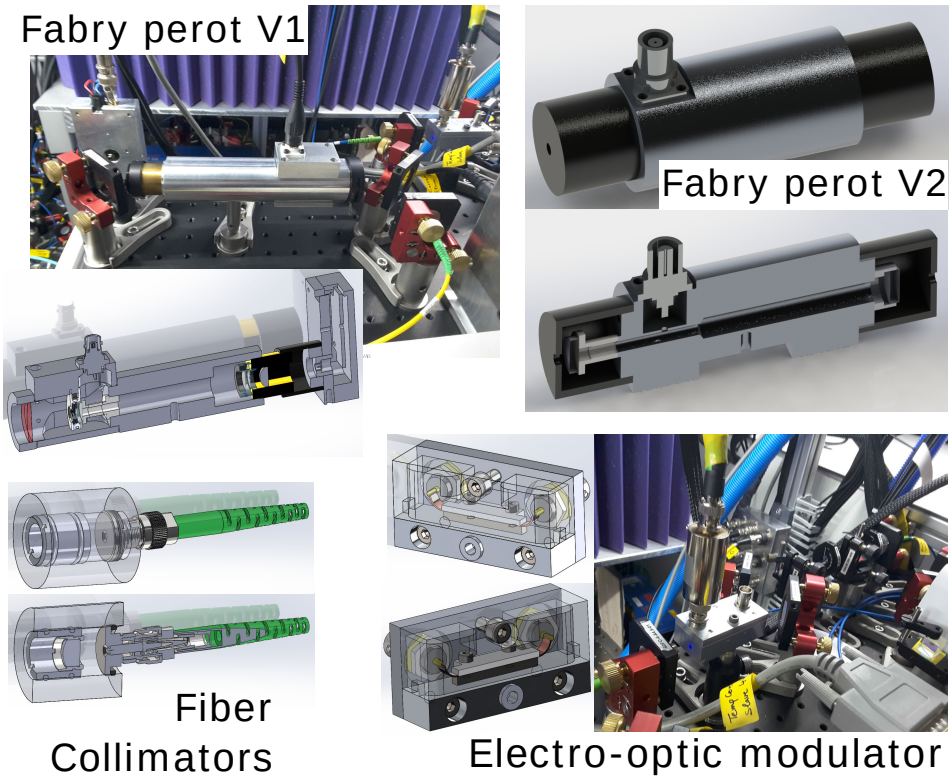

FIGURE 3.49: **A selection of other optics devices that we built for the SrCAL machine.**

within the original control system manuals written by Todd Meyrath and Florian from their time in Texas (see www.strontiumbec.com), which I would highly recommend for introducing the control system electronics.

Power line separation While I'm not sure if it really helps, we try to use separate building circuits for dirty equipment like fans and switched mode power supplies, in order to keep noise away from anything which might directly talk to the atoms. These are the red "dirty" lines found on the machine.

Power supplies With very few exceptions we used a rack of linear power supplies to run all our electronics. It might seem strange to be using big, expensive, inefficient linear power supplies when the switched mode equivalent could drive everything for a tiny fraction of the cost and space with excellent efficiency. This choice dates from Innsbruck, where switched mode power supplies were found to produce hard to trace noise in the 100 kHz range which permeated everything and caused headaches for precision experiments. The story goes that eventually the decision was made

FIGURE 3.50: **Electronics produced to run the SrCAL machine.**

to only use linear power supplies and get rid of anything switched mode from the experiments to finally be rid of this plague of noise. This decision stuck and the machine we have built was powered by linear power supplies. We have not been particularly strict on this rule and you will find switched mode power packs driving Andor cameras even close to the chamber but as all the core systems are linear it would not be hard to go through and remove switched mode supplies from the machine if we thought it was a problem.

Power supply location Power supplies are generally located in a rack 30 m from the machine and cabled in. This was done both to eliminate electrical/magnetic noise from the machine and perhaps more importantly to remove the heat load from the lab. Care must be taken when placing a linear power supply close to the machine. The transformers give a large oscillating 100 Hz magnetic field which can easily influence the atoms.

Cabling Details of the cabling can be found in table C.2. The cable shield should be grounded at one end and only one end but this generally wasn't done. A problem we had and continue to have is that the voltage drop on the 30 m long 5 V 12 A lines is large. If we set the power supply voltage and load the rack we end up with too small a voltage and if we turn up the supply voltage and reduce the load we end up over voltage. This could have been solved by remoting the sensing wires for the power

supply to the rack, but running 30 m of shielded sensing wires is a big job, so mostly we manually adjust the voltage as we load or unload the rack. A little feature you might want to note if a power outage means you need to unload and reload the racks.

Racking and grounding All the subracks are electrically isolated from the grounded framework upon which they are mounted. The racks on the SrCAL machine were wired by crimping connectors on the flatband cable and bolting them to the racks which was time consuming and sometimes unreliable. We purchased special 26AWG instead of the standard 28AWG flatband cable to try to reduce the voltage drops we get on the 135 MHz DDS racks (where each DDS consumes up to 0.5 A at 5 V). For the new iqClock racks we made a pcb backplane at jlcpcb.com which proved much easier and essentially eliminated the voltage drops due to the flatband cable.

New DDSs, new resources and new control system options The control system as is has proven ideal for our needs but there are a few new developments on the horizon which give cause to look around and want to extend it. We use the AD9852 and AD9858 DDS chips from analog devices in our 135 MHz and 500 MHz DDSs respectively. The AD9852 allows us to modulate our frequencies with a triangular frequency ramp which is essential for modulating our broadband red lasers but it is difficult to do complex sawtooth modulations of the kind required for performing SWAP cooling [311] in a pulse sequence. We use SWAP on ^{87}Sr but ramping the modulation parameters is not implemented, as multiple bus commands are needed to stop, adjust and restart the modulation for each point on a frequency ramp. For a steady-state machine like SrCAL this is not a problem but it is a capability we would like and it motivates our interest in other newer DDS chips. We also have looked at options for replacing the sometimes problematic flatband bus system with an ethernet system, plus a buffer and clock similar to the ARTIQ system (https://m-labs.hk/artiq/). A final little piece of electronics candy we recently discovered was the Open Hardware Repository (https://ohwr.org/welcome) which has a wealth of resources designed to excite.

Clock signals The DDSs all require a 1.2 GHz or 300 MHz clock input signal depending on the model. This is generated by a clock generator board from a 10 MHz signal derived from a rubidium clock in room D0.135. The clock generator board has a synthesiser chip which has provisions for locking to two external inputs. These are the external clock input which we use and a temperature compensated crystal oscillator. The crystal oscillator is not on our clock generator board. As a result, the frequency output will not be stabilized if the rubidium clock signal is disrupted. If the synthesiser frequency drifts by a large amount (which it can when no rubidium clock signal is provided), it is possible for the frequencies of the DDS outputs to drift by the same

proportion. If they drift too far, the AOMs will reflect the RF power back to the amplifiers potentially damaging the AOMs or the amplifiers or both. Since the clock controls around 50 amplifiers and AOMs the simultaneous destruction of all these amplifiers and AOMs could be very unfortunate. For this reason the rubidium clock is on a UPS and the first thing you should do when restarting the machine after a power outage is turn off all the amplifiers and check that the frequencies are correct. The clock signal must be applied before powering the clock generator board for the clock generator to lock. Adding the crystal oscillator to the clock generator boards is on my to do list.

Packaging We packaged a lot of boards into Fischer Elektronik rack insert modules. When we started this it was not something which had been done at scale here before. We waterjet (or laser) cut all our front and back panels into 2 mm thick aluminium sheet. When waterjet cutting is done with a slow speed the results are excellent (snijdenmetwater.nl), but we had mixed results with some of the waterjet cut batches. When cut too fast many holes ended up missing or not fully cut through. The laser cut pieces (247tailorsteel.com) tended to have sharp edges which needed post-processing work to debur. Overall the waterjet (and laser) cut option was however a very inexpensive and quick way to make a shelf full of panels for assembly. Labelling the front panels is something which was never done for the SrCAL electronics units and something which continues to bug me. All the labels were drawn up and we looked at trying to engrave them into anodised aluminium front panels but the cost was too high. Another option, the option we are currently pursuing for the iqClock electronics is to print colour labels onto waterproof plastic labelling material (Weerbestendige folie etiketten 4698, Staples 329064). The templates constructed in illustrator contain a separate layer with the cutout shape of the panel so the printed labels can then be cut out on our laser cutter. We will see how this goes shortly.

3.7.3 Data acquisition and analysis

Most of our data acquisition is based on using Vision (see www.strontiumbec.com) to capture frames from either an Andor Luca camera or a Point Grey Blackfly (BFLY-PGE-23S6M-C) (a vastly lower cost but more noisy alternative). This data is logged to the control computer hard drive and continuously synced to a NAS Synology DS214+, where it can be accessed by all computers on the SrCAL network for analysis. A series of script based matlab utilities was written to automate the analysis and plotting of this data so that the operator has near real time feedback to guide the machine operation.

A second set of Matlab/C++ programs is used to run the pointgrey cameras continuously and display video, subtract backgrounds and perform basic analysis with the results streamed to the screen in real time. This is used for aligning and optimizing the machine such as aligning the MOT or adjusting the repump locking cavity length to sit on resonance.

3.7.4 Monitoring, alarms and interlocks

Monitoring the bakeouts, the coil temperatures, water flows, vacuum pressures, the oven and the heated Zeeman slower back window are essential to maintaining the machine and reacting to avert catastrophes. A system was developed primarily to monitor the bakeouts which continues to be used today to monitor for problems and over time various other features have been added to supplement it.

Bakeout monitoring To monitor the temperatures of the machine and control the solid state relays for the heating bands during the bakeout we made six home made boards based on an ATMega chip using designs from previous machine bakes at Innsbruck. Each controller had 12 sensor channels and 12 pulse width modulated output channels (5 Hz) for driving relays. Different output channels had one of four pulse width modulation phases to try to even up the power load and reduce noise on the power lines. Originally a PID was written into the controller firmware to maintain a target temperature but when sensors fall off or fail as they often did this can result in unfortunate consequences. We rewrote much of the firmware to perform duty cycle ramps rather than a PID. The chip is controlled by a serial connection to a C++ based temperature controller-monitoring program run on a low power "Shuttle" computer (Type XS35V5Pro). The monitoring data is continuously updated and synced to a dropbox account so that it can be accessed and plotted at any time from the cloud. A program was written in matlab (and compiled so it was stand alone) to access and plot this data for visualizing the status and history in real time. The programs for monitoring and visualization are now used on all our machines for monitoring and visualizing temperature, vacuum and water flow data. The controller boards, the computer and the network switches are backed by a UPS so that in the event of a power failure the system will be able to continue to monitor the machine status and continuously report on it while crying for help. If a problem is detected alarms are activated and after two minutes the monitoring program will begin sending emails and SMSs every two minutes with updated information on the status of the problem. A web based service, uptimerobot.com continuously polls the network gateway for network failure and will also send email alerts in event of a disruption. We have not had a building wide power failure with the ovens on but we have had plenty of

occasions when the power has failed in the lab or on specific circuits so there has been some opportunity for system testing.

Oven and heated window monitoring At the end of the bakout the monitoring system was repurposed to monitor the oven, the Zeeman slower heated window, coil temperatures and ion pump currents with system left otherwise unchanged.

Water flow monitoring To keep track of cooling water flow in order to monitor for bursts[42], blockages and surprises, we attached a flow meter (Amazon 0.1-3L/min 1.2Mpa 7mm Water Flow Hall Sensor Meter for Coffer Maker from uxcell) to the return line on every water cooling circuit[43]. The flowmeters were polled by an ATMega arduino which is monitored, datalogged and alarmed by a C++ computer program, the same one used for monitoring the bakout and oven. This was all adapted from the temperature monitoring system by Benjamin. The flows are continuously visualised by the same matlab program I wrote for monitoring the ovens[44].

Coil temperature interlocks For the Zeeman slower coil a 60 °C bimetalic thermal switch (RS Components 176-9126) is mounted on the coil surface. The power supply driving ZS1 coil is interlocked through this switch to prevent any unfortunate meltdowns. A similar system is included for the other coils except that the 45 °C (RS Components 176-9081) switches are used instead as these coils do not get as hot in normal operation.

Camera systems A network of IP cameras watch the coil power supplies, the oven and back window power supplies, cavity transmissions on the locking cavities, spectroscopy locks, the Fabry Pérots and beat lock oscilloscopes, ion pump controllers and fluorescence from various parts of the machine. These are monitored from two PCs each with two 27" monitors running iSpy, an open source surveillance software package. This enables rapid debugging from the control terminal. By viewing these screens using a Galaxy S2 tablet running teamviewer we were able to monitor any signal from any part of the machine. This was used extensively for alignment, locking and optimization even aligning optical fibers by watching the power meter screen, I think we would struggle to cope without it. Most of the cameras used are D-link

[42] There is a reason they call the big condensed matter hall with glass walls "the aquarium".

[43] We used silicon gasket material as a 'glue' and secured the system with hose clamps but the success rate for leak proof connections was not great.

[44] Before we installed our flow monitoring system, a non return valve on the red spectroscopy cell in the RbSr lab blocked one friday night. They had deactivated their monitoring and alarm system so no-one knew the water had stopped flowing. The plastic tubing melted and emptied the water tank onto the optical table and shut down the water pump. The rubidium oven cold finger on the RbSr oven then overheated and large quantities of rubidium migrated from the oven to their ion pumps effectively shorting them. That was a good morning Monday. We all spent the next month rebuilding the red spectroscopy cell with better cooling and using copper piping and baking and high potting the ion pumps to try to bring them back to life. It was months before the RbSr ion pumps were back to normal. Don't turn the alarms off!

930L IP cameras as they were cheap at the time we built the machine. We have now found Unitoptek cameras from Aliexpress for as little as 13€ with much better performance and we are using these for the iqClock machine. A large array of IP cameras is bandwidth hungry so we operate our own private network behind a router to prevent IT from going nuts. It also avoids the need to negotiate with IT services every time we want to add or change a camera, which we sometimes do on a daily basis.

Beam position monitoring The performance of the D-link 930L IP cameras was not good enough to see the fluorescence from MOTs, particularly red MOTs so we used bullet cameras (RS components 493-5590) of the same type as those used on the RbSr machine. We also used these cameras for monitoring the positions of alignment critical beams such as dipole trap and transparency beams. These cameras produce an analog PAL output signal with can be monitored with old fashioned CRT screens or using quad camera video multiplexers. The video multiplexers we used died regularly and they are getting hard to find for the old fashioned non HD cameras. The price of these cameras is quite extreme at over 120€ each. Fortunately the Unitoptek IP cameras have similar sensitivity specifications as the bullet cameras and they have other more expensive models for starlight applications which are two orders more sensitive, so we will likely gradually transition all our monitoring to these IP cameras, certainly for new additions.

3.7.5 Plumbing

As much as I try to avoid plumbing and leave it until the very end, I have never managed to escape it. We use a heat exchanger based closed circuit cooling system (Van Der Heijden KÜHLMOBIL 512-WA-WA–B400-VP) running deionized water to cool all our coils as well as other devices. This system provides $1.6\,\mathrm{kl}\cdot\mathrm{h}^{-1}$ of cooling water at $\approx$6.4 bar and 23 °C with a stability of $\pm 0.1\,^{\circ}\mathrm{C}$ but it doesn't take much water loss to get a low water level pump shutdown. Other devices such as spectroscopy cells are sometimes cooled with house water. All cooling circuit components are made from copper, brass or stainless steel to avoid corrosion[45]. My policy is that there should never be any plastic pipework above the optical table as plastic is comparatively fragile, especially at the connection points. All cooling pipes above the optical table are copper with brass or stainless Swagelok connections. Possibly unnecessarily we also insulated all pipework above the table with plastic spiral wrap (natural for cold water, black for return) to reduce any potential issues with condensation. On copper pipes which flow current as well as water like the ZS3 and

[45] In the RbSr machine they had some aluminium, which corroded badly and led to blockages.

FIGURE 3.51: **Water manifolds and plumbing.**

compensation coils this spiral wrap insulation is essential and runs up to the point where Kapton tape insulation takes over. All the coils are cooled by a loop of 4 mm×4 mm square copper pipe. This is connected to our 8 mm outer diameter copper tubing using an 8 mm diameter brass adapter piece. The rectangular pipe had the corners filed off and was silver soldered into the brass adapters before being pressure tested for leaks.

Below the optical table all the pipes join to a LDPE (Teesing 70112100) pipe section which runs to the manifolds. This plastic section is easily changed and provides electrical and acoustic isolation as well as a way to include our low cost flowmeters on the return line. The manifold system for the closed circuit stabilized water is shown in figure 3.51. Pipework and mounting was also installed for a set of house water manifolds for cooling devices which do not require high temperature stability like beam dumps, but these were not installed. Our manifolds (Teesing 63001900) provide 20× 8 mm lines with fine regulation valves (Serto NV41C21-8) and 10 lines with standard 8 mm regulating valves (Serto NV41A21-8). Mini ball valves (Serto 32032420) are used to isolate the return lines. We considered using non-return valves in place of the ball valves but these were found by RbSr to regularly clog.

3.8 Summary

This chapter described the design and construction of a new strontium quantum degenerate gas machine. This machine is unique. It's aim is to produce the first steady-state source of degenerate gas. It was made to be flexible. The path to steady-state BEC is uncharted, it will have rocks, pitfalls and dead ends which we hope this machine will be able to navigate. I have tried to describe the technical detail needed to wield this tool with mastery. We

learned a lot constructing this machine. There is no book that teaches these things, it is not something you will learn in class, or from the literature, the best resources we have are the theses of those who came before us. I have tried to document some of that hard won knowledge to aid future builders in the construction of pulsed and steady-state degenerate gas machines alike. We now come to the part where we get to use this new capability to tackle new physics and try to make the impossible possible.

Chapter 4

V1.0: A protected BEC within a MOT

Our first plan for making a steady-state BEC was to develop a low temperature steady-state red MOT and then couple this to continuously replenish atoms in a dipole trap reservoir containing a dimple trap with a protected BEC (see section 1.5). Protection for the BEC from the 689 nm MOT light would be provided by an AC stark shift in the form of a "transparency" beam [192] while protection from the blue laser cooling photons would be achieved by our twin chamber machine design. The architecture is sketched in figure 4.1.

There are several steps needed to implement this plan:

Steady-state red MOT: We need to make a steady-state MOT using only the weak 7.4 kHz 689 nm transition. This MOT needs to be able to efficiently capture the flux from the upper chamber. This would represent the first steady-state MOT constructed using only such a weak transition. It also needs to be displaced by at least 3 cm so that there is no line of sight to the top blue chamber. A MOT temperature of $\approx$1 µK will be required since it will be directly coupled to the dipole trap reservoir that feeds our steady-state BEC, otherwise the hot atoms will melt the BEC.

Dipole traps: A series of dipole traps is needed. Firstly a reservoir dipole trap with a large surface area will collect cold atoms from the MOT and draw them in towards the BEC. An optional horizontal reservoir cross trap can be used to speed this capture process by increasing the effective trapping frequency in the long axis of the reservoir trap. Finally, a dimple dipole trap with high trapping frequencies will thermalize and concentrate the coldest of the atoms and provide the density boost needed to reach condensation.

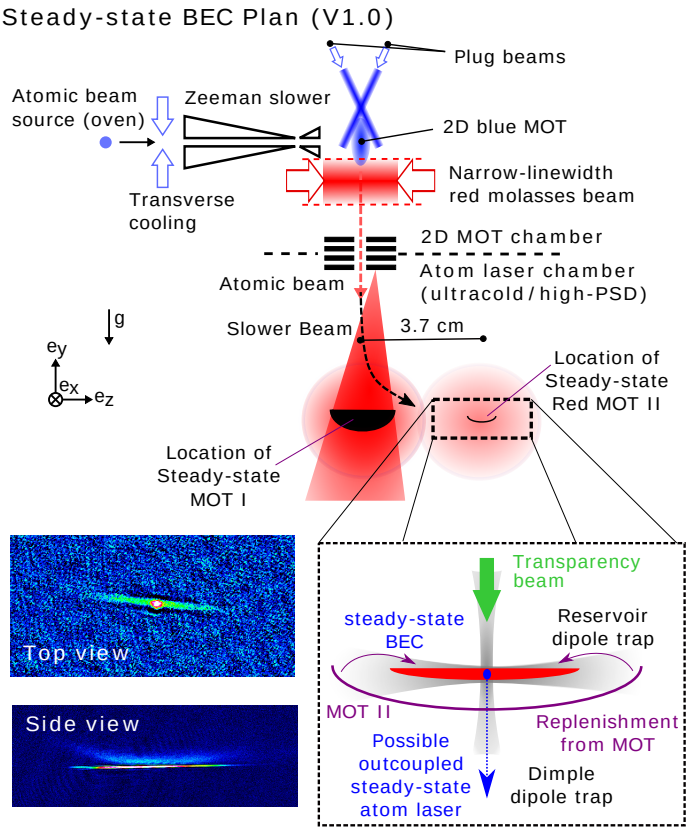

FIGURE 4.1: **Plan to make a steady-state BEC (V1.0).** Here we show our first plan to attempt to make a steady-state BEC.

Protection from MOT light: A transparency protection beam collinear with the dimple trap beam will AC Stark shift the dimple dipole trap region. This will protect the BEC contained within the dimple by preventing interacting with resonant red MOT light.

Protection validation: The protection levels achieved against both blue light from the top chamber and red MOT light need to be measured by making a pulsed BEC in the dimple trap and measuring its lifetime.

Optimization: We will begin by validating pulsed solutions both in terms of an evaporation ramp needed to go from steady-state conditions to having a BEC and in terms of repeating the pulsed work in [192]. By minimizing the gap between steady-state and what is needed to get a BEC the system should optimize to achieve steady-state degeneracy. A pulsed BEC may also be useful to provide an initial density boost increasing thermalization rates in the dimple.

Outcoupling an atom laser and beyond: Once a steady-state BEC is achieved we can try bragg outcoupling or another architecture to output an atom laser. The thought was that if we can get to degeneracy we may want (or need) to rework the machine or the architecture to get something more suitable for a steady-state atom laser attempt. We also imagined that we might want to move to or at least try evaporation from a guide, which might be quite a different architecture.

The results from the pulsed system in [192] provide a beacon to guide our way. It tells us the conditions (densities and temperatures) required for condensation in a very similar system. Our aim is to reach similar conditions in a steady-state system to what can be attained pulsed. This chapter will describe our first attempt and the results we achieved.

4.1 The first steady-state red MOT

The first big challenge for the new machine was to create a steady-state MOT in the atom laser chamber using only the 7.4 kHz, 689 nm transition. This is made challenging by the extremely weak radiation pressures that can be exerted by this transition, which makes catching atoms efficiently interesting.

A detailed account of our final solution and its performance is provided in chapter 5. I would *strongly* recommend reading that chapter before continuing. Rather than repeating the material we wrote in the paper here I will instead focus on discussing the problems we had and the solutions we came up with to make this system work for the first time, things which are not discussed when describing a final working system. This section will essentially be a supplement to the supplement in chapter 5.

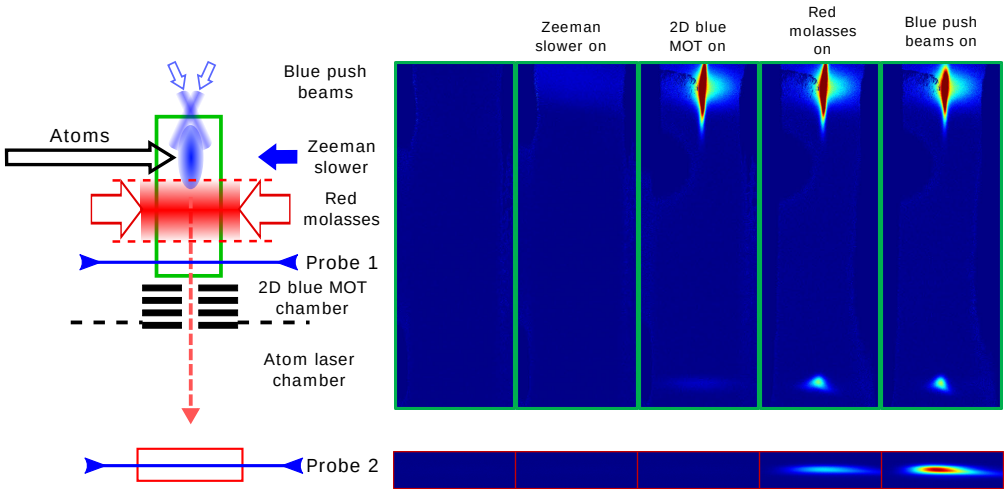

FIGURE 4.2: **Fluorescence Probe.** Recording the fluorescence from a retro-reflected probe beam was our main experimental method for optimizing the system before we had a steady-state MOT.

4.1.1 First edition

A steady-state red MOT had never been made before, nor had any MOT been made solely using such a weak transition so unsurprisingly, it wasn't quite "plug and play". The architecture of our steady-state red MOT is shown in figure 4.1. There were a number of key ingredients and realisations we needed to bridge the gap from our initial setup to arrive with a working steady-state red MOT. Here I will outline some of those.

Red MOT to molasses We never tried the 2D red MOT configuration in the upper chamber. A quick test of the red molasses configuration produced a suitable atomic beam which enabled us to simply move on and bypass all the headaches of the MOT. This may not have been necessary and it may not have improved performance, but it was certainly much simpler and eliminated a major risk from the machine. This was discussed in some detail in section 3.5.

Fluorescence probe We introduced retro-reflected fluorescence probe beams observed from the side by cameras (Point Grey Blackfly BFLY-PGE-23S6M-C) using the 461 nm transition. This enabled us to monitor the atomic beam flux and spread at several points along the path of the atoms. At various times we placed probes immediately below the red molasses, at the bottom of the upper chamber windows and in the center of the atom laser chamber along the Z axis and thus monitored the evolution of the atomic beam throughout the system. This was our main optimization technique until we had a steady-state MOT. Example data is shown in figure 4.2.

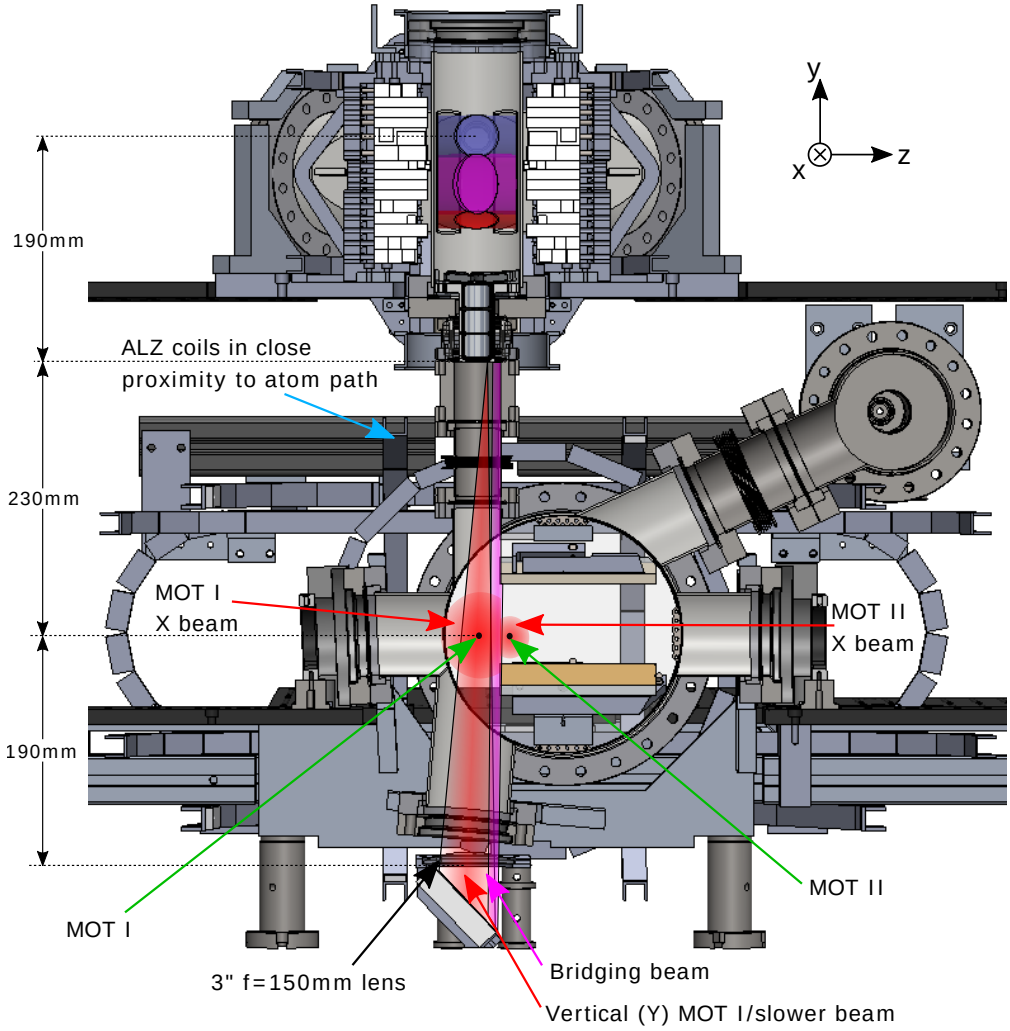

FIGURE 4.3: **Red MOT beams - side view.** The placement of the beams for the red MOT. Note that the MOT I X and MOT II X beams are clipped, tilted and tiled so that there is no gap or low intensity region between these beams.

Converging slower One of our major realizations was that we should use a converging beam for the MOT I vertical slower. This is illustrated in figure 4.3. With a collimated slower beam we either interfere with the atoms propagation in the upper chamber by shining red light through the baffle or we tilt the beam and push the atoms to the side. Both options are undesirable. By focussing the beam at the bottom baffle (viewed by a camera focussed on the baffle) we were able to use the beam curvature to provide a confining force pushing the atoms towards the beam center. We think this is an important aspect of what makes the architecture work.

Bigger and brighter In the course of trying to make the steady-state MOT work we completely rebuilt the red MOT optics twice to include much bigger beams and to remove retro-reflection optics to improve balance. This in turn required building several new red slave lasers to generate higher powers. The power in the vertical MOT beam (see figure 4.3) was increased from a couple of mW to around 12 mW and we found that the power in this beam is critical to getting a reasonable atom number. Increasing the vertical power was one of the key changes needed to make the system work. We now find that we can dramatically reduce the beam size of either the X or Z MOT beams[1] with little impact, but we do need at least one large beam in addition to the vertical slower beam to gather the atoms from the diffuse atomic beam input.

Modelling and simulation We developed a simulation and modelling library in Matlab which enabled us to test laser parameters and magnetic field configurations and visualize what this did to atom trajectories by making movies of how the atoms flowed through the system. While we did not rely on the quantitative numbers, we did use this to form and guide our intuition of how the system behaved. The model was a 3D Monte-Carlo simulation which took into account the 3D intensity profile of beams, polarization, their propagation, apertures in the system and a 3D magnetic field calculated using the Biot-Savart law from the 3D coil geometry. The model averaged forces and did not include the recoil kicks so it was not suitable for estimating temperatures. This code was used to generate the plots in figure 5.5. Some example trajectories can be seen in figure 4.5.

One of the issues that became clear from the modelling is that the location of one of the ALZ coils as shown in figure 4.3 (see also appendix C) is close to the atomic beam path from the blue MOT to the atom laser chamber. This results in inhomogeneities in the magnetic fields which impacts on the slowing performance in this region. It was expected that this problem would diminish in the longer term as the intent was to have our MOT located in the center of the chamber where large Helmholtz currents

[1] Z can be reduced from a 48 mm $1/e^2$ diameter to an 8 mm diameter with a ≈10% atom loss

would not be needed to drag the quadrupole centre to the side of the chamber where red MOT I is located.

Details of all the beams and imaging systems can be found in appendix D.

4.1.2 A steady-state MOT with high phase-space density

We had achieved for the first time a steady-state MOT on the weak 7.4 kHz red transition without any use of blue light in the bottom chamber. However, more was needed. The MOT needed to be much colder with a temperature ≈1 µK, it needed higher phase space density and a displacement of at least 2.7 cm so that a BEC would be protected from scattered blue photons from the 2D MOT chamber. These were the objectives for the second edition of our MOT, MOT II. Again, the details of this work are presented in chapter 5 which should be read before proceeding. The material here will be a supplement to the supplement in chapter 5 rather than reproduce that material. Here, the focus will be on some of the problems we encountered and our solutions.

Moving the location of the MOT to achieve protection from blue photons proved surprisingly easy. Simply displacing the quadrupole center for the MOT was sufficient to get atoms to transfer 3.7 cm and thus achieve the offset required. I say surprisingly because there were large gaps in the MOT beams between the initial location and the displaced location. As well as removing the line of sight to the blue chamber, this also removed MOT II from the strong broadband vertical MOT I beam which would otherwise prevent us from reaching very cold temperatures.

A consequence of focussing the vertical MOT I beam at the baffle was that you end up with a gap between the edge of the slower beam and the edge of the in-chamber mirrors which are used to direct the vertical MOT II beam upwards. Thus, there is a gap in which there is no vertical beam able to support atoms against gravity. We were very concerned about this so another beam was added to try to bridge the gap. The bridging beam is illustrated in figure 4.3. Surprisingly, we found that this bridging beam caused more trouble than help as it would tend to bounce the atoms up as they passed through it. Most of the time optimizations resulted in simply turning this beam off and eventually the power and AOM were used for another application[2].

In addition to displacing MOT II[3] from both the blue, the vertical and the X MOT I beams, there were other techniques needed to get our MOT colder and denser. Essentially, we made the location both spectrally and spatially darker.

[2]The optics for the bridging beam are still under the chamber.
[3]Also known as the high phase-space density (HPSD) MOT or the atom laser (AL) MOT.

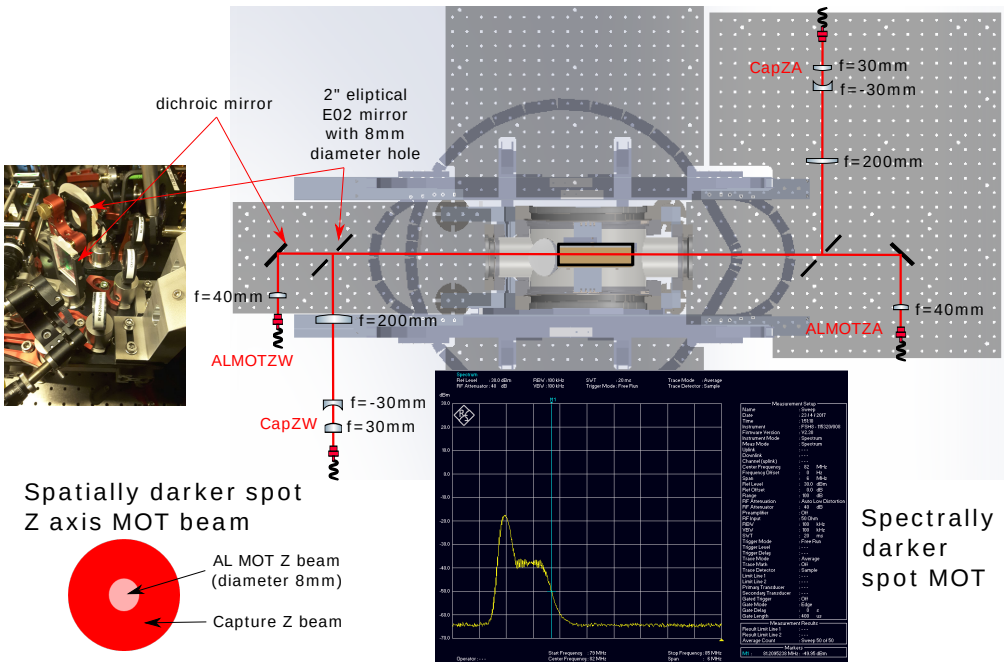

FIGURE 4.4: **'Darker' spot MOT.** The arrangement for creating a spatially darker region on the Z axis to get colder without reducing the gathering ability of the outer annular beam. Note the picture is from the current system which includes a lot of additional components rather than the initial configuration. (bottom right) Example of a signal used to drive an AOM giving a spectrally darker spot MOT.

Although we had displaced the MOT from both the vertical and X MOT I beams it remained in full view of the Z MOT I beam. Our solution was to put 8 mm diameter holes on a 45° angle in the mirrors steering the Z MOT I beam. This allowed us to place a weaker and narrower bandwidth MOT beam on the axis while leaving a high power broadband MOT beam in the outer regions for efficiently capturing atoms. These on axis beams were also reflected off dichroic mirrors to allow future multiplexing with a high power 1.07 µm dipole trap guide beam. In this way we created a 'darker' spot MOT on the Z axis. This is illustrated in figure 4.4.

The second trick we tried was to create a spectrally dark MOT. We did this by combining (with RF splitters) the outputs from initially two and later three[4] DDSs to drive each of the AOMs producing light for MOT II (X,Y and Z). This enabled us to reduce the intensity of the comb lines interacting with the MOT atoms and increase the intensity of the lines at greater detunings where the power essentially acts to capture atoms. This is illustrated in figure 4.4. Because the AOM is highly nonlinear (at least in the wings where there is overlap in spectra) it is difficult to know exactly what optical power we had in each spectral component. The optical power delivered by our AOM with both DDSs operating was much greater than the sum of the powers with any one DDS alone.

It is unclear how much each of these steps helped individually but the overall result was a MOT more than an order of magnitude colder than MOT I. There was however, a cost. The flux captured by MOT II is an order of magnitude smaller than that for MOT I. We can not definitively say what are the causes of this inefficiency, it is something that might be worth investigating further. The simulations did provide some possible insights by showing some trajectories which might be problematic as discussed in figure 4.5.

4.1.3 Summary

We demonstrated for the first time a steady-state MOT operating only on the narrow 7.4 kHz transition, a transition barely able to support atoms against gravity. The result was a MOT with temperatures approaching 1 µK and a phase-space density of $1.3(2) \times 10^{-3}$, 100 times better than any previous steady-state MOT.

The results published for ^{88}Sr are summarized in table 5.1 and in table 4.1 we show an extended edition including the results obtained for ^{84}Sr. It is ^{84}Sr which is what matters when we are trying to make a BEC and it is the ^{84}Sr results which matter for the next phase of our work. The results listed for ^{84}Sr used parameters optimized for ^{88}Sr (so the ^{84}Sr results can be better) and were collected at the same time as the ^{88}Sr results. All the data was collected at the same time. Many of these parameters like bias fields, intensities and

[4] An additional DDS was later added so that we could add an additional frequency to address atoms within the dipole trap on the non-magnetic line.

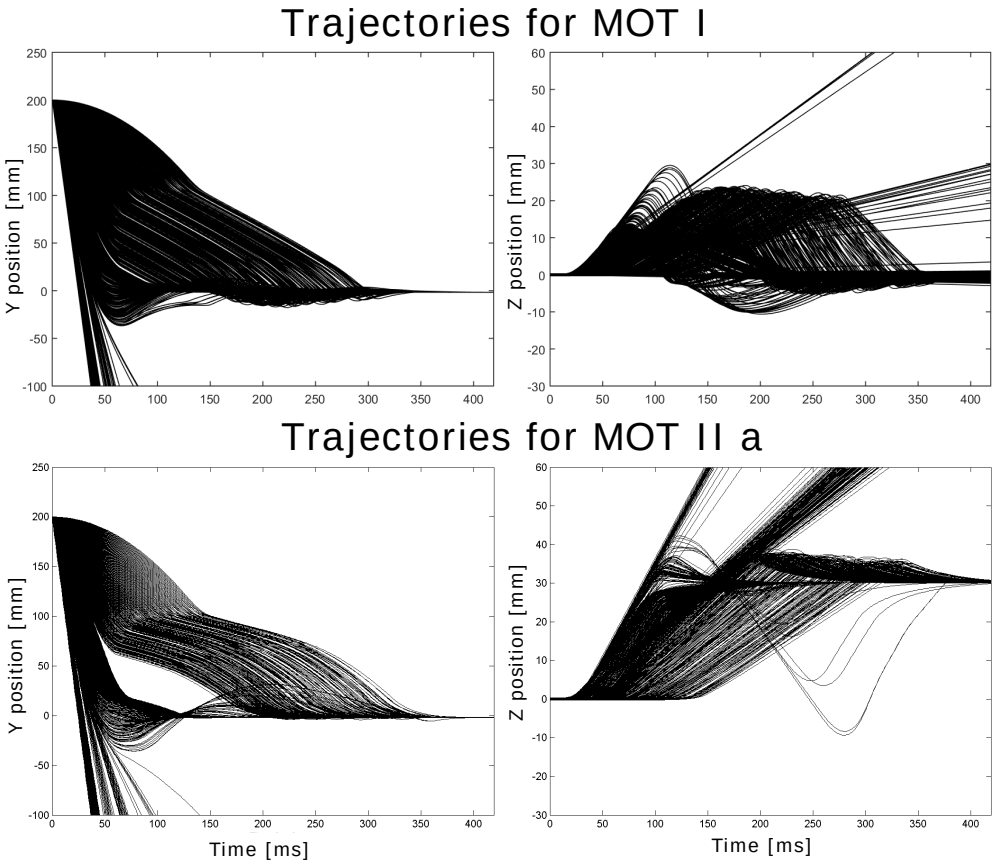

FIGURE 4.5: **Trajectories of atoms for MOT I and MOT II a.** To try to understand some of the loss mechanisms that reduced the flux captured by MOT II by an order of magnitude relative to MOT I models were made to simulate the trajectories of the atoms. Here simulations show losses from atoms falling through the vertical slower beam, bouncing and those gently captured. A concern is that the in-chamber mirrors sit between Y=25-75 mm depending on the X position. It is thought this might be an important loss mechanism for MOT II. These particular trajectories were calculated with no initial displacement or velocity in the X direction to give cleaner more easily interpreted results.

detunings were reoptimized daily so there was never any one particular definitive set of parameters which was optimized and then left for each isotope.

4.2 A strontium BEC

Here we briefly describe our dipole trap configuration and the evaporation sequence we use to make BECs of ^{84}Sr.

TABLE 4.1: Characteristics of the three Red MOT configurations for both ^{84}Sr and ^{88}Sr. All uncertainties are taken as $\pm 2\sigma$ from the fitted data. The parameters were optimized for ^{88}Sr, not ^{84}Sr. In some cases this resulted in a severe performance hit such as for the temperature for the z axis on the ^{84}Sr MOT. The MOT performances are sensitive to the parameters and need to be individually adjusted for each isotope to obtain optimal performance.

	^{88}Sr Red MOT I	^{88}Sr Red MOT II(a)	^{88}Sr Red MOT II(b)	^{84}Sr Red MOT I	^{84}Sr Red MOT II(a)	^{84}Sr Red MOT II(b)
Flux [atoms s^{-1}]	$5.1(7) \times 10^8$	$5.3(4) \times 10^7$	$5.3(9) \times 10^6$	4.85×10^6	$1.7(4) \times 10^6$	$4.7(15) \times 10^5$
Temperature x	-[a]	3.7(3) µK	2.01(6) µK	-[a]	-[b]	-[b]
Temperature y	20(5) µK	1.9(1) µK	1.42(3) µK	16(2) µK	2.3(3) µK	1.6(3) µK
Temperature z	26(7) µK	2.8(2) µK	1.91(9) µK	66(17) µK	8.4(12) µK	3.6(12) µK
Width σ_x	-[a]	385(4) µm	150(2) µm	-[a]	552(30) µm	351(4) µm
Width σ_y	725(61) µm	192(3) µm	88(1) µm	748(35) µm	245 µm	180(13) µm
Width σ_z	2086(41) µm	528(3) µm	247(3) µm	1571(49) µm	778(30) µm	386(11) µm
Atom number	$2.54(10) \times 10^9$	$1.71(5) \times 10^8$	$2.5(1) \times 10^7$	$6.69(8) \times 10^8$	$1.55(3) \times 10^8$	$5.9(2) \times 10^6$
Peak density [atoms cm^{-3}]	$5.1(7) \times 10^{10}$	$2.8(2) \times 10^{11}$	$4.8(4) \times 10^{11}$	$2.3(3) \times 10^{10}$	$9(1) \times 10^{10}$	$1.7(2) \times 10^{10}$
Peak PSD	$2.8(12) \times 10^{-6}$	$4(1) \times 10^{-4}$	$1.3(2) \times 10^{-3}$	$6.4(22) \times 10^{-7}$	$4.5(17) \times 10^{-5}$	$2.0(1) \times 10^{-5}$
$1/e$ lifetime	4.53(6) s	2.8(2) s	1.95(6) s	12.0 s	9.6 s	11.4 s

[a] At the location of Red MOT I no imaging system for the x axis was available so Red MOT I density and PSD calculations assume that temperature and width are the same as z along x.

[b] Top view data was not recorded so the temperature for the x axis is assumed to be the same as for the z axis.

4.2.1 Dipole traps

The dipole trap configuration which we used initially consisted of three dipole trap beams as shown in figure 4.6. This is similar to that used in previous machines [107]. A summary of the beam properties can be found in table 4.2. This geometry has a number of advantages. The sheet or reservoir trap is very large giving an excellent spatial overlap with and loading efficiency from a cold single frequency bosonic red MOT. The horizontal reservoir trap increases the trapping frequency in the long axis from a few hertz to something on the order of 40 Hz, increasing the efficiency of evaporation sequences (although this beam was often left off since it doesn't do much and after a while the beam line was re-purposed for a transport guide, see section 6.1). The third beam, the dimple, collects and concentrates the atoms in a trap with high trapping frequency for efficient evaporation. It is here that we make BECs by evaporating the rest of the atoms. While the horizontal and dimple beams adjust the trapping frequencies and the energy landscape, it is the sheet beam, which is the main determinant of the temperature of trapped atoms, and it is the sheet which controls the evaporation ramps.

The aim is to make a reservoir with as high a phase-space density as possible and with a volume sufficiently large that its distribution is unaffected by the dimple. If the reservoir is too big then our density will be low, and if the reservoir is too small then the reservoir

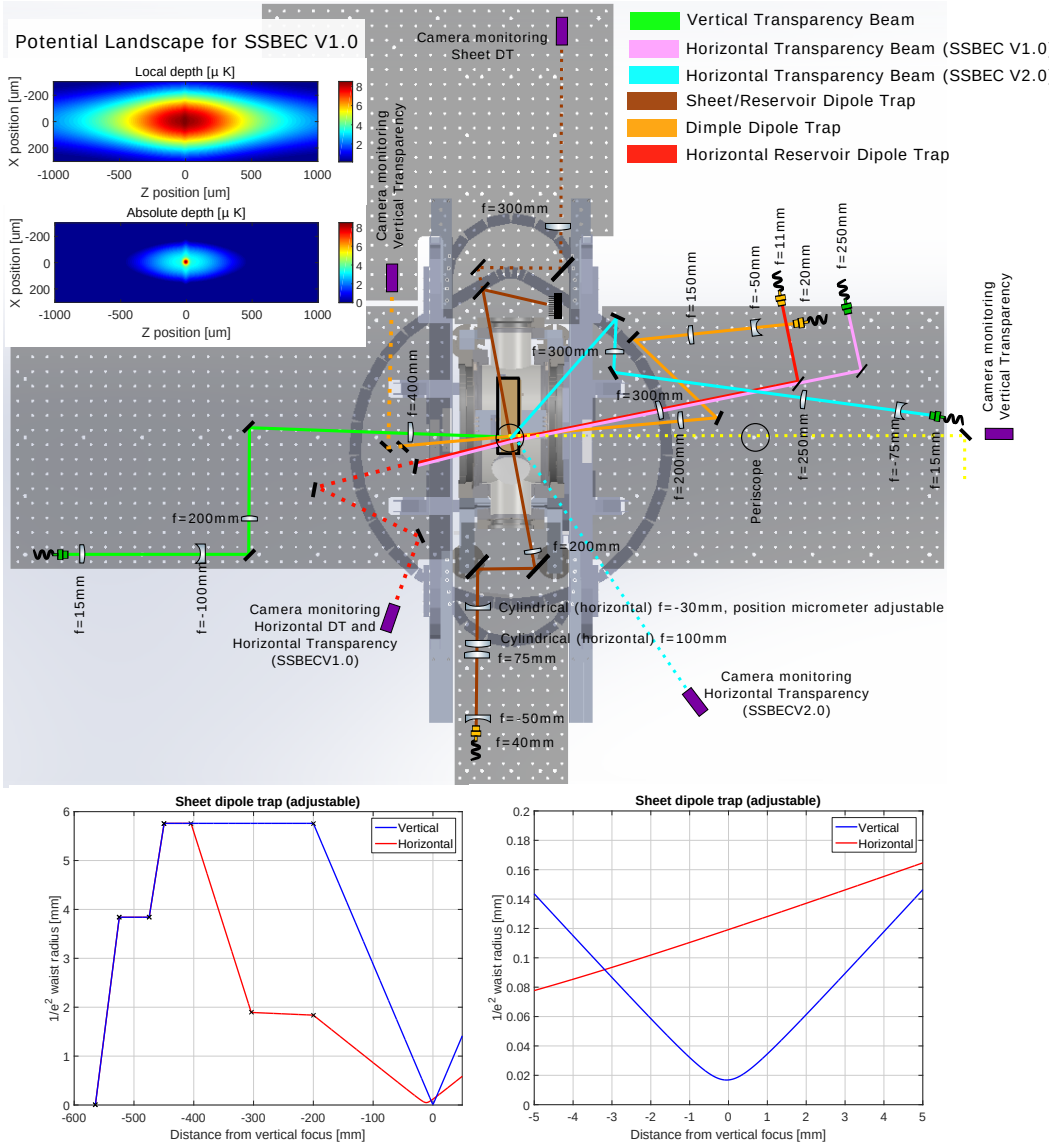

FIGURE 4.6: **Dipole trap geometry.** (top left) Potential landscapes for the first attempt at steady-state BEC. The local depth is the barrier height for an atom only able to travel in the vertical direction, whereas the absolute depth is the barrier height to the minimum for the entire trap. (middle) The chamber optics used to make the dipole traps and transparency beams and the camera systems for monitoring them. (bottom) Adjustable sheet dipole trap geometry - by adjusting the last cylindrical lens position the focus can be shifted generating large variations in the width of the sheet without shifting the trap location which is determined by the location of the focus in the vertical axis.

TABLE 4.2: **Dipole Trap Configuration.** Parameters of the dipole trap beams used for making BEC and the resulting trap properties. Trapping frequency estimates include window losses. Here, SSBEC stands for steady-state BEC architecture.

Parameter	First BEC	SSBEC V1.0	SSBEC V2.0
Sheet beam $1/e^2$ radius	18×305 µm	18×305 µm	13×120 µm
Sheet max power	2.8 W	4.6 W	1.47 W
Sheet max vertical trap frequency	721 Hz	925 Hz	1220 Hz
Sheet max horizontal trap frequency	43 Hz	55 Hz	137 Hz
Sheet max axial trap frequency	10 Hz	12 Hz	21 Hz
Sheet typical power[a]	2.8 W	1.37 W	0.9 W
Sheet typical vertical trap frequency[a]	722 Hz	505 Hz	980 Hz
Sheet typical horizontal trap frequency[a]	43 Hz	30 Hz	109 Hz
Sheet typical axial trap frequency[a]	10 Hz	7 Hz	11 Hz
Dimple beam $1/e^2$ radius		50 µm	26 µm
Dimple max power		430 mW	460 mW
Dimple max radial trap frequency		140 Hz	488 Hz
Dimple typical power[a]		305 mW	170 mW
Dimple typical radial trap frequency[a]		115 Hz	293 Hz
Horizontal reservoir beam $1/e^2$ radius	125 µm	125 µm	-
Horizontal reservoir max power	570 mW	1.76 W	-
Horizontal reservoir max radial trap frequency	26 Hz	46 Hz	-
Horizontal reservoir typical power[a]	0 mW	0 W	-
Horizontal reservoir typical radial trap frequency[a]	-	-	-
Transport guide $1/e^2$ radius	-	-	92 µm
Transport guide max power	-	-	12.76 W
Transport guide max radial trap frequency	-	-	205 Hz
Transport guide max axial trap frequency	-	-	0.5 Hz
Transport guide typical power[a]	-	-	12.0 W
Transport guide typical radial trap frequency[a]	-	-	205 Hz
Transport guide typical axial trap frequency[a]	-	-	0.5 Hz

.

[a] At the beginning of any ramps.

will start to look like little more than an extended dimple. In that case the dimple will not be able to produce a significant phase-space density increase beyond that in the reservoir. Ideally we want a dipole trap geometry that we can at least somewhat tune to try to get this balance right. We can also make estimates from models but they are just a guide.

There is a nice way to make a dipole trap with a tunable size, at least in one dimension [107]. By using an astigmatic sheet dipole beam, a cylindrical lens can be adjusted to tune the beam width at the location of the tight vertical focus without affecting the location or size of the tightly focused axis and thus without affecting the trap location. With the help of cameras to monitor the beam position at the focal plane, it is possible to rapidly explore different trap sizes. We used a number of dipole trap geometries. The first was conventional with waists in both axes in the same plane but the later (and current) sheet dipole trap uses this astigmatic geometry to provide wide tunability. This is illustrated in figure 4.6.

Our dipole trap beams were initially derived from a very old 5 W 1.07 µm IPG fiber laser. Over around 6 months of operation it gradually died and we eventually replaced it with a new incoherent[5] 20 W IPG fiber laser which was used for the rest of this work. Later the horizontal beam line was repurposed for a transport waveguide (see section 6.1). For best performance it is worth optimizing the polarization to minimize the Stark shift generated by the dipole trap. Our sheet dipole trap generates 50 kHz Stark shifts to the blue on the 7.4 kHz linewidth red transition, which is very significant and impacts the cooling performance because the optimal detuning depends on an atom's location in the trap. The Stark shifts and methods to calculate them are discussed in section 2.6. Initially we were quite careful to always use the polarization generating the smallest Stark shifts when placing our dipole traps.

The layout of the generation and distribution system for the dipole trap is in Chun-Chia's thesis [216]. We use Gooch & Housego, 3080-194 TeO_2 - 80 MHz AOMs for our modulation and power control, but it is the DDSs that are probably more important. The DDSs driving the dipole traps are 500 MHz DDSs which have a maximum attenuation of 31 dB[6].

[5] This laser has a linewidth of 1.115 nm corresponding to a coherence length of around 1 mm.

[6] At the time of assembly we didn't have any spare 135 MHz DDSs that can provide a 42 dB maximum attenuation. As a result the DDSs and their dipole traps are never fully off unless their frequency is also set to 0 Hz. This little issue caused much commotion when we first saw very cold atoms guided by a very weak but not quite off dimple dipole trap. This is the "copper pyrite" of ultracold physics. At first glance it looks similar to a BEC, a bimodal distribution after a time of flight expansion. There are two tells in our data that give this effect away, firstly the guided dimple beam is on a small angle relative to gravity so the stripe looks angled. The second tell is the distribution in the vertical axis. For a BEC you see a ball at the center of a thermal cloud, not a stripe through the entire vertical extent of the thermal could. An example of this stripe along side a real BEC can be observed in the cold thermal clouds of figure 6.11.

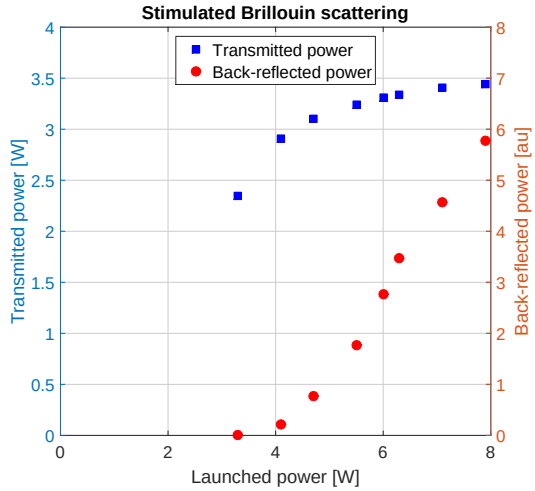

FIGURE 4.7: **SBS threshold.** We found the Stimulated Brillouin Scattering (SBS) threshold for a 12 m long OZ Optics PMJ-A3AHPC fiber. The fiber is a 0.12NA 6/125 core/cladding diameter fiber. We launched 1064 nm light with a linewidth on the order of 1 kHz from a 50 W Azur light (ALS-50) laser. The SBS threshold was found to be around 36 W · m.

There is no strong reason why we use three different frequencies[7] for the dipole trap AOMs. If we had a coherent laser it would be important to prevent interference and for that reason out of force of habit we generally choose different AOM frequencies and modulation frequencies for different beams. This is also the reason we use different modulation frequencies on our red MOT beams. We use vertical polarizations and collimated beams on the AOMs to reduce thermal effects, the beams are collimated to a waist to match a Schäfter and Kirchhoff (S&K) 6.2-03 collimator with coupling efficiencies of up to 90% although 80% was more common. Delivery is via 4 m long high power fibres (OZ optics PMJ-A3AHPC).

Towards the end of the work for this thesis we also borrowed some light from a coherent kHz linewidth 1.064 µm, 50 W fiber laser that was available from the SrMic machine. This laser from Azur light (ALS-50) was to be used for adding extra dimple dipole traps for evaporation sequences (see section 6.3.3). Initially we tried to pipe the light through a 12 m long 6/125 fiber from OZ Optics but we hit the Stimulated Brilllouin Scattering (SBS) threshold at 3 W transmitted (see figure 4.7) so we ended up improvising a connection using a 4 m fiber[8].

Aligning dipole traps can be a little tricky. Here is our approach:

1. Measure the dipole trap geometry at the waist on a camera to ensure the actual beam geometry is what you expected. Take careful note of the location of the focus to ensure

[7] 81.537 MHz, 79.386 MHz, 80.729 MHz.
[8] This is a little reminder to never ever forget about SBS, it is lurking just waiting to pounce on you.

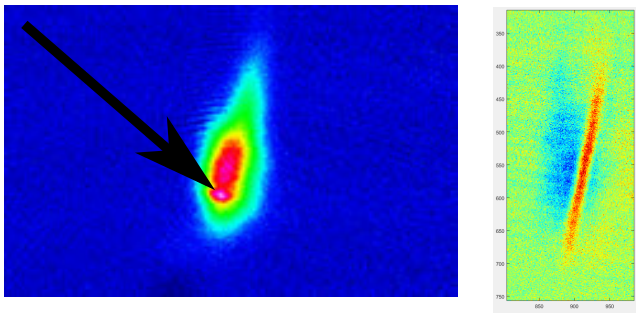

FIGURE 4.8: **Searching for dipole traps.** Typical images of newly found sheet dipole traps. (left) A small increase in the density of a MOT imaged from the side due to the presence of a nearby sheet dipole trap. (right) Using a poorly focussed dipole trap we found nothing searching from the side. Eventually we scanned out the XYZ parameter space for MOT locations with and without the dipole trap on and took the difference. The path of the dipole beam was then clear and we were able to adjust the focus to make it strong enough to load some atoms.

it will overlap with the MOT and your imaging system. This is done by placing a mirror in front of the vacuum chamber window, estimating the distance from that mirror to the MOT, and then measuring the parameters of the reflected beam on a camera along the reflected beam at the estimated distance.

2. Install a sensitive camera on the far side of the MOT you are trying to load and image the MOT (we used RS Components 493-5590 but for the iqClock system we are using IP cameras from Aliexpress/Unitoptek). For a MOT on the weak red strontium transition, this is a bit more difficult than it might seem because the fluorescence is so weak. We use as high a NA as possible for our imaging system to increase the fluorescence we can gather. We usually use several high reflectivity mirrors at 1 µm with polished back surfaces as filters against the dipole laser light.
3. Tweak the imaging lens to focus the dipole trap laser on the imaging camera. If the dipole trap was properly focussed at the MOT, this will be a small perturbation and the MOT should remain in focus.
4. Align the dipole laser so that its focus is co-located with the image of the MOT on the camera.
5. Try to load a cold MOT scanning all three axes of the MOT location using the bias fields. The target is loading a small number of atoms, or if that fails, looking for a stripe of increased density in the absorption image of the MOT cloud by subtracting images with the dipole trap on and off. Having two orthogonal imaging axes can make this much easier. The first signal will often be hard to pick from noise. I have provided some examples in figure 4.8 of a newly 'found' dipole trap.

A typical loading sequence takes around 850 ms and an example is shown in figure 4.9.

For ^{88}Sr we are able to load 50% of a single frequency red MOT cloud atom number (measured at a time equivalent to 10.66 s in figure 4.9). For ^{84}Sr we can load around 80% of a single frequency red MOT cloud atom number.

Characterizing the dipole trap is best done once you have a BEC by looking at the trapping frequency. We usually start by making a BEC and then modulating the dipole trap powers by a small amount (typically modulating the RF attenuation driving the AOM by between 0.1dB and 2dB) at a modulation frequency for a given time (typically 1s) and then looking at the loss as we scan the modulation frequency. This gives a rough idea of resonances and the absorption peaks can be made narrower by modulating for longer times at smaller depths, but it can be difficult to distinguish from harmonics and closely spaced frequencies between different axes. To get a better fix we usually use a second method where we perturb the trap and then look at the BEC (or atomic cloud) position, velocity or cloud width after a time of flight as a function of the evolution time. You can then fit a sine curve to get a trapping frequency. Here it is important to distinguish between the motion of a BEC and that of thermal atoms. An excitation spectrum for a thermal cloud is simple. It can be excited with a dipole or "center of mass" excitation at the trapping frequency or you can excite it parametrically where you will see heating and loss at harmonics of the trapping frequency. A BEC, on the other hand, will oscillate collectively and it can have a more complex spectrum. In addition to the standard dipole or "center of mass" oscillations it can also exhibit monopole, quadrupole, or higher order breathing oscillations at $\sqrt{X}\omega$, where X is a rational depending on geometry [312]. A good check for whether or not you are at the trapping frequency is to check that you see excitation or loss for both BEC and thermal atoms as both will oscillate at the trapping frequency.

4.2.2 Making a stable BEC

A typical evaporation sequence for making a pulsed BEC is described in figure 4.9. Since strontium MOTs can have a very high phase-space density it is actually quite easy to go from a MOT, to a loaded dipole trap, to a BEC. The key is starting with a good dipole trap geometry with a good atom number and loading it efficiently. We loaded our first atoms in a dipole trap, characterized the dipole trapping frequencies, and then made our first BEC, all in the same week.

For spectroscopy or lifetime measurements we typically begin with BECs of between 1×10^5 and 3×10^5 depending on the signal to noise required. Using a higher resolution imaging system is necessary for working with small BECs while maintaining signal to noise. We began with a 20 µm pixel resolution, which proved to be grossly inadequate and was shortly upgraded to a 4.48 µm pixel resolution.

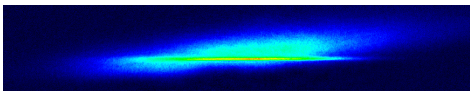

0s: Start the MOT
10s: Ramp on the sheet dipole trap (DT) at max power
10.11s: Ramp B fields to overlap the MOT and sheet DT (should overlap in 3D)
10.41s: Wait

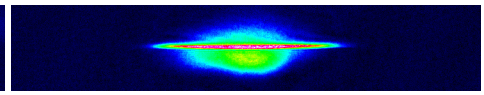

10.51s: Ramp off the MOT I beams,
Ramp off the high frequency components of MOT II beams,
Ramp bandwidth of low frequency MOT II beams to single frequency
Ramp B fields to maintain overlap with dipole trap

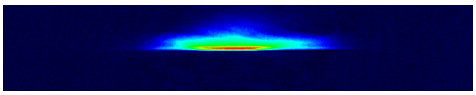

10.66s: Ramp down power of low frequency MOT II beams
Ramp B fields to maintain overlap with dipole trap

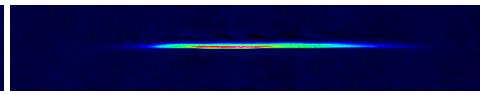

10.96s Set DDSs to single frequency
Ramp frequency of low frequency MOT II beams from 100kHz to 30kHz
Ramp down intensity of low frequency MOT II beams
Ramp B fields to maintain overlap with dipole trap
11.26s: Turn off red lasers and close shutters

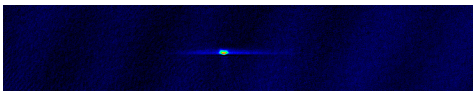

11.36s Ramp sheet DT to -7dB
Ramp dimple DT to 0dB
11.66s: Ramp sheet DT to -18dB
Ramp dimple DT to -18dB
12.36s: Wait

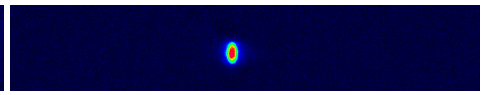

13.36s Turn off dipole traps and set their frequency to 0Hz
13.382s: Take Absorption Image

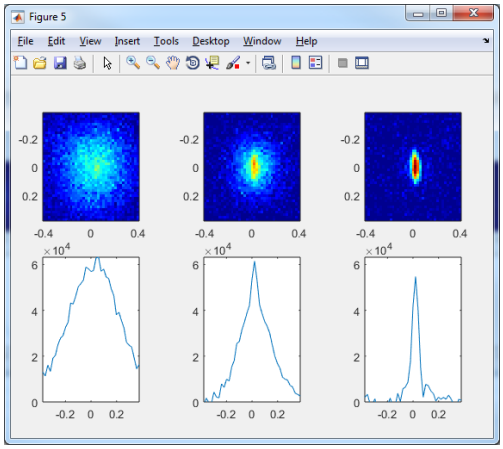

160808 - Our first BEC

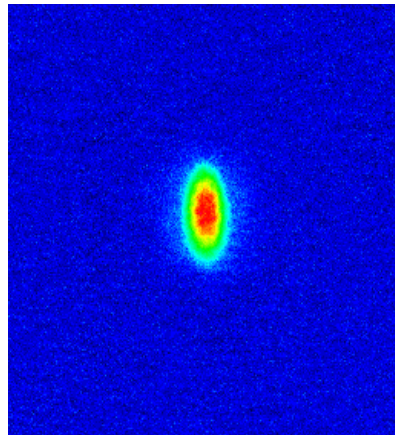

161103 - A nicer BEC
(better imaging system)

FIGURE 4.9: **Evaporation to BEC.** (above) The evaporation sequence used to make BEC. (below, left) Our first BEC from 8/8/2016 and (below, right) typical pure BEC of 3×10^5 atoms obtained 2 months later.

Making a pulsed BEC is easy. Making a pulsed BEC with a repeatable atom number is much harder, but this is what is needed for spectroscopy and lifetime scans. In the early days our machine stability was not ideal. This had a significant impact on the quality of our early scan data. Over the subsequent years the machine has become much more stable, but getting it into a stable condition and keeping it there requires daily checking and optimization of all the beam lines and parameters. When taking data we would always begin our day by checking the injection lock powers of all our lasers, the powers of all our beams lines and then we would adjust our magnetic field offsets to position the MOT for optimal dipole trap loading. Every day should begin and end with making a series of BECs to check the machine stability when taking data.

There were several important factors which dramatically improved the machine stability since taking the early data.

Camera software The Andor Luca cameras are able to collect multiple exposures and store them in the same on CCD chip frame buffer before sending the entire sequence back to the computer as a single image (Fast Kinetic Series (FKS) imaging). This allows the rapid collection of multiple exposures which improved the performance of background subtraction in absorption imaging. We wrote an improved camera interface so that we could use this mode, software which is now used on all our machines.

Magnetic fields The magnetic field gradients in the SrCAL machine are very small compared with typical machines, less than $0.5\,\mathrm{G}\cdot\mathrm{cm}^{-1}$. Unfortunately the machine chamber sits around 3 m from both the RbSr and SrMic machines that both have large Feshbach coils capable of running 1000 A. Worse still, the SrMic machine used cage coils with a cross section of several m^2 to adjust their bias fields. These coils also adjusted the bias field in the SrCAL chamber by almost the same amount. Initially this was dealt with by operating at nights but that became impossible once RbSr started leaving their machine scanning overnight. We implemented a feedforward compensation system using spare circuits on our bias coils and later built our own set of large cage coils with separate circuits to feedforward from both RbSr and SrMic. These are driven by home made bipolar 5 A laser current drivers. Rodrigo also designed and built a magnetic sensor circuit and planned to implement active feedback on the cage coils if problems persisted. We used these boards to calibrate our feedforward but have so far resisted the temptation to do it closed loop because of the likely havoc it would cause for the other machines. This will be a story for Rodrigo's thesis. One of the mistakes made during the machine construction was to assume a relatively benign

magnetic environment and I would recommend building a set of 1.5×1.5×1.5 m cage coils around every machine to guard against this problem.

Red master There are significant (-20 dBc) noise sidebands at around 1 MHz on the 689 nm red master laser from servo bumps. This caused large amounts of excess heating that affected the SrCAL machine, but which was not significant for the RbSr and SrMic machines, where small amounts of excess heating is not a significant concern. Fixing the source was not an option as it would interfere with the schedules of the other machines, but we eventually got some of the light transmitted through the locking cavity of the master and used that to seed a 'filter' slave to somewhat clean it. It might still be worth building a new red master laser for the SrCAL and iqClock machines so that we can finally eliminate this heating problem. This is detailed in Chun-Chia's thesis [216].

Blue master laser The group blue master laser was a frequency doubled commercial laser that also served as the blue light source for the RbSr machine. A double pass AOM was used to shift a portion of the laser output back to ^{88}Sr to maintain a spectroscopy lock and to injection lock slaves that seed the blue SrCAL and SrMic laser systems. As a result there was significant intensity noise on the injection locking seed when the RbSr machine was operated and at the end of every RbSr shot the laser would rapidly scan during a reset sequence. We were repeatedly assured that the spectroscopy lock PID could handle this punishment but our tree of injection locked blue slaves certainly could not[9]. Eventually we built our own blue master ECDL to try to combat this problem. The first edition [301] had a small mode-hop free tuning. This was upgraded to something that will stay locked to our spectroscopy cell for a day or more, but can sometimes start to run multimode and be troublesome to tune. I shortly plan to upgrade the SrCAL/iqClock blue master to our latest ECDL design used for our 448 nm and 487 nm lasers. We still need to design a better PID servo for this system.

Temperature stability Temperature fluctuations in the lab have a major impact on fibre coupling efficiencies throughout the laser systems. If temperatures drift by 1 °C all the fibre coupling efficiencies will fall and carefully optimized laser power levels will no longer be valid. A solution is to spend a day to go through and reoptimize all the laser systems and fibre couplings, but if the temperature is drifting around on a timescale of hours this becomes pointless. In summer, the building house water that cools the lab air conditioner would get quite warm and the room air conditioner capacity would plummet sending the room temperature up by 5 °C and cycling during the

[9] Thus we collected our early data when RbSr were not operating, which meant running from 8pm to 10am with maintenance and preparation activities during daylight hours.

day. To combat this we purchased and installed two mobile air conditioners which exhaust heat into the room air exhaust and invested effort to try to reduce the heat loads within the room. We removed all lab power supplies from the room and ran cabling so that they could be located in the remote electronic cabinets. Unnecessary lighting and equipment was turned off and the areas above the tables housing the electronics (the main heat load) were sealed off with plastic covers and tape creating a hot zone and increasing the heat extracted by the room air exhaust which draws its intake from these areas. This managed to bring the load down to a level that the room air conditioning could handle, even in summer.

4.3 Protecting a BEC from resonant light

A BEC needs to be protected from scattering resonant light. The great realization demonstrated in [192] was that it is possible to locally AC Stark shift the 689 nm cooling transition out of resonance and protect a region making a very dark dark spot [113]. This worked well enough for a BEC to form even in the presence of (a little) resonant cooling light.

This trick works because the 7.4 kHz red transition is so narrow that a Stark shift of many linewidths is feasible using current laser technology (even without a buildup cavity) and without introducing excess scattering. The same can not be said for the 30.5 MHz blue transition. To protect against blue light we rely on separation.

Here we will describe our efforts to protect against light on both the blue and the red cooling transitions and the results we achieved.

4.3.1 Protection from 461 nm light

Most of the measures introduced to protect against blue light have already been described in chapter 3. A brief summary can be found in figure 4.10 and as follows:

Separate chambers No blue beams are sent into the atom laser chamber (aside from imaging beams which are equipped with shutters). All the blue laser cooling stages take place in the separate 2D MOT chamber.

Baffles A series of four orifices made from 1" neutral density filters that are spaced with 20.5 mm centre separations form a baffle that was described in section 3.5.2. Each has an 8 mm diameter hole to allow the atomic beam to pass. This absorbs the blue light that does not pass directly through along the axis.

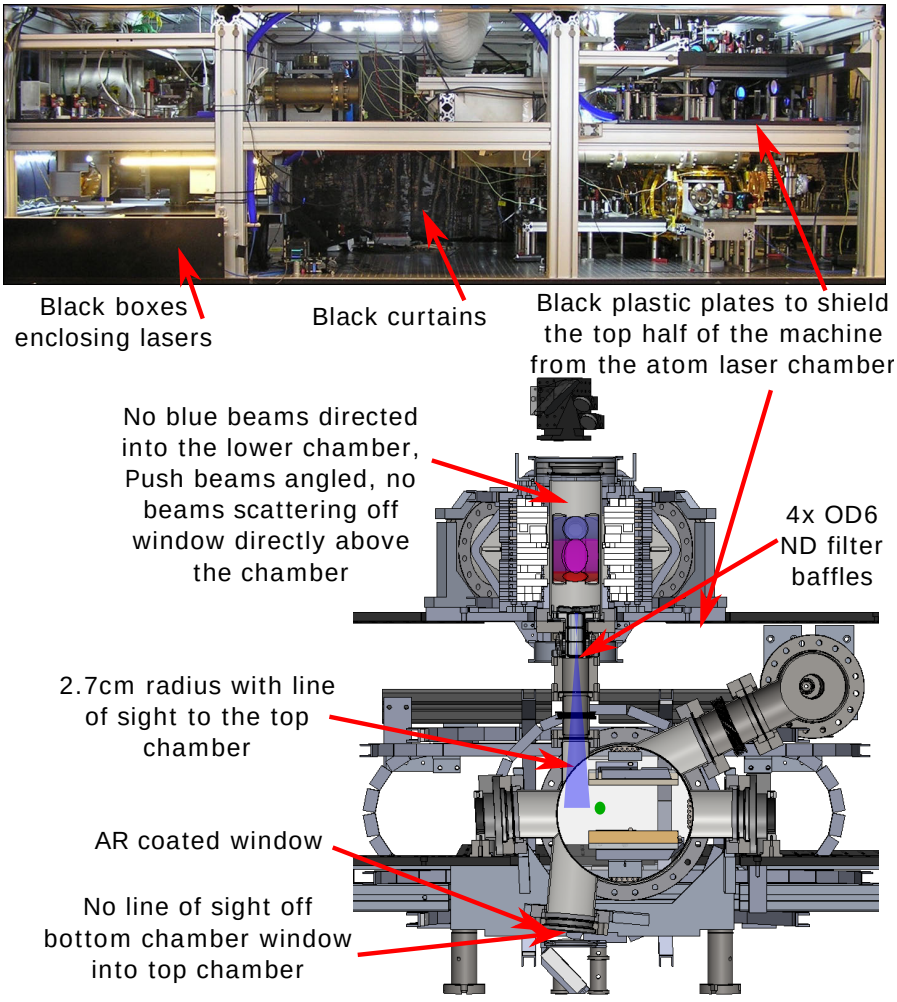

FIGURE 4.10: **Measures to protect against resonant blue light.** The range of measures used to protect a BEC from blue resonant light.

Transfer The location at which we make BECs is offset within the lower chamber to avoid a line of sight directly into the upper chamber. Our baffle geometry is such that an offset of 2.7 cm is required to achieve protection. We operate with an offset of ≈3.7 cm.

Shielding Boxes and shields were built to enclose all the laser and light distribution systems on the table and to shield the upper part of the machine from the lower part of the machine. All the roofs of these protection boxes were made from 5 mm thick black acrylic perspex (for strength) while the sides were all made from 6 mm thick black foamed PVC to also remove specular reflections (albeit with greatly reduced strength). The machine frame or additional 30 mm Boikon aluminium profile framework was used for support. Future boxes will all use acrylic as PVC can't be cut on our laser cutter (hydrochloric acid is produced).

To test the effectiveness of the blue light protection we compare the lifetime of a BEC with and without the blue lasers operating (but with the red lasers all off). The operating powers for the blue lasers and their frequency modulations were identical to the parameters for running the steady-state red MOT as listed in table 5.2. It is critical to take care to only count atoms in the BEC and exclude the trapped thermal cloud when analysing the lifetime data because a blue photon will scatter an atom out of a BEC but it will not scatter it out of the trap. Blue light will not change the total trapped atom number, just the BEC-thermal atom number ratio. The fitted 1/e lifetimes were 2.32(37) s without blue light and 2.11(30) s with the blue light operating[10].

We thus succeeded in protecting our BEC location from scattered 461 nm light by machine design.

4.3.2 Protection from 689 nm light

There are several transitions which can be used to significantly Stark shift the $^3P_1$ state. These were introduced in section 2.6.2. Since the 688 nm $^3P_1$-$^3S_1$ transition had already been successfully demonstrated to make a dark spot against $^1S_0$-$^3P_1$ light [192] this was considered a solved problem when we built the machine. It is only now that we are seriously pursuing other options, namely the 487 nm $^3P_1$-$^3D_2$ transparency transition (see section 6.3.2).

To characterize the Stark shifts achieved we initially performed loss spectroscopy on a trapped BEC around the 689 nm cooling transition. We observed up to six absorption lines with strengths depending on the optical polarizations and magnetic fields used. These

[10] If the entire data set is used for fitting these lifetimes the results are 3.05(79) s without blue light and 2.68(29) s with the blue light operating but the tail can be quite unreliable. For this reason, we shall quote the lifetimes fitting only data in which at least half the initial number remains.

correspond to the magnetic σ^- and σ^+ transitions and the non-magnetic π transition for both free atoms and the photo-association line at 330 kHz (see table 2.13 and [275, 276]). We are able to observe the photoassociation (PA) lines because the density in our BEC is high but they tend to be weak and tricky to pinpoint.

We began by mapping the Zeeman shifts which are plotted in figure 4.11 (top) alongside the curves from section 2.9 and 2.10. The agreement for small fields is excellent but at large fields we were unable to see the PA lines. A closer view of the spectra is plotted in figure 4.11 (bottom) and reveals that the lines become broad and weak as the field increases. This is very significant and goes way beyond the tiny variation in field strengths that could be attributed to the spatial extent of the BEC. We did not look into the origins of this effect but noted its impact for our application. A second effect is that the PA lines are not observable after the grazing crossing with the free atom lines. Maybe they are weaker and maybe the molecular and atomic states become mixed, coupled and broadened which would lead to a broad loss feature. I have no expertise in these matters but this might be an important limitation for the protection levels that can be achieved. For our first attempt at steady-state BEC we intended to operate near the MOT quadrupole center. The concept was to replenish our dipole trap reservoir with atoms from a neighbouring MOT, so these issues occurring at higher magnetic fields were not concerning. They are however an issue for the second architecture we implemented (chapter 6).

Our transparency 688 nm $^3P_1$-$^3S_1$ laser was a homemade ECDL based on the design from Tim van Leent's master's work [301]. This ECDL was a copy of our first UVA ECDL design and things have improved a lot since then, so it isn't exactly a fun system to work with. The ECDL was originally PDH locked to a high (5000) finesse in vacuum cavity using a zerodur spacer (see Jens' and Simon' thesis [107, 244] for something similar). We found the laser drift was low compared to the GHz precision required, so we usually just kept an eye on the laser frequency using Rene Gerritsma's High Finesse WSU-30 wavemeter. Eventually the locking optics were removed from around the cavity to improve the lock signal and performance for the repump lasers that were also locked to the same cavity (using different locking frequencies). More information can be found in section 3.7.1. To increase the power output a slave laser using an HL6738MG diode was injection locked. In later work still more power was needed and the output of the slave was then used to seed a tapered amplifier (TA). TAs were discussed in section 3.7.1.

To Stark shift the atoms we placed a vertical "transparency" laser almost counter-propagating with the dimple dipole trap beam as shown in figure 4.12. This was focussed to a (calculated) $1/e^2$ waist of 72 µm and overlaid with the dimple in the plane of the sheet dipole trap. Adjusting the alignment and focussing the transparency beam was a little tricky. First we located the beam by injecting blue and then red resonant light down the fibre and

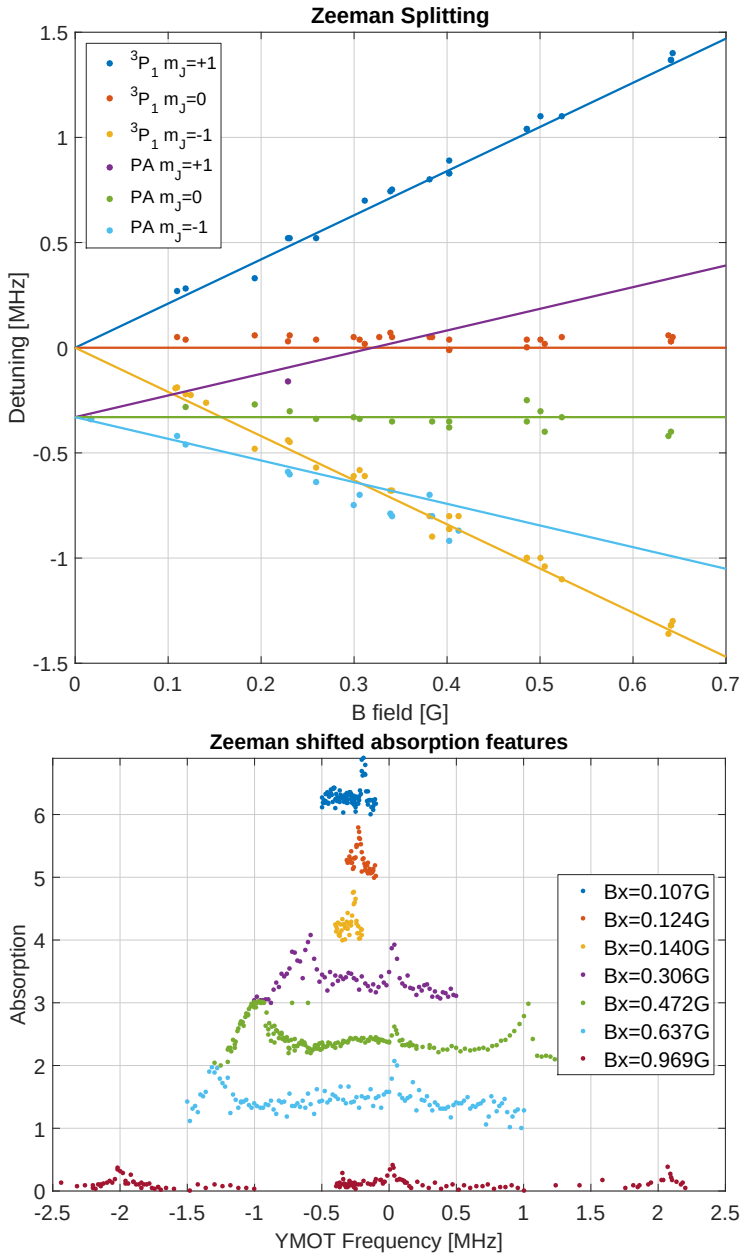

FIGURE 4.11: **Zeeman shifts by BEC loss spectroscopy.** (top) Locations of the absorption features and a comparison with the values from tables 2.13 and 2.14. All results are for ^{84}Sr. (bottom) Spectroscopy data shows the absorption lines becoming broader and deeper as the magnetic field increases. Probe light had components of σ^+, σ^- and π.

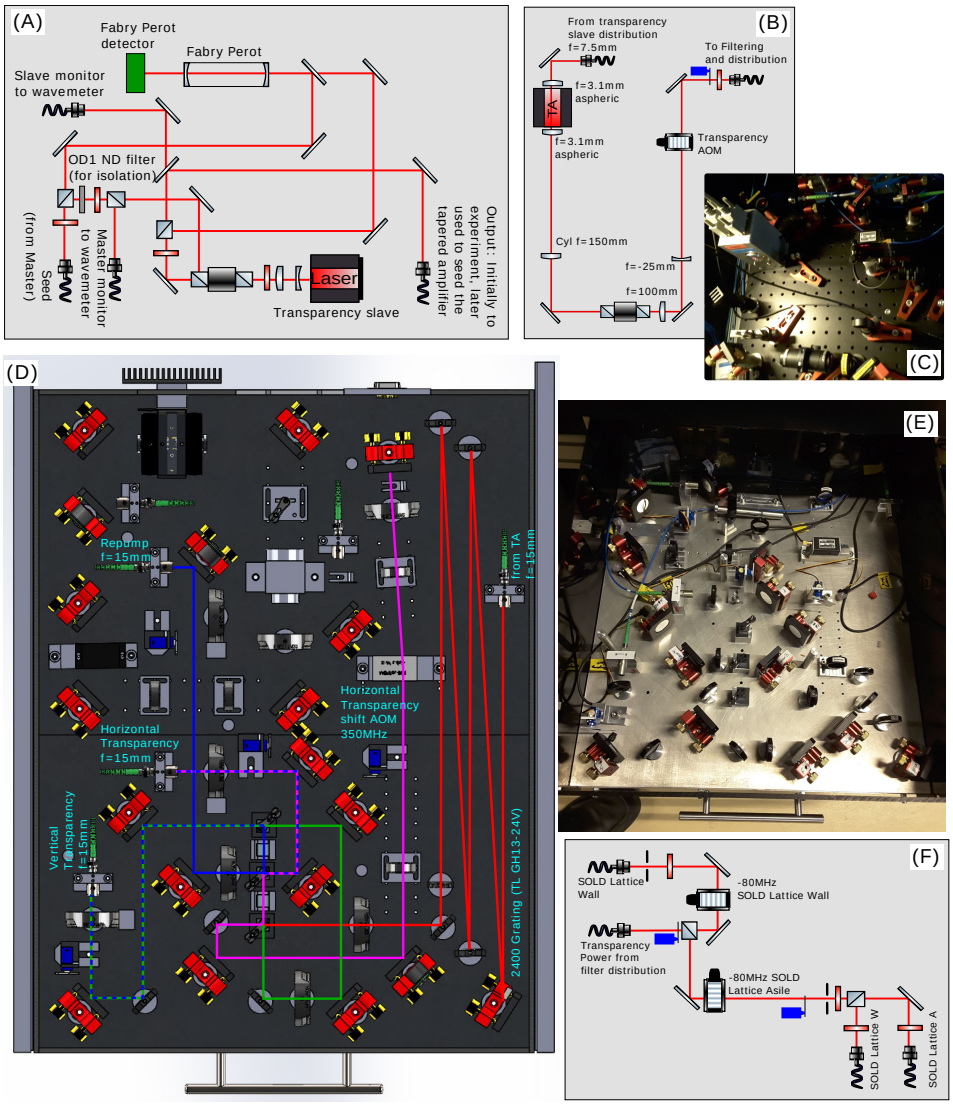

FIGURE 4.12: **Transparency laser system.** Here we show the optical configuration generating the transparency beams. (A) Transparency slave laser distribution system. (B) Tapered amplifier system. (C) Image of the tapered amplifier system. (D) Second edition of the Transparency filter and distribution system. (E) Image of the filter and distribution system. (F) SOLD lattice distribution system (see chapter 7).

looking for depletion in first a red MOT and later a cloud of atoms loaded in a sheet dipole trap. Once located, focussing was performed using the transparency beam to Stark shift the absorption frequency (with a magnetic field of ≈0.7G). Using a micrometer stage to adjust the focussing lens position, we sought a 500 kHz shift on the red magnetic line while minimizing the transparency power. Later implementations focussed higher powers to tighter focusses (26 µm) in order to generate greater Stark shifts and better protection.

When we first applied the transparency beam to our BEC we were surprised to find that our absorption features did not shift linearly away. Instead the Stark shift saturated and in some cases the features did not shift at all irrespective of the intensity applied. Typical shifts observed in the locations for the absorption features are shown in figure 4.13. This effect can also be observed in data contained within the supplementaries of [192] but in that case a Stark shift of a few hundred kHz was sufficient to provide protection against the tiny intensities of cooling light used.

For us, this posed a major problem. The light shifts we could produce, particularly near the MOT quadrupole center were very small, much too small to protect a BEC against scatter in a red MOT beam.

A recollection of selection rules for optical transitions would suggest that this behaviour is due to the existence of a dark state in any $^3P_1$-$^3S_1$ system. To understand this problem better we can calculate the eigenstates of the optical Bloch equations (equation 4.1 in box **??**) in the dressed state picture [223] as a function of the applied transparency beam power, detuning and polarization. The Stark shifts are plotted in figure 4.14.

Note that different polarization transparency beams shift different magnetic sublevels. Our solution to this problem is to try to *incoherently* add Stark shifts using two different polarization components at *different frequencies*. The different polarizations must not interfere in the atom so they need different frequencies to wash out coherences. Our solution is shown in figure 4.15. This solution uses beams from orthogonal (vertical and horizontal) directions and should work as long as the detuning between the transparency beams is large compared with the Stark shifts involved. To remove the coherence initially a 200 MHz single pass AOM was used to blue shift the horizontal arm. This was found to be marginal and we still saw what looked to be some coherences and absorption feature broadening as we tuned the transparency laser closer to the transition. In a later implementation the detuning was increased by using a double pass 350 MHz AOM to blue shift the horizontal transparency beam. The optical beam lines for the transparency beams are shown in figure 4.6. The waist size of the transparency beams was adapted over the course of the work trying to get ever greater protection levels. The waist sizes used during the first and second attempts at making steady-state BEC are listed in table 4.3.

We applied Stark shifts on both π and σ^+ using two orthogonal beams but one could

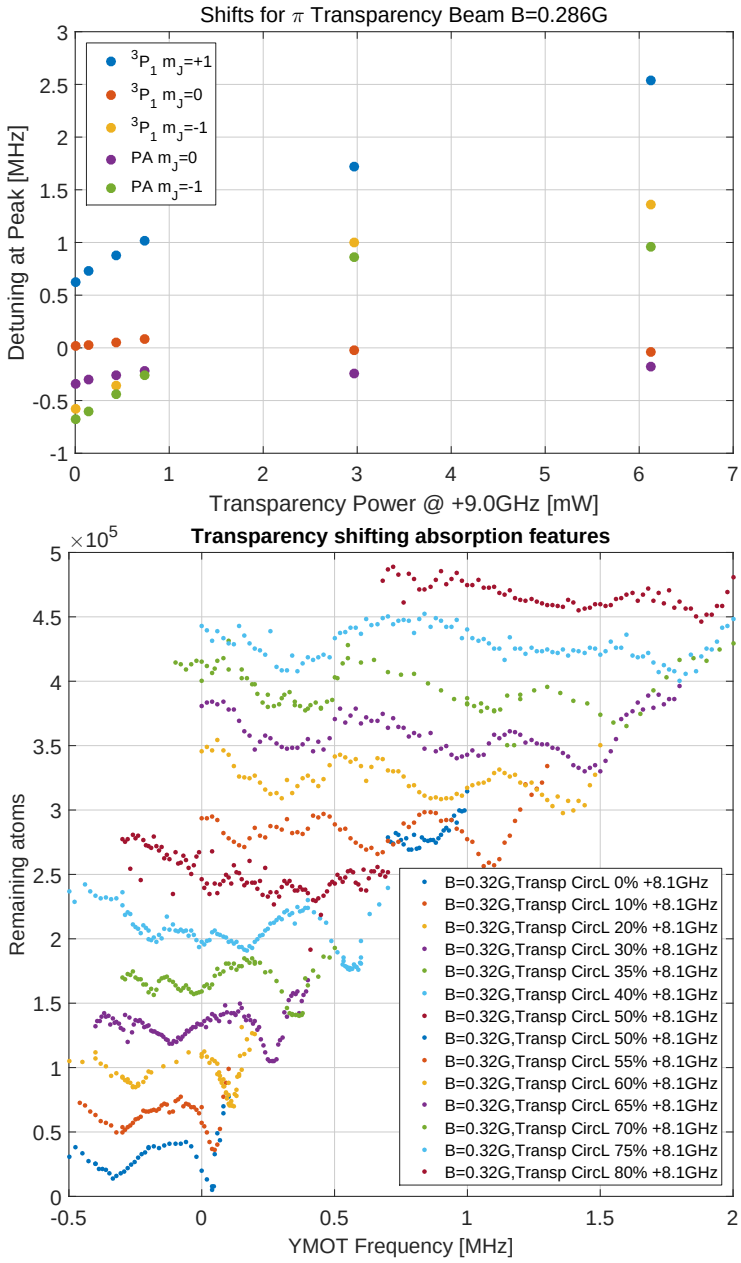

FIGURE 4.13: **Stark shifts by BEC loss spectroscopy.** (top) Stark shifts using a 6 mW π polarized transparency beam blue detuned by 9.0 GHz from $^3P_1$-$^3S_1$ with a 70 µm $1/e^2$ waist beam. No matter how much transparency power is applied some features do not shift. (bottom) Stark shifted lines broaden probably due to intensity variation across the sample causing a variable Stark shift.

Box 4.3.1: Calculating stark shifts.

$$\begin{bmatrix} -g_{3P1}\mu_B B & & & p_\pi C\Omega/2 & p_{\sigma^+} C\Omega/2 & \\ & 0 & & p_{\sigma^-} C\Omega/2 & & p_{\sigma^+} C\Omega/2 \\ & & g_{3P1}\mu_B B & & p_{\sigma^-} C\Omega/2 & p_\pi C\Omega/2 \\ p_\pi C\Omega/2 & p_{\sigma^-} C\Omega/2 & & -\Delta - g_{3S1}\mu_B B & & \\ p_{\sigma^+} C\Omega/2 & & p_{\sigma^-} C\Omega/2 & & -\Delta & \\ & p_{\sigma^+} C\Omega/2 & p_\pi C\Omega/2 & & & -\Delta + g_{3S1}\mu_B B \end{bmatrix} v = \lambda_E v \tag{4.1}$$

where:

Ω	$=$	Rabi frequency $\Omega = \Gamma\sqrt{I/(2I_{sat})}$
I	$=$	Transparency intensity [$W \cdot m^{-2}$]
I_{sat}	$=$	Saturation intensity
λ	$=$	Wavelength 688 nm
Γ	$=$	Linewidth [$2\pi\times 4$ MHz]
Δ	$=$	Detuning [typically $2\pi\times 30$ GHz]
$\begin{bmatrix} p_{\sigma^-} & p_\pi & p_{\sigma^+} \end{bmatrix}$	$=$	Transparency polarization vector (normalized in quadrature)
μ_B	$=$	Bohr magneton $\mu_B = e\hbar/(2m_e)$ =1.400 MHz/G
B	$=$	Magnetic field amplitude
C	$=$	Clebsch–Gordan coefficients
λ_E	$=$	eigenvalues/energy levels
v	$=$	vector of eigenstates

TABLE 4.3: **Transparency beam configuration.** Parameters of the transparency beams at the atoms.

Parameter	SSBEC architecture V1.0	SSBEC architecture V2.0
Vertical transparency $1/e^2$ radius	28(2) µm	28(2) µm
Vertical transparency maximum power	30 mW	8.5 mW
Horizontal transparency guide $1/e^2$ radius	35 µm	41 µm
Horizontal transparency maximum power	18 mW	12.5 mW
Typical detuning	20 GHz	14 GHz

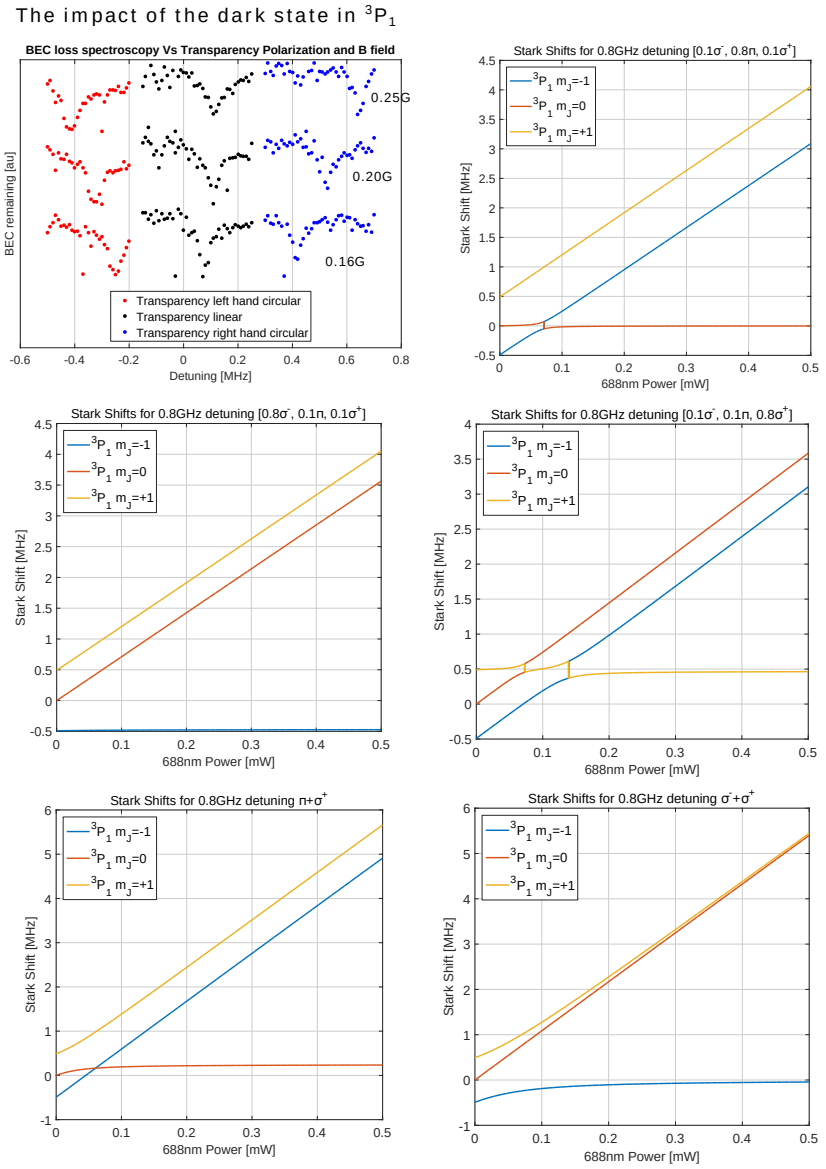

FIGURE 4.14: **The dark state problem.** When using a $^3P_1$-$^3S_1$ transition to Stark shift the $^3P_1$ state there will always be one fine state which is not Stark shifted. (bottom) Adding beams of different polarizations (which are coherent) will not solve the problem.

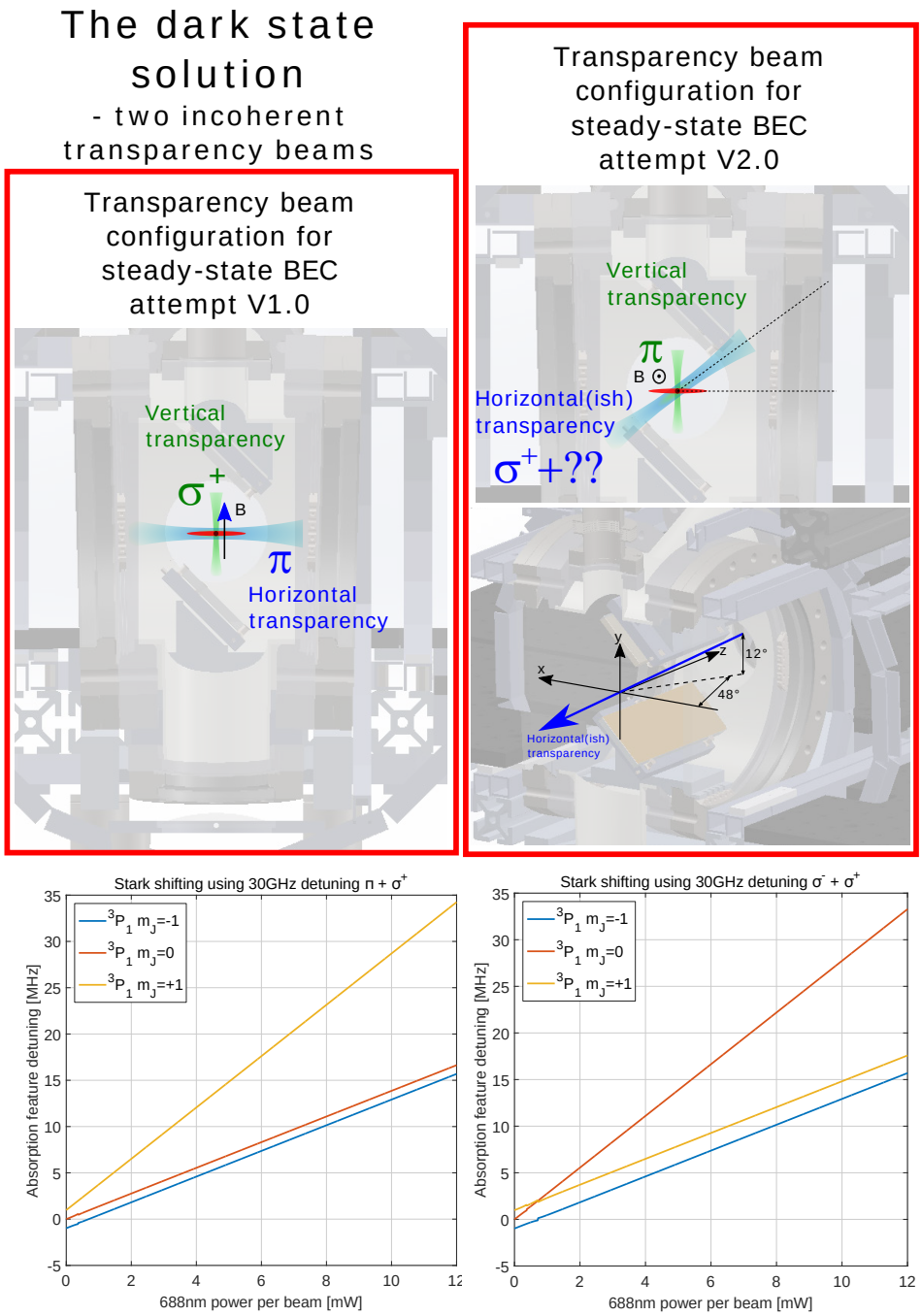

FIGURE 4.15: **The dark state solution.** Our solution to the dark state problem is to incoherently add the Stark shifts from two transparency beams with different polarizations and frequencies. Shown are the transparency beam configuration (top left) for steady-state BEC attempt V1.0 and (top right) for steady-state BEC attempt V2.0. (bottom left) The calculated Stark shifts for our targeted $\pi + \sigma^+$ transparency beam configuration. These are calculated for a 25 µm $1/e^2$ waist radius. (bottom right) The calculated Stark shifts for a $\sigma^- + \sigma^+$ transparency beam configuration, which we probably also could have used in our first attempt at BEC.

also imagine applying shifts on σ^- and σ^+. The beauty of using σ^- and σ^+ is that it could be implemented using a single beam line from a single direction with the simple addition of a polarizing beam splitter cube two add the two frequency components. In principle this could also be used to protect a copropagating waveguide, which is impractical if you need beams from orthogonal directions. We didn't think of the σ^- and σ^+ option at the time and since you need your transparency beam collinear with the magnetic field lines it isn't a configuration we can use in the current version of our system (see figure 4.15) but this would be worth revisiting if you need to protect a waveguide.

Now that we have a method for Stark shifting all the hyperfine levels without saturation, the next challenge is increasing the intensity to maximize the protection and allow further detuning of the transparency beam to reduce the scattering rate. This was done by using the transparency slave laser to seed a home made tapered amplifier (TA). More details on this system can be found in 3.7.1. A tapered amplifier has high gain and produces large amounts of amplified spontaneous emission (ASE) light. The ASE spectrum extends all the way from 688 nm to the laser transition at 689 nm and can cause substantial heating [192]. To counter this we spectrally filter the light with a Thorlabs grating (GH13-24V) as described in figure 4.12.

Rather than the ability to predict and generate Stark shifts, it is the lifetime of a BEC that matters. We measured the lifetime of a pure BEC for various levels of MOT light.

One has to be a little bit cautious when fitting BEC lifetimes as it is very easy to start counting thermal atoms if your dipole trap is deep enough to hold them. This can make your lifetime fit look fantastic. For this reason we now perform BEC lifetime measurements in a very shallow dipole trap barely able to hold a BEC against gravity so that even a single scattering event will probably eject an atom from both the BEC and the trap. The second measure we take is to fit only data corresponding to the loss of the first 50-75% of the original signal. Fitting the tails beyond this point can increase fitted lifetime measurements by 50% or more. We developed this procedure over time. If you collect your data at the same time comparisons can still be meaningful but comparing datasets is fraught with danger. When we started out we did neither of these things and simply relied on the integration region to select the BEC from the thermal atoms after a time of flight. Some great lifetime measurements were obtained this way. The opposite is true when measuring the BEC lifetime with transparency and red MOT light in a deep trap able to hold thermal atoms. Thermal atoms which remain in the trap stray out of the protection region, are heated by the MOT light and then return to slap the BEC around a little hastening its demise, usually dramatically.

Lifetime results are summarized in table 4.4. We actually went through numerous rounds of increasing powers first by adding a slave laser, then a tapered amplifier and then

TABLE 4.4: **BEC lifetime with and without protection.** The lifetime of a pure BEC in the presence of MOT light with and without transparency protection. Uncertainties are $\pm 2\sigma$ of the fitted results.

Configuration	Lifetime
Only red MOT (MOT II b configuration)	$2.5(5) \times 10^{-4}$ s
Only red MOT ($10 \times$ intensity used in [192])	$2.1(2) \times 10^{-3}$ s
Transparency[a] + red MOT (MOT II a configuration)	0.297(24) s
Transparency[a] + red MOT (MOT II b configuration)	0.438(23) s
Transparency[b] + red MOT (reduced powers[d])	0.78(10) s
Transparency[c] + red MOT (10x powers used in [192])[e]	2.49(12) s
Only blue light on	2.11(30) s[f]
No light on	2.32(37) s[g]

[a]The transparency laser had 29.5 mW on the vertical beam and 20.1 mW on the horizontal beam and was tuned to 3.11 GHz blue detuned vertical beam. The horizontal beam is 200 MHz blue detuned relative to the vertical beam.

[b]The transparency laser had 29.5 mW on the vertical beam and 20.1 mW on the horizontal beam and was tuned to 30.3 GHz blue detuned vertical beam. The horizontal beam is 200 MHz blue detuned relative to the vertical beam.

[c]The transparency laser had 18 mW on the vertical beam and 11 mW on the horizontal beam and was tuned to 3.11 GHz blue detuned vertical beam. The horizontal beam is 200 MHz blue detuned relative to the vertical beam.

[d]The powers used in red MOT IIb were reoptimized with a focus on reducing intensities rather than maximizing atom number. This was recorded with 8% power on the YMOT AOM instead of 15%. This was approximately the configuration used for single step evaporation to BEC.

[e]Illumination with single frequency optimized for in trap cooling in the configuration of [192] at 3.2 $\mu W \cdot cm^{-2}$, this was $10 \times$ the intensity used in [192]. This corresponded to 2.5% on the YMOT AOM.

by decreasing beam sizes trying to improve these lifetimes but going much beyond this point would have been very difficult and time consuming.

In the end the transparency protection that we achieved was able to increase the lifetime of a BEC in full view of the MOT beams by more than three orders of magnitude. For the configuration used in later work (see section 4.4.2) this corresponded to a lifetime of 0.78(10) s, which is only ≈30% of the background lifetime without the MOT beams. 0.78 s is a very marginal lifetime for making a BEC but the results from [192] showed the formation of a BEC in 160 ms, suggesting that it may still be reasonable for our purpose.

4.4 Steady-state BEC V1.0

The final step of our plan (figure 4.1) was to place our cold, high phase-space density MOT next to the dipole trap reservoir and gradually leak cold atoms from the MOT into the reservoir to replace atoms lost from the system. This reservoir is in thermal contact with a protected BEC and as long as we can compensate losses we should be able to maintain a BEC.

The first thing we found was that the presence of the transparency beams caused a very large (90%) loss to the MOT atom number.

4.4.1 Repump lasers

If both transparency beams are very intense and well overlapped, the probability of exciting an atom with the cooling light is small, the protection is good. But, in areas where the transparency beams do not overlap, the probability of excitation to the $^3P_1$ state can remain high even in the presence of a transparency beam. The linewidth of the transparency transition is 4 MHz, which is fast compared to the 21 µs $^3P_1$ lifetime, so many transparency photons can be scattered. Worse still, the $^3S_1$ branches strongly to the $^3P_0$ and $^3P_2$ metastable states from where atoms are effectively lost from the system. Hence the heavy losses. A solution is to include repump light on the 679 nm $^3P_0$-$^3S_1$ and 707 nm $^3P_2$-$^3S_1$ transitions to quickly return the atoms to the system.

For repump lasers we made two ECDLs again of the same design as Tim van Leent's ECDL [301] (section 3.7.1). These were assembled mostly by Chun-Chia and our second master's student Zhoumuyan Geng [302]. Like the transparency laser, they were locked to a high finesse cavity with a home made PID to prevent long term drift [216, 302]. It turned out that the 679 nm diode needed to be cooled below dew point to reach the required wavelength so a new design was partially implemented. The diodes on these

lasers degraded rapidly so slaves were built and injection locked to allow operating the diodes at a lower current while still obtaining sufficient output power from the laser system.

Although the use of repumps avoids the loss of atoms to the metastable states there is still a penalty. In the areas bordering the transparency protected region there is excess heating from atoms scattering both transparency and then repump photons. These atoms remain in the system heating it whereas without the repumps they would be mostly lost from the system and wouldn't contribute a heat load. This creates a hot zone at the edge of the protected region, increasing the effective reservoir temperature. This hot zone is large if the overlap is not good between the two transparency beams (which is inevitable given they come from different directions). It is an open question whether the heat load is significant and this partly motivates our present interest in the 487 nm repump where a single beam is sufficient.

The development of the repump lasers was also beneficial for the overall machine flux. By illuminating our 2D blue MOT with repump light (20 mm $1/e^2$ waist radius with 1 mW of 679 nm and 1 mW of 707 nm) we are able to improve our flux by around 30%[11]. Other groups have reported much higher flux improvements from the addition of repumps [107, 313]. This is most likely because the atoms in our machine only spend a very short time in the 2D blue MOT[12] compared to typical machines.

After a several month detour down repump lane, we returned to the task of coupling atoms from a steady-state MOT to replenish the reservoir of our dipole trap.

Cleaning

The first thing we found was that it is actually quite challenging to detect a very small BECs from within a large thermal cloud looking at the time of flight expansion images. But, this is exactly what a successful result would look like. We got to know the threshold parameters quite precisely when the machine was very stable and trained ourselves to tell the signs of BEC by operating at the threshold of BEC and playing games like "BEC or no BEC" with the machine operator knowing the ground truth. An example of a small BEC on a strong thermal background can be seen in figure 6.11.

A way to improve matters is to use a "cleaning pulse" as part of the imaging sequence [192]. The idea is that immediately prior to imaging you turn off your cooling light, protect the atoms in the dimple with transparency and then accelerate the atoms in the reservoir/sheet dipole trap with a flash of intense red MOT light (in the vertical axis). This pushes the atoms outside the protected dimple region from the reservoir while ideally leaving the dimple and any BEC untouched. After waiting a time for the pushed

[11] Using the 448 nm repump improved this to 50% but that was only tested recently [244].
[12] We measure a 15 ms 1/e loading time for our 2D blue MOT.

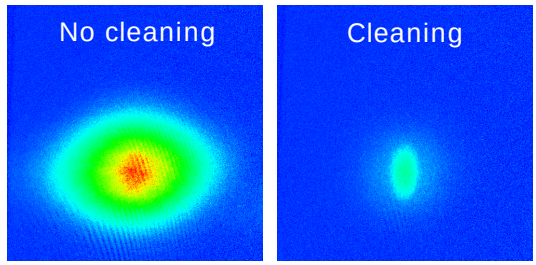

FIGURE 4.16: **The cleaning pulse.** In order to distinguish a small BEC from a large thermal cloud we found it valuable to apply a cleaning pulse as part of the imaging sequence (see [192]). This would kick atoms not protected by the transparency beams in the vertical direction separating the reservoir from the comparatively small proportion of atoms contained within the dimple. This removes much of the thermal noise improving the ratio of BEC to thermal atoms and thus the signal to noise ratio of the final image. We had a much smaller reservoir than was used in [192] so the improvements we see when we repeat the experiment of [192] are far less dramatic, therefore I have used data from [192] to illustrate this technique.

atoms to clear the field of view time-of-flight imaging can be performed. An example of the improvement possible from applying this cleaning technique is illustrated in figure 4.16.

If you take a system and you eject the hot atoms from the reservoir then you have potentially performed a one step evaporation sequence (if the time scales are long enough to allow thermalization). This is something you need to be careful of when using cleaning as this would not be steady-state. But there is a second effect, at the border of the protected region thermal atoms will be heated but not enough to escape the trap. These atoms remain trapped increasing instead of decreasing the temperature you will measure of the thermal cloud. In our case we have a large area with poor protection where the two transparency lasers are not overlapped and these areas can be heated noticeably. We actually found this second effect dominated, yet the ability to remove a large number of thermal atoms to improve our signal to noise ratio remained useful.

The cleaning sequence[13] that we tended to use was:

1. Switch off all laser cooling light.
2. Illuminate the sample with a 10 ms long pulse of single frequency blue detuned MOT light in the vertical upwards direction (we only had a single vertical MOT beam) at several I_{sat}. The frequency was adjusted to maximize the heating rate in order to evaporate the thermal atoms from the reservoir with the shortest possible illumination time. This is the same illumination time as was used in [192].
3. Turn off the vertical cooling laser

[13] Also referred to as "purification".

4. Wait 0-40 ms, typically 40 ms. This allowed time for the atoms to vacate the field of view of the camera. Without the wait time you will see a second cloud corresponding to the thermal atoms blown out of the dipole trap[14]. In [192] the wait time used was 25 ms, they also turned off their transparency lasers during the wait but we never saw any difference with them off or on.
5. Time-of fight absorption imaging sequence.

It is worth stressing that any final result would need to produce a BEC large enough to be observed in the presence of the full thermal background cloud, otherwise it would be hard to argue it is truly a steady-state BEC. That said, this technique remains a useful tool to help us get there.

4.4.2 Sitting on the edge of BEC

There were two general directions from which we approached the problem of going from a working pulsed system to a steady-state system. Given a steady-state MOT and a dipole trap, we know how to ramp the fields, laser powers and laser frequencies to make a (pulsed) BEC. One way to approach making a steady-state BEC is to adjust the parameters of the steady-state MOT and the dipole trap ramp parameters to try to make them as close as possible, minimizing this gap. If the gap can be eliminated we have a steady-state BEC.

The closest we got to steady-state operation was a single step change in our parameters (turn off the MOT light) to form a small BEC when we placed our steady-state MOT on top of the reservoir trap. Interestingly, we did not need to change any of the dipole trap powers and yet we could still make small BECs. The results are summarised in figure 4.17 (B) along side time-of-fight images of BECs of varying purities in this trap configuration in figure 4.17 (C).

A twist on this approach was the 'dual MOT'. By using multiple frequency components on our MOT beams we aimed to make a cold inner MOT together with a higher power outer MOT to recycle and capture atoms. The objective was to reduce the temperature of the inner MOT as far as possible by minimizing the power the cold atoms see and thus reducing the scattering rate to a bare minimum necessary in order to support them against gravity. By having a second higher intensity (frequency red detuned) outer MOT we can also recapture and recycle any atoms that fall through the weak inner MOT and greatly increase our capture velocity. While an interesting idea, we never saw improved results when we had two distinct and separated clouds of atoms forming a dual MOT. As the frequency gap between the inner and outer MOTs becomes small we end up with a single

[14] If we had a red beam pointing downwards the blown away atoms would always be below the signal cloud but because we kicked them up they would fall back and interfere with our signal without this wait.

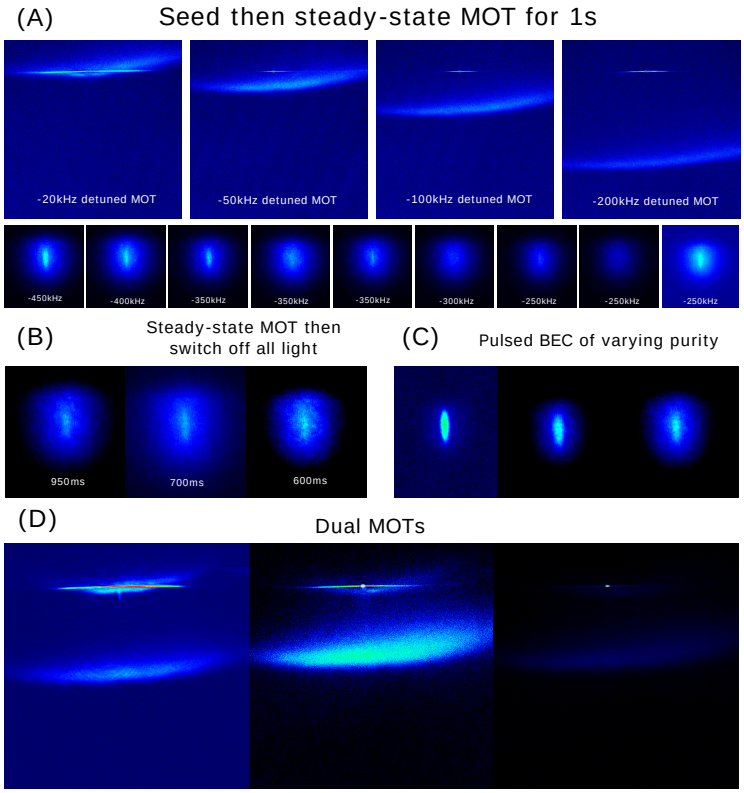

FIGURE 4.17: **Steady-state BEC attempt V1.0 results.** Results from our first attempt to make a steady-state BEC. (A) Load the reservoir in a pulsed mode and evaporate to degeneracy with a large thermal cloud then turn the machine to run a steady-state red MOT configuration for 1 s and see if we still have a BEC as a function of the detuning of the MOT. The top row contains in-situ images at the end of the sequence while the bottom row contains time-of-flight expansion images to check for the presence of a BEC. For large detunings the BEC survives, but for smaller detunings it usually melts. The right most image showing the results with a 250 kHz detuning was taken at the very end of our optimization work and was the closest we got to a steady-state system in this architecture. The in-situ images show that even with a detuning of 250 kHz there is no coupling of atoms into the reservoir. This indicated that the origins of our problems lay with the light as there was no thermal contact between the MOT atoms and the BEC. The number of atoms in the reservoir is difficult to reliably control yet this is very important to the outcome. A pure BEC will survive a long time as there are no thermal atoms in the reservoir to absorb resonant light while a system with a large quantity of thermal atoms will rapidly melt as unprotected atoms absorb and scatter MOT light and then transfer this heat to the BEC. It is possible that the variation that we see with a detuning of 250 kHz might be substantially due to variations in the number of reservoir atoms. (B) Time-of-flight expansion images are shown for a system in which a steady-state MOT is operated and then the light is switched off for a specified period of time but the dipole traps are left unchanged. These results are not clear, but they do show signs of the presence of BEC. (C) BECs of varying purity created using a pulsed sequence ending with a ramp to the same dipole trap configuration as was used in (B). (D) Dual MOTs supporting a low intensity inner MOT with a small detuning from the reservoir trap and an outer, high intensity MOT with a large detuning. The idea was that the outer MOT would capture and recycle atoms which can't be caught or which are lost from the inner MOT but we never found it to help with the performance of the inner MOT.

MOT that is indistinguishable from the "spectrally dark" MOTs we discussed and use to improve the performance in our high phase-space density MOT (section 4.1.2). Some results showing dual MOTs are included in figure 4.17 (D).

A second (related) angle from which we tried to approach a steady-state BEC was to create a BEC with parameters as close as possible to those of a steady-state MOT using the results of the "reduce the gap" or the laser cooling to degeneracy approach [192]. We then switch back to parameters closer to the MOT and see if we can extend the lifetime of the BEC by replenishing the depleted reservoir. The idea was that the process might be assisted by starting with a collisionally dense sample able to rapidly thermalize with new atoms in the reservoir and by beginning with a BEC we would begin with a strong Bose enhanced scattering within the reservoir. Results from this approach are shown in figure 4.17 (A). We found that if we detuned the MOT by a large frequency the lifetime of the BEC would be long whereas for detunings smaller than ≈200 kHz, maybe 350 kHz the BEC would melt rapidly. For such large detunings there was essentially no coupling of atoms from the MOT to the reservoir as indicated by the in-situ absorption images at the top of figure 4.17 (D). We also found that the survival time of the seed BEC depended critically on the number of thermal atoms in the reservoir. A pure BEC survived for times on the order of 1 s while systems with lots of thermal atoms in the reservoir had a lifetime that depended on the detuning of the steady-state MOT beams.

We found that in all cases the introduction of atoms to the dipole trap sheet reservoir (outside the laser protected region) leads to a reduction in the lifetime of the seed BEC.

4.4.3 Discussion

There is a minimum laser spectral intensity required for a MOT to support atoms against gravity. This minimum power level is much larger than that which was used in the Innsbruck experiment for applying the tiny amounts of laser cooling needed to demonstrate "laser cooling to degeneracy" [192]. The configuration used at Innsbruck (which we are able to repeat in our machine) does not require atoms to be captured or supported against gravity. Applying MOT laser light to atoms loaded in the reservoir (outside the protected region) heats rather than cools atoms. This problem is relieved slightly by the 50 kHz Stark shift in the dipole reservoir trap which pushes the transition frequency to the blue in the trap. If the MOT detuning is moved further red the heating rate is reduced but the MOT location moves away from the dipole trap and loading rates are reduced.

This was the core of the problem. To reduce the temperature in the reservoir the MOT lasers need to be either too weak to support atoms against gravity or too far detuned for the MOT to load into and couple with the dipole trapped reservoir.

The consequences of this problem are nicely demonstrated by looking at the lifetimes of a pure BEC compared to one with a surrounding thermal cloud. A protected pure BEC has a long lifetime ($\approx$1 s) even in the presence of a MOT beam while a BEC that has a surrounding thermal cloud extending beyond the protected region will melt rapidly. This is because the thermal atoms will be heated by the MOT light and then transfer the heat by elastic collisions to the protected region, thereby evaporating the BEC. Atoms transferred from the MOT to the dipole trap reservoir will also add a heat load but this is secondary and rapid melting occurs even with a negligible input flux.

There are at least two approaches that could be used to detune the atoms in the reservoir relative to the MOT, a Stark shift and a Zeeman shift.

If we could significantly increase the MOT magnetic field gradient we might be able to maintain physical proximity between the MOT and the reservoir while increasing the laser detuning. This might enable refilling from the MOT without the MOT lasers excessively heating the atoms in the reservoir. However, implementing this in our machine is not very practical. Increasing gradients would severely impact the operation of our steady-state red MOT where gentle gradients are essential for the red Zeeman slower to work. We also have long distances to the coils and the chamber edge so it is not realistic to try to locally change the gradients in the current design. These are not fundamental problems, they could be engineered away but they are road blocks for the built machine.

A second approach might be to Stark shift the reservoir dipole trap by choice of a reservoir trap wavelength. How well this might work is not at all clear. Usually we want to make our traps magic to minimize the Stark shifts in our trap, so that we can efficiently cool across the entire trap. This would do the opposite. Any light that efficiently cooled atoms in the center of the trap would be strongly blue detuned for atoms further out or in the MOT. Such a system would therefore need to rely on evaporation to cool atoms in the trap, a significant departure from the original plan.

A different approach is to try to improve laser cooling at high density to make the reservoir colder. One could implement ideas from degenerate Raman sideband cooling and cooling in deep lattices. Work from the 90s demonstrated improved phase-space densities of two orders of magnitude over conventional approaches [196–199, 314, 315]. More recently this approach has been shown to cool ^{87}Rb all the way to degeneracy [202]. Implementing this in our system is not a trivial matter. The schemes demonstrated capture atoms in a lattice and restrict their movement so it is not obvious how this should be translated to a continuous flow architecture. Again this approach would represent a major departure from our original plan with a highly uncertain outcome.

We have no definitive reason to believe that this approach can't in principle work, but, implementing these approaches on our current machine might open a Pandora's box of

challenges with an uncertain outcome so we looked at other configurations.

4.5 Summary

In this work we achieved the highest ever steady-state phase-space density in an ultracold atomic system. We improved the phase-space density of steady-state MOTs by more than two orders of magnitude. We show that we can protect a BEC even under intense resonant red light with lifetimes of 1 s and we showed we could protect a BEC from scattered resonant blue light. We can hold and protect a BEC within 2 mm of a steady-state red MOT and in full view of the MOT light. Our 9 month campaign pursuing this first architecture achieved numerous firsts but for the ultimate goal of a steady-state BEC, a new edition of the architecture was needed.

Chapter 5

A Steady-State MOT with 100 fold improved Phase Space Density

Physical Review Letters, Vol. **119**, 223202, (2017)[207]

Shayne Bennetts, Chun-Chia Chen, Benjamin Pasquiou*, and Florian Schreck

Van der Waals-Zeeman Institute, Institute of Physics, University of Amsterdam, Science Park 904, 1098XH Amsterdam, The Netherlands

We demonstrate a continuously loaded ^{88}Sr magneto-optical trap (MOT) with a steady-state phase-space density of $1.3(2) \times 10^{-3}$. This is two orders of magnitude higher than reported in previous steady-state MOTs. Our approach is to flow atoms through a series of spatially separated laser cooling stages before capturing them in a MOT operated on the 7.4-kHz linewidth Sr intercombination line using a hybrid slower+MOT configuration. We also demonstrate producing a Bose-Einstein condensate at the MOT location, despite the presence of laser cooling light on resonance with the 30-MHz linewidth transition used to initially slow atoms in a separate chamber. Our steady-state high phase-space density MOT is an excellent starting point for a continuous atom laser and dead-time free atom interferometers or clocks.

Laser cooled and trapped atoms are at the core of most ultracold quantum gas experiments [12], state-of-the-art clocks [45] and sensors based on atom interferometry [13]. Today, these devices typically operate in a time-sequential manner, with distinct phases for sample preparation and measurement. For atomic clocks a consequence is the need to bridge the dead time between measurements using a secondary frequency reference, typically a resonator. This introduces a problem known as the Dick effect [44] in which the sampling process inherent to a clock's cyclic operation down converts or aliases high frequency noise from the secondary reference into the signal band, thus degrading performance [316].

Recently, a new generation of atomic clocks using degenerate atoms in a three-dimensional optical lattice has been demonstrated using Sr [26]. To reach the potential of such a clock, it will be necessary to overcome the Dick effect, which can be achieved by reducing the dead time and/or by creating vastly improved secondary references. Our steady-state MOT can lead to significant advances in both directions. It approaches the high flux and low temperature requirements needed for a steady-state clock, which would completely eliminate the Dick effect. Furthermore, our MOT is created under conditions compatible with the creation of degenerate samples or an atom laser [16, 192]. This would be the ideal source for a secondary frequency reference based on superradiant lasing, which is expected to outperform current references [38, 39, 43, 317, 318]. Our source and a future atom laser based on it might also be valuable for atomic inertial sensors [16]. Improved clocks and inertial sensors will allow tests of fundamental physics [319] or be suitable for gravitational wave astronomy [13, 46, 59, 320].

Over the years many creative approaches have honed laser cooling to produce pulsed samples of ever increasing phase-space density (PSD) [193, 195, 197, 198, 200, 206, 321–326]. Pulsed MOTs using ^{88}Sr have demonstrated phase-space densities of 10^{-2} [327] while atoms held in dipole traps recently reached degeneracy [192, 202]. Despite the exquisite performances, these techniques suffer from extremely small capture velocities. As a consequence atoms must first be captured and precooled, and thus these techniques have only been used as part of time-varying sequences.

Several continuous high PSD MOT schemes have been demonstrated mostly based on bichromatic MOTs using alkaline earth atoms [328, 329]. The most successful reached a steady-state PSD of 1.2×10^{-5} [330]. This scheme used a MOT on a broad linewidth transition to capture atoms which then leak into a metastable state cooled by a MOT on a narrow transition. Narrow-line MOTs fed by a 2D MOT or Zeeman slower on the broad transition have been demonstrated for Yb and Er although steady-state PSDs are not measured [134, 331]. Another approach is the dark SPOT MOT [113], which creates a central spatial region of reduced laser interaction. Adding a further steady-state trapping and cooling stage to a MOT can increase the PSD substantially [203, 205, 332], with a steady-state PSD of $\sim 4 \times 10^{-4}$ reached for Cr atoms at a temperature of $\sim 50\,\mu$K [205].

In this Letter, we demonstrate a ^{88}Sr MOT at a temperature of $\sim 2\,\mu$K and a steady-state phase-space density of $1.3(2) \times 10^{-3}$, two orders of magnitude higher than reported for previous steady-state MOTs [330]. Combining our MOT with techniques such as [18, 192, 203, 205, 208, 332] promises yet higher PSDs and potentially a steady-state BEC and atom laser. Our result is achieved by flowing atoms through a series of spatially separated cooling stages as illustrated in Figure 5.1. First we use the high capture velocity of the broad-linewidth, "blue", $^1S_0 - {}^1P_1$ transition (30 MHz linewidth, 461 nm wavelength) in several

stages to slow and cool atoms to mK temperatures, finishing with a 2D "blue" MOT. Next, we capture the atoms in a 3D MOT using the narrow-linewidth, "red", $^1S_0 - {}^3P_1$ transition (7.4 kHz linewidth, 689 nm wavelength), which can reach temperatures close to the recoil limit [327]. We operate the two MOTs in separate chambers to avoid heating of the 3D "red" MOT by blue photons scattered from surfaces and from fluorescing atoms in the 2D blue MOT. The transfer of atoms between chambers is ensured by two key ingredients: firstly, the atomic beam from the 2D blue MOT is collimated by a red optical molasses and secondly, the atoms are slowed in the second chamber by a hybrid slower+MOT configuration operated on the low capture velocity red transition. We show that this approach allows the red MOT to produce clouds with unprecedented phase-space densities for a steady-state apparatus. Furthermore, we show that the red MOT location is sufficiently protected to form BECs even with all the blue cooling stages operating.

The path of atoms through the setup begins with a high-flux atomic beam source adapted from our previous design [106, 107]. In brief, this source is composed of an oven similar to [282], followed by a transverse cooling stage and a Zeeman slower, both using laser cooling on the broad-linewidth blue transition. A 2D blue MOT [116, 333, 334], whose non-confining axis is oriented in the direction of gravity, is located approximately 5 cm after the exit of the Zeeman slower (see Figure 5.1a). This MOT has a loading rate of $2.66(16) \times 10^9$ ^{88}Sr atoms/s (measured by absorption imaging) and cools atoms to about 1 mK in the radial (xz) plane. To prevent atoms from escaping upward, a pair of downward propagating blue "plug" beams are placed symmetrically to each other at an 8 ° angle from the y axis, increasing the flux by around 30 %.

The high phase-space density MOT must be operated on the narrow-linewidth red transition while being protected against photons from the broad-linewidth blue transition [328]. In order to ensure such protection, we position the red MOT in a separate chamber, 41 cm below the 2D blue MOT. The two chambers are separated and baffled by a set of four stacked 1-inch absorptive neutral density filters (Thorlabs NE60A). These filters are separated by 20 mm and have an 8 mm diameter center hole allowing atoms to pass.

Upon exiting the 2D blue MOT, atoms have a radial velocity of about 0.5 m/s, an average downward velocity of 3 m/s (see Section 5.1.2), and they fall accelerated by gravity towards the bottom chamber. Radial expansion during the 185 mm drop to the bottom of the baffle section would give a transfer efficiency less than 2 %. Accelerating the atoms downward is out of the question, since we can only use the low capture velocity red transition in the bottom chamber. Instead, we radially cool atoms emerging from the 2D MOT using a 2D molasses operating on the red $^1S_0 - {}^3P_1$ π transition, which is insensitive to the spatially varying magnetic field. To compensate the Doppler broadening of the atomic transition, which is more than 100 times the 7.4 kHz natural linewidth, it is necessary to modulate

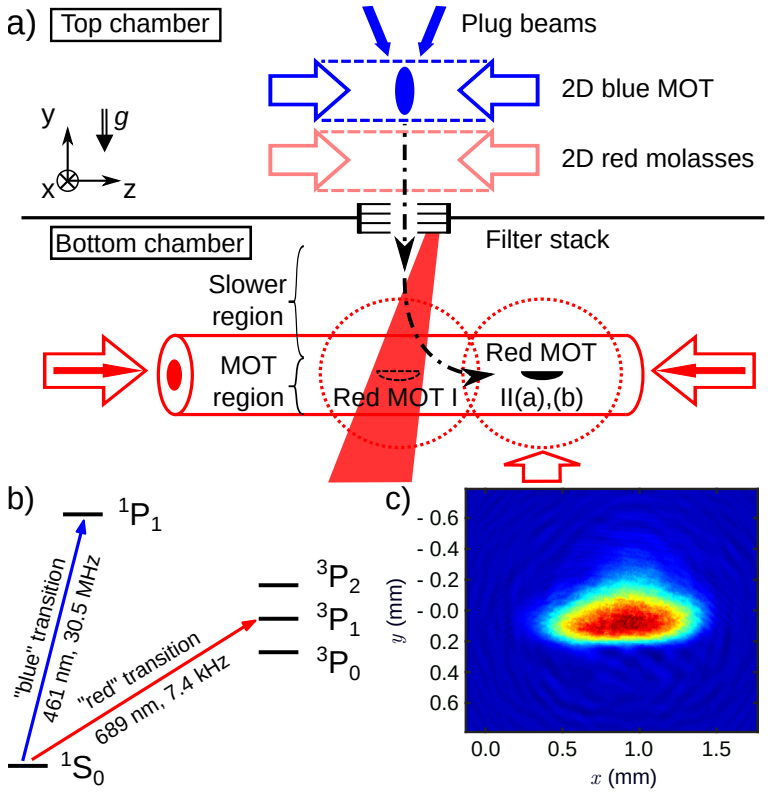

FIGURE 5.1: a) Schematic of our setup, showing the main cooling stages, and the position of the three "red" MOT configurations (see text). b) Electronic level scheme of strontium, with the "blue" and "red" transitions used for laser cooling. c) In situ absorption picture of a steady-state ^{88}Sr MOT with a PSD of $1.3(2) \times 10^{-3}$ (Red MOT II(b) configuration).

the frequency of the molasses laser beams forming a frequency comb spanning from 30 to 750 kHz to the red of the transition, with 25 kHz spacing [106]. This technique is used on all our red-transition laser beams. To prevent the two red $^1S_0 - {}^3P_1$ σ transitions towards the $m_{J'} = \pm 1$ states from hindering the radial slowing process, we produce a Zeeman shift of about 3 MHz by applying a bias magnetic field of 1.4 G in the vertical direction. Such a small field doesn't disturb the operation of the 2D blue MOT. This molasses reaches steady state after a few 10 ms, easily provided by four horizontal molasses beams with $1/e^2$ diameters of 45.6 mm along the y axis.

After a 41 cm fall from the top to the bottom chamber, the atomic beam has a measured downward velocity distribution peaked at 4 m/s. Our protection scheme necessitates slowing and capturing these falling atoms using only the red transition. However, the small scattering rate on this line allows a maximum deceleration of only $\sim 16\,g$, where g is earth

acceleration. To overcome this extreme limitation we implement a hybrid slower+MOT.

Our first hybrid setup configuration labeled "Red MOT I" (see Figure 5.1a) uses a magnetic quadrupole field centered 23 cm directly below the bottom baffle between chambers. The gradients are (0.55, 0.35, 0.23) $\mathrm{G}\cdot\mathrm{cm}^{-1}$ in the (x, y, z) directions. Horizontally propagating laser beams in the x, z axes are placed in a MOT configuration and provide radial cooling and confinement. On the y axis, a single, upward propagating beam is used, with circular polarization as needed for the MOT. Due to the weakness of the transition this upward propagating beam and gravity are sufficient to confine atoms in the vertical direction without a downward propagating MOT beam [335]. The vertical beam is directed slightly to the side of the baffle onto the lowest neutral density filter, to prevent it from affecting the cooling processes in the top chamber. This beam is converging to exert a restoring force towards the beam center during the slowing process [336].

Upon reaching the second chamber, atoms enter the region illuminated by the circularly-polarized upward-propagating beam, whose frequency is set to the red of the $^1\mathrm{S}_0 - {}^3\mathrm{P}_1$ transitions. We now describe the slowing process using an upward pointing quantization axis, see Figure 5.2a. The Doppler shift $\delta_{\mathrm{Doppler}}(v)$ of atoms with a downward velocity v brings them into resonance with the σ^+ transition from $^1\mathrm{S}_0$ to the state $m_{J'} = +1$ of $^3\mathrm{P}_1$. As radiation pressure slows atoms down, $\delta_{\mathrm{Doppler}}$ diminishes, which is partially compensated by the spatial variation of the magnetic field, following the principle of a Zeeman slower. The narrow linewidth of the red transition does not allow for a slowing process robust against magnetic and laser intensity fluctuations, so we modulate the laser frequency ν_{L} with a span of $\Delta\nu_{\mathrm{L}} = 4.05\,\mathrm{MHz}$, as used for example in "white light" slowing [337]. If atoms are successfully slowed and reach the region below the quadrupole field center, $\delta_{\mathrm{Doppler}}$ is small and atoms are resonant with the laser light as in a standard broadband narrow-line MOT [327]. Note that for the experimental configurations used the angle between the local magnetic field and the beam direction can be big, leading to significant additional absorption on the π transition during the slowing process.

We numerically model this hybrid setup by evolving classical atomic trajectories, first in an idealized 1D geometry with only a linear vertical magnetic field gradient and a uniform circularly polarized vertical beam, and then using a Monte Carlo approach in a realistic 3D geometry including all beams and details of the magnetic fields (see Section 5.1.4). The behavior of a falling atom can be obtained by analyzing the deceleration it experiences in dependence of time when dropped into the slower+MOT region with various starting velocities. The idealized 1D results shown in Figure 5.2b are qualitatively confirmed by the more realistic 3D model results shown in Figure 5.2c. With these simulations we estimate a maximum capture velocity of around 6 m/s for the hybrid slower+MOT setup, which is compatible with the measured velocity distribution of the atomic beam produced by the 2D

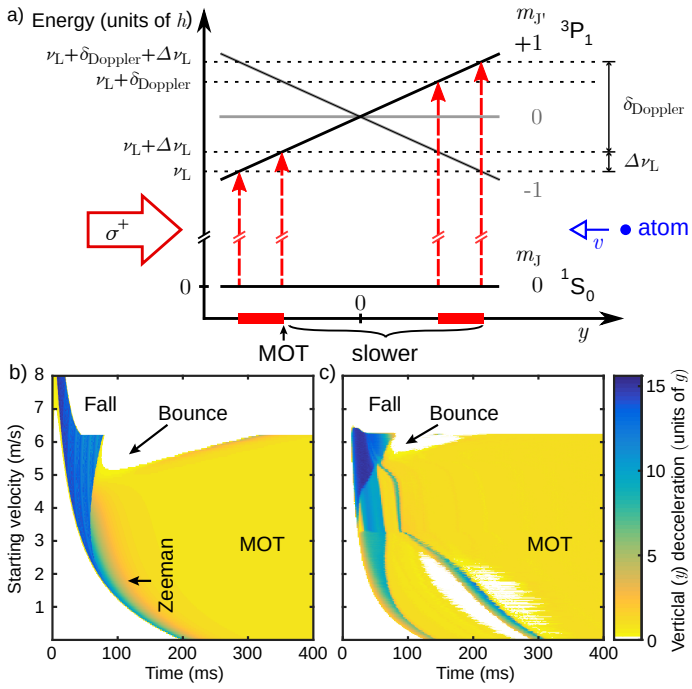

FIGURE 5.2: Working principle of the hybrid slower+MOT in Red MOT I configuration. a) Energy diagram of the $^1S_0, m_J$ and the $^3P_1, m_{J'}$ states in dependence of y for $x = z = 0$, where the coordinate origin lays in the quadrupole field center. An atom with velocity $v \neq 0$ along the y axis is addressed by the upward-propagating Red MOT I beam in a region delimited by the pair of red dashed arrows on the right. The range of this region is determined by the span of the laser frequency modulation $\Delta\nu_L$ and the magnetic field gradient. An atom with $v = 0$ is addressed in the region delimited by the pair of dashed arrows on the left. b) y deceleration from scattering of photons on the red transition (in units of earth acceleration g) in dependence of the initial velocity of atoms 20 cm above the quadrupole field center, obtained by an idealized 1D calculation. A horizontal path across the diagram corresponds to a 1D time-dependent trajectory along y. Annotations indicate regions dominated by Zeeman type slowing or red MOT type trapping. Atoms eventually captured in the MOT exhibit a time-independent non-zero force (yellow region at $\sim 1g$). The white regions show decelerations smaller than $0.25g$. The "Bounce" and "Fall" regions are undesirable cases described in (see Section 5.1.4). c) Equivalent deceleration data obtained by a full 3D Monte Carlo calculation with a realistic geometry.

blue MOT (see Section 5.1.2).

The characteristics of the hybrid Red MOT I are summarized in Table 5.1. The loading rate gives an estimated transfer efficiency of 19 % between the two chambers. Unfortunately, the high power broadband beams needed for the hybrid setup limit the PSD to $2.8(1.2) \times$

TABLE 5.1: Characteristics of the three Red MOT configurations. All uncertainties stated in this letter are taken as $\pm 2\sigma$ from the fitted data.

	Red MOT I	Red MOT II(a)	Red MOT II(b)
Flux [^{88}Sr/s]	$5.1(7) \times 10^8$	$5.3(4) \times 10^7$	$5.3(9) \times 10^6$
Temperature x	-[1]	3.7(3) µK	2.01(6) µK
Temperature y	20(5) µK	1.9(1) µK	1.42(3) µK
Temperature z	26(7) µK	2.8(2) µK	1.91(9) µK
Width σ_x	-[1]	385(4) µm	150(2) µm
Width σ_y	725(61) µm	192(3) µm	88(1) µm
Width σ_z	2086(41) µm	528(3) µm	247(3) µm
Atom number [^{88}Sr]	$2.54(10) \times 10^9$	$1.71(5) \times 10^8$	$2.5(1) \times 10^7$
Peak density [^{88}Sr/cm^3]	$5.1(7) \times 10^{10}$	$2.8(2) \times 10^{11}$	$4.8(4) \times 10^{11}$
Peak PSD	$2.8(1.2) \times 10^{-6}$	$4(1) \times 10^{-4}$	$1.3(2) \times 10^{-3}$
$1/e$ lifetime	4.53(6) s	2.8(2) s	1.95(6) s

10^{-6}, low compared to what can be achieved with a pure red MOT geometry in a time-varying sequence [327]. Moreover, with direct line-of-sight to a bright fluorescing blue MOT, this configuration does not provide protection against heating from blue photons sufficient to produce a steady-state BEC (see Section 5.1.3).

For these reasons, we implement a second MOT configuration, "Red MOT II(a)", located 3 cm in the z direction away from the Red MOT I position (see Figure 5.1a). This is achieved by adding another 5-beam geometry MOT (4 beams along x and z, 1 beam along y), whose beams make a smooth connection with the Red MOT I beams, and by displacing the center of the quadrupole field to the intersection of these new beams. Along the z axis the two additional beams are implemented as an 8 mm diameter low-intensity core within hollow 48 mm diameter Red MOT I beams. In this configuration, atoms entering the second chamber are decelerated by the hybrid slower plus Red MOT I beams, then continuously pushed to the Red MOT II(a) where they are confined and further cooled. The working principle of the hybrid setup remains unchanged, with the exception that the π transition becomes more important, since the magnetic field lines are more tilted with respect to the Red MOT I vertical beam.

Within this second red MOT, we have more freedom to adapt the beam parameters and thereby reach higher PSD. The main limitations to the PSD are firstly power broadening of the red transition effectively raising the Doppler cooling limit and secondly multiple scattering due to the high density. Both limitations recede with reduced MOT powers. For this reason, we implement a spectrally dark SPOT MOT by shaping the spectral intensity profile of our broadband MOT beams. At the steady-state MOT location, the effective scattering rate is just enough to hold atoms against gravity, while in the surrounding region

an effective high optical power captures fast atoms.

With Red MOT II(a) using the parameters given in Table 5.1, we reach a steady-state MOT with a PSD of $4(1) \times 10^{-4}$ for ^{88}Sr. The transfer efficiency from the top chamber to this MOT is 2 %, an order of magnitude lower than for Red MOT I. Simulations suggest significant losses may be attributed firstly to increased bouncing of atoms in the hybrid slower when the π transition is dominant and secondly to atom trajectories intersecting with mirrors inside the vacuum chamber.

We also produce a Red MOT II(a) using the much less abundant ^{84}Sr isotope, which is particularly suited to produce quantum degenerate gases, owing to its favorable scattering properties. This ^{84}Sr MOT contains up to $9.0(2) \times 10^6$ atoms at temperatures of 1.5(3) µK and 3.4(1.1)µK in the vertical and horizontal axes respectively. By loading this MOT into an optical dipole trap in a time sequential manner and applying a 3 s evaporative cooling sequence, we produce ^{84}Sr BECs of $3.0(2) \times 10^5$ atoms.

The protection provided by the dual chamber and baffle system against photons from the broad-linewidth blue transition is determined by comparing the BEC lifetime at the location of the Red MOT II(a) with and without the 2D blue MOT operating. The atomic flux is disabled by turning off the red transition beams during these measurements. The BEC lifetime in the dipole trap is 3.0(4) s without blue light and 2.7(2) s with blue light. Lifetimes were strongly limited by one-body collisions due to poor vacuum quality. These measurements confirm significant protection from blue photons thanks to our two-chamber design, making our system suitable for experiments aimed at developing a steady-state source of degenerate quantum gas.

Finally, “Red MOT II(b)" is a configuration designed to optimize phase-space density at the expense of transfer efficiency. This MOT reaches a steady-state PSD of $1.3(2) \times 10^{-3}$ for ^{88}Sr, which is two orders of magnitude higher than demonstrated in previous steady-state MOTs [330] (see Figure 5.1c and Table 5.1). Red MOT II(b) is the same as Red MOT II(a) except that we reduce the bandwidth of the MOT II beams to cover only -40 to -200 kHz detuning, resulting in three improvements. First, the smaller detuning of -40 kHz compresses the MOT, second, the reduced bandwidth reduces the total beam intensity required, and third, by ending the spectrum well before the photoassociation line located at -435 kHz detuning [274], we reduce losses due to molecule formation. The transfer efficiency from the top chamber to this MOT is 0.2 %, an order of magnitude lower than for Red MOT II(a). The $1/e$ lifetime of Red MOT II(b) measured after the atomic flux is suddenly stopped is 1.95(6) s, which is significantly smaller than the 4.53(6) s lifetime of Red MOT I. This reduction is due to two-body light-assisted collisions, which ultimately limits the maximum density achievable [274]. Both these losses and the need to compensate for gravity set the limits on the PSD achievable with this MOT configuration.

To summarize, we have demonstrated the operation of a MOT with a PSD of $1.3(2) \times 10^{-3}$ in the steady-state regime. This result requires the use of broad- and narrow-linewidth transitions to simultaneously achieve both high PSD and high capture efficiency. We use a dual chamber architecture to protect the MOT from heating by broad-linewidth transition photons, and efficient transfer between chambers is achieved using a hybrid slower+MOT configuration using only cooling on the narrow-linewidth transition. Although Sr is ideally suited to this architecture, our approach is broadly applicable to alkaline-earth metals, lanthanides and any other species with a strong transition to precool atoms and a weak transition supporting the operation of a MOT with a high PSD [338, 339]. Finally, we have shown that our design is compatible with the generation of quantum degenerate gases in the presence of a laser cooled influx. The use of this high-PSD source of matter, combined with a protection mechanism such as that demonstrated in [192], should allow the creation of a steady-state Bose-Einstein condensate and ultimately an atom laser with uninterrupted phase coherent output.

We thank Georgios Siviloglou for contributions during the early stages of the design and construction of the experiment. We thank the Netherlands Organisation for Scientific Research (NWO) for funding through Vici grant No. 680-47-619. This project has received funding from the European Research Council (ERC) under the European Union's Seventh Framework Programme (FP7/2007-2013) (Grant agreement No. 615117 QuantStro). B.P. thanks the NWO for funding through Veni grant No. 680-47-438 and C.-C. C. thanks the Ministry of Education of the Republic of China (Taiwan) for a MOE Technologies Incubation Scholarship. S.B. thanks the Australian Government and Nick Robins at the Australian National University for an Australian Postgraduate Award and support during the early stages of this work.

S.B. and C.-C. C. contributed equally to this work.

5.1 Supplemental Material

5.1.1 Details of the experimental setup

The atomic source is an oven producing a 10 mm diameter effusive jet of strontium atoms by heating Sr metal pieces (99.5 % from Alfa Aesar) to around 500 °C. While the oven was designed to operate at 550 °C for 18 months it is currently operated at only 500 °C as this has been found to deliver sufficient flux and will extend the operating life before needing to refill the Sr reservoir and rebake the oven section of the vacuum system. Increasing the temperature to 550 °C is expected to increase the flux by a factor of five, an important option when working with 0.5 % abundant ^{84}Sr. The oven output is collimated by an

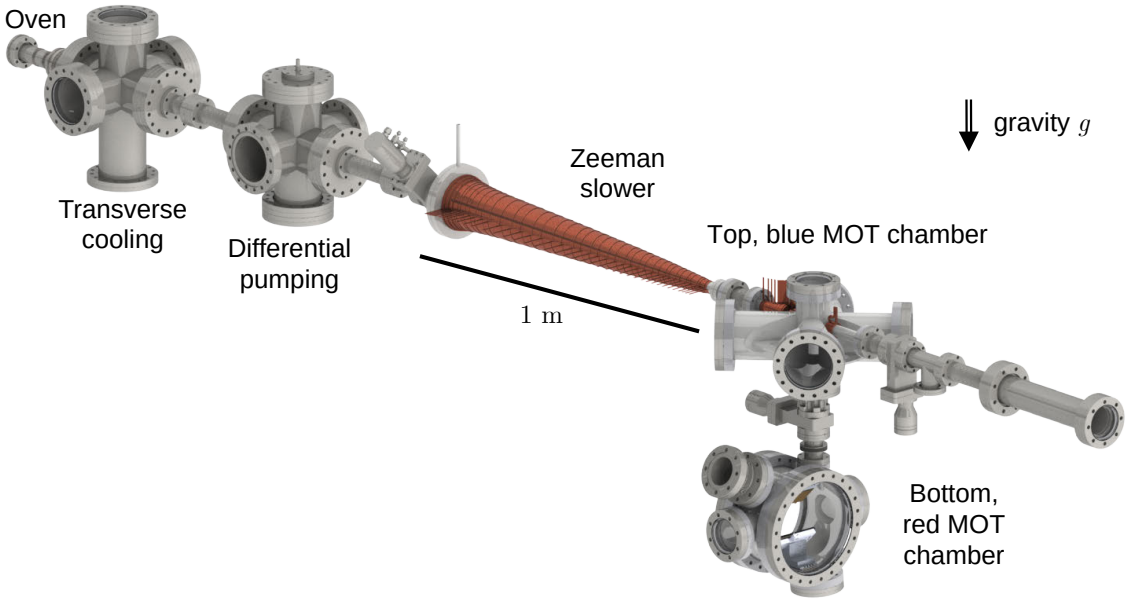

FIGURE 5.3: CAD drawing of the machine excluding vacuum pumping sections.

array of 8 mm long stainless steel microtubes with 80 µm inner diameter and 180 µm outer diameter, following a design inspired by [282]. The atoms are then transversely cooled in two dimensions over a 90 mm long region using for each axis a “zig-zag" configuration with four passes and retro-reflection of the laser beam. Finally a 105 cm long Zeeman slower, with a spin-flip design and a modeled maximum capture velocity of 500 m/s, slows the atoms to approximately 20 m/s.

The Zeeman slower output is captured by a 2D MOT using the blue 461 nm transition. The 2D MOT magnetic field gradient is created by two vertical permanent magnet arrays, facing each other with opposite pole orientation. The position and orientation of individual magnets stacked in each array can be independently adjusted to produce the desired radial gradient, which is approximately 10 G/cm in the region of the blue MOT and rapidly transitions to approximately 2 G/cm over about 15 mm. Helmholtz bias coils are used to trim the pointing and location of the 2D MOT in order to maximize capture by the 3D red MOT in the second chamber. Other details are described in the main text and illustrated in Figure 5.3. The parameters of all the beams for laser cooling on the blue transition are listed in Table 5.2. The parameters of the beams used for Red MOT I, Red MOT II(a) and Red MOT II(b) are listed in Table 5.3, Table 5.4 and Table 5.5, respectively.

TABLE 5.2: Properties of laser cooling beams using the blue $^1S_0 - {}^1P_1$ transition.

Beam name	Detuning [MHz]	Power [mW]	$1/e^2$ diameter [mm]	Comments
Transverse cooling	-18 (-0.6Γ)	30	23×9.6	Beam is passed 4 times side by side giving a 90 mm long cooling region. Same for both horizontal and vertical axes.
Zeeman slower	-424 (-14Γ)	64	25.4	Focused to 12 mm diameter at the oven exit.
2D MOT	-25 (-0.8Γ)	10.5	22.8	4 beams with centers at the same height as the Zeeman slower axis.
Plug beams	-13 (-0.4Γ)	0.017	9.6	2 symmetric beams inclined at 8° to the vertical (y axis) and aimed at the top half of the blue 2D MOT.

TABLE 5.3: Properties of laser beams used for Red MOT I. Under "detuning" $\Delta_1 : \delta : \Delta_2$ refers to a modulated comb of lines from Δ_1 to Δ_2 with a spacing of δ.[1]

Beam name	Detuning [MHz]	Power [mW]	$1/e^2$ diameter [mm]	Comments
2D Red molasses	-0.03 : 0.025 : -0.75	4.6	45.6×18.2	2 sets of 2 counter-propagating beams, centered 38 mm below Zeeman slower plane.
Red MOT I Y	-0.95 : 0.017 : -5	10.8	68	Waist given 22 cm below the quadrupole center. Beam focused on the bottom baffle 22 cm above the quadrupole center at $z = +10$ mm from the central axis of the falling atomic beam.
Red MOT I X	-0.7 : 0.015 : -3	3.3	47	2 counter-propagating beams
Red MOT I Z Outer	-0.7 : 0.016 : -3	1.14	48	2 counter-propagating beams with an 8mm hole to allow Red MOT I Z Inner beams to pass.
Red MOT I Z Inner	-0.73 : 0.017 : -1.1 -1.1 : 0.019 : -3.5	0.16[1]	8	2 counter-propagating beams

TABLE 5.4: Properties of laser beams used in the apparatus for Red MOT II(a). Under "detuning" $\Delta_1 : \delta : \Delta_2$ refers to a modulated comb of lines from Δ_1 to Δ_2 with a spacing of δ.

Beam name	Detuning [MHz]	Power [mW]	$1/e^2$ diameter [mm]	Comments
2D Red molasses	-0.03 : 0.025 : -0.75	4.6	45.6 × 18.2	2 sets of 2 counter-propagating beams, centered 38 mm below Zeeman slower plane.
Red MOT I Y	-0.5 : 0.017 : -4	10.8	68	Waist given 22 cm below the quadrupole center. Beam focused on the bottom baffle 22 cm above the quadrupole center at $z = +10$ mm from the central axis of the falling atomic beam.
Red MOT I X	-0.7 : 0.015 : -3	3.3	47	2 counter-propagating beams
Red MOT I Z Outer	-0.7 : 0.016 : -4	1.14	48	2 counter-propagating beams with an 8mm hole to allow Red MOT II Z Inner beams to pass.
Red MOT II Z Inner	-0.1 : 0.017 : -0.25 -0.26 : 0.015 : -2.85	0.063[1]	8	2 counter-propagating beams
Red MOT II Y	-0.1 : 0.016 : -0.25 -0.26 : 0.014 : -2.85	0.43[1]	36	1 upward-propagating beam
Red MOT II X	-0.1 : 0.017 : -0.25 -0.26 : 0.013 : -2.85	0.099 [1]	28.8	2 counter-propagating beams

TABLE 5.5: Properties of laser beams used in the apparatus for Red MOT II(b). Under "detuning" $\Delta_1 : \delta : \Delta_2$ refers to a modulated comb of lines from Δ_1 to Δ_2 with a spacing of δ.

Beam name	Detuning [MHz]	Power [mW]	$1/e^2$ diameter [mm]	Comments
2D Red molasses	-0.03 : 0.025 : -0.75	4.6	45.6 × 18.2	2 sets of 2 counter-propagating beams, centered 38 mm below Zeeman slower plane.
Red MOT I Y	-0.5 : 0.017 : -4	10.8	68	Waist given 22 cm below the quadrupole center. Beam focused on the bottom baffle 22 cm above the quadrupole center at $z = +10$ mm from the central axis of the falling atomic beam.
Red MOT I X	-0.7 : 0.015 : -3	3.3	47	2 counter-propagating beams
Red MOT I Z Outer	-0.7 : 0.016 : -4	1.14	48	2 counter-propagating beams with an 8mm hole to allow Red MOT II Z Inner beams to pass.
Red MOT II Z Inner	-0.04 : 0.017 : -0.2	0.016	8	2 counter-propagating beams
Red MOT II Y	-0.04 : 0.016 : -0.2	0.09	36	1 upward-propagating beam
Red MOT II X	-0.04 : 0.017 : -0.2	0.026	28.8	2 counter-propagating beams

5.1.2 Velocity distribution from the 2D Blue MOT

The atoms exiting the Zeeman slower enter the 2D MOT region. Due to the broad linewidth of the blue transition, they are rapidly cooled to about 1 mK in the radial direction, but are presumably unaffected in the 2D MOT, vertical axis. The velocity distribution along this axis depends mostly on the oven output collimation, the transverse cooling stage, and the transverse spread due to scattering from the Zeeman slower beam. This last contribution amounts to about 5×10^4 spontaneously emitted photons, which gives an energy increase in the slower transverse direction of $\sim 15\,\mathrm{mK}$, part of which will affect the vertical velocity distribution.

Aiming to measure the vertical velocity distribution, we place two cylindrical 4 mm $1/e^2$-diameter high by 16 mm $1/e^2$-diameter wide "gate" beams in the top chamber, which are actuated by fiber coupled acousto-optic modulator "switches" and centered 40.8 mm and 70.8 mm below the plane of the Zeeman slower. Each beam uses approximately 2 mW of light resonant with the blue transition to "blow away" any atoms attempting to travel to the bottom chamber. By sequentially opening these blocking beams a known velocity class can be selected. We find that opening any one beam for less than 5 ms (with the other beam off) results in no atoms transmitted to the lower chamber, so we use a 6 ms gate opening time resulting in an effective opening time of 1 ms. Atoms are collected in Red MOT I and then compressed by ramping up the gradient and decreasing the detuning to give a cloud dense enough to reliably measure the atom number using absorption imaging. By scanning the time between the opening of the two gate beams, we measure the velocity distribution of the atomic beam emanating from the top chamber that is capturable by Red MOT I, see Figure 5.4.

5.1.3 Heating from blue MOT photons

We now estimate the heating of Red MOT I by the scattering of fluorescence photons from the 2D blue MOT. The minimum scattering rate from atoms in a red MOT that is required to counter acceleration due to gravity is $\gamma_{\mathrm{min}} = mg/\hbar k$, where m is the atom mass, $\hbar$ is the reduced Planck constant and k is the photon wavenumber. Considering a blue transition photon scattering rate of 20 % of γ_{min} as acceptable, we can estimate the maximum allowable intensity of the blue photon flux at the location of the red MOT, $I_{\mathrm{max}} \approx 0.2 \times 2\gamma_{\mathrm{min}} I_{\mathrm{sat,blue}}/\Gamma_{\mathrm{blue}} \approx 0.13\,\mu\mathrm{W}\cdot\mathrm{cm}^{-2}$, with $I_{\mathrm{sat,blue}}$ and Γ_{blue} being the saturation intensity and the natural linewidth of the blue transition, respectively. Our blue MOT with optical frequency ν_{blue} has a flux of $F \approx 2.5 \times 10^9$ atoms/s and atoms spend around $t_{\mathrm{blue}} \approx 20\,\mathrm{ms}$

[1] Note that due to nonlinearities in the amplifiers and AOMs, it is not possible to separately measure the optical powers in each component of the spectrum.

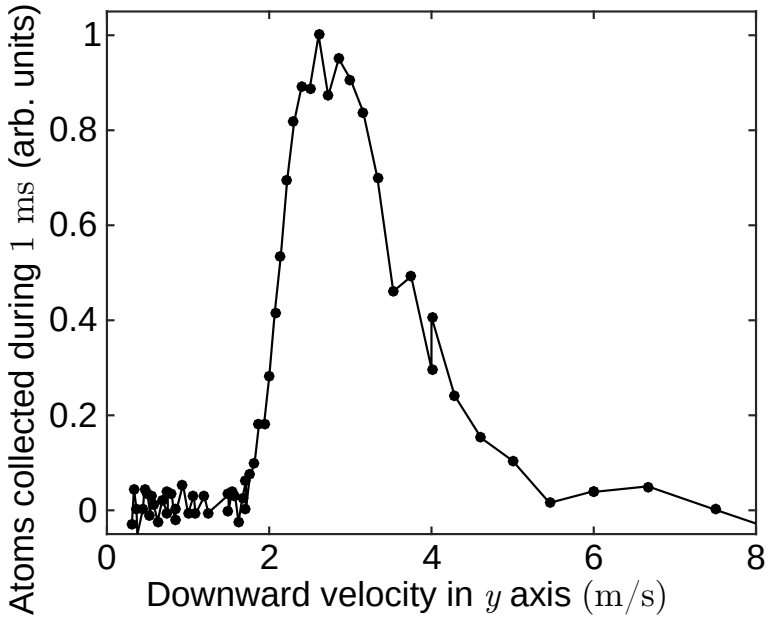

FIGURE 5.4: Velocity distribution of the atomic beam emitted downward by the blue 2D MOT and captured by Red MOT I, given for atoms located 55 mm below the plane of the Zeeman slower.

passing through the blue MOT. The intensity of the blue MOT light is $I_{\mathrm{MOT}} \approx I_{\mathrm{sat,blue}}/4$. The power scattered by the 2D blue MOT is thus $P = F t_{\mathrm{blue}} h\nu_{\mathrm{blue}} \Gamma_{\mathrm{blue}}/2\, I_{\mathrm{MOT}}/(I_{\mathrm{sat,blue}}(1 + I_{\mathrm{MOT}}/I_{\mathrm{sat,blue}})) \approx 4.1 \times 10^{-4}$ W. If we ignore all other sources of blue transition photons such as scattering off the chamber surfaces and windows, and consider only scattered light from the 2D MOT atoms, we need a minimum distance r of $r > \sqrt{P/(4\pi I_{\mathrm{max}})} \approx 16$ cm to reduce heating in the red MOT to an acceptable level. For the production of a degenerate gas where we require a scattering rate below 1 Hz for a reasonable lifetime, the corresponding distance is $r > 2.8$ m. This effectively requires there be no line of sight between a BEC and the 2D blue MOT, or any surface scattering light from the blue MOT, which dictates our apparatus design.

5.1.4 Numerical model results

We now describe the behavior of the hybrid slower+MOT setup, based on our numerical simulations. The results for the 1D idealized situation have already been presented in Figure 2b of the Letter and the 3D Monte Carlo simulations are shown in Figure 2c of the Letter and Figure 5.5. The 3D simulations begin with atoms released from the center of the aperture in the bottom baffle approximately 20 cm above the quadrupole field center

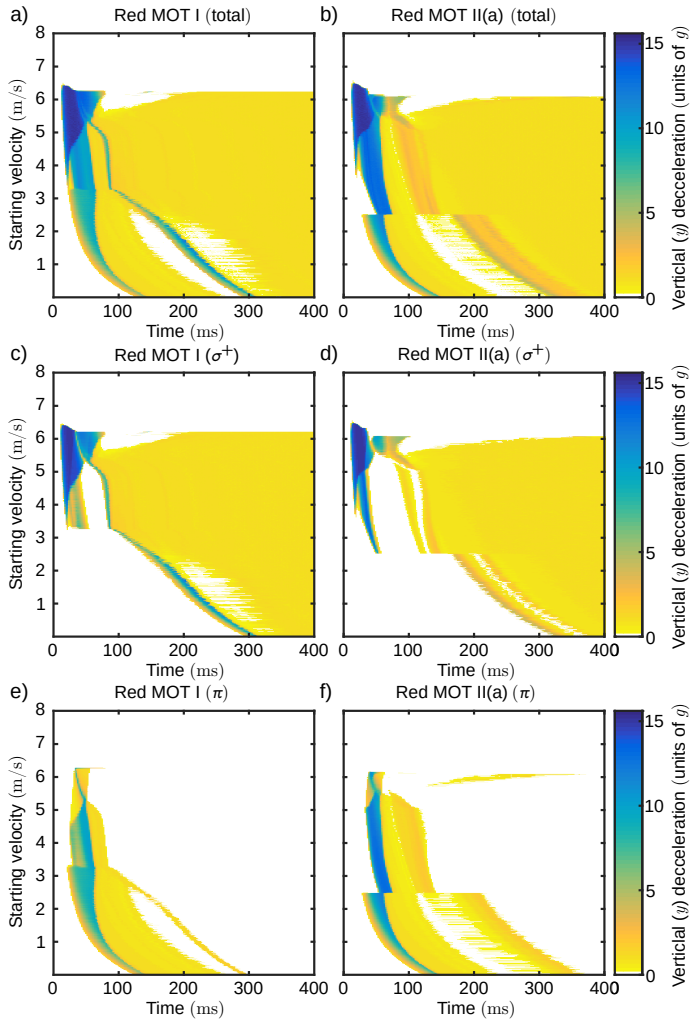

FIGURE 5.5: Monte Carlo numerical simulations of the hybrid slower+MOT. In these simulations, atoms start to fall from the center of the bottom baffle between the chambers, approximately 20 cm above the quadrupole center in the case of Red MOT I, with only a downward, y velocity component, which is indicated on the vertical axis. The horizontal axis corresponds to time during 1D trajectories along y. (left) Scattering in the Red MOT I configuration and (right) scattering in the Red MOT II(a) configuration. (a-b) Total scattering rate (in units of gravity g), (c-d) scattering from the σ^+ (MOT and Zeeman) and (e-f) scattering from the π (non magnetic) components separated. The white regions show decelerations smaller than $0.25g$.

in the case of Red MOT I, and with only a y velocity component. The atoms are then allowed to fall under gravity and experience radiation pressure from the various laser

beams and heating from spontaneous emission. Spontaneous emission heating is modeled as a lumped impulse in a random direction proportional to the root of the net radiation impulse absorbed.

In the idealized case, for a low starting velocity 20 cm above the quadrupole field center (below 5 m/s), the falling atoms first experience a Zeeman slower-like deceleration on the σ^+ transition with a scattering rate close to $\Gamma_{\mathrm{red}}/2$, where Γ_{red} is the natural linewidth of the red ${}^1\mathrm{S}_0 - {}^3\mathrm{P}_1$ transition. This scattering rate corresponds to a deceleration of about $16\,g$ (blue-colored region in Figure 2b of the letter). As atoms keep decelerating, the Doppler shift $\delta_{\mathrm{Doppler}}$ diminishes and a combination of the Zeeman effect and the broadening $\Delta\nu_{\mathrm{L}}$ of the laser beam frequency dictates the scattering rate at each spatial location. Eventually atoms are almost at rest in the vertical direction and $\delta_{\mathrm{Doppler}}$ becomes negligible. Atoms thus behave like in a standard broadband MOT, and they reach the height where the radiation pressure compensates exactly gravity, typically at the top of the spatial region addressed by the broadband MOT (yellow-colored region labeled “MOT" in Figure 2b and c of the letter). These atoms are thus captured in the MOT.

For medium starting velocities (between 5 and 6.2 m/s in the idealized case) the atoms' scattering is saturated for most of the time, until atoms are stopped in the vertical direction. This happens at a location deep within the region addressed by the broadband MOT. As a consequence, the scattering rate is way more than what is necessary to compensate gravity, and the hybrid setup acts as a spring and makes the atoms bounce up (see region labeled “Bounce" in Figure 2b and c of the letter). The relatively weak gravitational force is the only mechanism to push them downward. The simulations indicate that most atoms having bounced will then fall back into the MOT region and get captured there, provided they do not reach surfaces of the vacuum chamber. The horizontal confinement provided by Red MOT I X and Z beams is instrumental to this purpose.

For high starting velocities (above 6.2 m/s in the idealized case), the saturated scattering is insufficient to provide enough deceleration for the atoms before they reach the bottom of the spatial region addressed by the broadband MOT, and they are not captured (region labeled “Fall" in Figure 2b and c of the letter).

The main difference between the idealized case and the more realistic 3D simulation results is the influence of the π transition. Due to the tilted magnetic field orientation with respect to the hybrid vertical slower beam, a large part of the interaction occurs on the non-magnetic π transition and the σ^+ Zeeman slower-like transition is less important, as shown in Figure 5.5. Moreover, two main extra features appear in the results of the 3D simulations. The first is the disappearance of scattering for starting velocities above 6.5 m/s, which limits the maximum capture velocity. This originates from the Red MOT I vertical beam frequency boundaries, in combination with its location. Indeed, because of the tilt we

apply to the beam in order to hit the side of the bottom baffle, the fastest atoms enter the beam location only after having passed the spatial region where the light is on resonance with the slowing transitions, and thus they are never decelerated. The second feature is the kink in scattering rate appearing for starting velocities of 3.2 m/s for Red MOT I and 2.5 m/s for Red MOT II(a). This arises when atoms enter the vertical slower beam with a velocity smaller than the minimum velocity addressed by the σ^+ transition but within the frequency range of the π transition. In this case atoms are slowed entirely by the π transition before falling at the maximum velocity allowed by the π transition into the MOT region.

Chapter 6

V2.0: Trapped in a cold dark place

The take home message from our first attempt at making a steady-state BEC was that if MOT light is intense enough to hold atoms against gravity, it heats rather than cools dense atoms loaded in a reservoir dipole trap. To solve this conundrum our second architecture aimed to eliminate the need for intense MOT light in the vicinity of a BEC. Instead, we would remotely load atoms from a MOT into a dipole guide trap and shuttle them over to a dark place where they can be gently laser cooled hopefully eliminating our laser heating problem. A schematic of the plan for our second architecture is illustrated in figure 6.1.

Some readers will immediately recognize that this plan looks like it might also be suitable for cooling by evaporation from a guide [170, 172, 185, 188]. This is true but there are several issues like the inability to protect the atoms along this guide from resonant light and a perhaps inadequate trapping frequency which would make the implementation here unsuitable. We will however briefly discuss our hopes (and dreams) for implementing evaporative cooling in a guide in section 8.1.1.

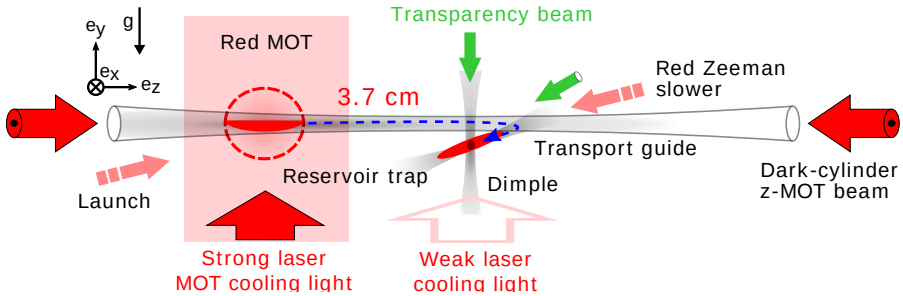

FIGURE 6.1: **Steady-state BEC (V2.0) plan.** A schematic of the plan for the second attempt at making a steady-state BEC. The objective is to load a dipole guide remotely from a steady-state red MOT and then transport the atoms along the dark guide to a dark reservoir where they can be condensed in a transparency protected dimple trap.

6.1 A guided atomic beam with high phase-space density

The first task for implementing our new architecture is finding a way to make a cold intense guided beam of atoms able to deliver atoms from a MOT to a remote site for condensation. Our concept design is to place a dipole trap guide beam through a MOT, darken the guide to protect atoms within from axial MOT light and launch atoms along the guide with a little push. Since the spatial overlap between the MOT and the guide is poor the loading efficiency might be expected to be low, but since the MOT catches and recycles atoms not loaded on any single pass, it is still possible to load high fluxes with good efficiencies. We demonstrate a beam output flux of around 30% of the total MOT loading flux even though the beam is significantly colder than the MOT from which it is loaded. This could be a powerful technique for generating high phase-space density beams for a range of applications including superradiant clock pump sources and high brightness ion beam sources[1]. We will now step through the elements described in figure 6.1 describing the details of how we made this beam and its performance.

6.1.1 Atom source

All the steady-state red MOT configurations described in chapter 5 could be used as sources of atoms from which to load an atomic beam. Their respective properties are summarized in table 4.1. Essentially the choice is one between flux and temperature. Initially we were sceptical about whether significant flux from MOT I[2] could be loaded into a dipole trap due to its relatively high 20 µK temperature. Nevertheless, this was the MOT we started with as our atom source because it was much easier than loading from MOT II. This perhaps surprising statement is because we could reuse all the imaging systems, dipole traps and MOT beams at the MOT II location where we made our pulsed BECs to receive, characterize and use the atomic beam. If the first attempt did not work well we would still have the option of building out the dipole traps, MOT beams and imaging systems for a third location beyond MOT II where the atomic beam could be received and hopefully condensed.

6.1.2 Transport dipole guide trap

To prevent atoms from accelerating (or decelerating) due to gravity our atomic beam must transfer atoms horizontally. A moving lattice or conveyor could also be used but this would require a coherent dipole trap laser and a more complex slowing and unloading scheme at the receiving end. We discussed in section 4.3.1 that we need to transfer atoms at least

[1] A paper is in preparation.
[2] Also known as the capture MOT.

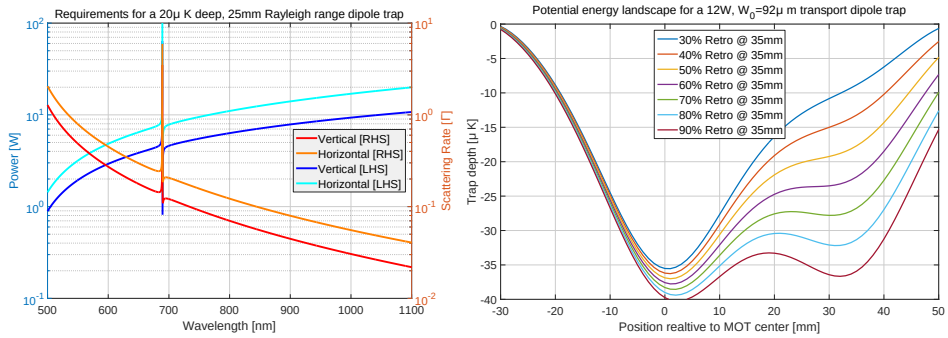

FIGURE 6.2: **Transport dipole guide.** (left - power requirements) Here we plot the power requirements and the resulting off-resonant scattering of photons for dipole traps that are 20 µK deep (at the Rayleigh range) for beams with a Rayleigh range of 25 mm. Both vertical (in the axis of gravity) and horizontal guide orientations are plotted showing the impact of gravitational sag. (right - potential landscape engineering) Engineering the transport guide potential energy landscape. Here we plot the potential energy landscape for the transport dipole trap in dependence of the power in the retro-reflected beam.

2.7 cm to avoid a line of sight to blue light from the upper 2D MOT chamber. It is possible to push the MOT across some of that distance by biasing the quadrupole center but the MOT atom numbers decrease rapidly as the MOT nears the vertical MOT beam edge (see figure 6.6). The further we transfer atoms along the dipole guide the faster the atoms need to travel to achieve a certain survival probability for a given lifetime. This, in turn, requires dissipating more energy at the destination, advocating shorter transfers. We chose a target transfer distance of around 3.7 cm, an apparently arbitrary choice until you realise that our existing dipole trap beams and imaging systems which were used to make BECs are located here. Furthermore, this location was found to be well protected from blue light in the characterization work described in (section 4.3.1).

We need a Rayleigh range of around 25 mm or longer in order to trap atoms against gravity over the entire transport distance. Since we have a MOT of 20 µK and we need to accelerate and decelerate atoms from this MOT, we can expect temperatures of the order of 20 µK. We also chose this as our target dipole guide depth one Rayleigh range away from the focus along the guide. The dipole trap powers required to achieve this as a function of wavelength are plotted in figure 6.2. We had around 12 W of power available after fiber coupling and AOMs from our 1.07 µm IPG (YLR-20-LP) laser (which is also used for our other dipole traps). An old 10 W 532 nm Verdi[3] was also considered. The power requirements at 532 nm are quite attractive but the scattering rate was more concerning at 1 Hz, so we focussed on the 1.07 µm option with our somewhat inadequately powered

[3]Which we thought was available but turned out not to work - we never saw more than 400 mW from it.

laser.

Figure 6.2 indicates that we need around 20 W at 1.07 µm. Our laser only produced 12 W so we retroreflected the beam which in principle can give us double the power. Forcing us to retro-reflect the beam (rather than buy or make a more powerful laser) actually turned out to be an advantage, because it allowed the engineering of the potential energy landscape that gave us additional fine control over the propagation of the atoms. Figure 6.2 plots out the potential energy landscape along the transport dipole trap for varying retro-reflection powers. The retro-reflection was assumed to be focused with a magnification of unity 35 mm from the focus in the forward pass. It is clear that the range of options is far greater than could have been obtained using a single pass beam.

We focussed the first pass beam at the location of MOT I (the capture MOT) with a calculated $1/e^2$ waist of 78 µm and a measured $1/e^2$ waist of 92 µm. The transport guide was geometrically aligned to the center of the chamber. We didn't have a good method for adjusting the focus location. We began by aligning the forward pass the same way that we align dipole trap beams (section 4.2.1). The problem here was that the transport has a very large Rayleigh range, red MOT I has a very large extent and red MOT I shifts daily with the magnetic bias field so it is difficult to pinpoint the focus precisely. The retro-reflection was first reverse coupled back through the launch fibre (OZ Optics PMJ-A3AHPC, S& K 6.2 mm collimator) using a photodiode monitoring the mirror leakage light on the other side of the fiber. We then imaged the leakage through a mirror from the retro-reflection beam before the chamber as shown in figure 6.3, allowing us to mark the location of the retro focus. Translating this imaging camera by the targeted focus position offset, 35 mm, gave us a target onto which we could offset the focus of the retro beam. With the retro beam at maximum power we loaded atoms from red MOT II into the second (retro-reflected) focus and we were (somewhat sketchily) able to image which way the cloud moved and thus estimate the direction towards the second trap minimum. With cameras monitoring the beam positions and micrometer stages adjusting the focussing lenses for both the forward and the retro-reflection beams we iterated towards a situation where there was a potential minimum around the location of the attempted BEC and where the foci of the forward and reverse passes had a relative offset of 35 mm. The extent of red MOT I is on the order of 1 cm and within the dark cylinder the extent grows substantially, so there is a good overlap between MOT I and the first potential minimum in the transport guide even if the first minimum might be offset by 5 mm compared with the geometric center. There were substantial uncertainties in this process and it can be seen in the data in figure 6.7 that the beam does become noticeably more dense as it propagates along the guide.

A waveplate was used to adjust the intensity of the retro-reflection beam and this was a parameter used to optimize performance for our second attempt at steady-state BEC. Later

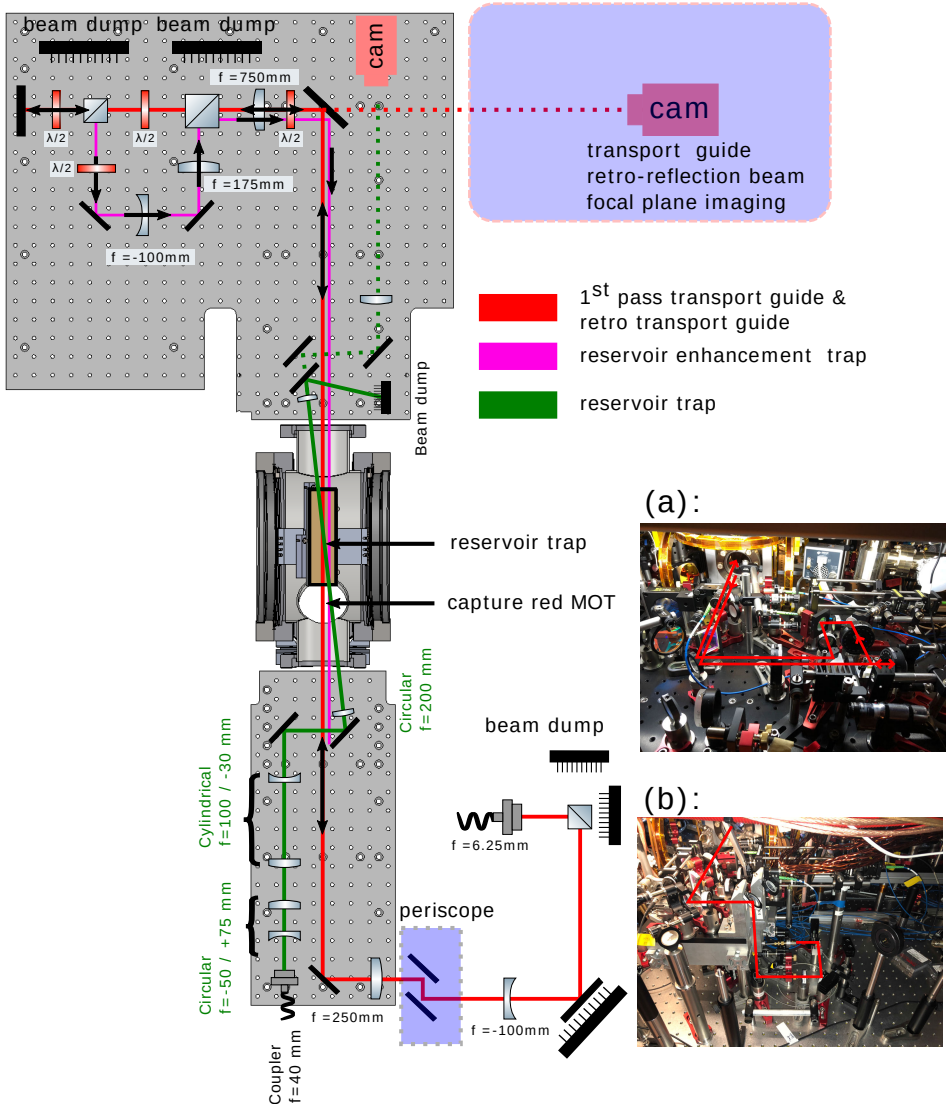

FIGURE 6.3: **Transport dipole trap setup.** The configuration of the guide and sheet/reservoir dipole traps. (a) Beam paths on the aisle side. (b) Beam paths on the wall side.

a second retro-reflection beam was generated from the transport beam as can be seen on figure 6.3, but this will not be discussed until section 6.2.

One concern we had was optical damage to the chamber windows. The beam waist at the windows for the transport beam is only 400 µm giving an intensity (including the retro-reflection) of around $10\,\mathrm{kW}\cdot\mathrm{cm}^{-2}$. For silica this is not high but high power beams can act as optical tweezers and seem to collect and attract dust. Our machine and lab are not exactly at clean room standard - we get dust damage to fibre tips from time to time which requires repolishing. If we damage the chamber windows this is not something we can fix so we designed a structure to hold a second AR coated window which could clamp onto the existing chamber windows with inputs for overpressurizing/feeding purge air or nitrogen to keep the area around the chamber window clean. We never ended up attaching the protection windows and we only had one instance where we did experience a dirt problem with a chamber window. During lifetime measurements we would often run the system in steady-state at full dipole trap power for a minute or more. On one such occasion we found that there was a sharp fall in atom number which did not recover. Eventually we tracked the problem to the input chamber window around the transport dipole trap beam but the dirt cleaned off and we haven't had further problems.

6.1.3 Protection from MOT light

If atoms travel along the transport dipole trap away from the MOT quadrupole center MOT light will simply push them back. You could try placing a push beam to fight the MOT, but this will most likely just heat the atoms radially until they fall from the trap. Another approach might be to protect the atoms with a "transparency beam". This was discussed in section 4.3.2 but the dark state in our 688 nm $^3\mathrm{P}_1$-$^3\mathrm{S}_1$ system means that we need two incoherent transparency beams with different polarizations. While the configuration we use of π and σ^+ is impractical for protecting a guide because it requires an exceptionally elongated beam shining onto the guide from the side, it might be possible to use a $\sigma^- + \sigma^+$ configuration (see section 4.3.2) or the $^3\mathrm{P}_1$-$^3\mathrm{D}_2$ transition (see section 6.3.2). Perhaps a bigger problem with transparency protection is that our MOT light is collinear with our transport guide. If we protect the entire guide we would also prevent laser slowing and unloading at the receiving end. If we don't protect the entire guide the MOT light would simply push the atoms back the moment they leave the protection[4]. Another approach is to use a moving molasses in combination with a 2D MOT. This has been used in a number of experiments, for example [171, 340], but our system thus far uses a 3D magnetic red MOT geometry.

[4] In the iqClock machines we will rotate our horizontal MOT beams by 45° so that after a short propagation distance along the z axis the region is free from MOT beams.

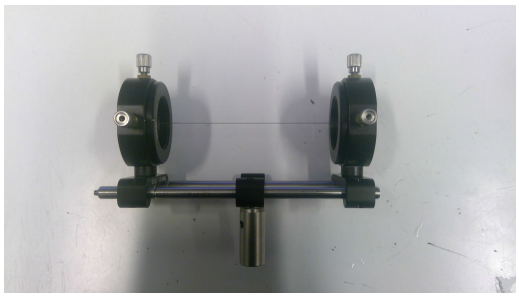

FIGURE 6.4: **Dark cylinder.** The dark cylinder used to block the MOT light from the transport dipole trap. Shown is the test unit rather than the final unit, which was similar but more than twice as long and constructed using a Thorlabs 30 mm cage frame and CXY1 mounts. The suspended capillary in the actual system is 200 mm long with a 600 µm diameter.

There is however a very simple technique, the dark SPOT [113], which we can adapt to our application. If our MOT beam is collinear with the dipole trap we can make a dark spot blocking the MOT beam from the dipole trap. We began by making and testing the performance of a variety of technologies that produce a dark region in the centre of the MOT beams, a dark spot, or rather dark cylinder in our case, since the MOT beams have to be dark along the whole transfer guide from MOT to target region. We tried gluing both black steel ball bearings and stainless steel ball bearings of a variety of sizes to microscope slides. We tried using microscope slides onto which black dots for labelling chemistry glassware had been heat transferred. We tried suspending stainless steel capillaries (of various diameters), in some cases blackened with ink or soot (similar to the material we used to make the oven nozzles but longer and wider). The ball bearings worked very well with attenuations of at least 80 to 200× but this was only in one image plane. Our dipole guide must be dark to MOT light over distances of at least 5 cm. For this reason we opted for the suspended capillary as our primary dark "spot" for its ability to darken a long cylinder corresponding to the entire propagation path of atoms down the transport dipole trap to an attenuation factor of 30-40.

To implement this we constructed a 1:1 image relay for our MOT beams using two f=500 mm lenses at (f, 2f, f) in the axis of the dipole guide and we placed our suspended capillaries at the image plane of the MOT. The cylinders were made from 200 mm long stainless steel capillaries with a 600 µm outer diameter and a 400 µm inner diameter. They were suspended by threading three 100 µm wires through the capillary and gluing them taut on the edges of a 1" ring. The whole structure was mounted within a Thorlabs 30 mm cage structure using a CXY1 translator at each end for alignment. Images of the initial test structure are shown in figure 6.4. The final system was very similar but used cage mounts instead.

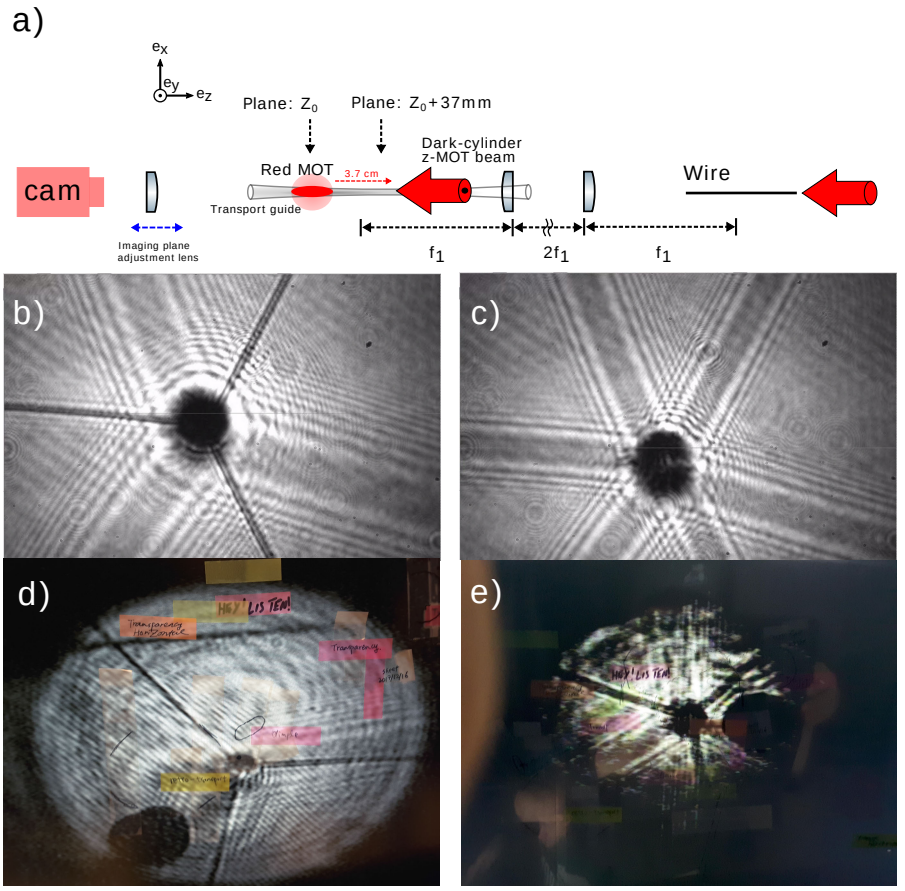

FIGURE 6.5: **Dark cylinder characterization.** (a) Tomography technique for aligning the position of the dark cylinder to block the MOT light from the transport dipole trap by using the transport dipole trap imaging cameras. (b) Imaging the plane of the suspension wires. (c) Imaging the MOT location after placing the dark spot. This technique also allowed initial alignment to make the cylinder coaxial with the MOT beams. (d-e) Images showing ball bearing dark spots "orbiting" the main dark spot. These are not mistakes or misalignments, the ball bearing dark spots were added to block secondary reflections from the tilted uncoated chamber windows (the images included are examples, they are not the current alignment).

The cameras we use to image the transport dipole laser from each direction focus the plane of the dipole trap. By adjusting the position of the dark cylinder the suspension wires at each end can also be brought into focus at which point we know the wires are in an image plane of the dipole trap and hence the MOT. In this way we can adjust the dark cylinder so that its image is centred on the transport dipole guide. The technique and results are summarized in figure 6.5.

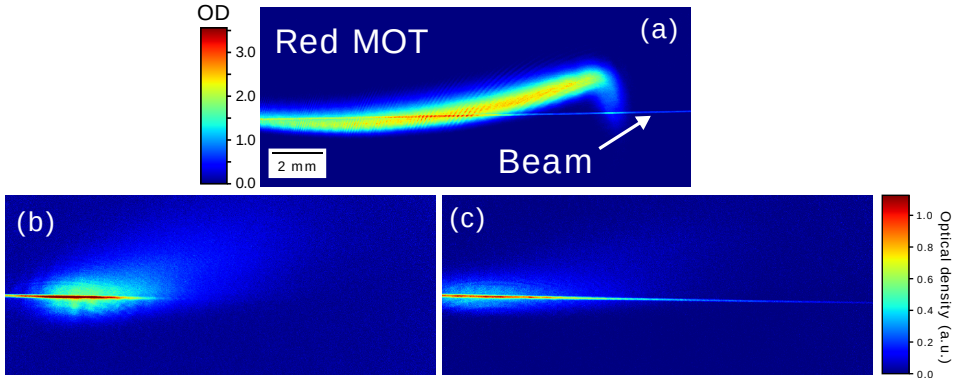

FIGURE 6.6: **Loading MOTs into a guide.**(a) If the red MOT I is shifted too close to the edge of the vertical MOT beam the atoms start to fall off the edge and the MOT becomes lossy. The MOT will also grow large in the axis of the guide if the Z-MOT power levels are low (as they are in this example). (b) If the Z intensity is too high the flux down the guide is low. (c) Red MOT I with reduced z-axis MOT beam intensity showing extension along the dark guide.

Fine alignment of the dark cylinder using the manual adjustments was made by observing the strength of the atomic beam arriving at the target location 3.7 cm from MOT I. For the MOT beam pushing atoms from the guide back into the MOT the cylinder position was optimized to continue to receive flux even as the MOT power on the transport axis beam was increased. The signal from this method was uncertain and noisy. One of the causes of problems was found to be reflections from the uncoated chamber windows. Our chamber is slightly tilted with respect to the MOT and dipole trap axis. Furthermore the first chamber window was intentionally tilted at 3° in the vertical to avoid interferences. To try to block some of the additional reflections, microscope slides with glued 1.6 mm diameter ball bearings were introduced to the MOT beams placed immediately before the dark cylinders. Using the same cameras as were used for dark cylinder tomography the MOT location could be imaged with high gain to see the reflections from the window surfaces. In this way the ball bearing locations were adjusted to block the reflections at the dark cylinder location. These ball bearings look like they are misaligned on the images in figure 6.5 but in fact their locations are correct and important for blocking these window reflections. With dark spots in place we find that the MOT cloud extends far down the transport guide. As can be seen in figure 6.6 this becomes more dramatic as the intensity of the MOT beams is reduced. The addition of the dark spots also has a detrimental effect on the number of atoms in and the lifetime of red MOT I. This is summarized in table 6.2.

Layouts of the MOT beam lines with the dark spots are provided in appendix D.

6.1.4 Push

A resonant π polarized 689 nm 30 nW push beam with a $1/e^2$ diameter of around 250 µm crosses the dipole guide at the center of the capture MOT (MOT I) with a 6° angle. This is used to give a somewhat controlled initial kick to send the atoms on their way down the transport guide. Atoms will arrive at the receiving end even without this kick, but we found it improved the system stability. Typical atom velocities when they arrive at the receiving end are 0.08-0.25 $\mathrm{m \cdot s^{-1}}$ (see figure 6.8), with the mean velocity adjustable by varying the power of the push beam.

6.1.5 Transverse cooling

We found the addition of a weak transverse cooling molasses using the red MOT II beams on the non-magnetic line to be extremely helpful for reducing radial beam temperatures and for greatly reducing the losses from the transport guide. There are only three transverse cooling beams: counter propagating horizontal beams and a vertical beam. These MOT beams have a 28.8 mm $1/e^2$ diameter and powers of 1.4 µW and 6.75 µW in the horizontal and vertical axes respectively, giving a total power of $0.5 I_{sat}$. More detail can be found in chapter 5 and section 4.1.2.

6.1.6 Results

The results we shall present here will be mostly for ^{88}Sr, which makes characterization much simpler and more accurate. ^{84}Sr is needed for a steady-state BEC but it is difficult to get a reasonable signal-to-noise ratio for a beam because of its low abundance. Only after the ^{84}Sr beam is slowed and the atoms trapped can a good signal be obtained. A summary of the results can be found in table 6.1. Uncertainties in individual measurements are generally derived statistically as $\pm 2\sigma$ from averaging many shots, but these will underestimate systematic variations that we will discuss and try to account for. We also tabulate in table 6.2 the vital statistics of the steady-state red MOT I that loads the guided beam for ^{84}Sr. By comparing its performance with red MOT I before adding the transport guide and push beams, we can gain insight into the impact these had on the system efficiency and lifetimes.

Radial temperature The radial beam temperature can be measured by ballistic expansion as shown in figure 6.7. A temperature decrease with propagation can be observed in the data. It is thought that this is largely due to the variation in the Stark shift of the transport guide as the beam diverges. As the trap depth decreases the resonant frequency shifts to the red getting closer to the transverse cooling frequency. This improves the performance of the radial cooling reducing temperature until it shifts

TABLE 6.1: **Results for guided beam.** Results are taken for an oven temperature of ≈500 °C. The data referenced in the notes is for a ^{88}Sr beam. Uncertainties reported are 2σ.

Parameter	Unit	^{88}Sr Beam	^{84}Sr Beam	Data
Radial temperature	μK	0.89(8)[a]	2.0(2)[b]	Figure 6.7
Axial temperature	μK	29(4)	29(4)[c]	Figure 6.8
λ_{dB}[d]	m	$1.10(6) \times 10^{-7}$	$8.5(5) \times 10^{-8}$	
Axial velocity[e]	$\mathrm{cm \cdot s^{-1}}$	8.4(8)	8.8(8)[c]	Figure 6.8
Linear density ρ_L	at $\mathrm{cm^{-1}}$	$3.88(16) \times 10^{6}$	$1.04(10) \times 10^{5}$	
Beam flux	at $\mathrm{s^{-1}}$	$3.25(28) \times 10^{7}$	$9.1(12) \times 10^{5}$	
Atomic beam $1/e^2$ radius	μm	46.6(16)	39.4(40)	Figure 6.7
Peak density	at $\mathrm{cm^{-3}}$	$1.14(8) \times 10^{11}$	$4.2(10) \times 10^{9}$	
Average density[j]	at $\mathrm{cm^{-3}}$	$5.7(4) \times 10^{10}$	$2.1(6) \times 10^{9}$	
Average elastic collision rate Γ_{el}[f]	Hz	$3.5(4) \times 10^{-4}$	0.11(4)	
Radial trapping frequency[g]	Hz	183(20)	187(20)	Calculated
Peak phase-space density[hd]		$1.5(4) \times 10^{-4}$	$2.7(8) \times 10^{-6}$	
Alternate peak phase-space density[id]		$1.3(4) \times 10^{-3}$	$7.1(24) \times 10^{-6}$	
Average phase-space density[kd]		$7.7(20) \times 10^{-5}$	$1.4(4) \times 10^{-6}$	

[a] The average values are known much more precisely. The uncertainty presented primarily estimates variation across the imaged region.

[b] The transverse cooling parameters were optimized including a reservoir dipole trap (for steady-state BEC). Without this dipole beam the transverse cooling is a little blue detuned to it doesn't cool well. It can be assumed that a temperature as good as that for ^{88}Sr is possible if optimized for.

[c] The axial temperature and velocity can not be measured for ^{84}Sr as the flux is not large enough. We assume the same values as for ^{88}Sr.

[d] Calculated in the moving frame.

[e] Depends on push beam power.

[f] The thermal elastic collision rate is given by $\Gamma_{el} = nv\sigma$ where n is the number density, $v = 4\sqrt{k_B T/\pi m}$ is the velocity and $\sigma = 8\pi a^2$ is the collision cross section [192]. For ^{84}Sr the elastic scattering length is $a = 124\ a_0$, for ^{88}Sr it is $a = -1 a_0$ from table 2.11. We use the axial temperature to estimate the velocity.

[g] Assumes a 50% retro-reflection power with a 12.0 watt beam.

[h] Calculated using equation 6.2.

[i] Alternate formulation based on equation 6.5.

[j] $n_{av} = \rho_L/(\pi W_0^2) = n_{peak}/2$ where N is the total number, W_0 is the $1/\mathrm{e}^2$ radius of the fitted radial Gaussian distribution.

[k] $PSD_{av} = PSD_{peak}/2$ assuming averaging over the $1/\mathrm{e}^2$ radius of the fitted radial Gaussian distribution.

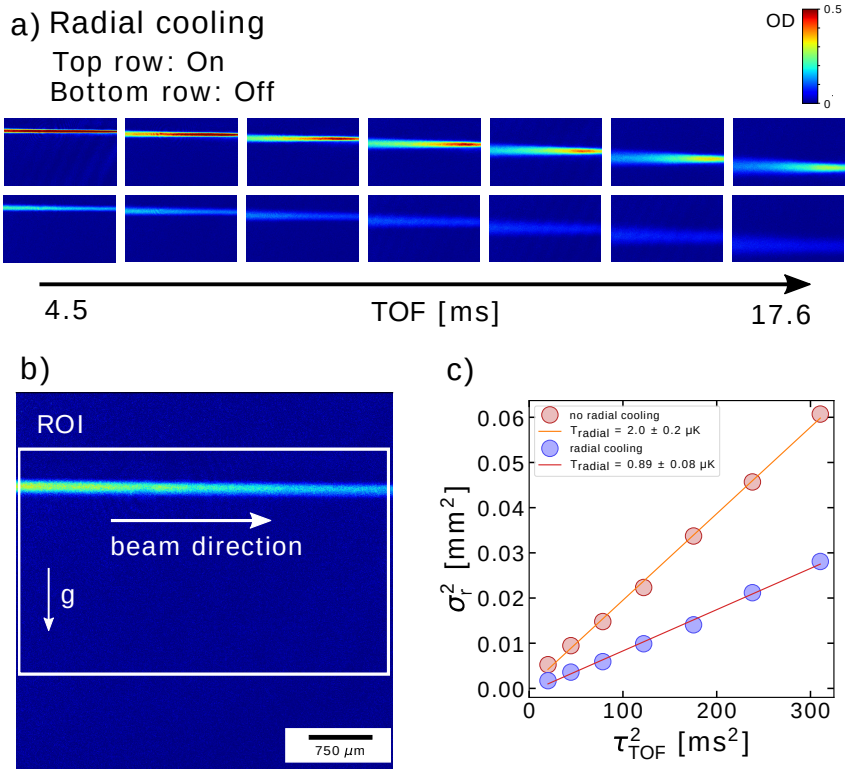

FIGURE 6.7: **^{88}Sr beam radial temperature.** (a) Absorption images of the ballistic expansion of the steady-state atomic beam after switching off the transport guide and transverse cooling beams for varying time of flight (TOF). We compare the behaviour of steady-state beams with or without transverse cooling light. (b) The full image has a field of view of 4.432 mm wide. The white box highlights the region of interest (ROI) shown in (a). We integrate along the horizontal axis of the ROI to derive the averaged radial temperature. (c) Atomic beam temperature along the radial direction is measured by integrating the ROI along the horizontal axis, fitting Gaussians to the profiles and analysing the expansion.

TABLE 6.2: **Steady-state red MOT I loading a beam.** Characteristics of the Red MOT I including the push beam and the transport dipole trap guide beam for ^{84}Sr. Also included are the previous results (in columns 1 and 2) for red MOT I without the transport or push from table 4.1. All uncertainties stated are taken as $\pm 2\sigma$ from the fitted data.

	^{88}Sr Red MOT I	^{84}Sr Red MOT I[a]	^{84}Sr Red MOT I+beam[b]
Incoming Flux [atoms s^{-1}]	$5.1(7) \times 10^8$	$4.85(98) \times 10^6$	$2.81(30) \times 10^6$
Temperature y	20(5) μK	16(2) μK	6.5(3) μK
Temperature z	26(7) μK	66(17) μK	10(33) μK[c]
Atom number	$2.54(10) \times 10^9$	$6.69(8) \times 10^8$	$6.44(20) \times 10^6$
$1/e$ decay lifetime	4.53(6) s	12.0(17) s	2.40(13) s
$1/e$ decay lifetime	-	-	4.76(16) s[d]
$1/e$ decay lifetime	-	-	6.03(38) s[e]

[a] ^{84}Sr Red MOT I and ^{88}Sr Red MOT I use the same parameter sets that were optimized for ^{88}Sr. For this reason some of the parameters like the z temperature were not good, reducing performance.
[b] Red MOT I including dark cylinders, transport and push beam and optimized for loading a guided beam.
[c] It is not possible to accurately measure this temperature due to the large size of the MOT.
[d] Push beam off.
[e] Push beam off and transport dipole guide trap off.

blue, after which we see the beam rapidly heat. It is this signature which we use to optimize the frequency of the transverse cooling light. The radial temperature averaged over the entire field of view was 0.89(8) μK. If we fit just the beginning or end 0.5 mm of the 4.432 mm field of view we get a temperature variation of 30%. In calculating the phase-space density we use the uncertainty across the entire field of view although the true temperature is probably at the lower end of this range.

Velocity and axial temperature Typically one would characterize the velocity distribution of an atomic beam by placing a probe beam partially in the direction of beam propagation and then measuring the Doppler shift in the fluorescence (or absorption) spectrum. In our case, only an absorption spectrum on the 689 nm transition has any hope of simultaneously resolving our very low velocities and delivering a measurable signal. Taking this data is on our "to do" list.

At the time our atomic beam was characterized by an alternate method. We apply a collimated 1 ms pulse of blue light perpendicular to the transport guide and orthogonal to gravity. We make the pulse intensity just high enough to eject a burst of atoms from the guide as viewed from above, see Fig. 6.8. Since the ejected atoms are not supported against gravity they accelerate away and gradually defocus from the image plane. This limits the maximum expansion times we can characterize, rather than the 4 mm imaging system field of view. We assume that spontaneously emitted photons are equally distributed during the ejection process, so that the z-axis mean velocity is

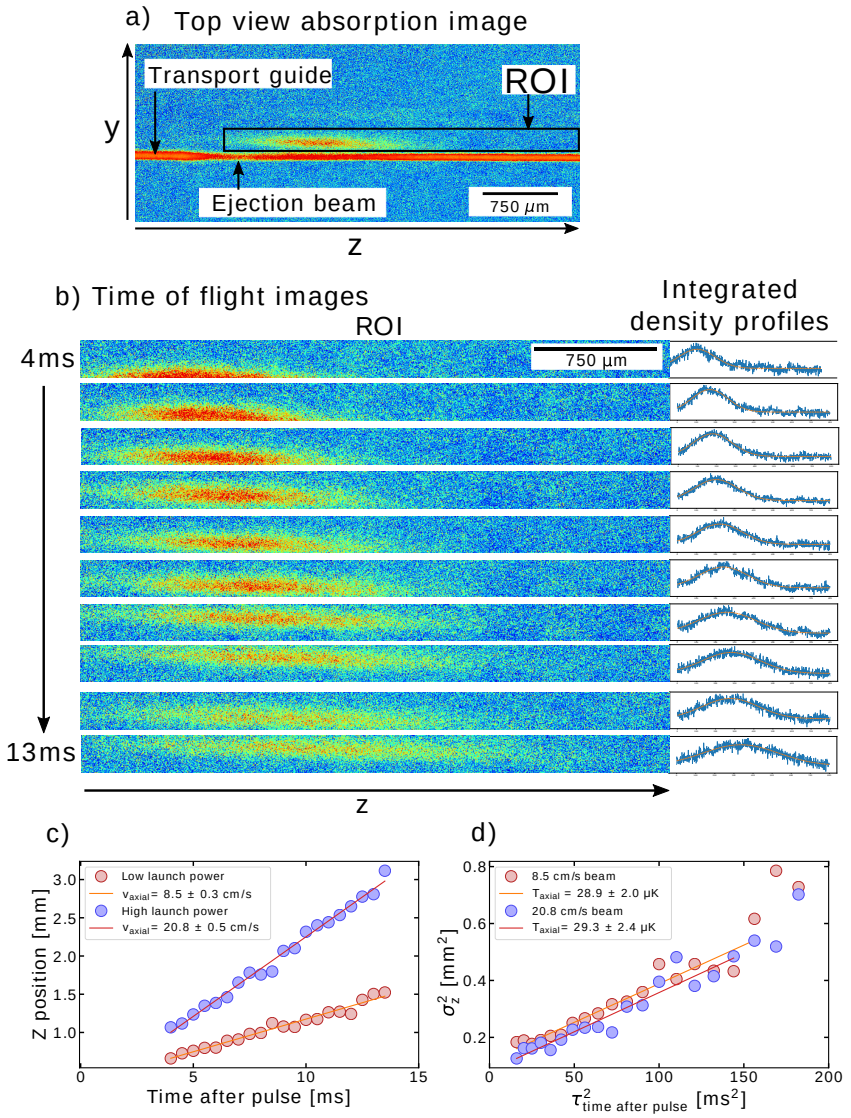

FIGURE 6.8: **Atomic beam axial velocity.** (a) Top view of the transport guide shortly after the ejection of a burst of atoms. The region of interest (ROI) used for fitting Gaussian clouds is shown. (b) Absorption images and respective density profiles of clouds of atoms ejected from the transport guide, taken 4 to 13 ms after ejection from the transport dipole guide. (c) Fitted axial velocities. (d) Evolution of the cloud width of two ejected clouds with different mean velocities. By fitting the width, we estimate the axial temperature.

not affected. If the number of photons scattered produces a heating which is small compared to the starting temperature of the beam it may also be assumed that the cloud expansion will reflect the initial beam temperature. Thus we can measure both the velocity and temperature of our beam.

Figure 6.8 shows the beam characterization results in the vicinity of our target BEC location. We assume the guide is flat and that the beam velocity at the ejection point is similar to that at the loading point[5] around 1.5 mm away. The results for several values of the push beam intensity are shown in figure 6.8. We measure a mean velocity ranging from 8.4 to 20.8 $\mathrm{cm} \cdot \mathrm{s}^{-1}$ and we fit an axial temperature of 29(4) µK. One might be concerned that the cloud expansion in the imaging system due to gravitational acceleration defocus could appear like a temperature. This however, would give a quadratic, rather than a linear expansion in the cloud size with time, which we do not see in the data. During the rest of our work we typically operate with a push beam intensity corresponding to a measured velocity of 8.4(8) $\mathrm{cm} \cdot \mathrm{s}^{-1}$.

Density Our imaging system resolution of 4.48 µm is sufficient to directly absorption image the beam density profile (with a 0.1 ms time of fight). A Gaussian profile is fitted to estimate the width and peak density yielding a $1/e^2$ radius of 46.6(16) µm. The linear density ρ_L can be estimated by integrating over the radial direction and averaging along the propagation axis giving a linear density of $3.88(16) \times 10^6$ atoms/cm.

Flux An estimate of the flux ϕ is given by $\phi = \rho_L v$ where ρ_L is the linear density and v is the velocity. This gives a flux of $3.25(28) \times 10^7$ ^{88}Sr/s.

Transport efficiency The loading efficiency from the MOT to the beam can be estimated from the decay rates of the MOT. Let us assume a simple rate model for our MOT. $dN/dt = \Phi_M - N\beta_{MOT} - N\beta_{Beam}$ where N is the atom number in the MOT, Φ_M is the flux captured by the MOT, β_{MOT} is the loss rate of the MOT alone and β_{Beam} is the additional loss rate due to the launching of atoms down the beam line. The lifetime τ can be related to the loss rate as $\tau = 1/\beta$. From the data for ^{84}Sr in table 6.2 we can estimate the transport efficiency in table 6.3. Around 30% of the total flux captured by the MOT is delivered in the form of a high phase-space density beam.

Phase-space density The deBroglie wavelength and phase-space density of the beam can be estimated in the moving frame of the atoms. The deBroglie wavelength λ_{dB} and the phase-space density PSD[6] can be calculated using the relations 6.1 and 6.2 respectively.

[5] Where the atoms will be stopped and loaded into a reservoir dipole trap as will be described in section 6.2.

[6] Normally ρ is used for the phase-space density but I have been using that for number densities of atoms so I will stick to PSD for the phase-space density to avoid confusion.

TABLE 6.3: **Estimating the transport efficiency.** Estimation is based on ^{84}Sr data.

Parameter	Result
Flux Φ_M[a]	$2.81(30) \times 10^6\,\mathrm{s}^{-1}$
MOT $1/e$ decay lifetime without beam τ_{MOT}[a]	$6.03(38)\,\mathrm{s}^{-1}$
MOT $1/e$ decay lifetime with beam $\tau_{MOT} + \tau_{Beam}$[a]	$2.40(13)\,\mathrm{s}^{-1}$
Calculated MOT lifetime due to beam losses only τ_{Beam}[b]	$3.99(46)\,\mathrm{s}^{-1}$
Steady-state MOT atom number measured [a]	$6.44(20) \times 10^6$
MOT atom number from loading /decay N_{MOT}[c]	$6.74(109) \times 10^6$
Launched beam flux Φ_B[d]	$1.69(53) \times 10^6$ ^{84}Sr/s
Measured arriving beam flux $\Phi_B\eta_B$[e]	$9.1(12) \times 10^5$ ^{84}Sr/s
MOT-beam loading efficiency Φ_B/Φ_M	60(39)%
Transport efficiency η_B	54(18)%
Total efficiency $\Phi_B\eta_B/\Phi_M$	32(18)%

[a] From table 6.2.
[b] $\tau_{MOT+Beam} = 1/(1/\tau_{MOT} + 1/\tau_{Beam})$
[c] $N_{MOT} = \Phi_M\tau_{MOT}$
[d] $\Phi_B = N_{MOT}/\tau_{Beam}$
[e] From table 6.1.

$$\lambda_{dB} = \frac{h}{\sqrt{2\pi m k_B T}} \tag{6.1}$$

$$PSD = n\lambda_{dB,x}\lambda_{dB,y}\lambda_{dB,z} \tag{6.2}$$

where:

T = temperature in the moving frame.
m = ^{88}Sr mass 1.4597×10^{-25} kg
n = number density

This yields a calculated peak phase-space density of $1.5(4) \times 10^{-4}$ for ^{88}Sr, a record phase-space density for a steady-state beam[7].

In tight traps it can be difficult to resolve the cloud size and thus determine the density. If we approximate the potential landscape in which the cloud sits by a harmonic trap with trapping frequencies (f_x, f_y, f_z) and assume a Boltzmann distribution with temperature T. We can then estimate the peak phase-space density within the system using equation 6.3.

[7] It must be remembered that ^{88}Sr is essentially non-interacting so it doesn't effectively thermalize. The phase-space densities we get with ^{84}Sr are lower due to the reduced abundance so the starting point for an evaporatively cooled guided beam based steady-state atom laser is still very challenging.

$$PSD = N\left(\frac{h(f_x f_y f_z)^{1/3}}{k_B T}\right)^3 \tag{6.3}$$

$$T = (T_x T_y T_z)^{1/3} \tag{6.4}$$

Since we can't really measure a trapping frequency in the axial direction of the transport guide but we can measure the linear density ρ_L, we can use a mixture of these two expressions as an alternate estimate of our beam phase-space density:

$$PSD_{alt} = \rho_L\left(\frac{hf_r}{k_B T_r}\right)^2 \frac{h}{\sqrt{2\pi m k_B T_z}} \tag{6.5}$$

In the case of ^{88}Sr where there is no thermalization and the beam is loaded from a MOT by laser cooling into the guide, we are committing some fairly egregious violations of the thermal equilibrium assumptions. For this reason it is expected that the phase-space density calculated by this method might be substantially higher than you might actually have as this method can overestimate the density.

We can numerically calculate the radial trapping frequency in our transport guide. This alternate method estimates the peak beam phase-space density for ^{88}Sr as PSD_{alt} =1.3(4) $\times 10^{-3}$ and for ^{84}Sr as PSD_{alt} =7.1(24) $\times 10^{-6}$. These are factors of 10 and 4 respectively, higher than the first method estimated. The first method used density estimates based on the observed atomic beam widths rather than calculated assuming a Boltzman distribution in a harmonic trap. We can understand this discrepancy from the absence of thermalization (which we see from variation in the axial and radial temperatures) and we will quote the earlier (lower) numbers as our phase-space density estimates.

Another (related) interesting question is the elastic collision rate within the atomic beam. The thermal elastic collision rate is given by $\Gamma_{el} = nv\sigma$ where n is the number density, $v = 4\sqrt{k_B T/\pi m}$ is the velocity and $\sigma = 8\pi a^2$ is the collision cross section [192]. For ^{84}Sr the elastic scattering length is $a = 124a_0$ and for ^{88}Sr it is $a = -1a_0$ (see table 2.11). We assume a velocity based on the axial temperature. This gives us average elastic collision rates for our ^{88}Sr beam of $\Gamma_{el,88}$ =3.5(4) $\times 10^{-4}$ Hz and $\Gamma_{el,84}$ =0.28(2) Hz or our ^{84}Sr beam. Given the propagation time from the MOT of less than 0.5 s it is easy to understand why our beams are not thermalized.

6.1.7 Possible applications and comparisons with other work

A guided atomic beam with very low temperature and high phase-space density is new and might have other applications beyond transport for our steady-state BEC. Past work

has focussed in particular on generating intense ion beams[341, 342], but such a source might also be valuable for precision measurement with atom interferometers [59, 343, 344], sympathetic cooling and cold chemistry [345, 346] and as a source of atoms for a superradiant clock [39, 41, 43].

Most of the notable work in high phase-space density beams has been performed in pursuit of quantum gases [170, 172, 187, 203, 332, 340, 347, 348] and ion beams [342, 349–354]. A particularly good review of the ion beam work is contained within [341]. Comparing performances across these two application areas is complicated by the fact that the quantum gases community tends to focus on flux and phase-space density while the ion beam community uses current and brightness. The ^{88}Sr beam presented here has a phase-space density around three orders of magnitude higher than previous work by Guery-Odelin's group where they demonstrated peak phase-space densities of $\sim 10^{-7}$ [170, 172][8].

6.1.8 Conclusions

To the best of our knowledge, our ^{88}Sr beam has the highest phase-space density ever achieved in a continuous ultracold beam experiment. Our steady-state guided atomic beam of ^{88}Sr has a peak phase-space density of $1.5(4) \times 10^{-4}$, a flux of $3.25(28) \times 10^{7}\,\mathrm{s}^{-1}$ and radial temperatures as low as $0.89(8)\,\mu\mathrm{K}$. This is around three orders of magnitude higher than previous work by Guery-Odelin's group where they demonstrated peak phase-space densities of $\sim 10^{-7}$ [170, 172].Furthermore, by demonstrating around 30% conversion efficiency from the flux captured by the MOT into a transported high phase-space density beam, we show the practicality of this technique for future steady-state beam sources for applications such as ion beams or superradiant clocks.

Using ^{84}Sr with its relatively low abundance our calculated beam peak phase-space density is $2.7(8) \times 10^{6}$ with a flux of $9.1(1.2) \times 10^{5}\ \mathrm{s}^{-1}$. This gives an average elastic collision rate of $0.11(4)\,\mathrm{Hz}$ indicating the beam is still a bit over an order of magnitude away from entering the collisionally dense regime. In the collisionally dense regime our transverse laser cooling might be expected to dramatically increase the phase space density by thermalizing and removing the axial temperature component.

6.2 Steady-state with unity phase-space density

Having transported a useful flux of atoms at high phase-space density to a dark place, our next tasks are to stop atoms from this beam, load them into a reservoir dipole trap, cool,

[8] In most of the ion beam literature insufficient information is provided to calculate their phase-space densities.

protect and hopefully condense them. Referring back to our design schematic in figure 6.1 we will once again step through the components and summarize the results.

6.2.1 Stop the beam

The first step is to stop the beam of atoms with minimal heating and without loss from the transport guide. To do this we constructed a Zeeman slower on the red MOT transition using the quadrupole magnetic field from our steady-state red MOT as our magnetic field source. A Zeeman slower has a number of advantages over a simple molasses. It uses the magnetic field to be able to address and slow a wider range of velocities, it requires less power because modulation is not required to address Doppler shifts and it stops the atoms at a well defined location irrespective of their initial velocity making it easier to capture them with a small volume trap giving higher phase-space density.

The magnetic field gradient from our steady-state red MOT in the axis of the transport guide is around $0.23\,\mathrm{G}\cdot\mathrm{cm}^{-1}$. Since the Zeeman shift is $2.1\,\mathrm{MHz}\cdot\mathrm{G}^{-1}$ (section 2.10) we can estimate the maximum deceleration rate required and hence the required slower intensity and stopping distance. These are plotted in figure 6.9 along with absorption images with and without the slower beam on. For the typical beam velocities we have of 0.1-0.2 $\mathrm{m}\cdot\mathrm{s}^{-1}$, we need Zeeman slower intensities of <0.05 I_{sat} and stopping distances of up to 3 mm[9].

Our Zeeman slower beam uses a beam focussed by a 7.5 mm S & K collimator with an estimated $1/e^2$ waist diameter of 300 µm at the atoms. It crosses the transport guide at an angle of 4° giving an overlap length of ≈4 mm. We modulate the frequency with a 50 kHz bandwidth triangular waveform at a modulation rate of 19 kHz as this was found to achieve the optimal flux. Broader bandwidths increase the light in the system without increasing the flux. The slower beam has a typical power of 5 nW giving an average spectral intensity of $0.3I_{sat}$ per unit linewidth, although there is a significant uncertainty in this number. The detuning of the Zeeman slower (which determines the beam stopping location) was around 1.72 MHz and this was optimized daily for optimally matching the dipole reservoir trap location to account for magnetic bias field variations.

Possible explanations for the slightly higher than expected optimized slower powers might include absorption by the optically dense cloud of atoms in the slower region. The dense "slower ball" is shown in figure 6.9.

The radial temperatures of the slower ball can be estimated from ballistic expansion (in the same way that we did for the beam in figure 6.7). We don't have a great way to measure the axial temperature as the atoms are not in equilibrium, they stop and then are

[9]For comparison, using the maximum scattering rate on the red transition a $0.1\,\mathrm{m}\cdot\mathrm{s}^{-1}$ beam could be stopped in less than 35 µm.

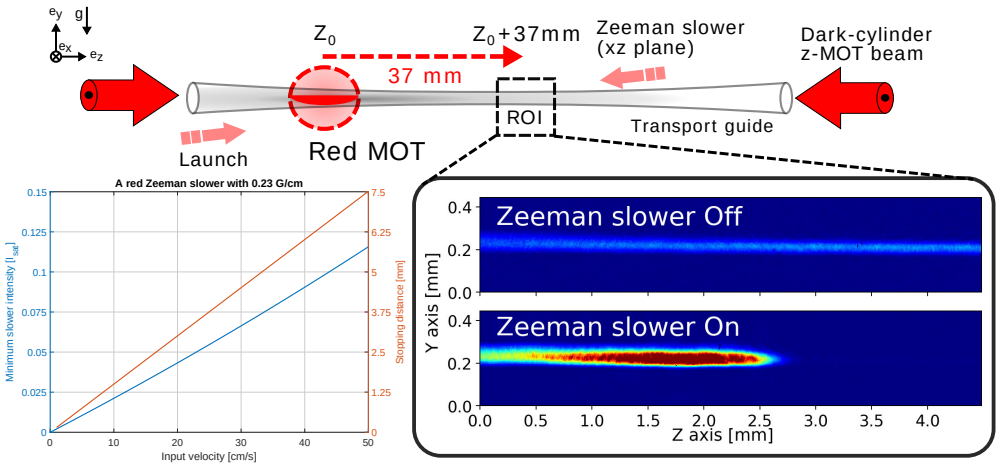

FIGURE 6.9: **Red Zeeman slower.** (left) The required intensities and stopping distances for a Zeeman slower using a single frequency of light near the red transition for a linear field gradient of $0.23\,\mathrm{G}\cdot\mathrm{cm}^{-1}$. (right) The "slower ball" of Zeeman slower atoms compared with the atomic beam without the slower.

accelerated backwards by the slower[10]. However, to get an estimate we perform a fit of the ballistic expansion at the edge of the slower ball in the axial direction. The flux can be estimated from a rate model in the same way that we estimated efficiencies for the beam. Let us assume a simple rate model for our MOT, $dN/dt = F - \beta_{Slower} N$, where N is the atom number in the slower ball, F is the incoming flux from the transport beam and β_{Slower} is the loss rate from the slower ball.

The results are summarized in table 6.4. The radial temperatures were found to be excellent at $0.88(26)\,\mu\mathrm{K}$ but the lifetime was very short at just $0.41(6)\,\mathrm{s}$. It is thought that this high loss is a result of the Zeeman slower pushing the atoms back and the lack of a trap in the system.

6.2.2 Trap and cool the atoms

The next step is to load a reservoir dipole trap from our cold atom supply. The atoms begin in the deep transport guide dipole trap. This trap is around $17\,\mu\mathrm{K}$ deep and strong in the radial direction with a trapping frequency of $200\,\mathrm{Hz}$. In short, it is not a simple thing to take atoms out the side. We began by simply overlapping the reservoir dipole trap with the transport guide beam. In this way we hoped to avoid yet another inefficient transfer stage.

[10] In a typical Zeeman slower, to prevent atoms from being pushed back you sharply change the magnetic field to rapidly detune the atoms, a trick we can not play here.

TABLE 6.4: **Zeeman slower "ball" results.** Results are taken for an oven temperature of ≈500 K. All data refers to ^{84}Sr. This data was taken with the reservoir dipole trap off.

Parameter	Units	Results
Radial temperature	μK	0.88(26)
Axial temperature	μK	5.8(42)
Atom number[a]	^{84}Sr	$3.57(35) \times 10^5$
Measured arriving beam flux[b]	^{84}Sr/s	$9.1(12) \times 10^5$
$1/e$ lifetime	s	0.41(6)

[a]The extent of the slower ball is poorly defined as it blurs into the incoming beam.
[b]From table 6.1.

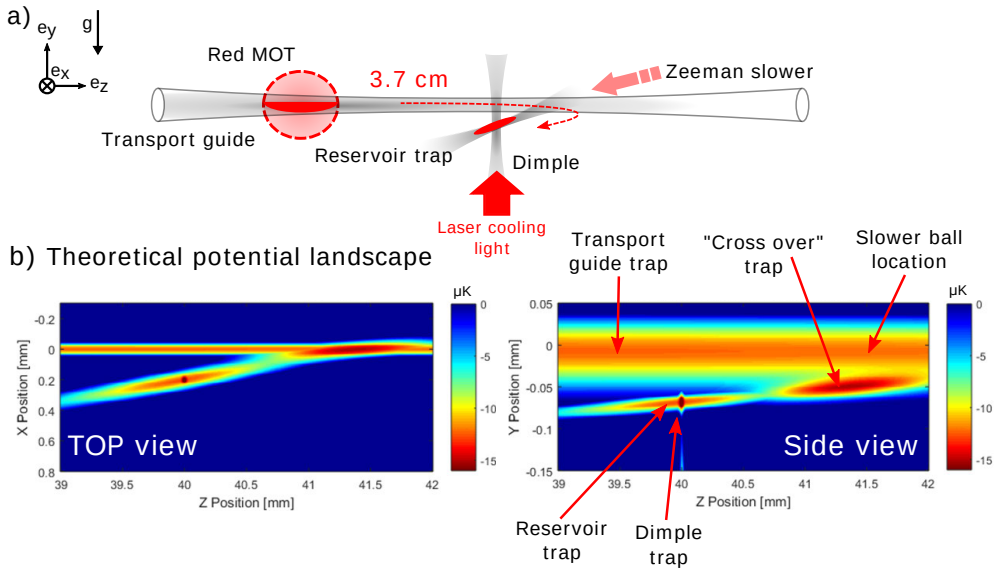

FIGURE 6.10: **Dipole trap geometry.** (a) A dipole trap geometry was developed to coax atoms out of the deeply trapped Zeeman slower ball and poke them into a reservoir dipole trap containing a dimple dipole trap. (b) Top and side views of calculated potential energy landscape for the $^1S_0$ state.

After a little while, trying to make a BEC in full view of a Zeeman slower beam in a place bombarded by hot atoms as they are decelerated started to sound like a bad idea. We then tried tilting and offsetting our reservoir trap from the transport guide in both the vertical and horizontal axes and worked on ways to lure and prod the atoms into our branching trap using gravity to assist sneaking through the 17 μK barrier. Our goal was to make a very gentle attractive slope from the Zeeman slower ball to the dimple to try to draw the atoms in but not to heat them. This also gives time for the laser beams to cool the (relatively hot) atoms emerging from the Zeeman slower ball before they arrive near the reservoir region.

In this way we planned to decouple the hot deceleration region from the cold reservoir. The geometry we ended up with is shown in figure 6.10. While it is not an idealized gentle monotonic slope it does gently draw atoms in towards the reservoir and dimple.

The direction of the tilt is also deliberate. We tried to create a geometry in which the Zeeman slower would nudge the atoms into our trap as it tried to push them back rather than fight the atom flow. It is necessary to very carefully adjust the height difference between the reservoir and the transport traps and, by fine tuning the transport retro beam alignment, the potential energy landscape can be engineered to try to get a fairly flat but slightly attractive branching reservoir trap. By looking at the atom distributions we fine tuned the beam alignments and powers to get the atoms to do what we wanted. It was a very fine and delicate geometry which needed constant attention and refinement. We tried to make this a little more robust by tapping another retro beam from the transport guide as shown in figure 6.3. We aligned this beam with the dimple region and, by adjusting the power, we were able to raise or lower the potential energy at the dimple region to make a trap which was attractive, but not one which would accelerate atoms into it.

We also placed several additional focussed red molasses beams into the system with the intention of performing "in-trap" cooling with frequencies optimized for the local Stark shifts within the trap. A pair of counter-propagating molasses beams focussed to $1/e^2$ diameters of $\approx 400\,\mu m$ each with a typical power of 0.13 nW (I=0.03 I_{sat}) were aligned with the reservoir trap (the Z in trap cooling beams). Most of the time the molasses beam co-aligned with the direction of the Zeeman slower was found to be unnecessary so it is thought that the main effect of these beams was to provide a counterforce to the Zeeman slowe,r preventing it from accelerating the atoms and throwing them out of the trap.

Based on modelling which indicated that we did not need such a large reservoir we also reduced the size of our reservoir dipole trap waists compared to what was used in the first attempt at steady-state BEC (section 4.2.1). With a smaller reservoir volume we hoped that our (rather limited) flux could better maintain the reservoir atom density. Our final reservoir geometry was a beam with a measured $1/e^2$ vertical waist radius of 13.5 µm and a horizontal waist of 120 µm. The dipole trap geometry and the optics used to produce it is shown in figure 4.6 and the properties are in table 4.2.

The temperatures of the atoms in the reservoir can be estimated from the ballistic expansion away from the location of the dimple. The temperature in the vertical axis for ^{84}Sr was measured at 0.61(4) µK, and 0.83(10) µK in the horizontal (x) axis.

6.2.3 Protect the dimple

As with our first attempt at a steady-state BEC, a critical aspect is protecting any potential BEC from both blue and red resonant light. The protection from blue remains unchanged from the first attempt (see section 4.3.1). The red light protection however required some adjustment from our previous system (see section 4.3.2). Since the 688 nm $^3P_1$-$^3S_1$ transition has a dark state, we needed to use two incoherent transparency beams from the vertical and horizontal directions to access both the π and the σ polarizations. Without this a BEC will not be sufficiently protected from red because our red light is still vastly more intense than the levels used in the original "laser cooling to degeneracy" experiment at Innsbruck [192].

To individually apply Stark shifts with a σ^+ or σ^- polarization we need to use a transparency beam collinear with the magnetic field. In the original configuration the field lines were vertical at the location of the intended BEC, so the σ polarization could be addressed with a circularly polarized transparency beam collinear with the dimple dipole trap. In the new system the magnetic field lines are collinear with the transport guide and we certainly do not dare apply a transparency beam collinear with that, for fear of breaking one or all of the loading, slowing and cooling processes. Our solution is illustrated in figure 4.15. The second transparency beam was inserted with a somewhat weird and unsatisfying angle of 45° offset in the X-Z plane and 23° offset in the Y-Z plane. This beam does however contain at least some σ^+ component allowing us to break the dark state. The weird angle also leads to a larger than desirable spot size for the transparency beam. Alignment procedures were the same as before. The beam parameters are listed in table refssbecV1:tab:TransparencyBeamData. The overall Stark shifts were less than what we had in our first steady-state BEC attempt but because the intended BEC location was much darker the resulting lifetimes were still improved. The lifetimes for a pulsed pure BEC in various configurations[11] is listed in table 6.5.

Typically we operated using a transparency beam blue detuned by 15-30 GHz, but during attempts at steady-state BEC we settled on 15 GHz since it maximized the Stark shifts while not introducing significant scattering. The repumps, which were critical in the first architecture to repump MOT atoms ending up in the metastable states, are of marginal importance here. Most of the reservoir is either strongly protected with both orthogonal polarizations or not illuminated by the transparency light eliminating the need for repumping in these regions. In the band around the dimple where the protection is partial, the MOT light illumination intensity is much lower than before so the loss rates are

[11] For these measurements the dipole reservoir trap was reduced to a level barely able to support the BEC against gravity. This way atoms scattered by photons will escape rather than remaining in the dipole trap reservoir where they would be poorly protected and can start to absorb resonant light. If they leave the confines of the protected dimple the heating rate and loss rate will rapidly rise melting the BEC. It will also create a thermal cloud which is difficult to separate from the BEC when integrating atom number.

TABLE 6.5: **Transparency protection.** Lifetime measurements for a BEC with blue light off. With transparency protection the BEC lifetime was indistinguishable with or without all red light on at the normal operating levels. If the intensity of the transparency beams is reduced to 10% of the normal operation the lifetime is reduced by nearly an order of magnitude. The transparency frequency was 16.2 GHz blue detuned. Power and beam modulation parameters are listed in appendix E, table E.5.

Configuration	Lifetime
BEC + transparency protection beams	2.22(22) s
BEC + protection + all red light	2.20(26) s
BEC + 10% protection power + all red light	0.26(6) s

comparably smaller. It is not clear if it is better to reduce the atom loss by repumping or reduce the heating by no repumping, so we usually tried both. While the repumps may or may not be useful in the reservoir they do significantly improve the flux from our 2D blue MOT so they remain locked and on when taking data.

The location of the intended BEC is relatively dark, certainly compared to the middle of a MOT, but there are still laser beams shining at this location. We also considered placing the MOT beams at 45° to the transport axis. That way no MOT beams would illuminate the BEC. Changing geometry would have required a lot of rebuilding and introduced potential for surprises, but it is something we will likely do in the future. A fully dark region is probably necessary for applications like interferometry. There were also other factors which dissuaded us from switching geometry. Firstly, our dark spot trick to protect the transport guide only works because the transport and MOT beam are collinear. You could use dark slits but with greater losses or we could implement a transparency laser to provide the protection but that is untried. Another factor is that it is not possible to get MOT beams in at 45° angles to the chamber and our magnetic field coils are rectangularly aligned with the chamber (annoyances rather than problems, you can always use smaller angles and the magnetic field can be reconfigured easily)[12].

6.2.4 Sitting on the edge

Once the system was fully built and the transparency protection levels validated we proceeded in much the same way as during our first attempt. We would operate the system in steady-state for typically 12 s and then change the parameters to make a BEC. The parameters were then adjusted to minimize the gap between the steady-state parameters and

[12]The geometry of the mHz iqClock machine now in design rotates the MOT beams by 45° relative to the transport guide. Here we plan to use several moving lattices in a 'multi-stroke' configuration to trap and transport atoms to a superradiant cavity maintaining its atom number.

those needed to reach BEC. As with our first attempt, cleaning pulses (see section 4.4.1) were usually used to blow away the thermal atoms in the reservoir in order to improve the signal to noise in the imaging system.

The closest we came to steady-state BEC was to simply turn off or reduce the power of the red Zeeman slower leaving all other parameters unchanged. This produced a (small) BEC within around 250 ms. The sequence consisted of a 12 s load to reach steady-state, after which the red Zeeman slower was turned off for 200 ms followed by a 50 ms long cleaning sequence (see section 4.4.1) and 22 ms time-of flight imaging. Figure 6.11 shows examples of typical results.

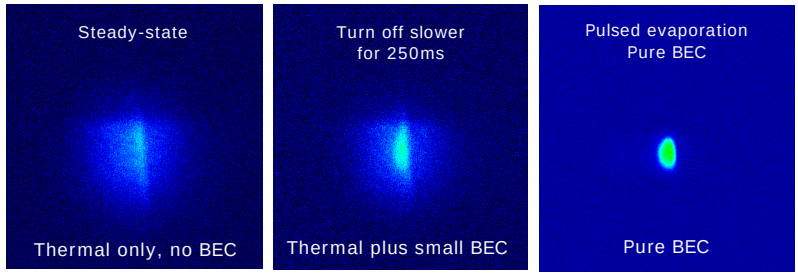

FIGURE 6.11: **Sitting on the edge of steady-state BEC (preliminary data).** Turning off the red Zeeman slower beam for 200 ms followed by a 50 ms long cleaning procedure (see section 4.4.1) is sufficient to eliminate the losses and allow the atoms in the reservoir to laser cool and condense. This data was taken during preliminary optimization work and includes a "stripe" in the thermal cloud from thermal atoms guided by residual dimple dipole trap power (see section 4.2.1). In later work the AOM frequency was also shifted during imaging eliminating the stripe from the thermal clouds, but this experimental work was not repeated.

6.2.5 Unity steady-state phase-space density

We can characterize the system for these final parameters (almost steady-state BEC) to estimate our steady-state phase-space density and to try to better understand where the best place is to target out improvements. In fact, all the data presented in this section along with the ^{84}Sr red MOT I+beam results from table 6.2 were collected at the same time with the same machine parameters (listed in appendix E) to try to get a complete snapshot of the system.

Our imaging system does not have the resolution to directly measure the atom number density in our dimple so we need an alternative approach for measuring our phase-space density. As we discussed in section 6.1.6, the phase-space density can also be formulated in terms of trapping frequencies (equation 6.3). This is the method by which we can estimate phase-space densities (and densities) within the reservoir and the dimple.

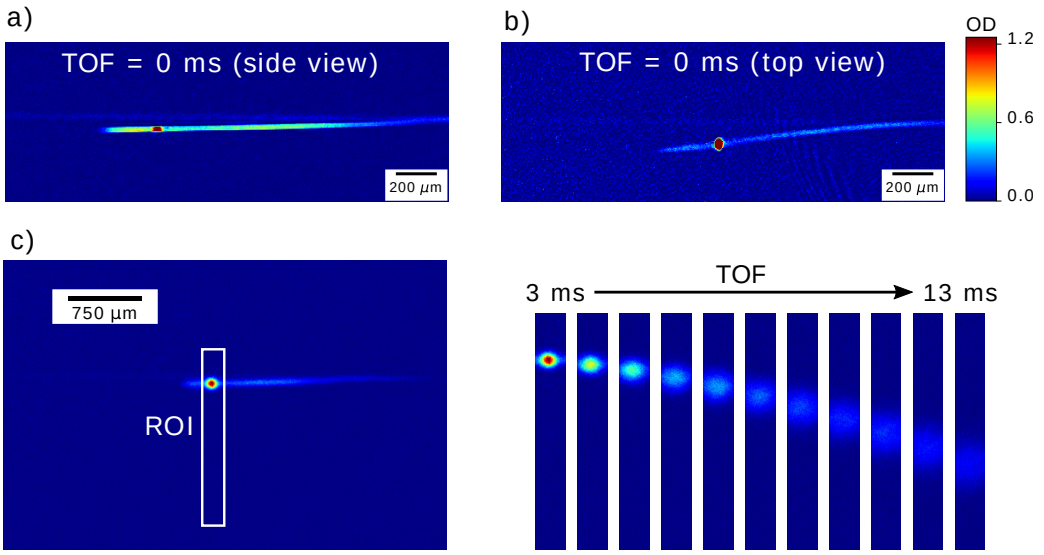

FIGURE 6.12: **Production of steady-state ultracold ^{84}Sr near quantum degeneracy.** (a,b) In-situ absorption images of density profiles of the atoms in the reservoir region taken from the side and from the top, respectively. (c) Time of flight of an ultracold ^{84}Sr sample. From the cloud expansion along the vertical direction we can derive the temperature by fitting the spatial profile of the atomic cloud. We also try to look for signs of a bimodal distribution in the cloud expansion images, a typical signature for a BEC.

It can be easy to overestimate the atom number in the dimple since the cloud is always overlapped with the reservoir trap to some extent. For this reason we also estimate the number knowing the loading rate of the dimple from a steady-state reservoir and the $1/e$ loading time. This results in a slightly lower atom number estimate. The results for the dimple section are tabulated in table 6.6.

We measure a steady-state phase-space density in the dimple of $1.7(11)$, almost the critical phase-space density to form a (very small) BEC.

With further analysis it is possible to gain some additional insight into what might be limiting our system. Fitting Gaussians to the cloud after a short, 5 ms, ballistic expansion can yield spatially resolved temperature and atom number information. We fit the clouds around the dimple and around the reservoir (see figure 6.10) to try to understand the temperature and atom number evolution within the system. Figure 6.13 shows typical raw data used for fitting and the fitted results. Analysis of the loss rates is tabulated in table 6.7.

A second important consideration is the elastic collision rate in both the reservoir and the dimple traps. We calculated this for the beam in section 6.1.6. The number density within the dimple can be estimated from the phase-space density which gives us an average elastic collision rate within the dimple of around $2.8(16)$ kHz. Estimating the number

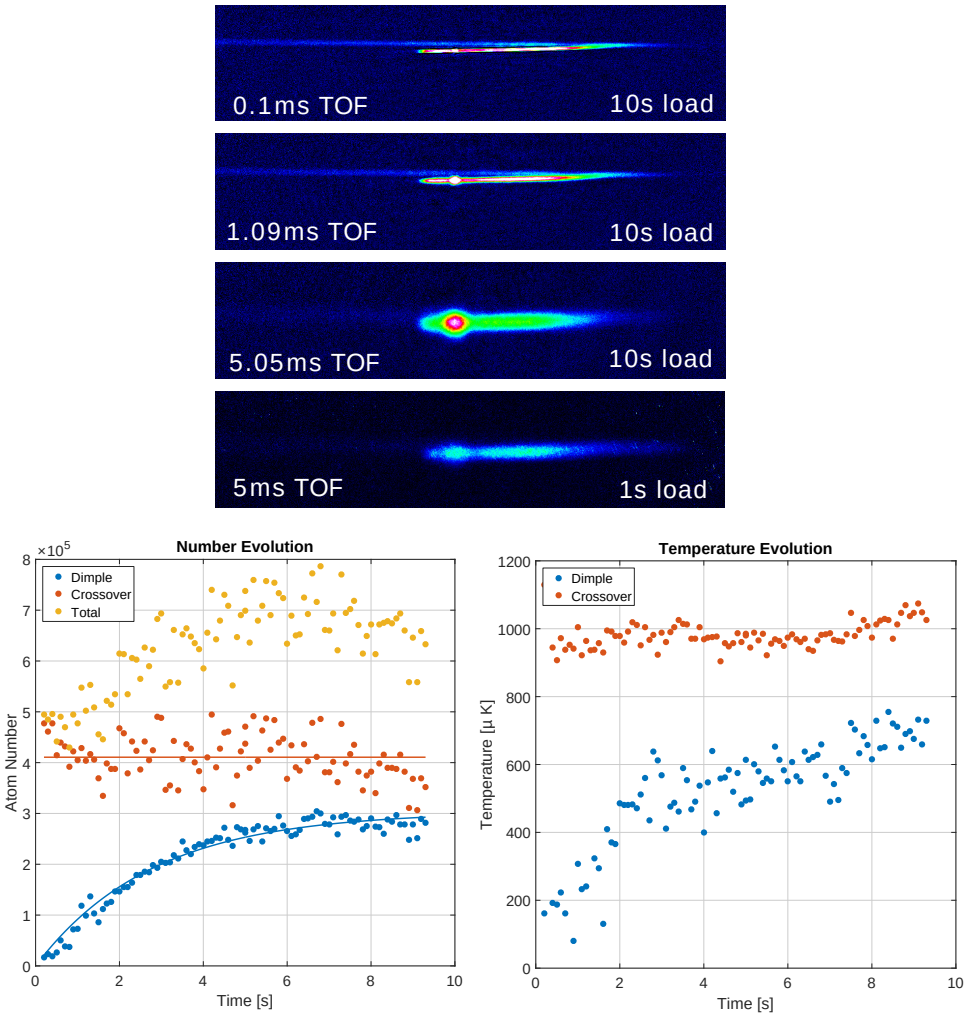

FIGURE 6.13: **Dimple analysis.** (top) Estimates of the atom number and temperature in both the dimple and "crossover" trap regions (see figure 6.10) can be made as a function of the loading time (in these top images load time refers to the time since all beams were switched on whereas the bottom images begin in steady-state but at the moment the dimple is switched on) by fitting Gaussians to the respective parts of the cloud after a 5 ms time of flight (TOF) for various loading times. Here we show example raw absorption images used for fitting. The bottom image has a different colour scale to the other images. (left) Evolution of the fitted atom numbers in the dimple and crossover reservoir clouds along with fitted curves when the dimple is switched on after loading the reservoir alone for 10 s. To estimate the initial cloud sizes the temperatures are scaled to match the final temperatures compiled from fitting the expansion curves. (right) Evolution of the fitted temperatures of the dimple and the crossover reservoir clouds in time since switching on the dimple after loading the reservoir alone for 10 s.

TABLE 6.6: **Dimple results.** Results are taken for an oven temperature of ≈500 K. All data refers to ^{84}Sr.

Parameter	Units	Results
Vertical trapping frequency	Hz	980(4)
Radial trapping frequency	Hz	293(17)
Vertical Temperature	μK	0.98(6)
X Temperature	μK	1.08(10)
Z Temperature	μK	1.16(8)
Average de-Broglie wavelength λ_{dB}	m	$1.97(22) \times 10^{-7}$
Dimple Loading $1/e$ lifetime[a]	s	2.4(5)
Dimple loading flux[b]	^{84}Sr s^{-1}	$9.3(26) \times 10^{4}$
Dimple number from flux/lifetime[c]	^{84}Sr	$2.2(10) \times 10^{5}$
Dimple number from integration[d]	^{84}Sr	$3.6(5) \times 10^{5}$
Peak Density	^{84}Sr cm^{-3}	$2.2(11) \times 10^{14}$
Phase-space density		1.7(11)

[a] This is the fitted loading time from figure 6.13 in which the reservoir is brought to steady-state over 10 s and then the dimple is switched on.
[b] The maximum slope in the loading curve of the dimple.
[c] The number can also be estimated from the loading rate and lifetime $N = f\tau$.
[d] Includes some atoms in the reservoir.

density in the reservoir is a little more tricky. We can easily measure the linear density from absorption imaging. For the density in the other two dimensions, we use from the temperatures and trapping frequency to give a peak density of $1.2(6) \times 10^{12}$ cm^{-3}. This results in an average collision rate in the reservoir of around 13(7) Hz. Although this is a low collision rate given the lifetime of just 0.77 s it is just fast enough to achieve some level of thermalization, even in the reservoir. Atoms in the dimple thermalize rapidly.

There is one thing that really sticks out from the analysis and that is the short lifetime of the reservoir at just 0.77(30) s. This is better than the 0.41(6) s we saw for the Zeeman slower ball (table 6.4) but only marginally so suggesting a similar loss mechanism. On the other hand the dimple demonstrates a much more reasonable lifetime of 2.4 s.

Another interesting question to ask is how close the steady-state parameters are to those needed to just reach BEC in pulsed mode (without refilling). For this we can compare with the data from [192] as shown in table 6.8. The principle conclusion which can be drawn from this comparison is that we have densities in our reservoir which are an order of magnitude less than what were needed in the pulsed case. We also have higher temperatures, which make the densities needed still higher. At the time we did push the flux to the point where little was gained from increasing the oven temperature.

TABLE 6.7: **Lifetime and efficiency analysis.** Results are taken for an oven temperature of ≈500 K. All data refers to ^{84}Sr.

Parameter	Units	Results
Measured arriving beam flux Φ_B[b]	^{84}Sr/s	$9.1(12) \times 10^5$
Reservoir number with dimple N_{R+D}	^{84}Sr	$4.1(5) \times 10^5$
Reservoir number without dimple N_R[g]	^{84}Sr	$4.8(3) \times 10^5$
Calculated reservoir $1/e$ lifetime τ_R[c]	s	0.77(30)
Calculated reservoir capture flux Φ_R[d]	^{84}Sr/s	$6.3(30) \times 10^5$
Calculated reservoir capture efficiency η_B[e]		69%
Linear density in the reservoir	^{84}Sr mm^{-1}	$3.5(5) \times 10^5$
Peak density in the reservoir	^{84}Sr cm^{-3}	$1.2(6) \times 10^{12}$
Average density in the reservoir	^{84}Sr cm^{-3}	$6(3) \times 10^{11}$
Peak collision rate in the reservoir[f]	Hz	27(14)
Average collision rate in the reservoir[f]	Hz	13(7)
Dimple loading $1/e$ lifetime τ_D	s	2.4(5)
Dimple loading flux Φ_D	^{84}Sr/s	$9.3(26) \times 10^4$
Dimple number from flux/lifetime N_D[a]	^{84}Sr	$2.2(10) \times 10^5$
Peak density in the dimple	^{84}Sr cm^{-3}	$2.2(12) \times 10^{14}$
Average density in the dimple	^{84}Sr cm^{-3}	$1.1(6) \times 10^{14}$
Peak collision rate in the dimple	kHz	5.5(31)
Average collision rate in the dimple	kHz	2.8(16)

[a] From table 6.6.
[b] From table 6.1.
[c] $\tau_R = 1/(\Phi_D/(N_R - N_{R+D}))$.
[d] $\Phi_R = \Phi_D + N_{R+D}/\tau_R$.
[e] $\eta_B = \Phi_R/\Phi_B$.
[f] For the reservoir we can not measure an axial temperature so we assume it is the same as we measure for the dimple.
[g] In this data the dimple trap is off and the reservoir atom number is integrated.

6.2.6 Conclusions

The steady-state phase-space density reached in the dimple of 1.7(11) is extraordinarily high. This is well over three orders of magnitude higher than the previous published[13] record steady-state phase-space density held by the Pfau group of 4×10^{-4} [205]. But this is not quite degeneracy.

[13] The reader may be wondering why these results have not been written up formally and published. At the time they were collected during January to March of 2018 we hoped that we were a few tweaks and tricks from our goal of a steady-state BEC. We didn't want to risk undermining the main result with a pre-result with similar performance from an almost identical system published a matter of weeks or months earlier. Priorities changed after we won the iqClock Quantum Flagship consortium grant. Since August 2018 I have focussed on building the new iqClock project so it has now been a year since we took this data. In the coming months we will finalize our upgrades discussed in the next section and try once again. One way or another we intend to publish the outcome before Chun-Chia, Benjamin or I move on.

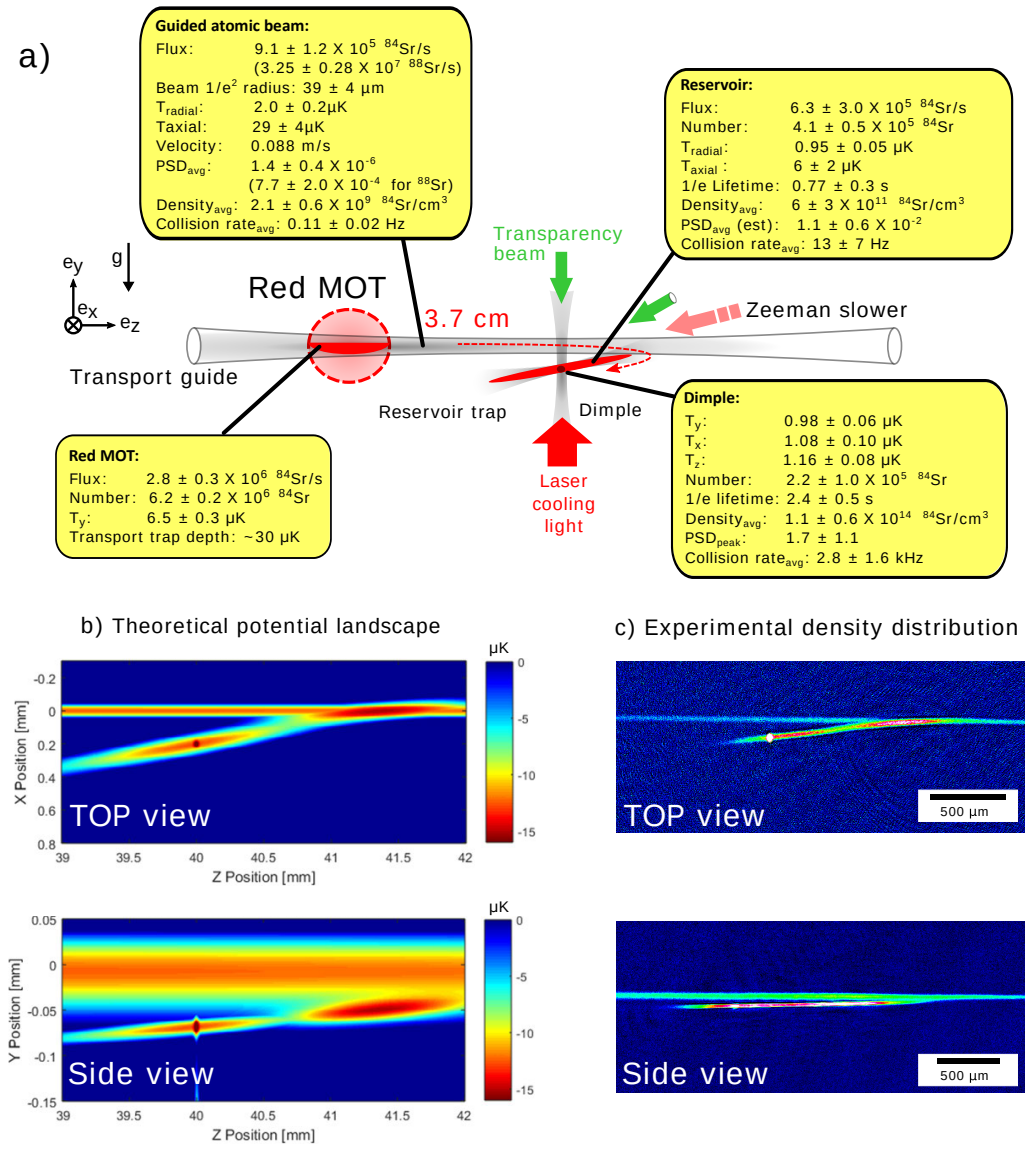

FIGURE 6.14: **Summary of the steady-state performance.** (a) Performances at various points throughout our transport architecture beginning with the steady-state red MOT, then the guided atomic beam and ending with the reservoir and the dimple trap in which we reach a steady state phase space density of 1.7(11). All values refer to ^{84}Sr unless otherwise stated. (c) Top and side view of calculated potential landscape for $^1S_0$ state. (c) Top and side view of ^{84}Sr atoms, continuously loaded into a reservoir trap.

TABLE 6.8: **The gap between pulsed requirements and steady-state results.** The gap between what we have in steady-state operation and what is sufficient in pulsed operation (using data taken from [192]).

Parameter	Steady-state	Pulsed [192]
Reservoir dipole trap power	790 mW	1748 mW
Reservoir dipole trap waist size	13 µm × 120 µm	17.3 µm × 298 µm
Reservoir dipole trap depth[a]	16.1 µK	11.73 µK
Dimple dipole trap power	135 mW	39.6 mW
Dimple dipole trap waist size	27 µm	22.4 µm
Dimple dipole trap depth	6.1 µK	2.73 µK
Vertical dipole trap power	-	743 mW
Vertical dipole trap waist size	-	297 µm
Vertical dipole trap depth	-	0.29 µK
Vertical trapping frequency	980(4) Hz	624 Hz
Dimple radial trapping frequency	293(17) Hz	244 Hz
Reservoir vertical trapping frequency	980 Hz	622 Hz
Reservoir X trapping frequency	108 Hz	37 Hz
Reservoir axial Z trapping frequency	18 Hz	8.4 Hz
Vertical Temperature	0.98(6) µK	0.944 µK
X Temperature	1.08(10) µK	0.944 µK
Axial Z Temperature	1.16(8) µK	0.944 µK
Number in dimple	$2.2(10) \times 10^5$	6.5×10^5
Number in reservoir	$4.1(5) \times 10^5$	5×10^6
Peak dimple density	$2.2(12) \times 10^{14}\,\mathrm{cm}^{-3}$	$1 \times 10^{15}\,\mathrm{cm}^{-3}$
Peak reservoir density	$1.2(5) \times 10^{12}\,\mathrm{cm}^{-3}$	$9.9 \times 10^{12}\,\mathrm{cm}^{-3}$
Peak dimple elastic collision rate	5.5(31) kHz	24 kHz[b]
Peak reservoir elastic collision rate	27(14) Hz	234 Hz[b]

[a] Ignoring gravitational sag.
[b] Values quoted in reference [192] appear to be missing a factor of 2π.

Our conclusion is that several aspects of the architecture need to be improved to reach steady-state degeneracy.

- The Zeeman slower is problematic. A Zeeman slower not only stops atoms but it also pushes them back and it partially overlaps with our reservoir[14]. We believe that our short lifetime of 0.77(30) s is primarily from the Zeeman slower although it is also possible that the high densities in the reservoir in combination with excess cooling laser power may play a role.

[14] We do include a counter-propagating molasses beam (Z in trap cooling) on the non-magnetic transition to try to help with this and without it the reservoir and dimple loading rates drop dramatically.

- Our ability to cool the reservoir while protecting the dimple from resonant light needs improvement. The temperatures we can reach of 1.1 μK are marginally high for the dimple to condense at an acceptable density in terms of 3-body scattering losses ($1 \times 10^{15}\,\mathrm{cm}^{-3}$). There are a number of factors that may be hurting here. The need for dual transparency beams from different orientations to achieve protection is one that particularly concerns me. This results in a region around the dimple with poor protection where the beams don't overlap. Here, atoms will scatter on the fast 4 MHz $^3P_1$-$^3S_1$ transparency transition and then on the repump transitions heating them. This creates a hot zone surrounding the dimple while at the same time reducing laser cooling capacity in this region. Another concern is the Stark shifts from the reservoir and transport guide dipole lasers that shift the transitions around preventing a global optimization of the laser cooling frequencies[15].
- Higher densities can still be obtained by increasing flux. Since taking these results we have improved flux and red MOT loading rates by more than an order of magnitude due to improvements to the blue Zeeman slower. This may already be sufficient to push our system to degeneracy.

To summarize, we believe that we do not reach sufficiently high densities for steady-state BEC because the lifetime of atoms in our reservoir dipole trap at $0.77(30)$ s is too short. It is thought that this is essentially a consequence of using a red Zeeman slower to stop our incoming atomic beam. We would also like to improve our reservoir cooling to reduce its temperature from $\approx$1.1 μK, which is marginal for making a strontium BEC even with a deep dimple and dense reservoir.

6.3 V2.1: Colder and darker

The results from our second attempt at steady-state BEC came tantalizingly close. Rather than wanting to rip it apart and try something new the urge was instead to tweak something or add something to nudge the system to degeneracy. We came up with a plan for several upgrades with an optional "sledge hammer".

1. **Improve or replace the Zeeman slower:** We developed a new deceleration technique, the Sysiphus Optical Lattice Decelerator (SOLD) that allows us to slow and load atoms from our beam without using radiation pressure. In principle it is more photon efficient than a Zeeman slower so it should also allow a significant reduction in laser

[15] We will be optimizing the polarizations of our dipole traps to minimize this and we will need to look into the affordability of moving to a magic wavelength.

intensities in the reservoir region and it is impossible for it to push atoms out of the reservoir trap so losses should be dramatically reduced.

2. **Improve the transparency protection and the laser cooling:** We are testing the 487 nm transparency transition for its ability to protect the dimple. Since there is no dark state for this transition a single beam matched to the dimple trap should be sufficient to fully protect the dimple from $^1S_0$-$^3P_1$. This will eliminate the presence of a partially protected region around the dimple where there is only one transparency beam that in turn should eliminate most of the heating from scattering on the transparency and repump transitions. It will also allow laser cooling the reservoir much closer to the dimple. The main concern is whether additional scattering due to proximity to the 461 nm line might cause excess heating for the BEC. In the case of the 487 nm transition there will be an optimal intensity beyond which off resonant scattering reduces the protection for the BEC.
3. **Use evaporation:** I sometimes think we have been fighting with one hand tied behind our backs. We have achieved these results with no deliberate evaporation in the system, only laser cooling. Yet we know that even small amounts of evaporation can rapidly reduce the temperature as long as the trap is protected from resonant light. With the introduction of dark state free transparency protection using a single beam, it will become much easier to protect dimple traps and reservoirs in close proximity to laser cooled clouds. This will open the potential for more complex cooling schemes that mix and match laser and evaporative cooling.

6.3.1 Colder: the Sisyphus Optical Lattice Decelerator (SOLD)

We used a Zeeman slower on the red transition to stop our atomic beam and load our reservoir but this caused high losses as it pushed atoms out of the reservoir trap (see section 6.2.6). The lifetime of our reservoir was only 0.77 s which had a big impact on the number of atoms we could accumulate and the density we could reach in the reservoir. The Sisyphus Optical Lattice Decelerator (SOLD) was our answer to this problem.

Benjamin had the idea that maybe we could use a Sisyphus mechanism in a state dependent lattice instead of radiation pressure to slow and stop our incoming atomic beam. The essence of the idea is to use a narrow transition to excite moving atoms when they are resonant with the bottom of a lattice on an excited state. They then climb the lattice hill in the excited state, loosing kinetic energy, before decaying spontaneously back to a flat potential landscape. If the lattice is deep, the atoms can lose much more than a photon recoil of energy during each cycle so it can in principle be an efficient process. This idea

has been bouncing around in various theoretical proposals for 25 years but doesn't seem to have been implemented experimentally [218, 355–357] so we tried it and it worked.

We wrote a paper on this technique which is included in chapter 7 so I will be very brief here in my remarks on this topic. Instead I would refer the reader to the following chapter that might be worth reading before continuing. I do however want to discuss why this technique has the potential to help push our system to degeneracy which is not a topic specifically addressed within the paper. There are many ways in which a SOLD lattice can help:

No unbalanced radiation pressure The SOLD technique is not based on radiation pressure like a Zeeman slower. There is no need for unbalanced beams that will cause loss for our reservoir.

More efficient SOLD can dissipate more kinetic energy per photon scattered and can in principle achieve faster rates of deceleration.

Much less resonant light No resonant light beams are required to run SOLD. It can simply rely on the transverse cooling for excitation reducing heating rates and reducing the amount of resonant light a BEC needs to be protected against.

Moderate Stark shifts required We only need a Stark shift of 500 kHz. With the powers of transparency light we have available this means we can use a large detuning of 30 GHz or more essentially eliminating off-resonant scattering and the need for repumpers (see figure 7.11).

Reduced impact of Stark shifts The performance of molasses cooling on the 7.4 kHz transition is very strongly impacted by Stark shifts. These can push the frequency of a beam optimized for a certain trap depth to the blue by many linewidths resulting in heating rather than cooling from the molasses beams in the outer parts of your dipole trap even though it might be optimal for the center. This prevents us from attaining optimal cooling performance in our landscape of variable potentials with variable Stark shifts. The SOLD architecture essentially reduces this sensitivity to our landscapes of variable Stark shifts.

A dark spot The SOLD lattice shifts atoms out of resonance throughout most of the reservoir so they interact only when they cross the nodes of the lattice. Essentially this will darken our reservoir reducing the scattering rate and allowing atoms to accumulate in a similar way to the way they accumulate in the dimple.

In principle, we can eliminate the need for both a Zeeman slower beam and the Z in-trap cooling molasses beam by using SOLD. Light from the transverse cooling beams is

sufficient to excite atoms into the excited state lattice that can dissipate the energy from the Z direction. This can completely eliminate the need for radiation pressure in the Z axis. In this way, SOLD can significantly reduce the resonant light in the reservoir. But it is not the resonant light that appears to be our main problem, it is the ability for the Zeeman slower to push and kick atoms out of our reservoir resulting in heavy losses. Here the SOLD can really help. It can cool the atoms in the Z axis with no need for unbalanced radiation pressure and without the Stark shift sensitivity of a molasses that disrupted the usefulness of our Z in trap cooling beams.

The SOLD will hopefully eliminate most of our losses while at the same time improving our cooling and making our reservoir and BEC darker. We are now implementing a SOLD decelerator overlapped with the reservoir dipole trap and large enough to also extend coverage to the end of the Zeeman slower. We also considered a second SOLD overlaid with the present location of the Zeeman slower but this will probably only marginally improve the system since a single SOLD is enough to eliminate a slower beam's destructive tendencies at the end where the atoms come to rest and we would then need to build additional transparency lasers to avoid interference. The angle between the reservoir and the slower location prevents a single beam covering both locations simultaneously.

To implement a SOLD decelerator we need counter-propagating transparency beams with a power on the order of 20 mW[16]. For our SOLD demonstration we used our horizontal and vertical protection beams but for implementation in the full system we need additional transparency lasers. SOLD and protection beams must be mutually incoherent with frequency separations of at least 700 MHz. Thus we are making new slave lasers and perhaps another master laser to seed them. We have recently tested injection locking 50 mW (Thorlabs HL6750MG) diodes and found they worked better than the 30 mW (Thorlabs HL6738MG) diodes we used in building the machine and the tapered amplifier chip we used on the transparency beams. These are now installed and the machine is being restabilized and optimized to get its performance back to what we had during our last campaign.

6.3.2 Darker: Better transparency protection

There are two ways in which we are improving the transparency protection for the dimple region. Firstly, we can increase the power in our protection beams and better focus and position our weirdly placed 'horizontal' transparency beam (see figure 4.15). The second approach is to switch to using the 487 nm $^3P_1$-$^3D_2$ transition, which has no dark state. We have implemented both.

[16]The more power the better at 688 nm as it affords a larger detuning, which reduces scatter on the $^3P_1$ - $^3S_1$.

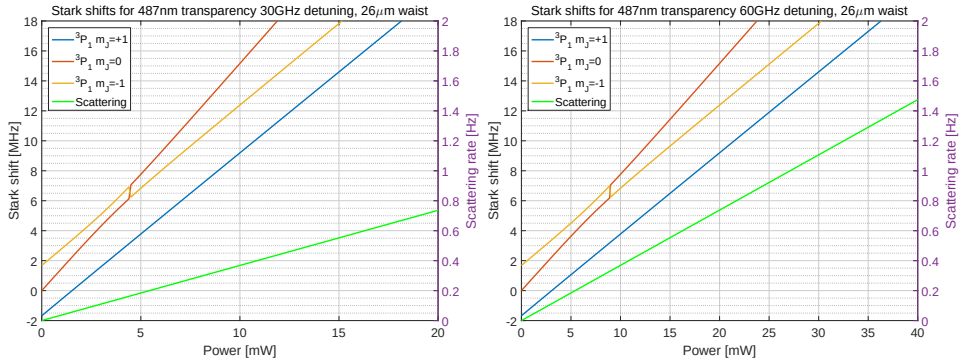

FIGURE 6.15: 487 nm **transparency laser.** Calculated Stark shifts and the off-resonant scattering rate for the ground state using a 487 nm $^3P_1$-$^3D_2$ transparency laser.

The lack of a dark state in the 487 nm $^3P_1$-$^3D_2$ transition means that only a single transparency beam is required to shift all the $^3P_1$ magnetic sublevels. This means that we no longer need to overlap two beams with their inevitable mismatch. This reduces the size of the partially protected boarder regions around the BEC protection zone reducing the incidence of excitation by a transparency beam and the subsequent heating.

A second important practical advantage of using 487 nm is that there is no need to overlap a 1.07 µm dipole trap beam with the transparency beam since the latter forms the trap by itself. This guarantees the BEC receives the maximum possible protection and that the alignment is always perfect.

Close proximity to 488 nm (argon ion laser replacement) makes 487 nm diodes relatively high power, cheap and easy to procure. Our 60 mW diodes came from CNI laser (LD-488-60). The main concern at 487 nm is the close proximity to 461 nm which will increase off resonant scattering rates. By solving for the eigenstates using the same methodology as we used in section 4.3.2 we can estimate the powers required to protect a BEC and the corresponding scattering rates. Figure 6.15 plots the results. We can see that off resonant scattering is indeed an important consideration and limits us to Stark shifts on the order of 5-10 MHz which is more than enough for our application. For this we will require a single beam with a power on the order of 10 mW detuned from the $^3P_1$-$^3D_2$ transition by $\approx$30 GHz.

6.3.3 V3.0: Use evaporation - the sledge hammer?

Compared to a typical pulsed strontium BEC machine the most notable difference from our work towards a steady-state BEC system is that our reservoir is much hotter. Typically when we make a pulsed BEC we evaporatively cool our reservoir and we start to see

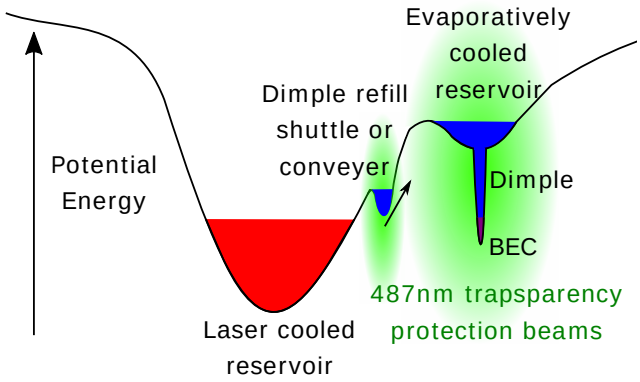

FIGURE 6.16: **Including evaporation to cool the reservoir.** Here we show one of many possible schemes that could be used to evaporatively cool the reservoir.

respectable condensates in our dimple for reservoir temperatures below around 0.2-0.3 µK. Making even very small BECs with a reservoir temperature above 0.8 µK starts to become problematic. We have a reservoir temperature of around 1.1 µK which requires loading huge numbers of atoms to reach very high densities. This temperature is limited by the fact that so far we have not deliberately used evaporative cooling. To make a reasonably pure BEC and to make this experiment much easier we *must* introduce evaporative cooling to the architecture to get our reservoir temperatures well below 1 µK.

Early last year we began implementing a final stage based on evaporative cooling with the introduction of an AOM for creating an array of dimple traps. These traps can be used to evaporate and shuttle atoms from our main reservoir to a second much colder reservoir trap off to the side. This scheme is illustrated in figure 6.16. So far it has been more of a side project in the hope that the earlier upgrades would do the job, but if we are ever going to make a steady-state system with even a moderately pure condensate evaporation will need to be incorporate as a final cooling stage in order to get the reservoir temperature down. An important part of making this work in a practical sense was the development of the 487 nm transparency transition that we are about to start testing. This new transparency beam dramatically simplifies evaporative architectures, the transparency makes the potential landscape at the same time as providing protection so it is much easier to paint guides with a dithered AOM and use an AOM to move dimple traps around to shuttle and evaporate atoms. If it is successful at demonstrating the necessary protection we will need to construct some higher power lasers so that we also have the power needed to protect an entire reservoir, not just a dimple. Fortunately, higher power diodes also exist and are relatively inexpensive at 487 nm so it is easy to imagine protecting an entire second (evaporatively cooled) reservoir containing a dimple.

6.3.4 Summary

The SOLD upgrade is essentially complete, the 487 nm transparency laser is being added to the machine and we are now getting the machine back to top performance. In the next couple of months the results from V2.1 will be finalized and depending on the outcome we may finish off the evaporation scheme described as V3 above or something similar. The fundamentals are all already there, the conditions needed to reach steady-state BEC are within our grasp and hopefully we will be able to finish this off over the coming months.

6.4 Summary

We began by producing a beam of ^{88}Sr with a steady-state peak phase-space density of $1.5(4) \times 10^{-4}$, a flux of $3.25(28) \times 10^{7}\,\mathrm{s}^{-1}$ and radial temperatures as low as $0.89(8)\,\mu\mathrm{K}$. To our knowledge, this is the highest phase-space density ever achieved in a continuous ultracold beam experiment, around three orders of magnitude higher than previous work by Guery-Odelin's group [170, 172]. Furthermore, we demonstrated 30% conversion efficiencies from the flux captured by our red MOT into a transported high phase-space density beam. This could have important implications for ultracold beam generation for applications from ion beams to sympathetic cooling and atom lasers.

We showed that we could decelerate, capture and cool this beam in a dipole trap where we produced steady-state samples with a phase-space density approaching degeneracy ($1.7(11)$). This result is another three orders of magnitude beyond the already record phase-space density produced by our red MOT [207]. In fact, from this steady-state sample a BEC can form within 250 ms simply by turning off the red Zeeman slower that loads new atoms from our guided atomic beam.

To tackle the heating and scattering from the slower we developed and demonstrated a new Sisyphus type slowing technique. The Sisyphus Optical Lattice Decelerator (SOLD) is able to slow atoms more efficiently than radiation pressure based approaches and can reduce the amount of light needed in the system. Unlike a Zeeman slower, the SOLD is able to bring atoms to a stop without pushing them back and it doesn't require a beam counter-propagating to the atoms. This should significantly reduce the loss in our reservoir trap. We will shortly be testing the SOLD together with a new dark state free transparency wavelength at 487 nm to see if these upgrades are sufficient to reach steady-state degeneracy.

Finally, we began developing approaches to incorporate a final evaporative cooling stage into our system. This is likely to be significantly helped by the development of a dark state free 487 nm transparency beam.

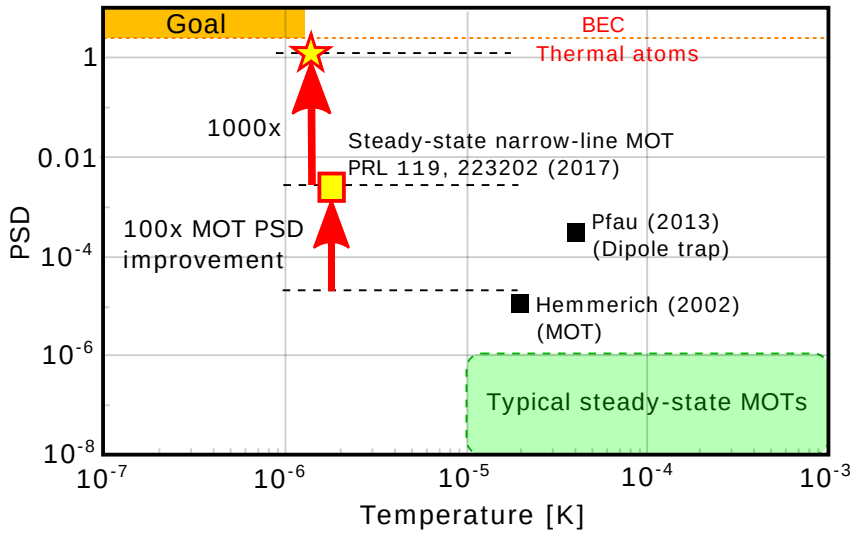

FIGURE 6.17: **Progress in steady-state ultracold samples.** The phase-space densities and temperatures from previous experiments are plotted along with our recent results. The yellow square shows our steady-state red MOT described in chapter 4 and 5 while the star indicates our current status with a phase-space density of 1.7(11). Hopefully we will soon break into the world of steady-state degeneracy.

When we started, the highest steady-state phase-space densities were on the order of 4×10^{-4}. We are now at 1, just a heartbeat away from the critical value of 2.6. This progress is illustrated in figure 6.17. We are preparing for a new campaign incorporating our latest upgrades and will shortly see if this is enough to reach the long awaited goal of steady-state degeneracy.

Chapter 7

Publication: Sisyphus Optical Lattice Decelerator

Physical Review A, Vol. **100**, 023401, (2019)[358]

Chun-Chia Chen, Shayne Bennetts, Rodrigo González Escudero, Florian Schreck and Benjamin Pasquiou*

Van der Waals-Zeeman Institute, Institute of Physics, University of Amsterdam, Science Park 904, 1098XH Amsterdam, The Netherlands

We experimentally demonstrate a variation on a Sisyphus cooling technique that was proposed for cooling antihydrogen. In our implementation, atoms are selectively excited to an electronic state whose energy is spatially modulated by an optical lattice, and the ensuing spontaneous decay completes one Sisyphus cooling cycle. We characterize the cooling efficiency of this technique on a continuous beam of Sr, and compare it with radiation pressure based laser cooling. We demonstrate that this new technique not only eliminates many of the constraints and limitations of traditional radiation pressure based approaches, it does so while delivering a similar atom number with lower final temperatures. This method can be instrumental in bringing new exotic species and molecules to the ultracold regime.

The asymmetry between matter and antimatter is one of the great mysteries of modern physics. A promising avenue to better understand this asymmetry is to precisely compare spectra of hydrogen with antihydrogen, but this requires the ability to generate robust trapped samples of ultracold antihydrogen [111, 359–363]. For this, laser cooling is needed at 121.6 nm, where performances remain strongly constrained by current laser technology [109, 364–366]. The proposal in Wu *et al.* [218] overcomes these limitations by allowing

the extraction of many photon recoils of momentum per scattering event by the simple addition of an optical lattice.

This method is not limited to cooling antihydrogen. Related proposals have considered a similar working principle to cool and localize atoms [355, 356] as well as to decelerate hot Yb atomic beams [357]. Slowing and cooling molecules [367–369] is perhaps the most topical application for this method today. Recent striking successes in molecule cooling have relied on adapting laser cooling to molecules, either by choosing species with close-to-diagonal Franck-Condon factors [370–372], or by using highly efficient laser cooling techniques [373, 374]. Applying this new cooling method can bring better cooling efficiency and a broader class of laser cooled molecules. In turn, progress in molecule cooling opens new ways to probe the very foundations of physics [375, 376]. Some of the most prominent include tests for the possible variation of fundamental constants [319] and for the validity of fundamental symmetries [377–382].

A range of approaches have been devised to achieve improved performance while relaxing constraints imposed by traditional Doppler cooling techniques. For example, rapid cycling using stimulated emission can provide stronger momentum transfer without spontaneous heating or loss from non closed cycling transitions. This is demonstrated in bichromatic force cooling [383], adiabatic rapid passage [384] and SWAP cooling [311] but it requires intense resonant light not available at the 121.6 nm transition needed for antihydrogen. Alternatively, Sisyphus-like cooling methods [322], where kinetic energy is converted into potential energy, can function effectively even at very low pumping rates and are routinely applied to beat the Doppler temperature limit [321]. Examples of this approach include Zeeman-Sisyphus decelerators [385] and Rydberg-Stark decelerators [386, 387], where a photon excitation changes the internal state allowing a significant part of the slowing to be done by an externally applied electromagnetic field gradient.

In this letter, we present a proof-of-principle demonstration of a class of proposals developed to laser cool antihydrogen [218] and other species [355–357]. Our demonstration uses a Sisyphus-like deceleration mechanism to slow a continuous stream of strontium atoms without using radiation pressure. The method uses a 1D optical lattice acting on the excited $^3P_1$ electronic state combined with a selective pumping mechanism that excites atoms to the lattice potential minima. We explore the performance of this technique, which we name a Sisyphus Optical Lattice Decelerator (SOLD). To compare with traditional radiation pressure schemes we also substitute the SOLD with a Zeeman slower on the same transition. In principle, by using a deep lattice very few pumping photons can be sufficient to bring fast atoms to rest, making SOLD a good decelerator candidate for exotic species and molecules without a closed cycling transition [368, 370–372, 374].

The working principle of the SOLD relies on a 3-level system coupled by two optical

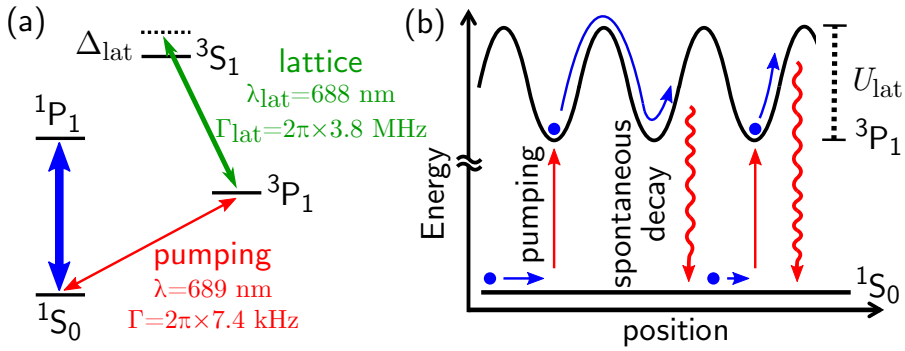

FIGURE 7.1: (a) Relevant electronic levels of strontium and the two transitions used for pumping and optical lattice creation, both necessary for the SOLD. (b) Schematic of two typical cooling cycles, from pumping to spontaneous decay.

transitions, something ubiquitous for both atomic and molecular species. Our implementation using strontium is depicted in Fig. 7.1(a). An optical lattice is formed using a pair of coherent counter-propagating beams with a frequency in the vicinity of the $^3P_1 - {}^3S_1$ transition. This produces a spatially modulated coupling between the $^3P_1$ and $^3S_1$ states and thus a spatially modulated light shift on the excited $^3P_1$ state. The ground $^1S_0$ state remains essentially unaffected. By applying a laser resonant with the $^1S_0 - {}^3P_1$ transition, atoms can be optically pumped into the $^3P_1$ state where they experience the force associated with the lattice potential, see Fig. 7.1(b). If the linewidth Γ of the $^1S_0 - {}^3P_1$ intercombination line is much smaller than the lattice height $U_{lat} \gg \hbar\Gamma$, this "pumping" laser can be tuned to selectively address the bottom of the lattice sites. For high enough velocity $v > \lambda_{lat}\Gamma$, atoms pumped into $^3P_1$ will then climb a significant fraction of the lattice potential hills and lose kinetic energy before spontaneously decaying to the ground state as shown in Fig. 7.1(b). As atoms in $^1S_0$ propagate along the lattice axis, this cooling cycle repeats like a Sisyphus mechanism. By making the lattice very high, it is theoretically possible to remove most forward kinetic energy within distances of a few lattice periods or with a single cycle, as in Rydberg-Stark decelerators [386, 387]. The temperature limit for this scheme is the higher of an effective Doppler temperature depending on Γ [356], or the recoil temperature.

To demonstrate experimentally the feasibility of the SOLD, we implement the setup shown in Fig. 7.2(a). We start with a magneto-optical trap (MOT) operating in a steady-state regime on the 7.4 kHz-linewidth $^1S_0 - {}^3P_1$ line, as described in our previous work (configuration "Red MOT I" in figure 5.1 of chapter 5). We overlap this MOT with an optical dipole trap acting as a "transport" guide (see Chapter 6). This 1D guide is $\sim 35\,\mu$K deep at the MOT location and propagates horizontally along the z axis. By adding a "launch"

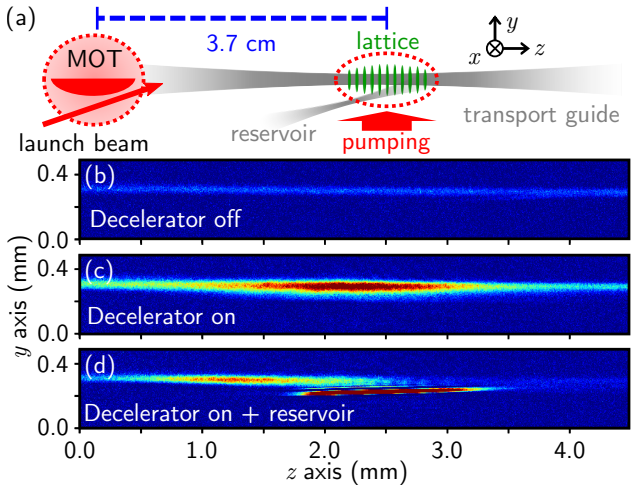

FIGURE 7.2: (a) Side view of the setup. (b,c,d) $^1S_0 - {}^1P_1$ absorption imaging pictures of the atomic beam at the decelerator location, (b) without lattice, (c) with lattice, and (d) with lattice and reservoir.

beam resonant with the $^1S_0 - {}^3P_1$ π transition and pointed at the overlap between the MOT and transport guide, we outcouple MOT atoms into the guide with a well-controlled mean velocity ranging from 0.08 to 0.25 m.s^{-1} (see Section 7.1.3). Atoms then propagate along the guide for ~ 3.7 cm until they reach the decelerator region.

We produce a 1D lattice potential with a pair of counter-propagating laser beams whose frequency is blue-detuned by $\Delta_{\text{lat}} \approx 2\pi \times 30$ GHz from the $^3P_1 - {}^3S_1$ transition. The lattice beams cross the transport guide at a shallow angle of 6°, overlapping the atomic beam for about 3.4 mm. Optical "pumping" from the $^1S_0$ to $^3P_1$ state is provided by illuminating the atoms from the radial direction. Pumping laser beams are 15 kHz red detuned from the π transition and their combined intensity corresponds to a saturation parameter of ~ 1. In addition to pumping, these beams provide an optical molasses effect, which brings the atoms' radial temperature to ~ 2 µK. Importantly, there is no near-resonant light capable of slowing atoms in the z axis in the absence of the SOLD optical lattice.

We operate the decelerator on a guided atomic beam continuously fed by the MOT, with a homogeneous axial density across the full field of view of our imaging system, see Fig. 7.2(b). When the lattice is switched on, the density in the overlap region between the atomic and lattice beams sharply increases, suggesting an accumulation of slowed atoms, as shown in Fig. 7.2(c). Without either lattice beam or with a large (160 MHz) frequency difference between the two lattice beams, this feature vanishes. Fig. 7.2(c) also shows that some atoms travel completely across the lattice region due to incomplete slowing or by diffusion. Note that our slowing mechanism is fully compatible with a steady-state

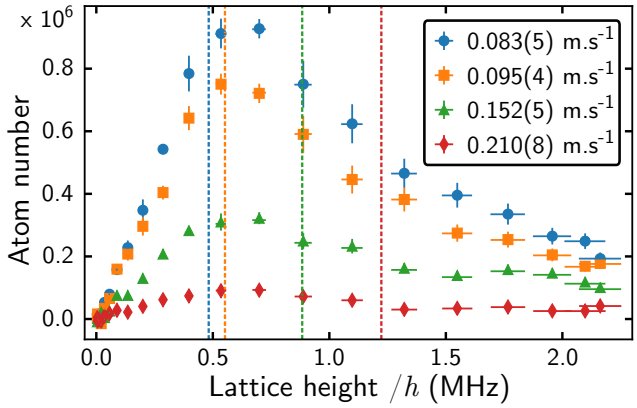

FIGURE 7.3: Measured steady-state number of atoms slowed by the SOLD and loaded in the reservoir, for varying lattice height and four different initial velocities. Dashed vertical lines give the criterion of eq. (7.1) for $m = 1$. The vertical error bars represent standard errors from binned data points. The horizontal error bars origin is described in (see Section 7.1.5).

apparatus, and we perform our measurements after reaching steady state.

For better characterization of the SOLD, and since we are concerned about diffusion of slowed atoms, we add a second "reservoir" dipole trap beam. This beam crosses below the transport guide at the lattice location, with an offset adjusted to allow slow atoms to pass from the guide into the reservoir while not significantly disturbing the potential landscape of the guide. With the help of optical molasses (see Fig. 7.2(a)), the reservoir collects and stores slowed atoms 2 mm away from the crossing. We measure the mean velocity selectivity of the loading of this reservoir (see Section 7.1.1), which matches a Gaussian centered around zero velocity with a width $\sigma_v = 0.0084(4)\,\mathrm{m.s}^{-1}$. We show one example of loading into this reservoir in Fig. 7.2(d), which also exemplifies a means of atom extraction from our ultracold atom source. We show in Fig. 7.3 the measured atom number loaded into the reservoir by the SOLD. The efficiency is poor for small lattices, as not enough kinetic energy is removed before atoms leave the lattice location. For increasing lattice height, we observe a clear loading optimum, followed by a slow decrease. These two features originate from the behavior of the pumping rate to $^3\mathrm{P}_1$.

We can better understand the observed SOLD slowing efficiency with a simple semi-classical model describing its various working regimes, which depends on the relative magnitude of the atoms' kinetic energy with respect to lattice height. Consider an atom initially pumped into the $^3\mathrm{P}_1$ state at the bottom of the lattice potential. In Fig. 7.4(a), we plot the dependence of the average energy lost per pump cycle E_{lost} with incoming velocity v and lattice height. For high kinetic energies compared to the lattice height $\frac{1}{2}mv^2 \gg U_{\mathrm{lat}}$,

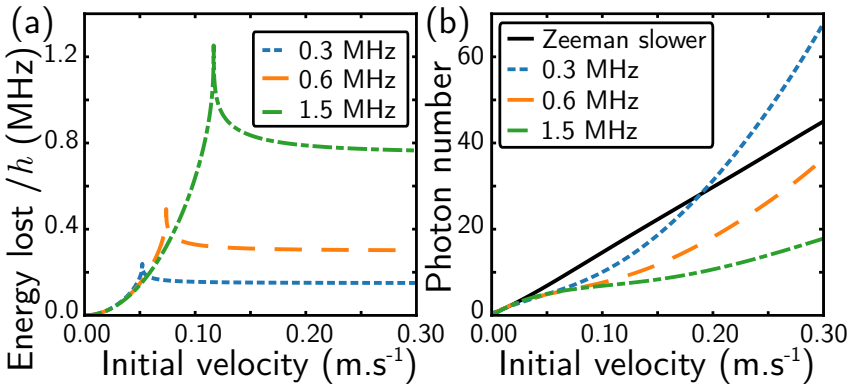

FIGURE 7.4: Efficiency of our cooling scheme for varying initial velocity. (a) Average energy E_{lost} lost during the first cooling cycle. (b) Number of cycles/pumping photons needed for the SOLD compared with a Zeeman slower. The black line shows the ZS behavior, while the dotted, dashed and dash-dotted lines are for the SOLD with various lattice heights.

atoms travel through several lattice sites and the energy lost saturates to $E_{\text{lost}} \to U_{\text{lat}}/2$ provided that $v \gg \lambda_{\text{lat}}\Gamma$. A striking feature of Fig. 7.4(a) is that E_{lost} exhibits an efficiency peak for $\frac{1}{2}mv^2 = U_{\text{lat}}$. In this case, atoms have just enough energy to climb one lattice maximum, where they spend most of their time and are thus more likely to undergo spontaneous emission. The energy lost asymptotically reaches $E_{\text{lost}} \to U_{\text{lat}}$ for $v \gg \lambda_{\text{lat}}\Gamma$ (see Section 7.1.2).

Laser cooling techniques can be benchmarked by the average number of photons that need to be scattered to slow atoms from some initial velocity to the technique's temperature limit. In Fig. 7.4(b) we calculate the number of pumping photons needed to reach a kinetic energy equivalent to a temperature below 2 µK. This temperature was arbitrarily chosen ~ 4 times larger than the recoil temperature for the $^1S_0 - {}^3P_1$ transition, the relevant cooling limit in our case. For comparison with radiation pressure based laser cooling methods, we also show in Fig. 7.4(b) the number of photons required in the case of a Zeeman slower (ZS) [118]. The SOLD always requires fewer cooling photons than the ZS for a lattice height satisfying $U_{\text{lat}}/h > v/\lambda_{\text{lat}}$.

The SOLD ability to slow atoms with high incoming velocities is strongly dependent on the pumping rate. We model this rate by solving the optical Bloch equations for a two-level system in dependence of velocity and lattice height. Assuming a constant velocity, we numerically solve (see Section 7.1.2) for the average population in $^3P_1$, which we show in Fig. 7.5(a). The remarkable feature in Fig. 7.5(a) is the presence of multiple resonances where there are high pumping rates. These can be explained by in-phase multiple π-over-N pulses. Indeed, only at the bottom of a lattice site is the detuning small enough to pump

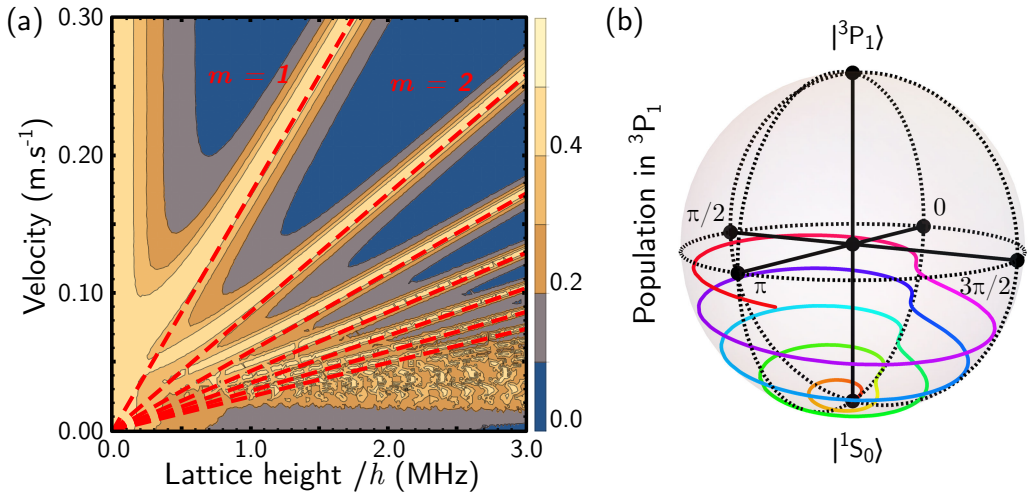

FIGURE 7.5: (a) Population transferred to the $^3P_1$ state depending on the lattice height and the atom velocity. For clarity of the figure, the population is calculated for a saturation parameter of the pumping transition of ~ 1600 instead of the $0.1 \sim 10$ typically used. Dashed red lines show the condition of eq. (7.1) for $m \in \{1...7\}$. (b) Short time evolution of the bloch vector (for 5 "pulses") in the case of in-phase excitation satisfying eq. (7.1) with $m = 1$.

a significant population to $^3P_1$. While the atoms propagate from one site to the next, the $^1S_0$ and $^3P_1$ states acquire different phases. Once at the next site, further population is efficiently pumped to $^3P_1$ only if the dephasing is equal to multiples of 2π, see Fig. 7.5(b). This criterion on the dephasing leads to the relation

$$\frac{U_{\text{lat}}}{h} = m \times \frac{4v}{\lambda_{\text{lat}}}, \tag{7.1}$$

with $m \in \mathbb{N}$ and h the Planck constant. The loading efficiency optimums observed in Fig. 7.3 correspond mainly to fulfilling this criterion for the case $m = 1$. Including both the average lost energy E_{lost} and the pumping rate, we model the behavior of the SOLD and reproduce qualitatively the features of the experimental data (see Section 7.1.2). The criterion of eq. (7.1) with $m = 1$ effectively dictates the capture velocity of the SOLD, $v_c = U_{\text{lat}}\lambda_{\text{lat}}/4h$. For a lattice height thus matching the atoms' velocity, the SOLD requires less photons than standard radiation pressure based laser cooling methods like the ZS.

We now compare experimentally the SOLD performance with that of a Zeeman slower. To this end, we add a laser beam counter-propagating to the transport guide, focused in the SOLD region and with a circular polarization set to address the $m_J = -1$ Zeeman sub-state. We demonstrated in previous work that it is possible to operate a ZS on the

TABLE 7.1: Comparison of the SOLD and the Zeeman slower (ZS). The rows give steady-state atoms numbers, fluxes, $1/e$ loading times, and reservoir radial (axial) temperatures T_{rad} (T_{z}). The various configurations are, in order, the SOLD in the transport guide, the SOLD plus the reservoir (R), the ZS plus reservoir and the combination of both.

	SOLD	SOLD+R	ZS+R	SOLD+ZS+R
Atom ($\times 10^6$)	0.78(01)	0.69(01)	1.87(04)	2.00(10)
Flux ($\times 10^6\,\mathrm{s}^{-1}$)	0.74(04)	0.65(03)	2.11(14)	2.80(15)
Loading (ms)	705(20)	625(52)	434(43)	507(55)
T_{rad} (µK)		1.53(02)	1.08(04)	1.34(02)
T_{z} (µK)		2.30(06)	5.67(94)	2.59(10)

narrow Sr intercombination line (see Chapter 5). We report in Tab. 7.1 a comparison between the two slowing methods. Both give similar results for fluxes and final atom numbers, with an advantage for the ZS, which we attribute mainly to the spatial selectivity of its optical excitation. However, we observe a clear difference in the final axial temperatures T_z within the reservoir, which effectively reflects the final mean velocities. For the SOLD, T_z is almost as low as the radial temperature T_{rad} provided by the molasses cooling, whereas T_z is 2.5 times hotter for the ZS. This is because a Zeeman slower is unable to decelerate atoms to zero velocity, as they remain somewhat resonant with ZS photons and are pushed backwards. By contrast, the final mean velocity for the SOLD is stationary in the frame of the optical lattice, which itself can be chosen arbitrarily [388, 389] (see Section 7.1.1).

An additional difference is that, since the SOLD does not rely on radiation pressure from the pumping beam to cool, it is possible to use a much broader class of transitions than for standard laser cooling methods. It is for example possible to use the ZS beam as a pumping beam that features both spatial and velocity selectivity. The lattice, now acting on atoms in $^3\mathrm{P}_1\, m_{\mathrm{J}} = -1$, is the one charged with decelerating atoms to zero axial velocity. In presence of both lattice and ZS beams, we observe the best number of atoms in the reservoir, while keeping the low temperature T_z due to the SOLD, see Tab. 7.1.

Let us now turn to considerations for further applications of this cooling scheme. Firstly, it is clear from Fig. 7.5(a) that, at high velocities, pumping rates are low unless the lattice height matches the conditions of eq. (7.1). This can be dealt with by temporal modulation of the lattice intensity, which varies the resonance locations. Secondly, for lattices much higher than the transport guide depth, we observe a clear spread of the atomic beam out of the guide. This is due both to the radial anti-confinement from the blue-detuned lattice beams and the slight angle between lattice and transport beams. A red-detuned

lattice could remedy this by confining the atoms radially, but this will make correctly tuning the pumping frequency dependent on the lattice intensity. Thirdly, if the lattice detuning Δ_{lat} is insufficient, atoms in the $^3P_1$ state can be optically pumped by the lattice light to $^3S_1$, where they can decay to the metastable $^3P_0$ and $^3P_2$ states. A higher detuning with correspondingly increased intensity (see Section 7.1.4) or the use of repumpers [390] solves this issue. Finally, the initial velocities decelerated in this proof of principle are low compared with several applications of interest, in part due to the small lattice height and deceleration region used. In the proposal of Wu *et al.* [218], the lattice is 78.5 MHz high and the capture velocity is set to $v_{c,\bar{H}} \approx 25\,\text{m.s}^{-1}$. It would take about 20 photon scattering events for the SOLD to bring antihydrogen close to the recoil limit, which, as seen in Fig. 7.4(b), is similar to the numbers demonstrated in this work.

To summarize, we experimentally demonstrate a Sisyphus-like deceleration mechanism to slow and cool strontium atoms without using radiation pressure. Our work validates a class of proposals developed for laser cooling antihydrogen [218] and other species [355–357]. We characterize the SOLD technique in the steady-state regime both experimentally and theoretically. We compare the SOLD with a typical radiation pressure based scheme (Zeeman Slower) and find similar atom numbers but lower axial temperature. By combining both techniques, we benefit from the ZS spatial/velocity selectivity and improved SOLD end temperatures. We also consider some improvements and applications to the case of antihydrogen. Using the SOLD method requires only three easily-met conditions: a three level system, selective pumping in a lattice with $U_{\text{lat}} \gg \hbar\Gamma$, and an initial velocity satisfying $v > \lambda_{\text{lat}}\Gamma$. Such simple requirements can be fulfilled by many systems where laser cooling to the ultracold regime remains a challenge, such as new exotic species and (polyatomic) molecules [368–374]. Furthermore, by careful choice of the time sequence for the lattice velocity and intensity, a pulsed version of the SOLD could bring an atom wavepacket to any desired velocity while scattering only a handful of photons.

Note added Recently, we became aware of related Sisyphus cooling in optical tweezers [224].

B.P. thanks the NWO for funding through Veni grant No. 680-47-438. We thank the NWO for funding through Vici grant No. 680-47-619 and the European Research Council (ERC) for funding under Project No. 615117 QuantStro. C.-C. C. thanks support from the MOE Technologies Incubation Scholarship from the Taiwan Ministry of Education.

C.-C. C. and S.B. contributed equally to this work.

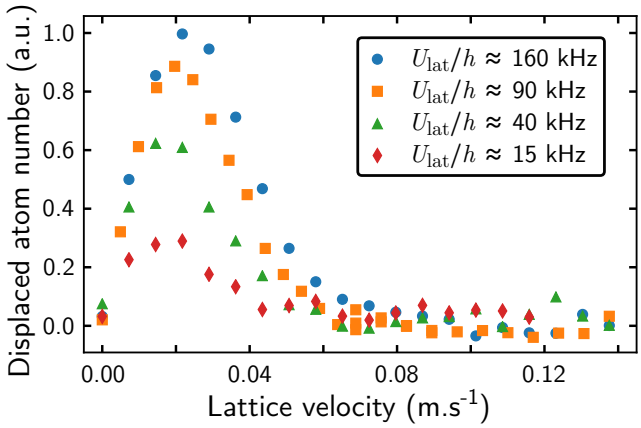

FIGURE 7.6: Acceleration of a stationary strontium cloud by a moving lattice, for various lattice heights. The abscissa gives the lattice velocity and the ordinate, in arbitrary units, is proportional to the fraction of atoms in the moving frame measured after 100 µs of acceleration followed by 20 ms of evolution.

7.1 Supplemental Material

7.1.1 Sisyphus Optical Lattice Accelerator

The SOLD deceleration scheme brings atoms ultimately to zero mean velocity in the reference frame of the lattice. By applying a small frequency difference between two lattice beams, a lattice will move at a well-controlled velocity [388, 389]. This implies that the SOLD can ideally decelerate or accelerate atoms to any desired velocity. We test this using a 1.53(2) µK stationary cloud produced by loading a MOT into a dipole trap, at the location of the lattice. We shine both lattice and pumping light onto this cloud for 100 µs, and after 20 ms observe the number of atoms in a displaced cloud corresponding to the moving lattice frame. The results are shown in Fig. 7.6. We observe an increase in the displaced fraction with lattice height, which we attribute to the increase in energy $\sim U_{\mathrm{lat}}/2$ given to the atoms for each scattering event. We also observe an optimal lattice velocity for a given lattice height, which roughly corresponds to our model criterion of eq. (7.7) with $m = 1$. The variation in the location of these efficiency peaks is more visible in Fig. 7.6 than in Fig. 3, because here the SOLD is pulsed for a short duration instead of operating in the steady-state regime, so the effects of each resonance corresponding to eq. (7.7) are more pronounced. Note that due to the initial size of the cloud and its location with respect to the lattice, our estimation of the effective lattice depth is much rougher than for the data of Fig. 3.

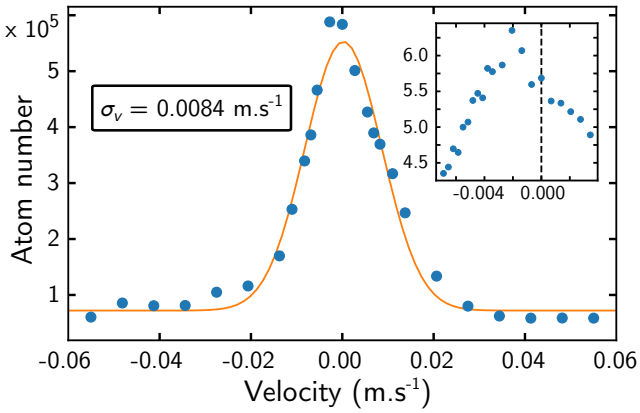

FIGURE 7.7: Velocity selectivity of the reservoir loading, measured by varying the lattice velocity. The line is a Gaussian fit of the data with width σ_v. The inset shows the same type of measurement on a much narrower velocity range, highlighting the center velocity of about $v_R \sim -0.002\,\mathrm{m.s^{-1}}$.

We can also use the moving lattice to characterize our reservoir dipole trap. The loading of this reservoir is both sensitive to the mean velocity of atoms and to the location they end up when reaching zero mean velocity. We characterize the velocity acceptance of the reservoir by varying the frequency difference between the two lattice beams. The loading efficiency of the reservoir depending on the lattice velocity is shown in Fig. 7.7. It can be fitted by a Gaussian whose width is $\sigma_v = 0.0084(4)\,\mathrm{m.s^{-1}}$, centered at $v_R \sim -0.002\,\mathrm{m.s^{-1}}$. This slight departure from zero velocity can be explained by the orientation of the reservoir relative to the guide, which favors the loading of atoms that move backward. We include this measured velocity selectivity of the reservoir in our model of the SOLD.

7.1.2 SOLD Model

Here we give a description of our model of the SOLD that is an extended version of the description given in the main text.

In order to model our cooling scheme in an insightful way, we split the problem into two parts: the average energy lost per cooling cycle and the pumping rate. We then use both results to simulate the time evolution of the atoms' velocity.

Energy lost

We begin with a study of the energy lost due to the presence of the lattice. We assume that the atoms are optically pumped into the $^3P_1$ state at the bottom of the lattice and we solve

the differential equation for the motion $z(t)$ along the lattice propagation axis:

$$\frac{1}{2}mv_0^2 = U_{\mathrm{lat}} \sin^2 k_{\mathrm{lat}} z + \frac{1}{2}m\left(\frac{dz}{dt}\right)^2,\ z(t=0) = 0, \tag{7.2}$$

with m and v_0 being respectively the mass and the initial velocity of the atom. U_{lat} is the lattice depth and $k_{\mathrm{lat}} = \frac{2\pi}{\lambda_{\mathrm{lat}}}$ is the wave vector of the lattice light with wavelength λ_{lat}. The solution of this equation can be written in terms of the Jacobi amplitude J_A:

$$z(t) = \frac{1}{k_{\mathrm{lat}}} J_A\left(k_{\mathrm{lat}} v_0\, t, \frac{2U_{\mathrm{lat}}}{mv_0^2}\right). \tag{7.3}$$

Since the process relies on spontaneous emission towards $^1\mathrm{S}_0$, we determine the average energy lost $E_{\mathrm{lost}}(U_{\mathrm{lat}}, v_0)$ by integrating the lattice height explored for a duration set by the natural linewidth Γ of the $^1\mathrm{S}_0 - {}^3\mathrm{P}_1$ transition,

$$E_{\mathrm{lost}} = \Gamma \int_0^\infty e^{-\Gamma t}\, U_{\mathrm{lat}} \sin^2(k_{\mathrm{lat}} z(t))\, dt. \tag{7.4}$$

In Fig. 4(a), we show the evolution of E_{lost} for several lattice heights and depending on the incoming velocity. We observe that for high incoming kinetic energies compared to the lattice height $\frac{1}{2}mv_0^2 \gg U_{\mathrm{lat}}$, the energy lost E_{lost} saturates. In this case, atoms travel through several lattice sites, and their propagation tends to $z(t) \to \frac{1}{k_{\mathrm{lat}}} J_A\left(k_{\mathrm{lat}} v_0\, t, 0\right) = v_0\, t$. Equation (7.4) gives the relation $E_{\mathrm{lost}} \to \frac{U_{\mathrm{lat}}}{2} / \left(1 + \left(\frac{\Gamma}{2k_{\mathrm{lat}} v_0}\right)^2\right)$. In our experiment $v_0 \gg \lambda_{\mathrm{lat}}\Gamma$, so the average energy lost saturates to $U_{\mathrm{lat}}/2$. One striking feature of Fig. 4(a) is that the energy lost exhibits a sharp resonance for $\frac{1}{2}mv_0^2 = U_{\mathrm{lat}}$, where cooling is the most efficient. In this case, atoms have just enough energy to climb on top of the first lattice hill, so they spend most of their time at this location, which makes them more likely to spontaneously emit there and therefore to lose most of their kinetic energy. Indeed, the explored lattice height becomes $U(t) \to U_{\mathrm{lat}} \tanh^2(k_{\mathrm{lat}} v_0\, t)$, which for $v_0 \gg \lambda_{\mathrm{lat}}\Gamma$ gives an average energy lost reaching asymptotically $E_{\mathrm{lost}} \to U_{\mathrm{lat}}$. Let us note that, in contrast to Ref. [218], which relies also on a spatial modulation of Γ, the effective rate of spontaneous emission in our case is higher on lattice hills only because of the increased time atoms spend there.

Pumping rate

We now examine the pumping rate in dependence of the incoming velocity and lattice height. We solve the optical Bloch equation for a two-level system corresponding to the $^1\mathrm{S}_0$ and $^3\mathrm{P}_1$ states, coupled by the pumping laser with Rabi frequency Ω. The time-dependent

Schrödinger - von Neumann equation for the density operator ρ is

$$\frac{d\rho}{dt} = -\frac{i}{\hbar}[H, \rho] + L, \tag{7.5}$$

with $\hbar$ the reduced Planck constant, L the usual term to account for the spontaneous emission due to Γ, and with the Hamiltonian H written as:

$$H = \begin{pmatrix} 0 & \Omega/2 \\ \Omega/2 & U_{\text{lat}} \sin^2(k_{\text{lat}} v_0\, t) \end{pmatrix}. \tag{7.6}$$

We numerically solve eq. (7.5) with time, starting with all the population in $^1S_0$ at $t = 0$. For this calculation, we assume a constant velocity v_0, which is valid for $\frac{1}{2}mv_0^2 \gg U_{\text{lat}}$. After a variable time, the $(\Omega, U_{\text{lat}}, v_0)$-dependent solution for the excited population reaches a steady-state only slightly perturbed by the time-dependent detuning produced by travelling within the lattice. Averaging over this small perturbation, we get the population in the $^3P_1$ state shown in Fig. 5.

The remarkable feature in this figure is the presence of sharp lines where the excited population is the highest. These can be simply explained by looking at the evolution of the Bloch vector associated with ρ, displayed in Fig. 7.8. When the atoms are not located at the bottom of a lattice site, the detuning is so strong that effectively the scattering rate vanishes, so the population distribution remains roughly constant for timescales short relative to Γ. Due to the dephasing between both states, the Bloch vector then evolves mainly horizontally, until the atoms reach the location of the bottom of the next lattice site. If at that moment the dephasing amounts to a multiple of 2π, then the effective pumping pulses add constructively, and the steady-state excited population is high. This leads to the resonance lines in Fig. 5.

We can give a simple quantitative criterion for the positions of these lines. The phase accumulated during the propagation through one lattice period is $\Phi = \Delta\, T$, with $T = \frac{\lambda_{\text{lat}}}{2v_0}$ the propagation time and Δ the dephasing, taken as the average detuning due to the lattice, giving $\Delta = 2\pi\, \frac{1}{h}\, \frac{U_{\text{lat}}}{2}$, with h the Planck constant. The condition $\Phi = m \times 2\pi$ (with $m \in \mathbb{N}$) gives the relation:

$$\frac{U_{\text{lat}}}{h} = m \times \frac{4v_0}{\lambda_{\text{lat}}}. \tag{7.7}$$

This criterion is shown as dashed red lines for $m \in \{1, ..., 7\}$ in Fig. 5.

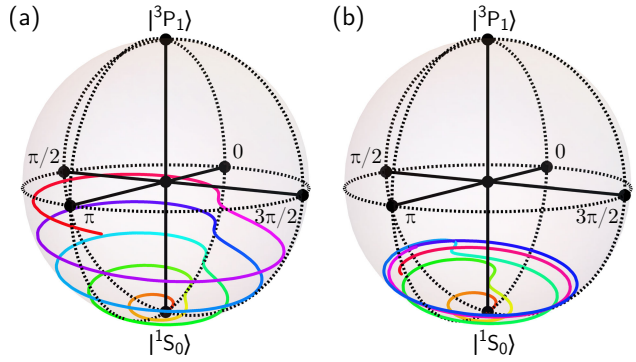

FIGURE 7.8: Evolution of the Bloch vector on the Poincaré sphere, shortly after the application of the SOLD. Atoms begin in the $^1S_0$ state at the location of a lattice site. The saturation parameter of the pumping to $^3P_1$ is set for clarity to about 60, and the lattice height is $h \times 600\,\mathrm{kHz}$. The velocity in (a) $v_0 = 0.1035\,\mathrm{m.s^{-1}}$ is such that the accumulated phase during the travel time between two sites is close to $\Phi = 2\pi$, while in (b) where $v_0 = 0.09\,\mathrm{m.s^{-1}}$ this condition is not met.

Overall evolution

In order to model the complete behavior of the SOLD, we solve classically the evolution of the atoms' velocity v with time, under the effective force $F(U_{\mathrm{lat}}, v) = -\Gamma \times \rho_{^3P_1}(U_{\mathrm{lat}}, v)\, E_{\mathrm{lost}}(U_{\mathrm{lat}}, v)$. We carry out this calculation for a packet of atoms whose velocity distribution follows a (1D) Boltzmann distribution corresponding to the temperature of our MOT of 6 µK summed with an offset corresponding to the measured mean velocity given by the launch beam. The capture probability in our reservoir is determined by the velocity-dependent efficiency extracted from the measurement shown in Fig. 7.7, corresponding to a Gaussian function with a width $\sigma_v = 0.0084\,\mathrm{m.s^{-1}}$. We thus simulate the time evolution of the loaded population in the reservoir depending on the lattice height, for the four mean starting velocities shown in Fig. 3. In Fig. 7.9 we compare the results from this model with our experimental data.

We see a good qualitative agreement concerning the overall behavior with both lattice height and starting mean velocity. In particular, the locations of the optimums of loading efficiency are well reproduced by our model. These correspond to the case when the starting mean velocity v_0 verifies the criterion of eq. (7.7) (with $m = 1$). Indeed, in that case atoms are efficiently pumped to the $^3P_1$ state, and lose typically a significant amount of energy $U_{\mathrm{lat}}/2$. After spontaneous emission, their velocity is much lower and atoms are in the (U_{lat}, v) region where the density of lines for $m \geq 2$ is high. They are therefore very likely to keep decelerating efficiently. On the contrary, for high velocity v_0, in the region $0 \ll \frac{U_{\mathrm{lat}}}{h} \ll \frac{4v_0}{\lambda_{\mathrm{lat}}}$, atoms will not get pumped to $^3P_1$. Our model is thus able to estimate the

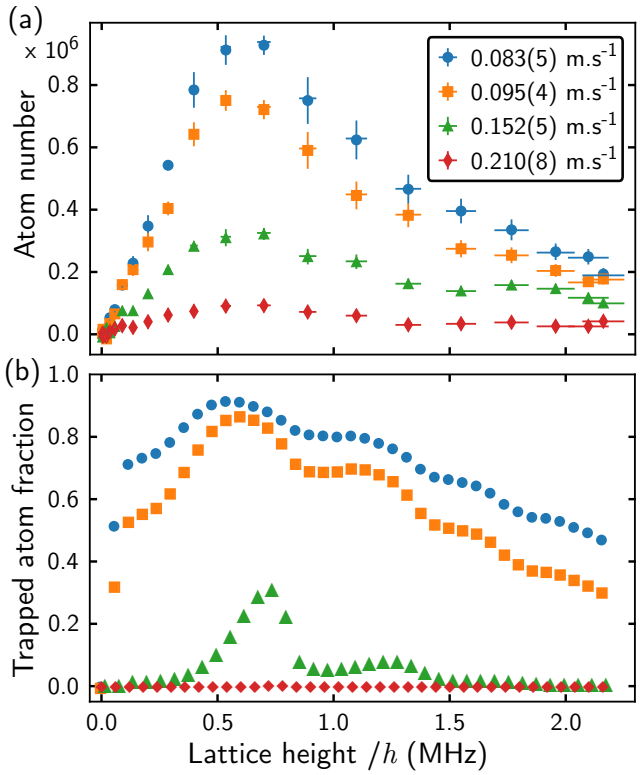

FIGURE 7.9: Comparison between (a) the experimental data already shown in Fig. 3 and (b) the results of the theoretical model (see text) for the same initial mean velocities.

capture velocity v_c of the SOLD, which is given by

$$v_c = \frac{U_{\text{lat}}\lambda_{\text{lat}}}{4h}. \tag{7.8}$$

Let us note that our model makes several approximations. Indeed the results of the calculations shown in Fig. 7.9(b) are given for one particular evolution time $t = 1.4\,\text{ms}$ that has been chosen for best match with the steady-state experimental data. Since no decay mechanism has been added in the model, the final loading would be with unity efficiency. This chosen deceleration time is rather short, because in this case the saturation parameter of the $^1S_0 - {}^3P_1$ transition is set to ~ 320, for which the calculations suffer less numerical errors compared to more realistic, lower saturation parameters. Nonetheless, the theory always exhibits the same overall behavior no matter the value of the saturation parameter. Another limitation of our model is that no selection criteria have been chosen for the position of atoms, whereas they must be in the vicinity of the crossing between the

transport guide and reservoir to be loaded. Similarly, atoms expelled from the guide by the barrier formed by the blue detuned lattice and the effects of the lattice's slight angle with the guide are not taken into account. Finally, the constant velocity approximation made when solving the optical Bloch equations is not valid for $\frac{1}{2}mv_0^2 \leq U_{\mathrm{lat}}$. To obtain a better quantitative agreement, Monte-Carlo simulations could be a straightforward option for further studies.

7.1.3 Atomic beam velocities

In order to characterize the dependence of the SOLD efficiency with incoming atom velocity, we need a measurement of the mean atom velocity within the transport guide before entering the lattice region. In the absence of the SOLD, we will assume the mean velocity to be constant throughout the lattice region, as the potential provided by the transport guide in this location is engineered to be flat in the axial direction.

We measure the atom velocity arriving at the location of the lattice by two methods. The first is to eject a burst of atoms out of the transport guide using a pulse of light resonant with the $^1\mathrm{S}_0 - {}^1\mathrm{P}_1$ transition. The pulse lasts 1 ms and the laser beam propagates horizontally perpendicular to the atomic beam. We assume that spontaneously emitted photons are equally distributed in all directions during the ejection process, so that the on-axis mean velocity is not affected by the light absorption. By examining the propagation of the packet of ejected atoms, we can infer the mean velocity, see Fig. 7.10. We were only able to measure the mean velocity with high accuracy, as measurements of the axial distribution or temperatures of these ejected clouds were limited by low signal to noise. Rough estimates were however consistent with the measured MOT temperature of 6 µK.

We use a second method as a cross-check for our determination of the atom mean velocity. It relies on the measurement of the loading in the transport guide region. Without the SOLD applied, we measure the steady-state atom number in the transport guide in the region corresponding to the extent of the lattice. We can extract the linear density ρ_{lin} in this region, if assumed to be homogeneous. By also assuming the mean velocity v_0 to be constant, we have the following relation for the steady-state incoming and outgoing flux:

$$F_{\mathrm{lat,out}} = F_{\mathrm{lat,in}} = \rho_{\mathrm{lin}} \times v_0. \tag{7.9}$$

We thus need to measure $F_{\mathrm{lat,out}} = F_{\mathrm{lat,in}}$, which we get from the loading curves of the MOT and the transport guide. The rate equations for both MOT and transport guide atom

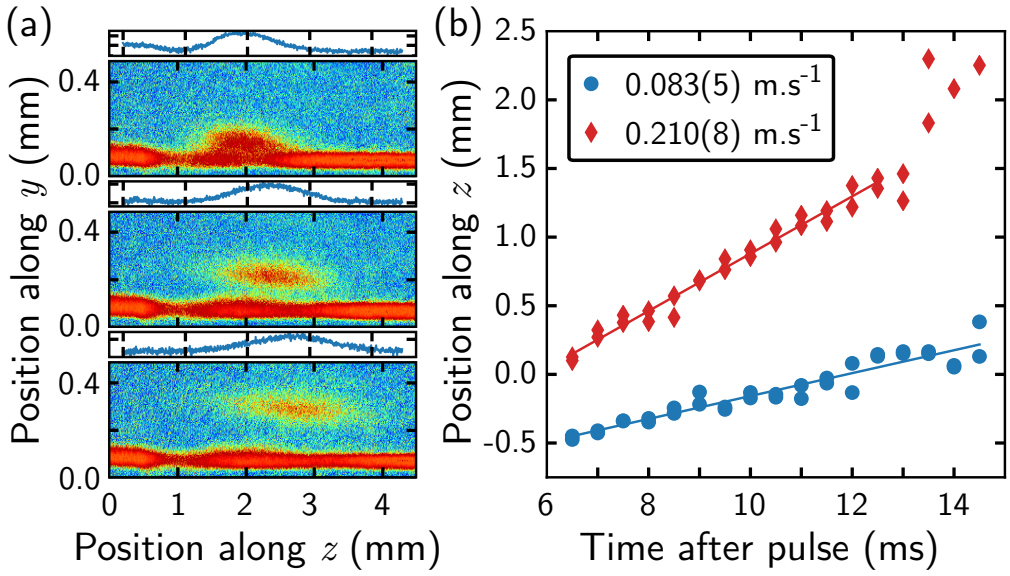

FIGURE 7.10: Measure of the atom beam velocity. (a) Absorption images and respective density profiles of clouds of atoms ejected from the transport guide, taken 5 ms (top), 8 ms (middle) and 10 ms (bottom) after the ejection pulse. The pulse is applied at $z \approx 1$ mm. (b) Evolution of the position along the z axis of two ejected clouds with different mean velocities. The lines are fits from which we extract the velocities.

numbers, N_{MOT} and N_{TG}, are

$$\begin{cases} \frac{dN_{\mathrm{MOT}}}{dt} = F_{\mathrm{in}} - \beta_{\mathrm{TG,in}}\, N_{\mathrm{MOT}} - \beta_{\mathrm{MOT,loss}}\, N_{\mathrm{MOT}} \\ \\ \frac{dN_{\mathrm{TG}}}{dt} = \eta_{\mathrm{TG}}\, \beta_{\mathrm{TG,in}}\, N_{\mathrm{MOT}} - \beta_{\mathrm{TG,out}}\, N_{\mathrm{TG}} \end{cases}, \tag{7.10}$$

where F_{in} is the flux coming into the MOT (see Chapter 5). The loss rate $\beta_{\mathrm{MOT,loss}}$ describes atoms lost from the MOT, while $\beta_{\mathrm{TG,in}}$ describes the rate of atoms coupled into the beginning of the transport guide. The efficiency η_{TG} accounts for the losses between the start and the end of the guide. Last, the rate $\beta_{\mathrm{TG,out}}$ describes atoms leaving the lattice region. We thus have $\beta_{\mathrm{TG,out}}\, N_{\mathrm{TG}}(t = \infty) = F_{\mathrm{lat,out}} = F_{\mathrm{lat,in}}$. From fitting the loading curves of both MOT and transport guide with the solutions of eq. (7.10), we extract the values of each β, F and η parameters, and ultimately get the value of v_0. We found a good agreement between the velocities derived from both methods, and we use the first one to determine the values provided in the main text.

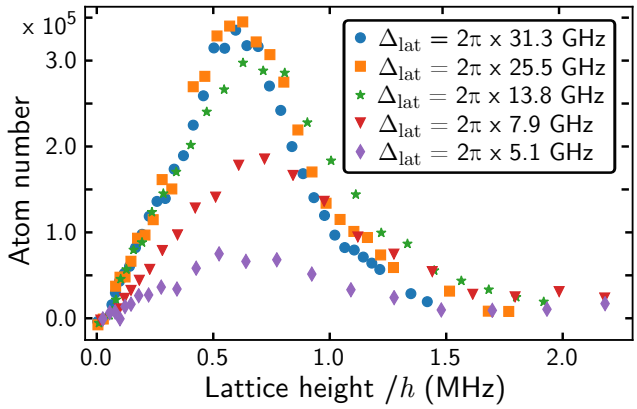

FIGURE 7.11: Effect of optical pumping by the lattice light to the $^3S_1$ state. The data show the number of atoms loaded into the reservoir as a function of the lattice height for various detunings of the lattice laser from the $^3P_1 - {}^3S_1$ transition.

7.1.4 Losses toward $^3S_1$

One limitation of our decelerator is the optical pumping by the lattice light of atoms in the $^3P_1$ state to the $^3S_1$ state. If such optical pumping occurs, atoms can decay from $^3S_1$ to the metastable $^3P_0$ and $^3P_2$ states and exit the cooling cycle. Fig. 7.11 shows, for several lattice laser detunings Δ_{lat}, the effect of optical pumping to $^3S_1$ depending on the lattice height. For detunings a few GHz away from the $^3P_1 - {}^3S_1$ transition we see a clear reduction of the atom number slowed and captured in the reservoir. For detunings above 20 GHz, the efficiency seems to converge toward a unique curve, indicating no significant optical pumping.

A repumping scheme such as the one used in Ref. [390] can optically pump atoms back to $^3P_1$. Apart from a few additional photon recoils, this method should not significantly affect the slowing process, providing the repumping time is short compared to the propagation of the atoms along the lattice. Another simple method is to detune the lattice laser frequency further away from the $^3P_1 - {}^3S_1$ transition, while adapting its power to keep the same lattice height. Aside from the data of Fig. 7.11, we operate at a lattice detuning of $\Delta_{\text{lat}} \approx 2\pi \times 30\,\text{GHz}$, for which optical pumping is negligible.

TABLE 7.2: Relative uncertainties on the relevant parameters used to calculate the lattice height for the $^3P_1$ state.

	uncertainty
Lattice beam power P	$\pm 3.0\,\%$
Lattice beam waist w_0	$\pm 1.4\,\%$
Lattice frequency detuning Δ_{lat}	$\pm 0.1\,\%$
Total transition rate $A_{^3P_J - {}^3S_1}$	$\pm 1.0\,\%$
Total uncertainty	$\pm 4.2\,\%$

7.1.5 Lattice height determination

An accurate determination of the lattice height is essential for the characterization of the SOLD. The potential of a 1D lattice acting on the $^3P_1$ state is given by

$$U(z) = -\frac{1}{2\epsilon_0 c}\,\alpha_i\, I(z) = -\frac{4P}{\pi\epsilon_0 c\, w_0^2}\,\alpha_i\, \sin^2 k_{\mathrm{lat}}\, z, \tag{7.11}$$

where α_i is the dynamic dipole polarizability of the $^3P_1$ state, P is the power of each lattice beam, and w_0 is their waist. In the two-level approximation,

$$\alpha_i \approx \frac{3\epsilon_0 \lambda_{\mathrm{lat}}^3}{8\pi^2}\,\frac{\Gamma_{\mathrm{eff}}}{\Delta_{\mathrm{lat}}}, \tag{7.12}$$

where ϵ_0 is the vacuum permittivity. The approximation is valid because the lattice laser detuning Δ_{lat} is only a few tens of GHz. The effective rate $\Gamma_{\mathrm{eff}} = \eta\, A_{^3P_1 - {}^3S_1}$ is the effective transition rate for the $5s5p\,^3P_1 - 5s6s\,^3S_1$ transition, with $\eta = 1/2$ due to the lattice laser polarization. The relative uncertainties of the parameters contributing to the determination of the lattice height are listed in Tab. 7.2. All parameters and their uncertainties are determined experimentally, except for the transition rate, which we derive from literature in the following manner.

The $^3P_J - {}^3S_1$ manifold transition rates are known accurately to the percent level. In Ref. [241], *ab-initio* calculated matrix elements for the relevant contributing transitions, together with experimental transition energies, are used to evaluate the $^3P_0$ polarizability. Constraints from both the measurement of the magic wavelength at 813 nm and the dc polarizability are then imposed to fine-tune the dominant matrix element terms, in order to agree with the experimental values. The fine-tuning of these matrix elements does not exceed 1.1 %, and the theoretical transition rate for $^3P_1 - {}^3D_1$ calculated from these matrix elements agrees with the measured value [391] to within 0.2 %.

From the dipole matrix elements of $5s5p\,^3\mathrm{P}_0 - 5s6s\,^3\mathrm{S}_1$ calculated in Ref. [241], we determine the value of $A_{^3\mathrm{P}_1 - ^3\mathrm{S}_1}$. To this end, we calculate the branching ratios of the $^3\mathrm{S}_1$ state to the three $5s5p\,^3\mathrm{P}_\mathrm{J}$ fine structure states using Wigner 6-j symbols. We take into account the fine structure splitting of the states, which is on the order of a few $100\,\mathrm{cm}^{-1}$, and apply the frequency dependent correction factors to the branching ratios. The resulting branching ratios are from $^3\mathrm{S}_1$ to $^3\mathrm{P}_0$, $^3\mathrm{P}_1$, $^3\mathrm{P}_2 = (12.02\%, 34.71\%, 53.27\%)$. Using these ratios, we derive the transition rate $A_{^3\mathrm{P}_1 - ^3\mathrm{S}_1} = 2.394(0.024) \times 10^7\,\mathrm{s}^{-1}$.

Chapter 8

Outlook: Steady-state ultracold atoms and atom lasers

We have only just begun to use the SrCAL machine. The range of ideas for both making and using steady-state degenerate gases is expansive and this machine is in a unique position to explore this previously uncharted space. In this final chapter I will briefly outline a few of the ideas this machine will hopefully allow us to explore over the coming years for both making and using steady-state quantum gases. I will also outline the iqClock project that aims to use the almost degenerate steady-state sample we have created as a gain medium for a superradiant clock. For this project I am now building a second edition of the SrCAL machine incorporating a cavity that will hopefully bring the exciting possibility of a superradiant clock into reality [39].

8.1 Paths to steady-state BEC not yet taken

The range of potential paths to steady-state BEC is extensive. We discussed some of these options in section 1.4, but we have only explored the tip of the iceberg experimentally. Here I will describe a few of the other paths I hope we can explore over the next few years in the hope that one day steady-state BEC will be as straightforward to produce as a pulsed ^{87}Rb BEC is today.

8.1.1 Evaporation from a guide

I have already described one possible evaporation scheme using a bucket chain or conveyor that we have begun to implement in section 6.3.3. Evaporation is the key to getting the temperatures of a reservoir down. I believe it is absolutely necessary to incorporate an evaporative cooling stage to make steady-state degenerate machines practical and easy. The

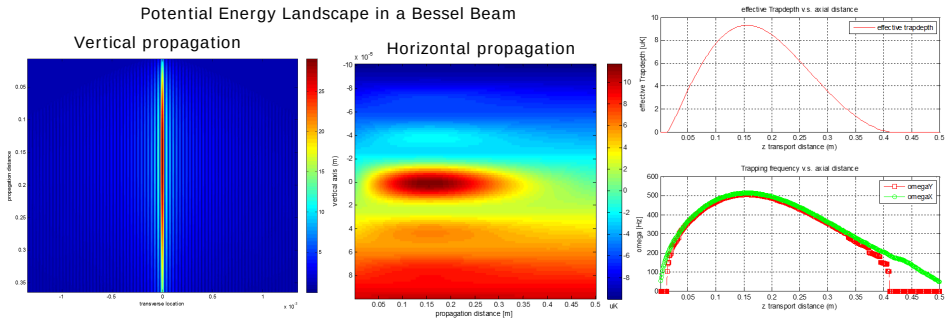

FIGURE 8.1: **A Bessel beam can be used to make optical guides for evaporative cooling.** (left) Cross section of trap depth vs propagation distance for beam propagation calculated using beam propagation method in the vertical direction (without the effects of gravity). (center) Propagation in the horizontal direction for a Bessel beam with wavelength 1064 nm, a power of 10 W and a 2° axicon angle and a beam waist of 5 µm. (right) Trap depth and trapping frequency for the center image along the propagation axis.

approach we described was based on painted potential landscapes and forcing evaporation in moving dimples or using a conveyor but there are also other perhaps simpler schemes.

When we designed the SrCAL machine we always imagined trying evaporation from a guide to degeneracy. This approach was explored in some depth by the groups of Guéry-Odelin [170] and Raithel [188]. This is one of the reasons that our atom laser chamber has a 130 mm long region with full optical access to image and monitor evaporation along a guide.

Our beam of ^{84}Sr gets close to the collisionally dense regime with elastic collision rates of around 0.28 Hz and a propagation time of around 0.4 s but much higher densities are needed to efficiently evaporatively cool such as beam. Since doing this work we have increased the machine flux by an order of magnitude which may well push this to the point where collisions become important but evaporation will not work in the current beam configuration.

To achieve efficient evaporation we need a tight trap which is not deep and has a long propagation length. This is a seeming contradiction in terms. The groups of Guery-Odelin and Raithel addressed this problem by using a material surface to strip the hot atoms from the beams in their very deep magnetic guides. This creative solution is however much more suited to magnetic guides than optical guides where such objects would absorb light from the guiding beams and create diffractive structures. The ground state of strontium is non-magnetic and the metastable states are lossy at high density so magnetic guides are not a realistic option for strontium.

If you interfere two plane waves you create an interference pattern that looks a little like

an array of tightly focussed beams. In a circular geometry this pattern consists of a tight central spot surrounded by rings, a "Bessel beam". A Bessel beam [392–397], created using an axicon is a way by which we can create a tight trap that propagates long distances. The tight trap is necessary for two reasons, firstly it increases trapping frequency and density improving the collision rates and evaporation efficiency. Secondly, it allows us to minimize the impact of gravitational sag. A few examples of Bessel beams based on the equations of [392] and modelled using the beam propagation method are shown in figure 8.1. We implemented a Bessel beam waveguide on the bench top and looked at the beam profiles we could generate experimentally but loading this tight trap experimentally is likely to be challenging.

A second challenge for us is protecting atoms in the guide from resonant 689 nm light. Previous machines that looked at this approach had apertures in the vacuum chamber to protect the guided beam from light used for loading. Our chamber has none of this. We always imagined using a transparency beam for this purpose. A single collinear Gaussian beam at 487 nm or a collinear 688 nm beam with two incoherent σ^++σ^- polarizations should work. A challenge maybe that the transparency protection is likely to interfere with the loading of atoms into the guide. One solution might be to implement a moving SOLD lattice at the loading point with a counter-propagating beam on a small angle to the guide. This would not only allow loading but might also cool the atoms in the axial direction and allow the launch with a highly controlled velocity. This loading mechanism is something that I will test in the new iqClock machines.

I find this system particularly appealing for the deep analogies it has to optical laser systems. Essentially this would be an equivalent of an active fiber for matter waves. How does phase noise vary with launch velocities in such a system? Does it break into domains of different phase? Can we make amplifiers and resonators and seeded amplifiers? It seems to me like a rich playground of possibility.

8.1.2 Cooling in a lattice

Another approach I remain excited about is sideband cooling in a deep lattice. Degenerate Raman sideband cooling was explored extensively as a means for potentially reaching degeneracy without evaporation, particularly in the late 90s. We briefly discussed the history in section 1.4.1, but I believe there remains much untapped potential in applying these ideas to strontium.

In species with more complex ground states some creative schemes are required to arrive with a unidirectional cooling scheme that will deliver a dark ground state. The notable one is degenerate Raman Sideband Cooling [196, 197, 202, 398] although there is

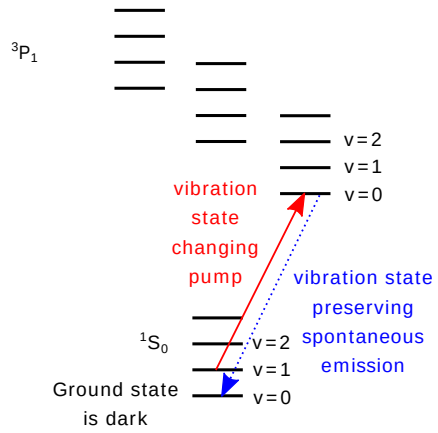

FIGURE 8.2: **Cooling strontium in a deep lattice** Consider cooling with σ^- on the 7.4 kHz $^1S_0$-$^3P_1$ transition. In our experiment we have a 1.7 MHz Zeeman splitting at the location of the dipole trap. Now let us apply a 1 MHz deep 3D lattice. Tune the cooling light to -2.7 MHz. The system will pump atoms to the $^1S_0$ $v = n$ to the $^3P_1$ $m_J = -1$ $v = n - 1$ state where v refers to the vibration level. Once excited, spontaneous emission will result in the $^3P_1$ $m_J = -1$ $v = n - 1$ decaying preferentially to $^1S_0$ $v = n - 1$ as this maximizes the Frank-Condon overlap. The lowest vibrational state is dark, that will end the cooling process.

also a collection of work from the Weiss group on laser cooling at high densities in deep lattices [198, 199, 314] which also explores these ideas in some depth.

I believe that this might actually be much simpler in strontium. Consider cooling with σ^- on the 7.4 kHz $^1S_0$-$^3P_1$ transition. In our experiment we have a 1.7 MHz Zeeman splitting at the location of the dipole trap. Now let us apply a 300 kHz deep 3D lattice. Tune the cooling light to -2 MHz. The system will pump atoms to the $^1S_0$ $v = n$ to the $^3P_1$ $m_J = -1$ $v = n - 1$ state where v refers to the vibration level. Once excited, spontaneous emission will result in the $^3P_1$ $m_J = -1$ $v = n - 1$ decaying preferentially to $^1S_0$ $v = n - 1$ as this maximizes the Frank-Condon overlap. The lowest vibrational state is dark which will end the cooling process. This process is depicted in figure 8.2. This looks a lot like degenerate Raman sideband cooling except we don't need the Raman in strontium as nature takes care of this for us.

One would probably be reluctant to apply a lattice to the dimple or BEC region in our system as it would dramatically increase scattering losses and heating but applying it to the reservoir might significantly help with cooling at high phase-space density. Fortunately the cooling light needed for this scheme at -2 MHz is detuned by many linewidths so it will only interact very weakly outside the lattice. One concern would be lattice uniformity so it might be advantageous to apply the cooling light only to the central uniform section of

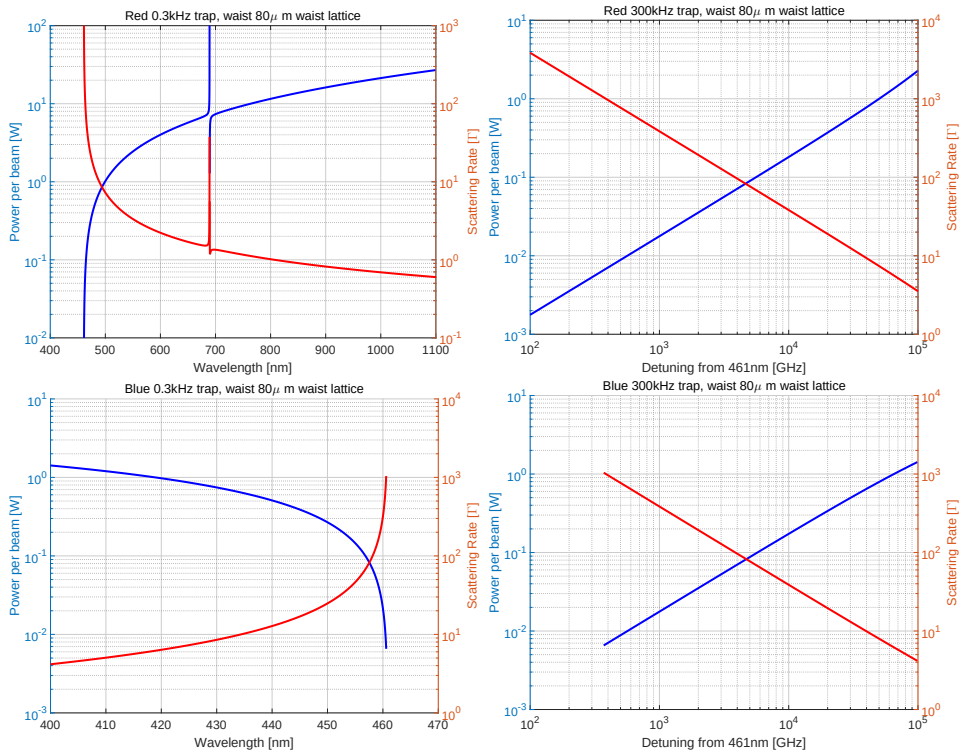

FIGURE 8.3: **Powers required to implement a deep cooling lattice** There are many potential wavelengths of interest 1064 nm which would require 25 W and scatter at 0.6 Hz, 479.8 nm(magic) which would require 480 mW and scatter at ≈15 Hz, 473.15 nm(magic) which would require 315 mW and scatter at ≈23 Hz and 464.5 nm which would require 91 mW and scatter at ≈75 Hz. The last option looks like the easiest and cheapest to implement but the scattering might be a problem and it isn't magic.

the lattice where the detunings are large. To cool the reservoir one could cycle the lattice on, apply a pulse of red cooling light and cycle the lattice off to allow the cloud to compress and then repeat. If the cycle was very fast we might call it a modulation and still consider even the reservoir essentially steady-state.

An obvious question is how much power is needed for such a lattice and how big and uniform a lattice would need to be. Let us consider a 300 kHz deep lattice with a $1/e^2$ waist of 80 µm. Figure 8.3 plots the required power in each counter-propagating (retro-reflected) beam and the peak scattering rate. 464.5 nm would probably be the easiest and quickest to implement as it can be done with a single diode. It would be low cost to implement a lattice in all three dimensions. The biggest concerns are the off resonant scattering rates which might be two orders of magnitude too high for a BEC. As already described, it will be

important to apply the lattice to the reservoir rather than the dimple with the BEC. A second concern is the relative polarizability of the ground and excited states. A large difference will likely reduce the effectiveness and the maximum lattice frequency that can be used. For this reason it might be interesting to also consider the magic wavelengths identified in figure 2.6 and table 2.9 possibly with the help of a build up cavity to achieve the required intensities. A few magic options are identified in figure 8.3.

If this approach worked it should be able to improve the phase-space density that can be reached for all the different isotopes of strontium. ^{88}Sr is very appealing because of its high natural abundance but it is fraught with the difficulty of having a small and negative scattering length. Let us for a moment consider the possibility of trying to condense ^{88}Sr in this way[1]. We know that we can reach a phase-space density of 0.1 using pulsed Doppler cooling in a dipole trap for ^{88}Sr [201]. Note that the dimple trick doesn't work with ^{88}Sr since there is no fast thermalization. An improvement of a factor of 30 is by no means assured but it is also not a ridiculous proposition as Chu's group demonstrated two orders of improvement with their first paper [196] and significantly exceeded that in more recent work [202]. But even if we can produce a phase-space density beyond 3 it still may take some time to see a phase change. Beyond densities of $1 \times 10^{14}\,\mathrm{cm}^{-3}$ it gets hard to make a lattice laser or we end up with multiply occupied sites. Since we can't use a dimple to push these densities higher we are stuck with needing a temperature below 350 nK giving us an elastic collision rate of 0.1 Hz. Maybe by loading multiple atoms into single lattice sites this process might be hastened. To summarize, although the prospect of trying to directly condense ^{88}Sr using this technique remains alluring it would seem that the thermalization rates would still pose a feasibility problem for this isotope.

For now, I hope to look a little deeper at the idea of using sideband cooling to bring the temperatures down and push the density up in our reservoir. This could be an important addition to our current architecture.

8.2 Outcoupling a steady-state atom laser

Once we have a steady-state BEC the next challenge is probably a steady-state atom laser. In section 1.3 we discussed at length some of the methods that have been used in the past to outcouple atom lasers from BECs. Most of them rely on changing atoms from a trapped to an untrapped state. For strontium this may be a challenge. The metastable states $^3P_{1,2}$ are a possibility in combination with a state dependent anti-trap to compensate the dimple and reservoir potentials but the metastable states can be lossy at high densities. Another

[1] The negative scattering length will mean the BECs will be tiny but maybe the production rate can be high.

possibility is a multi-photon Bragg transition [154–156] to a high momentum state able to escape the potential well in which the BEC forms.

Improving the purity of the BEC and atom laser is also likely to be important for many applications. This will likely motivate further work to improve the BEC production architecture particularly in the direction of evaporation. Improving the phase noise of the resulting atom laser is something that might be tackled by increasing the BEC size and by increasing lifetimes. Another important direction will be simplifying the system.

I dream that one day in the not too distant future we might have atom lasers and BEC sources you buy and simply bolt onto your experiment. The experiments we are trying to do in atomic physics are now hideously complicated yet we are still building our apparatus up from wire, steel and circuit boards. To continue moving forward and allow the time to think deeply about the physics we must find a way to dramatically simplify these machines. I can think of nothing better than to be able to buy an atom laser or condensate source and I really hope that this work will contribute to making such machines possible and affordable.

8.3 Superradiant clocks

Even before reaching degeneracy, the achievement of a steady-state sample of almost degenerate strontium has opened a range of new research directions and possibilities. Perhaps the most significant is the steady-state superradiant clock. Partly on the basis of the work described in this thesis the iqClock quantum technologies flagship project was established[2] to try to make a new generation of optical clocks [39]. I am now developing a second generation of the SrCAL machine incorporating a cavity, the lessons we learned and new ideas we wanted to try. We are manufacturing three new machines and trying new source concepts based on light-induced atomic desorption (LIAD) [399], a 300 °C hot 2D MOT and an oven in close proximity to a 2D MOT, where the Zeeman slower magnetic field is provided by the MOT magnets [334][3]. We will hopefully soon bring a steady-state superradiant clock to life and with it the world of possibilities such a device would enable. A brief introduction to superradiant lasers and their possible applications was provided in sections 1.1.1 and 1.1.2.

[2] www.iqclock.eu

[3] I would love to spend another 100 pages to describe these new machines but for now the time is better spent building them.

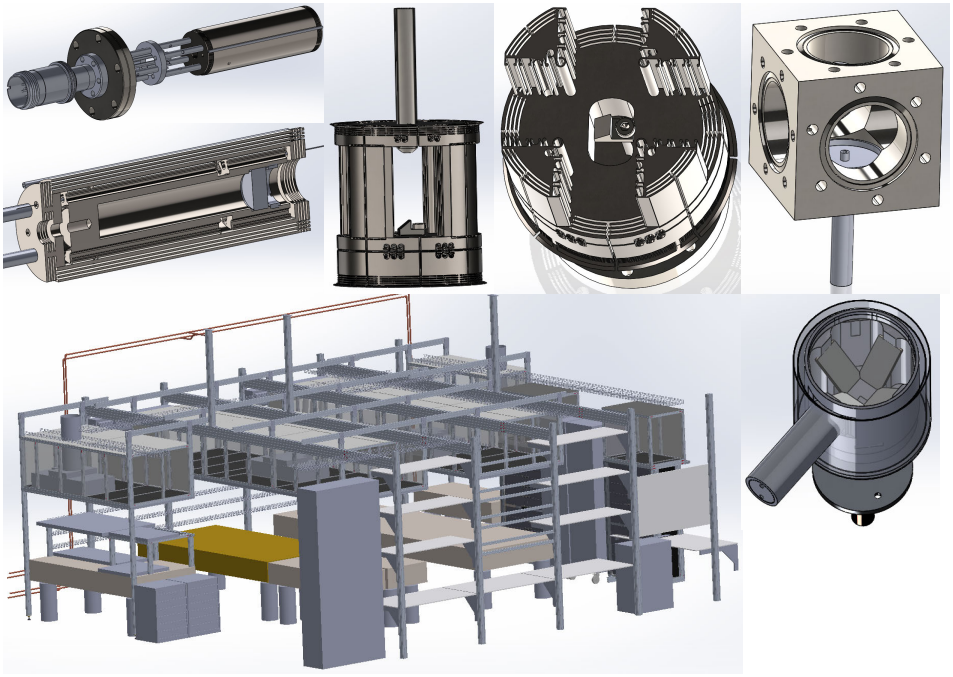

FIGURE 8.4: **Sources for the iqClock project and new lab infrastructure.** Several new source designs are being tested as a second generation of the SrCAL machine for the iqClock steady-state superradiant clock project. Along the top we have a new oven, a hot 2D MOT, a desorption system and along the bottom we have new lab infrastructre designed and built and a pyramid version of the hot 2D MOT source.

8.4 Concluding remarks

In the coming months I hope that we will nudge our machine over the edge and create a steady-state BEC. This will mark a milestone but we are still at the beginning of the story, not the end. In section 1.1 I described a world filled with new sensors, time standards and other possibilities this work might help to address.

Appendix A

Oven nozzle design equations

The choice of microtube dimensions and the appropriate number of tubes for the nozzle of an oven can best be addressed through flow calculations. This chapter contains technical details of these calculations and should be read in conjunction with the main text, section 3.1.1.

A.1 Molecular flow through a tube

In the molecular flow regime the flow rate f through a cylindrical tube may be described by [400]

$$f = Kf^* = K\frac{P_{in}\pi R^2}{\sqrt{2\pi m k_B T}},$$

where K is the Clausing factor (tabulated transmission probability of the tube) [401, 402] and f^* is the leak rate through a thin walled orifice of radius R. Since the tubes we use are long compared with their radius the Clausing factor K can be replaced by an analytic approximation [403] giving the flow rate

$$f = \frac{8R}{3L}\left(1+\frac{8R}{3L}\right)^{-1}\frac{P_{in}\pi R^2}{\sqrt{2\pi m k_B T}}. \tag{A.1}$$

A.2 Transitional flow through a tube

At higher temperatures we leave the molecular flow regime and enter the transitional flow regime, where analysis is more complicated.

Here we can estimate the flux from the equations in [280]. These equations were derived for flow in a highly elongated rectangular channel where the width is much greater than the height. We estimate the flow for our round tubes by calculating for a square channel of

the same area and then reduce the width by 6% in order to match the fluxes given by the molecular flow calculations in the limit of low temperatures and pressures. This evaluates to give an estimate for the flux in the transitional flow regime of

$$
\begin{aligned}
f &= \frac{1}{m}\left(\dot{M}_e^C + \left[\left(\dot{M}^D\right)^c + \left(\dot{M}^K\right)^c\right]^{\frac{1}{c}}\right) \\
&= \frac{1}{m}\left(\frac{h^3 w(P_{in}^2 - P_{out}^2)}{24\mu_e L R_s T} + \left[\left(\frac{\mu w h}{L}\ln\left(\frac{P_{in}}{P_{out}}\right)\right)^c + \left(\frac{wh^2}{3L}\sqrt{\frac{8}{\pi R_s T}}\left(P_{in} - P_{out}\right)\right)^c\right]^{\frac{1}{c}}\right) \\
&= \frac{hw}{mL}\left(\frac{h^2\left(P_{in}^2 - P_{out}^2\right)}{8\bar{v}P_{in}\left(\lambda^c + h^c\right)^{\frac{1}{c}}} + \left[\left(\frac{\bar{v}\lambda m P_{in}}{3k_B T}\ln\left(\frac{P_{in}}{P_{out}}\right)\right)^c + \left(\frac{h}{3}\sqrt{\frac{8m}{\pi k_B T}}\left(P_{in} - P_{out}\right)\right)^c\right]^{\frac{1}{c}}\right)
\end{aligned}
\tag{A.2}
$$

where:

c = -1.6
h = $\sqrt{\pi R^2}$, the channel height,
w = $(0.94)h$, the channel width,
λ = the mean free path,
ρ = $P_{in}/(k_B T)$, the number density,
m = the atomic mass,
L = the tube length,
R_s = k_B/m, the specific gas constant,
T = the source temperature,
$\bar{v}$ = $\sqrt{8k_B T/(\pi m)}$, the mean velocity,
k_B = Boltzmann's constant,
P_{in} = the source/oven pressure, and
P_{out} = the exit pressure.

It is not simple to estimate the output pressure as this depends on external factors such as pumping speed and outgassing rates so we assume P_{in}/P_{out} 1000. In any case this term is small at low pressures.

Several of these variables require further information. The partial vapour pressure for strontium [219, 220], P_{in} is given as a function of temperature T by equation A.3 and plotted in figure 2.1.

The mean free path λ is given by equation A.3 but depends critically on another property, the scattering length a_s.

$$\lambda = \frac{k_B T}{\sqrt{2}\pi P (2a_s)^2} \tag{A.3}$$

How to evaluate the scattering length is less clear. At least two approaches have been used in the literature. Schioppo *et al.* [219] estimated the scattering length as the diameter of the Sr_2 molecule $a_s = 8.13 \cdot a_o$ while another approach uses the Massey-Mohr equation [404]. The Massey-Mohr equation [404] estimates the collisional cross section σ between two Sr atoms with respect to their relative velocity v_{rel} and the C_6 Van de Waals coefficient. Using the value $C_6 = 3170 \cdot a_o$ calculated in [405] we obtain

$$\sigma = 4\pi a_s^2 = 7.7881 \times 10^{-18} \left(\frac{C_6}{v}\right)^{\frac{2}{5}} \tag{A.4}$$

The mean velocity in a Boltzmann distribution is given by $\bar{v} = \sqrt{8k_B T_s/(\pi m)}$ which could be one estimate of the relative velocity although adding two mean velocities in quadrature is probably more realistic giving $\bar{v}_{rel} = \sqrt{2}\bar{v}$. The resulting scattering length is weakly temperature dependent and around $a_s = 20.5 \cdot a_o$.

Schioppo *et al.* [219] found their measured brightness to be less than 30% of their predicted value and their divergence to be at least twice the predicted divergence and possibly much more as it was limited by an aperture in their system preventing accurate measurement. It is likely that they significantly understimated the scattering length which could substantially explain these divergences so we use the larger value of $a_s = 20.5 \cdot a_o$ based on the Massey-Mohr equation.

A.3 Centreline peaking factor

The peaking factor χ is defined as the on-axis flux per sterradian relative to that of a cosine emitter. In the molecular flow regime the peaking factor is $1/K$ where K is the Clausing factor [400]. Since our nozzle tubes are long and narrow we may approximate K by an analytic expression [403] as we did in equation A.1. At higher pressures intermolecular collisions reduce the peaking factor [403] and we are left with the expressions of equation A.7. The equations used follow the work of [403]. In theses expressions p^* is the pressure at which the mean free path equals the channel diameter as described in equation A.9 (the Knudsen number K_n is the ratio of p^* to the operating pressure p by definition). N^* is the reduced density at which the mean free path equals the tube length as shown in equation A.10.

Molecular flow: (K_n>10)

$$\chi = \frac{1}{K} \tag{A.5}$$

Transitional flow: (10>K_n>0.01)

$$\chi = \frac{1}{K}\frac{\sqrt{\pi}}{2}\mathrm{erf}\left(\sqrt{\frac{N^*}{2}}\right)/\sqrt{\frac{N^*}{2}} \tag{A.6}$$

$$\chi = \frac{1}{K}\frac{\sqrt{\pi}}{2}\mathrm{erf}\left(\sqrt{\frac{L\pi P_{in}(2a_s)^2}{\sqrt{2}k_BT}}\right)/\sqrt{\frac{L\pi P_{in}(2a_s)^2}{\sqrt{2}k_BT}} \tag{A.7}$$

High pressure flow from a nozzle for a monatomic gas:

$$\chi = 1.97 \tag{A.8}$$

$$p^* = P_{in}K_n = \frac{k_BT_s}{\sqrt{2}\pi(2a_s)^2(2R)} \tag{A.9}$$

$$N^* = L/\lambda = 1/K_n = L\sqrt{2}\pi P(2a_s)^2/\left(k_BT\right) \tag{A.10}$$

A.4 Angular distribution

The angular distribution in the molecular flow and transitional regimes is discussed in [400] and [403]. In the molecular flow regime the angular distribution $f(\theta)$ depends only on the tube geometry, not the pressure or temperature and is given approximately in [403]. The results are shown in equation A.11 and equation A.12, where $\zeta = L\tan(\theta)/(2R)$. The normalization of these equations is only approximate so we numerically normalize. We shall refer to this as being the 'molecular flow' angular distribution.

For $0 < \theta < \arctan\left(\frac{2R}{L}\right)$:

$$f(\theta) = \frac{\cos(\theta)}{\pi}\left(\frac{2}{K}\left(\left(1-\frac{K}{2}\right)\left[\arccos(\zeta) - \zeta\sqrt{1-\zeta^2}\right] + \frac{2}{3}(1-K)\left[1-\left(1-\zeta^2\right)^{\frac{3}{2}}\right]\zeta^{-1}\right) + \frac{\pi}{2}\right) \tag{A.11}$$

For $\arctan\left(\frac{2R}{L}\right) < \theta < \frac{\pi}{2}$:

$$f(\theta) = \frac{\cos(\theta)}{\pi}\left(\frac{8R}{3\tan(\theta)LK}(1-K) + \frac{\pi}{2}\right) \tag{A.12}$$

When the mean free path becomes short compared with the collimation tube length the tube is essentially opaque. In this regime only the end of the collimation tube contributes to defining the angular divergence of the beam. In the limit the resulting beam divergence resembles expansion from an aperture into free space.

If we assume a linear pressure drop along the collimation tube we may define a reduced tube length L' at which point the mean free path at that pressure is equal to the remaining length of tube and the flow is essentially molecular. This length is given by [403] $L' = \sqrt{L\lambda}$ where λ is the mean free path. L' thus provides a length scale over which the tube appears essentially transparent and may be expected to have an angular distribution that is approximately that for molecular flow.

For tubes sufficiently long that they are not operating in the molecular flow regime we shall assume an angular distribution given in equation A.11 and A.12 in which L is replaced by L', ie $L = \min(L, \sqrt{L\lambda})$ and where the Clausing factor K is replaced by the inverse peaking factor, $K = 1/\chi$ as given by equation A.7. The resulting angular distribution is only approximate and it is numerically normalized. There are significant deviations at the boundaries of the transitional flow regime. These shall be referred to as the 'transitional flow' angular distributions.

The matlab function used to evaluate the flow properties is included in section A.5.

A.5 Evaluation function

```
function [P,Flux,Consumption,Knudsen,Peaking,VelocityCaptureEfficiency,...
    Efficiency,CapturableFlux,NormalizedFlux,DeltaRelativeFlux,...
    CumDeltaRelativeFlux]=CalculateOvenPropertiesCommented(T,Theta,R,L,...
    OvenApertureRadius,DistanceToTC,TCRadius,MaxPhotonsScattered,TubeOD)

% [P,Flux,Consumption,Knudsen,Peaking,VelocityCaptureEfficiency,
% Efficiency,CapturableFlux,NormalizedFlux,DeltaRelativeFlux,
% CumDeltaRelativeFlux]=CalculateOvenProperties(T,Theta,R,L,
% OvenApertureRadius,DistanceToTC,TCRadius,MaxPhotonsScattered,TubeOD)
%
% This function evaluates the flow proerties of a microtube array nozzle
% Parameters:
% T - Temperature [degC] Array of values to evaluate at
% Theta - Output angle [rad] Array of values to evaluate at
% R - Microtube inner radius [um]
% L - Microtube Length [mm]
% OvenApertureRadius - Radius of oven aperture [mm]
```

```
% DistanceToTC - Distance to Angular aperture [mm]
% TCRadius - Angular Aperture radius [mm]
% MaxPhotonsScattered - Maximum Photons which can be scatter on 461nm due
%                           to non closed transition (typically <20,000) -
%                           used to evaluate vcapture, the capture velocity
% TubeOD - Microtube Outer Diameter [um]
%
% The following are returned as arrays with respect to temperature:
%
% P - The partial vapour pressure of Strontium [Pa]
% Flux - Output Flux [atoms/s]
% Consumption - Rate of consumption of Strontium [gramms/month]
% Knudsen - The Knudsen number
% Peaking - The Relative brightness on axis relative to that of a cosine
%           emitter
% VelocityCaptureEfficiency - The proportion of atoms within the velocity
%                             capture range
% Efficiency - The proportion of atoms in principle able to be captured
% Captureable Flux - [atoms/s] within velocity and angular capture ranges
%
% The following are returned as 2D arrays with respect to the temperature
% and output angle:
%
% NormalizedFlux - The Normalized flux per sterradian
% DeltaRelativeFlux - The angular distribution, note that there is very
%                       little solid angle at small angles from the axis.
% CumDeltaRelativeFlux - The normalized cumulative Flux angular distribution
%                       integrated from the axis out to the given angle


MaxTCAngle=atan(TCRadius/DistanceToTC);
Lambda461=461e-9;                 % wavelength of Zeeman Slower light
Plankh=6.626e-34;                % Planks constant
kB=1.3806488E-23;                % Boltzman constant
as=20.5;                         % scattering radius in units of a_o
ao=5.2917721092E-11;             % a_o, the Bohr radius
%TubeOD=190e-6;
m=83.913425*1.66053892E-27;      % atomic mass (Calculated for 84Sr)
vCapture=MaxPhotonsScattered*Plankh/Lambda461/m; % capture velocity of
                                                    % zeeman slower
TubeRatio=L/R;                   % length to radius ratio for tube
Kfactor=10^((0.0085*log10(TubeRatio)^4)-(0.0093*log10(TubeRatio)^3)...
    -(0.2052*log10(TubeRatio)^2)-(0.3316*log10(TubeRatio))-0.1733);
                                 % Clausing Factor assuming a long tube
NumberOfTubes=pi*OvenApertureRadius^2/(6*(TubeOD/2)^2*tan(pi/6));
                                 % Number of Tubes which fit into a circular
                                 % cross section
```

```
% evalusate parameters

cFactor=-1.6;
h=(pi*R^2)^0.5;
w=h*0.94;
Rspecific=kB/m;
LogPinPout=log(1000);

TempK=T+273.15;
P=10.^(14.232-8572./TempK-1.1926*log10(TempK)); % strontium partial pressure
NumDensity=P/kB./TempK/1000000; %n/cm^3
MFP=kB.*TempK./(2^0.5*pi.*P*(2*as*ao)^2);
NStar=L./MFP;
LDash=min(L,L./NStar.^0.5);
PStar=kB*TempK/2^0.5/pi/(2*as*ao)^2/(2*R);
PonPStar=P./PStar;
Knudsen=1./PonPStar;
LStar=P*pi*R^2./(2*pi*m*kB*TempK).^0.5;

VelocityCaptureEfficiency=erf(vCapture/2^0.5./(kB*TempK/m).^0.5)-...
    (2/pi)^0.5*vCapture.*exp(-(vCapture.^2/2/kB./TempK*m))...
    ./(kB*TempK/m).^0.5;
                % proportion of thermal atoms with speed less than Vcapture
KLStar=LStar*Kfactor;
Vbar=(8*kB*TempK/pi/m).^0.5;        % mean atom speed
D=Vbar.*(MFP)/3;
mu=NumDensity*1000000.*D*m;
Db=Vbar*h/3.*Knudsen;
Dk=Vbar*h/3;
De=(Db.^cFactor+Dk.^cFactor).^(1/cFactor);
mu_e=(NumDensity*1000000*m).*De;
MK=(P/L/3*w*h^2.*(8/pi/Rspecific./TempK).^0.5)/m;
MD=mu*h*w/L.*LogPinPout/m;
MC_e=h^3*w*P.^2./(24*mu_e*L*Rspecific.*TempK)/m;
FluxPerTube=MC_e+(MD.^cFactor+MK.^cFactor).^(1/cFactor);

Flux=FluxPerTube*NumberOfTubes;
Consumption=Flux*m*3600*24*365/12*1000;
Peaking=(1./Kfactor.*(pi^0.5/2*(NStar/2).^(-0.5).*erf((NStar/2).^0.5)));

DeltaThetaData=[0;Theta];
DeltaTheta=-cos(DeltaThetaData(2:end))+cos(DeltaThetaData(1:(end-1)));
AADeltaTheta=repmat(DeltaTheta,size(TempK));

AAPeaking=repmat(Peaking,size(Theta));
AATheta=repmat(Theta,size(TempK));
AALDash=repmat(LDash,size(Theta));
```

```
112
113 Zeta=AALDash.*tan(AATheta)/2/R;
114 SmallAngles=cos(AATheta)/pi.*(2*AAPeaking.*((1-(1/2./AAPeaking))...
115     .*(acos(Zeta)-(Zeta.*(1-(Zeta.^2)).^0.5))...
116     +2/3*(1-(1./AAPeaking)).*(1-((1-(Zeta.^2)).^(3/2)))./Zeta)+pi/2);
117 LargeAngles=cos(AATheta)/pi.*(1./tan(AATheta)*8*R.*AAPeaking/3./AALDash...
118     .*(1-(1./AAPeaking))+pi/2);
119 NormalizedFlux=(AATheta≤atan(2*R./AALDash)).*SmallAngles...
120     +(AATheta>atan(2*R./AALDash)).*LargeAngles;
121 DeltaRelativeFlux=NormalizedFlux*2.*AADeltaTheta;
122
123 % Do normalization
124 normalization=repmat(sum(DeltaRelativeFlux,1),size(Theta));
125 NormalizedFlux=NormalizedFlux./normalization;
126 DeltaRelativeFlux=NormalizedFlux*2.*AADeltaTheta;
127 CumDeltaRelativeFlux=cumsum(DeltaRelativeFlux,1);
128
129
130 AngularEfficiency=sum((AATheta≤MaxTCAngle).*DeltaRelativeFlux,1);
131 Efficiency=AngularEfficiency.*VelocityCaptureEfficiency;
132 CapturableFlux=Flux.*Efficiency;
```

Appendix B

Field measurement for the permanent magnet arrays

This appendix includes figures showing the designed and measured fields from the permanent magnet arrays in the 2D blue MOT. It is included to provide supporting detail for section 3.5.1.

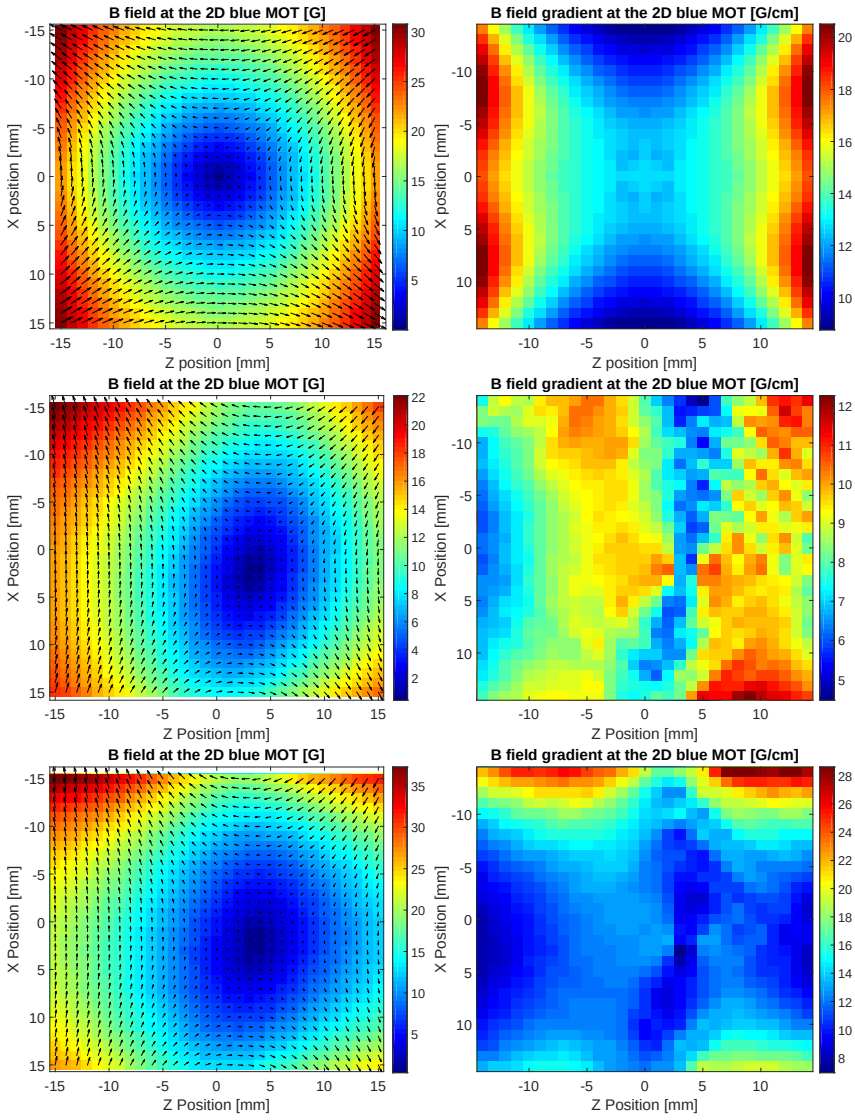

FIGURE B.1: **Designed and measured fields for the permanent magnet arrays around the 2D blue MOT.** The magnetic fields are plotted on the left hand side while the field gradients are on the right for field profiles at the height of the center of the 2D blue MOT. From top to bottom we have the deigned fields, the measured fields from the arrays and finally the measured fields from the arrays including the mu-metal shielding which sits next to the ZS3 coil. The z axis is parrallel to the Zeeman slower.

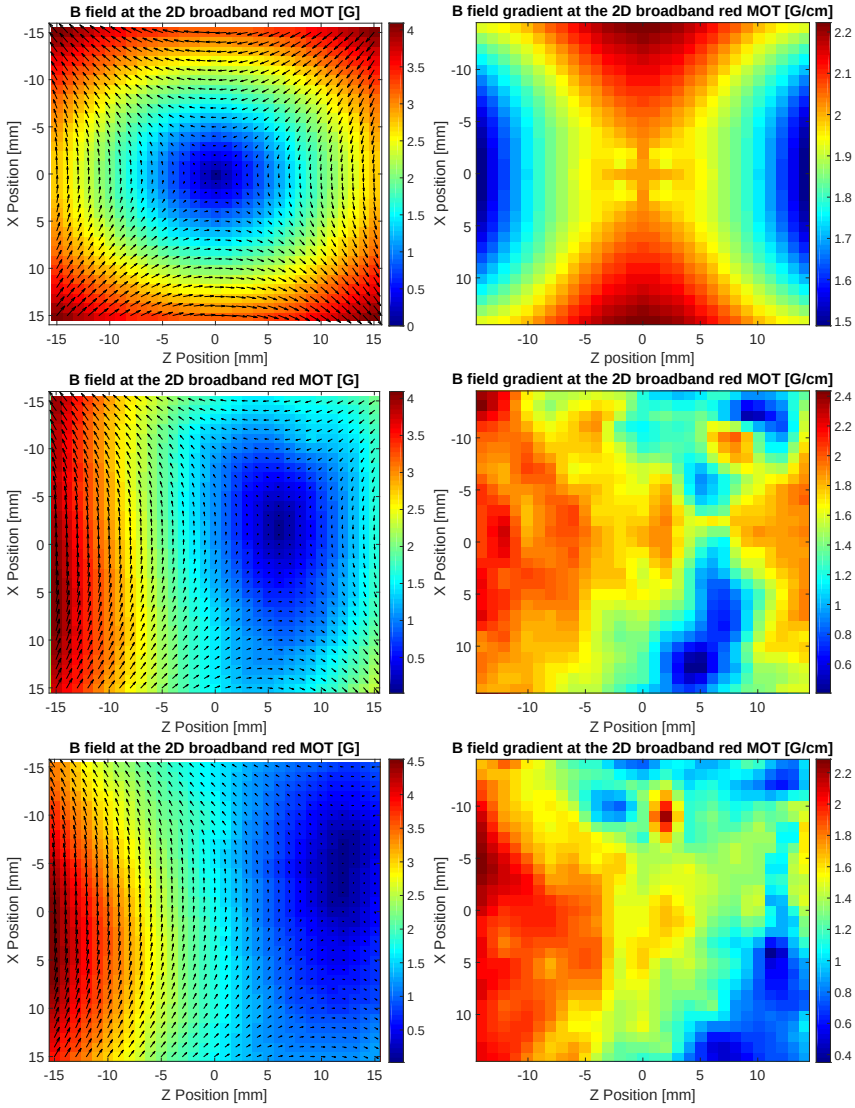

FIGURE B.2: **Designed and measured fields for the permanent magnet arrays near the 2D broadband red MOT.** The magnetic fields are plotted on the left hand side while the field gradients are on the right for field profiles at the height of the center of the 2D broadband red MOT. From top to bottom we have the designed fields, the measured fields from the arrays and finally the measured fields from the arrays including the mu-metal shielding which sits next to the ZS3 coil. The z axis is parrallel to the Zeeman slower.

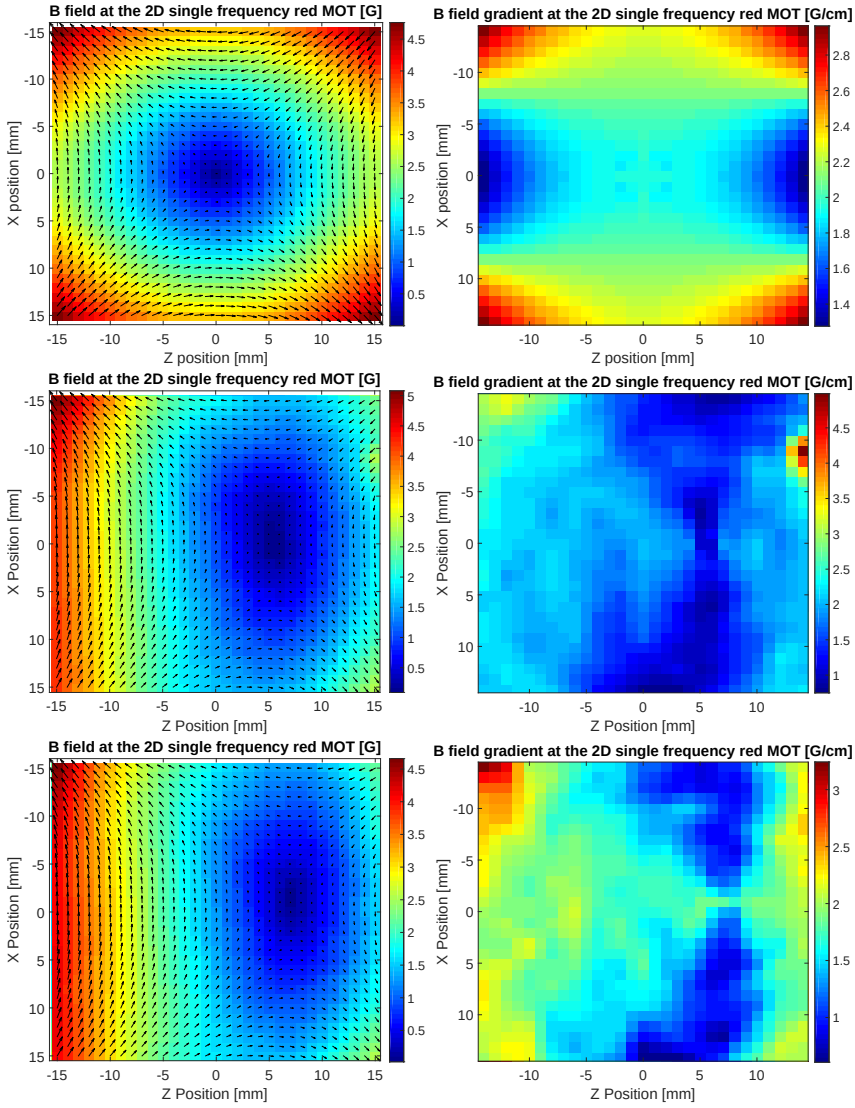

FIGURE B.3: **Designed and measured fields for the permanent magnet arrays around the 2D single frequency red MOT.** The magnetic fields are plotted on the left hand side while the field gradients are on the right for field profiles at the height of the center of the 2D single frequency red MOT. From top to bottom we have the deigned fields, the measured fields from the arrays and finally the measured fields from the arrays including the mu-metal shielding which sits next to the ZS3 coil. The z axis is parallel to the Zeeman slower.

Appendix C

Magnetic System

This appendix describes the technical parameters of the coils constructed.

The geometry of the coils on the machine is illustrated in figure C.1. Coils are typically referred to by their location within the room. "Wall" refers to negative on the z axis while "aisle" refers to positive on the z axis. "Oven" refers to negative on the x axis while "computer" is positive on the x axis. "Down" is negative on the y axis while "up" is positive on the y axis.

Table C.1 lists the currents and other critical parameters for all the coil sets. Table C.2 describes the cabling methods used to connect the machine to the power supply cabinet around 30 m away. Table C.5 describes the wire configuration of each circuit. Typically 2 to 4 individual circuits are connected in series to form a Helmholtz or anti-Helmholz coil set. These connections are made at terminal switch yards located around the machine and can be swapped to change the coil direction, strength or configuration. The power supplies are controlled by an analog output from our control system. The power supplies are all located in an adjacent room around 30 m from the machine.

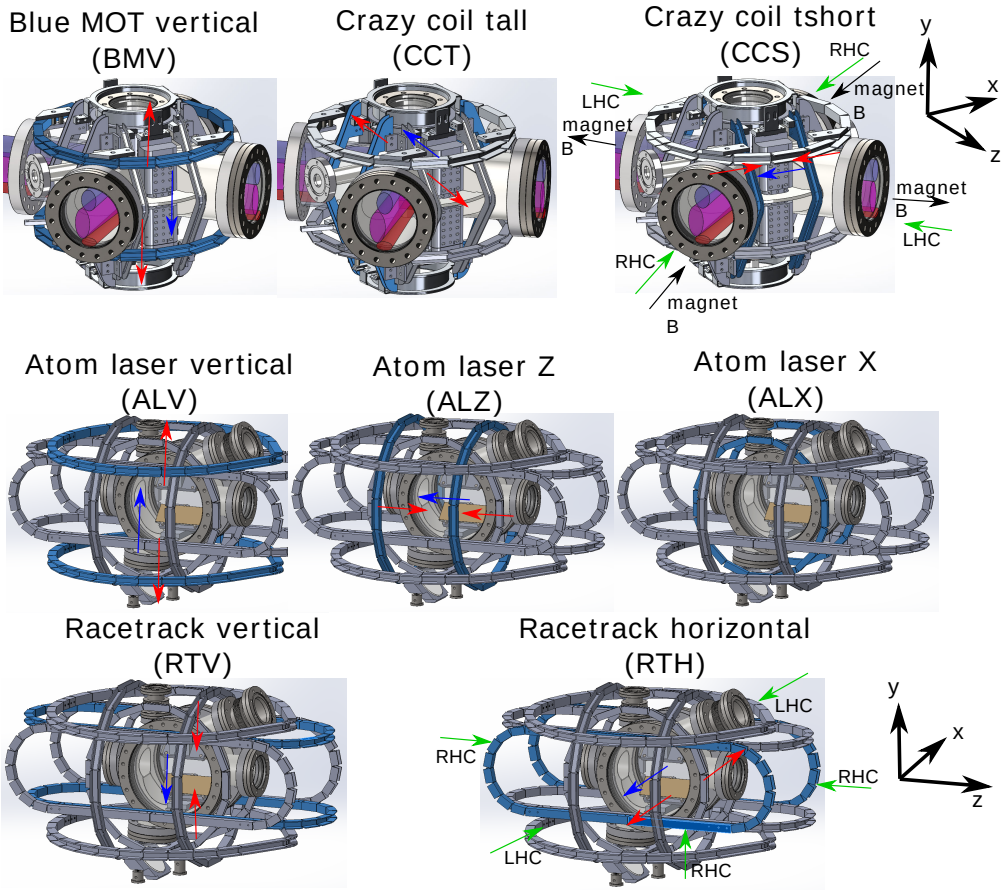

FIGURE C.1: **Coil geometry.** Here we show the geometry of the coils used in the machine. Overlaid are the current field directions for each coil in the Helmholtz (blue) and anti-Helmholtz (red) configuration and the polarizations of the MOT beams used in these axes (LHC-left handed circular, RHC-right handed circular).

TABLE C.1: **Coil parameters.**

Name	Abbreviation	Typical current [A] (Capture MOT)	Typical current [A] (High PSD MOT)	Maximum current [A]	Power supply (see table C.4)	Cabling (see table C.2)	Resistance [mΩ]	Turns per coil	Circuit config (see table C.5)
Zeeman Slower 1	ZS1	1.6	1.6	10	EA32-10	6 mm	2554		ZS1
Zeeman Slower 2	ZS2	14.0	14.0	20	EA16-20	6 mm	55		ZS2
Zeeman Slower 3	ZS3	128.0	128.0	200	GEN8-300	70 mm	14.7	5	ZS3
Compensation Coil	CC	0	0	200	UP6-132	70 mm	17	8	CC
Blue MOT Vertical Helmholtz	BMVH	5.0	5.0	20	EA32-10	6 mm	137	7	-BMT2-BMB2
Blue MOT Vertical Anti-Helmholtz	BMVAH	0.0	0.0	20	EA16-20	6 mm	499	30	BMT1+BMB1 -BMT3-BMB3
Crazy Coil Tall Helmholtz	CCTH	2.6	2.6	10	EA16-10	6 mm	726	21	CCW2+CCA2
Crazy Coil Tall Anti-Helmholtz	CCTAH	0.0	0.0	10	EA16-10	6 mm	507	14	-CCW1+CCA1
Crazy Coil Short Helmholtz	CCSH	0.3	0.3	10	EA16-10	6 mm	730	21	-CCO3-CCC3
Crazy Coil Short Anti-Helmholtz	CCSAH	0.0	0.0	10	EA16-10	6 mm	512	14	-CCO1+CCC1
Atom Laser Vertical Helmholtz	ALVH	1.357	0.66	20	ZUP10-20	6 mm	436	15	+ALT1+ALB1
Atom Laser Vertical Anti-Helmholtz	ALVAH	5.4	5.4	20	ZUP10-20	6 mm	1348	49	+ALT2-ALB2 +ALT3-ALB3
Atom Laser Z Helmholtz	ALZH	1.25	0.08	20	EA16-20	6 mm	256	12	+ALW2+ALA2
Atom Laser Z Anti-Helmholtz	ALZAH	0.0	0.0	20	EA16-20	6 mm	804	40	-ALW1+ALA1 -ALW3+ALA3
Atom Laser X Helmholtz	ALXH	0.0	0.0	20	None	6 mm	155	8	ALO1+ALO1
Atom Laser X Anti-Helmholtz	ALXAH	0.0	0.0	20	None	6 mm	293	16	ALO2-ALO2
Racetrack Vertical Helmholtz	RTVH	0.0	0.0	20	EA16-20	6 mm	303	10	-RTT3-RTB3
Racetrack Vertical Anti-Helmholtz	RTVAH	2.3	2.3	20	EA32-20*	6 mm	1339	49	-RTT1+RTB1 -RTT2+RTB2
Racetrack Horizontal Helmholtz	RTHH	0.95	1.20	20	EA16-20	6 mm	303	10	-RTO3-RTC3
Racetrack Horizontal Anti-Helmholtz	RTHAH	2.3	2.3	20	EA32-20*	6 mm	1340	49	-RTO1+RTC1 -RTO2+RTC2
Cage Coil X	CageX		≈0	10	LDD5	Direct	1780	22	
Cage Coil Y	CageY		≈0	10	LDD5	Direct	1780	22	
Cage Coil Z	CageZ		≈0	10	LDD5	Direct	1780	22	

TABLE C.2: **Cabling methods.** A description of the cabling methods used to connect the machine to the power supply racks, a 30 m distance away.

Cable type	Description
6 mm	Cabling is done using 6 mm^2 audio wire (LAT 600-50 from www.reichelt.at), which is shielded with tinned copper braid (91F453 from www.buerklin.com) and sheathed with a plastic sock to prevent interconnection between the bundles of cable shields (91F4206 from www.buerklin.com). The resistance to the power supply is around 200 mΩ. A 38 V, 2 kA, 26 J varistor (Farnell 1004275) is placed across the power supply terminals to arrest inductance voltage spikes and thus offer some protection for the power supply.
70 mm	Cabling is done using bundled (to minimize inductance) 70 mm^2 cables. There is no shielding. Termination is done by crimping using ring terminals (typically part 735790-89 from Conrad). A 38 V, 2 kA, 26 J varistor (Farnell 1004275) is placed across the power supply terminals to arrest inductance voltage spikes and thus offer some protection for the power supply.
Direct	Power supply is connected directly to the coils.

TABLE C.3: **Wire types.** The types of copper wire used to construct the coils. The thickness of the enamel insulation is nominally 100 µm. (*) Insulated by wrapping with 3 layers of kapton tape.

Wire type	Copper dimensions	Area [mm^2]	Supplier	Insulation	Notes
Flat	4.57 mm×1.01 mm	4.401	Hi Wire Ltd (spsx.com)	Magnetemp CA200 grade 2	Part CS4175
1.1 mm	1.12 mm diameter	0.985			
1.7 mm	1.70 mm diameter	2.27			Part CW1860
Square	4 mm×4 mm hollow, 1 mm wall	12	coleandswallow.com	None (*)	Annealed EN12441

TABLE C.4: **Power supply types.**

Type	Manf.	Part	Supplier	Part	Voltage [V]	Current [A]
EA16-10	EA Electro-Automatik	EA-PS 3016-10B	Farnell	1437497	16	10
EA16-20		EA-PS 3016-20B		1437543	16	20
EA32-10		EA-PS 3032-10B		1580523	32	10
EA32-20		EA-PS 3032-20B		1437545	32	20
EA16-10		EA-PS 3016-10B		1437497	16	10
EA16-10		EA-PS 3016-10B		1437497	16	10
ZUP10-20	TDK Lambda	ZUP10-20	Mouser	967-ZUP10-20	10	20
UP6-132		UP6-132		967-ZUP6-132/U	6	132
GEN8-300		GEN8-300	Conrad	1303971	8	300
LDD5	Home Made (LaserdiodeCurrentdriver V6.0 5A)				5	5

TABLE C.5: **Structure and properties of each coil circuit.**

Circuit name	Wire type (see table C.3)	Holder	Direction	Turns	Turns per layer (in order from bottom to top layer)	Resistance [mΩ] (before bake)	Resistance [mΩ] (after bake)	Typical cooling water flow [$l \cdot h^{-1}$] (Pump ≈ 4 bar)
ZS1	Flat				167, 165, 162, 160, 156, 153, 149, 146, 142, 138, 134, 130, 125, 121, 116, 112, 106, 101, 96, 90, 85, 79, 74, 67, 61, 55, 48, 42, 36, 28, 24, 19, 16, 13, 11, 9, 7, 5, 4, 3, 2, 1	2380		88.2
ZS2					18, 14, 12, 10, 8, 7, 5, 4, 3, 2, 2, 1	54.98		
ZS3	Square			5	5			29.5
Compensation				5	5			22.6
CCS Oven 1	1.1 mm Round	9×9	To Comp	14	7, 7	267.73		31.3
CCS Oven 2				13	4, 3, 3, 3	255.74		
CCS Oven 3				21	7, 7, 7	380.24		
CCS Comp 1				14	7, 7	262.78	243.87	31.5
CCS Comp 2				13	4, 3, 3, 3	256.53	235.79	
CCS Comp 3				21	7, 7, 7	391.95	349.93	
CCT Wall 1			To Wall	14	7, 7	272.83	253.97	27.3
CCT Wall 2				21	7, 7, 7	409.61	365.08	
CCT Wall 3				13	4, 3, 3, 3	265.69	241.85	
CCT Aisle 1				14	7, 7	272.33	252.96	26.3
CCT Aisle 2				21	7, 7, 7	402.90	361.04	
CCT Aisle 3				13	4, 3, 3, 3	267.34	243.87	
BMV Top 1	1.7 mm Round	13×11	Up	12	6, 6	105.49	102.46	30.4
BMV Top 2				7	3, 4	69.12	69.12	
BMV Top 3				18	6, 6, 6	147.91	146.90	
BMV Bottom 1				12	6, 6	105.49	104.48	33.3
BMV Bottom 2				7	3, 4	69.12	68.11	
BMV Bottom 3				18	6, 6, 6	147.91	144.88	
AL Aisle 1	1.7 mm Round	13×16	To Wall	24	8, 8, 8	237.45		27.9
AL Aisle 2				12	6, 6	128.29		
AL Aisle 3				16	8, 8	164.56		
AL Wall 1				24	8, 8, 8	237.45		29.3
AL Wall 2				12	6, 6	128.29		
AL Wall 3				16	8, 8	164.56		
AL Oven 1				8	4, 2, 2	82.26		29.7

TABLE C.5: **Structure and properties of each coil circuit.**

Circuit name	Wire type (see table C.3)	Holder	Direction	Turns	Turns per layer (in order from bottom to top layer)	Resistance [mΩ] (before bake)	Resistance [mΩ] (after bake)	Typical cooling water flow [$l \cdot h^{-1}$] (Pump ≈ 4 bar)
AL Oven 2	1.7 mm Round	13×8	To Comp	16	4, 4, 4, 4	151.41		29.7
AL Comp 1				8	4, 2, 2	79.62		31.4
AL Comp 2				16	4, 4, 4, 4	142.04		
AL Top 1		17×14	Up	15	5, 5, 5	217.16		26.4
AL Top 2				21	7, 7, 7	295.18		
AL Top 3				28	7, 7, 7, 7	379.33		
AL Bottom 1		17×14	Up	15	5, 5, 5	219.19		23.6
AL Bottom 2				21	7, 7, 7	295.41		
AL Bottom 3				28	7, 7, 7, 7	379.01		
RT Top 1		16×14	Up	21	7, 7, 7	293.12		26.3
RT Top 2				28	7, 7, 7, 7	377.03		
RT Top 3				10	5, 5	151.89		
RT Bottom 1				21	7, 7, 7	291.12		28.8
RT Bottom 2				28	7, 7, 7, 7	378.31		
RT Bottom 3				10	5, 5	151.41		
RT Oven 1			To Comp	21	7, 7, 7	293.12		28.1
RT Oven 2				28	7, 7, 7, 7	377.03		
RT Oven 3				10	5, 5	151.89		
RT Comp 1				21	7, 7, 7	291.12		29.3
RT Comp 2				28	7, 7, 7, 7	378.31		
RT Comp 3				10	5, 5	151.41		

Appendix D

Summary of MOT beams and imaging systems

The layouts of the MOT and imaging beam lines for the lower chamber is illustrated in figure D.1. A complete layout for the top and bottom layers of the breadboards launching beams into the atom laser chamber is provided in figure D.2 and figure D.3 respectively. A complete summary of figures containing optical layouts can be found in table D.1.

TABLE D.1: **Optics layout figures.**

Figure	Description	Page
Figure 3.10	Blue transverse cooling.	75
Figure 3.38	2D MOT optical configuration.	133
Figure 3.39	2D MOT vertical optical configuration.	134
Figure D.1	Red MOT and imaging systems for the lower chamber.	308
Figure 4.3	Red MOT beams - side view.	165
Figure D.2	Full beam layout for the lower chamber - main level.	309
Figure D.3	Full beam layout for the lower chamber - lower level.	310
Figure 4.6	Transparency and dipole trap geometry.	172
Figure 6.3	Transport dipole trap setup.	225
Figure 4.12	Transparency laser system.	186

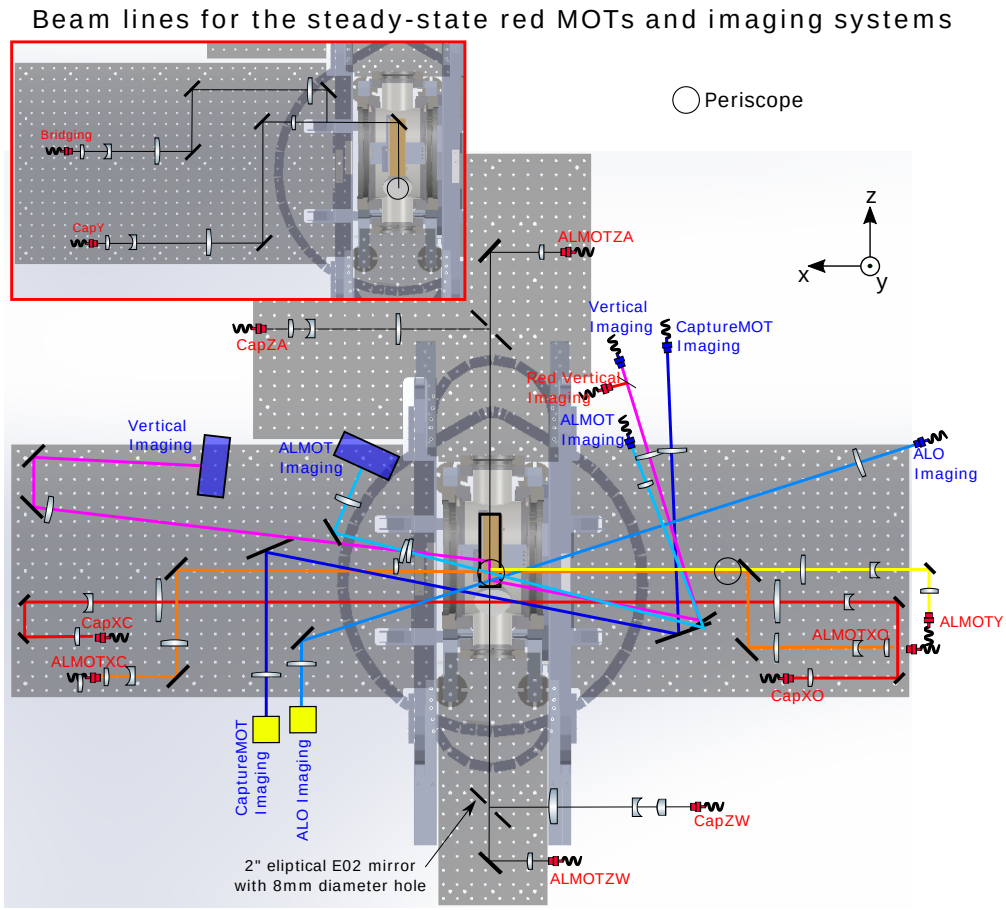

FIGURE D.1: **Red MOT and imaging systems for the lower chamber.**

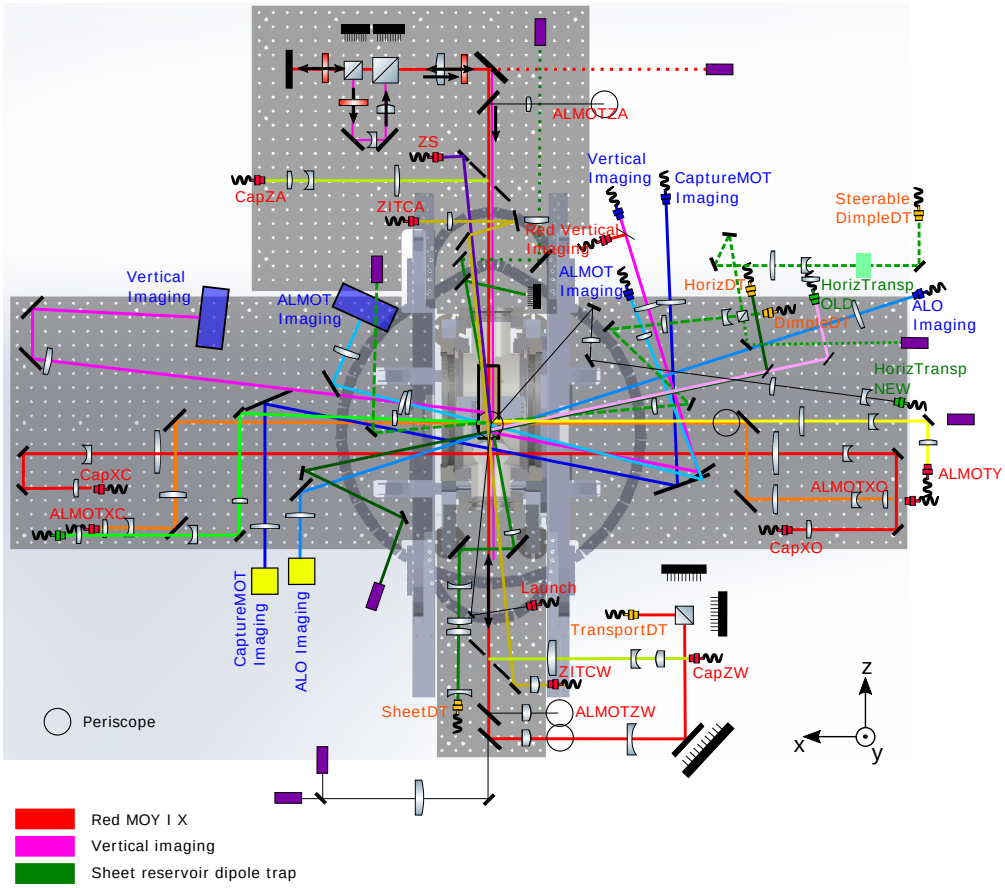

FIGURE D.2: **Full beam layout for the lower chamber - main level.**

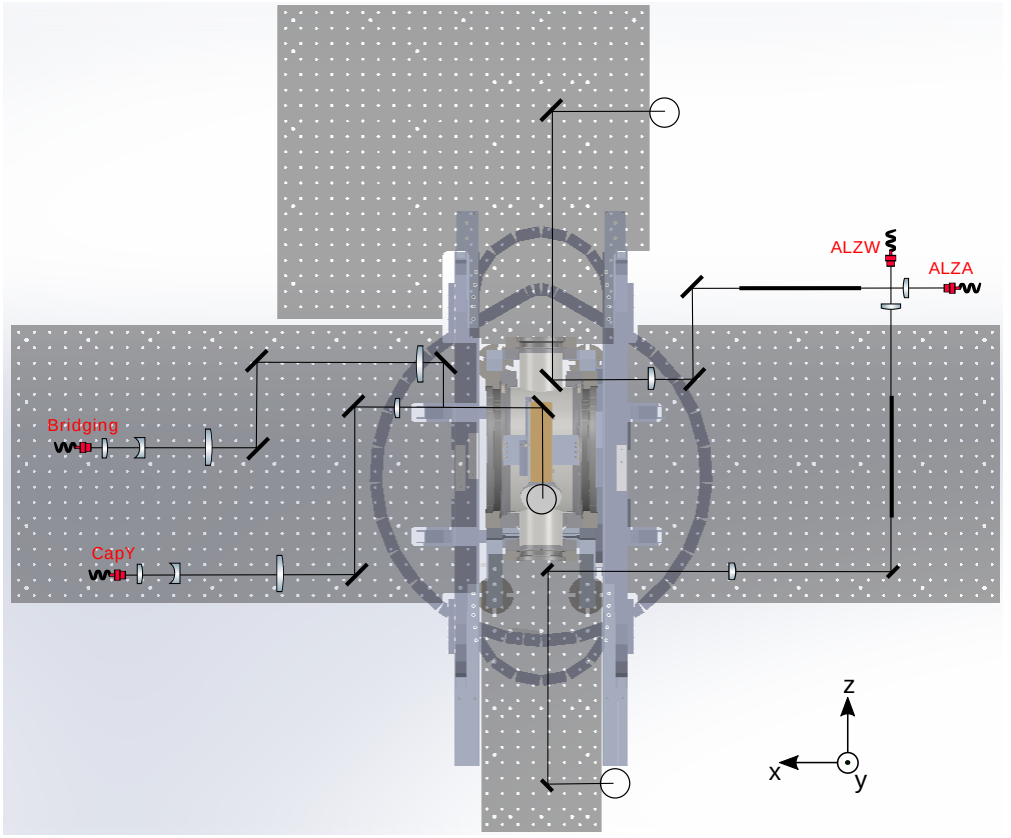

FIGURE D.3: **Full beam layout for the lower chamber - lower level.**

Appendix E

Laser parameters

Here we tabulate the laser parameters for the configurations discussed in this thesis.

TABLE E.1: Properties of laser cooling beams using the blue $^1S_0 - {}^1P_1$ transition.

Beam name	**Detuning [MHz]**	**Power [mW]**	$1/e^2$ **diameter [mm]**	**Comments**
Transverse cooling	-18 (-0.6Γ)	30	23×9.6	Beam is passed 4 times side by side giving a 90 mm long cooling region. Same for both horizontal and vertical axes.
Zeeman slower	-424 (-14Γ)	64	25.4	Focused to 12 mm diameter at the oven exit.
2D MOT	-25 (-0.8Γ)	10.5	22.8	4 beams with centers at the same height as the Zeeman slower axis.
Plug beams	-13 (-0.4Γ)	0.017	9.6	2 symmetric beams inclined at 8° to the vertical (y axis) and aimed at the top half of the blue 2D MOT.

TABLE E.2: Properties of laser beams used for Red MOT I. Under "detuning" $\Delta_1 : \delta : \Delta_2$ refers to a modulated comb of lines from Δ_1 to Δ_2 with a spacing of δ.[1]

Beam name	**Detuning [MHz]**	**Power [mW]**	$1/e^2$ **diameter [mm]**	**Comments**
2D Red molasses	-0.03 : 0.025 : -0.75	4.6	45.6 × 18.2	2 sets of 2 counter-propagating beams, centered 38 mm below Zeeman slower plane.
Red MOT I Y	-0.95 : 0.017 : -5	10.8	68	Waist given 22 cm below the quadrupole center. Beam focused on the bottom baffle 22 cm above the quadrupole center at $z = +10$ mm from the central axis of the falling atomic beam.
Red MOT I X	-0.7 : 0.015 : -3	3.3	47	2 counter-propagating beams
Red MOT I Z Outer	-0.7 : 0.016 : -3	1.14	48	2 counter-propagating beams with an 8mm hole to allow Red MOT I Z Inner beams to pass.
Red MOT I Z Inner	-0.73 : 0.017 : -1.1 -1.1 : 0.019 : -3.5	0.16[1]	8	2 counter-propagating beams

TABLE E.3: Properties of laser beams used in the apparatus for Red MOT II(a). Under "detuning" $\Delta_1 : \delta : \Delta_2$ refers to a modulated comb of lines from Δ_1 to Δ_2 with a spacing of δ.

Beam name	**Detuning [MHz]**	**Power [mW]**	$1/e^2$ **diameter [mm]**	**Comments**
2D Red molasses	-0.03 : 0.025 : -0.75	4.6	45.6 × 18.2	2 sets of 2 counter-propagating beams, centered 38 mm below Zeeman slower plane.
Red MOT I Y	-0.5 : 0.017 : -4	10.8	68	Waist given 22 cm below the quadrupole center. Beam focused on the bottom baffle 22 cm above the quadrupole center at $z = +10$ mm from the central axis of the falling atomic beam.
Red MOT I X	-0.7 : 0.015 : -3	3.3	47	2 counter-propagating beams
Red MOT I Z Outer	-0.7 : 0.016 : -4	1.14	48	2 counter-propagating beams with an 8mm hole to allow Red MOT II Z Inner beams to pass.
Red MOT II Z Inner	-0.1 : 0.017 : -0.25 -0.26 : 0.015 : -2.85	0.063[1]	8	2 counter-propagating beams
Red MOT II Y	-0.1 : 0.016 : -0.25 -0.26 : 0.014 : -2.85	0.43[1]	36	1 upward-propagating beam
Red MOT II X	-0.1 : 0.017 : -0.25 -0.26 : 0.013 : -2.85	0.099 [1]	28.8	2 counter-propagating beams

TABLE E.4: Properties of laser beams used in the apparatus for Red MOT II(b). Under "detuning" $\Delta_1 : \delta : \Delta_2$ refers to a modulated comb of lines from Δ_1 to Δ_2 with a spacing of δ.

Beam name	**Detuning [MHz]**	**Power [mW]**	$1/e^2$ **diameter [mm]**	**Comments**
2D Red molasses	-0.03 : 0.025 : -0.75	4.6	45.6 × 18.2	2 sets of 2 counter-propagating beams, centered 38 mm below Zeeman slower plane.
Red MOT I Y	-0.5 : 0.017 : -4	10.8	68	Waist given 22 cm below the quadrupole center. Beam focused on the bottom baffle 22 cm above the quadrupole center at $z = +10$ mm from the central axis of the falling atomic beam.
Red MOT I X	-0.7 : 0.015 : -3	3.3	47	2 counter-propagating beams
Red MOT I Z Outer	-0.7 : 0.016 : -4	1.14	48	2 counter-propagating beams with an 8mm hole to allow Red MOT II Z Inner beams to pass.
Red MOT II Z Inner	-0.04 : 0.017 : -0.2	0.016	8	2 counter-propagating beams
Red MOT II Y	-0.04 : 0.016 : -0.2	0.09	36	1 upward-propagating beam
Red MOT II X	-0.04 : 0.017 : -0.2	0.026	28.8	2 counter-propagating beams

[1]Note that due to nonlinearities in the amplifiers and AOMs, it is not possible to separately measure the optical powers in each component of the spectrum.

TABLE E.5: Properties of laser beams used in the apparatus for steady-state BEC attempt V2.0 in which we achieved unity phase-space density. Under "detuning" $\Delta_1 : \delta : \Delta_2$ refers to a modulated comb of lines from Δ_1 to Δ_2 with a spacing of δ. Powers are measured powers. Windows in the bottom chamber are uncoated. Beams are at 689 nm unless otherwise stated.

Beam name	**Detuning [MHz]**	**Power**	$1/e^2$ **diameter [mm]**
2D Red molasses[a]	-0.03 : 0.026 : -0.75	4.7 mW	45.6×18.2
Red MOT I Y[b]	-0.95 : 0.017 : -5.2	8.36 mW*	68
Red MOT I X[c]	-0.66 : 0.015 : -2.2	1.1 mW	47
Red MOT I Z Outer[d]	-0.82 : 0.016 : -2.2	219 µW	48
Red MOT II Z Inner[c]	-0.85 : 0.017 : -1.25	6.55 µW	8
Red MOT II Y[e]	+0.07	6.77 µW	36
Red MOT II X[c]	+0.07	1.38 µW	28.8
Z in-trap cooling[f]	+1.82	1.3 nW	0.3
Push[g]	+0.4:0.017:+0.9	30 nW	0.25
Slower[h]	-1.72:0.019:-1.77	5 nW	0.3
Transparency vertical +15 GHz 688 nm		9.0 mW	0.052
Transparency horizontal +15.7 GHz 688 nm		15.6 mW	0.082
Transparency vertical 679 nm repump		15.5 µW	0.052
Transparency vertical 707 nm repump		2.32 µW	0.052
Transparency horizontal 679 nm repump		54 µW	0.082
Transparency horizontal 707 nm repump		3.3 µW	0.082
2D MOT repump 679 nm		0.5 mW	40
2D MOT repump 707 nm		0.5 mW	40
Transport guide dipole trap[i] 1070 nm		12.1 W	0.184
Sheet dipole trap 1070 nm		850 mW	0.026×0.240
Dimple trap 1070 nm		156 mW	0.054
Blue transverse cooling vertical[j]	-18 (-0.6Γ)	31.2 mW	23×9.6
Blue transverse cooling horizontal[j]	-18 (-0.6Γ)	24.3 mW	23×9.6
Blue MOT beams[k]	-25 (-0.8Γ)	9.49 mW	22.8
Blue plug beams[l]	-13 (-0.4Γ)	17 µW	9.6
Blue Zeeman slower[m]	-424 (-14Γ)	64 mW	25.4

[a] 2 sets of 2 counter-propagating beams, centered 38 mm below Zeeman slower plane.

[b] Waist given 22 cm below the quadrupole center. Beam focused on the bottom baffle 22 cm above the quadrupole center at $z = +10$ mm from the central axis of the falling atomic beam. *Beam is apertured with an iris, 11 mW without the aperture.

[c] 2 counter-propagating beams.

[d] 2 counter-propagating beams with an 8mm hole to allow Red MOT II Z Inner beams to pass. Beam from the aisle side is blocked.

[e] 1 upward-propagating beam.

[f] 1 beam from the wall aligned to the reservoir trap with an angle of 0°.

[g] 1 beam from the aisle at 0° to the guide.

[h] 1 beam from the aisle at 4° to the guide.

[i] 60% relayed back to focus offset by 35 mm along with another 10% overlaid with the reservoir at the dimple location.

[j] Beam is passed 4 times side by side giving a 90 mm long cooling region.

[k] 4 beams with centers at the same height as the Zeeman slower axis.

[l] 2 symmetric beams inclined at 8 ° to the vertical (y axis) and aimed at the top half of the blue 2D MOT.

[m] Collimated.

Bibliography

[1] A. Einstein, *"Strahlungs-Emission und Absorption nach der Quantentheorie"*, Deutsche Physikalische Gesellschaft **18** 1916.

[2] A. Einstein, *"Zur Quantentheorie der Strahlung"*, Physikalische Zeitschrift **18** 1917.

[3] J. P. Gordon, H. J. Zeiger, and C. H. Townes, *"Molecular Microwave Oscillator and New Hyperfine Structure in the Microwave Spectrum of NH_3"*, Phys. Rev. **95**, 282–284, 1954, DOI: 10.1103/PhysRev.95.282.

[4] T. H. Maiman, *"Stimulated Optical Radiation in Ruby"*, Nature **187**, 493–494, 1960, DOI: 10.1038/187493a0.

[5] A. Javan, W. R. Bennett, and D. R. Herriott, *"Population Inversion and Continuous Optical Maser Oscillation in a Gas Discharge Containing a He-Ne Mixture"*, Phys. Rev. Lett. **6**, 106–110, 1961, DOI: 10.1103/PhysRevLett.6.106.

[6] Bose, *"Plancks Gesetz und Lichtquantenhypothese"*, Zeitschrift für Physik **26**, 178–181, 1924, DOI: 10.1007/BF01327326.

[7] A. Einstein, *"Quantentheorie des einatomigen idealen Gases"*, Sitzungber. Kgl. Akad. Wiss. 1924.

[8] M. H. Anderson, J. R. Ensher, M. R. Matthews, C. E. Wieman, and E. A. Cornell, *"Observation of Bose-Einstein Condensation in a Dilute Atomic Vapor"*, Science **269**, 198–201, 1995, DOI: 10.1126/science.269.5221.198.

[9] K. B. Davis, M. O. Mewes, M. R. Andrews, N. J. van Druten, D. S. Durfee, D. M. Kurn, and W. Ketterle, *"Bose-Einstein Condensation in a Gas of Sodium Atoms"*, Phys. Rev. Lett. **75**, 3969–3973, 1995, DOI: 10.1103/PhysRevLett.75.3969.

[10] W. Ketterle, D. S. Durfee, and D. M. Stamper-Kurn, *"Making, probing and understanding Bose-Einstein condensates"*, 1999, eprint: cond-mat/9904034.

[11] W. Ketterle, *"Nobel lecture: When atoms behave as waves: Bose-Einstein condensation and the atom laser"*, Rev. Mod. Phys. **74**, 1131–1151, 2002, DOI: 10.1103/revmodphys.74.1131.

[12] I. Bloch, J. Dalibard, and W. Zwerger, *"Many-body physics with ultracold gases"*, Rev. Mod. Phys. **80**, 885–964, 2008, DOI: 10.1103/RevModPhys.80.885.

[13] A. D. Cronin, J. Schmiedmayer, and D. E. Pritchard, *"Optics and interferometry with atoms and molecules"*, Rev. Mod. Phys. **81**, 1051–1129, 2009, DOI: 10.1103/RevModPhys.81.1051.

[14] T. J. Kippenberg and K. J. Vahala, *"Cavity Optomechanics: Back-Action at the Mesoscale"*, Science **321**, 1172–1176, 2008, DOI: 10.1126/science.1156032.

[15] M.-O. Mewes, M. R. Andrews, D. M. Kurn, D. S. Durfee, C. G. Townsend, and W. Ketterle, *"Output Coupler for Bose-Einstein Condensed Atoms"*, Phys. Rev. Lett. **78**, 582–585, 1997, DOI: 10.1103/PhysRevLett.78.582.

[16] N. P. Robins, P. A. Altin, J. E. Debs, and J. D. Close, *"Atom lasers: Production, properties and prospects for precision inertial measurements"*, Phys. Rep. **529**, 637, 2013, DOI: 10.1016/j.physrep.2013.03.006.

[17] I. Bloch, T. W. Hänsch, and T. Esslinger, *"Atom Laser with a cw Output Coupler"*, Phys. Rev. Lett. **82**, 3008–3011, 1999, DOI: 10.1103/PhysRevLett.82.3008.

[18] A. P. Chikkatur, Y. Shin, A. E. Leanhardt, D. Kielpinski, E. Tsikata, T. L. Gustavson, D. E. Pritchard, and W. Ketterle, *"A Continuous Source of Bose-Einstein Condensed Atoms"*, Science **296**, 2193–2195, 2002, DOI: 10.1126/science.296.5576.2193.

[19] W. Yi and L.-M. Duan, *"Adiabatic and nonadiabatic merging of independent Bose-Einstein condensates"*, Phys. Rev. A **71**, 043607, 2005, DOI: 10.1103/PhysRevA.71.043607.

[20] W. Ketterle, *"Atom Laser"*, Yearbook of Science & Technology, 1999.

[21] I. Ushijima, M. Takamoto, M. Das, T. Ohkubo, and H. Katori, *"Cryogenic optical lattice clocks"*, Nat. Photonics **9**, 185–189, 2015, DOI: 10.1038/nphoton.2015.5.

[22] B. J. Bloom, T. L. Nicholson, J. R. Williams, S. L. Campbell, M. Bishof, X. Zhang, W. Zhang, S. L. Bromley, and J. Ye, *"An optical lattice clock with accuracy and stability at the* 10^{-18} *level"*, Nature **506**, 71–75, 2014, DOI: 10.1038/nature12941.

[23] N. Hinkley, J. A. Sherman, N. B. Phillips, M. Schioppo, N. D. Lemke, K. Beloy, M. Pizzocaro, C. W. Oates, and A. D. Ludlow, *"An Atomic Clock with* 10^{-18} *Instability"*, Science **341**, 1215–1218, 2013, DOI: 10.1126/science.1240420.

[24] C. W. Chou, D. B. Hume, J. C. J. Koelemeij, D. J. Wineland, and T. Rosenband, *"Frequency Comparison of Two High-Accuracy* Al^+ *Optical Clocks"*, Phys. Rev. Lett. **104**, 070802, 2010, DOI: 10.1103/PhysRevLett.104.070802.

[25] C. W. Chou, D. B. Hume, T. Rosenband, and D. J. Wineland, *"Optical Clocks and Relativity"*, Science **329**, 1630–1633, 2010, DOI: 10.1126/science.1192720.

[26] S. L. Campbell, R. B. Hutson, G. E. Marti, A. Goban, N. D. Oppong, R. L. McNally, L. Sonderhouse, J. M. Robinson, W. Zhang, B. J. Bloom, and J. Ye, *"A Fermi-degenerate three-dimensional optical lattice clock"*, Science **358**, 90, 2017, DOI: 10.1126/science.aam5538.

[27] S. L. Campbell, *"A Fermi-degenerate three-dimensional optical lattice clock"*, PhD thesis, JILA, University of Colorado, USA, 2017.

[28] M. Takamoto, F.-L. Hong, R. Higashi, and H. Katori, *"An optical lattice clock"*, Nature **435**, 321, 2005, DOI: 10.1038/nature03541.

[29] B. C. Young, F. C. Cruz, W. M. Itano, and J. C. Bergquist, *"Visible Lasers with Subhertz Linewidths"*, Phys. Rev. Lett. **82**, 3799–3802, 1999, DOI: 10.1103/PhysRevLett.82.3799.

[30] C. Hagemann, C. Grebing, C. Lisdat, S. Falke, T. Legero, U. Sterr, F. Riehle, M. J. Martin, and J. Ye, *"Ultrastable laser with average fractional frequency drift rate below* $5 \times 10^{-19}/s$*"*, Opt. Lett. **39**, 5102, 2014, DOI: 10.1364/OL.39.005102.

[31] J. Ye, H. J. Kimble, and H. Katori, *"Quantum State Engineering and Precision Metrology Using State-Insensitive Light Traps"*, Science **320**, 1734, 2008, DOI: 10.1126/science.1148259.

[32] H. Katori and M. Takamoto, "Ultrastable Optical Clock with Neutral Atoms in an Engineered Light Shift Trap", *Conference on Lasers and Electro-Optics/International Quantum Electronics Conference and Photonic Applications Systems Technologies*, vol., Technical Digest (CD), San Francisco, California: Optical Society of America 2004, CMH3.

[33] S. G. Porsev and A. Derevianko, *"Hyperfine quenching of the metastable* $^3P_{0,2}$ *states in divalent atoms"*, Phys. Rev. A **69**, 042506, 2004, DOI: 10.1103/PhysRevA.69.042506.

[34] R. Santra, K. V. Christ, and C. H. Greene, *"Properties of metastable alkaline-earth-metal atoms calculated using an accurate effective core potential"*, Phys. Rev. A **69**, 042510, 2004, DOI: 10.1103/PhysRevA.69.042510.

[35] T. Kessler, C. Hagemann, C. Grebing, T. Legero, U. Sterr, F. Riehle, M. J. Martin, L. Chen, and J. Ye, *"A sub-40-mHz-linewidth laser based on a silicon single-crystal optical cavity"*, Nat. Photonics **6**, 687–692, 2012, DOI: 10.1038/nphoton.2012.217.

[36] K. Numata, A. Kemery, and J. Camp, *"Thermal-Noise Limit in the Frequency Stabilization of Lasers with Rigid Cavities"*, Phys. Rev. Lett. **93**, 250602, 2004, DOI: 10.1103/PhysRevLett.93.250602.

[37] M. Notcutt, L.-S. Ma, A. D. Ludlow, S. M. Foreman, J. Ye, and J. L. Hall, *"Contribution of thermal noise to frequency stability of rigid optical cavity via Hertz-linewidth lasers"*, Phys. Rev. A **73**, 031804, 2006, DOI: 10.1103/PhysRevA.73.031804.

[38] J. Chen, *"Active optical clock"*, Chin. Sci. Bull. **54**, 348–352, 2009, DOI: 10.1007/s11434-009-0073-y.

[39] D. Meiser, J. Ye, D. R. Carlson, and M. J. Holland, *"Prospects for a Millihertz-Linewidth Laser"*, Phys. Rev. Lett. **102**, 163601, 2009, DOI: 10.1103/PhysRevLett.102.163601.

[40] M. Gross and S. Haroche, *"Superradiance: An essay on the theory of collective spontaneous emission"*, Phys. Rep. **93**, 301–396, 1982, DOI: 10.1016/0370-1573(82)90102-8.

[41] J. G. Bohnet, Z. Chen, J. M. Weiner, D. Meiser, M. J. Holland, and J. K. Thompson, *"A steady-state superradiant laser with less than one intracavity photon"*, Nature **484**, 78–81, 2012, DOI: 10.1038/nature10920.

[42] M. A. Norcia and J. K. Thompson, *"Cold-Strontium Laser in the Superradiant Crossover Regime"*, Phys. Rev. X **6**, 011025, 2016, DOI: 10.1103/PhysRevX.6.011025.

[43] M. A. Norcia, M. N. Winchester, J. R. K. Cline, and J. K. Thompson, *"Superradiance on the millihertz linewidth strontium clock transition"*, Sci. Adv. **2**, e1601231, 2016, DOI: 10.1126/sciadv.1601231.

[44] R. Sydnow, ed., *Local oscillator induced instabilities in trapped ion frequency standards*, U.S. Naval Observatory, Washington, DC 1987, p. 133.

[45] A. D. Ludlow, M. M. Boyd, J. Ye, E. Peik, and P. O. Schmidt, *"Optical atomic clocks"*, Rev. Mod. Phys. **87**, 637–701, 2015, DOI: 10.1103/RevModPhys.87.637.

[46] S. Kolkowitz, I. Pikovski, N. Langellier, M. D. Lukin, R. L. Walsworth, and J. Ye, *"Gravitational wave detection with optical lattice atomic clocks"*, Phys. Rev. D **94**, 124043, 2016, DOI: 10.1103/PhysRevD.94.124043.

[47] T. M. Fortier *et al.*, *"Precision Atomic Spectroscopy for Improved Limits on Variation of the Fine Structure Constant and Local Position Invariance"*, Phys. Rev. Lett. **98**, 070801, 2007, DOI: 10.1103/PhysRevLett.98.070801.

[48] S. Blatt *et al.*, *"New Limits on Coupling of Fundamental Constants to Gravity Using* ^{87}Sr *Optical Lattice Clocks"*, Phys. Rev. Lett. **100**, 140801, 2008, DOI: 10.1103/PhysRevLett.100.140801.

[49] P. Wcislo, P. Morzynski, M. Bober, A. Cygan, D. Lisak, R. Ciurylo, and M. Zawada, *"Experimental constraint on dark matter detection with optical atomic clocks"*, Nat. Astron. **1**, 0009, 2016, DOI: 10.1038/s41550-016-0009.

[50] P. Wcisło *et al.*, *"New bounds on dark matter coupling from a global network of optical atomic clocks"*, Sci. Adv. **4**, eaau4869, 2018, DOI: 10.1126/sciadv.aau4869.

[51] A. Arvanitaki, P. W. Graham, J. M. Hogan, S. Rajendran, and K. Van Tilburg, *"Search for light scalar dark matter with atomic gravitational wave detectors"*, Phys. Rev. D **97**, 075020, 2018, DOI: 10.1103/PhysRevD.97.075020.

[52] A. Derevianko and M. Pospelov, *"Hunting for topological dark matter with atomic?clocks"*, Nat. Phys. **10**, 933–936, 2014, DOI: 10.1038/nphys3137.

[53] G. Cappellini, M. Mancini, G. Pagano, P. Lombardi, L. Livi, M. Siciliani de Cumis, P. Cancio, M. Pizzocaro, D. Calonico, F. Levi, C. Sias, J. Catani, M. Inguscio, and L. Fallani, *"Direct Observation of Coherent Interorbital Spin-Exchange Dynamics"*, Phys. Rev. Lett. **113**, 120402, 2014, DOI: 10.1103/PhysRevLett.113.120402.

[54] X. Zhang, M. Bishof, S. L. Bromley, C. V. Kraus, M. S. Safronova, P. Zoller, A. M. Rey, and J. Ye, *"Spectroscopic observation of SU(N)-symmetric interactions in Sr orbital magnetism"*, Science **345**, 1467, 2014, DOI: 10.1126/science.1254978.

[55] Wikipedia, *Iran–U.S. RQ-170 incident*, eprint: https://en.wikipedia.org/wiki/Iran%E2%80%93U.S._RQ-170_incident.

[56] M. Huynh and J. Lazio, *"An Overview of the Square Kilometre Array"*, 2013, arXiv: 1311.4288v1.

[57] G. A. Fabrizio, *"High frequency over-the-horizon radar : fundamental principles, signal processing, and practical applications"*, New York: McGraw-Hill Education 2013.

[58] G. Tino and M. Kasevich, *"Atom Interferometry"*, vol., International School of Physics Enrico Fermi Series, IOS Press 2014,

[59] P. W. Graham, J. M. Hogan, M. A. Kasevich, and S. Rajendran, *"New Method for Gravitational Wave Detection with Atomic Sensors"*, Phys. Rev. Lett. **110**, 171102, 2013, DOI: 10.1103/PhysRevLett.110.171102.

[60] Y. Bidel, N. Zahzam, C. Blanchard, A. Bonnin, M. Cadoret, A. Bresson, D. Rouxel, and M. F. Lequentrec-Lalancette, *"Absolute marine gravimetry with matter-wave interferometry"*, Nat. Commun. **9**, 627, 2018, DOI: 10.1038/s41467-018-03040-2.

[61] B. Canuel, F. Leduc, D. Holleville, A. Gauguet, J. Fils, A. Virdis, A. Clairon, N. Dimarcq, C. J. Bordé, A. Landragin, and P. Bouyer, *"Six-Axis Inertial Sensor Using Cold-Atom Interferometry"*, Phys. Rev. Lett. **97**, 010402, 2006, DOI: 10.1103/PhysRevLett.97.010402.

[62] P. Cheiney, L. Fouché, S. Templier, F. Napolitano, B. Battelier, P. Bouyer, and B. Barrett, *"Navigation-Compatible Hybrid Quantum Accelerometer Using a Kalman Filter"*, Phys. Rev. Applied **10**, 034030, 2018, DOI: 10.1103/PhysRevApplied.10.034030.

[63] T. Müller, M. Gilowski, M. Zaiser, P. Berg, C. Schubert, T. Wendrich, W. Ertmer, and E. M. Rasel, *"A compact dual atom interferometer gyroscope based on laser-cooled rubidium"*, Eur. Phys. J. D **53**, 273–281, 2009, DOI: 10.1140/epjd/e2009-00139-0.

[64] J. K. Stockton, K. Takase, and M. A. Kasevich, *"Absolute Geodetic Rotation Measurement Using Atom Interferometry"*, Phys. Rev. Lett. **107**, 133001, 2011, DOI: 10.1103/PhysRevLett.107.133001.

[65] A. Gauguet, B. Canuel, T. Lévèque, W. Chaibi, and A. Landragin, *"Characterization and limits of a cold-atom Sagnac interferometer"*, Phys. Rev. A **80**, 063604, 2009, DOI: 10.1103/PhysRevA.80.063604.

[66] Z.-W. Yao, S.-B. Lu, R.-B. Li, K. Wang, L. Cao, J. Wang, and M.-S. Zhan, *"Continuous Dynamic Rotation Measurements Using a Compact Cold Atom Gyroscope"*, Chin. Phys. Lett. **33**, 083701, 2016, DOI: 10.1088/0256-307x/33/8/083701.

[67] S. Stringari, *"Superfluid Gyroscope with Cold Atomic Gases"*, Phys. Rev. Lett. **86**, 4725–4728, 2001, DOI: 10.1103/PhysRevLett.86.4725.

[68] B. Canuel *et al.*, *"Exploring gravity with the MIGA large scale atom interferometer"*, Sci. Rep. **8**, 14064, 2018, DOI: 10.1038/s41598-018-32165-z.

[69] A. Peters, K. Y. Chung, and S. Chu, *"Measurement of gravitational acceleration by dropping atoms"*, Nature **400**, 849–852, 1999, DOI: 10.1038/23655.

[70] A. Peters, K. Y. Chung, and S. Chu, *"High-precision gravity measurements using atom interferometry"*, Metrologia **38**, 25–61, 2001, DOI: 10.1088/0026-1394/38/1/4.

[71] Z.-K. Hu, B.-L. Sun, X.-C. Duan, M.-K. Zhou, L.-L. Chen, S. Zhan, Q.-Z. Zhang, and J. Luo, *"Demonstration of an ultrahigh-sensitivity atom-interferometry absolute gravimeter"*, Phys. Rev. A **88**, 043610, 2013, DOI: 10.1103/PhysRevA.88.043610.

[72] N. Poli, F.-Y. Wang, M. G. Tarallo, A. Alberti, M. Prevedelli, and G. M. Tino, *"Precision Measurement of Gravity with Cold Atoms in an Optical Lattice and Comparison with a Classical Gravimeter"*, Phys. Rev. Lett. **106**, 038501, 2011, DOI: 10.1103/PhysRevLett.106.038501.

[73] J. B. Fixler, G. T. Foster, J. M. McGuirk, and M. A. Kasevich, *"Atom Interferometer Measurement of the Newtonian Constant of Gravity"*, Science **315**, 74, 2007, DOI: 10.1126/science.1135459.

[74] P. A. Altin, M. T. Johnsson, V. Negnevitsky, G. R. Dennis, R. P. Anderson, J. E. Debs, S. S. Szigeti, K. S. Hardman, S. Bennetts, G. D. McDonald, L. D. Turner, J. D. Close, and N. P. Robins, *"Precision atomic gravimeter based on Bragg diffraction"*, New J. Phys. **15**, 023009, 2013, DOI: 10.1088/1367-2630/15/2/023009.

[75] J. Rudolph, W. Herr, C. Grzeschik, T. Sternke, A. Grote, M. Popp, D. Becker, H. Müntinga, H. Ahlers, A. Peters, C. Lämmerzahl, K. Sengstock, N. Gaaloul, W. Ertmer, and E. M. Rasel, *"A high-flux BEC source for mobile atom interferometers"*, New J. Phys. **17**, 065001, 2015, DOI: 10.1088/1367-2630/17/6/065001.

[76] K. S. Hardman, P. J. Everitt, G. D. McDonald, P. Manju, P. B. Wigley, M. A. Sooriyabandara, C. C. N. Kuhn, J. E. Debs, J. D. Close, and N. P. Robins, *"Simultaneous Precision Gravimetry and Magnetic Gradiometry with a Bose-Einstein Condensate: A High Precision, Quantum Sensor"*, Phys. Rev. Lett. **117**, 138501, 2016, DOI: 10.1103/PhysRevLett.117.138501.

[77] Y. Bidel, O. Carraz, R. Charrière, M. Cadoret, N. Zahzam, and A. Bresson, *"Compact cold atom gravimeter for field applications"*, Appl. Phys. Lett. **102**, 144107, 2013, DOI: 10.1063/1.4801756.

[78] J. M. Hogan, D. M. S. Johnson, S. Dickerson, T. Kovachy, A. Sugarbaker, S.-W. Chiow, P. W. Graham, M. A. Kasevich, B. Saif, S. Rajendran, P. Bouyer, B. D. Seery, L. Feinberg, and R. Keski-Kuha, *"An atomic gravitational wave interferometric sensor in low earth orbit (AGIS-LEO)"*, Gen. Rel. Gravit. **43**, 1953–2009, 2011, DOI: 10.1007/s10714-011-1182-x.

[79] S. Dimopoulos, P. W. Graham, J. M. Hogan, M. A. Kasevich, and S. Rajendran, *"Atomic gravitational wave interferometric sensor"*, Phys. Rev. D **78**, 122002, 2008, DOI: 10.1103/PhysRevD.78.122002.

[80] I. Dutta, D. Savoie, B. Fang, B. Venon, C. L. Garrido Alzar, R. Geiger, and A. Landragin, *"Continuous Cold-Atom Inertial Sensor with* 1 nrad/sec *Rotation Stability"*, Phys. Rev. Lett. **116**, 183003, 2016, DOI: 10.1103/PhysRevLett.116.183003.

[81] J. E. Debs, P. A. Altin, T. H. Barter, D. Döring, G. R. Dennis, G. McDonald, R. P. Anderson, J. D. Close, and N. P. Robins, *"Cold-atom gravimetry with a Bose-Einstein condensate"*, Phys. Rev. A **84**, 033610, 2011, DOI: 10.1103/PhysRevA.84.033610.

[82] S. S. Szigeti, J. E. Debs, J. J. Hope, N. P. Robins, and J. D. Close, *"Why momentum width matters for atom interferometry with Bragg pulses"*, New J. Phys. **14**, 023009, 2012, DOI: 10.1088/1367-2630/14/2/023009.

[83] K. S. Hardman, C. C. N. Kuhn, G. D. McDonald, J. E. Debs, S. Bennetts, J. D. Close, and N. P. Robins, *"Role of source coherence in atom interferometry"*, Phys. Rev. A **89**, 023626, 2014, DOI: 10.1103/PhysRevA.89.023626.

[84] R. Karcher, A. Imanaliev, S. Merlet, and F. P. D. Santos, *"Improving the accuracy of atom interferometers with ultracold sources"*, New J. Phys. **20**, 113041, 2018, DOI: 10.1088/1367-2630/aaf07d.

[85] H. A. Haus, *"The noise figure of optical amplifiers"*, IEEE Photon. Technol. Lett. **10**, 1602–1604, 1998, DOI: 10.1109/68.726763.

[86] M. T. Johnsson and S. A. Haine, *"Generating Quadrature Squeezing in an Atom Laser through Self-Interaction"*, Phys. Rev. Lett. **99**, 010401, 2007, DOI: 10.1103/PhysRevLett.99.010401.

[87] B. Megyeri, G. Harvie, A. Lampis, and J. Goldwin, *"Directional Bistability and Nonreciprocal Lasing with Cold Atoms in a Ring Cavity"*, Phys. Rev. Lett. **121**, 163603, 2018, DOI: 10.1103/PhysRevLett.121.163603.

[88] J. M. Weiner, K. C. Cox, J. G. Bohnet, and J. K. Thompson, *"Phase synchronization inside a superradiant laser"*, Phys. Rev. A **95**, 033808, 2017, DOI: 10.1103/PhysRevA.95.033808.

[89] M. Xu, D. A. Tieri, E. C. Fine, J. K. Thompson, and M. J. Holland, *"Synchronization of Two Ensembles of Atoms"*, Phys. Rev. Lett. **113**, 154101, 2014, DOI: 10.1103/PhysRevLett.113.154101.

[90] J. Kim, D. Yang, S.-h. Oh, and K. An, *"Coherent single-atom superradiance"*, Science **359**, 662, 2018, DOI: 10.1126/science.aar2179.

[91] M. A. Norcia, R. J. Lewis-Swan, J. R. K. Cline, B. Zhu, A. M. Rey, and J. K. Thompson, *"Cavity-mediated collective spin-exchange interactions in a strontium superradiant laser"*, Science **361**, 259, 2018, DOI: 10.1126/science.aar3102.

[92] B. T. Seaman, M. Krämer, D. Z. Anderson, and M. J. Holland, *"Atomtronics: Ultracold-atom analogs of electronic devices"*, Phys. Rev. A **75**, 023615, 2007, DOI: 10.1103/PhysRevA.75.023615.

[93] R. A. Pepino, J. Cooper, D. Z. Anderson, and M. J. Holland, *"Atomtronic Circuits of Diodes and Transistors"*, Phys. Rev. Lett. **103**, 140405, 2009, DOI: 10.1103/PhysRevLett.103.140405.

[94] C.-C. Chien, S. Peotta, and M. Di Ventra, *"Quantum transport in ultracold atoms"*, Nat. Phys. **11**, 998–1004, 2015, DOI: 10.1038/nphys3531.

[95] L. D. Carr, D. DeMille, R. V. Krems, and J. Ye, *"Cold and ultracold molecules: science, technology and applications"*, New J. Phys. **11**, 055049, 2009, DOI: 10.1088/1367-2630/11/5/055049.

[96] R. V. Krems, *"Cold controlled chemistry"*, Phys. Chem. Chem. Phys. **10**, 4079–4092, 2008, DOI: 10.1039/B802322K.

[97] N. R. Hutzler, H.-I. Lu, and J. M. Doyle, *"The Buffer Gas Beam: An Intense, Cold, and Slow Source for Atoms and Molecules"*, Chem. Rev. **112**, 4803–4827, 2012, DOI: 10.1021/cr200362u.

[98] J. Lim, M. D. Frye, J. M. Hutson, and M. R. Tarbutt, *"Modeling sympathetic cooling of molecules by ultracold atoms"*, Phys. Rev. A **92**, 053419, 2015, DOI: 10.1103/PhysRevA.92.053419.

[99] E. B. Norrgard, D. J. McCarron, M. H. Steinecker, M. R. Tarbutt, and D. DeMille, *"Submillikelvin Dipolar Molecules in a Radio-Frequency Magneto-Optical Trap"*, Phys. Rev. Lett. **116**, 063004, 2016, DOI: 10.1103/PhysRevLett.116.063004.

[100] E. B. Norrgard, *"Magneto-optical trapping of diatomic molecules"*, PhD thesis, Yale University, USA, 2016.

[101] J. F. Barry, *"Laser cooling and slowing of a diatomic molecule"*, PhD thesis, Yale University, USA, 2013.

[102] M. R. Tarbutt, B. E. Sauer, J. J. Hudson, and E. A. Hinds, *"Design for a fountain of YbF molecules to measure the electron's electric dipole moment"*, New J. Phys. **15**, 053034, 2013, DOI: 10.1088/1367-2630/15/5/053034.

[103] L. R. Hunter, S. K. Peck, A. S. Greenspon, S. S. Alam, and D. DeMille, *"Prospects for laser cooling TlF"*, Phys. Rev. A **85**, 012511, 2012, DOI: 10.1103/PhysRevA.85.012511.

[104] K.-K. Ni, S. Ospelkaus, D. Wang, G. Quéméner, B. Neyenhuis, M. H. G. de Miranda, J. L. Bohn, J. Ye, and D. S. Jin, *"Dipolar collisions of polar molecules in the quantum regime"*, Nature **464**, 1324–1328, 2010, DOI: 10.1038/nature08953.

[105] A. Micheli, G. K. Brennen, and P Zoller, *"A toolbox for lattice-spin models with polar molecules"*, Nat. Phys. **2**, 341, 2006, DOI: 10.1038/nphys287.

[106] S. Stellmer, M. K. Tey, B. Huang, R. Grimm, and F. Schreck, *"Bose-Einstein Condensation of Strontium"*, Phys. Rev. Lett. **103**, 200401, 2009, DOI: 10.1103/PhysRevLett.103.200401.

[107] S. Stellmer, *"Degenerate quantum gases of strontium"*, PhD thesis, Institute of Experimental Physics, University of Innsbruck, Austria, 2013.

[108] I. F. Silvera and J. T. M. Walraven, *"Stabilization of Atomic Hydrogen at Low Temperature"*, Phys. Rev. Lett. **44**, 164–168, 1980, DOI: 10.1103/PhysRevLett.44.164.

[109] I. D. Setija, H. G. C. Werij, O. J. Luiten, M. W. Reynolds, T. W. Hijmans, and J. T. M. Walraven, *"Optical cooling of atomic hydrogen in a magnetic trap"*, Phys. Rev. Lett. **70**, 2257–2260, 1993, DOI: 10.1103/PhysRevLett.70.2257.

[110] T. W. Hijmans, Y. Kagan, G. V. Shlyapnikov, and J. T. M. Walraven, *"Bose condensation and relaxation explosion in magnetically trapped atomic hydrogen"*, Phys. Rev. B **48**, 12886, 1993, DOI: 10.1103/PhysRevB.48.12886.

[111] N. Masuhara, J. M. Doyle, J. C. Sandberg, D. Kleppner, T. J. Greytak, H. F. Hess, and G. P. Kochanski, *"Evaporative Cooling of Spin-Polarized Atomic Hydrogen"*, Phys. Rev. Lett. **61**, 935, 1988, DOI: 10.1103/physrevlett.61.935.

[112] D. G. Fried, T. C. Killian, L. Willmann, D. Landhuis, S. C. Moss, D. Kleppner, and T. J. Greytak, *"Bose-Einstein Condensation of Atomic Hydrogen"*, Phys. Rev. Lett. **81**, 3811–3814, 1998, DOI: 10.1103/PhysRevLett.81.3811.

[113] W. Ketterle, K. B. Davis, M. A. Joffe, A. Martin, and D. E. Pritchard, *"High densities of cold atoms in a dark spontaneous-force optical trap"*, Phys. Rev. Lett. **70**, 2253–2256, 1993, DOI: 10.1103/PhysRevLett.70.2253.

[114] S. Chu, L. Hollberg, J. E. Bjorkholm, A. Cable, and A. Ashkin, *"Three-dimensional viscous confinement and cooling of atoms by resonance radiation pressure"*, Phys. Rev. Lett. **55**, 48–51, 1985, DOI: 10.1103/PhysRevLett.55.48.

[115] V. S. Bagnato, G. P. Lafyatis, A. G. Martin, E. L. Raab, R. N. Ahmad-Bitar, and D. E. Pritchard, *"Continuous Stopping and Trapping of Neutral Atoms"*, Phys. Rev. Lett. **58**, 2194–2197, 1987, DOI: 10.1103/PhysRevLett.58.2194.

[116] K. Dieckmann, R. J. C. Spreeuw, M. Weidemüller, and J. T. M. Walraven, *"Two-dimensional magneto-optical trap as a source of slow atoms"*, Phys. Rev. A **58**, 3891–3895, 1998, DOI: 10.1103/PhysRevA.58.3891.

[117] Z. T. Lu, K. L. Corwin, M. J. Renn, M. H. Anderson, E. A. Cornell, and C. E. Wieman, *"Low-Velocity Intense Source of Atoms from a Magneto-optical Trap"*, Phys. Rev. Lett. **77**, 3331–3334, 1996, DOI: 10.1103/PhysRevLett.77.3331.

[118] W. D. Phillips and H. Metcalf, *"Laser Deceleration of an Atomic Beam"*, Phys. Rev. Lett. **48**, 596–599, 1982, DOI: 10.1103/PhysRevLett.48.596.

[119] D. G. Fried, *"Bose-Einstein Condensation of Atomic Hydrogen"*, PhD thesis, Massachusett Institute of Technology, 1999.

[120] K. M. R. van der Stam, E. D. van Ooijen, R. Meppelink, J. M. Vogels, and P. van der Straten, *"Large atom number Bose-Einstein condensate of sodium"*, Rev. Sci. Instrum. **78**, 013102, 2007, DOI: 10.1063/1.2424439.

[121] E. W. Streed, A. P. Chikkatur, T. L. Gustavson, M. Boyd, Y. Torii, D. Schneble, G. K. Campbell, D. E. Pritchard, and W. Ketterle, *"Large atom number Bose-Einstein condensate machines"*, Rev. Sci. Instrum. **77**, 023106, 2006, DOI: 10.1063/1.2163977.

[122] K. Dieckmann, *"Bose-Einstein Condensation with High Atom Number in a Deep Magnetic Trap"*, PhD thesis, University of Amsterdam, 2001.

[123] P. A. Altin, N. P. Robins, D. Döring, J. E. Debs, R. Poldy, C. Figl, and J. D. Close, *"^{85}Rb tunable-interaction Bose–Einstein condensate machine"*, Rev. Sci. Instrum. **81**, 063103, 2010, DOI: 10.1063/1.3430538.

[124] E. A. S. Daniel M. Farkas and J. Ramirez-Serrano, *"Production of Rubidium Bose-Einstein Condensates at a 1 Hz Rate"*, 2014, arXiv: 1403.4641.

[125] A. S. Tychkov, T. Jeltes, J. M. McNamara, P. J. J. Tol, N. Herschbach, W. Hogervorst, and W. Vassen, *"Metastable helium Bose-Einstein condensate with a large number of atoms"*, Phys. Rev. A **73**, 031603, 2006, DOI: 10.1103/PhysRevA.73.031603.

[126] F. Pereira Dos Santos, J. Léonard, J. Wang, C. J. Barrelet, F. Perales, E. Rasel, C. S. Unnikrishnan, M. Leduc, and C. Cohen-Tannoudji, *"Bose-Einstein Condensation of Metastable Helium"*, Phys. Rev. Lett. **86**, 3459–3462, 2001, DOI: 10.1103/PhysRevLett.86.3459.

[127] A. Robert, O. Sirjean, A. Browaeys, J. Poupard, S. Nowak, D. Boiron, C. I. Westbrook, and A. Aspect, *"A Bose-Einstein Condensate of Metastable Atoms"*, Science **292**, 461–464, 2001, DOI: 10.1126/science.1060622.

[128] S. Stellmer, R. Grimm, and F. Schreck, *"Production of quantum-degenerate strontium gases"*, Phys. Rev. A **87**, 013611, 2013, DOI: 10.1103/PhysRevA.87.013611.

[129] Y. N. Martinez de Escobar, P. G. Mickelson, M. Yan, B. J. DeSalvo, S. B. Nagel, and T. C. Killian, *"Bose-Einstein Condensation of ^{84}Sr"*, Phys. Rev. Lett. **103**, 200402, 2009, DOI: 10.1103/PhysRevLett.103.200402.

[130] R. L. D. Campbell, R. P. Smith, N. Tammuz, S. Beattie, S. Moulder, and Z. Hadzibabic, *"Efficient production of large ^{39}K Bose-Einstein condensates"*, Phys. Rev. A **82**, 063611, 2010, DOI: 10.1103/PhysRevA.82.063611.

[131] G. Roati, M. Zaccanti, C. D'Errico, J. Catani, M. Modugno, A. Simoni, M. Inguscio, and G. Modugno, *"^{39}K Bose-Einstein Condensate with Tunable Interactions"*, Phys. Rev. Lett. **99**, 010403, 2007, DOI: 10.1103/PhysRevLett.99.010403.

[132] S. Stellmer, M. K. Tey, R. Grimm, and F. Schreck, *"Bose-Einstein condensation of ^{86}Sr"*, Phys. Rev. A **82**, 041602, 2010, DOI: 10.1103/PhysRevA.82.041602.

[133] S. Kraft, F. Vogt, O. Appel, F. Riehle, and U. Sterr, *"Bose-Einstein Condensation of Alkaline Earth Atoms: ^{40}Ca"*, Phys. Rev. Lett. **103**, 130401, 2009, DOI: 10.1103/PhysRevLett.103.130401.

[134] S. Dörscher, A. Thobe, B. Hundt, A. Kochanke, R. L. Targat, P. Windpassinger, C. Becker, and K. Sengstock, *"Creation of quantum-degenerate gases of ytterbium in a compact 2D-/3D-magneto-optical trap setup"*, Rev. Sci. Instrum. **84**, 043109, 2013, DOI: 10.1063/1.4802682.

[135] Y. Takasu, K. Maki, K. Komori, T. Takano, K. Honda, M. Kumakura, T. Yabuzaki, and Y. Takahashi, *"Spin-Singlet Bose-Einstein Condensation of Two-Electron Atoms"*, Phys. Rev. Lett. **91**, 040404, 2003, DOI: 10.1103/PhysRevLett.91.040404.

[136] K. Aikawa, A. Frisch, M. Mark, S. Baier, A. Rietzler, R. Grimm, and F. Ferlaino, *"Bose-Einstein Condensation of Erbium"*, Phys. Rev. Lett. **108**, 210401, 2012, DOI: 10.1103/PhysRevLett.108.210401.

[137] J. Ulitzsch, D. Babik, R. Roell, and M. Weitz, *"Bose-Einstein condensation of erbium atoms in a quasielectrostatic optical dipole trap"*, Phys. Rev. A **95**, 043614, 2017, DOI: 10.1103/PhysRevA.95.043614.

[138] P. G. Mickelson, Y. N. Martinez de Escobar, M. Yan, B. J. DeSalvo, and T. C. Killian, *"Bose-Einstein condensation of* ^{88}Sr *through sympathetic cooling with* ^{87}Sr*"*, Phys. Rev. A **81**, 051601, 2010, DOI: 10.1103/PhysRevA.81.051601.

[139] A. Griesmaier, J. Werner, S. Hensler, J. Stuhler, and T. Pfau, *"Bose-Einstein Condensation of Chromium"*, Phys. Rev. Lett. **94**, 160401, 2005, DOI: 10.1103/PhysRevLett.94.160401.

[140] S. B. Papp, *"Experiments with a two-species Bose-Einstein condensate utilizing widely tunable interparticle interactions"*, PhD thesis, University of Colorado, USA, 2007.

[141] T. Weber, J. Herbig, M. Mark, H.-C. Nägerl, and R. Grimm, *"Bose-Einstein Condensation of Cesium"*, Science **299**, 232–235, 2003, DOI: 10.1126/science.1079699.

[142] T. Fukuhara, S. Sugawa, and Y. Takahashi, *"Bose-Einstein condensation of an ytterbium isotope"*, Phys. Rev. A **76**, 051604, 2007, DOI: 10.1103/PhysRevA.76.051604.

[143] M. Lu, N. Q. Burdick, S. H. Youn, and B. L. Lev, *"Strongly Dipolar Bose-Einstein Condensate of Dysprosium"*, Phys. Rev. Lett. **107**, 190401, 2011, DOI: 10.1103/PhysRevLett.107.190401.

[144] G. Modugno, G. Ferrari, G. Roati, R. J. Brecha, A. Simoni, and M. Inguscio, *"Bose-Einstein Condensation of Potassium Atoms by Sympathetic Cooling"*, Science **294**, 1320–1322, 2001, DOI: 10.1126/science.1066687.

[145] C. C. Bradley, C. A. Sackett, and R. G. Hulet, *"Bose-Einstein Condensation of Lithium: Observation of Limited Condensate Number"*, Phys. Rev. Lett. **78**, 985–989, 1997, DOI: 10.1103/PhysRevLett.78.985.

[146] C. C. Bradley, C. A. Sackett, J. J. Tollett, and R. G. Hulet, *"Evidence of Bose-Einstein Condensation in an Atomic Gas with Attractive Interactions"*, Phys. Rev. Lett. **75**, 1687–1690, 1995, DOI: 10.1103/PhysRevLett.75.1687.

[147] A. B. Deb, T. McKellar, and N. Kjærgaard, *"Optical runaway evaporation for the parallel production of multiple Bose-Einstein condensates"*, Phys. Rev. A **90**, 051401, 2014, DOI: 10.1103/PhysRevA.90.051401.

[148] J.-F. Riou, W. Guerin, Y. L. Coq, M. Fauquembergue, V. Josse, P. Bouyer, and A. Aspect, *"Beam Quality of a Nonideal Atom Laser"*, Phys. Rev. Lett. **96**, 070404, 2006, DOI: 10.1103/PhysRevLett.96.070404.

[149] Y. Le Coq, J. H. Thywissen, S. A. Rangwala, F. Gerbier, S. Richard, G. Delannoy, P. Bouyer, and A. Aspect, *"Atom Laser Divergence"*, Phys. Rev. Lett. **87**, 170403, 2001, DOI: 10.1103/PhysRevLett.87.170403.

[150] E. W. Hagley, L. Deng, M. Kozuma, J. Wen, K. Helmerson, S. L. Rolston, and W. D. Phillips, *"A Well-Collimated Quasi-Continuous Atom Laser"*, Science **283**, 1706–1709, 1999, DOI: 10.1126/science.283.5408.1706.

[151] N. P. Robins, C. Figl, S. A. Haine, A. K. Morrison, M. Jeppesen, J. J. Hope, and J. D. Close, *"Achieving Peak Brightness in an Atom Laser"*, Phys. Rev. Lett. **96**, 140403, 2006, DOI: 10.1103/PhysRevLett.96.140403.

[152] J. E. Debs, D. Döring, P. A. Altin, C. Figl, J. Dugué, M. Jeppesen, J. T. Schultz, N. P. Robins, and J. D. Close, *"Experimental comparison of Raman and rf outcouplers for high-flux atom lasers"*, Phys. Rev. A **81**, 013618, 2010, DOI: 10.1103/PhysRevA.81.013618.

[153] M. Jeppesen, J. Dugué, G. R. Dennis, M. T. Johnsson, C. Figl, N. P. Robins, and J. D. Close, *"Approaching the Heisenberg limit in an atom laser"*, Phys. Rev. A **77**, 063618, 2008, DOI: 10.1103/PhysRevA.77.063618.

[154] G. D. McDonald, C. C. N. Kuhn, S. Bennetts, J. E. Debs, K. S. Hardman, M. Johnsson, J. D. Close, and N. P. Robins, *"80ℏk momentum separation with Bloch oscillations in an optically guided atom interferometer"*, Phys. Rev. A **88**, 053620, 2013, DOI: 10.1103/PhysRevA.88.053620.

[155] H. Müller, S.-w. Chiow, Q. Long, S. Herrmann, and S. Chu, *"Atom Interferometry with up to 24-Photon-Momentum-Transfer Beam Splitters"*, Phys. Rev. Lett. **100**, 180405, 2008, DOI: 10.1103/PhysRevLett.100.180405.

[156] S.-w. Chiow, T. Kovachy, H.-C. Chien, and M. A. Kasevich, *"102ℏk Large Area Atom Interferometers"*, Phys. Rev. Lett. **107**, 130403, 2011, DOI: 10.1103/PhysRevLett.107.130403.

[157] B. P. Anderson and M. A. Kasevich, *"Macroscopic Quantum Interference from Atomic Tunnel Arrays"*, Science **282**, 1686–1689, 1998, DOI: 10.1126/science.282.5394.1686.

[158] S. Krinner, D. Stadler, D. Husmann, J.-P. Brantut, and T. Esslinger, *"Observation of quantized conductance in neutral matter"*, Nature **517**, 64–67, 2015, DOI: 10.1038/nature14049.

[159] S. Inouye, A. P. Chikkatur, D. M. Stamper-Kurn, J. Stenger, D. E. Pritchard, and W. Ketterle, *"Superradiant Rayleigh Scattering from a Bose-Einstein Condensate"*, Science **285**, 571–574, 1999, DOI: 10.1126/science.285.5427.571.

[160] S. Inouye, T. Pfau, S. Gupta, A. P. Chikkatur, A. Görlitz, D. E. Pritchard, and W. Ketterle, *"Phase-coherent amplification of atomic matter waves"*, Nature **402**, 641–644, 1999, DOI: 10.1038/45194.

[161] D. Schneble, Y. Torii, M. Boyd, E. W. Streed, D. E. Pritchard, and W. Ketterle, *"The Onset of Matter-Wave Amplification in a Superradiant Bose-Einstein Condensate"*, Science **300**, 475–478, 2003, DOI: 10.1126/science.1083171.

[162] O. Zobay and G. M. Nikolopoulos, *"Spatial effects in superradiant Rayleigh scattering from Bose-Einstein condensates"*, Phys. Rev. A **73**, 013620, 2006, DOI: 10.1103/PhysRevA.73.013620.

[163] M. Kozuma, Y. Suzuki, Y. Torii, T. Sugiura, T. Kuga, E. W. Hagley, and L. Deng, *"Phase-Coherent Amplification of Matter Waves"*, Science **286**, 2309–2312, 1999, DOI: 10.1126/science.286.5448.2309.

[164] D. Schneble, G. K. Campbell, E. W. Streed, M. Boyd, D. E. Pritchard, and W. Ketterle, *"Raman amplification of matter waves"*, Phys. Rev. A **69**, 041601, 2004, DOI: 10.1103/PhysRevA.69.041601.

[165] Y. Yoshikawa, T. Sugiura, Y. Torii, and T. Kuga, *"Observation of superradiant Raman scattering in a Bose-Einstein condensate"*, Phys. Rev. A **69**, 041603, 2004, DOI: 10.1103/PhysRevA.69.041603.

[166] G. M. Moy, J. J. Hope, and C. M. Savage, *"Atom laser based on Raman transitions"*, Phys. Rev. A **55**, 3631–3638, 1997, DOI: 10.1103/PhysRevA.55.3631.

[167] P. D. Drummond, A. Eleftheriou, K. Huang, and K. V. Kheruntsyan, *"Theory of a mode-locked atom laser with toroidal geometry"*, Phys. Rev. A **63**, 053602, 2001, DOI: 10.1103/PhysRevA.63.053602.

[168] T. Erdogan, *"Fiber grating spectra"*, J. Light. Technol. **15**, 1277–1294, 1997, DOI: 10.1109/50.618322.

[169] C. M. Fabre, P. Cheiney, G. L. Gattobigio, F. Vermersch, S. Faure, R. Mathevet, T. Lahaye, and D. Guéry-Odelin, *"Realization of a Distributed Bragg Reflector for Propagating Guided Matter Waves"*, Phys. Rev. Lett. **107**, 230401, 2011, DOI: 10.1103/PhysRevLett.107.230401.

[170] T. Lahaye, J. M. Vogels, K. J. Günter, Z. Wang, J. Dalibard, and D. Guéry-Odelin, *"Realization of a Magnetically Guided Atomic Beam in the Collisional Regime"*, Phys. Rev. Lett. **93**, 093003, 2004, DOI: 10.1103/PhysRevLett.93.093003.

[171] P. Cren, C. F. Roos, A. Aclan, J. Dalibard, and D. Guéry-Odelin, *"Loading of a cold atomic beam into a magnetic guide"*, Eur. Phys. J. D **20**, 107–116, 2002, DOI: 10.1140/epjd/e2002-00106-3.

[172] T. Lahaye, Z. Wang, G. Reinaudi, S. P. Rath, J. Dalibard, and D. Guéry-Odelin, *"Evaporative cooling of a guided rubidium atomic beam"*, Phys. Rev. A **72**, 033411, 2005, DOI: 10.1103/PhysRevA.72.033411.

[173] C. F. Roos, P. Cren, D. Guéry-Odelin, and J. Dalibard, *"Continuous loading of a non-dissipative atom trap"*, EPL **61**, 187, 2003, DOI: 10.1209/epl/i2003-00211-3.

[174] G. Reinaudi, T. Lahaye, A. Couvert, Z. Wang, and D. Guéry-Odelin, *"Evaporation of an atomic beam on a material surface"*, Phys. Rev. A **73**, 035402, 2006, DOI: 10.1103/PhysRevA.73.035402.

[175] C. F. Roos, P. Cren, J. Dalibard, and D. Guéry-Odelin, *"A Source of Cold Atoms for a Continuously Loaded Magnetic Guide"*, Phys. Scr. **T105**, 19, 2003, DOI: 10.1238/Physica.Topical.105a00019.

[176] T. Lahaye and D. Guéry-Odelin, *"Kinetics of the evaporative cooling of an atomic beam"*, Phys. Rev. A **73**, 063622, 2006, DOI: 10.1103/PhysRevA.73.063622.

[177] T. Lahaye and D. Guéry-Odelin, *"Discrete-step evaporation of an atomic beam"*, Eur. Phys. J. D **33**, 67–75, 2005, DOI: 10.1140/epjd/e2005-00007-y.

[178] C. F. Roos, P. Cren, T. Lahaye, J. Dalibard, and D. Guéry-Odelin, *"Injection of a cold atomic beam into a magnetic guide"*, 2003, arXiv: cond-mat/0212147.

[179] G. Reinaudi, Z. Wang, A. Couvert, T. Lahaye, and D. Guéry-Odelin, *"A moving magnetic mirror to slow down a bunch of atoms"*, Eur. Phys. J. D **40**, 405–410, 2006, DOI: 10.1140/epjd/e2006-00244-6.

[180] T. Lahaye, P. Cren, C. Roos, and D. Guéry-Odelin, *"Propagation of guided cold atoms"*, Commun. Nonlinear Sci. Numer. Simul. **8**, 315–328, 2003, DOI: 10.1016/s1007-5704(03)00032-7.

[181] F. Vermersch, C. M. Fabre, P. Cheiney, G. L. Gattobigio, R. Mathevet, and D. Guéry-Odelin, *"Guided-atom laser: Transverse mode quality and longitudinal momentum distribution"*, Phys. Rev. A **84**, 043618, 2011, DOI: 10.1103/PhysRevA.84.043618.

[182] G. L. Gattobigio, A. Couvert, M. Jeppesen, R. Mathevet, and D. Guéry-Odelin, *"Multimode-to-monomode guided-atom lasers: An entropic analysis"*, Phys. Rev. A **80**, 041605, 2009, DOI: 10.1103/PhysRevA.80.041605.

[183] A. Couvert, T. Kawalec, G. Reinaudi, and D. Guéry-Odelin, *"Optimal transport of ultracold atoms in the non-adiabatic regime"*, EPL **83**, 13001, 2008, DOI: 10.1209/0295-5075/83/13001.

[184] L. Kindt, *"Shock wave loading of a magnetic guide"*, PhD thesis, University of Utrecht, The Netherlands, 2011.

[185] E. P. Power, L. George, B. Vanderelzen, P. Herrera-Fierro, R. Murphy, S. M. Yalisove, and G. Raithel, *"Design and Fabrication of a Chip-based Continuous-wave Atom Laser"*, 2012, arXiv: 1202.0479.

[186] B. K. Teo and G. Raithel, *"Loading mechanism for atomic guides"*, Phys. Rev. A **63**, 031402, 2001, DOI: 10.1103/PhysRevA.63.031402.

[187] S. E. Olson, R. R. Mhaskar, and G. Raithel, *"Continuous propagation and energy filtering of a cold atomic beam in a long high-gradient magnetic atom guide"*, Phys. Rev. A **73**, 033622, 2006, DOI: 10.1103/PhysRevA.73.033622.

[188] S. E. Olson, G. Raithel, and A. J. Christlieb, *"Pressure-driven evaporative cooling in atom guides"*, Phys. Rev. A **90**, 043612, 2014, DOI: 10.1103/PhysRevA.90.043612.

[189] J. Williams, R. Walser, C. Wieman, J. Cooper, and M. Holland, *"Achieving steady-state Bose-Einstein condensation"*, Phys. Rev. A **57**, 2030–2036, 1998, DOI: 10.1103/PhysRevA.57.2030.

[190] M. A. Macovei and J. Evers, *"Loading atom lasers by collectivity-enhanced optical pumping"*, Phys. Rev. A **81**, 013626, 2010, DOI: 10.1103/PhysRevA.81.013626.

[191] S. Bhongale and M. Holland, *"Loading a continuous-wave atom laser by optical pumping techniques"*, Phys. Rev. A **62**, 043604, 2000, DOI: 10.1103/PhysRevA.62.043604.

[192] S. Stellmer, B. Pasquiou, R. Grimm, and F. Schreck, *"Laser Cooling to Quantum Degeneracy"*, Phys. Rev. Lett. **110**, 263003, 2013, DOI: 10.1103/PhysRevLett.110.263003.

[193] M. Kasevich and S. Chu, *"Laser cooling below a photon recoil with three-level atoms"*, Phys. Rev. Lett. **69**, 1741–1744, 1992, DOI: 10.1103/PhysRevLett.69.1741.

[194] N. Davidson, H. J. Lee, M. Kasevich, and S. Chu, *"Raman cooling of atoms in two and three dimensions"*, Phys. Rev. Lett. **72**, 3158–3161, 1994, DOI: 10.1103/PhysRevLett.72.3158.

[195] A. Aspect, E. Arimondo, R. Kaiser, N. Vansteenkiste, and C. Cohen-Tannoudji, *"Laser Cooling below the One-Photon Recoil Energy by Velocity-Selective Coherent Population Trapping"*, Phys. Rev. Lett. **61**, 826–829, 1988, DOI: 10.1103/PhysRevLett.61.826.

[196] V. Vuletić, C. Chin, A. J. Kerman, and S. Chu, *"Degenerate Raman Sideband Cooling of Trapped Cesium Atoms at Very High Atomic Densities"*, Phys. Rev. Lett. **81**, 5768–5771, 1998, DOI: 10.1103/physrevlett.81.5768.

[197] A. J. Kerman, V. Vuletić, C. Chin, and S. Chu, *"Beyond Optical Molasses: 3D Raman Sideband Cooling of Atomic Cesium to High Phase-Space Density"*, Phys. Rev. Lett. **84**, 439–442, 2000, DOI: 10.1103/PhysRevLett.84.439.

[198] D.-J. Han, S. Wolf, S. Oliver, C. McCormick, M. T. DePue, and D. S. Weiss, *"3D Raman Sideband Cooling of Cesium Atoms at High Density"*, Phys. Rev. Lett. **85**, 724–727, 2000, DOI: 10.1103/PhysRevLett.85.724.

[199] S. L. Winoto, M. T. DePue, N. E. Bramall, and D. S. Weiss, *"Laser cooling at high density in deep far-detuned optical lattices"*, Phys. Rev. A **59**, R19–R22, 1999, DOI: 10.1103/PhysRevA.59.R19.

[200] S. E. Hamann, D. L. Haycock, G. Klose, P. H. Pax, I. H. Deutsch, and P. S. Jessen, *"Resolved-Sideband Raman Cooling to the Ground State of an Optical Lattice"*, Phys. Rev. Lett. **80**, 4149–4152, 1998, DOI: 10.1103/PhysRevLett.80.4149.

[201] T. Ido, Y. Isoya, and H. Katori, *"Optical-dipole trapping of Sr atoms at a high phase-space density"*, Phys. Rev. A **61**, 061403, 2000, DOI: 10.1103/PhysRevA.61.061403.

[202] J. Hu, A. Urvoy, Z. Vendeiro, V. Crépel, W. Chen, and V. Vuletić, *"Creation of a Bose-condensed gas of ^{87}Rb by laser cooling"*, Science **358**, 1078–1080, 2017, DOI: 10.1126/science.aan5614.

[203] M. Falkenau, V. V. Volchkov, J. Rührig, A. Griesmaier, and T. Pfau, *"Continuous Loading of a Conservative Potential Trap from an Atomic Beam"*, Phys. Rev. Lett. **106**, 163002, 2011, DOI: 10.1103/PhysRevLett.106.163002.

[204] M. Falkenau, V. V. Volchkov, J. Rührig, H. Gorniaczyk, and A. Griesmaier, *"Evaporation-limited loading of an atomic trap"*, Phys. Rev. A **85**, 023412, 2012, DOI: 10.1103/PhysRevA.85.023412.

[205] V. V. Volchkov, J Rührig, T Pfau, and A Griesmaier, *"Sisyphus cooling in a continuously loaded trap"*, New J. Phys. **15**, 093012, 2013, DOI: 10.1088/1367-2630/15/9/093012.

[206] J. Rührig, T. Bäuerle, A. Griesmaier, and T. Pfau, *"High efficiency demagnetization cooling by suppression of light-assisted collisions"*, Opt. Express **23**, 5596–5606, 2015, DOI: 10.1364/OE.23.005596.

[207] S. Bennetts, C.-C. Chen, B. Pasquiou, and F. Schreck, *"Steady-State Magneto-Optical Trap with 100-Fold Improved Phase-Space Density"*, Phys. Rev. Lett. **119**, 223202, 2017, DOI: 10.1103/PhysRevLett.119.223202.

[208] N. P. Robins, C. Figl, M. Jeppesen, G. R. Dennis, and J. D. Close, *"A pumped atom laser"*, Nat. Phys. **4**, 731–736, 2008, DOI: 10.1038/nphys1027.

[209] L. Santos, F. Floegel, T. Pfau, and M. Lewenstein, *"Continuous optical loading of a Bose-Einstein condensate"*, Phys. Rev. A **63**, 063408, 2001, DOI: 10.1103/PhysRevA.63.063408.

[210] J. I. Cirac and M. Lewenstein, *"Pumping atoms into a Bose-Einstein condensate in the boson-accumulation regime"*, Phys. Rev. A **53**, 2466–2476, 1996, DOI: 10.1103/PhysRevA.53.2466.

[211] T. Salzburger and H. Ritsch, *"Twin stimulated amplification of light and matter waves in an atom-photon pair laser"*, Phys. Rev. A **77**, 063620, 2008, DOI: 10.1103/PhysRevA.77.063620.

[212] L. Deng, E. W. Hagley, J. Wen, M. Trippenbach, Y. Band, P. S. Julienne, J. E. Simsarian, K. Helmerson, S. L. Rolston, and W. D. Phillips, *"Four-wave mixing with matter waves"*, Nature **398**, 218–220, 1999, DOI: 10.1038/18395.

[213] A. C. Doherty and K. Jacobs, *"Feedback control of quantum systems using continuous state estimation"*, Phys. Rev. A **60**, 2700–2711, 1999, DOI: 10.1103/PhysRevA.60.2700.

[214] S. S. Szigeti, M. R. Hush, A. R. R. Carvalho, and J. J. Hope, *"Feedback control of an interacting Bose-Einstein condensate using phase-contrast imaging"*, Phys. Rev. A **82**, 043632, 2010, DOI: 10.1103/PhysRevA.82.043632.

[215] *NIST Atomic Spectra Database Lines*, 2019, eprint: https://physics.nist.gov/PhysRefData/ASD/lines_form.html.

[216] C.-C. Chen, *"An atomic marble run to unity phase-space density"*, PhD thesis, Institute of Physics, University of Amsterdam, The Netherlands, 2019.

[217] C. Chen, S. Bennetts, R. G. Escudero, F. Schreck, and B. Pasquiou, *"Sisyphus Optical Lattice Decelerator"*, 2018, arXiv: 1810.07157.

[218] S. Wu, R. C. Brown, W. D. Phillips, and J. V. Porto, *"Pulsed Sisyphus Scheme for Laser Cooling of Atomic (Anti)Hydrogen"*, Phys. Rev. Lett. **106**, 213001, 2011, DOI: 10.1103/PhysRevLett.106.213001.

[219] M. Schioppo, N. Poli, M. Prevedelli, S. Falke, C. Lisdat, U. Sterr, and G. M. Tino, *"A compact and efficient strontium oven for laser-cooling experiments"*, Rev. Sci. Instrum. **83**, 103101, 2012, DOI: 10.1063/1.4756936.

[220] M. Asano and K. Kubo, *"Vapor Pressure of Strontium below 660°K"*, J. Nucl. Sci. Technol. **15**, 765–767, 1978, DOI: 10.1080/18811248.1978.9735585.

[221] C. E. John Wagner, *"Strontium Dog: v. 1: Search/destroy Agency Files (2000 Ad Strontium Dog 1)"*, 2000 AD Graphic Novels 2007.

[222] R. Scott, *The Martian*, 2015.

[223] C. J. Foot, *"Atomic Physics"*, Oxford University Press 2005.

[224] A. Cooper, J. P. Covey, I. S. Madjarov, S. G. Porsev, M. S. Safronova, and M. Endres, *"Alkaline-Earth Atoms in Optical Tweezers"*, Phys. Rev. X **8**, 041055, 2018, DOI: 10.1103/PhysRevX.8.041055.

[225] X. Xu, T. H. Loftus, J. L. Hall, A. Gallagher, and J. Ye, *"Cooling and trapping of atomic strontium"*, J. Opt. Soc. Am. B **20**, 968–976, 2003, DOI: 10.1364/josab.20.000968.

[226] C. W. Bauschlicher, S. R. Langhoff, and H. Partridge, *"The radiative lifetime of the $^1D_2$ state of Ca and Sr: a core-valence treatment"*, Journal of Physics B **18**, 1523–1532, 1985, DOI: 10.1088/0022-3700/18/8/011.

[227] M. Yasuda and H. Katori, *"Lifetime Measurement of the $^3P_2$ Metastable State of Strontium Atoms"*, Phys. Rev. Lett. **92**, 153004, 2004, DOI: 10.1103/PhysRevLett.92.153004.

[228] D. A. Miller, L. You, J. Cooper, and A. Gallagher, *"Collisional energy transfer between excited-state strontium and noble-gas atoms"*, Phys. Rev. A **46**, 1303–1309, 1992, DOI: 10.1103/PhysRevA.46.1303.

[229] P. G. Mickelson, Y. N. Martinez de Escobar, P. Anzel, B. J. DeSalvo, S. B. Nagel, A. J. Traverso, M. Yan, and T. C. Killian, *"Repumping and spectroscopy of laser-cooled Sr atoms using the* $(5s5p)^3P_2 - (5s4d)^3D_2$ *transition"*, Journal of Physics B **42**, 235001, 2009, DOI: doi:10.1088/0953-4075/42/23/235001.

[230] S. Ye, X. Zhang, T. C. Killian, F. B. Dunning, M. Hiller, S. Yoshida, S. Nagele, and J. Burgdörfer, *"Production of very-high-n strontium Rydberg atoms"*, Phys. Rev. A **88**, 043430, 2013, DOI: 10.1103/PhysRevA.88.043430.

[231] J. D. Whalen, F. Camargo, R. Ding, T. C. Killian, F. B. Dunning, J. Pérez-Ríos, S. Yoshida, and J. Burgdörfer, *"Lifetimes of ultralong-range strontium Rydberg molecules in a dense Bose-Einstein condensate"*, Phys. Rev. A **96**, 042702, 2017, DOI: 10.1103/PhysRevA.96.042702.

[232] J. Millen, G. Lochead, G. R. Corbett, R. M. Potvliege, and M. P. A. Jones, *"Spectroscopy of a cold strontium Rydberg gas"*, Journal of Physics B **44**, 184001, 2011, DOI: 10.1088/0953-4075/44/18/184001.

[233] A. Derevianko, *"Feasibility of Cooling and Trapping Metastable Alkaline-Earth Atoms"*, Phys. Rev. Lett. **87**, 023002, 2001, DOI: 10.1103/PhysRevLett.87.023002.

[234] M. M. Boyd, *"High Precision Spectroscopy of Strontium in an Optical Lattice: Towards a New Standard of Frequency and Time"*, PhD thesis, University of Colorado, USA, 2007.

[235] M. M. Boyd, T. Zelevinsky, A. D. Ludlow, S. Blatt, T. Zanon-Willette, S. M. Foreman, and J. Ye, *"Nuclear spin effects in optical lattice clocks"*, Phys. Rev. A **76**, 022510, 2007, DOI: 10.1103/PhysRevA.76.022510.

[236] R. M. Sandner, M. Müller, A. J. Daley, and P. Zoller, *"Spatial Pauli blocking of spontaneous emission in optical lattices"*, Phys. Rev. A **84**, 043825, 2011, DOI: 10.1103/PhysRevA.84.043825.

[237] G. K. Campbell, A. D. Ludlow, S. Blatt, J. W. Thomsen, M. J. Martin, M. H. G. de Miranda, T. Zelevinsky, M. M. Boyd, J. Ye, S. A. Diddams, T. P. Heavner, T. E. Parker, and S. R. Jefferts, *"The absolute frequency of the* ^{87}*Sr optical clock transition"*, Metrologia **45**, 539–548, 2008, DOI: 10.1088/0026-1394/45/5/008.

[238] P. Morzynski *et al.*, *"Absolute measurement of the* $^1S_0$ - $^3P_0$ *clock transition in neutral* ^{88}*Sr over the 330 km-long stabilized fibre optic link"*, Sci. Rep. **5**, 17495, 2015, DOI: 10.1038/srep17495.

[239] A. J. Daley, M. M. Boyd, J. Ye, and P. Zoller, *"Quantum computing with alkaline-earth-metal atoms"*, Phys. Rev. Lett. **101**, 170504, 2008, DOI: 10.1103/PhysRevLett.101.170504.

[240] T. Middelmann, S. Falke, C. Lisdat, and U. Sterr, *"High Accuracy Correction of Blackbody Radiation Shift in an Optical Lattice Clock"*, Phys. Rev. Lett. **109**, 263004, 2012, DOI: 10.1103/PhysRevLett.109.263004.

[241] M. S. Safronova, S. G. Porsev, U. I. Safronova, M. G. Kozlov, and C. W. Clark, *"Blackbody-radiation shift in the Sr optical atomic clock"*, Phys. Rev. A **87**, 012509, 2013, DOI: 10.1103/PhysRevA.87.012509.

[242] R. Santra, E. Arimondo, T. Ido, C. H. Greene, and J. Ye, *"High-Accuracy Optical Clock via Three-Level Coherence in Neutral Bosonic* ^{88}Sr", Phys. Rev. Lett. **94**, 173002, 2005, DOI: 10.1103/PhysRevLett.94.173002.

[243] O. Onishchenko, S. Pyatchenkov, A. Urech, C.-C. Chen, S. Bennetts, G. A. Siviloglou, and F. Schreck, *"The frequency of the ultranarrow* $^1S_0$-$^3P_2$ *transition in* ^{87}*Sr"*, 2018, arXiv: 1812.02115.

[244] J. Samland, *"A 448nm repump for Strontium"*, MA thesis, University of Amsterdam, The Netherlands, 2019.

[245] S. Stellmer and F. Schreck, *"Reservoir spectroscopy of* $5s5p^3P_2 - 5snd^3D_{1,2,3}$ *transitions in strontium"*, Phys. Rev. A **90**, 022512, 2014, DOI: 10.1103/PhysRevA.90.022512.

[246] H. G. C. Werij, C. H. Greene, C. E. Theodosiou, and A. Gallagher, *"Oscillator strengths and radiative branching ratios in atomic Sr"*, Phys. Rev. A **46**, 1248–1260, 1992, DOI: 10.1103/PhysRevA.46.1248.

[247] V. Schkolnik, O. Fartmann, and M. Krutzik, *"An extended-cavity diode laser at 497 nm for laser cooling and trapping of neutral strontium"*, Laser Phys. **29**, 035802, 2019, DOI: 10.1088/1555-6611/aaffc8.

[248] T. Kurosu and F. Shimizu, *"Laser Cooling and Trapping of Alkaline Earth Atoms"*, Jpn. J. Appl. Phys. **31**, 908–912, 1992, DOI: 10.1143/jjap.31.908.

[249] K. R. Vogel, *"Laser Cooling on a narrow atomic transition and measurement of the two-body cold collision loss rate in a strontium magneto-optical trap"*, PhD thesis, University of Colorado, Boulder, USA, 1999.

[250] Y. Bidel, *"Piégeage et refroidissement laser du strontium; Etude de l'effet des interférences en diffusion multiple"*, PhD thesis, Université de Nice, France, 2002.

[251] L. R. Hunter, W. A. Walker, and D. S. Weiss, *"Observation of an atomic Stark–electric-quadrupole interference"*, Phys. Rev. Lett. **56**, 823–826, 1986, DOI: 10.1103/PhysRevLett.56.823.

[252] S. G. Porsev, M. G. Kozlov, Y. G. Rakhlina, and A. Derevianko, *"Many-body calculations of electric-dipole amplitudes for transitions between low-lying levels of Mg, Ca, and Sr"*, Phys. Rev. A **64**, 012508, 2001, DOI: 10.1103/PhysRevA.64.012508.

[253] R. Grimm, M. Weidemüller, and Y. B. Ovchinnikov, *"Optical dipole traps for neutral atoms"*, Adv. At. Mol. Opt. Phys. **42**, 95, 2000, DOI: 10.1016/s1049-250x(08)60186-x.

[254] X. Zhou, X. Xu, X. Chen, and J. Chen, *"Magic wavelengths for terahertz clock transitions"*, Phys. Rev. A **81**, 012115, 2010, DOI: 10.1103/PhysRevA.81.012115.

[255] E. W. Weisstein, *Wigner 3j-Symbol*, eprint: http://mathworld.wolfram.com/Wigner3j-Symbol.html.

[256] M. S. Safronova, Z. Zuhrianda, U. I. Safronova, and C. W. Clark, *"Extracting transition rates from zero-polarizability spectroscopy"*, Phys. Rev. A **92**, 040501, 2015, DOI: 10.1103/PhysRevA.92.040501.

[257] A. D. Ludlow, *"The Strontium Optical Lattice Clock: Optical Spectroscopy with Sub-Hertz Accuracy"*, PhD thesis, University of Colorado, Boulder, USA, 2008.

[258] M. Takamoto, H. Katori, S. I. Marmo, V. D. Ovsiannikov, and V. G. Pal'chikov, *"Prospects for optical clocks with a blue-detuned lattice"*, Phys. Rev. Lett. **102**, 063002, 2009, DOI: 10.1103/PhysRevLett.102.063002.

[259] A. D. Ludlow, M. M. Boyd, T. Zelevinsky, S. M. Foreman, S. Blatt, M. Notcutt, T. Ido, and J. Ye, *"Systematic Study of the ^{87}Sr Clock Transition in an Optical Lattice"*, Phys. Rev. Lett. **96**, 033003, 2006, DOI: 10.1103/PhysRevLett.96.033003.

[260] A. Brusch, R. Le Targat, X. Baillard, M. Fouché, and P. Lemonde, *"Hyperpolarizability Effects in a Sr Optical Lattice Clock"*, Phys. Rev. Lett. **96**, 103003, 2006, DOI: 10.1103/PhysRevLett.96.103003.

[261] M. M. Boyd, A. D. Ludlow, S. Blatt, S. M. Foreman, T. Ido, T. Zelevinsky, and J. Ye, *"^{87}Sr Lattice Clock with Inaccuracy below 10^{-15}"*, Phys. Rev. Lett. **98**, 083002, 2007, DOI: 10.1103/PhysRevLett.98.083002.

[262] Q. Wang, Y.-G. Lin, F. Meng, Y. Li, B.-K. Lin, E.-J. Zang, T.-C. Li, and Z.-J. Fang, *"Magic Wavelength Measurement of the ^{87}Sr Optical Lattice Clock at NIM"*, Chin. Phys. Lett. **33**, 103201, 2016, DOI: 10.1088/0256-307x/33/10/103201.

[263] T. Ido and H. Katori, *"Recoil-free spectroscopy of neutral Sr atoms in the Lamb-Dicke regime"*, Phys. Rev. Lett. **91**, 053001, 2003, DOI: 10.1103/PhysRevLett.91.053001.

[264] I. Courtillot, A. Quessada-Vial, A. Brusch, D. Kolker, G. D. Rovera, and P. Lemonde, *"Accurate spectroscopy of Sr atoms"*, Eur. Phys. J. D **33**, 161, 2005, DOI: 10.1140/epjd/e2005-00058-0.

[265] A. Quessada-Vial, *"Développement d'une horloge optique à atomes de strontium piégés: réalisation d'un laser ultra-stable et stabilité de fréquence"*, PhD thesis, Université de Paris VI, France, 2005.

[266] T. Mukaiyama, H. Katori, T. Ido, Y. Li, and M. Kuwata-Gonokami, *"Recoil-limited laser cooling of ^{87}Sr atoms near the Fermi temperature"*, Phys. Rev. Lett. **90**, 113002, 2003, DOI: 10.1103/PhysRevLett.90.113002.

[267] Y. N. Martinez de Escobar, P. G. Mickelson, P. Pellegrini, S. B. Nagel, A. Traverso, M. Yan, R. Côté, and T. C. Killian, *"Two-photon photoassociative spectroscopy of ultracold ^{88}Sr"*, Phys. Rev. A **78**, 062708, 2008, DOI: 10.1103/PhysRevA.78.062708.

[268] A. Stein, H. Knöckel, and E. Tiemann, *"Fourier-transform spectroscopy of Sr_2 and revised ground-state potential"*, Phys. Rev. A **78**, 042508, 2008, DOI: 10.1103/PhysRevA.78.042508.

[269] A. Traverso, R. Chakraborty, Y. N. Martinez de Escobar, P. G. Mickelson, S. B. Nagel, M. Yan, and T. C. Killian, *"Inelastic and elastic collision rates for triplet states of ultracold strontium"*, Phys. Rev. A **79**, 060702(R), 2009, DOI: 10.1103/PhysRevA.79.060702.

[270] M. Bishof, M. J. Martin, M. D. Swallows, C. Benko, Y. Lin, G. Quéméner, A. M. Rey, and J. Ye, *"Inelastic collisions and density-dependent excitation suppression in a ^{87}Sr optical lattice clock"*, Phys. Rev. A **84**, 052716, 2011, DOI: 10.1103/PhysRevA.84.052716.

[271] C. Lisdat, J. S. R. Vellore Winfred, T. Middelmann, F. Riehle, and U. Sterr, *"Collisional Losses, Decoherence, and Frequency Shifts in Optical Lattice Clocks with Bosons"*, Phys. Rev. Lett. **103**, 090801, 2009, DOI: 10.1103/PhysRevLett.103.090801.

[272] T. Zelevinsky, M. M. Boyd, A. D. Ludlow, T. Ido, J. Ye, R. Ciuryło, P. Naidon, and P. S. Julienne, *"Narrow Line Photoassociation in an Optical Lattice"*, Phys. Rev. Lett. **96**, 203201, 2006, DOI: 10.1103/PhysRevLett.96.203201.

[273] B. H. McGuyer, C. B. Osborn, M. McDonald, G. Reinaudi, W. Skomorowski, R. Moszynski, and T. Zelevinsky, *"Nonadiabatic Effects in Ultracold Molecules via Anomalous Linear and Quadratic Zeeman Shifts"*, Phys. Rev. Lett. **111**, 243003, 2013, DOI: 10.1103/PhysRevLett.111.243003.

[274] M. Borkowski, P. Morzynski, R. Ciuryło, P. S. Julienne, M. Yan, B. J. DeSalvo, and T. C. Killian, *"Mass scaling and nonadiabatic effects in photoassociation spectroscopy of ultracold strontium atoms"*, Phys. Rev. A **90**, 032713, 2014, DOI: 10.1103/PhysRevA.90.032713.

[275] B. J. Reschovsky, B. P. Ruzic, H. Miyake, N. C. Pisenti, P. S. Julienne, and G. K. Campbell, *"Narrow-line photoassociation spectroscopy and mass-scaling of bosonic strontium"*, 2018, arXiv: 1808.06507.

[276] S. Stellmer, B. Pasquiou, R. Grimm, and F. Schreck, *"Creation of Ultracold Sr_2 Molecules in the Electronic Ground State"*, Phys. Rev. Lett. **109**, 115302, 2012, DOI: 10.1103/PhysRevLett.109.115302.

[277] S. Blatt, T. L. Nicholson, B. J. Bloom, J. R. Williams, J. W. Thomsen, P. S. Julienne, and J. Ye, *"Measurement of Optical Feshbach Resonances in an Ideal Gas"*, Phys. Rev. Lett. **107**, 073202, 2011, DOI: 10.1103/PhysRevLett.107.073202.

[278] M. Yan, B. J. DeSalvo, B. Ramachandhran, H. Pu, and T. C. Killian, *"Controlling Condensate Collapse and Expansion with an Optical Feshbach Resonance"*, Phys. Rev. Lett. **110**, 123201, 2013, DOI: 10.1103/PhysRevLett.110.123201.

[279] A. Ciamei, A. Bayerle, C.-C. Chen, B. Pasquiou, and F. Schreck, *"Efficient production of long-lived ultracold Sr_2 molecules"*, Phys. Rev. A **96**, 013406, 2017, DOI: 10.1103/PhysRevA.96.013406.

[280] N. Dongari, A. Sharma, and F. Durst, *"Pressure-driven diffusive gas flows in micro-channels: from the Knudsen to the continuum regimes"*, Microfluid. Nanofluid. **6**, 679–692, 2009, DOI: 10.1007/s10404-008-0344-y.

[281] E. Wille, *"Preparation of an Optically Trapped Fermi-Fermi Mixture of ^{6}Li and ^{40}K Atoms and Characterization of the Interspecies Interactions by Feshbach Spectroscopy"*, PhD thesis, Institute of Experimental Physics, University of Innsbruck, Austria, 2009.

[282] R. Senaratne, S. V. Rajagopal, Z. A. Geiger, K. M. Fujiwara, V. Lebedev, and D. M. Weld, *"Effusive atomic oven nozzle design using an aligned microcapillary array"*, Rev. Sci. Instrum. **86**, 023105, 2015, DOI: 10.1063/1.4907401.

[283] V. O. Altemose, *"Helium Diffusion through Glass"*, J. Appl. Phys. **32**, 1309–1316, 1961, DOI: 10.1063/1.1736226.

[284] J. A. Rushton, M. Aldous, and M. D. Himsworth, *"Contributed Review: The feasibility of a fully miniaturized magneto-optical trap for portable ultracold quantum technology"*, Rev. Sci. Instrum. **85**, 121501, 2014, DOI: 10.1063/1.4904066.

[285] Pfeiffer, eprint: https://www.pfeiffer-vacuum.com/en/know-how/introduction-to-vacuum-technology/fundamentals/conductance/.

[286] B. Suurmeijer, T. Mulder, and J. Verhoeven, *"Vacuum Science and Technology"*, 2016, eprint: hightechinstitute.nl.

[287] *Instruction Manual New Duniway Ion Pumps*, eprint: https://www.duniway.com/images/_pg/manual-duniway-ion-pumps.pdf.

[288] I. R. Hill, Y. B. Ovchinnikov, E. M. Bridge, E. A. Curtis, and P. Gill, *"Zeeman slowers for strontium based on permanent magnets"*, Journal of Physics B **47**, 075006, 2014, DOI: 10.1088/0953-4075/47/7/075006.

[289] Y. B. Ovchinnikov, *"A permanent Zeeman slower for Sr atomic clock"*, EPJ Special Topics **163**, 95–100, 2008, DOI: 10.1140/epjst/e2008-00812-x.

[290] M. Bober, J. Zachorowski, and W. Gawlik, *"Designing Zeeman slower for strontium atoms - towards optical atomic clock"*, 2010, arXiv: 1006.1554.

[291] C. J. H. Pagett, P. H. Moriya, R. Celistrino Teixeira, R. F. Shiozaki, M. Hemmerling, and P. W. Courteille, *"Injection locking of a low cost high power laser diode at 461 nm"*, Rev. Sci. Instrum. **87**, 053105, 2016, DOI: 10.1063/1.4947462.

[292] J. Huckans, W. Dubosclard, E. Maréchal, O. Gorceix, B. Laburthe-Tolra, and M. R. de Saint-Vincent, *"Note on the reflectance of mirrors exposed to a strontium beam"*, 2018, arXiv: 1802.08499.

[293] M. Cadoret, E. de Mirandes, P. Cladé, S. Guellati-Khélifa, C. Schwob, F. m. c. Nez, L. Julien, and F. m. c. Biraben, *"Combination of Bloch Oscillations with a Ramsey-Bordé Interferometer: New Determination of the Fine Structure Constant"*, Phys. Rev. Lett. **101**, 230801, 2008, DOI: 10.1103/PhysRevLett.101.230801.

[294] P. Cladé, S. Guellati-Khélifa, F. m. c. Nez, and F. m. c. Biraben, *"Large Momentum Beam Splitter Using Bloch Oscillations"*, Phys. Rev. Lett. **102**, 240402, 2009, DOI: 10.1103/PhysRevLett.102.240402.

[295] H. Busche, *"Efficient loading of a magneto-optical trap for experiments with dense ultracold Rydberg gases"*, PhD thesis, Department of Physics and Astronomy, University of Heidelberg, Germany, 2011.

[296] K. Metzger, *"Dreidimensionale Feldberechnung starr magnetisierter Permanentmagnete mit einer Anwendung in eisenlosen elektrischen Maschinen"*, Archiv für Elektrotechnik **59**, 229–242, 1977, DOI: 10.1007/BF01573988.

[297] B. O. Kock, *"Magneto-Optical Trapping of Strontium for use as a Mobile Frequency Reference"*, PhD thesis, University of Birmingham, UK, 2013.

[298] R. R. Mhaskar, *"Toward an Atom Laser: Cold Atoms in a Long, High-gradient Magnetic Guide"*, PhD thesis, University of Michigan, USA, 2008.

[299] M. A. Traxler, *"Linear Atom Guides: Guiding Rydberg Atoms and Progress Toward an Atom Laser"*, PhD thesis, University of Michigan, USA, 2013.

[300] S. Bennetts, G. D. McDonald, K. S. Hardman, J. E. Debs, C. C. N. Kuhn, J. D. Close, and N. P. Robins, *"External cavity diode lasers with 5kHz linewidth and 200nm tuning range at 1.55μm and methods for linewidth measurement"*, Opt. Express **22**, 10642–10654, 2014, DOI: 10.1364/OE.22.010642.

[301] T. B. M. van Leent, *"Narrow-linewidth External Cavity Diode Lasers for Atomic Physics"*, MA thesis, University of Amsterdam, The Netherlands, 2017.

[302] Z. Geng, *"Repumping Strontium: from Laser Construction to Repumping Characterization"*, MA thesis, University of Amsterdam, The Netherlands, 2017.

[303] L. Nilse, H. J. Davies, and C. S. Adams, *"Synchronous tuning of extended cavity diode lasers: the case for an optimum pivot point"*, Appl. Opt. **38**, 548–553, 1999, DOI: 10.1364/AO.38.000548.

[304] P. McNicholl and H. J. Metcalf, *"Synchronous cavity mode and feedback wavelength scanning in dye laser oscillators with gratings"*, Appl. Opt. **24**, 2757–2761, 1985, DOI: 10.1364/AO.24.002757.

[305] M. Gilowski, C. Schubert, M. Zaiser, W. Herr, T. Wübbena, T. Wendrich, T. Müller, E. Rasel, and W. Ertmer, *"Narrow bandwidth interference filter-stabilized diode laser systems for the manipulation of neutral atoms"*, Opt. Commun. **280**, 443 –447, 2007, DOI: 10.1016/j.optcom.2007.08.043.

[306] P. Zorabedian and W. R. Trutna, *"Interference-filter-tuned, alignment-stabilized, semiconductor external-cavity laser"*, Opt. Lett. **13**, 826–828, 1988, DOI: 10.1364/OL.13.000826.

[307] X. Baillard, A. Gauguet, S. Bize, P. Lemonde, P. Laurent, A. Clairon, and P. Rosenbusch, *"Interference-filter-stabilized external-cavity diode lasers"*, Opt. Commun. **266**, 609 –613, 2006, DOI: 10.1016/j.optcom.2006.05.011.

[308] Z. Xu, S. Zhang, Y. Li, and W. Du, *"Adjustment-free cat's eye cavity He-Ne laser and its outstanding stability"*, Opt. Express **13**, 5565–5573, 2005, DOI: 10.1364/OPEX.13.005565.

[309] D. J. Thompson and R. E. Scholten, *"Narrow linewidth tunable external cavity diode laser using wide bandwidth filter"*, Rev. Sci. Instrum. **83**, 023107, 2012, DOI: 10.1063/1.3687441.

[310] R. G. Escudero, *"Magnetic Field Control and Laser Frequency Stabilization for Strontium Magneto-Optical Traps"*, MA thesis, Ludwig–Maximilians–Universität München, Germany, 2016.

[311] M. A. Norcia, J. R. K. Cline, J. P. Bartolotta, M. J. Holland, and J. K. Thompson, *"Narrow-line laser cooling by adiabatic transfer"*, New J. Phys. **20**, 023021, 2018, DOI: 10.1088/1367-2630/aaa950.

[312] G. Bismut, B. Pasquiou, E. Maréchal, P. Pedri, L. Vernac, O. Gorceix, and B. Laburthe-Tolra, *"Collective Excitations of a Dipolar Bose-Einstein Condensate"*, Phys. Rev. Lett. **105**, 040404, 2010, DOI: 10.1103/PhysRevLett.105.040404.

[313] M. A. Norcia and J. K. Thompson, *"Simple laser stabilization to the strontium ^{88}Sr transition at 707 nm"*, Rev. Sci. Instrum. **87**, 023110, 2016, DOI: 10.1063/1.4942434.

[314] S. Wolf, S. J. Oliver, and D. S. Weiss, *"Suppression of Recoil Heating by an Optical Lattice"*, Phys. Rev. Lett. **85**, 4249–4252, 2000, DOI: 10.1103/PhysRevLett.85.4249.

[315] D. J. Han, M. T. DePue, and D. S. Weiss, *"Loading and compressing Cs atoms in a very far-off-resonant light trap"*, Phys. Rev. A **63**, 023405, 2001, DOI: 10.1103/PhysRevA.63.023405.

[316] P. G. Westergaard, J. Lodewyck, and P. Lemonde, *"Minimizing the Dick effect in an optical lattice clock"*, IEEE Trans. Ultrason. Ferroelectr. Freq. Control **57**, 623, 2010, DOI: 10.1109/TUFFC.2010.1457.

[317] D. Meiser and M. J. Holland, *"Steady-state superradiance with alkaline-earth-metal atoms"*, Phys. Rev. A **81**, 033847, 2010, DOI: 10.1103/PhysRevA.81.033847.

[318] D. G. Matei, T. Legero, S. Häfner, C. Grebing, R. Weyrich, W. Zhang, L. Sonderhouse, J. M. Robinson, J. Ye, F. Riehle, and U. Sterr, *"1.5 μm Lasers with Sub-10 mHz Linewidth"*, Phys. Rev. Lett. **118**, 263202, 2017, DOI: 10.1103/PhysRevLett.118.263202.

[319] J.-P. Uzan, *"The fundamental constants and their variation: observational and theoretical status"*, Rev. Mod. Phys. **75**, 403–455, 2003, DOI: 10.1103/RevModPhys.75.403.

[320] N. Yu and M. Tinto, *"Gravitational wave detection with single-laser atom interferometers"*, Gen. Relat. and Gravit. **43**, 1943–1952, 2011, DOI: 10.1007/s10714-010-1055-8.

[321] P. D. Lett, R. N. Watts, C. I. Westbrook, W. D. Phillips, P. L. Gould, and H. J. Metcalf, *"Observation of Atoms Laser Cooled below the Doppler Limit"*, Phys. Rev. Lett. **61**, 169–172, 1988, DOI: 10.1103/PhysRevLett.61.169.

[322] J. Dalibard and C. Cohen-Tannoudji, *"Laser cooling below the Doppler limit by polarization gradients: simple theoretical models"*, J. Opt. Soc. Am. B **6**, 2023–2045, 1989, DOI: 10.1364/JOSAB.6.002023.

[323] G. Salomon, L. Fouche, P. Wang, A. Aspect, P. Bouyer, and T. Bourdel, *"Gray-molasses cooling of ^{39}K to a high phase-space density"*, EPL **104**, 63002, 2013, DOI: 10.1209/0295-5075/104/63002.

[324] G. Colzi, G. Durastante, E. Fava, S. Serafini, G. Lamporesi, and G. Ferrari, *"Sub-Doppler cooling of sodium atoms in gray molasses"*, Phys. Rev. A **93**, 023421, 2016, DOI: 10.1103/PhysRevA.93.023421.

[325] C. Y. Yang, P. Halder, O. Appel, D. Hansen, and A. Hemmerich, *"Continuous loading of $^1S_0$ calcium atoms into an optical dipole trap"*, Phys. Rev. A **76**, 033418, 2007, DOI: 10.1103/PhysRevA.76.033418.

[326] N. Radwell, G. Walker, and S. Franke-Arnold, *"Cold-atom densities of more than 10^{12} cm^{-3} in a holographically shaped dark spontaneous-force optical trap"*, Phys. Rev. A **88**, 043409, 2013, DOI: 10.1103/PhysRevA.88.043409.

[327] H. Katori, T. Ido, Y. Isoya, and M. Kuwata-Gonokami, *"Magneto-Optical Trapping and Cooling of Strontium Atoms down to the Photon Recoil Temperature"*, Phys. Rev. Lett. **82**, 1116–1119, 1999, DOI: 10.1103/PhysRevLett.82.1116.

[328] A. Kawasaki, B. Braverman, Q. Yu, and V. Vuletić, *"Two-color magneto-optical trap with small magnetic field for ytterbium"*, J. Phys. B **48**, 155302, 2015, DOI: 10.1088/0953-4075/48/15/155302.

[329] J. Lee, J. H. Lee, J. Noh, and J. Mun, *"Core-shell magneto-optical trap for alkaline-earth-metal-like atoms"*, Phys. Rev. A **91**, 053405, 2015, DOI: 10.1103/PhysRevA.91.053405.

[330] J. Grünert and A. Hemmerich, *"Sub-Doppler magneto-optical trap for calcium"*, Phys. Rev. A **65**, 041401, 2002, DOI: 10.1103/PhysRevA.65.041401.

[331] A. Frisch, K. Aikawa, M. Mark, A. Rietzler, J. Schindler, E. Zupanic, R. Grimm, and F. Ferlaino, *"Narrow-line magneto-optical trap for erbium"*, Phys. Rev. A **85**, 051401, 2012, DOI: 10.1103/PhysRevA.85.051401.

[332] J Mahnke, I Kruse, A Hüper, S Jöllenbeck, W Ertmer, J Arlt, and C Klempt, *"A continuously pumped reservoir of ultracold atoms"*, J. Phys. B **48**, 165301, 2015, DOI: 10.1088/0953-4075/48/16/165301.

[333] T. Yang, K. Pandey, M. S. Pramod, F. Leroux, C. C. Kwong, E. Hajiyev, Z. Y. Chia, B. Fang, and D. Wilkowski, *"A high flux source of cold strontium atoms"*, Eur. Phys. J. D **69**, 226, 2015, DOI: 10.1140/epjd/e2015-60288-y.

[334] I. Nosske, L. Couturier, F. Hu, C. Tan, C. Qiao, J. Blume, Y. H. Jiang, P. Chen, and M. Weidemüller, *"Two-dimensional magneto-optical trap as a source for cold strontium atoms"*, Phys. Rev. A **96**, 053415, 2017, DOI: 10.1103/PhysRevA.96.053415.

[335] M. K. Tey, S. Stellmer, R. Grimm, and F. Schreck, *"Double-degenerate Bose-Fermi mixture of strontium"*, Phys. Rev. A **82**, 011608, 2010, DOI: 10.1103/PhysRevA.82.011608.

[336] J. V. Prodan, W. D. Phillips, and H. Metcalf, *"Laser Production of a Very Slow Monoenergetic Atomic Beam"*, Phys. Rev. Lett. **49**, 1149–1153, 1982, DOI: 10.1103/physrevlett.49.1149.

[337] M. Zhu, C. W. Oates, and J. L. Hall, *"Continuous high-flux monovelocity atomic beam based on a broadband laser-cooling technique"*, Phys. Rev. Lett. **67**, 46–49, 1991, DOI: 10.1103/physrevlett.67.46.

[338] A. J. Berglund, J. L. Hanssen, and J. J. McClelland, *"Narrow-Line Magneto-Optical Cooling and Trapping of Strongly Magnetic Atoms"*, Phys. Rev. Lett. **100**, 113002, 2008, DOI: 10.1103/PhysRevLett.100.113002.

[339] T. Kuwamoto, K. Honda, Y. Takahashi, and T. Yabuzaki, *"Magneto-optical trapping of Yb atoms using an intercombination transition"*, Phys. Rev. A **60**, R745–R748, 1999, DOI: 10.1103/PhysRevA.60.R745.

[340] A. Griesmaier, A. Aghajani-Talesh, M. Falkenau, J. Sebastian, A. Greiner, and T. Pfau, *"A high flux of ultra-cold chromium atoms in a magnetic guide"*, Journal of Physics B **42**, 145306, 2009, DOI: 10.1088/0953-4075/42/14/145306.

[341] J. J. McClelland, A. V. Steele, B. Knuffman, K. A. Twedt, A. Schwarzkopf, and T. M. Wilson, *"Bright focused ion beam sources based on laser-cooled atoms"*, Appl. Phys. Rev. **3**, 011302, 2016, DOI: 10.1063/1.4944491.

[342] A. J. McCulloch, R. W. Speirs, J. Grimmel, B. M. Sparkes, D. Comparat, and R. E. Scholten, *"Field ionization of Rydberg atoms for high-brightness electron and ion beams"*, Phys. Rev. A **95**, 063845, 2017, DOI: 10.1103/PhysRevA.95.063845.

[343] L. Hu, N. Poli, L. Salvi, and G. M. Tino, *"Atom Interferometry with the Sr Optical Clock Transition"*, Phys. Rev. Lett. **119**, 263601, 2017, DOI: 10.1103/PhysRevLett.119.263601.

[344] R. H. Parker, C. Yu, W. Zhong, B. Estey, and H. Müller, *"Measurement of the fine-structure constant as a test of the Standard Model"*, Science **360**, 191, 2018, DOI: 10.1126/science.aap7706.

[345] E. Narevicius and M. G. Raizen, *"Toward Cold Chemistry with Magnetically Decelerated Supersonic Beams"*, Chem. Rev. **112**, 4879–4889, 2012, DOI: 10.1021/cr2004597.

[346] N. Balakrishnan, *"Perspective: Ultracold molecules and the dawn of cold controlled chemistry"*, J. Chem. Phys. **145**, 150901, 2016, DOI: 10.1063/1.4964096.

[347] A Aghajani-Talesh, M Falkenau, V. V. Volchkov, L. E. Trafford, T Pfau, and A Griesmaier, *"Laser cooling of a magnetically guided ultracold atom beam"*, New J. Phys. **12**, 065018, 2010, DOI: 10.1088/1367-2630/12/6/065018.

[348] G. Kleine Büning, J. Will, W. Ertmer, C. Klempt, and J. Arlt, *"A slow gravity compensated atom laser"*, Appl. Phys. B **100**, 117–123, 2010, DOI: 10.1007/s00340-010-4078-7.

[349] B. Knuffman, A. V. Steele, and J. J. McClelland, *"Cold atomic beam ion source for focused ion beam applications"*, J. Appl. Phys. **114**, 044303, 2013, DOI: 10.1063/1.4816248.

[350] A. V. Steele, A. Schwarzkopf, J. J. McClelland, and B. Knuffman, *"High-brightness Cs focused ion beam from a cold-atomic-beam ion source"*, Nano Futures **1**, 015005, 2017, DOI: 10.1088/2399-1984/aa6a48.

[351] W. DeGraffenreid, J. Ramirez-Serrano, Y.-M. Liu, and J. Weiner, *"Continuous, dense, highly collimated sodium beam"*, Rev. Sci. Instrum. **71**, 3668–3676, 2000, DOI: 10.1063/1.1289683.

[352] B. M. Sparkes, D. Murphy, R. J. Taylor, R. W. Speirs, A. J. McCulloch, and R. E. Scholten, *"Stimulated Raman adiabatic passage for improved performance of a cold-atom electron and ion source"*, Phys. Rev. A **94**, 023404, 2016, DOI: 10.1103/PhysRevA.94.023404.

[353] S. H. W. Wouters, G. ten Haaf, R. P. M. J. W. Notermans, N. Debernardi, P. H. A. Mutsaers, O. J. Luiten, and E. J. D. Vredenbregt, *"Performance predictions for a laser-intensified thermal beam for use in high-resolution focused-ion-beam instruments"*, Phys. Rev. A **90**, 063817, 2014, DOI: 10.1103/PhysRevA.90.063817.

[354] A. J. McCulloch, B. M. Sparkes, and R. E. Scholten, *"Cold electron sources using laser-cooled atoms"*, Journal of Physics B **49**, 164004, 2016, DOI: 10.1088/0953-4075/49/16/164004.

[355] R. Taïeb, R. Dum, J. I. Cirac, P. Marte, and P. Zoller, *"Cooling and localization of atoms in laser-induced potential wells"*, Phys. Rev. A **49**, 4876–4887, 1994, DOI: 10.1103/PhysRevA.49.4876.

[356] V. V. Ivanov and S. Gupta, *"Laser-driven Sisyphus cooling in an optical dipole trap"*, Phys. Rev. A **84**, 063417, 2011, DOI: 10.1103/PhysRevA.84.063417.

[357] V. V. Ivanov, *"Continuous loading of an atom beam into an optical lattice"*, Opt. Commun. **324**, 258–263, 2014, DOI: 10.1016/j.optcom.2014.03.042.

[358] C.-C. Chen, S. Bennetts, R. González Escudero, F. Schreck, and B. Pasquiou, *"Sisyphus optical lattice decelerator"*, Phys. Rev. A **100**, 023401, 2019, DOI: 10.1103/PhysRevA.100.023401.

[359] G. B. Andresen *et al.*, *"Trapped antihydrogen"*, Nature **468**, 673, 2010, DOI: 10.1038/nature09610.

[360] G. Gabrielse *et al.*, *"Trapped Antihydrogen in Its Ground State"*, Phys. Rev. Lett. **108**, 113002, 2012, DOI: 10.1103/PhysRevLett.108.113002.

[361] M. Ahmadi *et al.*, *"Observation of the 1S-2S transition in trapped antihydrogen"*, Nature **541**, 506, 2017, DOI: 10.1038/nature21040.

[362] M. Ahmadi *et al.*, *"Observation of the hyperfine spectrum of antihydrogen"*, Nature **548**, 66, 2017, DOI: 10.1038/nature23446.

[363] M. Ahmadi *et al.*, *"Observation of the 1S-2P Lyman-α transition in antihydrogen"*, Nature **561**, 211–215, 2018, DOI: 10.1038/s41586-018-0435-1.

[364] G. Gabrielse *et al.*, *"Lyman-α source for laser cooling antihydrogen"*, Opt. Lett. **43**, 2905–2908, 2018, DOI: 10.1364/OL.43.002905.

[365] K. S. E. Eikema, J. Walz, and T. W. Hänsch, *"Continuous Coherent Lyman-α Excitation of Atomic Hydrogen"*, Phys. Rev. Lett. **86**, 5679–5682, 2001, DOI: 10.1103/PhysRevLett.86.5679.

[366] P. H. Donnan, M. C. Fujiwara, and F. Robicheaux, *"A proposal for laser cooling antihydrogen atoms"*, Journal of Physics B **46**, 025302, 2013, DOI: 10.1088/0953-4075/46/2/025302.

[367] L. De Marco, G. Valtolina, K. Matsuda, W. G. Tobias, J. P. Covey, and J. Ye, *"A degenerate Fermi gas of polar molecules"*, Science **363**, 853–856, 2019, DOI: 10.1126/science.aau7230.

[368] B. K. Stuhl, B. C. Sawyer, D. Wang, and J. Ye, *"Magneto-optical Trap for Polar Molecules"*, Phys. Rev. Lett. **101**, 243002, 2008, DOI: 10.1103/PhysRevLett.101.243002.

[369] T. Isaev and R. Berger, *"Polyatomic Candidates for Cooling of Molecules with Lasers from Simple Theoretical Concepts"*, Phys. Rev. Lett. **116**, 063006, 2016, DOI: 10.1103/PhysRevLett.116.063006.

[370] J. F. Barry, D. J. McCarron, E. B. Norrgard, M. H. Steinecker, and D. DeMille, *"Magneto-optical trapping of a diatomic molecule"*, Nature **512**, 286, 2014, DOI: 10.1038/nature13634.

[371] L. Anderegg, B. L. Augenbraun, E. Chae, B. Hemmerling, N. R. Hutzler, A. Ravi, A. Collopy, J. Ye, W. Ketterle, and J. M. Doyle, *"Radio Frequency Magneto-Optical Trapping of CaF with High Density"*, Phys. Rev. Lett. **119**, 103201, 2017, DOI: 10.1103/physrevlett.119.103201.

[372] A. L. Collopy, S. Ding, Y. Wu, I. A. Finneran, L. Anderegg, B. L. Augenbraun, J. M. Doyle, and J. Ye, *"3D Magneto-Optical Trap of Yttrium Monoxide"*, Phys. Rev. Lett. **121**, 213201, 2018, DOI: 10.1103/PhysRevLett.121.213201.

[373] I. Kozyryev, L. Baum, L. Aldridge, P. Yu, E. E. Eyler, and J. M. Doyle, *"Coherent Bichromatic Force Deflection of Molecules"*, Phys. Rev. Lett. **120**, 063205, 2018, DOI: 10.1103/PhysRevLett.120.063205.

[374] S. Truppe, H. J. Williams, M. Hambach, L. Caldwell, N. J. Fitch, E. A. Hinds, B. E. Sauer, and M. R. Tarbutt, *"Molecules cooled below the Doppler limit"*, Nat. Phys. **13**, 1173, 2017, DOI: 10.1038/nphys4241.

[375] M. S. Safronova, D. Budker, D. DeMille, D. F. J. Kimball, A. Derevianko, and C. W. Clark, *"Search for new physics with atoms and molecules"*, Rev. Mod. Phys. **90**, 025008, 2017, DOI: 10.1103/RevModPhys.90.025008.

[376] D. DeMille, *"Diatomic molecules, a window onto fundamental physics"*, Phys. Today **68**, 34–40, 2015, DOI: 10.1063/pt.3.3020.

[377] I. Kozyryev and N. R. Hutzler, *"Precision Measurement of Time-Reversal Symmetry Violation with Laser-Cooled Polyatomic Molecules"*, Phys. Rev. Lett. **119**, 133002, 2017, DOI: 10.1103/PhysRevLett.119.133002.

[378] S. K. Tokunaga, C. Stoeffler, F. Auguste, A. Shelkovnikov, C. Daussy, A. Amy-Klein, C. Chardonnet, and B. Darquié, *"Probing weak force-induced parity violation by high-resolution mid-infrared molecular spectroscopy"*, Mol. Phys. **111**, 2363–2373, 2013, DOI: 10.1080/00268976.2013.821186.

[379] S. B. Cahn, J. Ammon, E. Kirilov, Y. V. Gurevich, D. Murphree, R. Paolino, D. A. Rahmlow, M. G. Kozlov, and D. DeMille, *"Zeeman-Tuned Rotational Level-Crossing Spectroscopy in a Diatomic Free Radical"*, Phys. Rev. Lett. **112**, 163002, 2014, DOI: 10.1103/PhysRevLett.112.163002.

[380] J. J. Hudson, D. M. Kara, I. J. Smallman, B. E. Sauer, M. R. Tarbutt, and E. A. Hinds, *"Improved measurement of the shape of the electron"*, Nature **473**, 493, 2011, DOI: 10.1038/nature10104.

[381] J. Baron *et al.*, *"Order of Magnitude Smaller Limit on the Electric Dipole Moment of the Electron"*, Science **343**, 269–272, 2013, DOI: 10.1126/science.1248213.

[382] W. B. Cairncross, D. N. Gresh, M. Grau, K. C. Cossel, T. S. Roussy, Y. Ni, Y. Zhou, J. Ye, and E. A. Cornell, *"Precision Measurement of the Electron's Electric Dipole Moment Using Trapped Molecular Ions"*, Phys. Rev. Lett. **119**, 153001, 2017, DOI: 10.1103/PhysRevLett.119.153001.

[383] J. Söding, R. Grimm, Y. B. Ovchinnikov, P. Bouyer, and C. Salomon, *"Short-Distance Atomic Beam Deceleration with a Stimulated Light Force"*, Phys. Rev. Lett. **78**, 1420–1423, 1997, DOI: 10.1103/PhysRevLett.78.1420.

[384] X. Miao, E. Wertz, M. G. Cohen, and H. Metcalf, *"Strong optical forces from adiabatic rapid passage"*, Phys. Rev. A **75**, 011402, 2007, DOI: 10.1103/PhysRevA.75.011402.

[385] N. J. Fitch and M. R. Tarbutt, *"Principles and Design of a Zeeman-Sisyphus Decelerator for Molecular Beams"*, ChemPhysChem **17**, 3609–3623, 2016, DOI: 10.1002/cphc.201600656.

[386] S. D. Hogan and F. Merkt, *"Demonstration of Three-Dimensional Electrostatic Trapping of State-Selected Rydberg Atoms"*, Phys. Rev. Lett. **100**, 043001, 2008, DOI: 10.1103/PhysRevLett.100.043001.

[387] S. D. Hogan, C. Seiler, and F. Merkt, *"Rydberg-State-Enabled Deceleration and Trapping of Cold Molecules"*, Phys. Rev. Lett. **103**, 123001, 2009, DOI: 10.1103/PhysRevLett.103.123001.

[388] M. Ben Dahan, E. Peik, J. Reichel, Y. Castin, and C. Salomon, *"Bloch Oscillations of Atoms in an Optical Potential"*, Phys. Rev. Lett. **76**, 4508–4511, 1996, DOI: 10.1103/PhysRevLett.76.4508.

[389] S. R. Wilkinson, C. F. Bharucha, K. W. Madison, Q. Niu, and M. G. Raizen, *"Observation of Atomic Wannier-Stark Ladders in an Accelerating Optical Potential"*, Phys. Rev. Lett. **76**, 4512–4515, 1996, DOI: 10.1103/PhysRevLett.76.4512.

[390] T. P. Dinneen, K. R. Vogel, E. Arimondo, J. L. Hall, and A. Gallagher, *"Cold collisions of* $Sr^* - Sr$ *in a magneto-optical trap"*, Phys. Rev. A **59**, 1216–1222, 1999, DOI: 10.1103/PhysRevA.59.1216.

[391] T. Nicholson, S. Campbell, R. Hutson, G. Marti, B. Bloom, R. McNally, W. Zhang, M. Barrett, M. Safronova, G. Strouse, W. Tew, and J. Ye, *"Systematic evaluation of an atomic clock at* 2×10^{-18} *total uncertainty"*, Nat. Commun. **6**, 6896, 2015, DOI: 10.1038/ncomms7896.

[392] O. Brzobohatý, T. Cizmár, and P. Zemánek, *"High quality quasi-Bessel beam generated by round-tip axicon"*, Opt. Express **16**, 12688–12700, 2008, DOI: 10.1364/OE.16.012688.

[393] J. Durnin, J. J. Miceli, and J. H. Eberly, *"Comparison of Bessel and Gaussian beams"*, Opt. Lett. **13**, 79–80, 1988, DOI: 10.1364/OL.13.000079.

[394] J. Arlt, T. Hitomi, and K. Dholakia, *"Atom guiding along Laguerre-Gaussian and Bessel light beams"*, Appl. Phys. B **71**, 549–554, 2000, DOI: 10.1007/s003400000376.

[395] J. Arlt, K. Dholakia, J. Soneson, and E. M. Wright, *"Optical dipole traps and atomic waveguides based on Bessel light beams"*, Phys. Rev. A **63**, 063602, 2001, DOI: 10.1103/PhysRevA.63.063602.

[396] S. Schmid, G. Thalhammer, K. Winkler, F. Lang, and J. H. Denschlag, *"Long distance transport of ultracold atoms using a 1D optical lattice"*, New J. Phys. **8**, 159–159, 2006, DOI: 10.1088/1367-2630/8/8/159.

[397] S. Akturk, B. Zhou, B. Pasquiou, M. Franco, and A. Mysyrowicz, *"Intensity distribution around the focal regions of real axicons"*, Opt. Commun. **281**, 4240–4244, 2008, DOI: 10.1016/j.optcom.2008.05.027.

[398] X. Li, T. A. Corcovilos, Y. Wang, and D. S. Weiss, *"3D Projection Sideband Cooling"*, Phys. Rev. Lett. **108**, 103001, 2012, DOI: 10.1103/PhysRevLett.108.103001.

[399] O. Kock, W. He, D. Swierad, L. Smith, J. Hughes, K. Bongs, and Y. Singh, *"Laser controlled atom source for optical clocks"*, Sci. Rep. **6**, 37321, 2016, DOI: 10.1038/srep37321.

[400] R. H. Jones, D. R. Olander, and V. R. Kruger, *"Molecular-Beam Sources Fabricated from Multichannel Arrays. I. Angular Distributions and Peaking Factors"*, J. Appl. Phys. **40**, 4641–4649, 1969, DOI: 10.1063/1.1657245.

[401] W. Steckelmacher, *"Knudsen flow 75 years on: the current state of the art for flow of rarefied gases in tubes and systems"*, Rep. Prog. Phys. **49**, 1083–1107, 1986, DOI: 10.1088/0034-4885/49/10/001.

[402] R. Cole, *"Complementary Variational Principles for Knudsen Flow Rates"*, IMA J. Appl. Math. **20**, 107–115, 1977, DOI: 10.1093/imamat/20.1.107.

[403] H. C. W. Beijerinck and N. F. Verster, *"Velocity distribution and angular distribution of molecular beams from multichannel arrays"*, J. Appl. Phys. **46**, 2083–2091, 1975, DOI: 10.1063/1.321845.

[404] C. A. Stan and W. Ketterle, *"Multiple species atom source for laser-cooling experiments"*, Rev. Sci. Instrum. **76**, 063113, 2005, DOI: 10.1063/1.1935433.

[405] S. G. Porsev and A. Derevianko, *"High-accuracy relativistic many-body calculations of van der Waals coefficients* C_6 *for alkaline-earth-metal atoms"*, Phys. Rev. A **65**, 020701, 2002, DOI: 10.1103/PhysRevA.65.020701.

List of publications

E.1 Publications presented in this thesis

Steady-State Magneto-Optical Trap with 100-Fold Improved Phase-Space Density

Bennetts S, Chen CC, Pasquiou B, and Schreck F, Phys. Rev. Lett. **119**, 223202 (2017), DOI: https://doi.org/10.1103/PhysRevLett.119.223202

Chapter 5 of this thesis: Together with CC, BP and FS I designed and constructed the machine and made the red MOT work. I collected most of the data and analysed it. I was heavily involved in drafting and editing the paper.

Sisyphus Optical Lattice Decelerator

Chen CC, Bennetts S, González Escudero. R., Schreck F, and Pasquiou B, Phys. Rev. A **100**, 023401 (2019), DOI: https://doi.org/10.1103/PhysRevA.100.023401

Chapter 7 of this thesis: Together with CC, BP and FS I designed and constructed the machine and made it work. I worked with BP to do the first proof of principle tests and then with CC to implement the modifications to the machine needed to collect the SOLD data. I collected and analysed parts of the data and I was heavily involved in drafting and editing the paper.

Continuous guided strontium beam with high phase-space density

Chen CC, Bennetts S, González Escudero. R., Pasquiou B, and Schreck F, Phys. Rev. Applied (2019), Accepted August 28 (2019), https://arxiv.org/abs/1907.02793

Section 6.1 of this thesis: Together with CC, BP and FS I designed and constructed the machine and made it work. I collected most of the data for ^{84}Sr and ^{88}Sr and did a large part of the analysis. I proposed the motivation for the paper

.

E.1.1 Publications in preparation that were presented in this thesis

Steady-state strontium with unity phase-space density

Bennetts S, Chen CC, González Escudero. R., Pasquiou B, and Schreck F, (Order to be determined), (2019 - in preparation)

Section 6.2 of this thesis: Together with CC, BP and FS I designed and constructed the machine and made it work. I collected most of the data and did a large part of the analysis. We decided to shelve submitting this work for publication because it is too close to our final goal, a much bigger

and more important result, a steady-state BEC. The fear was that a premature publication might damage the impact from achieving the main goal of a steady-state BEC. This work will be submitted for publication before SB, CC or BP leave.

E.2 Other publications with major contributions

External cavity diode lasers with 5 kHz **linewidth and** 200 nm **tuning range at** 1.55 µm **and methods for linewidth measurement**

Bennetts S, McDonald GD, Hardman KS, Debs JE, Kuhn CCN, Close JD, and Robins NP, Optics Express, **22** (9), 10642 (2014), DOI: https://doi.org/10.1364/OE.22.010642

11W narrow linewidth laser source at 780nm for laser cooling and manipulation of Rubidium

Sane SS, Bennetts S, Debs JE, Kuhn CCN, McDonald GD, Altin PA, Close JD and Robins NP, Optics Express, **20** (8), 8915 (2012), DOI: https://doi.org/10.1364/OE.20.008915

High power operation of cladding pumped holmium-doped silica fibre lasers

Hemming A, Bennetts S, Simakov N, Davidson A, Haub J and Carter A, Optics Express, **21** (4), 4560 (2013), DOI: https://doi.org/10.1364/OE.21.004560

99W mid-IR operation of a ZGP OPO at 25% duty cycle

Hemming A, Richards J, Davidson A, Carmody N, Bennetts S, Simakov N, Haub J, Optics Express, **21** (8), 10062 (2013), DOI: https://doi.org/10.1364/OE.21.010062

Efficient, polarised, gain-switched operation of a Tm-doped fibre laser

Simakov N., Hemming A., Bennetts S., and Haub J. Optics Express, **19** (16), 14949 (2011), DOI: https://doi.org/10.1364/OE.19.014949

A high power hybrid mid-IR laser source

Hemming A., Richards J., Bennetts S., Davidson A., Carmody N., Davies P., Corena L., and Lancaster D., Optics Communications, **283** (20), 4041 (2010), DOI: https://doi.org/10.1016/j.optcom.2010.05.078

Gain-switched holmium-doped fibre laser

Wu K., Ottaway D., Munch J., Bennetts S., Lancaster D.G., Jackson S.D., Optics Express, **17** (23), 20872 (2009), DOI: https://doi.org/10.1364/OE.17.020872

E.2.1 Other publications with minor contributions

Frequency of the ultranarrow $^1S_0$-$^3P_2$ transition in ^{87}Sr

Onishchenko O, Pyatchenkov S, Urech A, Chen CC, Bennetts S, Siviloglou GA, and Schreck F, Phys. Rev. A **99**, 052503 (2019), https://doi.org/10.1103/PhysRevA.99.052503

80$\hbar$k Momentum Separation with Bloch Oscillations in an Optically Guided Atom Interferometer

McDonald GD, Kuhn CCN, Bennetts S, Debs JE, Hardman KS, Johnsson M, Close JD, and Robins NP, Phys. Rev. A **88**, 053620 (2013), DOI: https://doi.org/10.1103/PhysRevA.88.053620

A faster scaling in acceleration-sensitive atom interferometers

McDonald GD, Kuhn CCN, Bennetts S, Debs JE, Hardman KS, Close JD and Robins NP, EPL, **105**, 63001 (2014), DOI: https://doi.org/10.1209/0295-5075/105/63001

A Bright Solitonic Matter-Wave Interferometer

McDonald GD, Kuhn CCN, Hardman KS, Bennetts S, Everitt PJ, Altin PA, Debs JE, Close JD, and Robins NP, Phys. Rev. Lett. **113**, 013002 (2014), DOI: https://doi.org/10.1103/PhysRevLett.113.013002

A Bose-condensed, simultaneous dual species Mach-Zehnder atom interferometer

Kuhn CCN, McDonald GD, Hardman KS, Bennetts S, Everitt PJ, Altin PA, Debs JE, Close JD and Robins NP, New J. Phys. **16**, 073035 (2014), DOI: https://doi.org/10.1088/1367-2630/16/7/073035

The Role of Source Coherence for Atom Interferometry

Hardman KS, Kuhn CCN, McDonald GD, Debs JE, Bennetts S, Close JD and Robins NP, Phys Rev A **89**, 023626 (2014), DOI: https://doi.org/10.1103/PhysRevA.89.023626

Construction and Characterization of External Cavity Diode Lasers for Atomic Physics

Hardman KS, Bennetts S, Debs JE, Kuhn CCN, McDonald GD, and Robins NP, J. Vis. Exp. **86**, e51184 (2014), DOI: https://doi.org/10.3791/51184

Optically guided linear Mach Zehnder atom interferometer

McDonald GD, Keal H, Altin PA, Debs JE, Bennetts S, Kuhn CCN, Hardman KS, Johnsson MT, Close JD, and Robins NP, Phys. Rev. A **87**, 013632 (2013), DOI: https://doi.org/10.1103/PhysRevA.87.013632

Precision atomic gravimeter based on Bragg diffraction

Altin PA, Johnsson MT, Negnevitsky V, Dennis GR, Anderson RP, Debs JE, Szigeti SS, Hardman KS, Bennetts S, McDonald GD, Turner LD, Close JD, and Robins NP, New J. Phys. **15** 023009 (2013),

DOI: https://doi.org/10.1088/1367-2630/15/2/023009

High power, narrow bandwidth and broadly tunable Tm^{3+}, Ho^{3+}-co-doped aluminosilicate glass fibre laser

Hemming A, Jackson SD, Sabella A, Bennetts S, and Lancaster DG, Electronics Letters, **46** (24), 1617 (2010), DOI: https://doi.org/10.1049/el.2010.2809

Highly narrow linewidth, CW, all-fiber oscillator with a switchable linear polarization

Jovanovic, N., Marshall, G.D., Fuerbach, A., Town, G.E., Bennetts, S., Lancaster, D.G., Withford, M.J., IEEE Photonics Technology Letters, **20** (10), 809 (2008), DOI: https://doi.org/10.1109/LPT.2008.921111

High-power 83 W holmium-doped silica fiber laser operating with high beam quality

Jackson, S.D., Sabella, A., Hemming, A., Bennetts, S., Lancaster, D.G., Optics Letters, **32** (3), 241 (2007), DOI: https://doi.org/10.1364/OL.32.000241

Acknowledgements

Encouraged by my parents, my passion for making toys began at an early age. First, it was tree houses, gardens, fish ponds and carts but with inspiration from *Star Trek*, *Stargate*, *Firefly*, *Babylon 5*, *Battlestar Galactica* and more recently *The Expanse* I gravitated towards wanting to make totally new toys, toys from the realm of science fiction.

In high school I had some great teachers, but my physics teacher Terry Werner and my chemistry teacher Ed Gilmore had a particularly strong influence. Terry Werner had a somewhat unconventional teaching style. Occasionally he would lecture but most of the time he reigned over a classroom filled with anarchy. He taught that physics was not some abstract theory but the simplest description of reality that made sense and encouraged us to measure and test all these "theories" experimentally. He asked us to measure gravity, crash carts and show momentum conservation and make clocks. We measured diffraction patterns and mapped magnetic and electric fields (and made giant sparks). More than anyone else Terry Werner sparked my passion for experimental physics. This continued with my time with the IPhO (Rodney Jory) where I finally became hooked on physics rather than engineering.

The Australian National University was a unique playground for an undergraduate. ANU was initially set up as a research only national institution based on the Princeton IAS but after some time it grew a small undergraduate teaching school to provide student labour. The result was that as undergrads we got to play with all the old equipment from the research labs curated by Andrew Papworth and taught by passionate experts across the full range of disciplines like Hans Bachor, Craig Savage, David McClelland, John Close and Paul Davies. We had accelerators, nuclear physics, shock tubes for hypersonic flows, plasma physics experiments and a wealth of optics and spectroscopy labs and on top of that our teachers created summer projects and 6 month lab projects in their research labs so that we could really get involved in their research work. Because it was real (and old) equipment it often didn't work the way it was supposed to so there was lots of fun disassembling the monochromator or spectrum analyser to figure out how to fix it. This is something you would never get with a canned push button demonstration which sadly is often considered "lab work" in other places. With Hans Bachor and my then lab partner Nick Robins I did projects on making bright squeezed light, frequency comb generation and making and

characterizing lasers. Nick went off and tried to make a continuous atom laser where as I did more optics and lasers. I spent a short time at Laser Zentrum Hannover where I worked with some of the first stretch pulsed modelocked fiber lasers for frequency combs and then I switched direction and joined an applied lab, maybe not the best choice with hindsight.

The DSTO was an applied government lab where I learned a lot of engineering and about how government and industry work. I am particularly grateful to Olivia Samardzic and Nikita Simakov who helped keep me sane but there were also many fantastic technicians, engineers and physicists who taught me so many of the skills I have come to rely on. I would like to thank Don Koks, Jae Daniel, Alan Davidson, Phil Davies, Alex Hemming, David Lancaster, Patrick Klovekorn, Victor Florea, Victor Karaganov, Jesper Munch, Jim Richards, Mark Hughes, Neil Carmody, Alex Sabella, Simon Rees, Michael Gillyon, Ka Wu and Valerian Kuznetsov for many happy experiences while I was there. Eventually though, I grew disillusioned with government and again I sought meaning by returning to academia.

Back at ANU I hoped to recreate the golden days of my undergrad working with my old lab partner, Nick Robins on the still unsolved problem of making a continuous atom laser (using rubidium). The funding stars did not align and after two years I realised that I needed a new plan. At the time an exciting new paper from Florian Schreck's group in Innsbruck had just been published using strontium, *Laser cooling to degeneracy*. This looked like the key to making a continuous atom laser, in fact, it almost seemed like an 18 month project. Excited, I moved to join Florian's group just as he was moving from Innsbruck to Amsterdam and here I started designing the atom laser machine (hoping funding to build it would soon materialize).

The last five and a half years in Amsterdam have been a wild, intense, roller coaster ride filled with amazing experiences. It felt like every day we pushed up against our physical and mental limits and then extended them a little further. I look back with immense satisfaction at how far we have come and what we as a team managed to do. But, it was not the physics or the engineering that I treasure most, it was the experiences and the joy of spending this time with such an exceptional group of people and the exhilaration of trying to make the impossible, possible.

Without ChunChia Chen, Benjamin Pasquiou and Florian Schreck, the atom laser project could never have achieved what it did.

ChunChia is not only an outstanding physicist and engineer, he is the most generous, gentle, humble and yet capable workaholic I have ever met and I was lucky enough to have him as my lab partner(!!). I can't think how I would have survived this time without ChunChia and I don't know how the machine could have been built without his dedication and relentless drive. Together, we were at our most creative bouncing ideas

off the whiteboard or implementing some new scheme at 2am in a junk food fuelled push to break a problem. ChunChia is also a library, he knows every experiment and group in the community, he reads veraciously and he has contacts and friends all across the world streaming the latest gossip. Every week he taught me about new ideas and experiments he found not just in physics, but broadly. We did the Y-Combinator marathon, the Musk videos, SpaceX launches and presentations, numerous courses on deep learning and robotics as well as short trips into biophysics, particle physics and an innumerable number of other directions. He was invariably playing the latest videos from a new workshop, course, conference or lindau meeting while we built or ran the machine. It has been an incredible team and I have come to rely in so many ways on ChunChia.

For me, Benjamin was "the rock" of stability. Every time I freaked out thinking it wasn't going to work it was Benjamin who calmly steadied the ship. The eternal optimist. He was there when the first vacuum parts were laid, when the vacuum broke, at 6am when we tried making the first MOTs and when the oven was aligned and loaded during an all night effort before he needed to jump on a plane to China. Benjamin was the one who took us to the bar when all hope seemed lost and who organized parties and "bad movie" festivals to lighten the load. Benjamin is a teacher, he insists on taking whatever time is needed to do something right, he insists on standards and he will make a fantastic professor. Whenever I am uncertain of something or have a silly idea in my head, Benjamin is my sounding board and the filter whose judgement I rely on. After 8 years Benjamin keeps the strontium group running. He is the reservoir of group knowledge, he teaches new students, he keeps the infrastructure running and fixes whatever fails. When things go wrong Benjamin takes on the unenviable task of putting them right and ensuring they don't go wrong again.

Florian is unusual for a professor in my experience. Firstly, he is exceptionally approachable, he keeps his office in the lab so that he can always help and stay involved in the experiments and yet he also gives complete freedom offering suggestions and advice and hoping they will be embraced rather than seeking to direct the research projects. In this way he trains independent researchers and gives them the space to grow (and to make mistakes). Another thing that is special about Florian is his dedication. Most nights and weekends you see him here until late correcting a student's report or writing grant proposals to keep these expensive machines going or trying to help someone with one of their problems. Before he leaves, he will take the time to wander around and discuss with everyone else their problems and offer advice. It always seems such a shame to have someone of Florian's talents spending so much precious time chasing funding, networking and dealing with the bureaucracy just to give us the space to focus on science. I wish I could wave a wand and make all that go away so that we might better utilize his skill and insight. I hope that I can in some way repay him for all the help he has given me and the faith he has placed in

me. Florian made this project happen. He got the funding that made this machine possible risking much to tackle a big unknown goal even though it was neither fashionable nor easy. Finally, Florian's gentleness and generosity is legendary. I admire his temperance, his calmness and his ability to always see the good in people.

Two years ago, Rodrigo González Escudero joined us and brought so much new life to our experiment. From passionate dinner conversations to dragging me to the bar (still sitting on my chair) Rodrigo has made me smile. Rodrigo even started confiscating my junk food insisting that I stick around a few more years. Rodrigo is always ready to help, he offers advice and gives whatever he can. I am so very glad we have Rodrigo.

Sergei Piatchenkov had a more challenging time than most. I admire his tenacity in remaining positive and finding a uniquely Russian perspective on life with quotes like *"There is no happiness, only units of standard suffering"*. I was lucky to spend many weekends with Sergei and ChunChia on long bike rides through Holland and we spent Christmas and New Year's Eve dinners together as well as innumerable passionate discussions over dinner and late at night. Sergei's dedication could always be counted on from early morning to midnight any day of the week. I also enjoyed many stimulating conversations with Georgios Siviloglou from the microscope project and Vincent Barbé from the RbSr project.

Francesca Famà and Sheng Zhou joined us for the new iqClock project only a few months ago yet already I would be lost without them. Their contagious positivity, their resourcefulness, initiative and humility again make me feel so incredibly lucky to be working with such fantastic people. I am looking forward to this exciting adventure building a new machine together.

There are many other strontium BEC group members whom I have enjoyed working with and who have brought so much joy to my time here. I would like to thank our master's students Jens Samland, Zhou Geng, Tim van Leent, Namrata Dutta-Mazumdar and Wouter Meinster. On the other experiments I enjoyed working with Alex Urech from the microscope and Lucas Reichsöllner, Severin Charpignon, Prem Thekkeppat, Alessio Ciamei and Alex Bayerle from the RbSr experiment. Denis Kurlov and Jiri Minar have provided many interesting theoretical insights.

Arthur La Rooij from the magnetic chips/Rydberg group was the beating heart of the original Amsterdam group when I arrived. He made me feel welcome and like I belonged here from the very first day I met him. Arthur showed us the Amsterdam I have grown to love from bokbier festivals in Haarlem to birthday parties and first Thursday of the month beers. He also translated my thesis summary to Dutch for which I owe him! Maarten Soudijn held the desk next to mine and I enjoyed many a long conversation on physics and life. Like Arthur, Maarten made me feel welcome and I will be forever grateful for making the move to Amsterdam so easy. Graham Lochead, David Davtyan, Carla Sanna,

Julian Naber, Shimon Machluf, Sophie Botsi, Nus Nusselder, Daniel Nicolai, Julius de Hund and Nataly Cisternas San Martin from the atom chips group were great office mates and colleagues. More recently I have also had the pleasure of learning a little about ions from Matteo Mazzanti and Henrik Hirzler in Rene Gerritsma's group. I would also like to thank the other PIs Robert Spreeuw, Klaasjan van Druten, Ben van Linden van den Heuvell and Rene Gerritsma for their insightful and supportive suggestions and comments during journal clubs and more generally as well as for numerous stimulating lunchtime conversations. I would particularly like to thank Robert for pointing out several errors in this thesis as well as helpful advice. Daniel Bonn, Mark Golden and Rudolf Sprik also provided great advice and words of encouragement over the years.

A machine like the atom laser would be impossible to make without skilled craftsmen. The workshop here in Amsterdam is something special and unlike anything I have seen before. Two people in particular were crucial to the construction of the atom laser machine; Jan Kalwij and Ron Manuputy. I have worked with many workshops in the past and the skills, professionalism, efficiency and quality I have seen here is exceptional. In five and a half years I don't think Jan has ever made a mistake, in fact he sees through the errors in my drawings and makes what I need. Jan and Ron, I am in your debt. In the subsequent time there have been many additions and modifications to the machine to try this idea or that and over the time I also had the pleasure of working with Sven Koot, Tristan van Klingeren, Johan Mozes, Fred van Anrooij, Tjerk van Goudoever, Alix Wattjes, Gertjan Bon, Tijs van Roon, Daan Giesen, Hans Ellermeijer, Harry Beukers and as well as having many interesting and enjoyable discussions with Gerrit Hardeman, Joost Overtoom and Theo van Lieshout. Since the new iqclock project started and we are building again I have had a whole new mountain of work to do for which again I am firmly in debt to Jan, Sven, Tristan, Johan, Tjerk, Clint Ederveen Janssen and Alix as well as Daan, Gertjan, Tijs, Tjeerd Weijers, Mattijs Bakker, Hans and Udo van Hes.

Joost van Mameren, Natalie Wells, Anne-Marieke Commentuijn and Rita Vinig made my transfer here as painless as possible and took care of (and continue to take care of) all the bureaucratic headaches. Boudewijn, Natalie, Mohamed, Mike, Peter and many others from inkoop have done a fantastic job over the years processing and receiving many hundreds of orders and making them turn out right. My good friends at the security desk always had a friendly face as we arrived or left at 4am or huddled during a 3am fire alarm and our institute secretaries always quickly sorted out the little problems that continually turned up.

Lastly I want to thank my parents Heather and Peter, my sister Rebecca and her family Mike, Matthew and Andrew for their patience and understanding with a absentee son, brother and uncle.

Finally, I would like to thank the Dutch people for the joy of sharing the past five years with this wonderful country in the amazing city of Amsterdam. Amsterdam is a special place, I have never felt so safe, so welcomed and the warmth of so many happy, generous people. Risky, expensive research like ours would not be possible without the generous support we have received from the Dutch and European people. I hope that I can find ways to repay this debt.

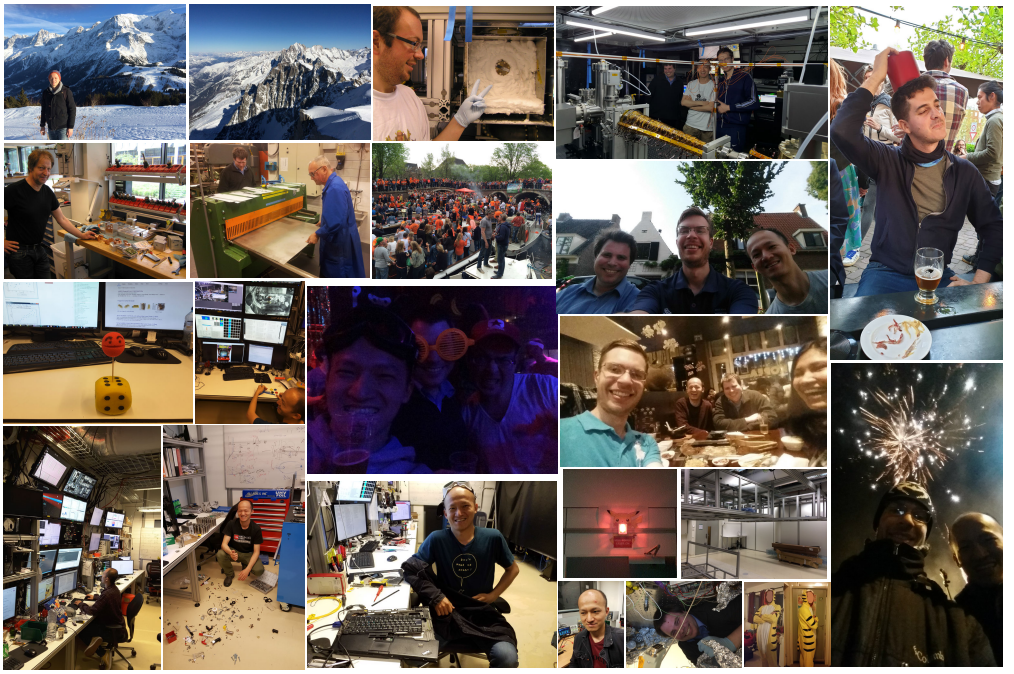

FIGURE E.1: **Thank You.**